

Durability and Service Life Modelling of Alkali-Activated Concrete

Tamara Janey Chidiac

Supervisors:

Prof. John L. Provis

Dr. Brant Walkley

Industry Mentors:

Prof. Bjorn Van Belleghem

Dr. Tim Soetens

A thesis submitted in fulfilment of the requirements for the degree of
Doctor of Philosophy



Department of Materials Science and Engineering

The University of Sheffield

2023

Abstract

The serviceability limit state of a concrete structure exposed to a corrosive environment has often been calculated by service life models solely based on Fick's second law for chloride diffusion. The main limitation of this type of model is that it does not account for various modes of transport and reactions that occur when the concrete is exposed to unsaturated conditions; moisture transport, chloride ingress and carbonation reactions can occur at the same time and influence the durability of the structure. The primary objective of this research is on the construction and implementation of a modelling framework which includes the durability characteristics that define the resistance of concrete to chloride ingress and carbonation reaction in an environment with a variable relative humidity condition. The model is implemented for alkali-activated materials, which are an alternative type of energy-saving construction material, to calculate the service life until the point of corrosion initiation across the reinforcement embedded in the concrete.

The durability response of alkali-activated materials (AAMs) has been investigated via an extensive literature review, in the case when the construction material has been tested in a single type of deterioration condition that is either submerged in aqueous chloride solutions or exposed to natural and/or accelerated carbonation conditions, as well as in real service condition where the concrete is simultaneously exposed to these deterioration conditions. The main conclusion that can be drawn is that alkali-activated materials have similar performance properties to Portland cement (PC) in corrosive conditions, but the service life has not been previously estimated quantitatively by including the impact of carbonation on the permeability of corrosive species towards the steel reinforcement.

A well-established service life model known in the literature as *fib* Bulletin 34 service life design code, is adapted to predict the time taken for reinforcement corrosion to initiate in alkali-activated concretes. The model approach is based on the calculation of the time needed for a certain critical concentration of chloride ions, migrating from the external environment, to reach the steel reinforcement and initiate the corrosion reaction. The service life of alkali-activated concretes is predicted probabilistically by taking into account the distribution of the available durability data. The findings indicate that alkali activated concretes with high calcium content can exhibit promising characteristics as a construction material applied for structural application in chloride-rich corrosive environments. However, the sensitivity analysis

conducted in this research reveals a wide range of values in service life predictions for a single type of alkali-activate concrete.

The moisture transport in alkali-activated materials is investigated in this research because the moisture state in these porous materials is an essential durability factor that should be accurately predicted in order to model the simultaneous ingress of chlorides and CO₂ in marine conditions. Three moisture transport models, namely the single, dual, and mechanistic permeability models, are implemented to assess the moisture transport in AAMs during wetting and drying cycles. This enables to study the significance in each model, accounting for the complex porous microstructure of the material, on predicting the degree of saturation as a function of the external relative humidity. In comparison with data for PC, it can be concluded that the dual permeability model is a suitable model to simulate and predict the degree of saturation in the pores of Alkali-activated cements. This is due to its better description of the transport of moisture in large and small pore regions of a cement along with the interconnectivity between the two pore regions.

Finally, a numerical model has been developed and validated for service life prediction of alkali-activated concrete in marine conditions by including transport and reactions that occur when the concrete is exposed in unsaturated conditions; moisture transport, chloride ingress and carbonation reactions. The model is set to probabilistically predict the service life of alkali-activated concrete by taking into account the distribution of critical chloride concentrations. Sensitivity analysis is conducted to systematically vary the durability properties in the model to provide a range of possible values for service life. It can be concluded that moisture transport can have an equal impact as carbonation on the distribution of service life when alkali-activated concrete is exposed to a wetting cycle. Furthermore, the developed service life model can be used as an efficient decision-making tool in material design of concrete for suitable structural applications with low environmental impact.

Table of Contents

Abstract	2
List of Abbreviations	8
List of Symbols	9
List of Chemical Compounds and Elements	13
Acknowledgement	14
List of Figures	16
List of Tables	32
Chapter 1: Introduction	36
1.1 Background	36
1.2 Objective and Scope of Research	39
1.3 Thesis Outline	39
Chapter 2: Literature review	42
2.1 Alkali-Activated Materials- Historical Background	42
2.2 Chemistry of Alkaline Activating Solutions	44
2.3 Aluminosilicate Raw Materials	46
2.3.1 High-Calcium Alkali-Activated Binders.....	46
2.3.2 Low Calcium Alkali-Activated Systems.....	48
2.4 Role of Concrete Against Corrosion of Steel Reinforcement	49
2.5 Mechanisms of Steel Corrosion in Reinforced Concrete	50
2.6 Critical Chloride Threshold	53
2.7 Test Methods Used for the Detection of Steel Corrosion in Reinforced Concrete	54
2.8 Mechanism of Steel Corrosion in AAMs	56
2.8.1 Corrosion of Steel in SG-Based AAMs	56
2.8.2 Corrosion of Steel in Low Calcium Based AAMs.....	57
2.8.3 Critical Chloride Thresholds in AAMs	58
2.9 Moisture Transport in Cement Based Materials	60
2.10 Fundamental Relations	63
2.10.1 Degree of Saturation	63
2.10.2 Models for Isotherms	64
2.10.3 Moisture Transport Models.....	66
2.11 Chloride Ingress	78
2.11.1 The Resistance of PC Against Chloride Ingress	78

2.11.2	The Resistance of AAMs Against Chloride Ingress	79
2.11.3	Chloride Ingress in High Calcium Based AAMs	79
2.11.4	Chloride Ingress in Low Calcium AAMs	81
2.11.5	Variability of Chloride Binding in AAMs with Mixed Low and High Calcium Precursors.....	82
2.11.6	Test Methods for Chloride Transport Properties	84
2.12	Carbonation.....	84
2.12.1	Portland Cement Carbonation	85
2.12.2	Alkali-Activated Cement Carbonation.....	88
2.12.3	Comparison of Carbonation Effect on Pore Solution Alkalinity Between Low and High Ca-AAMs.....	94
2.12.4	Ingress of CO ₂ in Alkali-Activated Concretes	95
2.12.5	Effects of Carbonation on Microstructure of Portland Cements and Alkali-Activated Cements	97
2.13	Chloride and Carbonation Resistance of AAMs.....	100
2.13.1	The Impact of Carbonation on Chloride Ingress in PC and AAM Based Materials ...	100
2.14	Service Life	103
2.14.1	Analytical Models	103
2.14.2	<i>fib</i> Bulletin 34 code.....	104
2.15	Conclusion	107
Chapter 3:	Materials and Methods.....	109
3.1	Raw Materials and Mix Proportions.....	109
3.1.1	Precursors.....	109
3.2	Preparation of Alkali-activated Cements and Mortars.....	110
3.2.1	Alkaline Activating Solution	110
3.2.2	Alkali Activated Cements	110
3.2.3	Alkali Activated Mortars	110
3.3	Test Methods	111
3.3.1	Dynamic Vapor Sorption	111
3.3.2	Thermogravimetry Analysis	113
3.3.3	Mercury Intrusion Porosimetry	113
3.3.4	Embedded Electrode Methods - Bulk Resistivity	114
3.3.5	Particle Size Analysis.....	115
3.4	Software	115
3.4.1	Cement Pore Solution Ions	115
3.4.2	Coupled System of Partial Differential Equations.....	117
3.5	Conclusion	122

Chapter 4: Probabilistic Service Life Prediction of Alkali Activated Concretes Exposed to Chloride Induced Corrosion	123
4.1 Introduction.....	124
4.2 Durability and Service Life.....	125
4.2.1 Chloride Threshold	125
4.2.2 Chloride Ingress	126
4.2.3 Aging of Concretes	128
4.3 Materials and Methods.....	129
4.3.1 Mix designs selected for detailed analysis.....	129
4.3.2 Calculation of Chloride Threshold.....	131
4.3.3 Calculation of Pore Solution Alkalinity.....	132
4.3.4 Aging factor	132
4.3.5 Service Life Prediction Model	132
4.4 Results and Discussion.....	134
4.4.1 Chloride threshold.....	134
4.4.2 Service Life Predictions	138
4.4.3 Sensitivity Analysis.....	146
4.5 Conclusions.....	150
Chapter 5: Moisture Permeability in Alkali-Activated Materials	152
Abstract.....	152
5.1 Introduction.....	152
5.2 Methodology	163
5.2.1 Mix Design of Alkali-Activated Cements.....	163
5.2.2 Characterizations.....	164
5.2.3 Moisture Permeability Transport Parameters.....	165
5.2.4 Prediction of WVSIs	166
5.2.5 Moisture Permeability Models.....	166
5.3 Statistical Criterion for Curve Fitting	171
5.4 Comparison of Saturation Profile Data between PC and AAMs.....	172
5.5 Results and Discussion.....	173
5.5.1 Characterization	173
5.5.2 Prediction of WVSIs	178
5.5.3 Cyclic Water Vapour Sorption Isotherms	181
5.5.4 Moisture Transport in Alkali-Activated Cements.....	188
5.5.5 Simulation of Moisture Transport in Alkali-activated Cements	191
5.5.6 Upscaling of Moisture Transport Properties from Cement to Mortar and Concrete...	214

5.6	Conclusions	228
Chapter 6:	Coupling Chloride Ingress and Carbonation for Service Life Prediction of Alkali-Activated Concrete	231
6.1	Introduction and aim	232
6.2	Materials and Methodology	233
6.2.1	Raw Materials and Mix Designs:.....	233
6.2.2	Test Methods.....	233
6.2.3	Estimation of Chloride Profile of Alkali-Activated Concrete in Real Service Conditions	233
6.3	Fundamental Relations	234
6.3.1	Coupled Reactive Mass Transport Model.....	234
6.3.2	Aging Factor of Concrete.....	237
6.3.3	Moisture Permeability Models.....	241
6.3.4	Transport of Ions and Carbonation Reaction	243
6.3.5	Transport of Heat in Concrete.....	252
6.4	Spatial Discretization, Boundary and Initial Conditions	253
6.4.1	Spatial Discretization	253
6.4.2	Boundary and Initial Conditions	254
6.5	Critical Chloride Threshold	255
6.6	Modelling Summary	256
6.7	Results and Discussion	259
6.7.1	Aging Factor of Alkali-Activated Concrete.....	259
6.7.2	Calcium Carbonate Precipitation Rates	270
6.7.3	Estimation of Total Chloride Profile of a Structure in Real Service Conditions	270
6.7.4	Extent of Aging Factor.....	271
6.8	Service Life Prediction of Alkali-Activated Concretes	274
6.8.1	Summary of Inputs for Numerical Model.....	274
6.8.2	Computational Study.....	278
6.8.3	Probabilistic service life prediction.....	291
6.9	Conclusion	302
Chapter 7:	Conclusion and Future Research	304
Appendix	308
References	321

List of Abbreviations

AAMs	Alkali-activated materials
PC	Portland cement
SCMs	supplementary cementitious materials
SG	Ground Granulated Blast Furnace Slag
FA	Fly ash
AAS	Alkali-activated blast furnace slag
AAF	Alkali-activated fly ash
RCS	Reinforced Concrete Structures
AAC	Alkali-Activated Concrete
CT	Chloride Threshold
C_{crit}	Critical Chloride Content
RH	Relative Humidity
SEM	Scanning Electron Microscope
WVSI	Water vapor sorption isotherms
FF	Feng and Fredlund's model
VG	Van Genuchten model
FX	Fredlund and Xing's Model
KM	Kosugi model
Multi	Multimodal Model
MK	metakaolin
RC	Reinforced Concrete
d_{avg}	average particle size
DVS	Dynamic vapour sorption
TGA	Thermogravimetric analysis
LCR	Inductance (L), Capacitance (C) and resistance (R) meter
CT_{Concrete}	chloride ion concentrations by wt.% of concrete
CT_{Cement}	chloride ion concentrations by wt.% of binder
NME	normalized mean error

List of Symbols

t	tons
S	Degree of Saturation
V_l	Water volume fraction
V_p	Void volume
Φ	Effective porosity
Φ_l	liquid phase of the pore
Φ_g	gaseous phase of the pore
P_c	capillary pressure, Pa
θ	evaporable water content at certain relative humidity
θ_r	water content at dry reference state
θ^{max}	water content at saturated state
ρ_l	liquid water density, kg.m ⁻³
R	Universal gas constant, Pa.m ³ .K ⁻¹ .mol ⁻¹
T	absolute temperature, K
M_v	molar mass of the water molecule, kg.mol ⁻¹
φ	relative humidity
J_l	liquid flux, kg.m ⁻² . s ⁻¹
ρ_l	density of the liquid water, kg.m ⁻³
k	liquid permeability, m ²
η	dynamic viscosity of liquid water, Pa.s
P_l	liquid pressure, Pa
k_{rl}	relative permeability
D_a	apparent moisture diffusion coefficient, m ² . s ⁻¹
D_l	liquid water diffusivity, m ² . s ⁻¹
D_v	water vapour diffusivity, m ² . s ⁻¹
P_{vs}	saturated vapor pressure at 20°C, Pa
a	air entry flow pressure, Pa
m and n	shape factors for the sorption isotherm
D_{v0}	free vapor diffusion coefficient in the air, m ² . s ⁻¹
f	resistance factor of the pore network for gaseous diffusion

x_D	material parameter
ϕ_l	porosity in the large pore region
ϕ_s	porosity in the small pore region
Γ_ω	Mass exchange between two porosity regions
β_w	first order rate coefficient
ξ	moisture transfer factor ($\text{kg} \cdot \text{s}^{-1} \cdot \text{m}^{-3}$)
w_f	Volumetric fraction of the large pore region
$w_{f,D}$	Contribution factor of large pore region to moisture transport
$f_V(\theta)$	scaling function for vapour diffusion
μ_{dry}	vapour diffusion resistance factor
n_{sp}	a shape parameter that accounts for the serial-parallel connectivity of the pores in the cement.
n_{cap}	a scaling parameter used to adjust the liquid permeability factor
K_{eff}	effective liquid permeability
$f_l(S)$	scaling function for liquid flow
$K_{l,rel}(S)$	relative conductivity function
pC_i	the inflexion points within the moisture storage curve
s_i	slope at the inflexion points
$\Delta\theta_i$	represents the difference between the plateau levels in the moisture storage curve
C_{tb}	total bound chloride concentration, $\frac{\text{mg of Cl}}{\text{g of binder}}$
C_f	Free chloride concentration, $\text{mol} \cdot \text{L}^{-1}$
α and β	binding constants
C_{crit}	critical chloride threshold (% by mass of binder)
C_0	initial chloride content (% by mass of binder)
$C_{s,\Delta x}$	Surface chloride content (% by mass of binder)
d	concrete cover (mm)
Δx	depth of the concrete convection zone (mm).
D_{nssm}	non-steady state chloride migration coefficient (mm^2/year)
D_{app}	Apparent coefficient of chloride diffusion (mm^2/year)
b_e	regression variable (K)
T_{ref}	standard test temperature (K)

T_{real}	temperature of the structural element or the ambient air (K)
k	transfer parameter
t_0	reference point of time, 0.0767 years
n	aging factor
t	time increment from last equilibrium stage, s
M_0	mass value at end of previous equilibrium stage, g
M_e	mass value at equilibrium at the current stage, g
M_t	mass value at time t, g
l	thickness of the powder sample, m
D	diffusion coefficient of moisture in the current stage, m^2/s
r	meniscus curvature radius (pore entry radius), m
γ	surface tension of mercury, N/m
θ	contact angle of mercury/cement interface, °
pK_w	the ionic product of water
$D_{\text{H}_{\text{cp}}}$	Moisture diffusivity in cement phase, m^2/s
g_i	Volume fraction of aggregates
$S_{\text{meas.}}$	measured degree of saturation
S_{ref}	reference degree of saturation at 50% RH.
D_i	diffusion of ionic species in water, m^2/s
F	formation factor
ρ_c	resistivity of concrete, $\Omega.\text{cm}$
ρ_s	resistivity of pore solution, $\Omega.\text{cm}$
λ_i^0	equivalent conductivity of the ionic species, in the pore solution, at infinite dilution, $\text{cm}^2.\text{S}.\text{mol}^{-1}$
G_i	empirical coefficient for each ionic species at a given temperature, $(\text{mol}.\text{L}^{-1})^{-0.5}$
I	molar ionic strength, $\text{mol}.\text{L}^{-1}$
σ_y	conductivity recorded at temperature T_y , $(\Omega.\text{cm})^{-1}$
σ_x	conductivity at reference temperature T_x , $(\Omega.\text{cm})^{-1}$
D_0	initial effective chloride diffusion coefficient obtained on the 28 th day, m^2/year
m	aging factor
E_a	activation energy, $\text{kJ}.\text{mol}^{-1}$

$T_{0,e}$	initial and final temperature, K
v	liquid flow velocity, $m \cdot year^{-1}$
C_{Cl}	free chloride concentration, $mol \cdot L^{-1}$
D_{Cl}	effective chloride diffusion coefficient, $m^2 \cdot year^{-1}$
$\frac{\partial C_{cl,B}}{\partial t}$	rate of chloride to be adsorbed or bound to the cement hydrates, $mol \cdot L^{-1} \cdot year^{-1}$
ρ_b	binder density, kg of cement per L of cement
M_{Cl}	Molar mass of chloride, g/mol
f_b	volumetric fraction of the binder in concrete
$\frac{\partial C_{cl,B}}{\partial C_{Cl}}$	Langmuir binding isotherm for alkali-activated cements, $((mg \text{ Cl. L}) / (g \text{ binder. mol Cl}))$
$D_{CO_2}^0$	CO ₂ diffusion coefficient in air, m^2/s
$r_{CO_2(aq)}$	rate of CO ₂ dissolution into pore solution, $mol \cdot L^{-1} \cdot year^{-1}$
k_t	interfacial gas-liquid mass transfer coefficient for CO ₂ , $year^{-1}$
k_{henry}	Henry's Law constant for equilibrium partitioning of CO ₂ gas to water
$D_{CO_3^{2-}}$	effective diffusivity of carbonate ions, $m^2 \cdot year^{-1}$
$r_{CO_3^{2-}}$	rate of production of carbonate from dissolved CO _{2(aq)}} , $mol \cdot L^{-1} \cdot year^{-1}$
r_C	rate of consumption of carbonate ions to form carbonate phases, $mol \cdot L^{-1} \cdot year^{-1}$
k_c	rate constant for calcium carbonate formation, $mol \cdot year^{-1}$
$K_{sp,CaCO_3}$	solubility product constant, $mol^2 L^{-2}$
φ_u	updated porosity of the concrete
φ_0	initial porosity of the concrete
V_j	molar volume of the solid phase j, m^3/mol
Δn	change in the molar amount of the solid phase, mol
V_{CASH}	molar volume of the C-A-S-H phase, m^3/mol
V_{CaCO_3}	molar volume of the CaCO ₃ phase, m^3/mol
k	thermal conductivity of concrete, $W \cdot m^{-1} \cdot K^{-1}$
C_p	Heat capacity of concrete, $J \cdot Kg^{-1} \cdot K^{-1}$
c_{aq}	concentration of CO ₂ in the aqueous phase, $mol \cdot L^{-1}$
c_{gas}	concentration of CO ₂ in the gaseous phase, $mol \cdot L^{-1}$

List of Chemical Compounds and Elements

CaCO₃	limestone
Ca	Calcium
SiO₂	Silicon Dioxide
CaO	Calcium oxide
Al	Aluminum
C-A-S-H	Calcium AluminoSilicate Hydrate
N-A-S-H	Alkaline AluminoSilicate Hydrate
C-S-H	Calcium Silicate Hydrate
Afm	aluminate ferrite mono-sulfate
C	CaO
A	Al ₂ O ₃
\$	SO ₃
H	H ₂ O
S	SiO ₂
F	Fe ₂ O ₃
H	H ₂ O
N	Na ₂ O
K	K ₂ O
c̄	CO ₂
C₃A·CaCl₂·nH	Friedel's salt
HCO₃⁻	bicarbonate
CO₃²⁻	carbonate
CH	portlandite
CaCO₃	calcium carbonate
Cc̄	Calcium carbonate
Na₂CO₃·10H₂O	Natron
NaHCO₃	nahcolite

Acknowledgement

This PhD is the result of guidance and support from many people, and including the funding agency, I have received during my time as a member of DuRSAAM and Cements@Sheffield group. So, I would like to express my sincere gratitude in no particular order:

Thanks to Prof. John Provis and Dr. Brant Walkley for offering me the golden opportunity to pursue a PhD at the University of Sheffield and working with you at the Cements@Sheffield group. I also thank you for recruiting me as an early stage researcher at the PhD Training Network on Durable, Reliable and Sustainable Structures with Alkali-Activated Materials (DuRSAAM) where this project has received funding from the European Union's Horizon 2020 research and innovation programme under Grant Agreement #813596.

Thanks to Dr. Neven Ukrainczyk and Dr. Dale Prentice, the unofficial second supervisors, for your time and support, beyond the call of duty, to guide me through this project and make it more fun and interesting. The patience and effort you put in to assist me is priceless and your discussions along with feedback on mathematical and thermodynamic modelling is absolutely invaluable.

Thanks to Dr. Tim Soetens and Prof. Bjorn Van Belleghem, the industry mentors from SANACON, for your help in obtaining experimental data at Magnel-Vandepitte Laboratory, Department of Structural Engineering and Building Materials, Ghent University, Belgium. Also, thank you for your teachings on applying scientific knowledge to practice in real life technical problems. Your discussions and guidance have shaped my project.

On a little more serious note, I want to thank two very special people, of whom without this project would not have succeeded. The first is my primary supervisor and mentor Prof. John Provis. I am sincerely grateful to Prof. John Provis for his teachings and supervision during our countless meetings. His guidance and support helped to put my ideas into practice and then in paper. His mentorship for over three years and a half has inspired me to become an enthusiastic researcher with endless curiosity to apply known knowledge to uncover new knowledge. The second person is my mother Jacqueline Anne Chidiac. Her encouragement helped me remain motivated to work on the project during the lockdown followed by COVID-19 despite the isolation I have gone through during that period. Her inspiration, as a woman of

science, has taught me to always remain focus and to chase my dreams no matter what hardships may come in my way.

Last but definitely not least, I have to thank God. God helped me cross paths with all these wonderful people and God gave me an amazing family to cherish forever.

After this list of thanks, I hope I have not forgotten anyone; if so, I ask for forgiveness. I would like to end with an inspirational quote from the Lebanese writer Gibran Khalil Gibran:

“Knowledge and understanding are life’s faithful companions who will never prove untrue to you. For knowledge is your crown, and understanding your staff; and when they are with you, you can possess no greater treasures.”

"المعرفة والفهم رفيقان مخلصان للحياة ولن يثبت لك أبدًا أنهما غير صحيحين. لان العلم تاجك وفهم صولجانك. وعندما يكونون معك ، لا يمكنك امتلاك المزيد من الكنوز ."

List of Figures

Figure 1.1 Thesis outline summarizing the key work related to Chapters 4,5 and 6 and their interrelations to achieve the research objective stated in Chapter 1. The durability data and models obtained from literature review and experimental measurements, discussed in Chapters 2 and 3, form the basis of Chapters 4, 5 and 6 followed by future work suggested in Chapter 7.	41
Figure 2.1 Classification of AAMs and its subset Geopolymers, with comparison to PC and calcium sulfoaluminate binder chemistry. The shading specifies approximate alkali content; darker shading links to higher concentration of sodium and/or potassium [2]...	43
Figure 2.2 Schematic representation of Al sites within C-A-S-H type gels cross-linking q^3 Al tetrahedral (green triangle), bridging q^2 (B) Al tetrahedra (blue triangle), pairing q^2 (P) Al tetrahedra (brown triangle), and charge-balancing Al^V (orange square). Si tetrahedra are shown by the grey triangles, and charge-balancing alkali cations and protons have been omitted by the authors for clarity in [31].....	47
Figure 2.3 3D representation of a polymerized section of the N-A-S-H gel indicating various constituent environments [35].	49
Figure 2.4 Theoretical conditions of corrosion, immunity and passivation of iron depicted through the Pourbaix diagram, at 25°C. The red area and the blue box denote normal pH values and electrode potentials in reinforced-concretes (in the absence of aggressive species) respectively [41].	52
Figure 2.5 Pourbaix diagram for the iron-water system. Adapted from [43].	52
Figure 2.6 Schematic representation of the concept used for the prediction of corrosion initiation including two parts: 1) chloride content prediction at the level of the steel surface, and 2) critical chloride content for corrosion initiation, C_{crit} . [44].	53
Figure 2.7 Long-term cumulative capillary absorption i versus $t^{1/2}$ for water and n-decane into a mortar 1:2 Portland cement:sand by weight, 0.4 water:cement ratio by weight, cured under water for 28 days, dried at 40 °C for 24 h and then at 105 °C to constant weight [60]. White box symbol; water and black cross symbol; n-decane.....	60
Figure 2.8 SEM micrographs of alkali-activated and cement paste samples (magnification level is the same for all micrographs) [69]. Where: AAP1:90%FA+10%SG,	

AAP3:50%FA+50%SG, AAP4:75%FA+25%SG, AAP5:25%FA+75%SG, and HCP:100%PC.....	62
Figure 2.9 The moisture storage function, obtained from sorption data, and illustrates the parameters contained in Equation 2.58 [88]......	76
Figure 2.10 The liquid water permeability function from hygroscopic to saturated moisture content. Data in the saturated moisture range are from permeameter or infiltrometer test. The slope in between is derived by the relative liquid conductivity function and can be calibrated by adjusting ncap and nsp obtained from wet and dry cup tests [88].	77
Figure 2.11 Comparison of total and free chloride profiles of alkali-activated cement based mortar with 75%FA-25%SG (a) and alkali-activated cement based mortar with 25%FA-75%SG (b) after immersion in 16.5% NaCl aqueous solution for 45 days [55]	84
Figure 2.12 C/S ratio present in C-S-H as a function of β_{CH} (left) and solubility product of C-S-H as a function of its C/S content (right), adapted from [5].	86
Figure 2.13 Changes in compressive strength of sodium carbonate activated slag mortar exposed in different carbonation conditions and corresponding carbonation depths. Samples were cured for 28 days in sealed conditions before carbonation exposure. Graph obtained from [132]......	89
Figure 2.14 Phase diagram as a function of temperature and gas phase CO ₂ concentration for the Na ₂ CO ₃ —NaHCO ₃ —CO ₂ —H ₂ O system in an air atmosphere at ambient pressure. The dashed line represents a temperature of 23 °C. Graph from [129].	90
Figure 2.15 Natural carbonation depth of silicate-activated slag cements as a function of MgO content (by wt.%) in slag. Adapted from [134]......	91
Figure 2.16 Plot of pH (solid lines) and carbonate/bicarbonate ratio (dashed lines) as a function of NaOH addition and CO ₂ concentration, for simulated AAS pore solutions. Black lines are at 0.04% CO ₂ , and grey lines at 4% CO ₂ . Graph from [129]......	93
Figure 2.17 Evolution of pH of the pore solution and compressive strength of alkali-activated metakaolin paste cured under natural CO ₂ conditions. Adapted from [136]......	94
Figure 2.18 Carbonation of alkali-activated concretes under natural outdoor conditions protected from rainfall. Error bars represent one standard deviation in each direction from the average value. The number and small letters next to each concrete label indicate the use of the same precursor but in a different mix design. Figure from [114].	95
Figure 2.19 Comparison between the experimental carbonation depths in Portland cement concrete, type CEMI binder with different w/c, and the predicted depths by Meta, Papadakis', and Yang's model. Graph from [144]......	97

Figure 2.20 (a) C-S-H molar volume change, due to carbonation, as a function of C/S for both CN (CEM I with w/c=0.45) and CP (CEM I with w/c=0.6) materials, (b) influence of the choice of molar volume of calcium carbonate in molar volume change of CSH, based on the data obtained for various polymorphic forms of calcium carbonate formed from C-S-H in carbonated CN system. Figure adapted from [146].	99
Figure 2.21 Schematic showing permeability of the concrete as the main controlling factor for steel corrosion. Figure adapted from [148].	100
Figure 2.22 Service life of reinforced concrete subject to steel corrosion. Figure obtained from [148].	103
Figure 2.23 Histogram for time to depassivation of RC with (left) 40 mm cover replacement and (right) 80 mm cover replacement predicted by the fib Bulletin 34 design code. Figure adapted from [47].	106
Figure 2.24 Data (shown by symbols) of chloride profile for samples obtained from real service conditions and chloride transport curve (shown by solid line) estimated by Fick's diffusion model [162].	107
Figure 3.1 Embedded Electrodes Method (EEM) [173].	115
Figure 3.2 Graphical representation of explicit finite difference method use to characterise multi-species transport through alkali-activated concrete.	118
Figure 4.1 Critical chloride thresholds (C_{crit}) for alkali-activated mortars derived from mixed high- and low-Ca precursors (wt.% slag and fly ash as indicated for each group of data), as a function of alkali activator dosage; data from [55].	126
Figure 4.2 Chloride migration coefficients of high calcium alkali-activated concretes as a function of alkali dosage, compiled from the available literature [98, 114, 152, 186, 187].	127
Figure 4.3 Chloride migration coefficients of low calcium alkali-activated concretes as a function of water/binder (w/b), compiled from the available literature [98, 114, 152, 186, 187].	127
Figure 4.4 Algorithm of the probabilistic service life model “fib Bulletin 34 code” for service life design of reinforced concrete assuming depassivation of the reinforcement to be the serviceability limit state. The input data can be found in sections 4.2.1-4.2.3 that describe the durability performances of high and low Ca-AAMs with specified mix proportions (i.e. w/b, alkali dosage and ratio of slag to fly ash precursors).	134
Figure 4.5 C_{crit} (wt.% of binder) of high calcium AAMs (100%SG), as a function of alkali dosage (wt.% of binder), calculated using the pore solution alkalinity in Table S1 (A); and	

C_{crit} (wt.% of binder) calculated by including the reduction of pore solution alkalinity, between 13.5 and 13.2, at the surface of the steel reinforcement (B).	137
Figure 4.6 C_{crit} (wt.% of binder) of high calcium AAMs (50%SG+50%FA), as a function of alkali dosage (wt.% of binder), calculated using the pore solution alkalinity in Table S1 (A); and C_{crit} (wt.% of binder) calculated by including the reduction of pore solution alkalinity, between 13.5 and 13.2, at the surface of the steel reinforcement (B).	137
Figure 4.7 C_{crit} (wt.% of binder) of low calcium AAMs (100%FA), as a function of alkali dosage (wt.% of binder), calculated using the pore solution alkalinity in Table S1 (A); and C_{crit} (wt.% of binder) calculated by including the reduction of pore solution alkalinity, between 13.5 and 13.2, at the surface of the steel reinforcement (B).	138
Figure 4.8 Cumulative probability plot for C_{crit} in SG100. Data are the set of possible C_{crit} values obtained for 100%SG, containing Na_2O at 3 wt.% of binder, as shown in Figure 4 part-B.	139
Figure 4.9 Cumulative probability plot for C_{crit} in 50SG50FA. Data are the set of possible C_{crit} values obtained for 50%FA/50%SG, containing Na_2O of 4 wt.% of binder, as shown in Figure 5-part B.....	139
Figure 4.10 Cumulative probability plot for C_{crit} in FA100. Data are the set of possible C_{crit} values obtained for 100%FA, containing Na_2O of 10 wt.% of binder, as shown in Figure 6-part B.	140
Figure 4.11 Cumulative probability plot for D_{nssm} . Data are the set of possible chloride migration values obtained for 100%SG and 50%FA/50%SG containing Na_2O of 3 and 4 wt.% of binder, respectively, as shown in Figure 4.2.....	140
Figure 4.12 Cumulative probability plots for D_{nssm} in FA100. Data are the set of possible chloride migration values obtained for 100%FA, containing Na_2O of 10 wt.% of binder, as shown in Figure 4.3.....	141
Figure 4.13 Simulated histogram (A) and cumulative distribution plot (B) for service life for SG100 concrete. $P_f = 0.1$ is indicated by a star and horizontal line in (B).	143
Figure 4.14 Simulated histogram (A) and cumulative distribution plot (B) for service life of SG50FA50 concrete. $P_f = 0.1$ is indicated by a star and horizontal line in (B).	143
Figure 4.15 Simulated histogram (A) and cumulative distribution plot (B) for service life of FA100 concrete. $P_f = 0.1$ is indicated by a star and horizontal line in (B).	144
Figure 4.16 Service life of SG100 computed using 0.767 years as a reference point in time (t_0) to match the value of Lepech et al. [47].	145

Figure 4.17 Sensitivity analysis in service life predictions for SG100 concretes of different cover depths (i.e. 35, 45 and 55 mm) as shown in the legend of each panel, showing the predicted service life as a function of C_{crit} , temperature, D_{nssm} , and aging factor. Note the differences in vertical scale between panels.....	147
Figure 4.18 Sensitivity analysis in service life predictions for 50SG50FA concretes of different cover depths (i.e. 50, 60 and 70 mm) as shown in the legend of each panel, showing the predicted service life as a function of C_{crit} , temperature, D_{nssm} , and aging factor. Note the differences in vertical scale between panels.....	148
Figure 4.19 Sensitivity analysis in service life predictions for FA100 concretes of different cover depths (i.e. 100, 200 and 300 mm) as shown in the legend of each panel, showing the predicted service life as a function of C_{crit} , temperature, D_{nssm} , and aging factor. Note the differences in vertical scale between panels.....	149
Figure 5.1 Desorption isotherms of various cements. Data obtained from [62, 69, 70] and replotted. Note that the drop in degree of saturation in the pink curve (i.e. 75SG25FA*) at 93% RH is in the original data set found in [69] and appears to be an analytical error.	155
Figure 5.2 Desorption isotherms of geopolymers based cements and Portland cement [62, 69].	156
Figure 5.3 Adsorption isotherms of alkali-activated cements and Portland cement. Data obtained from [69, 70, 205].	157
Figure 5.4 A diagram of the C-S-H structure containing the solid components (Ca-O sheets, with attached silicate tetrahedra) with chemisorbed/hydroxylated water, and physisorbed, or liquid water kept in the gel and capillary pores during the wetting stage (left) and drying stage (right). Figure obtained from [208].	158
Figure 5.5 Effect of drying and wetting on the morphology of cement hydrates. Drying results in the collapse of the structure and only part of the structure can be recovered after wetting, Figure obtained from [62].	159
Figure 5.6. C-S-H in Portland cement, containing interlayers and gel pores, undergoing microstructural changes during a drying and then wetting cycle [210].	160
Figure 5.7. Apparent moisture diffusion coefficient D_a vs. degree of liquid water saturation S_l , assessed from sorption kinetics (under non-steady-state conditions for adsorption – “ads” – and desorption – “des”), on various samples of Portland cement pastes and concretes. Comparison with effective titrated water diffusion coefficient $D_{e(HTO)}$ (under steady-state conditions), Figure obtained from [82].	161

Figure 5.8. Apparent moisture diffusivity in the small and large pores during desorption state, Figure obtained from [62].	162
Figure 5.9 Degree of saturation in small and large pore regions of a cement. Abbreviations are s and l for small and large pores, respectively, w for evaporable water occupied volume and p for pore volume. Figure obtained from [62].	168
Figure 5.10 TGA of alkali-activated binders-effect of calcium oxide content in mineralogical composition.	174
Figure 5.11 TGA of alkali-activated binders - effect of alkali dosage in mix design.	175
Figure 5.12. Pore size distribution (A and B) and cumulative pore volume (C and D) of alkali-activated cement pastes.	176
Figure 5.13. Cumulative pore volume of alkali-activated binders, denoted as AAP#, and Portland cement, noted as HCP, obtained from BJH analysis of the adsorption branch in water vapour sorption isotherms and normalized by the total pore volume. Graph obtained from [69].	177
Figure 5.14 Water vapour adsorption isotherms of 90FA10SG* (A), 75SG25FA* (B), 50SG50FA* (C), with predictions from different models: VG, Van Genuchten model, VG-Dual, Dual-Porosity Van Genuchten model, Multi, multimodal model, KM, Kosugi model ,FX, Fredlund and Xing's Model, and FF, Feng and Fredlund's model, according to the equations presented in chapter 2 section 2.10.	179
Figure 5.15 Water vapour desorption isotherms of 90FA10SG* (A), 75SG25FA* (B), 50SG50FA* (C), with predictions from different models: VG, Van Genuchten model, VG-Dual, Dual-Porosity Van Genuchten model, Multi, multimodal model, KM, Kosugi model ,FX, Fredlund and Xing's Model, and FF, Feng and Fredlund's model, according to the equations presented in Chapter 2 section 2.10.	180
Figure 5.16 Comparison of NME for desorption isotherms. Each column in the figure stands for one type of binder according to the legend.	180
Figure 5.17 Comparison of NME for adsorption isotherms. Each column in the figure stands for one type of binder according to the legend.	181
Figure 5.18 Scanning curves of water vapour sorption isotherms. AB and BA are the main adsorption and desorption curves respectively. CB and DE are the first scanning curves in wetting and drying respectively. EB is the second scanning curve in wetting. Figure from [70].	182
Figure 5.19 Change in mass of 100SG (A), 75SG25FA (B), 50SG50FA (C) and 100SG8 (D) during three sorption/desorption cycles.	183

Figure 5.20 Water vapor sorption isotherms of 100SG (A), 75SG25FA (B), 50SG50FA (C) and 100SG8 during three sorption/desorption cycles.....	185
Figure 5.21 Water vapor desorption isotherms (DES) of 100SG (A), 75SG25FA (B), 50SG50FA (C), obtained from the third desorption cycle, and predictions from different isotherm models: VG, Van Genuchten model, and VG-Dual, Dual-Porosity Van Genuchten model.....	186
Figure 5.22 Water vapor sorption isotherms (ADS) of 100SG (A), 75SG25FA (B), 50SG50FA (C), obtained from the third adsorption cycle, and predictions from different isotherm models: VG, Van Genuchten model, and VG-Dual, Dual-Porosity Van Genuchten model.	187
Figure 5.23 Fits for desorption isotherm (A) and adsorption isotherm (B) by VG and VG-Dual models.....	188
Figure 5.24 Circular symbols represent experimental D_a data obtained during the desorption of 100SG (A), 75SG25FA(B) and 50SG50FA (C) binders. The measured curves of D_a , lines, are fitted by means of implementing Equations 2.34 and 2.35 in Equation 2.33.....	192
Figure 5.25. Saturation profile at the end of drying from 100% to 50% RH for 100SG(A), 75SG25FA (B). and 50SG50FA (C) binders simulated by implementing equations 2.34 and 2.35 in equation 2.33 and using the moisture transport parameters presented in Tables 5.12-5.13.....	194
Figure 5.26 Circular symbols represent experimental D_a data obtained during the adsorption of 100SG (A), 75SG25FA(B) and 50SG50FA (C) binders. The measured curves of D_a , lines, are fitted by means of implementing Equations 2.34 and 2.35 in Equation 2.33.....	195
Figure 5.27 Saturation profile at the end of wetting from 50% to 100% RH for 100SG(A), 75SG25FA (B). and 50SG50FA (C) binders simulated by implementing equations 2.34 and 2.35 in the single permeability model and using the moisture transport parameters present in Table 5.15.	196
Figure 5.28 Saturation profile at the end of drying from 100% to 50% RH (A) and at the end of wetting from 50% to 100%RH (B) simulated by the single permeability model.	197
Figure 5.29 Saturation profiles in 3D for 75SG25FA binder as function of its thickness, in mm, during wetting for 1 year (A) (i.e. 365 days) and during drying for 5 years (B) (i.e. 1825 days) simulated by the single permeability moisture transport model.	197
Figure 5.30 Simulated saturation profile, dashed line, for AAMs and data, circle symbol, of measured profiles for PC-0.45 at the end of wetting after 315 days, from 53.5% to 97%	

RH (A) and at the end of drying after 370 days from 89% to 53.5% RH (B). Data obtained from [179].	198
Figure 5.31 Circular symbols represent experimental D_a data obtained during the desorption of 100SG. The measured curves of D_a (lines) are obtained by means of fitting the overall moisture transport equation (Eq. 2.42) which includes moisture transport in the large pore region (Eq. 2.44) and small pore region (Eq.2.46) along with the transport contribution factor from the large pore region ($w_{f,D}$).	199
Figure 5.32 Circular symbols represent experimental D_a data calculated from the diffusivity data obtained during the desorption of 75SG25FA. The measured curves of D_a (lines) are obtained by means of fitting the overall moisture transport equation (Eq. 2.42) which includes moisture transport in the large pore region (Eq. 2.44) and small pore region (Eq.2.46) along with the transport contribution factor from the large pore region ($w_{f,D}$).	199
Figure 5.33 Circular symbols represent experimental D_a data calculated from the diffusivity data obtained during the desorption of 50SG50FA. The measured curves of D_a (lines) are obtained by means of fitting the overall moisture transport equation (Eq. 2.42) which includes moisture transport in the large pore region (Eq. 2.44) and small pore region (Eq.2.46) along with the transport contribution factor from the large pore region ($w_{f,D}$).	200
Figure 5.34 Saturation profile at the end of drying from 100% to 50% RH for 100SG in the large pore region (A) and in the small pore region (B). Profiles are simulated by implementing equations 2.43 and 2.45 in the dual permeability model and using the moisture transport parameters present in Tables 5.16-5.17.	201
Figure 5.35 Saturation profile at the end of drying from 100% to 50% RH for 75SG25FA in the large pore region (A) and in the small pore region (B). Profiles are simulated by implementing equations 2.43 and 2.45 in the dual permeability model and using the moisture transport parameters present in Tables 5.16-5.17.	201
Figure 5.36 Saturation profile at the end of drying from 100% to 50% RH for 50SG50FA in the large pore region (A) and in the small pore region (B). Profiles are simulated by implementing equations 2.43 and 2.45 in the dual permeability model and using the moisture transport parameters present in Tables 5.16-5.17.	202
Figure 5.37 Circular symbols represent experimental D_a data obtained during the adsorption of 100SG. The measured curves of D_a (lines) are obtained by means of fitting the overall moisture transport equation (Eq. 2.42) which includes moisture transport in the large pore	

region (Eq. 2.44) and small pore region (Eq.2.46) along with the transport contribution factor from the large pore region ($w_{f,D}$).....	202
Figure 5.38 Circular symbols represent experimental D_a data obtained during the adsorption of 75SG25FA. The measured curves of D_a (lines) are obtained by means of fitting the overall moisture transport equation (Eq. 2.42) which includes moisture transport in the large pore region (Eq. 2.44) and small pore region (Eq.2.46) along with the transport contribution factor from the large pore region ($w_{f,D}$).....	203
Figure 5.39 Circular symbols represent experimental D_a data obtained during the adsorption of 50SG50FA. The measured curves of D_a (lines) are obtained by means of fitting the overall moisture transport equation (Eq. 2.42) which includes moisture transport in the large pore region (Eq. 2.44) and small pore region (Eq. 2.46) along with the transport contribution factor from the large pore region ($w_{f,D}$).....	203
Figure 5.40 Saturation profile at the end of wetting from 50% to 100% RH for 100SG in the large pore region (A) and in the small pore region (B). Profiles are simulated by implementing equations 2.43 and 2.45 in the dual permeability model and using the moisture transport parameters present in table 5.18-5.19.....	205
Figure 5.41 Saturation profile at the end of wetting from 50% to 100% RH for 75SG25FA in the large pore region (A) and in the small pore region (B). Profiles are simulated by implementing equations 2.43 and 2.45 in the dual permeability model and using the moisture transport parameters present in table 5.18-5.19.....	205
Figure 5.42 Saturation profile at the end of wetting from 50% to 100% RH for 50SG50FA in the large pore region (A) and in the small pore region (B). Profiles are simulated by implementing equations 2.43 and 2.45 in the dual permeability model and using the moisture transport parameters present in table 5.18-5.19.....	206
Figure 5.43 100SG Saturation profiles in 3D for 100SG binder as a function of its thickness, in mm, during drying for 5 years (i.e. 1825 days) in the large and small pore regions simulated by implementing Equations 2.43 and 2.45 in the dual permeability model.	206
Figure 5.44 100SG Saturation profiles in 3D for 100SG binder as a function of its thickness, in mm, during wetting for 1 years (i.e. 365 days) in the large (A) and small pore regions (B) simulated by implementing Equations 2.43 and 2.45 in the dual permeability model...	206
Figure 5.45 Saturation profile at the end of drying from 100% to 50% RH (A) and at the end of wetting from 50% to 100% RH (B) for 100SG, 75SG25FA and 50SG50FA of the alkali-activated binder simulated by the dual permeability model.	207

- Figure 5.46. Simulated saturation profile, dashed line, for AAMs 100SG, 75SG25FA,50SG50FA and data, circle symbol, of measured profiles for PC-0.45 at the end of wetting after 315 days, from 53.5% to 97% RH (A) and at the end of drying after 370 days from 89% to 53.5% RH (B). Data obtained from [179]..... 208
- Figure 5.47 The moisture storage curves obtained from the adsorption isotherm of 50SG50FA* that is replotted in terms of the degree of saturation as a function of pC which is $\log(Pc/Pref)$ with $Pref = 1 \text{ Pa}$ [88]. The parameters shown in this graph are the pore maxima pC_i which are the inflection points within the moisture storage curves indicated by vertical dashed lines. The other parameters are the slopes, s_i , of the moisture storage curve at the inflection points and are equal to the slope of straight lines drawn tangent to the curve at those points. The parameter ΔS_i represents the difference between the plateau levels, which are indicated by horizontal dashed line, in the moisture storage curves. Note that the subscript “i” is a number ranging from 1 to 3. 209
- Figure 5.48 The moisture storage curves obtained from the desorption isotherm of 50SG50FA* that is replotted in terms of the degree of saturation as a function of pC which is $\log(Pc/Pref)$ with $Pref = 1 \text{ Pa}$ [88]. The parameters shown in this graph are the pore maxima pC_i which are the inflection points within the moisture storage curves indicated by vertical dashed lines. The other parameters are the slopes, s_i , of the moisture storage curve at the inflection points and are equal to the slope of straight lines drawn tangent to the curve at those points. The parameter ΔS_i represents the difference between the plateau levels, which are indicated by horizontal dashed line, in the moisture storage curves. Note that the subscript “i” is a number ranging from 1 to 3. 210
- Figure 5.49 Relative permeability curves obtained from the mechanistic relative permeability function and the van Genuchten-Mualem model in the case of adsorption (A) and desorption (B) for 50SG50FA*. 211
- Figure 5.50 Saturation profile at the end of drying from 100% to 50% RH (A) and wetting from 50% to 100% RH (B) for 50SG50FA binder. Profiles are simulated by Equation 2.33 where the apparent moisture diffusivity parameter is obtained implementing Equations 2.50 and 2.55 in Equation 2.49. The moisture transport parameters are presented in Table 5.19 with liquid permeability factors of $1.2 \times 10^{-22} \text{ m}^2$ and..... 212
- Figure 5.51 Saturation profiles in 3D for 50SG50FA binder as a function of its thickness, in mm, during wetting for 1 year (A) (i.e. 365 days) and during drying for 5 years (B) (i.e. 1825 days) simulated by the single permeability moisture transport model. 213

Figure 5.52 Simulated saturation profile, dashed line, for 50SG50FA and data, circle symbol, of measured profiles for PC-0.45 at the end of wetting after 315 days, from 53.5% to 97% RH (A) and at the end of drying after 370 days from 89% to 53.5% RH (B). Data obtained from [179]..... 214

Figure 5.53 The cement and mortar skin of the concrete cover affected by the contact with formwork during the process of concrete casting. Figure obtained from [221]. 215

Figure 5.54 Water vapour desorption isotherms for Portland cement at cement, mortar and concrete scale. Data obtained from [69, 205, 222]..... 215

Figure 5.55 D_a vs. RH data from the desorption of 100SG (A) 75SG25FA(B) 50SG50FA(C) from cement to mortar and concrete resulting from the upscaling procedure..... 217

Figure 5.56 D_a vs. RH data from the adsorption of 100SG (A) 75SG25FA(B) 50SG50FA(C) from cement to mortar and concrete resulting from the upscaling procedure..... 218

Figure 5.57 Circular symbols represent experimental D_a data obtained during the desorption of 100SG (A), 75SG25FA(B) and 50SG50FA (C) mortars. The measured curves of D_a , lines, are fitted by means of implementing equations 2.34 and 2.35 in equation 2.33. 220

Figure 5.58 Saturation profile at the end of drying from 100% to 50% RH for 100SG(A), 75SG25FA (B). and 50SG50FA (C) binders simulated by implementing Equations 2.34 and 2.35 in Equation 2.33 and using the moisture transport parameters present in Tables 5.24-5.25..... 221

Figure 5.59 Circular symbols represent experimental D_a data obtained during the adsorption of 100SG (A), 75SG25FA(B) and 50SG50FA (C) mortars. The measured curves of D_a , lines, are fitted by means of implementing Equations 2.34 and 2.35 in Equation 2.33. 221

Figure 5.60 Saturation profile at the end of wetting from 50% to 100% RH for 100SG(A), 75SG25FA (B). and 50SG50FA (C) binders simulated by implementing equations 2.34 and 2.35 in the single permeability model and using the moisture transport parameters present in Tables 5.26 and 5.27. 222

Figure 5.61 Circular symbols represent experimental D_a data obtained during the desorption of 100SG (A), 75SG25FA (B) and 50SG50FA (C). The measured curves of D_a (lines) are obtained by means of fitting the overall moisture transport equation (Eq. 2.42) which includes moisture transport in the large pore region (Eq. 2.44) and small pore region (Eq.2.46) along with the transport contribution factor from the large pore region ($w_{f,D}$). 224

Figure 5.62 Saturation profile at the end of drying from 100% to 50% RH for alkali-activated concretes in the large pore region (A), in the small pore region (B) and total saturation (C).

Profiles are simulated for 100SG, 75SG25FA and 50SG50FA by implementing Equations 2.43 and 2.45 in the dual permeability model and using the moisture transport parameters presented in Tables 5.28-5.29.....	225
Figure 5.63 Circular symbols represent experimental D_a data obtained during the desorption of 100SG (A), 75SG25FA (B) and 50SG50FA (C). The measured curves of D_a (lines) are obtained by means of fitting the overall moisture transport equation (Eq. 2.42) which includes moisture transport in the large pore region (Eq. 2.44) and small pore region (Eq.2.46) along with the transport contribution factor from the large pore region ($w_{f,D}$).	226
Figure 5.64 Saturation profile at the end of wetting from 50% to 100% RH for 100SG 75SG25FA, 50SG50FA in the large pore region (A), in the small pore region (B) and total saturation (C) . Profiles are simulated by implementing Equations 2.43 and 2.45 in the dual permeability model and using the moisture transport parameters presented in Tables 5.30-5.31.	228
Figure 6.1 C_{crit} (mol.L ⁻¹) of high calcium AAMs, 100%SG and 50%SG50%FA, as a function of alkali dosage (wt.% of binder).	256
Figure 6.2 Algorithm of the developed numerical service life model. Where “x” in $C_{cl}(t,x)$ is the location of the rebar in reinforced alkali-activated concrete and “t” is time in years.	258
Figure 6.3 Measured resistivity of Portland cement (PC) mortar, by EEM test, as a function of time and relative humidity. Figure obtained from [173].	260
Figure 6.4 Resistivity measurements of 100SG in submerged conditions as a function of time and temperature.	261
Figure 6.5 Resistivity measurements of 100SG in unsaturated conditions, 60% RH, as a function of time and temperature.....	261
Figure 6.6 Resistivity measurements of 75SG25FA in submerged conditions as a function of time and temperature.	262
Figure 6.7 Resistivity measurements of 75SG25FA in unsaturated conditions, 60%RH, as a function of time and temperature.....	262
Figure 6.8 Resistivity measurements of SG50FA50 in submerged conditions as a function of time and temperature.	263
Figure 6.9 Resistivity measurements of SG50FA50 in unsaturated conditions, 60% RH, as a function of time and temperature.....	263

Figure 6.10 Resistivity measurements of CEM III in submerged conditions as a function of time and temperature.	264
Figure 6.11 Resistivity measurements of CEM III in unsaturated conditions, 60%RH, as a function of time and temperature.....	264
Figure 6.12 Phase assemblages of alkali-activated binders and CEM III, as calculated by thermodynamic simulations in GEM-Selektor. Note that aq_gen is the pore fluid (evaporable/free water with dissolved ions) present in the binders.....	266
Figure 6.13 Pore solution resistivity measurements calculated theoretically using the NIST model [240] based on thermodynamic calculations of pore fluid compositions.	267
Figure 6.14 Effective chloride diffusion in alkali-activated mortars, in submerged condition, as a function of time and temperature.	269
Figure 6.15 Effective chloride diffusion in CEM III mortars, in submerged condition, as a function of time and temperature.....	270
Figure 6.16 Total chloride profile (mol/L) of a structure, made of CEM II cement, in service conditions for more than 25 years at 40 mm above sea level [163], compared to the profiles modelled in this study for the AAM concretes as indicated.	271
Figure 6.17 Time-dependence of chloride diffusion coefficients of 100SG concrete.	272
Figure 6.18 Time-dependence of chloride diffusion coefficients of 75SG25FA concrete....	273
Figure 6.19 Time-dependence of chloride diffusion coefficients of alkali-activated 50SG50FA concrete.....	273
Figure 6.20 Chloride profiles for 100SG concrete in marine splash zone environment at 100% RH and 30°C. The chloride profiles in 100SG concrete are predicted by implementing the Langmuir isotherm with the coefficients determined at the level of the cement (A) and at the level of the concrete (B).	280
Figure 6.21 Chloride profiles for 100SG concrete within 1.5 km of the ocean at 50% RH and 30°C. The chloride profiles in 100SG concrete are predicted by reducing the total amount of bonded chloride predicted by the Langmuir isotherm for 100SG binder by 0% A and 100% B.	281
Figure 6.22 Chloride profiles for 100SG concrete within 1.5 km of the ocean at 100% RH and 30°C. The chloride profiles in 100SG concrete are predicted by accounting for the total amount of bonded chloride predicted by the Langmuir isotherm for 100SG binder (A) and by reducing the total amount of bonded chloride predicted by the Langmuir isotherm for 100SG binder by 100% (B).	281

Figure 6.23 Chloride profiles for 100SG concrete in marine splash zone environment (A), marine spray zone (B), within 800 m of the ocean (C), and within 1.5 km of the ocean (D), at 100% RH and 30°C. The chloride profiles in 100SG concrete are predicted by accounting for the total amount of bonded chloride predicted by the Langmuir isotherm for 100SG binder. 282

Figure 6.24 3D profile for CO₂ transport (A) and CO₂ with **C032** – transports, represented as solid line (-) and star sign (*) respectively, (B) in 100SG concrete, with cover of 50 mm, within 1.5 km of the ocean at 50% RH and 30°C. These are initial outputs from the proposed numerical model..... 284

Figure 6.25 Updated 3D profile for CO₂ transport (A) and CO₂ with **C032** – transports, represented as solid line (-) and star sign (*) respectively, (B) in 100SG concrete, with cover of 50 mm, within 1.5 km of the ocean at 50% RH and 30°C. These outputs are from the updated numerical model that has included the reduction factor of values 0.05 and 0.04 for CO₂ transport in the skin layer and concrete cover, respectively. 284

Figure 6.26 CO₂ with **C032** – profiles, represented as solid line and star sign respectively, in 100SG concrete, with cover within 800 m of the ocean at 50% RH and 30°C with carbonation kinetics (A) and without carbonation kinetics (B)..... 285

Figure 6.27 Chloride profile for 50SG50FA concrete within 800 m of the ocean at 50% RH and 30°C with carbonation kinetics (A) and without carbonation kinetics (B)..... 286

Figure 6.28 Chloride profile for 75SG25FA concrete within 800 m of the ocean at 50% RH and 30°C with carbonation kinetics (A) and without carbonation kinetics (B)..... 286

Figure 6.29 Output messages obtained while initially running the codes for 75SG25FA (A) and 50SG50FA (B) containing the initial rates of precipitation of calcium carbonate (i.e. k parameter as presented in Table 6.8). 287

Figure 6.30 CO₂ with **C032** – profiles in 75SG25FA concrete, with cover of 50 mm, in marine spray zone environment at 100% RH and 30°C. with chloride binding (A) and without chloride binding (B)..... 288

Figure 6.31 saturation profiles for 75SG25FA concrete, with cover of 50 mm,, in marine spray zone environment at 100% RH and 30°C with chloride binding (A) and without chloride binding (B)..... 288

Figure 6.32 CO₂ with **C032** – profiles in 75SG25FA concrete, with cover of 50 mm, in marine spray zone environment at 50% RH and 30°C. with chloride binding (A) and without chloride binding (B)..... 289

Figure 6.33 saturation profiles for 75SG25FA concrete, with cover of 50 mm, in marine spray zone environment at 50% RH and 30°C with chloride binding (A) and without chloride binding (B).....	289
Figure 6.34 Model validation for 100SG concrete, with cover 50 mm, located in a marine splash zone. The circular symbols are the data set and the dashed lines are the predicted curves by the model in case when the concrete is exposed to wetting and drying conditions at 30°C.	290
Figure 6.35 Model validation for 75SG25FA concrete, with cover 50 mm, located in a marine splash zone. The circular symbols are the data set and the dashed lines are the predicted curves by the model in case when the concrete is exposed to wetting and drying conditions at 30°C.	291
Figure 6.36 Model validation for 50SG50FA concrete, with cover 50 mm, located in a marine splash zone. The circular symbols are the data set and the dashed lines are the predicted curves by the model in case when the concrete is exposed to wetting and drying conditions at 30°C.	291
Figure 6.37 Distribution of critical chloride thresholds for 100SG and 50SG50FA concretes.	292
Figure 6.38 Probability service life distribution of 100SG concrete, with cover of 65 mm, in various zones at 50% RH and 30°C.....	293
Figure 6.39 Probability service life distribution of 75SG25FA concrete, with cover of 65 mm, in various zones at 50% RH and 30°C.....	293
Figure 6.40 Probability service life distribution of 100SG concrete, with cover of 65 mm, in various zones at 100% RH and 30°C.....	294
Figure 6.41 Probability service life distribution of 75SG25FA concrete, with cover of 65 mm, in various zones at 100% RH and 30°C.....	294
Figure 6.42 Cumulative probability service life prediction of 50SG50FA concrete, with cover of 100 mm, in various zones at 50% RH and 30°C (A) and at 50% RH and 30°C (B)..	296
Figure 6.43 Cumulative probability service life prediction of 50SG50FA concrete, with cover of 100 mm, within 800 m of the ocean and exposed to drying and wetting conditions at 30°C . The prediction of service life is set with and without change in porosity of 50SG50FA concrete.	298
Figure 6.44 Cumulative probability service life prediction of 75SG25FA concrete, with cover of 65 mm, within 800 m of the ocean and exposed to drying and wetting conditions 30°C.	

The prediction of service life is set with and without change in porosity of 75SG25FA concrete.....	298
Figure 6.45 Probability service life distribution of 75SG25FA concrete, with cover of 65 mm, located in marine splash zone exposed to wetting with severe wetting condition A and drying with severe drying condition B at 30°C. In the case of severe drying condition, the impact of change in porosity is also included.....	300
Figure 6.46 Probability service life distribution of 100SG concrete, with cover of 65 mm, located in marine splash zone exposed to drying and wetting conditions with and without chloride binding at level of the cement.	301
Figure 6.47 Cumulative probability service life prediction of 100SG concrete, with cover of 65 mm, located in marine splash zone and exposed to drying and wetting conditions also at different exposure temperatures of 5°C, 20 °C and 50°C.	302

List of Tables

Table 2.1 List of C_{crit} values obtained for low and high Ca-AAMs.	59
Table 2.2 Chloride binding capacities of AAS hydrates.....	80
Table 2.3 Concrete mix design and the corresponding Langmuir parameters α and β from the study of Mangat et al. [104].....	81
Table 2.4 Fitted parameters for Langmuir isotherms for AAMs, from [113].....	83
Table 2.5 In-service carbonation rates of AAC. Data obtained from [55].	97
Table 2.6 Change in porosity of naturally carbonated alkali-activated FA and SG based cements. Data obtained from [147].	99
Table 2.7 Carbonation effect on chloride ingress in PC and AAMs.	102
Table 2.8 Model distribution parameters corresponding to the simulations in Figure 2.23. .	106
Table 3.1 Averaged (Avg.) chemical composition and average particle size (i.e. d_{avg}) of SG, and FA for cement samples, as determined by X-ray fluorescence (XRF) and laser diffraction [165].....	109
Table 3.2 Chemical composition and average particle size (i.e. d_{avg})of SG and FA for mortar samples, as determined by X-ray fluorescence (XRF) and laser diffraction [167].	109
Table 3.3 Mix designs of alkali-activated pastes.	110
Table 3.4 Materials used in alkali-activated mortars.	111
Table 3.5 Mix design of alkali-activated mortars.	111
Table 4.1 Aging factors of alkali-activated concretes as reported in the literature	129
Table 4.2 Mix designs of alkali-activated concretes described in the simulations here. All samples were cured at room temperature and in saturated conditions.	130
Table 4.3 Maximum recommended $D_{nssm,28}^*$ for various cover depths for binder type CEM III	130
Table 4.4 Mineralogical composition (M.C.) of AAMs used in thermodynamic calculations to estimate the pore solution alkalinity of AAMs; along with other parameters including porosity and mix design of alkali-activated concretes needed to calculate the critical chloride thresholds, in wt.% of binder, by implementation of Equation 4.1-4.2.	135
Table 4.5 fib Bulletin 34 code parameters used for service life prediction of alkali-activated concretes.	142
Table 4.6 Sensitivity parameters for service life prediction of AAC.	146

Table 5.1 Mix designs of Portland cement pastes obtained from the literature.....	154
Table 5.2 Mix designs of AAMs obtained from the literature.....	154
Table 5.3 Chemical composition of precursors as determined by X-ray fluorescence (XRF) [165].....	163
Table 5.4. Mix designs of alkali-activated cements discussed in this chapter.....	163
Table 5.5 Initial moisture condition functions, where $S(x)$ is the degree of saturation, S , as a function of distance, x , which is the thickness of the cement sample. Data obtained from [179].....	173
Table 5.6 Volumetric fraction of large pore region, w , and effective porosity ϕ as measured by MIP.	177
Table 5.7 Volumetric fraction of large pore region estimated through BJH analysis [69]....	178
Table 5.8. Apparent moisture diffusivity during desorption process as determined from DVS instrument.	189
Table 5.9, Apparent moisture diffusivity during adsorption process as determined from DVS instrument.	189
Table 5.10 Apparent moisture diffusivity during desorption process as determined from DVS experimental data.....	190
Table 5.11 Apparent moisture diffusivity during adsorption process as determined from DVS experimental data.....	191
Table 5.12 Parameters of the Van Genuchten model used to simulate desorption isotherms of alkali-activated binders.....	193
Table 5.13. Parameters obtained from fitting D_a - S desorption data by means of implementing equations 2.34 and 2.35 in the single permeability moisture transport model.	193
Table 5.14 Parameters of the Van Genuchten model used to simulate adsorption isotherms of alkali-activated binders.....	195
Table 5.15 Parameters obtained from fitting D_a - S adsorption data by means of implementing equations 2.34 and 2.35 in the single permeability moisture transport model.	196
Table 5.16 Parameters of the VG-Dual model used to simulate desorption isotherms for alkali-activated binders.	200
Table 5.17 Parameters obtained from fitting D_a - S desorption data by means of implementing equation 2.44 for moisture transport in large pore region.	200
Table 5.18 Parameters of the VG-Dual model used to simulate adsorption isotherms for alkali-activated binders.....	204

Table 5.19 Parameters obtained from fitting D_a -S adsorption data by means of implementing equation 2.44 for moisture transport in large pore region.	204
Table 5.20 Parameters of the Van Genuchten model used to simulate WVSIs of 50SG50FA*.	210
Table 5.21 The scaling factors nsp and ncap determined by fitting the mechanistic relative permeability curve with the curve generated by the van Genuchten-Mualem model. The normalized mean error (NME) is used to assess the accuracy of the curve fitting results in Figure 5.49.	211
Table 5.22 Parameters of the Van Genuchten model used to simulate WVSIs of 50SG50FA and implemented in the mechanistic permeability model.	212
Table 5.23 values of porosity of alkali-activated mortars and concretes obtained from	218
Table 5.24 Parameters of the Van Genuchten model used to simulate desorption isotherms of alkali-activated mortars.	220
Table 5.25 Parameters obtained from fitting D_a -S desorption data of alkali-activated mortars by means of implementing equations 2.34 and 2.35 in the single permeability moisture transport model.	220
Table 5.26 Parameters of the Van Genuchten model used to simulate adsorption isotherms of alkali-activated mortars.	222
Table 5.27 Parameters obtained from fitting D_a -S adsorption data, of alkali-activated mortars, by means of implementing equations 2.34 and 2.35 in the single permeability moisture transport model.	222
Table 5.28 Parameters of the VG-Dual model used to simulate desorption isotherms for alkali-activated concretes.	225
Table 5.29 Parameters obtained from fitting $D_a(l)$ desorption data, of alkali-activated concretes, by means of implementing equation 2.44 for moisture transport in the large pore region.	225
Table 5.30 Parameters of the VG-Dual model used to simulate adsorption isotherms for alkali-activated concretes.	227
Table 5.31 Parameters obtained from fitting $D_a(S)_l$ adsorption data, of alkali-activated concretes, by means of implementing equation 2.44 for moisture transport in the large pore region.	227
Table 6.1 Mix design of alkali-activated mortars.	233
Table 6.2 Properties of ionic species in concrete pore solution [106].	239

Table 6.3 Change in porosity of naturally carbonated alkali-activated fly ash and slag based cements. MIP data obtained from [147].	251
Table 6.4 Build-up rates and maximum surface concentration, dependent on various zones. Data obtained from [262].	255
Table 6.5 Pore solution chemistry of alkali-activated binders and CEM III binder.	266
Table 6.6 Chloride and carbonate ion transport models for alkali-activated mortars.	268
Table 6.7 Chloride and carbonate ion transport models, in $m^2/year$, in alkali-activated concretes.	268
Table 6.8 Calculated calcium concentration, activity coefficients and precipitation rate constants for $CaCO_3$ for carbonated AAMs.	270
Table 6.9 Mix designs of alkali-activated concretes.	274
Table 6.10 Parameters used in the numerical model for transport in the mortar phase (i.e. skin layer) and concrete phase for the studied alkali-activated concretes.	275
Table 6.11 Moisture permeability parameters for 100SG concrete with 5 mm skin layer of mortar phase. The moisture transport parameters have been already calculated in in “Chapter 5: Moisture Permeability in Alkali-Activated Materials”.	276
Table 6.12 Moisture permeability parameters for 75SG25FA concrete with 5 mm skin layer of mortar phase. The moisture transport parameters have been already calculated in in “Chapter 5: Moisture Permeability in Alkali-Activated Materials”.	277
Table 6.13 Moisture permeability parameters for 50SG50FA concrete with 5 mm skin layer of mortar phase. The moisture transport parameters have been already calculated in in “Chapter 5: Moisture Permeability in Alkali-Activated Materials”.	278
Table 6.14 Fitted parameters, α and β , for Langmuir isotherms for AAMs obtained at the cement level from [113] and at concrete level [104].	279
Table 6.15 Lognormal distributions fit of critical chloride thresholds for 100SG and 50SG50FA concretes.	292
Table 6.16 Normal distribution fit of service life for 100SG and 75SG25FA concretes, with cover of 65 mm, in various zones and exposed to drying condition.	295
Table 6.17 Normal distribution fit of service life for 100SG and 75SG25FA concretes, with cover of 65 mm, in various zones and exposed to wetting condition.	295
Table 6.18 Normal distribution fit of service life for 50SG50FA concrete, with cover of 100 mm, in various zones and exposed to drying and wetting condition.	296

Chapter 1: Introduction

1.1 Background

Concrete, a man-made rock composed of cement, water, sand and aggregate, is the most used building material on earth. Its use ranges from the construction of energy systems to the construction of gravity defying skyscrapers. The high consumption of concrete is attributed to the fact that no material has been found to be capable of replacing reinforced concrete at a low economic cost and with long lasting service performance [1]. Portland cement (PC), the mineral binder that joins all the components together in concrete, is produced by the decomposition of carbonates to obtain its main component known as the clinker. Around 90% of the cement sector's CO₂ emissions can be attributed to the production of clinker by heating a mixture of raw materials up to a high temperature range of 1400-1500°C in the rotary kiln and then by cooling the mixture to form the clinker from a semi-molten state to a solid state. The reason for the high calcination temperature is to decompose the major raw material, limestone (CaCO₃), as a source of calcium to chemically combine with the other ground raw materials which are usually shales or clays [2]. **Equation 1.1** depicts the decomposition reaction of limestone in the rotary kiln;



It is reported that a value of 0.53 t CO₂ was emitted per ton of clinker produced and an average of 0.34 t CO₂ emitted per ton of cement due to the combustion of non-renewable resources required to heat the raw materials in the kiln [2]. These amounts make the process of CO₂ emissions from the cement sector contribute to approximately 8% of global CO₂ anthropogenic emissions [2]. This contribution factor will rise because of the surge in demand for concrete to meet the needs of the global population expected to increase by 2.5 billion by 2050 [3].

Efforts for the reduction of carbon footprint of the cement industry have been implemented which include: energy efficiency manufacturing processes with the replacement of alternative fuels, carbon capture and storage, increased degree of clinker substitution and production of alternative cements [3]. Habert et al. [3] have estimated the strategies for optimization of clinker content of cement, with supplementary cementitious materials, and implementation of alternative cements in construction could drop the CO₂ budget of concrete production by 45

and 41% respectively [3]. They have also emphasized the use of alkali-activation technology as a suitable alternative for valorization of large streams of industrial wastes and by-products, to produce low carbon cementitious materials [3].

Alkali-activated materials (AAMs) are made by chemical reactions between an alkaline activator, that is source of alkali cations, and reactive aluminosilicate materials mixed with water either at room temperature or at a slightly elevated temperature (up to 80°C). The main raw materials typically used as aluminosilicate precursors for alkali-activation are those which are also used as supplementary cementitious materials (SCMs) in Portland cement blends, such as blast furnace slag and fly ashes which are industrial by-products obtained from the production of steel and electricity respectively [2]. Another source for aluminosilicate precursors used for alkali-activation is metakaolin, also known as calcined kaolin clays, that exist as a natural resource in abundance around the world [2, 4].

Regardless of the type of binder used in reinforced concrete, whether it is PC or AAMs with its potential environmental benefits, corrosion reaction occurs at the level of the rebar and the required time to corrosion initiation is termed as the serviceability limit state of the structure. Corrosion reaction occurs when concrete in an unsaturated state (i.e. not in submerged conditions) is exposed to an environment consisting of a combined action of carbonation and chloride ingress. This combined action exists in a typical situation where aerosol chlorides, which are chloride-contained liquid droplets originated either from sea water or during the application of chloride contained de-icing salts, deposit on concrete surface while carbonation occurs at the same time [5]. Carbonation occurs by the diffusion of atmospheric CO₂ through the pore network of the concrete cover, also partly in a dissolved state in the pore solution which induces a drop in pH of the pore solution, from its normal passive values (i.e. pH \cong 13.5) to near neutrality, and induces an overall increase in porosity and pore size of the concrete matrix [6]. This leads to bound chlorides from the hydrated phases to become liberated, diffuse to the rebar, and accumulate across the surface of the rebar [7]. Once a certain concentration of chloride ions has been reached then corrosion occurs through localized de-passivation (i.e. pitting) over areas of the protective thin oxide layer initially formed around the rebar because of the highly alkaline environment of the surrounding concrete, as an inherent property. This concentration of chloride ions needed to initiate corrosion in reinforced concrete is termed as critical chloride threshold (C_{crit}) [8]. The effect of corrosion can lead to reductions in cross-sectional area of the rebar which reduces its capacity to absorb tensile and shear stress

to withstand the compressive load that the structure was initially designed for in a construction project [9].

The resistance of concrete cover, also known by the term durability, against corrosive agents for the steel reinforcement has been adequately researched in the literature to obtain data of the performance of AAMs in corrosive conditions for structural applications, where in some cases AAMs have been proven to have similar and/or better performance than PC[10]. For example, NTBUILD 492 test [11] has been used to calculate the non-steady state chloride migration towards the rebar with the influence of ionic interaction from different ions simultaneously present in the pore solution (i.e. aqueous phase of the concrete). Another transport test method used is the NTBUILD 443 test to calculate the effective chloride diffusion and possible chloride binding capacity of the concrete matrix by the use of ASTM C 1218 [12] and ASTM C 1152 [13] techniques. Electrical impedance spectroscopy has been applied to investigate the permeability, in other words microstructural evolution, of alkali-activated binders as a function of time [14]. Furthermore, thermodynamic modelling has been implemented to predict the phase evolution of the binders exposed to chloride and carbonate ions from the environment [15, 16]. This technique is a useful tool to predict the changes in the porosity of the cement and alkalinity of the pore solution as a function of changes in pore solution composition [17, 18].

However, some gaps are still existent in the literature which can decrease the chances for AAMs to be placed as a commercial product in the market. For example, most of the research that has been conducted to test the durability of AAMs were in lab scale and only in single deterioration condition. As well as the transport tests used are the ones originally made to test the PC and are mostly conducted without considering the difference in the chemistry of each binder which can have an impact on the results. Another gap in the literature is the lack of long-term service performance data for AAMs in service conditions. Therefore, the main challenge is to prove the reliability of AAMs by predicting the time for corrosion initiation (i.e. known as the serviceability limit state [9]), through the use of a numerical model describing combined modes of degradation occurring in reinforced alkali-activated concrete exposed to a corrosive environment.

1.2 Objective and Scope of Research

The general aim of this thesis is the construction of a multi-transport numerical model that interplays the reaction and ingress of chloride ions and CO₂ in the liquid phase and gaseous phase of the concrete, respectively, based on the saturation state of alkali-activated concrete which is also predicted by moisture permeability transport models. The numerical model will couple moisture, chloride and carbonation transport-reaction equations, that have been separately pre-established to describe the durability performance of PC concrete exposed to a single type of environmental condition, with durability data of AAMs as inputs. Hence, the service life for alkali-activated concrete exposed to combined modes of degradation will be predicted until the point of corrosion initiation. Additionally, the service life will be calculated in a probabilistic mode by accounting the variability of durability data, as inputs for the numerical model, obtained for a single type of alkali-activated concrete from literature and experimental work carried out in this research. Thus, the scope of this study is solely on degradation via mass transport of moisture, chloride ion and CO₂ from the external environment into alkali-activated concrete (AAC) without including other modes of chemical attack such as the impact of freeze-thaw cycle on the permeability of concrete located in cold climate regions.

1.3 Thesis Outline

The work described in this thesis to achieve the main objective falls generally into six chapters described as follow:

- **Chapter 2** is on the literature that provides a thorough discussion on durability aspects of AAMs exposed to carbonation reaction and chloride ingress in comparison to Portland cement. It also includes moisture permeability models used to predict evaporable water content across the porous cementitious matrix and a commonly used service life model implemented to predict the service life of reinforced concrete.
- **Chapter 3** presents the materials and experimental methods used in this research. The materials used in this research are AAMs with different mix designs and are presented in detail. Some of the experimental methods are implemented to obtain data for parameters used in the numerical models described in **Chapters 5** and **6**. Additionally, the computational technique implemented to run the numerical models is discussed in the chapter.

- **Chapter 4** is on applying a well-established service life model, *fib* Bulletin 34, based on the distribution of the durability data of AAMs obtained from the literature. The distribution of C_{crit} for AAMs is also estimated by implementing a model that includes the ratio of chloride concentration to pore solution alkalinity which serves as corrosion indicating factor in AAMs also obtained from the literature. It is revealed that AAMs with high calcium content in the mineralogical composition can be a suitable low carbon construction material for structural applications in a submerged aqueous marine chloride environment. Gaps in the model are also identified for further development done in this research to improve its predictions.
- **Chapters 5** primarily describes anomalous moisture transport in cement, which is the deviation of transport of evaporable water from Fick's second law of diffusion, and that it is mainly caused by the complex microstructure of the binder. Three moisture permeability models have been implemented for AAMs exposed to wetting and drying cycles, and predicted profiles of degree of saturation are compared with data for Portland cement attained from the literature. The dual permeability model is found to be a suitable model because it includes the anomaly effect of moisture transport by accounting the fast and slow transport of moisture through two different pore size regions, classified as large and small pores, of a material with a complex microstructure such as the case of blended cements.
- **Chapters 6** is on the construction of a numerical model that implements carbonation-chloride induced reactive transport models combined with moisture permeability models to predict the service life of alkali-activated concrete in unsaturated conditions (i.e. not in submerged conditions). The calculation of the degree of saturation is the key parameter in the model that can interplay the ingress of CO_2 in the gas phase and chloride ions in the aqueous phase of the concrete. The developed model also implements reactive transports in the skin layer of the concrete cover, which is more of a mortar phase, and is usually ignored in existing service life models present in the literature. The model is also validated against chloride profile data for a structure exposed in unsaturated conditions. Finally, the distribution of C_{crit} for AAMs, determined in **Chapter 4**, is built in the numerical model to probabilistically predict the service life of alkali-activated concrete exposed to combined environmental conditions. Sensitivity analysis is also included in this study to determine the variation

of the distribution of service life when some of the durability parameters are systematically varied in the model.

- Finally, **Chapter 7** contains overall conclusions for **Chapters 4-6**. It also includes discussions on the limitations of the developed numerical model which can be subjects of future research in the field of durability of alkali-activated materials.

Figure 1.1 represents a flow chart indicating the main outcome obtained from each chapter outlined in the thesis along with their interrelations to achieve the main objective of this research.

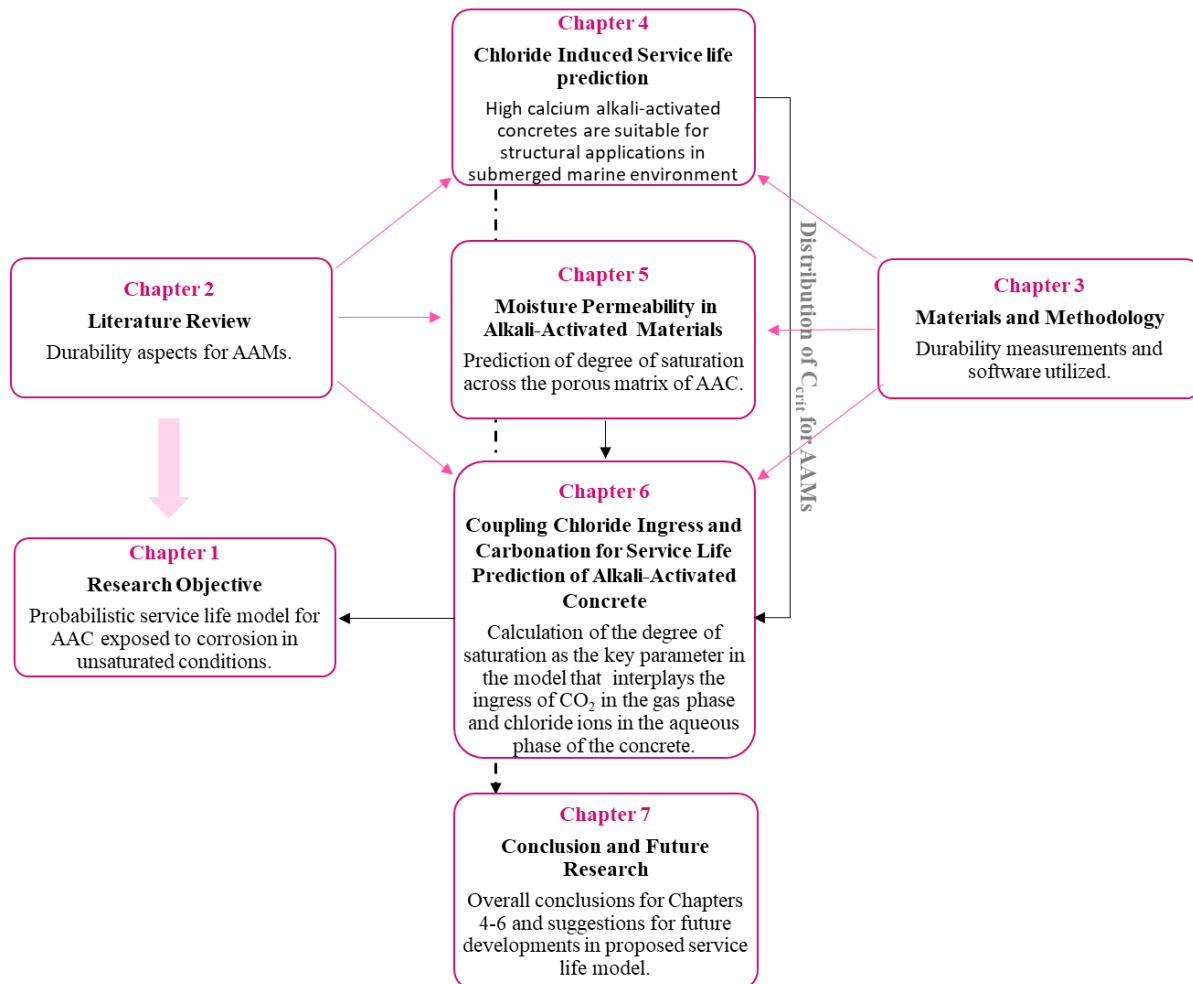


Figure 1.1 Thesis outline summarizing the key work related to **Chapters 4,5 and 6** and their interrelations to achieve the research objective stated in Chapter 1. The durability data and models obtained from literature review and experimental measurements, discussed in **Chapters 2 and 3**, form the basis of **Chapters 4, 5 and 6** followed by future work suggested in **Chapter 7**.

Chapter 2: Literature review

2.1 Alkali-Activated Materials- Historical Background

The reaction of an alkali source with an alumina- and silica-containing solid precursor as means of forming a solid material comparable to Portland cement (PC) was first patented by Whiting, a cement scientist, in 1895 [19]. Later on, in 1908 Kühl, a German cement chemist and engineer, marked a mixture of a vitreous slag and an alkali sulfate or carbonate, with or without added alkaline earth oxides or hydroxides, as a ‘developing material’ because of its comparable usage as Portland cement [2].

Purdon, in an important journal article published in 1940, established the scientific basis of alkali-activated cementitious binders in more detail, where he noted the enhanced tensile and flexural strength of slag-alkali cements compared to Portland cements of similar compressive strength. Other key notes from that study were the low solubility of these slag binders, and low heat evolution during the reaction into hardened state [2].

However, the first real contribution to the research in cement science of alkali-activated materials was given by Glukhovsky in 1959 [20] [2]. He claimed that these binders inherently show good durability properties because of the presence of aluminosilicate hydrates in their chemical composition, compared to PC composed of calcium silicate hydrates. For this reason, he developed a similar binder called “soil-cement”, in order to reflect its likeness to natural minerals, which is obtained from the reaction of low-calcium or calcium-free aluminosilicates (e.g. clays) with alkali metal solutions [2, 21]. Nevertheless, much of the degradation observed in modern concretes is due to the corrosion of embedded steel reinforcement, while intact unreinforced ancient structures have not been subject to this mode of decay.

From the early 1980s developments of low-calcium (including calcium-free) binders were led by the work of Davidovits who, in 1978, first applied the name “Geopolymer” to these materials. Geopolymers were manufactured through the alkali-activation of calcined clays, particularly metakaolin. These geopolymers have been used as a fire-resistant replacement for organic polymeric materials and as cementitious binders [21].

Following all the above initial investigations, research in alkali-activated materials (AAMs) has since diffused worldwide with different names such as F-cement in Finland, Pyrament in

the USA, E-Crete™ in Australia, Geocements in Ukraine, and ASCEM in the Netherlands. With this excess of names applied to the description of AAMs, three different categories were defined and adopted to identify the variety in alkali-activated materials based on their chemical compositions, as shown in **Figure 2.1** [22].

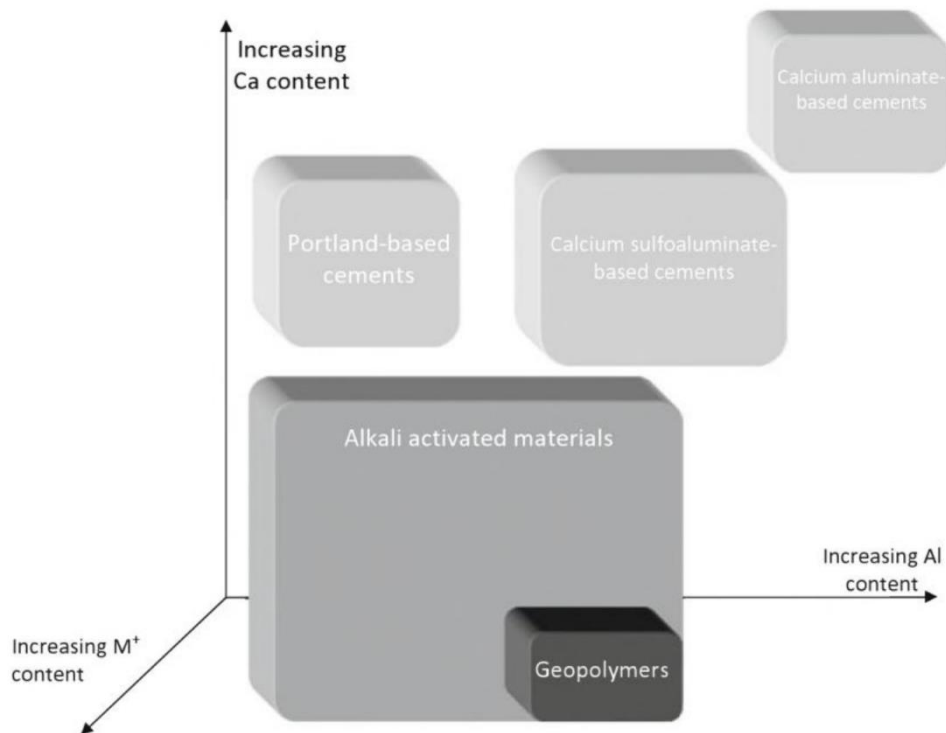


Figure 2.1 Classification of AAMs and its subset Geopolymers, with comparison to PC and calcium sulfoaluminate binder chemistry. The shading specifies approximate alkali content; darker shading links to higher concentration of sodium and/or potassium [2].

- Alkali activated materials is the broadest term, including any cementitious material made by the reaction of an alkaline salt, in solid or dissolved state, with a solid aluminosilicate powder. The alkaline salt has to be soluble and can raise the alkalinity of the reaction mixture to accelerate the dissolution of the solid precursor. This solid can also contain calcium silicate hydrates, through the alkali-activation of conventional clinkers, or precursor with an aluminosilicate-rich content such as a metallurgical slag, natural pozzolan, fly ash or bottom ash[22].
- Geopolymers are a subgroup of AAMs, that are mainly composed of aluminosilicate as the binding phase to form the solid material. Its formation is from low calcium (Ca) content raw materials such as low-Ca fly ash and calcined clays (i.e. metakaolin)[22].

Furthermore, the terms AAMs and geopolymers should not be used interchangeably as AAMs made from high-Ca raw materials have a chain structure of calcium silicate hydrate (C-S-H) type phases and geopolymers have a pseudo-zeolitic network structure. This difference in chemical structure is enough to distinguish their durability performances within the same environmental service conditions [2].

2.2 Chemistry of Alkaline Activating Solutions

Similarly, to the use of water to binder ratio (w/b) as key parameter used for manufacturing of binders in the PC system, it is also used for production of AAMs. However, in AAMs an alkali activator is introduced to create an alkaline environment to dissolve the aluminosilicate precursors for the formation of the gel-like reaction products [21]. Therefore, in AAMs w/b is presented in three different ways:

1. Water to binder ratio (w/b): the ratio of total mass of water (water in alkaline solutions with additional water) to total mass of precursors.
2. Liquid to binder ratio (l/b): the ratio of total mass of alkaline liquids (alkaline solutions with additional water) to total mass of precursors.
3. Water to solid ratio (w/s): the ratio of total mass of water (water in alkaline solutions with additional water) to total mass of solid (precursors and the dissolved solids in the alkaline solutions). Also this ratio is sometimes termed as w/b with the binder (b) defined as the total solids.

In this research the notation w/b is used to describe the ratio of the total mass of water (water in alkaline solutions with additional water) to total mass of solid (precursors and the dissolved solids in the alkaline solutions) in the mix design for the studied alkali-activated materials.

In addition, it is necessary to understand the chemistry of the alkaline activating solutions that are combined with aluminosilicate precursors to produce cementitious materials;

Alkali silicates are the most widely used activators and can be written as $\text{Na}_2\text{O}-\text{SiO}_2-\text{H}_2\text{O}$. These can be produced via two processes: melting carbonate salts with silicon dioxide to form a glass and then dissolving in water, or dissolving silicon dioxide in highly alkaline solutions. Most of the silicate sites present in the activating solutions used in manufacture of AAMs will be deprotonated either once or twice, making the activating solution buffer at approximately pH 11-13.5 [2, 23].

Alkali hydroxide is produced industrially as the product of the chlor-alkali process, which is the electrolysis of an aqueous solution containing alkali chlorides. The high use of sodium and potassium hydroxides is due to their solubility in water that can reach up to concentrations of 30 mol/kg at 20 °C [24]. In addition, alkali-hydroxide can produce a highly alkaline solution at a relatively low cost. However, one of the main disadvantages is the potential for the excess alkali present in the pore solution to react with atmospheric CO₂ and form efflorescence. This can serve as a durability problem as the presence of formed carbonates can limit the chloride binding capacity of cement hydrates in order to prevent steel corrosion [2, 14]. Another related durability issue by hydroxide activation is the poor microstructural development of the binder, making it more porous, which can negatively impact the compressive strength of the concrete [25]. Furthermore, there is a difficulty in handling the activators because they are hazardous to human health [26].

Alkali carbonate can be obtained either by the Solvay process or by the mining of carbonate salt deposits. Its alkalinity is lower than that of other alkali-activating solutions, which means that the selection of aluminosilicate raw materials that can be used with carbonate containing activators may be quite limited. Moreover, the potential of formation of hydrous sodium carbonate salts (e.g. the decahydrate Na₂CO₃·10H₂O) due to presence of carbonate ions already in the pore solution, can bind to large amounts of water and cause difficulties related to water demand in mix designs [2]. However, Bernal reported that the consumption of carbonates, during advanced curing times of alkali-activated slags, can lead to an increase in alkalinity of the pore solution and can make the reaction process form similar reaction products as the ones observed in case of slags activated by alkali hydroxide [27]. In addition, it was reported that slags with high magnesium oxide content can overcome the known issues with delayed setting time in carbonate activated binders [27].

Alkali sulfates can either be extracted from mining processes or be a by-product from the manufacturing of other chemical materials such as boric acid, silica pigments or ascorbic acid. This kind of activator has not very often been used in the preparation of alkali-activated binders, but it has been reported that the addition of clinker is usually required for enough strength development of the material [2]. In addition, Bernal [27] reported that slags activated by sodium sulfate can have setting times faster than in the case of sodium carbonate activation, but their process to harden takes a longer time than the slags activated by sodium silicate.

Finally, alkali sulfates and carbonates, compared to alkali hydroxides and silicates, provide significant scope for greenhouse gas savings in cement production, but the manufacturing conditions must first be identified to form binders with properties that can meet performance standards [2, 27].

2.3 Aluminosilicate Raw Materials

The aluminosilicate-rich raw materials used in AAMs can be natural resources, such as clay that is calcined to obtain metakaolin, and industrial by-products such as ground granulated blast furnace slag (SG) or fly ash (FA). Depending on the reactive calcium oxide content in these materials and the type of alkali-activator used, the binder made up of the final reaction products can be divided into two main groups:

- A calcium- and silicon- rich material, in the case of blast furnace slag, having a composition of silicon dioxide (SiO_2) and calcium oxide (CaO) greater than 70% with CaO of at least 40% , activated under relatively moderate alkaline conditions leads to the formation to calcium aluminosilicate hydrate (C-A-S-H) gel as the main reaction product [28]. This product is similar to the one obtained from the hydration of PC, but the difference is the incorporation of aluminum (Al) in the structure of C-A-S-H [21].
- An aluminum- and silicon rich material, such as class F fly ash (according to ASTM C618 [29]) with low calcium oxide content, and metakaolin, also with low CaO content, will require more severe conditions for the alkali-activation reaction to take place. Conditions such as high alkalinity and the right curing temperatures for certain mix designs would be needed to obtain acceptable strength properties. The hydration reaction leads to the formation of the main hydrate product that is an alkaline aluminosilicate hydrate (N-A-S-H) gel, which is sometimes termed as a geopolymer gel [21].

2.3.1 High-Calcium Alkali-Activated Binders

Ground-granulated blast-furnace slag is commonly used as a calcium-rich aluminosilicate precursor for the production of alkali-activated materials. Blast furnace slag, which is a by-product of manufacture of iron in blast furnaces, consists of silicate and aluminate impurities from the iron ore and coke. The type of reaction products formed in alkali-activated blast furnace slag (AAS) is mainly dependent on type of activator, composition of the precursors, curing conditions, and extent of slag reaction [2, 30].

The main reaction product of alkali activated blast furnace slag (AAS) is the C-(N)-A-S-H type gel, and the secondary reaction products, which may be zeolites and/or hydrotalcites, are dependent on the magnesium oxide (MgO) content in the mineralogical composition of the slag. Slags containing low MgO content can lead to the formation of the C-(N)-A-S-H gel with a higher incorporation of Al and alkali (N) content in its network structure, and to the formation of strätlingite as the dominant secondary product. However, for more MgO-rich slags, much of the Al is consumed in the formation reaction of secondary Mg-Al rich hydration products termed as hydrotalcite-like phases [30].

Overall, the molecular interactions govern the nanostructure of C-(N)-A-S-H gel and are controlled by precursor composition and mix formulation. The structure of C-(N)-A-S-H gel is generally a mix of cross-linked/noncross-linked tobermorite units, as seen in **Figure 2.2**. This form of structure has been found to be similar to the calcium silicate hydrate phase (C-S-H) seen in Portland cement [31].

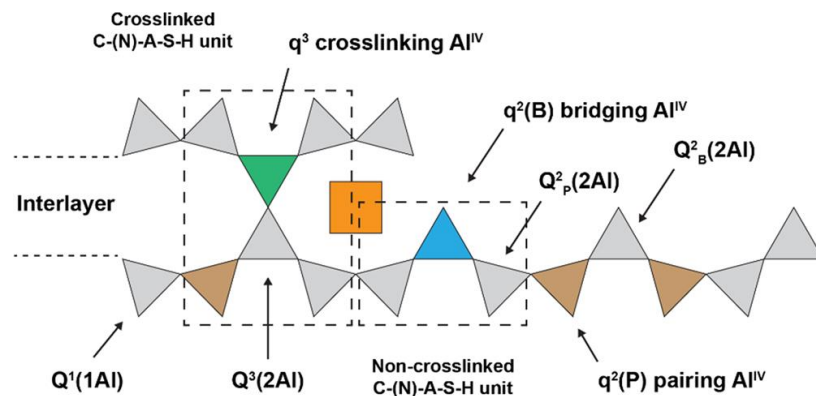


Figure 2.2 Schematic representation of Al sites within C-A-S-H type gels cross-linking q^3 Al tetrahedral (green triangle), bridging $q^2(B)$ Al tetrahedra (blue triangle), pairing $q^2(P)$ Al tetrahedra (brown triangle), and charge-balancing Al^V (orange square). Si tetrahedra are shown by the grey triangles, and charge-balancing alkali cations and protons have been omitted by the authors for clarity in [31].

Walkley et al. have studied the structural framework of C-(N)-A-S-H gel through the variation of the chemical composition of slag by the application of ^{17}O , ^{23}Na , and ^{27}Al 3Q MAS NMR spectroscopy to multiphase ^{17}O -enriched gels [31]. They have noted that with an increase of bulk calcium (Ca) content within the reaction mixture, the formation of low-Al, high-Ca containing C-(N)-A-S-H occurs. This type of hydrate has exhibited a highly ordered structure and with less cross-linking sites. Also more coordination between calcium and oxygen atoms occurred which led to an increase of protons connecting with CaO layers to form Ca-OH sites

[31]. In addition, they have noted that the increase of bulk Ca content can promote the formation of hydroxy-AFm and monocarbonate-AFm phases. Whereas in the case of the reaction mixture containing a high bulk of Al content, this ionic species will substitute more in the C-(N)-A-S-H gel, leading its structure to have a higher degree of cross linking sites and a disordered form. Furthermore, the increase in the bulk Al content has resulted in an increased in the formation of additional disordered N-A-S-H gel with high Al and sodium (Na) contents [31].

2.3.2 Low Calcium Alkali-Activated Systems

Fly ash, as the by-product of coal combustion for the production of electricity, has been used to make low-calcium alkali-activated binders whereas calcined clays, known as metakaolin, are the precursors used to make free-calcium alkali-activated binders [2]. Most of the fly ashes used in alkali-activation are grouped within class F (low calcium content) category as defined by ASTM C618, a commonly used standard for the classification of supplementary cementitious materials (SCMs). However, the activation process for these precursors differ from AAS production as sometimes thermal or steam curing (60-80°C) and strong alkaline activators are required for the activation reaction [32]. Class C (high calcium content) fly ash is less frequently used because it is less abundant compared to other SCMs and the alkali-activated binder produced will have rapid setting properties that affect the workability of the material during concrete casting [33].

Looking further into the formation of hydrates of geopolymer type binders, the main reaction product is a polymeric network with amorphous zeolite-like phases, named N-A-S-H gel. The secondary reaction products are mainly zeolite-like crystalline structures such as analcite, sodalite, Na-chabazite, hydroxysodalite and faujasite [34]. Additionally, the composition and structure of these formed zeolites vary according to the type of activator and precursor used, along with the conditions used for curing stage [2]. Walkley et al. have proposed a structural model for alkali aluminosilicate gel (N-A-S-H) frameworks based on data obtained from solid-state nuclear magnetic resonance spectroscopy (^{17}O , ^{23}Na , and ^{27}Al). In **Figure 2.3** the proposed conceptual model for the structure of N-A-S-H gel is shown with charge-balancing of the partial negative charges on bridging oxygen associated with tetrahedral Al provided by sodium and by extra-framework Al [35].

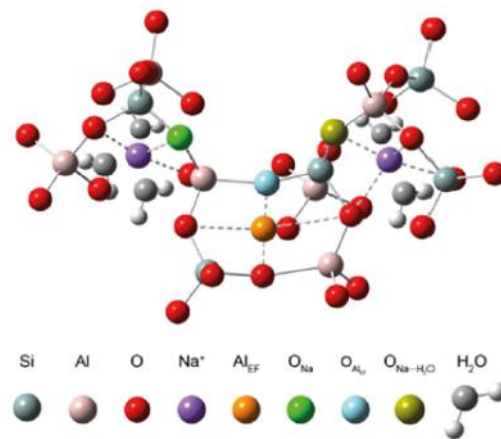


Figure 2.3 3D representation of a polymerized section of the N-A-S-H gel indicating various constituent environments [35].

Overall, insights into the nanostructure of the main hydrates formed in AAMs (i.e. C-(N)-A-S-H and N-A-S-H hydrates in high and low Ca-AAMs, respectively) is crucial for understanding the solubility and reactivity of the cement hydrates that control the macroscale engineering properties of the concrete such as the compressive and tensile strength [31]. In addition, the chemical composition of cementitious material, also known as the phase assemblage of formed cement hydrates, control the durability properties of the concrete cover which serves as a protective barrier for steel reinforcement against corrosion [30]. Consequently, the cement hydrates play a major role in the prediction of long-term service performance of the reinforced concrete structure.

2.4 Role of Concrete Against Corrosion of Steel Reinforcement

In general, the concrete matrix, made up of cement, sand and aggregates, acts as a physical barrier against penetration of aggressive agents mainly through its pores. This means that the less permeable and thicker the concrete cover is, the more durable the material is to prevent steel corrosion, and the longer the service life of the reinforced concrete structure (RCS) will be. In addition, the chemistry of the pore solution and cement hydrates play a role in interacting and binding to the corrosive agents leading to less flow of the ions towards the steel rebar [36].

The durability of Portland cement based concrete in corrosive environment has been studied for many years with standard performance tests developed along with recommended types of raw materials and mix designs for concrete material used for the infrastructure [37].

However, the durability performance of alkali-activated concrete (AAC) in combined chemical attack of carbonation and chloride ingress is still not clearly understood up to this date [38]. One of the main reasons is due to the lack of standardized tests needed to evaluate the durability of AAMs exposed to the weathering conditions [39]. Consequently, the use of AAC in construction and especially in marine exposure conditions (i.e. corrosive environment) has not been widely implemented. The following section provides a general description of corrosion across the rebar in reinforced concrete.

2.5 Mechanisms of Steel Corrosion in Reinforced Concrete

Reinforced concrete is a concrete matrix with a steel rebar embedded in such a way that the two materials act together to resist loads in a structure. Reinforced concrete combines the good compressive strength properties of concrete and the excellent mechanical strength properties of steel because of its ability to absorb the tensile and shear stress that prevents the concrete from crumbling under high loads. Thus, reinforced concrete materials can provide high mechanical strength, fire resistance, shape adaptability and durability [21].

However, with time, severe steel corrosion can occur in the concrete structures that can lead to the concrete spalling and then structural failure. Corrosion of the reinforcement occurs when corroding agents from the environment permeate through the concrete matrix, towards the rebar and dissolve the protective (passivating) thin oxide layer that was formed around the surface of the steel as soon as it was embedded in the highly alkaline environment of the concrete.

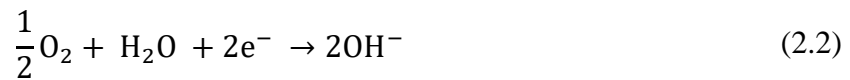
The entry of chloride ions from the external environment, either by capillary absorption, hydrostatic pressure and/or diffusion process, into the concrete can act as a catalyst to accelerate the corrosion process. The infiltration of chloride ions into concrete, as free ions in the pore solution, provides the electrolyte needed to sustain the electrochemical reactions that cause localized pitting around the passive film of the reinforcement.

The presence of absorbed chlorides around the steel causes the formation of acids such as hydrochloric acid (HCl) and hydrogen sulfide (H₂S) that create pits inside the rebar and become the deposit areas for formed rust products [40]. The overall effect of the corrosion induced by chlorides together with oxygen and water is a substantial reduction in the cross section area of the rebar.

In addition, carbonation is also a coupling corrosive agent with the chloride ions around the steel reinforcement. The carbonate ions, resulting from the flow of carbon dioxide and its partial dissolution into the concrete pore solution, can cause the drop of alkalinity of the pore

solution surrounding the rebar which causes the dissolution of the passive film layer. Thus, in the combined case (i.e. presence of chloride and carbonate ions) the corrosion reaction can take place over wide areas of the reinforcement making it a more uniform process [21].

Steel corrosion, an electrochemical process, must have four main conditions simultaneously present in order for the reaction to remain sustained. The first condition is the provision of two half-cell reactions considered to be the anodic, **Equation 2.1**, and the cathodic, **Equation 2.2**, reactions that can be shown as follows:



The second condition is the maintenance of an electrical circuit where the ferrous ions migrate through the pore water of the concrete to the cathodic sites where they react to form rust (represented here as $\text{Fe}(\text{OH})_2$) through equation (2.3):



The third and fourth conditions are the presence of moisture and oxygen that act as catalysts for corrosion reactions by providing more hydroxides (OH^{-}) for the production of the main rust component $\text{Fe}(\text{OH})_2$.

The use of the Pourbaix diagram, as shown in **Figures 2.4** and **2.5**, can indicate when steel is likely to corrode based on insights of pore solution alkalinity of the concrete matrix and the value of electrode potential of the rebar which can indicate the occurrence of a reduction process that forms part of the corrosion process [41]. These Figures are originally adapted from [42] and simplified to indicate the corrosion state of steel reinforcement in concrete.

As shown in **Figure 2.5**, iron (Fe, the main element of steel) can be theoretically categorized into two major regions – where corrosion is likely to occur (areas of corrosion) and regions where corrosion is unlikely to occur (regions of passivation and regions of immunity) [41].

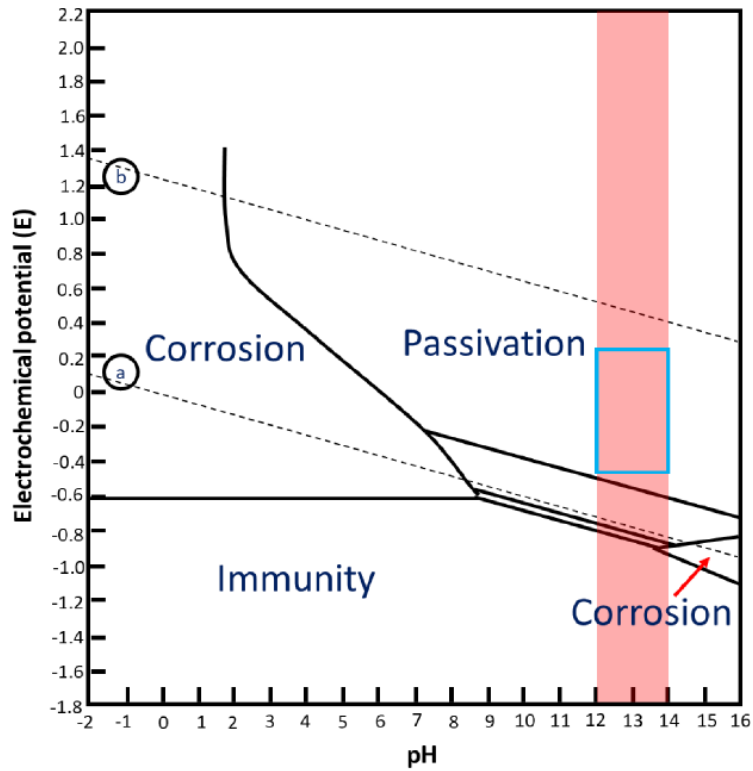


Figure 2.4 Theoretical conditions of corrosion, immunity and passivation of iron depicted through the Pourbaix diagram, at 25°C. The red area and the blue box denote normal pH values and electrode potentials in reinforced-concretes (in the absence of aggressive species) respectively [41].

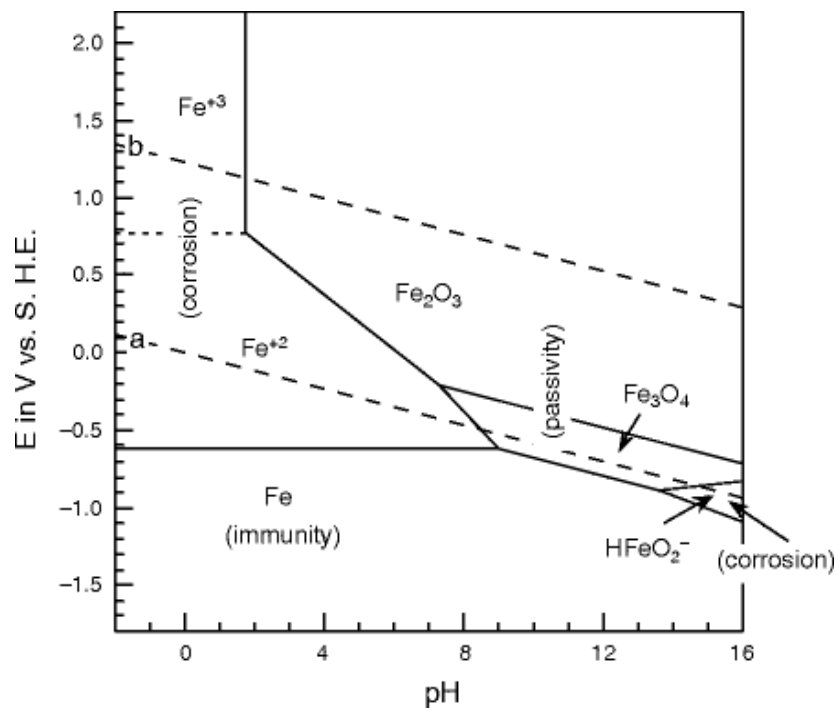


Figure 2.5 Pourbaix diagram for the iron-water system. Adapted from [43].

The following sections will focus on the concept of chloride threshold (CT) and the standardized tests used to detect the corrosion initiation of the rebar. These tests have been designed to calculate the value of chloride threshold which can be used to predict the service limit state of the infrastructure before the end of life [40].

2.6 Critical Chloride Threshold

One of the main concepts that has set the direction of corrosion research in reinforced concretes is the correlation between a certain concentration of chlorides in concrete and the onset of steel corrosion. That concept is now known as the chloride threshold value or the critical chloride content, termed as C_{crit} [44]. In **Figure 2.6**, Angst (2019) has schematically represented two parts for corrosion initiation where the first part is on the model that depicts the evolution of the chloride content at the surface of the rebar and the second part is on the comparison of the estimated value, obtained by the model, to the C_{crit} . The value of C_{crit} is relative to the type of binder used because the chemistry of the pore solution, responsible for forming the passive film around the steel rebar, will be altered. In addition, the steel potential, for the corrosion reaction, can be different for every type of embedded steel rebar [8]. Furthermore, Angst (2019) in his research has pointed out in **Figure 2.6** that the main parameters used for the model and C_{crit} are seen as deterministic, or single value, parameters but in reality both values could be in widely spread distributions [44].

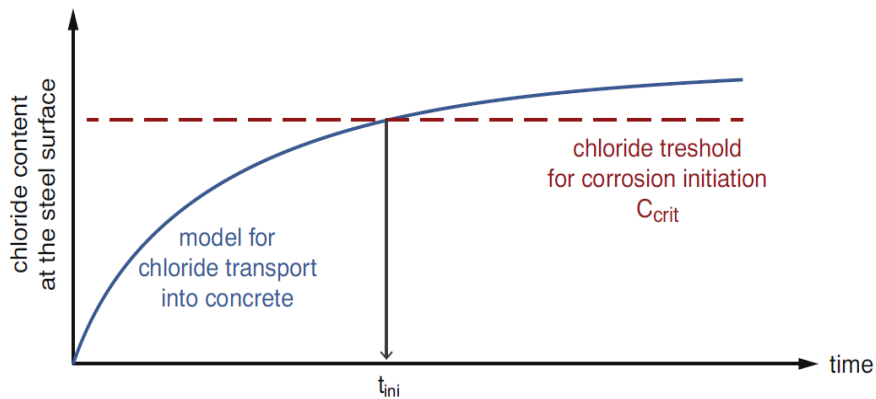


Figure 2.6 Schematic representation of the concept used for the prediction of corrosion initiation including two parts: 1) chloride content prediction at the level of the steel surface, and 2) critical chloride content for corrosion initiation, C_{crit} . [44].

The variations could be the result of different experimental methodology, in terms of specimen design and the experimental setup conditions that are used to determine the chloride transport properties and the chloride threshold [44]. Also, the definition used for corrosion initiation could vary in various testing techniques for steel bar corrosion [40, 44]. Additionally, corrosion initiation may not solely depend on the concentration of chloride ions but also on the concentration of other ionic species present in the pore solution [45]. Yet, C_{crit} remains a valuable parameter to use during the modelling of chloride ingress and the prediction of corrosion onset [46, 47]. It will also be used in this research for predicting service life of alkali-activated concretes until the point of corrosion initiation.

The following section describes some of the standard test methods used to assess steel corrosion in reinforced concrete.

2.7 Test Methods Used for the Detection of Steel Corrosion in Reinforced Concrete

The permeation of chloride ions and drop of alkalinity, as a result of carbonation, has led the ratio of free chloride ions to alkalinity of pore solution (i.e. Cl^-/OH^-) to be used as a corrosion risk indicator. In other words, it is used to calculate the concentration of critical chloride content (i.e. C_{crit}) needed to predict the likelihood of the onset of steel corrosion [40]. Several electrochemical techniques, including visual inspection, have been employed for the assessment of steel corrosion and estimation of the value of C_{crit} .

The first electrochemical technique is the half-cell potential (E_{corr} , mV_{SCE}) measurement with its procedure described in ASTM C876 [48]. This test can qualitatively identify the levels of steel corrosion by the following conditions: if E_{corr} is more positive than $-126 mV_{SCE}$ (vs. saturated calomel electrode (SCE)), the steel remains passive and if E_{corr} is more negative than $-276 mV_{SCE}$ than the steel is in an active corrosion developing stage. However, this test method is not suitable for slag-based AAMs (i.e. when slag is used as the main precursor of the binder) because there is still uncertainty and limited information about the state of the rebar when the measured value of E_{corr} is between -200 and $-350 mV_{SCE}$. The main cause of the misinterpretation is that slag precursors contain sulfide ions that can reduce the redox potential of the pore solution and maintain the steel in a passive state with the E_{corr} reaching much more negative values than those usually obtained as an indication of corrosion in PC based concrete [40]. Recently, Runci et al. [49] have proposed a value for E_{corr} of lower than $-400 mV_{SCE}$ to be the limiting value for distinguishing between active and passive states of steel in AAMs.

The second technique is linear polarization resistance (LPR) used to measure the corrosion rate (R_p) and estimate the value of the corrosion current density by **Equation 2.4**;

$$I_{\text{corr}} = \frac{\beta_a \beta_c}{2.3R_p(\beta_a + \beta_c)} = \frac{B}{R_p} \quad (2.4)$$

Where, B is the Stern-Geary constant with value ranging from 13 to 52 mV, β_a and β_c are anodic and cathodic constants. Andrade et al. [50] specified that I_{corr} can be utilized to assess the active and passive zones of the rebar when values for B are assumed to be 26 mV and 52 mV for corroding and passive steel states respectively. However, Babaei et al. [51] have reported that these reference values for PC are different for the case of alkali-activated binders. They suggested values for B to be between 13 and 20 mV for the passive steel state and B to be between 45 and 58 mV for the corroding steel state in the case of AAMs [51]. These values are within the ranges suggested by Runci et al. [49] where B between 15-25 mV corresponds to steel in a passive condition and B between 55-63 mV indicates that steel is in an active corroding condition.

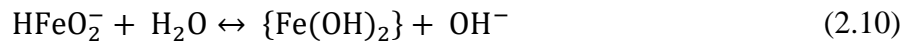
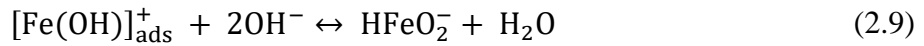
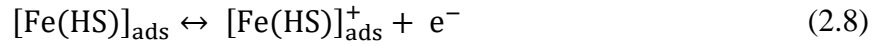
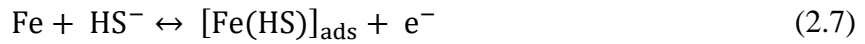
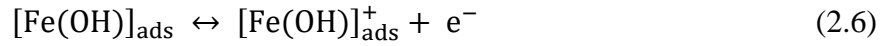
The third electrical technique is electrochemical impedance spectroscopy (EIS), a frequency based test where an alternating current is emitted and propagates through the concrete towards the rebar. The obtained result is an electrochemical impedance spectrum that can provide information around the polarization resistance, which is used to calculate the rate of steel corrosion [40].

The corrosion reactions can differ between low and high calcium based AAMs, and from the process seen in Portland cement based concrete, in a way that the chloride concentration may not solely play the dominant role because the interactions of steel with other pore solution ions can also have an impact [44, 52]. This is due to the high alkalinity of the pore solution in geopolymers, and the reduced sulfur species in pore solution of alkali-activated slag cements that can cause the formation of a sulfide film on the surface of the rebar, leading to a more complex corrosion reaction [44, 45]. The following sections describe the corrosion reaction mechanisms in high and low calcium based AAMs.

2.8 Mechanism of Steel Corrosion in AAMs

2.8.1 Corrosion of Steel in SG-Based AAMs

Mundra and Provis [45] have verified the complex passivation layer that forms on the steel surface in pore fluid conditions simulating SG-based AAMs to be Fe-S complexes instead of the usual iron oxide seen for the case of PC. In addition, they have described the formation of the passive layer and rust products as routes for the anodic peaks in their obtained cyclic voltammograms described in **Equations 2.5-2.10**. The chemical compounds placed between square brackets represent intermediate species and the chemical compounds in the curly braces represent species that may undergo changes upon aging.



In **Equation 2.7** the presence of HS^- in the alkaline pore solution of alkali-activated slag competes with OH^- , in **Equation 2.5**, for adsorption on the surface layer of the steel, and forms adsorbed layers of $[\text{Fe(HS)}]_{\text{ads}}^+$ and $[\text{Fe(OH)}]_{\text{ads}}^+$ according to **Equations 2.8** and **2.6**, respectively. Next, in the presence or absence of HS^- , $[\text{Fe(OH)}]_{\text{ads}}^+$ species, in **Equation 2.9**, converts to Fe(OH)_2 as a final corrosion product [45].

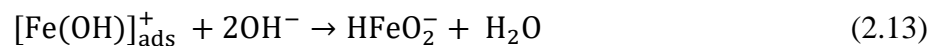
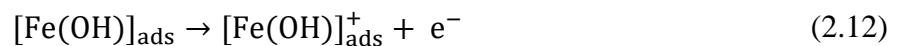
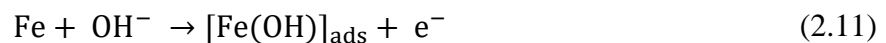
In addition, Mundra and Provis [45] have proposed another novel relationship for the onset of corrosion and that it is not dependent on chloride ion concentration. They conducted experiments where they have exposed the steel specimens to simulated pore solutions of alkali-activated slag with varying $[\text{HS}^-]/[\text{OH}^-]$ and alkalinity (from 0.8 to 1.36 M) with the steel specimen kept in saturated conditions with respect to sodium chloride solution (NaCl). They have deduced that corrosion initiation would occur when the steel is exposed to a pore solution containing a concentration ratio of HS^- to OH^- ranging between 0.007 and 0.1125. However, Mundra and Provis have noted that the actual pore solution of alkali-activated slag was for $[\text{HS}^-$

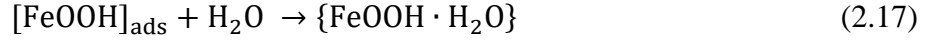
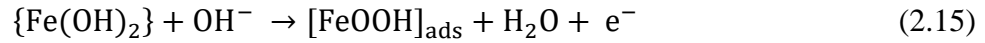
$]/[\text{OH}^-] \geq 0.33$ and that corrosion did not take place at any chloride concentration in the simulated pore fluid experiments under these conditions [45].

Mangat et al. [53] have investigated their exposed alkali-activated concretes to accelerated corrosive conditions for 1750 days and obtained the C_{crit} in terms of Cl^-/OH^- concentration ratio in a range of 2.1 to 2.8. The implemented experimental conditions contained multiple wetting and drying cycles to attain levels of oxygen, chloride and temperature enough for initiating steel corrosion within their research time frame of 1750 days [53]. Hence, the difference between this exposure condition and the simulated pore solution used by Mundra and Provis [45] is the lack of extra amount of dissolved oxygen, in the latter case, that diffuses from the environment into the capillary pores of the concrete. The quantity of available dissolved oxygen at the steel and pore solution interface plays an essential role in the formation of passive layer around the reinforcement and can also impact the extent of corrosion reaction [45].

2.8.2 Corrosion of Steel in Low Calcium Based AAMs

Mundra et al. [54] obtained a novel relationship for predicting the onset of corrosion as a function of the high alkalinity pore solution found in low-Ca AAMs (not containing sulfide). In terms of C_{crit} , $[\text{Cl}^-]/[\text{OH}^-]^3 = 1.25$ is the power law relationship that can predict corrosion pitting as a function of the alkalinity of the pore solution. In addition, they have also described the formation of the passive layer and rust products in low Ca-based AAMs according to **Equations 2.11-2.14**. Where the passivation layer is the formation of $[\text{Fe}(\text{OH})]_{\text{ads}}$ that can change into $[\text{Fe}(\text{OH})]_{\text{ads}}^+$ and the amount is dependent on the concentration of OH^- in the pore solution. Also in concentrated alkaline solution ($\text{pH} > 14$) the $[\text{Fe}(\text{OH})]_{\text{ads}}^+$ changes to HFeO_2^- ions which undergoes a hydrolysis reaction to form $\text{Fe}(\text{OH})_2$, according to **Equation 2.14**. Furthermore, $\{\text{Fe}(\text{OH})_2\}$ in concentrated alkaline solution can change into a film layer of $[\text{FeOOH}]_{\text{ads}}$ and upon aging can be transformed into two types of rust product that are $\text{Fe}_2\text{O}_3 \cdot \text{H}_2\text{O}$ and $\text{FeOOH} \cdot \text{H}_2\text{O}$, according to **Equations 2.15-2.17** [54].





2.8.3 Critical Chloride Thresholds in AAMs

In literature, C_{crit} is most commonly expressed in terms of % total chloride content relative to the weight of the unhydrated cement, %TotalCl/cem. Babae and Castel [55] identified steel depassivation during a corrosion test on reinforced alkali-activated mortars, having been submerged in a 3.5 wt.% NaCl solution for a period of nine months, and measured the chloride content at the interface between the steel and cementitious matrix. The protocol used to measure the chloride content is found in the ASTM C1152 technique [13] used to measure acid-soluble chloride in mortar and concrete. Thus, Babae and Castel [55] measured C_{crit} in terms of %TotalCl/cem because acid soluble chloride represents the total chloride content present in the cementitious matrix. However, this chloride content was initially present as free ions in the pore solution due to the absence of chloride binding to the cement hydrates of the alkali-activated mortars reported by Babae and Castel [55]. Additionally, the C_{crit} is reported in terms of wt.% of binder by taking into account the amount of fly ash and slag precursors with the anhydrous part of the activator present in the alkali-activated mortars. Furthermore, Babae and Castel [55] obtained the C_{crit} values for a mix of alkali-activated mortars activated by sodium hydroxide with sodium silicate solution and by sodium hydroxide+potassium hydroxide with sodium silicate solution. In the case of sodium hydroxide with sodium silicate solution activator, the C_{crit} obtained for Fly ash dominated samples (75% fly ash and 25%) was between 0.341 and 0.692 of Cl in wt.% by binder mass. The values obtained for mixture of slag and fly ash (50% fly ash and 50% slag) was between 0.335 and 0.436 of Cl in wt.% by binder mass. The values obtained for slag dominated samples (75% slag and 25% fly ash) was between 0.19 and 0.30 of Cl in wt.% by binder mass. The reason for the variation of C_{crit} was due to the alkali dosage and silica modulus used in the mix design of the activating solution. The samples activated with a solution containing higher alkali dosage and silica modulus had higher C_{crit} than the samples activated with a solution containing lower alkali dosage and silica modulus. As for the one case of Fly ash dominated sample activated by sodium hydroxide+potassium

hydroxide with sodium silicate solution, the measured C_{crit} values varied between 0.511 and 0.548 of Cl in wt.% by binder mass. These values are higher than the ones obtained for the fly ash dominated sample activated by sodium hydroxide with sodium silicate solution. However, the values obtained for the fly ash dominated samples are beyond the values suggested for geopolymers found in [40] that range between 0.2 and 0.4 wt.% of the binder.

Moreover, C_{crit} has been expressed in the literature in terms of the percentage of free chloride in the cement (%FreeCl/cem) which depicts the amount free chloride ions present in the pore solution that is primarily responsible for the corrosion initiation. In addition, C_{crit} is expressed in terms of the chloride concentration to the hydroxide concentration ($[Cl^-]/[OH^-]$) of the concrete pore solution. This definition is often used to identify the condition of the pore solution for corrosion to occur in reinforced concrete.

The following **Table 2.1** summarizes the values of C_{crit} , expressed in different forms and determined by different test methods, for low and high calcium based AAMs.

Table 2.1 List of C_{crit} values obtained for low and high Ca-AAMs.

Type of Cement	Corrosion Test Method	C_{crit}	Ref.
Low Ca-AAM	Linear Polarization Resistance measurements of steel exposed in simulated pore solution with different $[Cl^-]/[OH^-]$ concentration ratios.	$[Cl^-]/[OH^-]^3=1.25$	[54]
High Ca-AAM	Corrosion potential and corrosion current density measurements of concrete exposed to corrosion inducing conditions for 1750 days	$2.1 < [Cl^-]/[OH^-] < 2.8$	[53]
High Ca-AAM	Linear Polarization Resistance measurements of steel exposed in simulated pore solutions with different $[Cl^-]/[OH^-]$ ratios	$0.007 < [HS^-]/[OH^-] < 0.1125$	[45]

In this thesis, the prediction of service life for alkali-activated concretes is based on C_{crit} in terms of $[Cl^-]/[OH^-]$. This is to account only for the concentration of free chlorides responsible for corrosion initiation. Thus, values in the first two rows of **Table 2.1** will be used to estimate the serviceability limit state of low and high calcium based alkali-activated concretes in **Chapter: 6**.

The ingress of chloride ions and CO_2 in the concrete matrix is dependent on the degree of pore solution saturation and flow of moisture through the interconnected capillary pores, towards

the rebar, during drying and wetting conditions. The following section discusses moisture transport and degree of pore solution saturation across the porous cementitious material where both mechanisms are dependent upon the external relative humidity (RH).

2.9 Moisture Transport in Cement Based Materials

Conventionally, moisture transport in cementitious materials was modelled based on Darcy's or Fick's law to predict the moisture state or the degree of saturation of pores inside the concrete matrix [56-58]. However, anomalous moisture transport properties of Portland and blended cement-based materials have been reported in the literature [59-63]; this means that the water sorption measurements of cement-based materials, on a long timescale, have shown that the mass change versus square root of time ($t^{0.5}$) does not follow a linear relation that depicts the behaviour of a Fickian process [60]. In addition, Hall [59] noted that the absorption behavior of water by Portland cement mortars has deviated progressively below the $t^{1/2}$ line, but when tested with an organic liquid (n-decane) the adsorption has followed the $t^{1/2}$ line as shown in **Figure 2.7** [60].

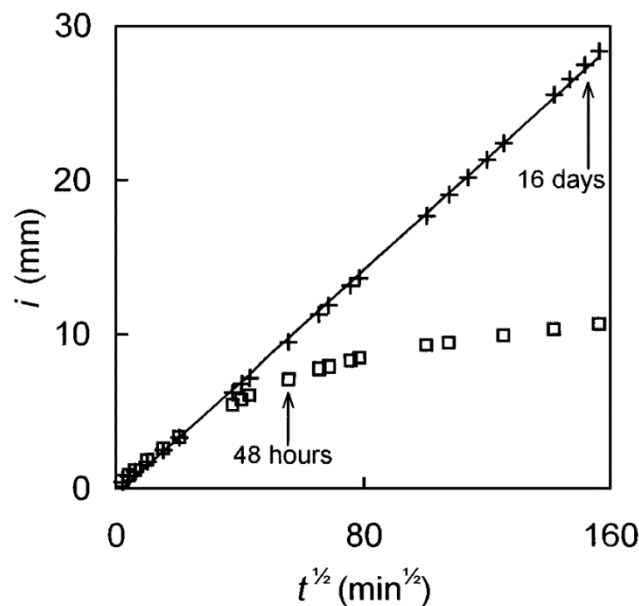


Figure 2.7 Long-term cumulative capillary absorption i versus $t^{1/2}$ for water and n-decane into a mortar 1:2 Portland cement:sand by weight, 0.4 water:cement ratio by weight, cured under water for 28 days, dried at 40 °C for 24 h and then at 105 °C to constant weight [60]. White box symbol; water and black cross symbol; n-decane.

In addition, Ren et al. [64] have noted in their study that the mass change versus $t^{0.5}$ curve for the water absorption process of cement-based materials has two linear stages. The first one

follows the conventional single-porosity model, while the second deviates from the first, which is why such a mass change curve is called anomalous. One of the main reasons for the deviation from the square root of time law is because of the effect of the continuous swelling of the C–S–H gel because of its hygroscopic nature. Consequently, this expansion effect during capillary absorption will make cement-based materials elongate at a macroscopic scale, change the pore structure, and gradually slow down the rate of water absorption [64] [60] [62].

Furthermore, the hysteresis, or the anomaly effect, can delay the diffusion of moisture and make it difficult for the moisture equilibrium state to be reached during drying or wetting stages. Several authors have suggested the reason for the hysteresis can be due to rehydration and/or dehydration of the cement hydrates (which changes the microstructure of the cement) and the heterogeneous microstructure of the cement due to the existence of a wide range of pore sizes [65-68]. The scanning electron microscope (SEM) images in **Figure 2.8** show the complex microstructure of AAMs made of varying compositions of fly ash (FA) and slag (SG).

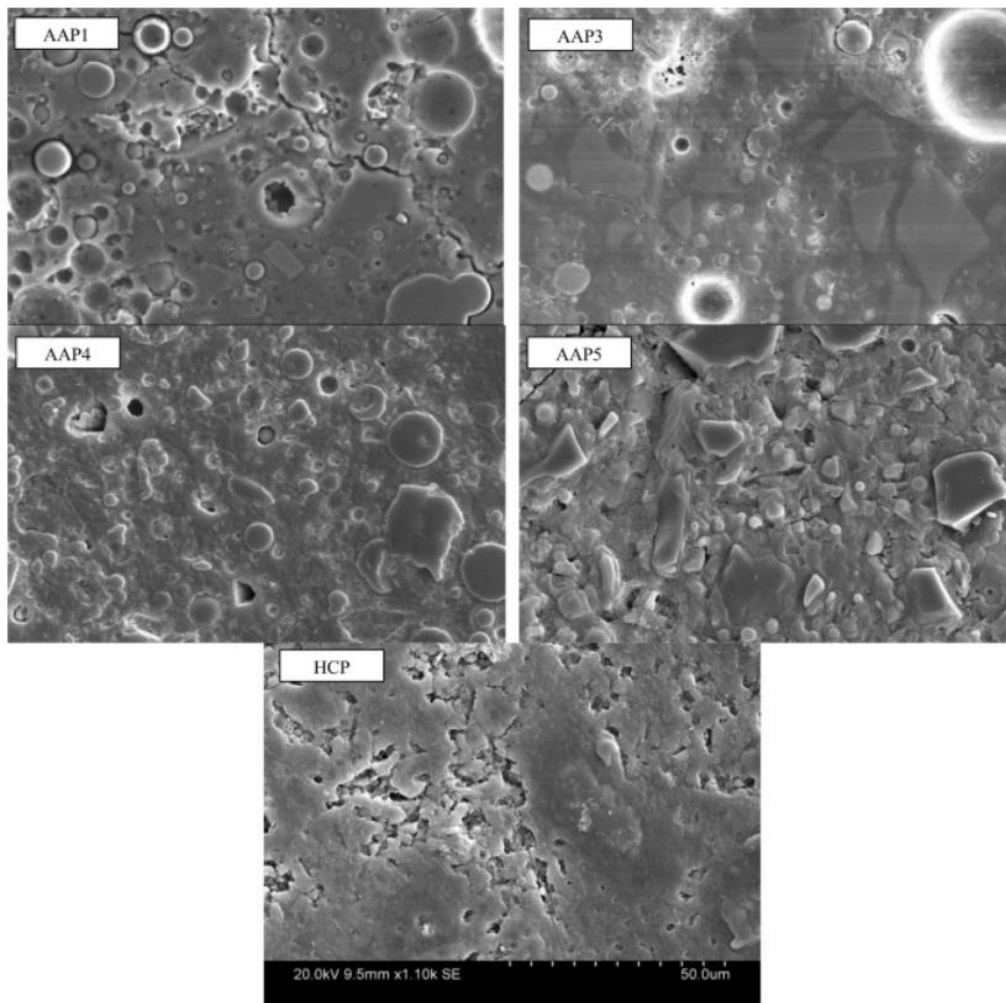


Figure 2.8 SEM micrographs of alkali-activated and cement paste samples (magnification level is the same for all micrographs) [69]. Where: AAP1:90%FA+10%SG, AAP3:50%FA+50%SG, AAP4:75%FA+25%SG, AAP5:25%FA+75%SG, and HCP:100%PC.

Therefore, advanced mathematical models are needed to be implemented to predict the saturation profile in a concrete matrix – AAC or conventional PC – by taking into account the complex microstructure of the cementitious binder. The following section describes the empirical equations and predictive models used to predict the degree of saturation and saturation profile in cements as a function of external RH.

2.10 Fundamental Relations

2.10.1 Degree of Saturation

Concrete is considered to be a porous material that can be fully or partially filled with liquid water. This level of liquid water is dependent on the relative humidity (RH) of the environment and effective porosity (i.e. connected pores) of the material. The concrete is considered to be fully saturated only when the effective pores are filled with water and partially saturated when part of these pores is occupied by the gas phase. The relation between the degree of water saturation, S , and pore volume of the material is introduced by **Equation 2.18**.

$$S = \frac{V_l}{V_p} \quad (2.18)$$

V_l ; Water volume fraction

V_p ; Void volume

Another equation used to assess the degree of saturation is with the use of effective porosity according to Equation 2.19.

$$S = \frac{\phi_l}{\phi} \quad (2.19)$$

Where the effective porosity, ϕ , may contain both liquid phase, ϕ_l , and gaseous phase ϕ_g based on **Equation 2.20** :

$$\phi = \phi_l + \phi_g \quad (2.20)$$

Relation between relative humidity and degree of saturation

Water vapor sorption isotherms (WVSIs), measured by experiments and/or Dynamic Vapor Sorption (DVS) instruments, are determined to correlate the external relative humidity to amount of evaporable water, also known as free and unbounded water in the cement sample at constant temperature [70]. For the prediction of degree of saturation, moisture transport models utilize the relation between capillary pressure, P_c , and degree of saturation. The following **Equation 2.21** is employed for the conversion of evaporable water, θ , to S .

$$S = \frac{\theta - \theta_r}{\theta^{\max} - \theta_r} \quad (2.21)$$

θ ; evaporable water content at certain relative humidity

θ_r ; water content at dry reference state

θ^{\max} ; water content at saturated state

The Kelvin equation [71], **Equation 2.22**, is used to convert the value of relative humidity to capillary pressure:

$$P_c = -\frac{\rho_l RT}{M_v} \ln RH \quad (2.22)$$

ρ_l ; liquid water density 997 kg.m⁻³.

R ; gas constant, 8.314 Pa.m³.K⁻¹.mol⁻¹.

T ; absolute temperature, 293.15 K

M_v ; molar mass of the water molecule, 0.018 kg.mol⁻¹

RH ; relative humidity, as a fraction

2.10.2 Models for Isotherms

Several models were studied by Zhang et. al [70] to predict the degree of saturation at a certain relative humidity. Most of the studied models were obtained from the field of geology and used to predict moisture transport in soil systems, but have also been validated for studies of cementitious materials. A brief description of each model is presented in the following section.

2.10.2.1 Feng and Fredlund's model

This model (FF) is an empirical relationship which was used to fit WVSIs for a ceramic material by the following **Equation 2.23** [72]:

$$S = \frac{a_F}{a_F + P_c^{b_F}} \quad (2.23)$$

Where the two parameters, a_F , in Pa, and b_F , dimensionless, are determined by means of curve fitting the adsorption and desorption isotherms. However, this model cannot be applicable for

the cementitious materials because of the effect of C-S-H swelling in high humidity conditions [73].

2.10.2.2 Van Genuchten's model

The Van Genuchten model (VG) is used to predict the degree of water saturation in soil using the following S-shaped curve **Equation 2.24** [74]:

$$S = \left[\left(1 + \left(\frac{P_c}{a} \right)^n \right) \right]^{-m} \quad (2.24)$$

Where a , in Pa, m and n , dimensionless, are three empirical parameters obtained by curve fitting the WVSIs. In addition, the above equation has been simplified into a two parameter equation by the use the of following relation, **Equation 2.25**, for shape parameters [74]:

$$m = 1 - 1/n \quad (2.25)$$

2.10.2.3 Fredlund and Xing's Model

Fredlund and Xing's Model (FX) is based on the Van Genuchten model to account for the pores in the high capillary pressure region, according to **Equation 2.26** [75]:

$$S = \left[\ln \left[e + \left(\frac{P_c}{a_x} \right)^{n_x} \right] \right]^{-m_x} \quad (2.26)$$

e ; Euler number (2.71828, a mathematical constant)

2.10.2.4 The Kosugi Model

The Kosugi model (KM) includes a lognormal pore size distribution function in the following **Equation 2.27** [76];

$$S = Q \left(\sigma^{-1} \ln \frac{P_c}{P_{cm}} \right) \quad (2.27)$$

P_{cm} ; capillary pressure, Pa, related to the median pore radius

σ ; standard deviation of log-transformed pore radii; related to the width of the pore size distribution

Q ; complementary normal distribution function as defined by **Equation 2.28**;

$$Q(x) = (2\pi)^{-1/2} \int_x^{\infty} \exp\left(\frac{-x^2}{2}\right) dx \quad (2.28)$$

2.10.2.5 Multimodal model

The multimodal model (Multi) is written as **Equation 2.29** [70]:

$$S = \sum_{i=1}^N w_i S_i(P_c) \quad (2.29)$$

N ; the number of pore systems

w_i ; ranging between 0-1 is the weighing factor characterizing the pore system i and $w_i S_i$ represents the water content contribution of pore system i to the total water content in the material. For instance, when $n=2$ then **Equation 2.29** becomes a bimodal model. An example of the use of the bimodal model is when Zhang and Angst [62] applied the VG equation for the small and large pore regions of the cement paste as will be explained in section 2.10.3.3.2 .

2.10.3 Moisture Transport Models

2.10.3.1 Darcy's Model

The most commonly used moisture transport model is Darcy's law for flow in a saturated matrix, according to **Equation 2.30** [77].

$$J_l = -\rho_l \frac{K}{\eta} \nabla P_l \quad (2.30)$$

J_l ; liquid flux ($\text{kg}\cdot\text{m}^{-2}\cdot\text{s}^{-1}$)

ρ_l ; density of the liquid water ($\text{kg}\cdot\text{m}^{-3}$)

k ; liquid permeability (m^2)

η ; dynamic viscosity of liquid water, 0.001 Pa.s

P_l ; liquid pressure, Pa

2.10.3.2 Buckingham model

The Buckingham law [78] is a modified version of the above Darcy moisture transport equation and accounts for unsaturated conditions by the following **Equation 2.31**:

$$J_l = -\rho_l k_{rl} \frac{K_l}{\eta} \nabla P_l \quad (2.31)$$

k_{rl} ; relative permeability that is a function of liquid water saturation

The van Genuchten-Mualem equation [74] is used to model the relative permeability as a function of the degree of saturation according to the following **Equation 2.32**:

$$k_{rl}(S) = S^{0.5} [1 - (1 - S^{1/m})^m]^2 \quad (2.32)$$

2.10.3.3 The single-porosity model

2.10.3.3.1 The S-Based form of Richards' Equation

Zhang et al. [79] have modeled the moisture transport in cement pastes based on a diffusion approach with an apparent diffusion coefficient that combines water vapor and liquid water in the moisture transport. The state variable in the model is the moisture content in which the degree of saturation, S , has been chosen. The model is the S-based form of Richards' equation according to **Equation 2.33** that is also based on Fick's second law of diffusion:

$$\frac{\partial S}{\partial t} = D_a \frac{\partial^2 S}{\partial x^2} \quad (2.33)$$

The apparent moisture diffusion coefficient, D_a in $m^2 \cdot s^{-1}$, is the sum of the liquid water and water vapour diffusivities, D_l and D_v , which are modelled based on **Equations 2.34** and **2.35**. This is because moisture transport in an unsaturated porous medium is governed by the transport of three phases: liquid water, water vapour and dry air. However, dry air is neglected because it contributes the least to the mass transport [80]. Thus, **Equations 2.34** and **2.35** are combined, with the assumption of equilibrium between liquid water and water vapour [79], to include the contributions of both phases in the moisture transport represented by the parameter D_a in **Equation 2.33** [79].

$$D_l(S) = -k_{rl} \frac{K_l}{\phi \eta} \frac{\partial P_c}{\partial S} \quad (2.34)$$

$$D_v(S) = - \left(\frac{M_v}{\rho_l RT} \right)^2 D_{v0} f(S, \phi) \frac{P_{vs} \phi}{\phi} \frac{\partial P_c}{\partial S} \quad (2.35)$$

P_{vs} ; saturated vapor pressure at 20°C, 2338.54 Pa

M_v ; Molar weight of water, 0.0018 (kg/mol)

R ; universal gas constant, 8.3144 (Pa.m³.K⁻¹.mol⁻¹)

T ; absolute temperature (K), 20°C ≡ 293.15 K

ϕ ; Relative humidity

P_c ; Capillary pressure (Pa)

η ; dynamic viscosity of liquid water, 0.001 Pa.s at 20°C

Where the capillary pressure is a function of the degree of saturation according to the following

Equation 2.36;

$$P_c(S) = a(S^{-\frac{1}{m}} - 1)^{\frac{1}{n}} \quad (2.36)$$

a ; air entry flow pressure (Pa)

m and n ; shape factors for the sorption isotherm and $n = \frac{1}{1-m}$

Where $\frac{\partial P_c}{\partial S}$ factor in the liquid and vapour diffusivities is the derivative of the capillary pressure (P_c) with respect to degree of saturation (S) according to **Equation 2.36.i** adapted from [81].

$$\frac{\partial P_c}{\partial S} = -\frac{a}{nm} S^{\left(\frac{-1}{m}-1\right)} \times \left(S^{\left(\frac{-1}{m}\right)} - 1\right)^{\left(\frac{1}{n}-1\right)} \quad (2.36.i)$$

The transport of water vapor is governed by the effective water vapor diffusion coefficient, D_{ve} , in the porous medium by the following **Equation 2.37;**

$$D_{ve}(S) = D_{v0} \cdot f(S, \phi) \quad (2.37)$$

D_{v0} ; free vapor diffusion coefficient in the air, 2.47×10^{-5} (m².s⁻¹) between 20°C and 25°C [82].

f ; resistance factor of the pore network for gaseous diffusion

The Millington equation is used to calculate the diffusion in porous materials as a function of saturation state and tortuosity that is a microstructural property of the material [83]. This equation is further refined in [84] where the equation for the resistance factor, which takes into account the effect of liquid water saturation and tortuosity of the cementitious material, is obtained according to **Equation 2.38**:

$$f(S, \phi) = \phi(1 - S) \cdot \phi^{x_D-1}(1 - S)^{x_D+1} \quad (2.38)$$

x_D ; material parameter, constant value of 2.74

$\phi(1 - S)$; space available for vapor diffusion

$\phi^{x_D-1}(1 - S)^{x_D+1}$; description of tortuosity and connectivity effects

Zhang et al. [79] have set x_D to a value of 2.74 based on the experimental data, found in the literature, on the diffusion properties of CO₂ and O₂ into concrete and mortar test samples.

In general, K_1 and x_D are two fitting parameters in the apparent diffusion coefficient. The effects of the permeability K_1 and x_D can be easily separated in most ranges of RH. This point is very important to take into consideration when discussing the dominant contributing factor for each D_l and D_v at a certain relative humidity, RH. For example, in the high RH range the liquid transport coefficient is prominent, whereas vapor diffusion plays a key role in the low RH range. In addition, there is a very narrow range in which both D_l and D_v have comparable influences on moisture transport.

In this research, all available measured curves of D_a as a function of degree of saturation are fitted by means of the equations for D_v and D_l to obtain the intrinsic permeability factor, K_1 , and the material parameter, x_D .

2.10.3.3.2 The dual-porosity moisture transport model

Zhang and Angst [62] have considered that hydrated cement paste can be viewed as a dual-porosity material with two pore size regions, the large pore region and the small pore region. They assumed that pores in each region are well connected, meaning that fluids can move in each region, as well as communicate between the two regions [62]. The volumetric fraction of the large pore region, w_f , was obtained when the Van Genuchten (VG) equation has been applied for each porosity region to obtain a bimodal equation (i.e. VG-Dual) according to **Equation 2.39.a** [62]:

$$S = w_f \left[1 + \left(\frac{P_c}{\alpha_l} \right)^{\frac{1}{1-m_l}} \right]^{-m_l} + (1 - w_f) \left[1 + \left(\frac{P_c}{\alpha_s} \right)^{\frac{1}{1-m_s}} \right]^{-m_s} \quad (2.39.a)$$

Where l and s stand for large and small pores respectively.

In addition, the shape parameters m_l and m_s have been considered as a single constant value such that $m_l = m_s = m$ and is set as 0.45 for Portland cement binders [70]. However, in this research the shape parameters m_l and m_s are also set as a single value “m” but it is determined by fitting the WVSIs of AAMs with **Equation 2.39.a**. Additionally, **Equation 2.39.a** also represents the sum of degree of saturation in large and small pore regions of the cement as interpreted by **Equation 2.39.b**.

$$S = w_f S_l + (1 - w_f) S_s \quad (2.39.b)$$

The porosities attributed to the large and small pore regions are calculated by **Equations 2.40** and **2.41**;

$$\phi_l = w_f \phi \quad (2.40)$$

$$\phi_s = (1 - w_f) \phi \quad (2.41)$$

ϕ ; total porosity of the material

ϕ_l ; porosity in the large pore region

ϕ_s ; porosity in the small pore region

The moisture diffusivities in the large and small pore regions of the cement are combined with the contribution factor of the large pore region to the moisture transport (i.e. $w_{f,D}$) as shown in **Equation 2.42** to calculate the overall apparent moisture diffusivity parameter D_a used in **Equation 2.33**. Note that $w_{f,D}$ is not the same parameter as w_f (i.e. the volumetric fraction of the large pore region in cement) implemented in **Equation 2.39 a+b**.

$$D_a = w_{f,D} D_{a,l} + (1 - w_{f,D}) D_{a,s} \quad (2.42)$$

Zhang and Angst [62] have also modified the Richards equation into a coupled partial differential equation according to **Equations 2.43-2.46**. Where, **Equations 2.44** and **2.46** are

implemented in **Equations 2.43** and **2.45** to simulate the moisture transport in large and small pore regions of the cement respectively.

$$\frac{\partial S_l}{\partial t} = \frac{\partial}{\partial x} \left(D_{a,l} \frac{\partial S_l}{\partial x} \right) + \frac{\Gamma_\omega}{\rho_w \phi w_f} \quad (2.43)$$

$$D_{a,l} = -k_{r,l} \frac{K_{w,l}}{\phi_l n} \frac{\partial P_{c,l}}{\partial S_l} - \left(\frac{M_v}{\rho_w RT} \right)^2 D_{v0} f_l \frac{P_{VS} \phi_l}{\phi_l} \frac{\partial P_{c,l}}{\partial S_l} \quad (2.44)$$

$$\frac{\partial S_s}{\partial t} = \frac{\partial}{\partial x} \left(D_{a,s} \frac{\partial S_s}{\partial x} \right) - \frac{\Gamma_\omega}{\rho_w \phi (1 - w_f)} \quad (2.45)$$

$$D_{a,s} = -k_{r,s} \frac{K_{w,s}}{\phi_s n} \frac{\partial P_{c,s}}{\partial S_s} - \left(\frac{M_v}{\rho_w RT} \right)^2 D_{v0} f_s \frac{P_{VS} \phi_s}{\phi_s} \frac{\partial P_{c,s}}{\partial S_s} \quad (2.46)$$

Γ_ω ; Mass exchange between two porosity regions

subscripts l and s; relate to the large and small pores of cementitious material respectively

In addition, the equation of the resistance factor of the pore network for gaseous diffusion in large and small pore regions (i.e. f_l and f_s) is the same as **Equation 2.38** (i.e. $f(S, \phi)$) but based on the degree of saturation (i.e. S_l and S_s) and porosity (ϕ_l and ϕ_s) in each pore region [62].

The linear and nonlinear mass transfers between the large and small pores have been studied in the literature for fractured media. It has been shown that the linear mass exchange was able to accurately represent the mass exchange between two porosity regions according to [85]. The following **Equation 2.47** describes the linear mass exchange between the two porosity regions and is also included in the moisture transport in large and small pore regions.

$$\Gamma_\omega = \beta_w (\phi_s - \phi_l) \quad (2.47)$$

β_w ; first order rate coefficient ($\text{kg} \cdot \text{s}^{-1} \cdot \text{m}^{-3}$)

β_w is generally assumed to be dependent on the geometry of the small pore region, the length scale of the large pores region and permeability at the interface of two regions [85, 86]. For concrete, Smyl et al. [87] have considered β_w to be a function of the liquid conductivity in two

porosity regions. Zhang and Angst [62] then simplified the relation as the following **Equation 2.48**. In addition, Zhang and Angst (2020) [62] determined the moisture transfer factor, ξ , by fitting the mass change curve measured during drying/wetting tests, to be 10^{-3} .

$$\beta_w = \xi k_{r,l} k_{r,s} \quad (2.48)$$

ξ ; moisture transfer factor ($\text{kg} \cdot \text{s}^{-1} \cdot \text{m}^{-3}$)

$k_{r,i}$; relative liquid permeability, i ; l, s where l is for the large pore region and s for the small region.

2.10.3.3.3 *The mechanistic model*

Scheffler et al. [88] have utilized the following moisture transport model, **Equation 2.49**, and have considered the pore size distribution of cement, obtained from the derivative of the moisture storage function, in the relative liquid permeability factor, $K_l(S)$. They have also considered vapor resistant factor, $f_v(\theta)$, in the vapor diffusion, $D_v(S)$, by a different form of equation as shown in **Equation 2.50**.

$$D_a = -\frac{K_l(S)}{\phi \eta} \frac{\partial P_c}{\partial S} - \left(\frac{M_v}{\rho_w RT} \right)^2 D_v(S) \frac{P_{VS} \phi}{\phi} \frac{\partial P_c}{\partial S} \quad (2.49)$$

Where, $D_v(S)$ is a function of the moisture content according to **Equation 2.50** and $K_l(S)$ is also a function of the saturation degree according to **Equations 2.54** and **2.55** [88]:

$$D_v(\theta, T) = \frac{D_{v,air}(T)}{\mu_{dry}} f_v(\theta) = \frac{D_{v,air}(T)}{\mu_{dry}} \left[\frac{1 - \left(\frac{\theta}{\phi} \right)}{\left(\frac{\theta}{\phi} \right)^{n_{sp}} + \left(1 - \frac{\theta}{\phi} \right)^2 \cdot \left(1 - \left(\frac{\theta}{\phi} \right)^{n_{sp}} \right)} \right] \quad (2.50)$$

θ ; moisture content $\left(\frac{\text{Volume of liquid, m}^3}{\text{Volume of solid, m}^3} \right)$

ϕ ; porosity $\left(\frac{\text{Volume of pore, m}^3}{\text{Volume of solid, m}^3} \right)$

$f_v(\theta_1)$; scaling function for vapour diffusion

The relative moisture content also known as the degree of saturation is the ratio of the moisture content, θ , and porosity, ϕ , as shown in **Equation 2.51**.

$$S = \frac{\theta}{\phi} \quad (2.51)$$

Therefore, **Equation 2.50** can be rewritten in the form of **Equation 2.52**:

$$D_v(S) = \frac{D_{v,air}(T)}{\mu_{dry}} \left[\frac{1 - S}{(S)^{n_{sp}} + (1 - S)^2 \cdot (1 - S^{n_{sp}})} \right] \quad (2.52)$$

μ_{dry} ; vapour diffusion resistance factor, 13.5 (dimensionless), and is used to define the reduction of vapour diffusivity in air, $D_{v,air}(T)$, for the cementitious material. This value is determined from dry-cup test where water vapour transport is the only type of mass transport occurring while the cement sample is exposed to a very low relative humidity environment [88]. More information on the experimental set up can be found in [82] .

n_{sp} ; a shape parameter that accounts for the serial-parallel connectivity of the pores in the cement. It is material dependent and is determined from the measured data obtained by the dry-cup test [88].

$D_{v,air}(T)$; vapour diffusivity in air is expressed as a function of temperature and pressure according to **Equation 2.53** obtained from [89].

$$D_{v,air} = 0.083 \frac{P_0}{P} \left(\frac{T}{273.15} \right)^{1.81} \quad (2.53)$$

P_0 ; Reference gas pressure of 101,325 Pa

T ; ambient temperature (K)

The liquid moisture flow can be expressed by two ways as shown in **Equations 2.54** and **2.55**, where **Equation 2.54** is used when the sample is submerged in water and **Equation 2.55** is used when the sample is exposed to wetting and drying cycles.

$$K_l(S) = K_{l,sat}(S) \quad \text{sample under submerged conditions} \quad (2.54)$$

$$K_l(S) = K_{l,hyg}(S) + n_{cap} K_{eff} f_l(S) K_{l,rel}(S) \quad \text{if } S \leq 1 \quad (2.55)$$

n_{cap} ; a scaling parameter used to adjust the liquid permeability factor when the sample is exposed to a high relative humidity environment. This value is determined from a wet-cup test where moisture diffusion (including vapour and liquid) is considered to be the mass transport occurring while the cement sample is exposed to a high relative humidity environment [88]. More information on the experimental setup can be found in [82].

$K_{l,hyg}(\theta_1)$; is the liquid permeability in hygroscopic conditions at extremely low RH condition, according to **Figure 2.10**. The value is relatively less important in a practical sense because concrete structures are not exposed at such low RH conditions in real service conditions [90].

K_{eff} ; effective liquid permeability used to describe the liquid flow in the sample with pores mainly filled with liquid water.

$f_l(S)$; scaling function for liquid flow as shown in **Equation 2.56**.

$$f_l(S) = \left[\frac{S^{n_{sp}}}{(S)^{n_{sp}} + (1 - S)^2 \cdot (1 - (S)^{n_{sp}})} \right] \quad (2.56)$$

$K_{l,rel}$; is a parameter that contains information on the pore structure of the porous media [18].

The relative conductivity function $K_{l,rel}(S)$ is numerically determined by implementing **Equation 2.57** and using information on the pore structure obtained from the moisture storage function, $S(pC)$, presented as **Equation 2.58** [18, 88].

$$K_{l,rel}(S) = \left[\frac{\int_0^S P_c(s)^{-1} ds}{\int_0^1 P_c(s)^{-1} ds} \right]^2 \quad (2.57)$$

Initially, pC , in the moisture storage function, is taken as log of the capillary pressure P_c according to [88]. However, a quantity should be dimensionless to implement the natural log [91]. Hence, pC is implemented, in this research, as $\log(P_c/P_{ref})$ where $P_{ref} = 1$ Pa. Next, **Equation 2.58** is implemented to determine the moisture storage function [88].

$$S(pC) = \sum_{i=1}^N \left[\frac{\Delta\theta_i}{\sqrt{2}} \left(1 + \operatorname{erf} \left(\frac{pC_i - pC}{\sqrt{2}s_i} \right) \right) \right] \quad (2.58)$$

An illustration of the parameters contained in **Equation 2.58** is shown in **Figure 2.9** where the moisture content, θ_1 , is plotted as a function of pC . Additionally, the parameters are briefly explained in the following:

N ; which is used in the summation factor (i up to N) has a value of 3 based on the number of plateau surfaces the moisture storage curve contains (i.e. **Figure 2.9**)

pC_i ; the inflexion points within the moisture storage curve (i.e. the point where the curve changes from plateau to linear shape)

pC ; $\log(P_c/P_{ref})$ where $P_{ref} = 1$ Pa

s_i ; slope at the inflexion points

$\Delta\theta_i$; represents the difference between the plateau levels (i.e. **Figure 2.9**) and can also be estimated by **Equation 2.59**:

$$\Delta\theta_i = \theta_i - \theta_{i+1} \quad \text{for } i < N \quad \Delta\theta_N = \theta_N \quad (2.59)$$

Note in **Equation 2.59**, when moisture content is used to plot the moisture storage curve, the summation of $\Delta\theta_i$ should be equal to the maximum moisture content of the sample when saturated. In addition, when the degree of saturation, S , is used to plot the moisture storage curve the sum of ΔS_i must equal to 1 [88]. The latter method is used for this research to plot the moisture storage function of alkali-activated cement.

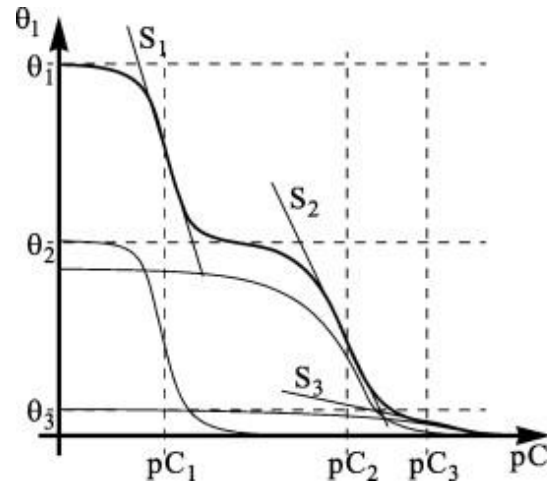


Figure 2.9 The moisture storage function, obtained from sorption data, and illustrates the parameters contained in **Equation 2.58** [88].

Next, **Equation 2.60**, which is obtained from combining **Equations 2.57** and **2.58**, describes the implementation of the relative permeability factor as a function of degree of saturation S ;

$$K_{l,rel}(S) = \frac{\left[\int_0^S \sum_{i=1}^N \left[\frac{\Delta S_i}{\sqrt{2}} \left(1 + \operatorname{erf} \left(\frac{pC_i - \log(a(s^{-\frac{1}{m}} - 1)^{\frac{1}{n}})}{\sqrt{2}S_i} \right) \right) \right] ds \right]^2}{\left[\int_0^1 \sum_{i=1}^N \left[\frac{\Delta S_i}{\sqrt{2}} \left(1 + \operatorname{erf} \left(\frac{pC_i - \log(a(s^{-\frac{1}{m}} - 1)^{\frac{1}{n}})}{\sqrt{2}S_i} \right) \right) \right] ds \right]^2} \quad (2.60)$$

Finally, **Figure 2.10** shows the permeability function vs. the moisture content ranging from hygroscopic to saturated conditions.

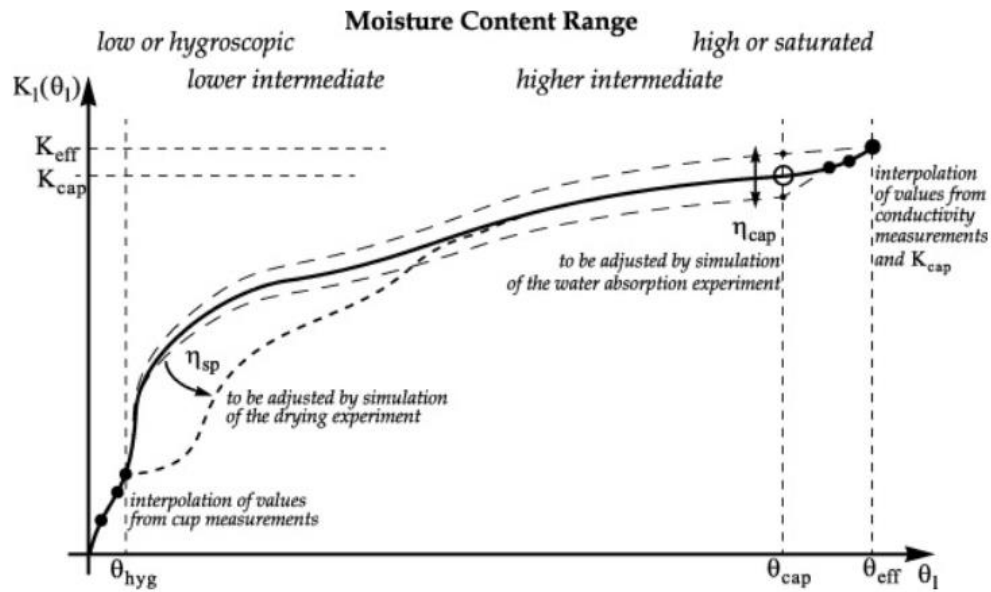


Figure 2.10 The liquid water permeability function from hygroscopic to saturated moisture content. Data in the saturated moisture range are from permeameter or infiltrometer test. The slope in between is derived by the relative liquid conductivity function and can be calibrated by adjusting n_{cap} and n_{sp} obtained from wet and dry cup tests [88].

In this research, the moisture transport in AAMs simulated by using the mechanistic model utilizes the intrinsic permeability coefficient (K_{eff}) obtained from the single moisture model. The scaling factors n_{sp} and n_{cap} are determined by fitting the mechanistic relative permeability curve ($K_{r,mechanistic}$), which function is obtained by multiplying the parameters: n_{cap} , $f_l(S)$ and $K_{l,rel}(S)$, with the curve generated by the Mualem model for relative permeability (i.e. k_{r1}) [92]. This is because wet and dry cup tests were not done for this research. In addition, for this research the value of $D_{v,air}(T)$ in **Equation 2.50** is set to $2.47 \times 10^{-5} \text{ m}^2 \cdot \text{s}^{-1}$, which is also used in the single and dual moisture permeability models, because this is the right value of water vapour diffusivity in air [93]. Furthermore, all the above analytical and predictive models have been implemented in this research to study anomalous moisture transport in alkali-activated cements. The choice of permeability model for each type of binder has been discussed in **Chapter 5 “Moisture Permeability in Alkali-activated Materials”**.

Quantitative prediction of the long term durability performance of cement requires first to quantify the effect of single mode of degradation (e.g. carbonation and or chloride ingress) on the durability of the binder. The physical mechanisms of degradation effect should be described at the level of the microstructure of the cement which is characterized by three main aspects:

the assemblage of hydrate phases, the pore structure and the composition of the pore solution. The impacts of any mode of degradation on each of these three aspects need to be quantified in a service life model to predict the time taken for the structure to reach its serviceability limit state in a corrosive environment [36]. The following sections discuss the durability of alkali-activated cement and Portland cement separately exposed to each corrosion mechanism (i.e. carbonation and chloride ingress), and then in combined degradation conditions.

2.11 Chloride Ingress

The presence of chloride ions in concrete is from two sources: internal from the mineralogical composition of the components of the concrete, and external from: marine conditions and de-icing salt applications on iced roads. The penetrability of chlorides into concrete is a combined process of diffusion coupled with migration into the pore liquid phase and convection in the pore liquid by liquid transport (i.e. flow of pore solution). Furthermore, the flow of these ions can be retarded because of interaction between the ions in the pore solution and the formed hydrates through chloride binding [37]. This kind of interaction (i.e. chloride binding) can be chemical and/or physical reactions dependent on the nature of the cementitious hydrates [53]. The multiple species present in the pore solution could also have a retarding effect on the chloride migration [5]. Another main factor affecting chloride ion penetration is the heterogeneous nature of the microstructure of concrete in which continuous dissolution, precipitation and hydration reactions could occur, in long term service conditions, affecting the porosity of the cement and the overall permeability of the concrete [23].

Therefore, durability studies of cementitious binders around the microstructure, pore solution chemistry and chloride binding potential are crucial to predict the transport of chlorides in concrete [23]. The following sections discuss the durability response of PC and AAM systems against chloride ingress.

2.11.1 The Resistance of PC Against Chloride Ingress

The phase assemblage of Portland cement contains a well-known hydrate called aluminato ferrite mono-sulfate, termed as AFm. The AFm hydrate with a chemical composition of $C_3A \cdot C\$ \cdot nH$ (where $C=CaO$, $A=Al_2O_3$, $\$=SO_3$ and $H=H_2O$) is a layered double hydroxide that has positively charged layers, with a capacity to bind to anions such as Cl^- [94]. It usually starts to form during the hydration reaction of the clinker phases at the point where gypsum is depleted and formation of ettringite halts [95]. The main reaction product between AFm hydrate and Cl^- is Friedel's salt, with a chemical composition of $C_3A \cdot CaCl_2 \cdot nH$, and which is

usually stable at 25°C and 1 bar [94]. Additionally, it has been noted that with an increase in the alite phase, C₃S, of the clinker, an increase in the resistance of free chloride migration occurred [96].

2.11.2 The Resistance of AAMs Against Chloride Ingress

The nature of the dense microstructure and the formation of hydrotalcite-like phases in AAS binders have proven to give better resistance and binding capacity to chlorides than PC binders [97]. Nevertheless, the form of water present in the pore solution after the hydration reactions plays an important role in chloride resistance because it is the carrying media for the corrosive ions. The free pore solution water in alkali-activated slag, AAS, is lower than in the case for alkali-activated fly ash, AAF, due to the presence of chemical binding of water by the hydrates formed in AAS. This could also explain the reasons for the low chloride diffusivity in AAS [97].

2.11.3 Chloride Ingress in High Calcium Based AAMs

Calcium-rich AAMs are considered to have better resistance to chloride penetration than PC since it has been noted that with an increase in age, the chloride resistance of AAS exceeds PC [10]. Although some concretes containing blended Portland cement with 50-80% of slag replacement (i.e. CEM III cement) have shown to have similar resistance to chloride ingress compared to concretes made of AAS [98] [37]. The following sections discuss multiple factors that contribute to the durability of high and low calcium based AAMs in a chloride environment.

2.11.3.1 Importance of calcium content

Blast furnace slag is primarily composed of glassy phases of CaO, SiO₂, Al₂O₃, MgO, and minor Fe₂O₃ and sulfide. When this raw material is used to produce alkali-activated slag cements, the weight percentage of CaO will range between 30 and 50 wt.%. This range is still lower than the CaO content found in PC, which is above 50 wt.% [99]. The glassy nature of blast furnace slags, usually above 90% glass, imparts a very high extent of reactivity which can facilitate its dissolution in the alkaline media, that can rapidly release calcium ions and form C-A-S-H gels responsible for a more uniform and dense microstructure, similar to the case of C-S-H gel in PC [99]. This is due to the structure of C-A-S-H and C-S-H gels that have significant amounts of bound water, leading to the reduction of porosity and water permeability in the binder [10, 100].

2.11.3.2 Chloride binding phases

The ingress of chloride ions into concrete is a complex process because at one point the chloride ion can be present in three forms: acid soluble (chemically bonded), water soluble (physically bonded) and free chlorides ions [101]. Ke et al. [102] have estimated the chloride binding capacities of the main cement hydrates found in AAS, when produced separately as synthetic phases, as shown in **Table 2.2**.

Table 2.2 Chloride binding capacities of AAS hydrates.

	Components	Chloride binding capacity	Ref.
Synthetic phase	C-(N-)A-S-H	137 mg/g	[102]
	Strätlingite	200 mg/g	[103]
	Mg-Al-OH LDH	250 mg/g	[103]

The magnesium-aluminum hydrotalcite (i.e. Mg-Al-OH LDH) and strätlingite, which are known as secondary reaction products containing a layered double hydroxide structure, have the capacity to bind to chloride ions through different mechanisms. The hydrotalcite structures bind to the chloride ions through surface adsorption, and strätlingite through an ion exchange mode to form into a hydrocalumite-like phase [10, 23]. In addition, the chloride binding mechanism by the C-A-S-H gel is through surface adsorption and with the possibility of a chemisorption reaction via the replacement of the interlayer hydroxyl groups by chloride ions. Furthermore, the binding capacities were fitted through the Freundlich adsorption isotherm and included in the free chloride ion diffusion model developed by Mundra et al. [30]. The following **Equation 2.61** describes the Freundlich adsorption isotherm:

$$C_{tb} = \alpha * C_f^\beta \quad (2.61)$$

C_{tb} ; total bound chloride concentration, $\frac{\text{mg of Cl}}{\text{g of binder}}$

C_f ; Free chloride concentration, mol.L^{-1}

α and β ; binding constants

Mangat et al. [104] have also deduced that the Langmuir binding isotherm is also a suitable adsorption isotherm to relate the bound and free chloride ions in alkali-activated slag based concretes. In their study, uncoated faces of the slabs were immersed in a 5 wt.% sodium

chloride solution for 540 days. They carried out concrete coring at 180, 270 and 540 days of chloride exposure in order to perform pore fluid extractions from concrete cores representing 0-20, 20-40 and 40-60 mm depths. Then, the free chloride concentration of the pore solution was determined by dipping a chloride ion selective electrode into the pore solution. The concrete mix design used in their study and fitted Langmuir parameters are summarized in **Table 2.3**.

Table 2.3 Concrete mix design and the corresponding Langmuir parameters α and β from the study of Mangat et al. [104].

	Precursor	Sand/Aggregate	Na ₂ O (wt.%binder)	Ms	w/b	Langmuir		Ref
						α	β	
Concrete	Slag	0.4	6	2	0.47	1.8	7	[104]
	Slag	0.4	5	2	0.47	1.3	7	
	Slag	0.4	4	2	0.47	1.2	7	

According to Mangat et al., chloride binding isotherms were modelled by the Langmuir isotherm but most of the bound chlorides were later reported, by the same authors, to be 77.78% physically adsorbed and 16.67% chemically bonded [104, 105]. This can show that there is a weak interaction between the cement hydrates and chlorides in the pore solution for AAS. In addition, usually, the electron-sharing or covalent bond is the strongest of all bond types. This means that minerals bonded in this manner display general insolubility and greater stability than minerals bonded in the physical manner. Furthermore, there is still a controversy on how much of the hydrated products are available for chloride binding and there is also limited information on binding kinetics of the hydrated phases [106].

Hence, the chloride binding capacity of this material has not been assured yet, as some researchers reported and quantified the significant chloride binding capacity, while others stated that there was not any chloride binding and postulated that prevention of steel corrosion of alkali-activated slag concrete is dependent only on the pore size distribution around the reinforcement [55, 103].

2.11.4 Chloride Ingress in Low Calcium AAMs

The main hydration product in low-Ca AAMs is N-A-S-H gel with a structure containing large macro-pores and small gel pores [107]. This gel could continue to densify due to a process called “continued gelation” which can reduce the pore size over time and reduce the diffusivity

of chloride ions. However, leaching of alkalis from the pore solution occurs when the binder is exposed to an aqueous environment, leading to the reduction of gelation reactions in the N-A-S-H systems with time that could lower the long-term durability of low-Ca AAMs [10, 23]. In addition, low-Ca AAMs contain less bound water compared to high Ca-AAMs [108]. This issue can speed the passage of corroding agents, in the aqueous phase, towards the rebar and accelerate the corrosion reaction.

2.11.4.1 Chloride binding phases

Fu et al. [109] have conducted chloride binding tests on alkali-activated fly and metakaolin binders and have deduced that chloride ions do not chemically react with the formed hydrates which are N-A-S-H and zeolitic phases. They also explained that the chloride ions only get physically adsorbed onto the surface of the N-A-S-H gel without undergoing any chemical reaction [109]. In addition, Runci et al. [110] have shown that there is chloride binding in geopolymer systems by comparing the total and free chloride profiles obtained from alkali-fly ash mortars after being exposed to a 16.5% NaCl solution for 35 days (i.e. NT BUILD 443 test method [111]).

2.11.5 Variability of Chloride Binding in AAMs with Mixed Low and High Calcium Precursors

Zhang et al. (2019) have implemented the equilibrium procedure proposed by Tang and Nilsson [112] to determine the chloride binding isotherms of AAMs [113]. They reported that the Langmuir isotherm fits better than the Freundlich isotherm for chloride adsorption by most of the alkali-activated slag/fly ash binders according to **Equation 2.62**;

$$C_{tb} = (\alpha * C_f)/(1 + \beta C_f) \quad (2.62)$$

Zhang et al. [113] have concluded in their study that the chloride binding capacity of AAMs increases with the increase of water/binder and decrease with the increase of alkali dosage. These effects may be because the amount of bound chloride is greatly influenced by the concentration of Cl^- in the pore solution, and with a decrease in OH^- the Cl^- becomes the dominant ion. Also the influence of silica modulus can have an effect on reaction products of AAS because C-A-S-H plays the dominant role in chloride binding, compared to N-A-S-H in alkali-activated fly ash (AAF). **Table 2.4** contains the values of the fitted parameters of the Langmuir isotherm for AAMs [113].

Table 2.4 Fitted parameters for Langmuir isotherms for AAMs, from [113].

	Slag(%)	Fly Ash(%)	Na ₂ O (wt.%binder)	Ms	w/b	Langmuir		Ref
						α	β	
Paste	100	-	6	1.5	0.5	22.2	0.17	[113]
	80	20	6	1.5	0.5	21.5	0.12	
	60	40	6	1.5	0.5	23.7	0.08	
	40	60	6	1.5	0.5	18.3	0.14	
	20	80	6	1.5	0.5	15.1	0.11	
	100	-	4	1.5	0.5	17.5	0.07	
	100	-	8	1.5	0.5	15.8	0.03	
	60	40	8	1.5	0.5	16.9	0.05	
	20	80	8	1.5	0.5	10.9	-0.02	
	100	-	6	-	0.5	23.6	0.15	
	100	0	6	0.5	0.5	23.2	0.14	
	100	0	6	1	0.5	25.4	0.24	
	60	40	6	0	0.5	21.4	0.24	
	60	40	6	0.5	0.5	20.6	0.15	
	60	40	6	1	0.5	21.3	0.14	
	20	80	6	0	0.5	18.3	0.13	
	100	-	6	1.5	0.3	18.2	0.15	
	100	-	6	1.5	0.7	38.2	0.31	
	60	40	6	1.5	0.3	11.7	0.06	
	20	80	6	1.5	0.3	10.4	0.10	

However, for the case of alkali-activated cement based mortars exposed to concentrated aqueous chloride solutions, there was no evidence of chloride binding according to **Figure 2.11**.

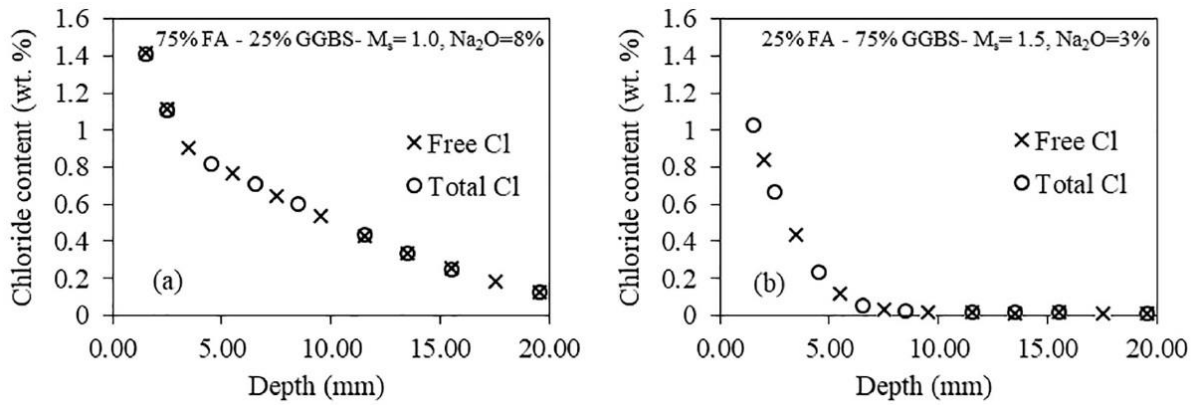


Figure 2.11 Comparison of total and free chloride profiles of alkali-activated cement based mortar with 75%FA-25%SG (a) and alkali-activated cement based mortar with 25%FA-75%SG (b) after immersion in 16.5% NaCl aqueous solution for 45 days [55] .

2.11.6 Test Methods for Chloride Transport Properties

Some of the test methods used to estimate the chloride transport properties for concrete are: NordTest NTBUILD 492 [11] used to calculate the non-steady state chloride migration (under an electrical field gradient) with the influence of ionic interaction from different ions simultaneously present in the pore solution and the NordTest NTBUILD 443 test [111] used to calculate the effective chloride diffusion along with estimation of chloride binding capacity by the use of ASTM C 1218 [12] and ASTM C 1152 [13] techniques as implemented in [114-117]. In addition, the NordTest NTBUILD 492 [11] has also been recalibrated by the use of the chemistry of the pore solution of AAMs in order to precisely determine the depth of chloride ingress into AAC [98].

2.12 Carbonation

Except for the situation of water-immersed or buried concretes, essentially all structural concretes are exposed to atmospheric CO₂ and undergo a degradation called carbonation reaction. This is also known to occur simultaneously with other durability-related processes such as chloride ingress in air-borne chloride environments [5, 21].

In normal atmospheric conditions CO₂ in the gaseous state diffuses through the pore network of the concrete cover where it partially undergoes a gas-liquid mass transfer to the pore aqueous phase while the rest of it permeates through the pore fraction filled with air.

The process of CO₂ gas dissolution into the pore solution induces the carbonation reaction where the CO₂ in an aqueous state reacts with the pore solution ions and some of the hydrate products, particularly portlandite in PC, which leads to the drop in alkalinity of pore solution from a high value, that usually passivates the steel reinforcement, to near neutrality. This causes changes in the microstructure of the cement. This CO₂ gas diffusion-reaction process in porous media is controlled by both the concentration gradient of CO₂ and the rate of chemical reaction in the pore solution [118]. The carbonation rate and degree is dependent on the exposure environmental conditions (i.e. relative humidity (RH), CO₂ concentration, temperature and duration of exposure) but more importantly on the durability properties of PC-based binders and AAMs [119].

However, PC-based binders and AAMs exhibit different reaction mechanisms during carbonation, due to formation and interactions of different phases in these two systems. Where the main difference is the absence of portlandite as a hydrate in AAMs and the presence of higher alkali content in the pore solution of AAMs compared to the pore solution composition of PC [120].

2.12.1 Portland Cement Carbonation

2.12.1.1 Carbonation Mechanism

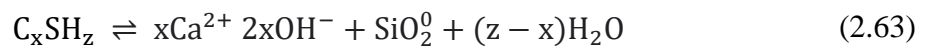
The carbonation mechanism of PC occurs by the diffusion of carbon dioxide through the capillary pores of the cementitious matrix then reacts with the pore water to form bicarbonate (HCO₃⁻) and carbonate ions (CO₃²⁻). Papadakis et al. [121] simulated the carbonation process of PC based materials, where C-S-H gel and portlandite are the main cement hydration products prone to this reaction. In their model, the first step was that CO₂ diffuses into the pores of cement-based materials while the hydration product portlandite (CH) dissolves in the pore solution. Then, CO₂ dissolves in the pore solution, to form the above-mentioned ions (i.e. HCO₃⁻ and CO₃²⁻) and reacts with portlandite to form calcium carbonate, CaCO₃. This is accompanied by a decrease of the pH value of concrete pore solution from an initial value above 13 to as low as 8 [10]. The main products of natural carbonation of portlandite are calcite and aragonite.

2.12.1.2 Effects of Carbonation

The decrease in the pH accelerates the decomposition of ettringite and Friedel's salt (calcium monochloroaluminate hydrate, or Cl-AFm) in hardened cement paste that can increase both the porosity and the diffusion of chlorides into concrete [10, 122]. Another effect is the

decalcification of C-S-H gel which polymerizes into an amorphous gel and changes the pore size distribution of the binder. However, CaCO_3 precipitation can block the pores and reduce damage in the structure of the C-S-H that would otherwise increase the porosity. Which type of carbonation mechanism dominates in the cement is dependent on the amount of portlandite present in the cement.

Xie et al. [5] have modelled the carbonation reaction of C-S-H as a variable dissolution process where it is a function of the calcium to silica ratio, C/S, in its gel structure [5]. The reaction below, **Equation 2.63**, depicts the dissolution and is considered in their kinetic model as an intermediate or slow step reaction:



x; C/S ratio set as a continuous variable

z; H/S ratio set to be constant during the carbonation of Portland cement

Additionally, their model framework sets for every time step the solubility of C-S-H as a function of the C/S ratio, which means the x in **Equation 2.63** is set as a continuous variable. This approach has also led to a correlation between the C/S present in C-S-H, and the saturation index of portlandite (CH), β_{CH} , according to **Figure 2.12**, although it is unrealistic for C-S-H to contain a calcium to silica ratio below 0.5 [123].

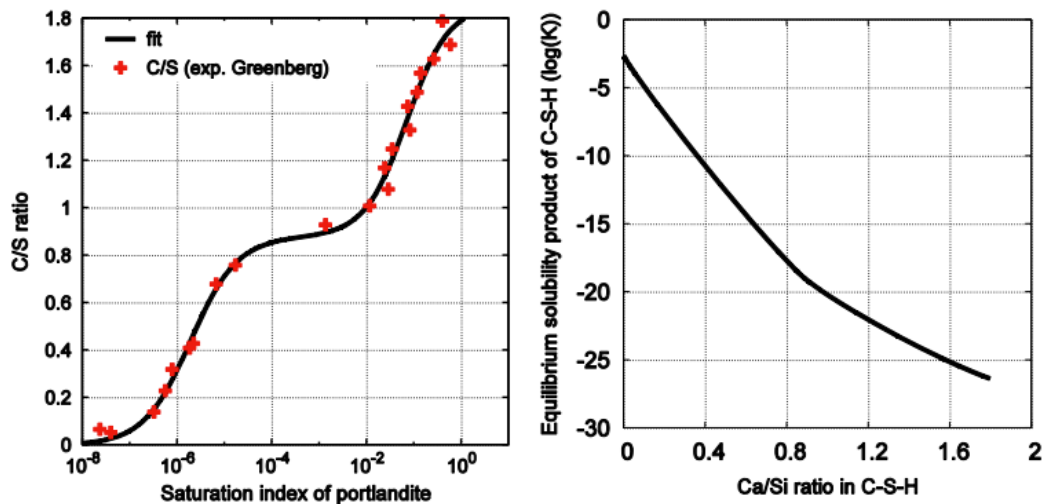
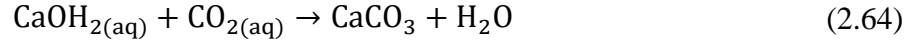


Figure 2.12 C/S ratio present in C-S-H as a function of β_{CH} (left) and solubility product of C-S-H as a function of its C/S content (right), adapted from [5].

Furthermore, in their model, the impact of the formed carbonation product, calcium carbonate ($C\bar{c}$), has been included in the dissolution rate of CH, upon carbonation reaction [5], where the authors have considered the decrease in rate of CH dissolution because of the growing thickness of $C\bar{c}$ coating around the CH spheres. The following **Equations 2.64-2.65** describe the dissolution reaction and rate in which the effect of $C\bar{c}$ has been implemented by the use of a correction factor termed as f_{coating} .



$$\frac{dn_{\text{CH}}}{dt} = \frac{n_{\text{CH}}^0}{\tau_{\text{CH}}} f_{\text{coating}} \ln \beta_{\text{CH}} \quad (2.65)$$

n_{CH} and n_{CH}^0 ; the current and initial CH content in concrete (mol.m^{-3})

τ_{CH} ; characteristic time, of 720s, associated with dissolution of CH spherical crystals with initial radius of $R_0 = 40\mu\text{m}$

β_{CH} ; saturation index of CH

f_{coating} ; correction factor taking into account the impact of calcium carbonate, $C\bar{c}$, coating around CH crystals to decrease its dissociation reaction rate, as shown in **Equation 2.66**.

$$f_{\text{coating}} = \frac{r_p^2}{1 + c \frac{r_p}{r_c} (r_c - r_p)} \quad (2.66)$$

c ; Dimensionless factor of 0.32×10^6 obtained by accelerated carbonation experiment (at 50% CO_2 exposure condition) on Portland cement.

r_p ; relative radius from the internal point of CH to its outermost point

r_c ; relative radius from the internal point of CH to the outermost point of $C\bar{c}$ coating CH.

The two geometry factors, r_p and r_c are dependent on the molar quantities of CH and volume of calcium carbonate, $V_{C\bar{c}}$, according to the following **Equation 2.67**;

$$r_p = \left(\frac{n_{\text{CH}}}{n_{\text{CH}}^0} \right)^{\frac{1}{3}}, \quad r_c = \left(\frac{n_{\text{CH}}}{n_{\text{CH}}^0} + \frac{V_{C\bar{c}}}{V_{\text{CH}}} \left(1 - \frac{n_{\text{CH}}}{n_{\text{CH}}^0} \right) \right)^{\frac{1}{3}} \quad (2.67)$$

2.12.2 Alkali-Activated Cement Carbonation

The carbonation reaction mechanisms between high-Ca and low-Ca AAMs are different. In the carbonation reaction of high-Ca AAMs, CO₂ dissolves into the pore solution, forms carbonic acid and reacts with C-A-S-H gel to produce CaCO₃ [124]. Whereas in low-Ca AAMs, the N-A-S-H gel does not decalcify and sodium carbonate is formed from the reaction between the alkalis, found in the pore solution, and the carbonate ions [125] [10].

2.12.2.1 High calcium content AAMs carbonation

2.12.2.1.1 Carbonation Mechanism

Products of AAS hydration are mainly C-A-S-H gels of low crystallinity or amorphous structure, with uniform and dense structural features. During the carbonation reaction, and since portlandite does not exist in the composition of AAMs, decalcification of C-A-S-H gel occurs where calcium ions are released from the gel and into the pore solution [119]. The decalcification of the gel starts by the removal of calcium ions from the interlayer and then the gel starts to decompose to form an amorphous alumina-silica gel [126]. The aluminum present in the gel precipitates and is integrated in the amorphous silica phase to form tetrahedral Al(-OSi)₄ sites. Due to this process, C-A-S-H gel undergoes volume shrinkage and an increase in its degree of polymerization, which leads to loss of mechanical strength of the material [126].

2.12.2.1.2 Effects of Carbonation

The reaction between free calcium and carbonate ions, present in the pore solution, forms calcium carbonate. Usually, the first polymorphs of calcium carbonate to form are aragonite and vaterite, with an orthorhombic and hexagonal structural features respectively, because they are the least stable phases and closer in formation energy to the original state, according to the Ostwald Step Rule [127]. Then, calcite, with a rhombohedral structural feature, is formed [128]. However, in many cases CaCO₃ in the amorphous state cannot be immediately identified [129]. The calcite is the main calcium carbonate polymorph formed under natural carbonation, whereas aragonite and vaterite are the main polymorphs formed under accelerated carbonation conditions [130]. In some cases, the formation of calcium carbonate phases may have a positive impact on the durability by refining the pore structure which makes the construction material more resistant to CO₂ diffusion [131].

Ke et al. [132] have observed a similar effect with alkali-activated slag mortars, activated by sodium carbonate, exposed to natural carbonation conditions (i.e. 0.04 wt.% CO₂). After their samples were cured for a 28-day period, in sealed conditions, they placed each set of samples

in different carbonation conditions which were at 0, 0.04 and 1 wt.% CO₂ atmospheric conditions. Next they measured the evolution of compressive strength and carbonation rate as a function of time as shown in **Figure 2.13**. The data plotted in **Figure 2.13** shows that samples in natural carbonation conditions exhibited the same evolution in compressive strength as non-carbonated samples but slightly higher. However, the samples exposed in accelerated conditions retained their 28-day compressive strength but showed a higher depth of carbonation than the naturally carbonated samples. Hence for samples in natural carbonation condition, the formation of calcium carbonate blocked the connected pores, reduced further carbonation reaction and increased the compressive strength of the materials [132, 133].

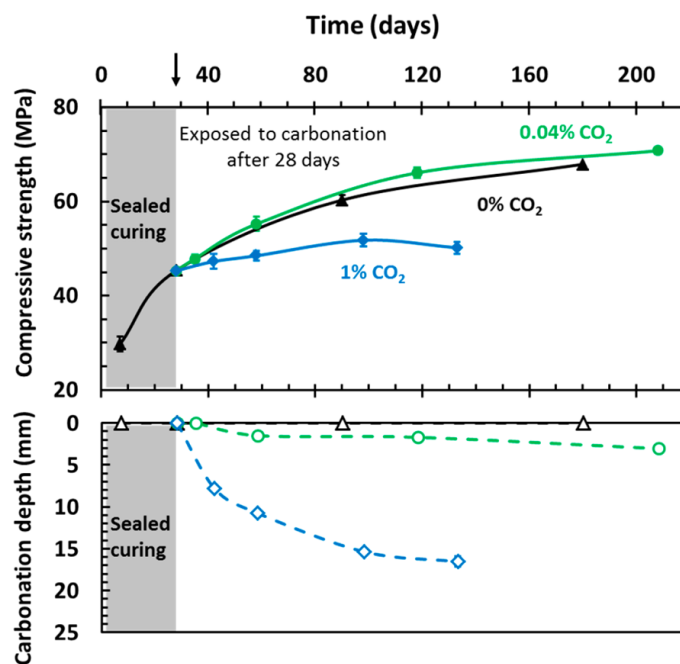


Figure 2.13 Changes in compressive strength of sodium carbonate activated slag mortar exposed in different carbonation conditions and corresponding carbonation depths. Samples were cured for 28 days in sealed conditions before carbonation exposure. Graph obtained from [132].

2.12.2.1.3 Role of pore solution

The pore solution ions that contribute to high alkalinity (i.e. pH around 13) are mainly the hydroxide and alkalis that are from the activating solution. These ions also react with the dissolved carbon dioxide, in the form of carbonate ions, to form sodium rich carbonates. The main carbonation product under natural conditions, is natron, Na₂CO₃.10H₂O, and the product under accelerated conditions is nahcolite, NaHCO₃ [129]. Therefore, polymorphs of sodium carbonate in the cement paste are formed dependent on the concentration of CO₂ in the atmosphere as shown in **Figure 2.14**.

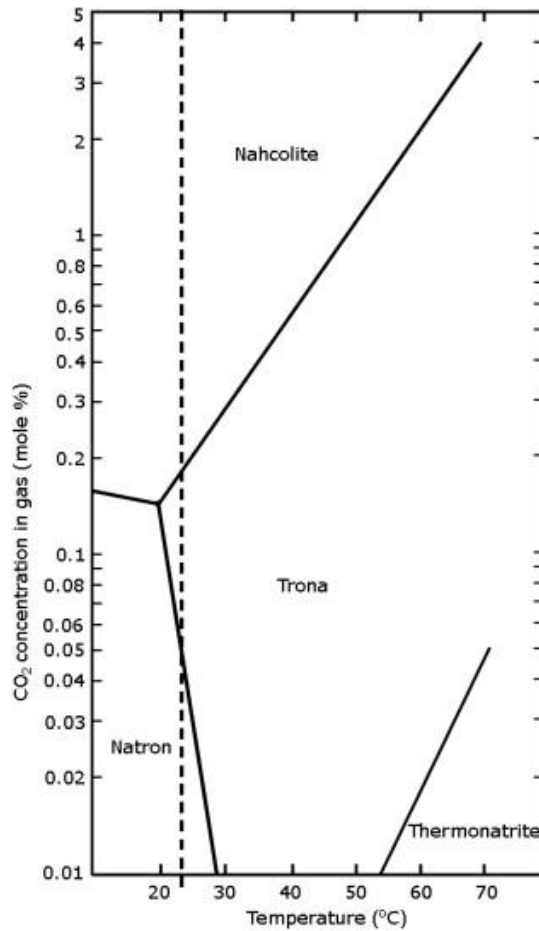
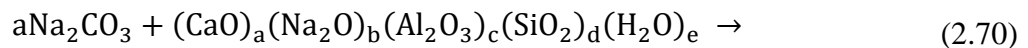
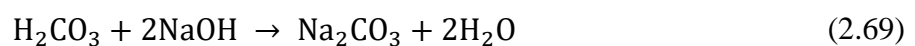
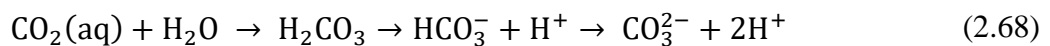
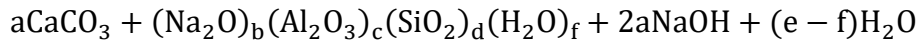


Figure 2.14 Phase diagram as a function of temperature and gas phase CO₂ concentration for the Na₂CO₃—NaHCO₃—CO₂—H₂O system in an air atmosphere at ambient pressure. The dashed line represents a temperature of 23 °C. Graph from [129].

Furthermore, under natural carbonation condition the diffusion of CO₂ will be lower than under accelerated carbonation due to the pore blockage by natron because of its higher molar volume compared to nahcolite (i.e. that is formed under accelerated carbonation condition) [129]. However, these formed sodium carbonates tend to react with the C-A-S-H gel and form CaCO₃ as the final carbonation product, according to the following set of **Equations 2.68-2.70**.





Where a,b,c,d,e and f are the stoichiometric coefficients for the respective oxide components that are: calcium oxide (CaO), sodium oxide (Na₂O), aluminum oxide (Al₂O₃), silicon dioxide, (SiO₂) and water (H₂O) which vary due to the variability of the mineralogical composition of slag [130] .

2.12.2.1.4 Importance of magnesium oxide (MgO) content

Slags with high magnesium oxide content can reduce the negative impact of carbonation on AAMs. Carbonated alkali-activated slag with a high magnesium oxide content has been shown to contain high amount of Mg-Al-hydrotalcite phase (Mg-Al-OH-LDH) that can chemically bind with CO₂ and prevent the loss of mechanical strength by the reduction of decalcification of C-A-S-H gel [27, 134]. **Figure 2.15** shows that the carbonation depth of alkali-activated slag (AAS) with high MgO content was smaller than AAS containing a lower weight percentage of MgO. This can be because the microstructure of carbonated high-Mg AAS has less capillary pores and more tortuosity that enhances its resistance to not only to CO₂ diffusion but also to subsequent types of chemical degradation such as sulfate and chloride ingress [134, 135].

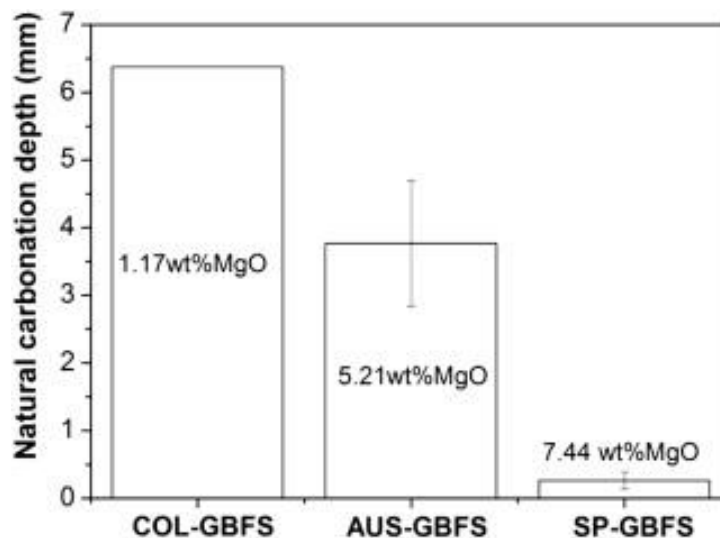


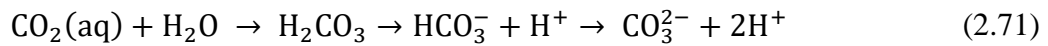
Figure 2.15 Natural carbonation depth of silicate-activated slag cements as a function of MgO content (by wt.%) in slag. Adapted from [134].

Moreover, thermodynamic modelling of the phase assemblage of carbonated AAS has shown that the effect of high MgO content in the slag can increase the secondary phases (i.e. Mg-Al-hydrotalcite), that bind CO₂ and partially buffer the pore solution pH which can help to lower

the extent in reduction of C-(N)-A-S-H gel (i.e. C-A-S-H gel containing a high composition of alkali content). All these factors assist to maintain the high alkalinity of the pore solution around the steel reinforcement [16].

2.12.2.1.5 *Use of accelerated carbonation tests*

The effect of carbonation on the durability of the construction material is the change of the pore solution composition. In natural carbonation conditions CO₂ gas partially dissolves into the pore solution and forms carbonate ions. These carbonate ions play a role in reduction of the pore solution alkalinity [118]. Whereas under continuous exposure to a CO₂ gas rich environment, that is the accelerated carbonation test, bicarbonate ions begin to form and dominate among other dissolved carbonate species according to the following reaction, Equation 2.71;



The presence of bicarbonate ions, that are not detected at such high concentrations in natural carbonation conditions, can induce a difference in the carbonate/bicarbonate ionic equilibrium. The bicarbonate ions are more acidic than carbonate ions and cause a great reduction of the pore solution alkalinity [118, 129].

In addition, a developed thermodynamic model estimated that the pH of the pore solution exposed to natural carbonation is above 11 while the pH of the same solution exposed to 4% CO₂ is around 9 as shown in **Figure 2.16**. Consequently, the results obtained from accelerated carbonation tests underestimate the service life of alkali-activated materials [129].

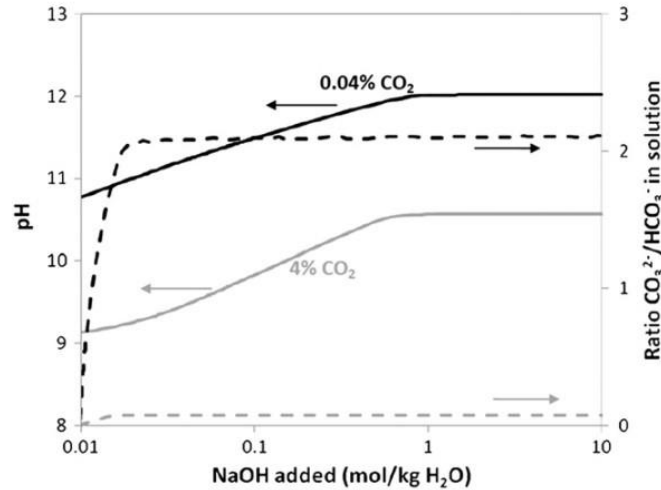


Figure 2.16 Plot of pH (solid lines) and carbonate/bicarbonate ratio (dashed lines) as a function of NaOH addition and CO₂ concentration, for simulated AAS pore solutions. Black lines are at 0.04% CO₂, and grey lines at 4% CO₂. Graph from [129].

2.12.2.2 Low-calcium AAMs carbonation

2.12.2.2.1 Carbonation mechanism

Pouhet et al. [136] have described the natural carbonation reaction in the pore solution of calcium-free AAMs into two steps; first, the formation of Na₂CO₃ and reduction of pore solution pH to around 12, and second, the evolution of the ratio of carbonate/bicarbonate phase equilibrium where bicarbonate ions start to dominate and reduce the pH further to 10.5. However, the final pH reached is still higher than the limit, which is 9, for steel depassivation to occur [136].

2.12.2.2.2 Effect of carbonation

It has been proposed that the main hydrate of low-calcium AAMs, N-A-S-H gel, remains stable during carbonation reactions despite changes in the pore solution composition [137]. However, the only condition that would lead the N-A-S-H gel to dissociate is when hydroxide ions react with carbonic acid (H₂CO₃) in the pore solution [136, 137].

A case study of alkali-activated metakaolin (MK) paste exposed to natural carbonation conditions showed that the evolution of its compressive strength was not affected by the drop of alkalinity of its pore solution, as shown in **Figure 2.17**. The reason could be the possible reaction between carbonates and alkali ions in the pore solution to form efflorescence, which are Na₂CO₃ precipitates, and that potentially fill up the pores inside the material [136].

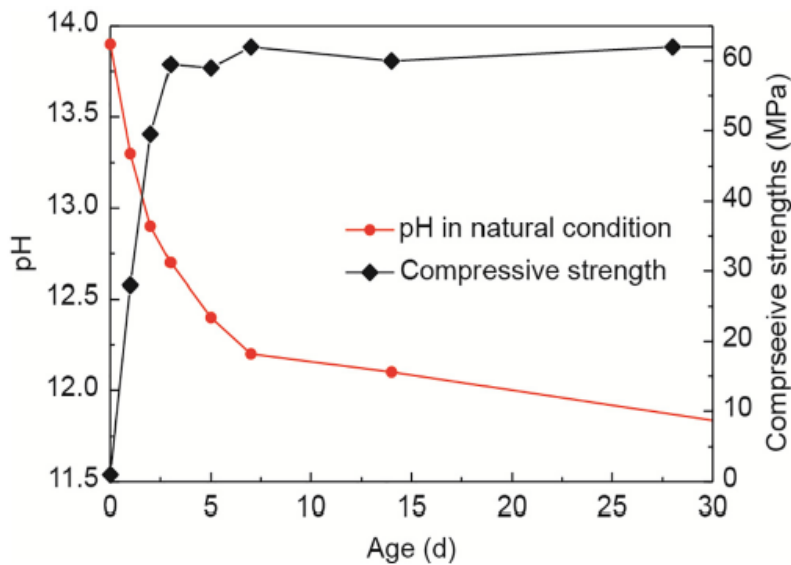


Figure 2.17 Evolution of pH of the pore solution and compressive strength of alkali-activated metakaolin paste cured under natural CO₂ conditions. Adapted from [136].

2.12.3 Comparison of Carbonation Effect on Pore Solution Alkalinity Between Low and High Ca-AAMs

The reduction of the pore solution alkalinity by carbonation reactions is greater in the case of low-calcium AAMs than high-calcium AAMs, because of low concentration of alkali ions present in the pore solution of low-calcium AAMs. The dissolution of fly ash in the alkaline media consumes large concentrations of sodium and hydroxide ions in order to form cementitious hydrates, especially the main N-A-S-H gel. Therefore, the binding of sodium ions by the gel phases reduces the effective alkali concentration in the pore solution and consequently the alkalinity of the pore solution. Whereas, the hydrates in AAS have a lower alkali binding capacity and hence a higher concentration of free alkali ions in the pore solution. This ensures a buffering effect for the pore solution alkalinity to remain high during natural carbonation reaction. Overall, the availability of free alkalis in the pore solution is a preventative measure for obtaining carbonation resistance in AAMs. However, the presence of free calcium ions in the pore solution found in blended AAMs, especially in the case of AAMs composed of a 50:50 ratio of SG and FA precursors, can lower the resistance to carbonation reaction [138]. However in terms of alternative mix designs for blended AAMs, Bernal et al. [139] reported that the addition of metakaolin to AAS at only up to 10 wt.% improved the carbonation resistance of the alkali-activated cement.

2.12.4 Ingress of CO₂ in Alkali-Activated Concretes

The extent of carbonation reaction in the concrete cover is indicated by a carbonation depth which serves as a piece of data in calculating the service life of reinforced concrete. The carbonation depth is determined by spraying phenolphthalein solution on the surfaces of the concrete samples, exposed in natural conditions, and observing the change in color where pink indicates the pH of the pore solution is above 9.5, and colorless if it is below [140]. The line between these two colors indicates the depth of the carbonation reaction in the concrete cover and is also termed as the carbonation front. However, for some carbonated AAMs it has been reported in the literature that the pH of the pore solution has remained above 9.5, which can make the carbonation depth results from the phenolphthalein test quite misleading [6, 129, 136]. The graph in **Figure 2.18** describes the carbonation depths, obtained from the phenolphthalein test, in alkali-activated concretes exposed to natural outdoor carbonation conditions. These results are from the RILEM TC 247-DTA round robin testing of carbonation on five different alkali-activated concretes based on fly ash (FA), slag (S) and metakaolin (MK) that took place in different laboratories [114].

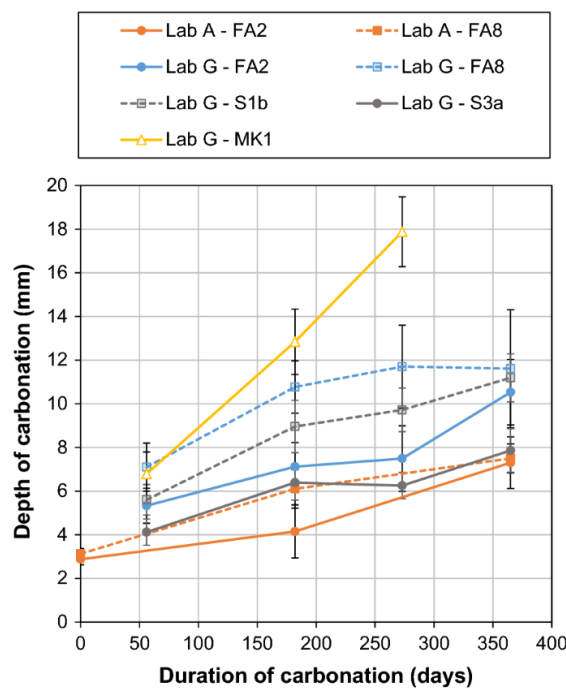


Figure 2.18 Carbonation of alkali-activated concretes under natural outdoor conditions protected from rainfall. Error bars represent one standard deviation in each direction from the average value. The number and small letters next to each concrete label indicate the use of the same precursor but in a different mix design. Figure from [114].

In addition, the prediction of the carbonation depth has been estimated by many analytical, reactive transport and thermodynamic models [16, 121, 141, 142]. In which the analytical models, such as Papadakis' model [143] and Yang's model [142], and reactive transport models account for the carbonation rate with chemical reactions between CO₂ and cementitious hydrates found in Portland cements.

A meta-model has been developed to calculate the carbonation front based on the analytical solution of Fick's first law and incorporating the effect of the mix design of Portland cement concrete as well as the environmental conditions such as temperature and relative humidity [144]. This model is based on the following **Equation 2.72**;

$$x_{\text{CO}_3}(t) = \sqrt{\frac{2D_{\text{CO}_2} \cdot c_{\text{CO}_2}}{a}} \sqrt{t} \quad (2.72)$$

x_{CO_3} ; depth of carbonation

D_{CO_2} ; diffusion coefficient for carbon dioxide

c_{CO_2} ; concentration of carbon dioxide at the surface of the concrete

a ; amount of carbon dioxide required to carbonate a unit volume of concrete

t ; time

The predictions of this model are close to the data of PC reported in the literature, as seen in **Figure 2.19**.

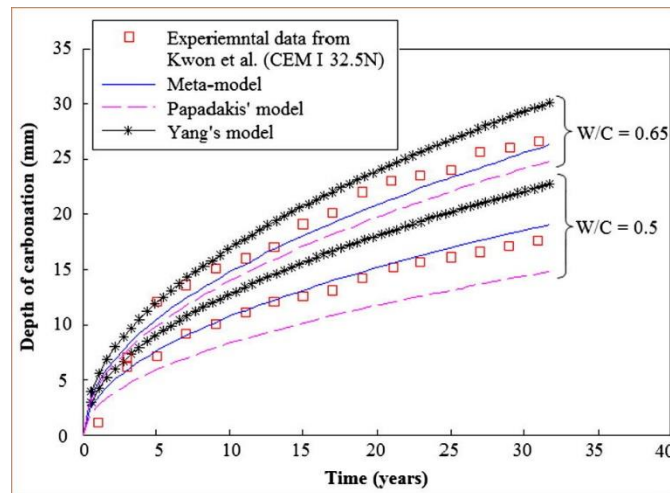


Figure 2.19 Comparison between the experimental carbonation depths in Portland cement concrete, type CEMI binder with different w/c, and the predicted depths by Meta, Papadakis', and Yang's model. Graph from [144].

Finally, **Table 2.5** contains carbonation rates of old in-service structures made of alkali-activated materials.

Table 2.5 In-service carbonation rates of AAC. Data obtained from [55].

Location	Application	Date	Compressive Strength (MPa)	Average Carbonation Rate (mm/year)
Odessa, Ukraine	Drainage collector	1966	62 (34 years)	<0.1
Krakow, Poland	Precast floor slabs and wall panels	1974	43 (27 years)	0.4
Zaporozhye Oblast, Ukraine	Silage trenches	1982	39 (18 years)	0.2-0.4
Magnitogorsk, Russia	Heavy duty road	1984	86 (15 years)	1
Lipetsk, Russia	High-rise residential buildings	1986	35 (14 years)	0.4
Tchudovo, Russia	Prestressed railway sleepers	1988	82 (12 years)	0.7-1

2.12.5 Effects of Carbonation on Microstructure of Portland Cements and Alkali-Activated Cements

The dominant hydrate in PC system is the calcium silicate hydrate gel, C-S-H, with a calcium to silica ratio, Ca/Si >1.5. However, alkali-activated slag cements are mainly composed of calcium aluminosilicate hydrate gel (i.e. C-A-S-H) or of C-(N)-A-S-H gel containing high alkali content in its composition to reflect the high concentration of alkali ions present in the activating solution which is used in the mix design of AAMs. The Ca/Si ratio (C/S) present in

the composition of these hydrates (i.e. C-A-S-H and C-(N)-A-S-H gel) has been reported to be close to 1 [145], although this ratio can change with the variability of the mineralogical composition of the precursors [16, 123]. Furthermore, the Ca/Si ratio is a crucial parameter in carbonation kinetics as it depicts the extent of change in porosity and effect of possible clogging due to the formation of formed carbonate products which are mainly calcium carbonate and its polymorphs vaterite and aragonite [146]. Morandea et al. [146] have conducted accelerated carbonation tests (10% CO₂, 25°C, and 65% RH) on type-I PC cements to investigate the carbonation of portlandite and C-S-H gel found in this cement. They have been able to link the change in chemical composition of the cement, due to the extent of carbonation, to the evolution of the porosity based on the following **Equation 2.73**;

$$\Delta\phi_{\text{CSH}} = n_{\frac{\text{CSH}}{\text{CC}}} V_{\text{CC}}^{\text{CSH}} + n_{\text{CSH}}(t_0)(V_{\text{CSH}}(t) - V_{\text{CSH}}(t_0)) \quad (2.73)$$

$n_{\text{CSH}}(t_0)(V_{\text{CSH}}(t) - V_{\text{CSH}}(t_0))$; C-S-H decalcification related to increase in porosity

$V_{\text{CC}}^{\text{CSH}}$; Formation of calcium carbonate related either to portlandite or C-S-H

However, the molar volume of the carbonate phase formed by the dissolution of C-S-H is based on the type of polymorph of calcium carbonate formed, since it can affect the overall porosity of the cement according to **Figure 2.20(b)**. Furthermore, carbonation in PC systems can lead to a reduction in the porosity, due to the formation of calcium carbonate from the dissolution of portlandite that can compensate the loss in volume of C-S-H. The following **Equation 2.74** describes the changes in the volume of C-S-H based on its Ca/Si ratio, ranging from 0.4 to 1.7, with **Figure 2.20(a)** showing the results.

$$(V_{\text{CSH}}(t_0) - V_{\text{CSH}}(t)) = \beta \left(1 - \frac{\frac{C}{S}(t)}{\frac{C}{S}(t_0)} \right) \quad (2.74)$$

where;

$$0.02 < \beta < 0.04 \text{ (L. mol}^{-1}\text{)}$$

$$\frac{C}{S}(t_0) = 1.7$$

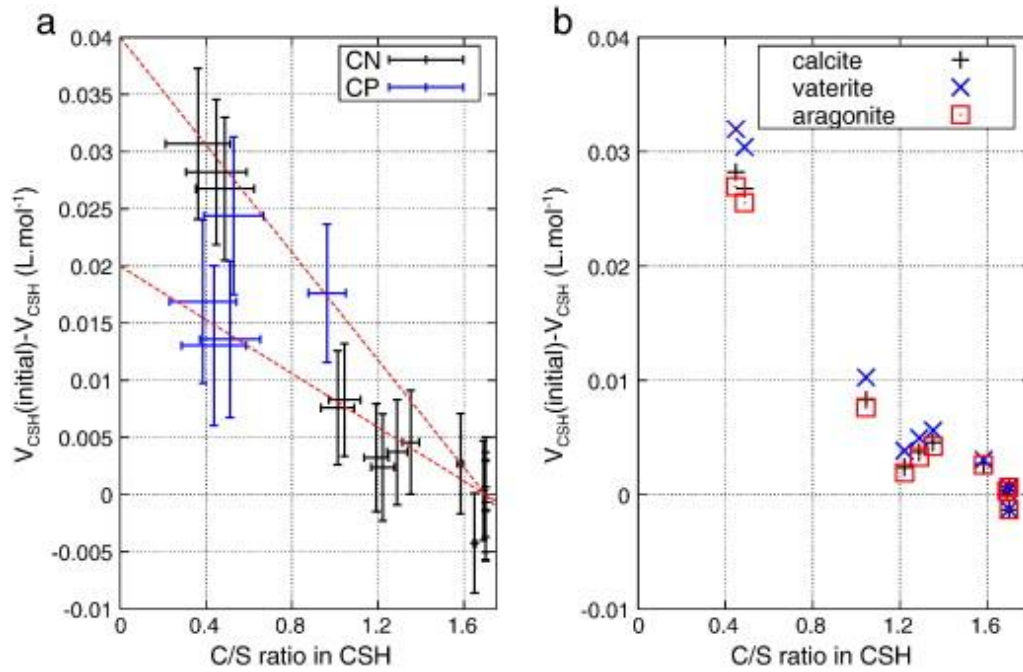


Figure 2.20 (a) C-S-H molar volume change, due to carbonation, as a function of C/S for both CN (CEM I with $w/c=0.45$) and CP (CEM I with $w/c=0.6$) materials, (b) influence of the choice of molar volume of calcium carbonate in molar volume change of CSH, based on the data obtained for various polymorphic forms of calcium carbonate formed from C-S-H in carbonated CN system. Figure adapted from [146].

Unfortunately, similar studies for the case of C-A-S-H gel found in AAMs system have not been conducted until this point. However, Nedeljković et al. [147] have measured the changes in the porosity of alkali-activated cements exposed to natural laboratory carbonation conditions (55% RH and 20°C) for a period of 1 year by the use of mercury intrusion porosimetry. The results are reported in **Table 2.6** that contains the percentage of porosity for reference samples (i.e. not carbonated) and in carbonated samples. They concluded that AAMs made with more than 50 wt.% slag were more resistant to carbonation reactions and that the alkalinity of the pore solutions of all the tested alkali-activated cements remained above 10.5 [147].

Table 2.6 Change in porosity of naturally carbonated alkali-activated FA and SG based cements. Data obtained from [147].

Mixtures	Total porosity (vol.%) – reference	Total porosity (vol.%) – carbonated
100%FA	43.72	30.41
30%SG&70%FA	26.04	26.22
50%SG&50%FA	9.404	17.09
70%SG&30%FA	6.538	9.66
100%SG	3.57	3.38

2.13 Chloride and Carbonation Resistance of AAMs

The combined action of carbonation and ingress of chloride ions exists in splash zones from sea water or salt lakes, where chlorides deposit on the surface of concrete with carbonation occurring at the same time. The combined action also exists in cold regions where de-icing salt is applied on roads and then rain splashes the chloride ions on concrete structures [5]. In addition, the effect of corrosion rate (i.e. from chloride ingress) is at its highest impact on the reinforcement of concrete when it is in water submerged conditions [37].

The uptake of chloride ions by the cement is sensitive to changes in: alkalinity and ionic strength of its pore solution, chloride ion concentration, and microstructure that is a common effect induced by the carbonation reaction. Therefore, a coupling effect of carbonation on chloride ingress should be characterized and/or quantified [10, 37, 116].

One of the main impacts carbonation has on the durability of concrete is the change in the microstructure of the cement that impacts the permeability of corrosive species towards the steel reinforcement as shown in **Figure 2.21**. In addition, **Figure 2.21** describes that the type of raw materials and method of manufacture of concrete can shape its overall permeability to corroding agents [148].

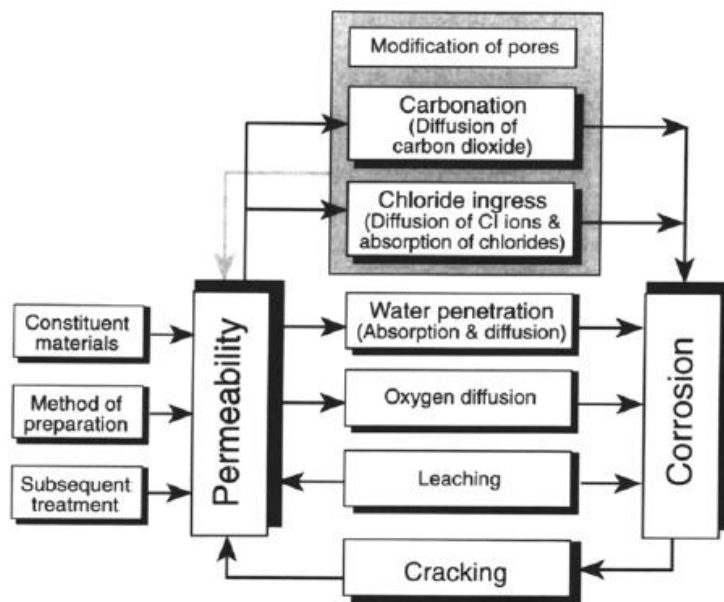


Figure 2.21 Schematic showing permeability of the concrete as the main controlling factor for steel corrosion. Figure adapted from [148].

2.13.1 The Impact of Carbonation on Chloride Ingress in PC and AAM Based Materials

Xie et al. [5] in their reactive transport model have included the impact of carbonation on chloride ingress in Portland cement based concrete. The adsorption of chlorides was modelled

by **Equation 2.75** that takes into account the loss of chloride sorption sites, calcium ions, during the carbonation of C-S-H as described in section 2.12.1;

$$s_{\text{Cl|Na}}(c_{\text{Cl}}) = \frac{\alpha_{\text{Cl|Na}}\left(\frac{C}{S}\right)c_{\text{Cl}}}{1 + \beta_{\text{Cl|Na}}\left(\frac{C}{S}\right)c_{\text{Cl}}} \quad (2.75)$$

$s_{\text{Cl|Na}}(c_{\text{Cl}})$; C-S-H binding capacity in sodium chloride solution.

$\alpha_{\text{Cl|Na}}\left(\frac{C}{S}\right)$ and $\beta_{\text{Cl|Na}}\left(\frac{C}{S}\right)$; Fitted parameters for Langmuir isotherm.

c_{Cl} ; chloride concentration, mol.L^{-1}

Where $\alpha_{\text{Cl|Na}}$ and $\beta_{\text{Cl|Na}}$ are set to vary as a function of calcium to silica ratio (C/S) in the C-S-H as shown in **Equation 2.76**.

$$\alpha_{\text{Cl|Na}}, \beta_{\text{Cl|Na}} = \begin{cases} 0.222, 2.10 & C/S \leq 0.5 \\ 0.022 + 0.16\left(\frac{C}{S} - 0.5\right), 2.1 + 1.157\left(\frac{C}{S} - 0.5\right) & 0.5 < C/S \leq 1.5 \\ 0.182, 3.26 & \frac{C}{S} > 1.5 \end{cases} \quad (2.76)$$

However, the authors have highlighted that incorporating supplementary cementitious materials (SCMs) with PC would change the reactants for carbonation and chloride binding isotherms because of the formation of different hydrates in the system. Thus, the modified chloride binding isotherm cannot be directly implemented for the case of AAMs.

Table 2.7 describes the impact of carbonation on microstructure, pore solution chemistry and chloride ingress in each type of binder (i.e. PC, low and high-Ca AAMs).

Table 2.7 Carbonation effect on chloride ingress in PC and AAMs.

	Portland cement	High Ca-AAMs	Low Ca-AAMs	Reference
Microstructure change caused by carbonation	Reduction of the total porosity because of the precipitation of calcium carbonate around Portlandite (CH) crystals. This can slow down the dissolution reaction of CH and increase its solid volume.	Decalcification of the CASH that can form micro cracks in the concrete.	Reduction of the total porosity due to the precipitation of sodium carbonate in the pore space.	[10, 120, 149, 150] [147]
Chloride transport	Decrease in chloride sorption capacity due to the decalcification of the main chloride adsorbent hydrate (i.e. C-S-H) and degradation of formed Friedel's salt.	Decrease in chloride sorption capacity due to the decalcification of the main chloride adsorbent hydrate (i.e. C-A-S-H)	The initial presence of un-reacted fly ash particles in the Geopolymer binder causes high porosity in the concrete which leads to a high transfer of chloride ions into the surface of the concrete.	[10, 120, 151, 152]
Pore solution chemistry	Increase of free chloride ions along with a rise in the degree of saturation of the pores.	Formation of efflorescence (i.e. Na_2CO_3) and calcium carbonate phases.	Formation of efflorescence (i.e. Na_2CO_3).	[116, 130, 138]

It is known in the literature that the rate of chloride ingress into concretes made with “geopolymer” (low-Ca AAM) binders is high in saline environments, and it also has lower resistance to carbonation when compared to Portland cement concrete. This may make the steel reinforcement in geopolymer concrete to be more susceptible to corrosion reactions [151]. This is in contrast to AAS based concretes which proved to have better resistance to corrosion than PC based concrete [120, 153].

2.14 Service Life

The service life of a reinforced concrete structure is divided into two stages [154]. The first stage is the initiation phase in which free chloride ions accumulate up to a certain concentration level adequate to onset the corrosion of steel reinforcement. This concentration, as discussed in section 2.6, is termed as the critical chloride threshold (C_{crit}). The second stage is called the propagation phase, where the steel is in an active state and continuous corrosion reactions are occurring which yield corrosion products. These products tend to expand the volume between the surface of the concrete and the reinforcement, leading to cracks that will eventually cause spalling of the concrete structure [155].

In this research, the service life for alkali-activated concrete is predicted only until the point of corrosion initiation. Although the propagation phase is a significant component in reinforced concrete structures [156] [157], the prediction of corrosion initiation should be first assessed carefully by including other modes of degradations (carbonation reaction and moisture transport) while modelling chloride ingress towards the rebar in reinforced concrete. Moreover, **Figure 2.22** describes the overall service life of reinforced concrete exposed to steel corrosion.

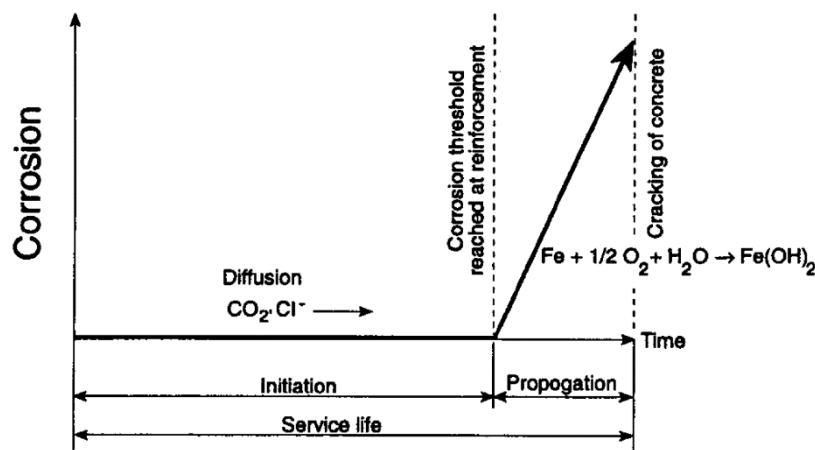


Figure 2.22 Service life of reinforced concrete subject to steel corrosion. Figure obtained from [148].

The following section briefly describes some of the analytical service life models existing in the literature.

2.14.1 Analytical Models

Colleparidi et al. [158] were the first authors to quantify the kinetics of chloride penetration using a mathematical expression proposed by Fick in 1855 [159]. The expression is used to describe the diffusion of matter in permeable media, according to **Equation 2.77**;

$$\frac{\partial c(x, t)}{\partial t} - D^* \frac{\partial^2 c(x, t)}{\partial x^2} = 0 \quad (2.77)$$

D^* ; apparent diffusion coefficient

c ; chloride concentration in the pore solution

x ; concrete cover depth

t ; time

There are various analytical models, mainly based on modified versions of the classical error function solution to Fick's second law, that are used to solely model the diffusion transport of chloride ions. The HETEK model implements a variable surface chloride boundary condition in modelling the chloride diffusion in concrete. The ClinConc model simulates the chloride diffusion by taking into account the non-linear chloride binding along the concrete cover [159, 160]. The *fib* Bulletin 34 code is a probabilistic model that predicts the service life based on the distribution values of its durability parameters in the error function solution model [47].

2.14.2 *fib* Bulletin 34 code

Based on **Equation 2.77**, the *fib* Bulletin 34 code for Service Life Design of Reinforced Concrete (RC) defined the time to corrosion initiation according to **Equation 2.78** [161], assuming de-passivation of the reinforcement to be the serviceability limit state, and characterizing this by the critical chloride threshold [47].

$$C_{\text{crit}} = C_0 + (C_{s,\Delta x} - C_0) \left[1 - \operatorname{erf} \frac{d - \Delta x}{2\sqrt{D_{\text{app},c}t}} \right] \quad (2.78)$$

C_{crit} ; critical chloride threshold (% by mass of binder)

C_0 ; initial chloride content (% by mass of binder)

$C_{s,\Delta x}$; surface chloride content (% by mass of binder)

d ; concrete cover (mm)

Δx ; depth of the concrete convection zone (mm).

The apparent coefficient of chloride diffusion (i.e. $D_{app,C}$) through concrete is obtained from non-steady state chloride migration tests (D_{nssm}) (i.e. NTBUILD 492 [11]), according to **Equation 2.79** which is an approximation (and simplification) of the full time-dependent solution to Fickian diffusion. D_{nssm} has been measured for concrete, at an age of $t_0 = 28$ days, with the NTBUILD 492 test, and it is modified by the variation in temperature as an environmental factor.

$$D_{app,C} = \exp\left(b_e \left(\frac{1}{T_{ref}} - \frac{1}{T_{real}}\right)\right) D_{RMCK} k \left(\frac{t_0}{t}\right)^n \quad (2.79)$$

b_e ; regression variable (K)

T_{ref} ; standard test temperature (K)

T_{real} ; temperature of the structural element or the ambient air (K)

D_{nssm} ; chloride migration coefficient (mm²/year)

k ; transfer parameter, assumed to be 1 ([46]; [47])

t_0 ; reference point of time, 0.0767 years (28 days)

t ; time (years)

n ; aging factor

Lepech et al. [47] used the *fib* Bulletin 34 code in a case study where chloride-induced corrosion of reinforcement was the mode of failure and the service limit state. They computed the probability for RC with two different cover replacements, 40 and 80 mm, and obtained the histograms, with a lognormal distribution shown in **Figure 2.23**, which have been developed by using Monte Carlo analysis (i.e. computed with 100,000 runs) from this model:

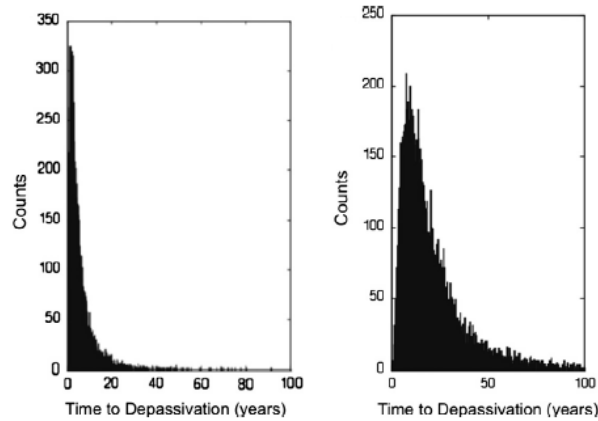


Figure 2.23 Histogram for time to depassivation of RC with (left) 40 mm cover replacement and (right) 80 mm cover replacement predicted by the fib Bulletin 34 design code. Figure adapted from [47].

The environmental and material performance parameters that are needed to be given into the model to obtain the above histograms, shown in **Figure 2.23**, are shown in **Table 2.8**.

Table 2.8 Model distribution parameters corresponding to the simulations in **Figure 2.23**.

Variable	Unit	Distribution
C_{crit}	Wt% of cement	Beta
C_0	Wt% of cement	Deterministic
$C_{s, \Delta x}$	Wt% of cement	Normal
d	mm	Normal
Δx	μm	Deterministic
b_e	-	Normal
T_{ref}	K	Deterministic
T_{real}	K	Normal
$D_{RMC,0}$	m^2/year	Normal
k	-	Deterministic
t_0	year	Deterministic
n	-	Beta

Data from some extracted concrete samples, that had been exposed to real service conditions, did not have the same chloride ingress curvature as predicted by Fick's second law of diffusion [162, 163]. The real service condition is a cyclic drying-wetting environment, and the chloride profile shown in **Figure 2.24** can indicate that diffusion is not the sole transport mechanism of chloride ingress.

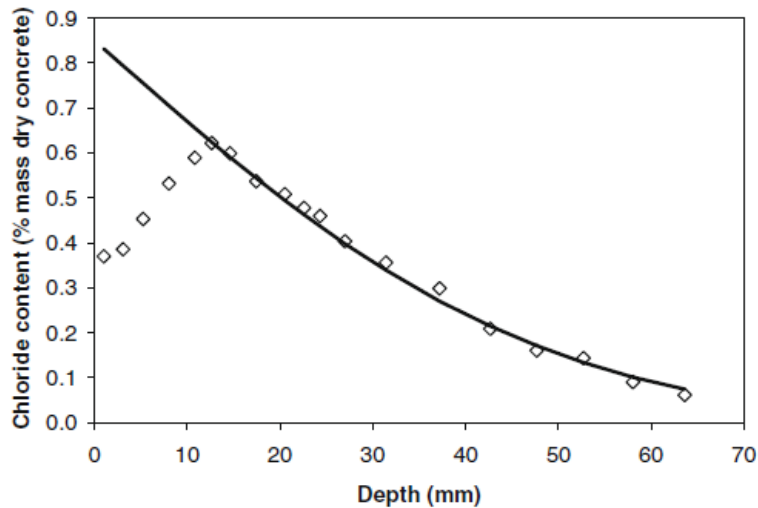


Figure 2.24 Data (shown by symbols) of chloride profile for samples obtained from real service conditions and chloride transport curve (shown by solid line) estimated by Fick's diffusion model [162].

The chloride content in the vicinity of the surface layer tends to increase to a maximum and then decrease along the depth of the concrete cover [7]. Ožbolt et al. [164] have explained that this increase is the combined effect of capillary suction and moisture evaporation that can cause the chloride to accumulate at a certain depth, and not only in the surface layer, due to hysteric moisture behaviour [164]. Chang et al. [7] have further researched the cause of this chloride peak and have found that it is a coupled effect of carbonation and capillary suction/moisture evaporation. They have explained that the chloride peak was also because of the decomposition of Friedel's salt as an effect of carbonation which occurs during the drying stage [7]. Therefore, service life models that do not account for the combined moisture and carbonation effect on the durability of concrete can lead to misleading service life calculations.

2.15 Conclusion

According to the conducted literature review, the serviceability limit state of AAC exposed to the combined modes of corrosion conditions still needs to be quantitatively predicted to assess the reliability of AAMs as low carbon construction material for structural applications with a target service life of at least 100 years. Consequently, the main scope of this research is the construction and implementation of a modelling framework in which the durability characteristics that define the resistance of AAC to chloride ingress and carbonation reaction is implemented. The following chapters provide the main insights towards constructing a service life model for AAMs by first testing an already existing service life model that has already been developed for PC concrete (i.e. *fib* Bulletin 34 code). The results from the *fib* Bulletin 34 code provide insights about the impact of environmental condition (e.g.

temperature) on the durability of AAC. This impact of environmental condition has then led to the study of the relation between the relative humidity of the environment and the degree of saturation of the concrete through the implementation of moisture permeability models. Finally, quantitative prediction of the degree of saturation of the pores across the concrete, cover has been set as a key parameter to model the interplay of ingress of CO₂ and chloride ions into the concrete with the durability response of AAMs to predict the service life of AAC in carbonation-chloride induced corrosion. In addition, similar to the *fib* Bulletin 34 code, the developed coupled mass transport model is set to probabilistically predict the service life of AAC to account for the variation of composition and reactivity of the precursors (i.e. SG and FA) by including a range of performance values for each durability parameter in the proposed service life model.

Chapter 3: Materials and Methods

3.1 Raw Materials and Mix Proportions

In this research the durability and service life of high calcium based alkali-activated binders are mainly measured and predicted since it has been considered that calcium-rich AAMs have better resistance to chloride penetration than PC [10]. Thus, alkali-activated binders composed of ground granulated blast furnace slag mixed with fly ash precursors that has a maximum amount of 50 wt.% replacement of the total mix design is produced and studied in this thesis.

3.1.1 Precursors

Ground granulated blast furnace slag (SG), and fly ash (FA) were used in this research for the preparation of cement samples. The mineralogical compositions, measured by X-ray fluorescence, of these precursors, are shown in **Table 3.1** and can also be found in [165]. The SG was supplied from ECOCEM (France), and the FA from Baumineral (Germany).

Table 3.1 Averaged (Avg.) chemical composition and average particle size (i.e. d_{avg}) of SG, and FA for cement samples, as determined by X-ray fluorescence (XRF) and laser diffraction [165].

Precursor	CaO	SiO ₂	Al ₂ O ₃	MgO	SO ₃	Fe ₂ O ₃	TiO ₂	K ₂ O	Na ₂ O	LOI
SG (d_{avg} ;11.8 μ m)	42.6	36.1	11.1	6.4	0.8	0.4	0.5	0.4	0.2	0.6
FA (d_{avg} ;12.8 μ m)	6.2	51.8	22.2	2.5	0.6	7.9	1	2.2	1	3.1

In addition, SG, FA and Portland cement of type CEM III/B 42.5 were used in this research for the preparation of mortar samples. The study on alkali-activated and PC mortars was done in Belgium at the company SANACON in collaboration with Magnel-Vandepitte Laboratory, Department of Structural Engineering and Building Materials, Ghent University. The CEM III/B 42.5 was supplied from S.A. Cimenteries CBR Cementbedrijven N.V. (Belgium), SG from ECOCEM (The Netherlands) and FA from VLIEGASUNIE (The Netherlands). The CEM III/B 42.5 has a composition of 20-34 wt.% of clinker and 66-80 wt.% of SG as reported in [166]. Whereas the mineralogical composition of FA and SG is shown in **Table 3.2**.

Table 3.2 Chemical composition and average particle size (i.e. d_{avg}) of SG and FA for mortar samples, as determined by X-ray fluorescence (XRF) and laser diffraction [167].

Precursor	CaO	SiO ₂	Al ₂ O ₃	MgO	SO ₃	Fe ₂ O ₃	TiO ₂	K ₂ O	Na ₂ O	LOI
SG (d_{avg} ;8.28 μ m)	40.9	31.1	13.7	9.16	2.31	0.40	1.26	0.69	-	0.1
FA (d_{avg} ;8.48 μ m)	3.74	56.7	24	1.75	1.04	6.34	1.16	2.3	-	2.86

3.2 Preparation of Alkali-activated Cements and Mortars

3.2.1 Alkaline Activating Solution

The alkaline activating solution was prepared by dissolution of sodium hydroxide, NaOH, pellets (Sigma Aldrich) into sodium silicate solution (PQ Silicates), with silica modulus Ms (moles SiO₂/ moles Na₂O) of value 2 and 55.9 wt.% water), to obtain an alkaline activating solution of desired Ms, and an alkali (Na₂O) dosage defined as a certain weight percentage of the binder. The binder here includes the precursors and the dissolved-solids part of the activating solution. Then water was added to the activating solution to reach the desired water/binder ratio for each cement sample. The activating solution was left overnight to cool down to room temperature prior to preparation of the samples.

3.2.2 Alkali Activated Cements

The cement samples were produced by first manually mixing the precursors, to ensure a homogeneous mixture, and then adding the activating solution. Next the samples were mixed for two minutes under a slow rate (200-400 revolutions per minute, rpm) and then mixed for eight minutes under a higher rate (2000 rpm). All the samples were cast in sample tubes, made of plastic, then sealed and stored at room temperature (20 ± 3°C) until testing. The mix designs of the produced cements are shown in **Table 3.3**. These cement samples are studied in **Chapter 5**.

Table 3.3 Mix designs of alkali-activated pastes.

Mix of Low and High Calcium based Alkali-Activated Cements				
Precursor	Type of activator	w/b	Na₂O (wt.%Binder)	Ms (moles SiO₂/moles Na₂O)
50% Slag and 50% Fly ash	NaOH-Na ₂ Si ₂ O ₅	0.4	4	1.5
75% Slag and 25% Fly ash	NaOH-Na ₂ Si ₂ O ₅	0.45	4	1.5
High-Calcium based Alkali-Activated Cements				
Precursor	Type of activator	w/b	Na₂O (wt.%Binder)	Ms (moles SiO₂/moles Na₂O)
100% Slag	NaOH-Na ₂ Si ₂ O ₅	0.5	4	1.5
100% Slag	NaOH-Na ₂ Si ₂ O ₅	0.47	8	1.5

3.2.3 Alkali Activated Mortars

The mortars were prepared in 10 L batches with a planetary mixer. The Quartz sand, with 0-4 mm particle size, and solid precursors were first dry blended for ninety seconds. Then the alkaline activating solution was gradually added, in thirty seconds, and further mixed for two

minutes to derive homogeneous mixtures. Next, the mortars were cast into moulds in two layers, and each layer was compacted on a vibrating table for thirty seconds. The moulds, made of wood, have dimensions of 100 mm x 100 mm x 50 mm and contain two embedded stainless steel bars, of diameter 6 mm, that are positioned 50 mm apart. The amount of each material used is shown in **Table 3.4** in order to obtain the final mix designs of alkali-activated mortars as shown **Table 3.5**. In addition, Portland cement of type CEM III/B 42.5N (according to EN 197-1) was used to produce Portland cement based mortars. These samples are studied in **Chapter 6**.

Table 3.4 Materials used in alkali-activated mortars.

Sample	Amount of NaOH (g)	Amount of Na ₂ Si ₂ O ₅ (g)	Amount of Water (g)	Amount of Precursor (g)			Amount of Sand (g)
				SG	FA	CEM III/B	
100SG	60	1050	1935	4500	-	-	15069
75SG25FA	60	1050	1665	3386.25	1128.75	-	15114.15
50SG50FA	60	1050	1425	2250	2250	-	15069.15
CEMIII/B	-	-	2153	-	-	4305	12915

Table 3.5 Mix design of alkali-activated mortars.

Sample	Na ₂ O (Wt.% of Binder)	Ms (nSiO ₂ /nNa ₂ O)	water/binder (mass ratio)	Sand/binder (mass ratio)
100SG	4	1.5	0.5	3
75SG25FA	4	1.5	0.45	3
50SG50FA	4	1.5	0.4	3
CEM III	-	-	0.5	3

3.3 Test Methods

3.3.1 Dynamic Vapor Sorption

Dynamic vapour sorption, DVS, is used for **Chapter 5** to study the moisture permeability in cement and the water vapour sorption isotherms (WVSIs) including adsorption and desorption isotherms of the binder. So that to model moisture transport and estimate free water content, or degree of water saturation, in cement as a function of RH of the external environment [79].

DVS is a gravimetric technique that measures the mass gain during wetting, or loss during drying, in each RH step carried out in order to obtain WVSIs by means of a directly-generated controlled RH condition. During the experiment, small RH steps, by 5%, were carried out so it can be assumed that the apparent moisture diffusivity, $D_a(S)$, is constant within each RH interval. Therefore, the apparent moisture diffusivity can be calculated by Fick's second law of diffusion according to **Equation 3.1**;

$$\frac{\partial S}{\partial t} = D_a(S) \frac{\partial^2 S}{\partial x^2} \quad (3.1)$$

Where S is the degree of saturation of the cement paste.

In this study, WVSIs of the cement samples were obtained by monitoring the mass changes from 50% to 95% relative humidity. In this case, the calculation of the degree of saturation is according to **Equation 3.2**;

$$S = \frac{m - m_d}{m_m - m_d} \quad (3.2)$$

m_d ; mass change at lowest relative humidity, 50%

m_m ; mass change at highest relative humidity, 95%

m ; mass change at certain relative humidity

The apparent moisture diffusion coefficients, fitted through water sorption mass change curves, are based on a simplification that water diffuses into a thin slab of cement powder from its top surface in the sample pan. Hence, a one dimensional slab model is implemented with the assumption that the cement powder particles are uniformly distributed on the sample pan. The solution that has been used, in the literature, to numerically solve **Equation 3.1** is known as the slope method by using **Equation 3.3**, for the wetting process, and **Equation 3.4**, for the drying process [168].

$$\frac{M_t}{M_e} = 2 \left(\frac{Dt}{\pi l^2} \right)^{\frac{1}{2}} \left(\text{for sorption process, when } \frac{M_t}{M_e} < 0.6 \right) \quad (3.3)$$

$$\frac{M_t - M_e}{M_0 - M_e} = 1 - 2 \left(\frac{Dt}{\pi l^2} \right)^{\frac{1}{2}} \quad \left(\text{for desorption process, when } 0.4 < \frac{M_t - M_e}{M_0 - M_e} < 1 \right) \quad (3.4)$$

t ; time increment from last equilibrium stage, s

M_0 ; mass value at end of previous equilibrium stage, g

M_e ; mass value at equilibrium at the current stage, g

M_t ; mass value at time t , g

l ; thickness of the powder sample, m

D ; diffusion coefficient in the current stage, m^2/s

3.3.2 Thermogravimetry Analysis

Thermogravimetric analysis (TGA) for all cements was carried out in a Perkin Elmer TGA 4000 instrument coupled with a Hiden mass spectrometer. The amount of sample used was 40 mg and it was tested from 20°C to 1000°C at a heating rate of 10°C/min, in an alumina crucible. Commercial-grade nitrogen was used as inert gas at a flow rate of 20 mL/min. The purpose of this characterization, studied in **Chapter 5**, is to identify the presence of carbonated cement hydrate phase that may possibly form in alkali-activated binders exposed to natural carbonation in the surrounding ambient environment.

3.3.3 Mercury Intrusion Porosimetry

Mercury intrusion Porosimetry, MIP, has been used for **Chapter 5** research to determine the percentage of porosity (i.e. total pore volume) of the cementitious material, along with information about its pore size distribution. The main source of error in MIP is its inability for the mercury to pass through all the closed pores, and also the ink-bottle effect which means that the pore entry diameter, rather than the actual pore diameter, is measured. As well as the way the material is being tested, through varying contact angles of mercury per test can affect the results [169]. The estimation of the pore radius and pore pressure is calculated by the Washburn equation [170], **Equation 3.5**, which is the base calculation surrounding the equipment.

$$P = - \frac{2\gamma \cos(\theta)}{r} \quad (3.5)$$

P; pore pressure, Pa

r; meniscus curvature radius (pore entry radius), m

γ ; surface tension of mercury, N/m

θ ; contact angle of mercury/cement interface, °

Samples of the alkali-activated binders are cut into small bulk pieces of total mass around 2 g and are analysed using the Autopore V instrument where the contact angle and surface tension are set to 130° and 0.485 Nm⁻¹, according to the recommendations discussed in [170-172]. Multiple samples, 3-4 per mix, are collected in order to create a statistical average and a standard deviation of MIP data in order to estimate the porosity of the binders.

Finally, this instrument has been used to estimate; effective porosity of the cements, the volumetric fraction of the large pore region, as well as the length factor of the large pore to the small pore regions, as will be discussed in **Chapter 5**.

3.3.4 Embedded Electrode Methods - Bulk Resistivity

The embedded electrode method (EEM) is a validated method used to measure the resistivity of repair mortars in order to assess their compatibility with the parent concrete prior to cathodic protection, as explained in [173]. Cathodic protection is a technique that can reduce or even stop the corrosion process of steel in reinforced concrete structure. In this research, the EEM method is used to evaluate the transport properties of alkali-activated mortars that will be determined in **Chapter 6**.

Resistivity measurements have been conducted by measuring the resistance between two stainless steel bars that are embedded into mortar prisms, with dimensions of 100 mm × 100 mm × 50 mm, by means of an LCR (Inductance (L), Capacitance (C) and resistance (R)) meter, set at a measurement frequency of 120 Hz, as shown in **Figure 3.1**;



Figure 3.1 Embedded Electrodes Method (EEM) [173].

Then the resistivity measurement is calculated by multiplying the measured resistance by a cell constant, C , that is dependent on the geometry of the mortar mould and embedded electrodes. The value of the cell constant, $C = 7.62$ cm, has already been determined in [173] for the exact cell setup used in this research. In summary, the mortar prism, with the embedded electrodes, was filled with a potassium chloride solution, of concentration 0.01 mol/L, and resistance was measured, using the LCR meter, between the electrodes. The conductivity of the electrolyte solution was already determined and used to calculate its resistivity which is then divided by the measured resistance in order to obtain the cell constant.

3.3.5 Particle Size Analysis

A Mastersizer 3000 particle size analyser (Malvern Company) was used for the quantification of particle size distribution of the studied cements, in powder form, for analytical sizes ranging from 0.01 μm – 2mm. Non-aqueous solution, isopropanol, was used as dispersing agent in the medium of the test. The average particle sizes of the crushed cement powders have been used to calculate the apparent moisture diffusivities based on the water sorption kinetic data obtained from the DVS, as mentioned in section 3.3.1.

3.4 Software

3.4.1 Cement Pore Solution Ions

A thermodynamic modelling programme was used to predict the concentration of pore solution ions and pore solution alkalinity in alkali-activated cements and used for **Chapters 4 and 6**. The open source software GEM-Selektor v.3 (<https://gems.web.psi.ch/GEMS3/>) was utilised to perform the prediction where the mineralogical composition, extent of degree of reaction for the precursors and mix design of the alkali-activated binders were set as inputs in order to obtain the concentration of ions present in the aqueous phase of the cements. This output is

used in Chapter 6 in order to calculate the resistivity of the pore solution because all ions contribute to the electrolytic conductivity of the solution. In addition, the extent of degree of reaction for slag and fly ash, used in the thermodynamic calculations, is discussed in **Chapter 4** and **6**.

Thermodynamic data for solid, aqueous and gas phases in alkali-activated cements were acquired from the Slop98.dat and Cemdata18 database, with the ideal solid solution end member models for alkali-substituted calcium aluminate silicate hydrate gel (CNASH_ss) and for hydroxylated hydrotalcite (MgAl-OH-LDH_ss) as detailed in [123, 145, 174].

The following **Equation 3.6** is the extended Debye-Hückel equation used to calculate the activity coefficients of the aqueous species in order to estimate the real concentration of the ions participating in the hydration reactions;

$$\log_{10}\gamma_i = \frac{-Az_i^2\sqrt{I}}{1 + Ba\sqrt{I}} + bI + \log_{10} \frac{x_{iw}}{X_w} \quad (3.6)$$

γ_i ; activity coefficient of the i^{th} aqueous species

z_i ; charge of the i^{th} aqueous species

A ($\text{kg}^{0.5}\text{mol}^{-0.5}$) and B ($\text{kg}^{0.5}\text{mol}^{-0.5}\text{cm}^{-1}$); temperature and pressure dependent electrostatic parameters

x_{iw} ; molar quantity of water

X_w ; molar amount of the total aqueous phase

The values for the average ionic radius, a , and the parameter for short-range interactions of charged species, b , are set to be 3.31 \AA and $0.098 \text{ kg}\cdot\text{mol}^{-1}$ respectively in order to represent a NaOH-dominated aqueous phase, as specified according to [175].

I is the total ionic strength of the aqueous solution and it is calculated according to the **Equation 3.7**.

$$I = \frac{1}{2} \sum c_i \cdot z_i^2 \quad (3.7)$$

c_i ; concentration of the i^{th} ionic species

z_i ; charge of the i^{th} ionic species

Finally, the formation of quartz, dolomite, thaumasite, and magnesite are excluded in the calculations because their kinetics of formation under ambient conditions is considered to be slow [176].

3.4.2 Coupled System of Partial Differential Equations

In saturated conditions, or in complete submerged water conditions, chloride ingress into the concrete cover occurs mainly through a diffusion process because of the presence of concentration gradient [159]. Fick's second law of diffusion has been used in the literature for modelling chloride ingress in concrete according to the following partial differential equation (pde), **Eq.3.8**, with the initial and boundary conditions set accordingly:

$$\begin{cases} \frac{\partial C}{\partial t} = D \frac{\partial^2 C}{\partial x^2}, & x > 0, \quad t > t_{\text{ex}} \\ C(0, t) = C_{S,0}, & t > t_{\text{ex}}, \quad \text{Boundary Condition} \\ C(x, t_{\text{ex}}) = 0, & x > 0, \quad \text{Initial Condition} \end{cases} \quad (3.8)$$

C ; Chloride concentration, mol/L, at a certain time of exposure, t in year, and distance, x in m, in the concrete cover.

$C_{S,0}$; Surface chloride concentration at the surface of the concrete cover, m.

D ; Constant diffusion coefficient, m^2/s

t_{ex} ; Initial time of exposure, year

The analytical solution to the above pde is often calculated using the simplified form of the error function solution of Fick's second law according to **Equation 3.9** with the definition of complementary error function shown in **Equation 3.10**.

$$C(x, t) = C_{s,0} \operatorname{erfc} \left(\frac{x}{2\sqrt{D(t - t_{\text{ex}})}} \right), \quad x > 0, \quad t > t_{\text{ex}} \quad (3.9)$$

$$\operatorname{erfc}(z) = 1 - \frac{2}{\sqrt{\pi}} \int_0^z e^{-t^2} dt \quad (3.10)$$

Where $C_{s,0}$ and D are experimentally determined from curve fitting the chloride profile obtained from the NTBUILD 443 Test.

There are several numerical methods for solving **Equation 3.8** under more complex physical circumstances, including where the diffusion constant is not constant, but one common method is the finite explicit method using the forward Euler method, where the derivation to obtain this method can be found in [177]. First consider a space, x (distance) vs. t (time) as shown in **Figure 3.2**.

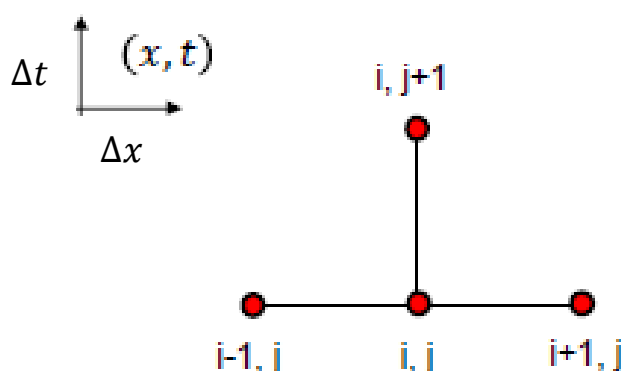


Figure 3.2 Graphical representation of explicit finite difference method use to characterise multi-species transport through alkali-activated concrete.

Where the x and t coordinates are divided by intervals Δx and Δt that allows the space to be regarded as a grid of rectangles of size $(\Delta x \times \Delta t)$. Then the coordinate of a point in the grid is marked as $(i\Delta x, j\Delta t)$ where i and j are positive integers. Hence, the concentration of a species is denoted as $c_{i,j}$ at coordinates $(i\Delta x, j\Delta t)$ and the neighbouring values are pinpointed in **Figure 3.2**. The derivation of the finite explicit method is done by applying Taylor's series in t -direction while keeping x constant,

$$c_{i,j+1} = c_{i,j} + \Delta t \left(\frac{\partial c}{\partial t} \right)_{i,j} + \frac{1}{2} (\Delta t)^2 \left(\frac{\partial^2 c}{\partial t^2} \right)_{i,j} + \dots \quad (3.11)$$

Then rearranging to obtain;

$$\left(\frac{\partial c}{\partial t}\right)_{i,j} = \frac{c_{i,j+1} - c_{i,j}}{\Delta t} + O(\Delta t) \quad (3.12)$$

Where $O(\Delta t)$ is the order of error which are the neglected terms having an order of Δt or higher when the left and right hand side of **Equation 3.11** is divided by Δt .

Next applying Taylor's series in the x-direction, while keeping the time constant, the following equations, **Equation 3.13** and **Equation 3.14**, are obtained.

$$c_{i+1,j} = c_{i,j} + \Delta x \left(\frac{\partial c}{\partial x}\right)_{i,j} + \frac{1}{2}(\Delta x)^2 \left(\frac{\partial^2 c}{\partial x^2}\right)_{i,j} + \dots \quad (3.13)$$

$$c_{i-1,j} = c_{i,j} - \Delta x \left(\frac{\partial c}{\partial x}\right)_{i,j} + \frac{1}{2}(\Delta x)^2 \left(\frac{\partial^2 c}{\partial x^2}\right)_{i,j} + \dots \quad (3.14)$$

Then adding **Equation 3.13** and **Equation 3.14**,

$$\left(\frac{\partial^2 c}{\partial x^2}\right)_{i,j} = \frac{c_{i+1,j} - 2c_{i,j} + c_{i-1,j}}{(\Delta x)^2} + O(\Delta x)^2 \quad (3.15)$$

As well as neglecting the error terms found in $O(\Delta x)^2$, next step is substituting **Equation 3.15** and **Equation 3.12** into **Equation 3.8** to get **Equation 3.16**.

$$\frac{C_i^{j+1} - C_i^j}{\Delta t} = D \frac{C_{i-1}^j - 2C_i^j + C_{i+1}^j}{\Delta x^2} \quad (3.16)$$

Then rearranging to obtain the final form of the equation:

$$C_i^{j+1} = C_i^j + \frac{D\Delta t}{\Delta x^2} [C_{i-1}^j - 2C_i^j + C_{i+1}^j] \quad (3.17)$$

In addition, the discretisation should be done in such a way to nearly and accurately predict the value of the concentration of the ionic species at a given Δx and this can be done by increasing the number of time steps of small step size such that $\Delta t \leq \frac{\Delta x^2}{2D}$. This can ensure stability for optimal predictions done by the model as discussed in [178].

However, in unsaturated conditions, diffusion is not necessarily the main transport phenomenon. In cases where the concrete is subjected to cyclic wetting and drying cycles the diffusion of chloride ions is mainly dependent on the degree of water saturation in the capillary pores of the concrete because the mode of chloride ion transfer is through the aqueous phase of the pores. Hence, diffusional transport is accompanied by capillary suction, from capillary action inside capillary pores of the concrete cover, permeation due to a pressure gradient, and migration due to an electrical potential gradient [37]. In addition, chloride binding and aging, due to the impact of pozzolanic activity, must also be considered while modelling the chloride ingress [30].

Therefore, appropriate moisture transport models are essential for the prediction of the degree of evaporable water content (i.e. free water) in capillary pores as a function of the external environmental relative humidity. Conventionally, moisture transport has been modelled using Darcy's or Fick's law without accounting for the anomaly effect present in such materials [62]. In addition, CO₂ simultaneously diffuses through the gaseous part of the pores and partially dissolves into the pore solution and initiate carbonation reactions that can lead to changes in the microstructure of the cement [5]. Therefore, a multi-species and multi-mechanism reactive transport modelling framework is needed to predict the durability performance of concrete. Consequently, an advanced solver is needed to model this highly non-linear mass transport problem [179]. The following section describes the `pdepe` function that contains the built-in solver available in MATLAB.

3.4.2.1 *pdepe Function*

The equations, that are discussed in **Chapters 5 and 6**, along with their initial and boundary conditions are being solved by using the `pdepe` function available in MatLab according to the following format;

$$\text{sol} = \text{pdepe}(m, \text{pdefun}, \text{icfun}, \text{bcfun}, \text{xmesh}, \text{tspan})$$

Where;

`pdefun`; elliptical and or parabolic partial differential equation

icfun; initial value conditions

bcfun; boundary value conditions

xmesh; spatial mesh

tspan; temporal mesh

Considering the partial differential equation, pdefun, the pdepe solver expects it in the form of **Equation 3.18**.

$$c\left(x, t, u, \frac{\partial u}{\partial x}\right) \frac{\partial u}{\partial t} = x^{-m} \frac{\partial}{\partial x} \left(x^m f\left(x, t, u, \frac{\partial u}{\partial x}\right) \right) + s\left(x, t, u, \frac{\partial u}{\partial x}\right) \quad (3.18)$$

The terms in the equation above are:

m ; scalar parameter that represents the symmetry of the system (i.e. 0 for slab, 1 for cylindrical and 2 for spherical coordinates).

$c\left(x, t, u, \frac{\partial u}{\partial x}\right)$; diagonal matrix that governs the type of pde which can be elliptical, when the elements of this matrix are zero, and parabolic when the elements are non-zero and positive.

$f\left(x, t, u, \frac{\partial u}{\partial x}\right)$; flux term.

$s\left(x, t, u, \frac{\partial u}{\partial x}\right)$; source term.

The algorithm used in the pdepe function is the ode15s solver that is based on implicit finite difference method and is well known for solving stiff ordinary differential equations [180]. Stiffness is an efficiency issue where very small step size is required in a region to obtain a very smooth solution curve that represents reliable results for the differential equation. The ode15s solver speeds up the computation process through implementing a moderate number of steps, of very small size, and function evaluations that satisfy the accuracy requirement set as a default in the solver [181].

The pdepe function outputs the values of the solution, for the coded pde in the MATLAB script, on the spatial mesh provided in xmesh after they are computed by integration to obtain approximate solutions at the times specified in tspan.

The values of the initial conditions, I.C., for the pdes used in this research, are set constant with positive values for the initial time t_0 . Additionally, this I.C. can be set either as a constant number or as a function of distance, x , into the concrete cover. The former type can create an initial uniform profile whereas the latter an un-uniform profile at time t_0 across the thickness of the concrete cover. The I.C. is coded in the icfun of the pdepe function.

The boundary conditions, B.C., can be modified based on the type of condition the transport occurs. In this case the boundary condition can be set as constant (Dirichlet), a flux (Von Neumann), or a mix between the two called the Robin [182]. The B.C. is coded in the bcfun of pdepe function and in the form of **Equation 3.19**.

$$p(x, t, u) + q(x, t) f\left(x, t, u \frac{\partial u}{\partial x}\right) \quad (3.19)$$

$f\left(x, t, u \frac{\partial u}{\partial x}\right)$; flux term

$p(x, t, u)$ and $q(x, t)$; coefficients

Finally, a MATLAB script has been developed to simulate anomalous moisture transport in alkali-activated cements and reactive transport that accounts for carbonation and chloride ingress in unsaturated alkali-activated concrete. A detailed description of the numerical models coded in the MatLab scripts can be found in **Chapters 4-6**.

3.5 Conclusion

The Matlab software, section 3.4.2, is implemented throughout **Chapters 4-6**. In **Chapter: 4** the software is used to fit distribution of durability data with mathematical functions and to perform service life calculations using an analytical model. It is also applied in **Chapters 5** and **6** to numerically solve single and coupled nonlinear differential equations. The thermodynamic modelling programme, described in section 3.4.1, is used for **Chapters 4** and **6**. The methods described in sections 3.3.1-3.3.3 and 3.3.5 correspond to the methodology used in **Chapter: 5** to obtain the moisture permeability data for alkali-activated cements. Whereas the method described in section 3.3.4 corresponds to the methodology used in **Chapter: 6** to obtain the ionic transport data for alkali-activated mortars.

Chapter 4: Probabilistic Service Life Prediction of Alkali Activated Concretes Exposed to Chloride Induced Corrosion

Note: This chapter is based on the manuscript “Probabilistic Service Life Prediction of Alkali Activated Concretes Exposed to Chloride Induced Corrosion” T.J. Chidiac, N. Ukrainczyk, D. P. Prentice, and J. L. Provis published in Journal of Advanced Concrete Technology.

Abstract

In this study, the well-established service life design code defined in *fib* Bulletin 34 is adapted to predict the time to initiation of reinforcement corrosion in alkali-activated concretes submerged in marine conditions. The model approach is based on the probabilistic calculation of the time needed for a critical concentration of chloride ions, migrating from the external environment towards the rebar, to accumulate at the surface of the steel reinforcement and initiate the corrosion reaction. The information required to define the parameters of the model is derived from literature data, relating the concrete mix designs with accelerated laboratory test results. The findings indicate that alkali activated concretes with high calcium content can exhibit promising characteristics as a construction material applied for structural application in chloride-rich corrosive environments. The probabilistic approach adopted in this model provides the opportunity to assess the influence of variability in mineralogical composition and reactivity of the precursors with the alkaline activating solution, that influence the chemical evolution and microstructure of the binder matrix. The predicted service life is quite sensitive to these factors, with very high service lives predicted for some alkali-activated concretes but rather short service lives predicted for others, and this must be incorporated into any engineering assessment of future material performance.

Keywords: Alkali-activated concrete; chloride; durability; service life; probabilistic modelling

4.1 Introduction

The service life of a reinforced concrete structure is often controlled by chloride ions diffusing throughout the interconnected capillary pores of the concrete and accumulating at the surface of the rebar until reaching a certain concentration, known as the critical chloride threshold (C_{crit}). This causes corrosion through localized (i.e. pitting) de-passivation over areas of the protective film around the rebar [7]. Consequently, reductions in cross-sectional area of the rebar occur, reducing the capacity of the reinforced element to withstand mechanical load [9]. This process takes place in conventional Portland cement concretes, and also in alkali-activated concretes (AACs) which are the main topic of investigation here. The protection given by concrete cover as a protective barrier against corrosive agents for the steel reinforcement has been extensively researched for AACs, with the aim of obtaining data regarding their performance in corrosive conditions [183].

Service life modelling of Portland cement (PC) based concretes has adopted the term critical chloride threshold (C_{crit}), in terms of wt.% of the binder, as a limit state function to estimate the time needed for a certain concentration of chloride ions to accumulate across the steel and initiate corrosion. Various analytical models, based on modified versions of the classical error function solution of Fick's second law, have been used to calculate the service life of structures by modelling the diffusional transport of chloride ions into the concrete cover. The HETEK model [184] implements a variable surface chloride boundary condition in modelling the chloride diffusion in concrete. The ClinConc model [160] simulates the chloride diffusion by taking into account non-linear chloride binding within the concrete cover [159, 160]. However, these models are deterministic; they provide single output values for service life, without explicitly considering distributions of input parameters. A probabilistic approach is preferred here, because the performance properties of multiple elements made from any given concrete are intrinsically scattered, leading to variation in the performance of the overall structure [114].

The *fib* Bulletin 34 code [161, 185] describes a probabilistic model that predicts the service life based on the distribution values of its durability parameters in the error function solution to Fickian diffusion [47]. This code is chosen here as the basis to probabilistically predict the service life of AAC, and to identify how variations in the material parameter impact the predicted service life. In summary, the purpose of this research is to demonstrate the importance of incorporating reactivity and mineralogical composition of precursors as experimental parameters in durability test designs for AAC. Thus, setting the direction for future design in

service life models to account the variability in durability performance of any given AAC because of the inconsistency in production conditions which impact mineralogical composition of raw materials (i.e. industrial wastes) needed for the manufacture of AACs across the concrete industries. Examples of production conditions are the composition of raw materials and methods of steel manufacture where slag as a by-product is obtained and used as precursors for AAMs.

The first section of this paper reviews the mechanisms underlying chloride-induced corrosion in high-calcium (>30% CaO) AAMs and low-calcium (<15% CaO) AAMs, drawing upon existing durability data available in the literature. The second section describes the *fib* Bulletin 34 code for service life design, which is applied together with thermodynamic prediction of the pore solution alkalinity of AACs, as a key input parameter for the calculation of C_{crit} . Subsequently, the collected data are used in service life calculations for three specific types of alkali-activated concretes: alkali-activated slag concrete (denoted 100%SG), alkali-activated slag-fly ash concrete (50%SG/50%FA), and alkali-activated fly ash concrete (100%FA).

4.2 Durability and Service Life

Most of the AAC durability data available in the literature focus on the transport properties of corrosive agents into alkali-activated concretes, with a smaller but still significant number of studies presenting aging factors (i.e. time-dependent refinement of the pore structure of the concrete), or critical chloride thresholds C_{crit} [44]. So, the established *fib* Bulletin 34 design code [161], which uses distributions of chloride transport parameters, critical chloride thresholds, and aging factor is adapted here to probabilistically predict the service life of AAMs. The key controlling factors are now discussed in turn.

4.2.1 Chloride Threshold

Corrosion reactions in AAMs, with both low and high calcium contents, differ from those observed in Portland cement-based concrete due to the high alkalinity of the pore solution in AAMs and the possible presence of reduced sulfur species (sulfides) in the pore solution of alkali-activated slag, which can lead to the formation of a sulfide film on the metal surface, resulting in a more complex corrosion reaction sequence [44] [45] [183] [49]. Despite the complexity of corrosion chemistry in AAMs, several studies have successfully determined critical chloride thresholds, C_{crit} , in terms of chloride content by wt.% of binder, as well as the ratio of chloride to hydroxide concentration (as shown in Figure 4.1 and Table 2.1) [55]. The

values of C_{crit} are given for alkali-activated mortars containing different amounts of slag (SG) and fly ash (FA) precursors in their mix designs, **Figure 4.1**.

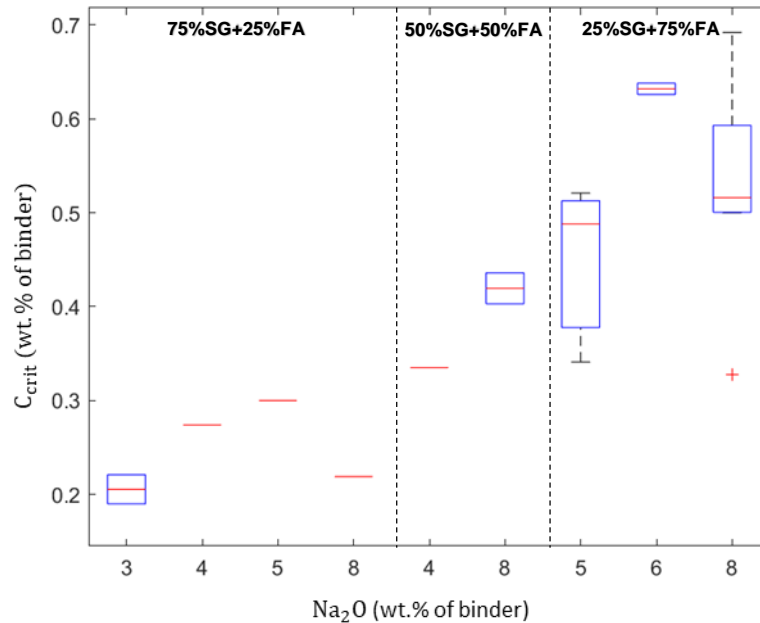


Figure 4.1 Critical chloride thresholds (C_{crit}) for alkali-activated mortars derived from mixed high- and low-Ca precursors (wt.% slag and fly ash as indicated for each group of data), as a function of alkali activator dosage; data from [55].

Table 2.1 in section 2.8.3 of Chapter 2: “Literature Review” provides a summary of published corrosion risk indicators in terms of the chloride and hydroxide concentrations ($[Cl^-]$ and $[OH^-]$) as well as the various test methods employed, for both low and high calcium AAMs, where it is assumed that ground granulated blast furnace slag is the main source of calcium. Sulfide content is also important in slag-based AAMs, due to the high content of reduced sulfur. This is due to a significant role played by HS^- ions in the pore solution, leading to the formation of a complex Fe-S passivating film on the steel surface [45].

4.2.2 Chloride Ingress

Chloride penetration into concrete is a complex phenomenon because diffusion is also coupled with migration (defined via the non-steady state migration coefficient, D_{nssm}) and/or convection (i.e. flow of solvent) phenomena, in laboratory tests and in field exposure. For the prediction of service life, the *fib* Bulletin 34 code for service life design utilises chloride migration data as input for the transport of chloride ingress, neglecting the potential influence of other forms of transport.

Figures 4.2 and 4.3 show the variations of chloride migration coefficient values obtained by the rapid chloride migration test NTBUILD 492 [11], for high-Ca, 50/50 slag/fly ash-based, and low-Ca AAMs as reported in the literature [98, 114, 152, 186, 187].

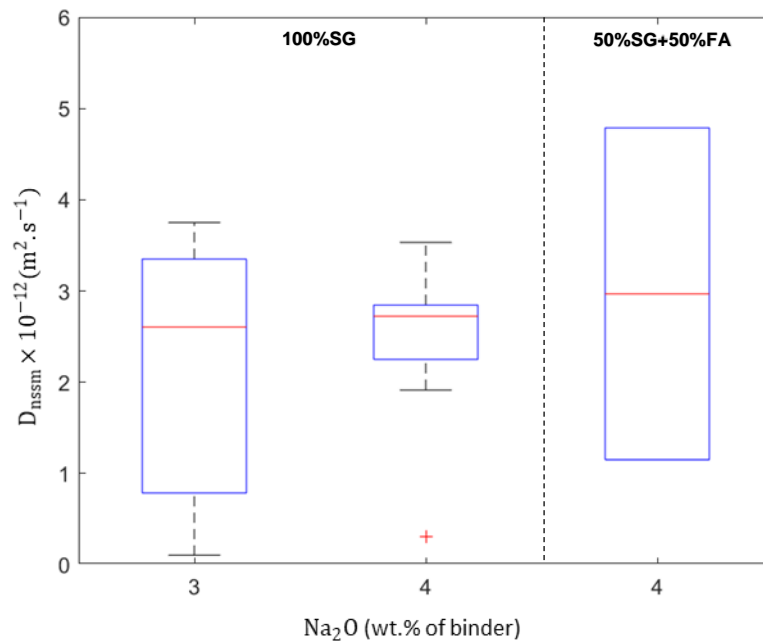


Figure 4.2 Chloride migration coefficients of high calcium alkali-activated concretes as a function of alkali dosage, compiled from the available literature [98, 114, 152, 186, 187].

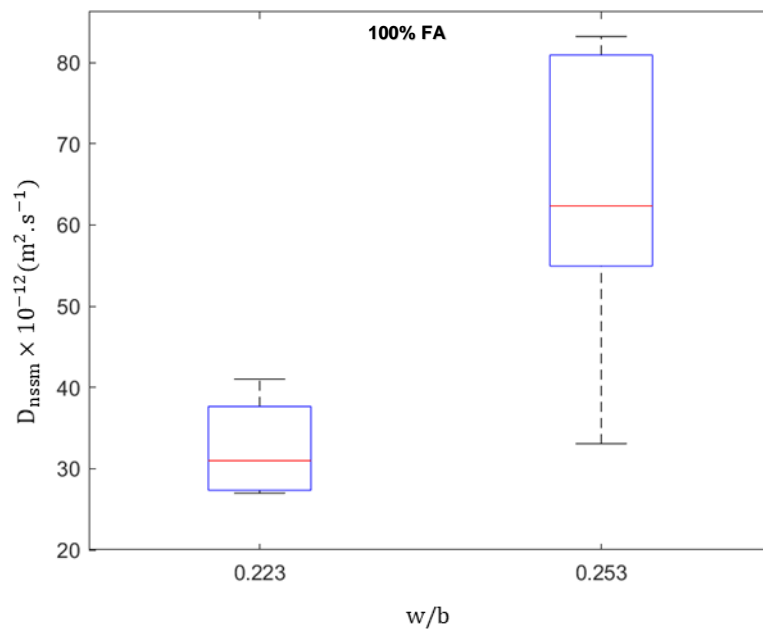


Figure 4.3 Chloride migration coefficients of low calcium alkali-activated concretes as a function of water/binder (w/b), compiled from the available literature [98, 114, 152, 186, 187].

The chloride migration coefficient values for 100% SG alkali-activated concrete, with alkali dosages of 3 and 4 wt.% of binder, are within the range 0.1 to 3.75×10^{-12} m²/s. The lower boundary of this distribution indicates very low or almost negligible chloride mobility according to the classification of [188], whereas the values obtained for 50%SG/50%FA alkali-activated concretes are somewhat higher, from 1.15 to 4.78×10^{-12} m²/s. However, these are still lower than the maximum recommended values for concretes based on CEM III (blended PC containing 36-95% slag) under chloride exposure [37].

The chloride migration coefficients of 100%FA alkali-activated concretes (Figure 4.3), with similar mix design composition except for the ratio of water to binder, range from 26.98 to 83.2×10^{-12} m²/s, which are very high compared to the standard values [37]. The reason for such a difference in chloride migration values is because the pore structure of 100%FA alkali-activated concretes is very open and connected compared to most other cementitious materials, making the material permeable [108]. In addition, there is less chemical binding of free water in low calcium AAMs compared to high calcium AAMs [109]. There are also potential differences in chloride binding between different types of AAM, but this topic requires further analysis and insight, and is not invoked here as a detailed explanation for differences in concrete performance.

4.2.3 Aging of Concretes

Over time, the microstructure of a concrete tends to densify because of the chemical evolution of the binder. More hydration products are formed, leading to further refinement of the pores in the microstructure. Several methods have been used to measure the aging factor of alkali-activated concretes; **Table 4.1** summarises the reported aging factors of alkali-activated concretes, represented as the power-law exponents describing the reduction in diffusion or migration coefficients as a function of time.

Table 4.1 Aging factors of alkali-activated concretes as reported in the literature

Mix Design (%SG+%FA)	Na ₂ O (wt.% binder ^a)	Mr ^b	w/b ^c	Curing condition	Test method	Aging factor (exponent)	Ref
100% FA	15	1.375	0.37	80 °C for 24h	AASHTO T259 salt ponding	0.234	[189]
	15	1.375	0.37	80 °C for 24h	AASHTO T259 salt ponding	0.309	[189]
50% SG / 50% FA	4	1	0.425	100% RH	ASTM C1202 charge passed	0.604	[190]
100% SG	7	1.2	0.47	Under water	NordTest 443 bulk diffusion	0.574	[105]
	5	1.2	0.47	Under water	NordTest 443 bulk diffusion	0.55	[105]
	4	1.2	0.47	Under water	NordTest 443 bulk diffusion	0.512	[105]
	4	0.6	0.26	100% RH	Chloride penetration depth	0.74	[117]

^a binder; total amount of solids (precursors + anhydrous activator)

^b Mr; silica modulus in the activating solution (molar ratio of SiO₂ to Na₂O)

^c water/binder mass ratio; includes water within the activating solution and any extra water added in the mix

According to **Table 4.1** the values of the aging factors for the 50% SG / 50%FA mix, and the 100%SG mix of [117], are higher than the other reported values. The aging factor obtained for 50% SG / 50% FA was obtained by the rapid chloride permeability test where the measurement is done on the total charge passed through the concrete [190]. This test is designed based on the chemistry of the pore solution of PC which may not be suitable for AAMs containing a higher concentrated pore solution with ionic species (Zuo et al. 2019). The high aging factor for one 100%SG concrete was obtained from a single specimen exposed to a marine splash zone environment for two years. The aging factor was calculated by using the chloride diffusion obtained for this concrete after two years and with an assumed value for chloride diffusion after 4 years [117]. The authors of that study have suggested further research to validate this high value, 0.74, for the aging factor.

4.3 Materials and Methods

4.3.1 Mix designs selected for detailed analysis

Table 4.2 contains the mix designs of SG100, FA100 and 50SG50FA Alkali-activated concretes that are discussed in this paper. The durability data for each concrete are taken from literature reporting durability studies of alkali-activated concretes with similar mix designs (i.e. **Figures 4.1-4.3** and **Tables 2.1** and **4.1**) to create distributions in the model input data.

Table 4.2 Mix designs of alkali-activated concretes described in the simulations here. All samples were cured at room temperature and in saturated conditions.

Mix name	Sand/coarse aggregate mass ratio	Precursor amount (kg/m ³ concrete)		28 day compressive strength(MPa)	w/b ^a	Na ₂ O	Mr ^b	Ref.
		FA	SG					
FA100	0.667	425	-	42.4	0.253	10	1.1	[114]
SG100	0.667	-	357	33.9	0.42	3	0.33	[114]
50SG50FA	0.818	205	205	46	0.40	4	1.5	[98]

^a water/binder mass ratio; includes water within the activating solution and any extra water added in the mix

^b Mr; silica modulus in the activating solution (molar ratio of SiO₂ to Na₂O)

The depths of concrete cover to be assessed for service life calculations of SG100, 50SG50FA and FA100 in seaborne chloride environment, are 45, 60, and 200 mm, respectively. The high cover depth for FA100 is due to the high value of the chloride migration coefficient, Figure 4.3, that exceeds the limits specified by [37] and necessitates a very high cover depth to reach a meaningful service life under the model assumptions. The concrete cover depths for SG100 and 50SG50FA concretes are chosen based on their chloride migration values, **Figure 4.2**, which fall within the range of $D_{nssm,28}$ values (i.e. chloride migration test conducted on concretes cured for 28 days) that are conventionally used to recommend cover depths as shown in **Table 4.3**. The effect of the depth of the concrete cover on service life is also assessed in section 4.1 by sensitivity analysis.

Table 4.3 Maximum recommended $D_{nssm,28}$ * for various cover depths for binder type CEM III and specified chloride exposure classes, for a design service life of 100 years [37].

Mean Cover (mm) to reinforcing steel	Maximum value $D_{RMC,28}$ (10^{-12} m ² /s)	
	CEM III (50-80% slag)	
	XD1/2/3, XS1 *	XS2, XS3
35	2.0	1.0
40	4.0	1.5
45	6.0	2.5
50	8.5	3.5
55	12	5.0
60	15	6.5

* XD represents corrosion induced by de-icing salts, and XS represents corrosion induced by a seaborne chloride environment. The number indicates the severity of the environmental condition from a scale of 1 to 3 [191].

* $D_{nssm,28}$; chloride migration value for concrete measured after 28 days of curing

4.3.2 Calculation of Chloride Threshold

The defined ratios of chloride to hydroxide concentration for low-Ca AAMs and high Ca AAMs, from **Table 2.1**, are used to obtain the ranges of critical chloride thresholds, denoted as CT_{Concrete} and CT_{Cement} , in terms of chloride ion concentrations by wt.% of concrete and binder, respectively. These thresholds were calculated using **Equations 4.1** and **4.2**, derived from [192].

$$\frac{CT_{\text{concrete}}}{\frac{[\text{Cl}^-]}{[\text{OH}^-]}} = \frac{M_{\text{Cl}} S \phi_s}{10 \rho_c} 10^{-(\text{pK}_w - \text{pH})} \quad (4.1)$$

Where ρ_c is the density of the concrete (g/cm^3); S is pore saturation, set at 0.8 for concrete [192]; ϕ_s is concrete volume fraction porosity; pK_w is the ionic product of water, set to 14 at 25°C ; pH describes the alkalinity of the pore solution; and M_{Cl} is the molar mass of chloride, 35.453 g/mol .

$$\frac{CT_{\text{cement}}}{CT_{\text{concrete}}} = \frac{W_{\text{tot}}}{W_{\text{cement}}} \quad (4.2)$$

Where W_{tot} is total weight of the concrete; and W_{cement} is total weight of the binder used in the concrete.

It should be noted that the influence of sulfide concentration on corrosion indicators [183] is not implemented in the *fib* Bulletin 34 design code, as the model solely predicts service life based on chloride concentration. Furthermore, for low Ca-AAMs, the corrosion indicator is included in the model without the cubic power law on hydroxide concentration, shown in **Table 2.1**. The cubic formulation was initially developed for steel bars exposed to a hyperalkaline simulated pore solution of low-Ca AAM binders (i.e., pH approximately 14-14.5) [54], while leaching effects are likely to reduce the pH below this level in the exposure conditions of interest here. For example, when low-calcium fly ash based concrete was exposed to a 16.5 wt.% NaCl solution for 35 days, the measured pH across the 25 mm mortar cover ranged from 11 to 11.8 [110]. The impact of the critical chloride threshold on service life is assessed through sensitivity analysis in section 4.3.

4.3.3 Calculation of Pore Solution Alkalinity

The open source software GEM-Selektor v.3 (<https://gems.web.psi.ch/>; [193]) was utilised to predict the alkalinity of pore solution in AAMs by thermodynamic simulation, where the mineralogical composition and degree of reaction of precursors along with the mix design of alkali-activated binders (e.g. free water content and composition of activating solution) were set as inputs. The assumed degrees of reaction of slag and fly ash were 70% and 35%, respectively, based on values reported for the reactivity of supplementary cementitious materials in blended cements [194]. A code typed in the GEM-Selektor v.3 software to account for the extent of reactivity for slag precursors at 70% and for fly ash precursors, at 35% used in AAMs is included in Appendix 4. The code also accounts for the composition of activating solution and amount of free water used in the mix design to produce 100 g of alkali-activated binder.

4.3.4 Aging factor

Values for the aging factor of around 0.6 or higher are considered to be unrealistic in real service conditions, because this represents a very extensive decrease in chloride mobility over an extended period of aging. This could lead to overestimation of the service life because the aging exponent is the dominant factor in modelling the chloride ingress with a time dependent diffusivity parameter [159]. Therefore, all the values of aging factor are taken to be around 0.5 for service life calculations of SG100 and SG50FA50, and the values for FA100 are taken to be between 0.234 and 0.309, according to **Table 4.1**.

4.3.5 Service Life Prediction Model

The *fib* Bulletin 34 code is applied in this research to probabilistically calculate the service life for alkali-activated reinforced concretes by implementing **Equation 4.3**, which is a rearranged form of **Equation 2.78**, and by including defined distributions of the environmental and material performance parameters. The available data for durability or material performance, sections 4.2.1-4.2.3, are described by normal and lognormal distribution functions (**Equations 4.4 and 4.5** respectively) using a distribution filter application in Matlab.

$$t = \left[\left[\frac{2}{x} \cdot \text{erf}^{-1} \left[\frac{c_{\text{crit}} - c_s}{c_i - c_s} \right] \right]^{-2} \cdot \frac{1}{k \cdot D_{\text{app,C}} \cdot (t_0)^n} \right]^{\frac{1}{1-n}} \quad (4.3)$$

$$f(x) = \frac{1}{\sigma\sqrt{2\pi}} e^{-\frac{1}{2}\left(\frac{x-\mu}{\sigma}\right)^2} \quad (4.4)$$

$$f(x) = \frac{1}{x\sigma\sqrt{2\pi}} e^{-\frac{(\ln x - \mu)^2}{2\sigma^2}} \quad (4.5)$$

Where $f(x)$ is the probability density function; σ is the standard deviation, and μ is the mean.

Figure 4.4 describes the algorithm implemented in the numerical model *fib* Bulletin 34 code for service life design of reinforced concrete assuming depassivation of the reinforcement to be the serviceability limit state, and characterizing this by the critical chloride threshold (C_{crit}). Where the durability data for chloride transport ($D_{app,C}$), aging factor (n) and corrosion risk indicators for high and low Ca-AAMs are collected from literature and set as inputs, along with their specified distributions, in the numerical model. The numerical model also includes the impact of ambient temperature (T) and extent of densification of concrete on chloride transport to probabilistically predict the service life of reinforced AAC exposed to a certain chloride concentration (C_s) and containing an initial chloride content (C_i) in its mineralogical composition. Finally, the transfer parameter (k) in the numerical model is assumed to be 1 according to [46, 47].

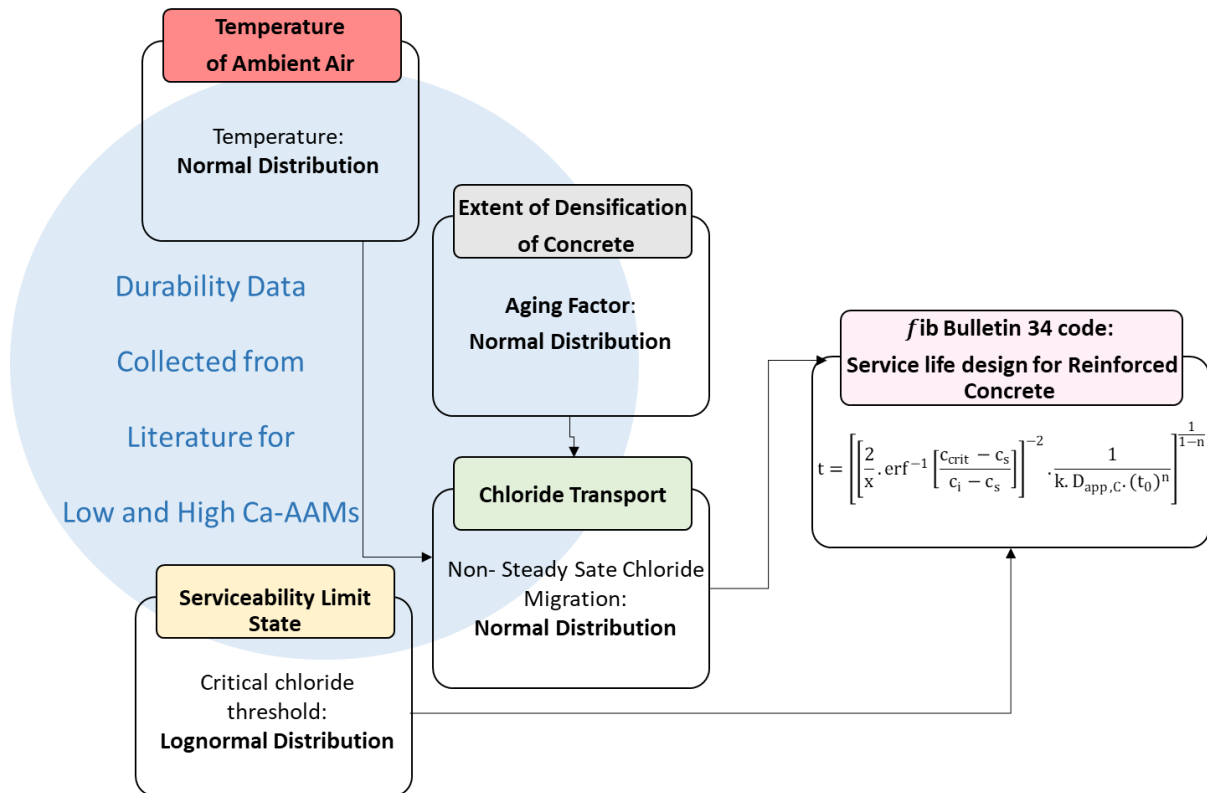


Figure 4.4 Algorithm of the probabilistic service life model “fib Bulletin 34 code” for service life design of reinforced concrete assuming depassivation of the reinforcement to be the serviceability limit state. The input data can be found in sections 4.2.1-4.2.3 that describe the durability performances of high and low Ca-AAMs with specified mix proportions (i.e. w/b, alkali dosage and ratio of slag to fly ash precursors).

Sensitivity analysis is also performed to understand the impact of each parameter on the output result, service life, by using **Equation 4.3**.

4.4 Results and Discussion

4.4.1 Chloride threshold

In PC concrete, alkalinity is buffered by portlandite ($\text{Ca}(\text{OH})_2$) and increased further by the concentration of additional alkalis (e.g. Na^+ and K^+). However, for AAC, the alkalinity of the pore solution depends on the alkali dosage and silicate modulus used in the activating solution, and there can be variations between high and low calcium AAMs [101]. **Table 4.4** presents the range of mineralogical compositions of the precursors, along with the variability in mix design components used for slag-based and fly ash-based AACs, in durability case studies as reported in the literature. The mix design and extent of reactivity of the precursors (i.e. slag and fly ash)

have served as inputs for the thermodynamic software (i.e. GEM-Selektor v.3) to estimate the variation of pore solution alkalinity for alkali-activated cements also shown in Table 4.4.

Table 4.4 Mineralogical composition (M.C.) of AAMs used in thermodynamic calculations to estimate the pore solution alkalinity of AAMs; along with other parameters including porosity and mix design of alkali-activated concretes needed to calculate the critical chloride thresholds, in wt.% of binder, by implementation of Equation 4.1-4.2.

	Alkali-Activated Slag			Alkali-Activated Slag and Fly Ash		Alkali-Activated Fly Ash		Ref
	Slag (kg/m ³)			Slag (kg/m ³)	Fly Ash (kg/m ³)	Fly Ash (kg/m ³)		
	300	400	500	200	200	400		
Porosity	0.13	0.084-0.156	0.111	0.135		0.12		[152, 195, 196]
M.C. of SG & FA precursors	M.C.	Avg.	std.	Avg.	std.	Avg.	std.	[100, 104, 105, 152, 187, 188, 190, 197-201]
	SiO ₂	34.64	2.21	42.5	2.31	51.33	6.57	
	Al ₂ O ₃	12.03	1.95	20.63	0.94	22.49	1.61	
	CaO	42.0	2.0	24.0	0.9	6.99	5.4	
	Fe ₂ O ₃	0.93	1.61	4.49	1.77	8.54	3.17	
	Na ₂ O	0.27	0.21	0.68	0.26	1.71	1.14	
	MgO	6.78	1.02	3.48	0.30	2.17	1.05	
	SO ₃ [*]	0.31	0.30	0.67	0.15	0.67	0.61	
K ₂ O	0.43	0.13	0.73	0.14	1.94	0.46		
Pore solution alkalinity	pH	13.96	0.20	13.02	0.45	14.01	1.00	
Mix Design of alkali-activated concretes	Precursor (g/cm³)	avg.	std.	avg.	std.	avg.	std.	
	Concrete (g/cm ³)	0.41	0.07	0.40	0.003	0.43	0.04	
	w/b	2.41	0.05	2.42	0.04	2.37	0.07	
	Na ₂ O	0.47	0.06	0.43	0.04	0.26	0.05	
	Mr	5	1.7	4	1.1	9	1.5	
		1	0.5	1.3	0.3	1.2	0.2	

* The sulfur present in the slag is simulated to be present in reduced form (sulfide), but is represented in oxide form in this table for consistency with the broader literature.

The literature data collected as **Table 4.4** reveal a wide range of simulated pore solution alkalinity values for alkali-activated concretes [100, 104, 105, 152, 187, 188, 190, 197-201], and corresponding representative porosity (volume of permeable voids) values [152, 195, 196]. Notably, 50SG50FA and FA100 exhibit relatively low pore solution alkalinity, reaching pH values of 12.3 and 11, respectively; this may represent a limitation of the thermodynamic simulation approach used here which assumes congruent dissolution of the fly ash, where the acidic silicates are simulated to dissolve more than would be the case if they were considered to be present in unreactive phases. However, for a simulation based on literature data it is not possible to give more precise determination and representation of the differences in reactivity between different fly ash constituent phases.

Next, the critical chloride thresholds are estimated for each type of alkali-activated concrete and grouped based on the alkali dosage (in terms of Na₂O by wt.% of binder) used in the mix design of the activating solution. The resulting distributions of critical chloride thresholds are depicted in part A of Figures 4.4-4.6, showing the variations in C_{crit} as a function of alkali dosage in the AAM activating solution.

Conversely, the critical chloride thresholds calculated based on the pore solution alkalinity are rather high compared to the data presented in Figure 4.1, while still falling within the range of corrosion initiation values reported by [192]. However, it is important to consider that in AAMs, pH may also be significantly affected by leaching or washout of the pore solution. The high pH in AAMs creates a hydroxide concentration gradient between the inner material and the external environment, resulting in leaching of hydroxide (and alkali) ions. Research conducted by [101] demonstrated that in a high calcium AAM concrete, the hydroxyl ion concentration reduced from 0.155 to 0.017 mol/L between 180 and 1750 days at a cover depth of 10 mm. In comparison, the OH⁻ concentration in PC concrete ranged from 0.014 to 0.009 mol/L under an accelerated corrosive environment with multiple wetting and drying cycles within the same time frame of 1750 days. Considering the greater extent of pore solution alkalinity reduction in alkali-activated materials compared to Portland cement-based concrete, the pH values for the pore solution of SG100, 50SG50FA and FA100 were set to vary between 13.5-13.2 when calculating the critical chloride thresholds. The updated values for the distribution of critical chloride thresholds are displayed in Figures 4.4-4.6, comparing part A to part B of each respective Figure. Significantly, the median values of the updated thresholds fall within the range of critical chloride thresholds obtained for alkali-activated mortars, as shown in Figure 4.1. So, the distribution values for C_{crit} shown in Figures 4B-6B are implemented in the *fib* Bulletin 34 code to probabilistically calculate the service life of AAC. A calculation example of critical chloride threshold, in wt.% of binder, for SG100 concrete by implementation of Equations 4.1-4.2 based on variability of pore solution alkalinity along with other parameters including porosity, mix design and saturation state of the concrete is shown in **Tables 4.A.1-4.A.3** presented in Appendix 4.

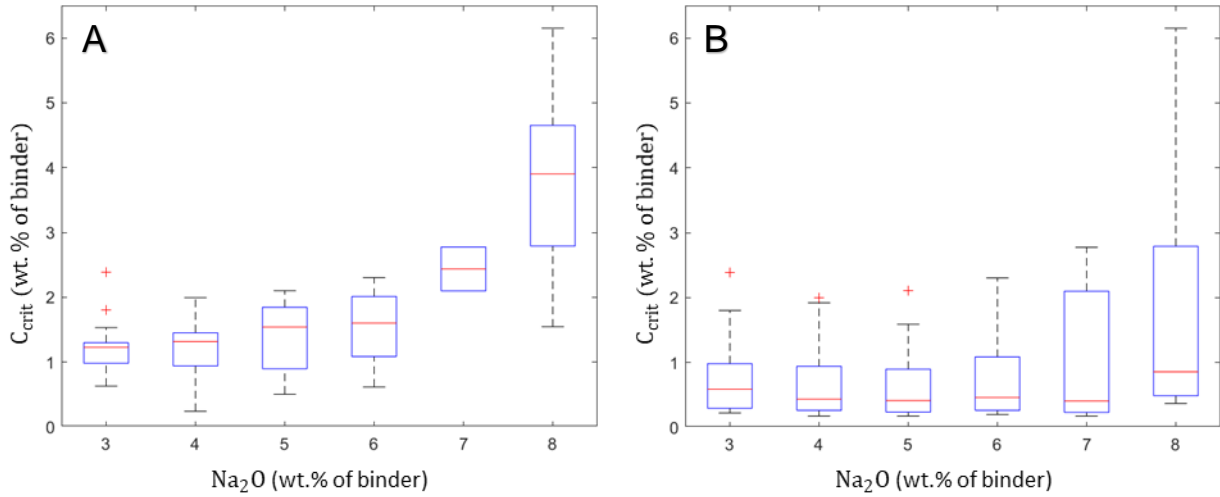


Figure 4.5 C_{crit} (wt.% of binder) of high calcium AAMs (100%SG), as a function of alkali dosage (wt.% of binder), calculated using the pore solution alkalinity in Table S1 (A); and C_{crit} (wt.% of binder) calculated by including the reduction of pore solution alkalinity, between 13.5 and 13.2, at the surface of the steel reinforcement (B).

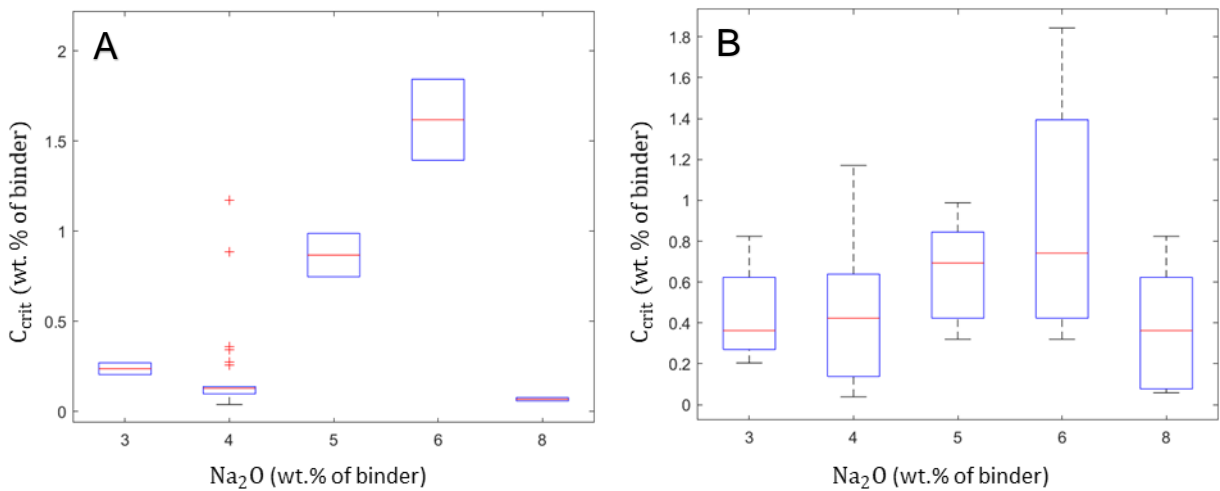


Figure 4.6 C_{crit} (wt.% of binder) of high calcium AAMs (50%SG+50%FA), as a function of alkali dosage (wt.% of binder), calculated using the pore solution alkalinity in Table S1 (A); and C_{crit} (wt.% of binder) calculated by including the reduction of pore solution alkalinity, between 13.5 and 13.2, at the surface of the steel reinforcement (B).

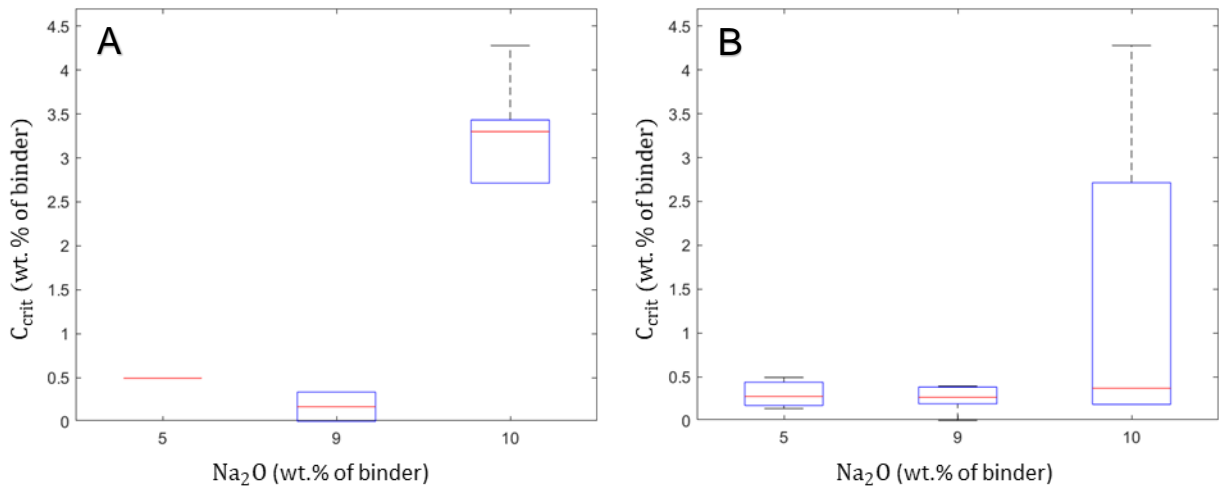


Figure 4.7 C_{crit} (wt.% of binder) of low calcium AAMs (100%FA), as a function of alkali dosage (wt.% of binder), calculated using the pore solution alkalinity in Table S1 (A); and C_{crit} (wt.% of binder) calculated by including the reduction of pore solution alkalinity, between 13.5 and 13.2, at the surface of the steel reinforcement (B).

4.4.2 Service Life Predictions

Figures 4.7-4.11 represent durability data in probability and cumulative plots, where the data are the set of critical chloride thresholds and chloride migration coefficients of 100%SG, 50%SG 50%FA and 100%FA alkali-activated concretes as already discussed in sections 4.2.1 and 4.2.2, respectively. A lognormal function is chosen to model the distribution of chloride thresholds because its generated curve fits the data better than the normal function, and has previously been chosen to model the distribution of chloride thresholds for PC [192]. The normal distribution function is selected to model the distribution of chloride migration coefficients [46]. The average and standard deviation for the aging factor are estimated using the data presented in **Table 4.1**. A normal distribution is selected to model the distribution of aging factors, instead of the beta distribution implemented in the *fib* Bulletin 34 code, because of limited data values reported for AAMs. The distributions for all the durability data are truncated between upper and lower boundaries, based on the maximum and minimum values achieved in the literature. The data for variation in temperature, and chloride concentration on the surface of the concrete, are set using normal distribution functions [46, 47].

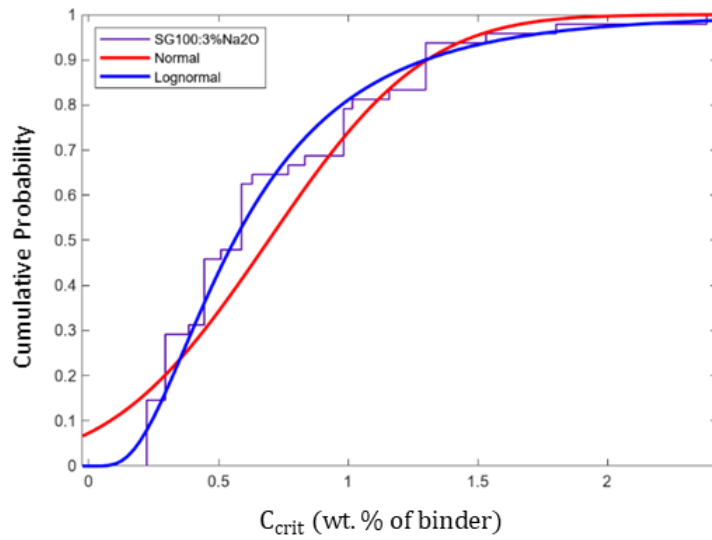


Figure 4.8 Cumulative probability plot for C_{crit} in SG100. Data are the set of possible C_{crit} values obtained for 100%SG, containing Na_2O at 3 wt.% of binder, as shown in Figure 4 part-B.

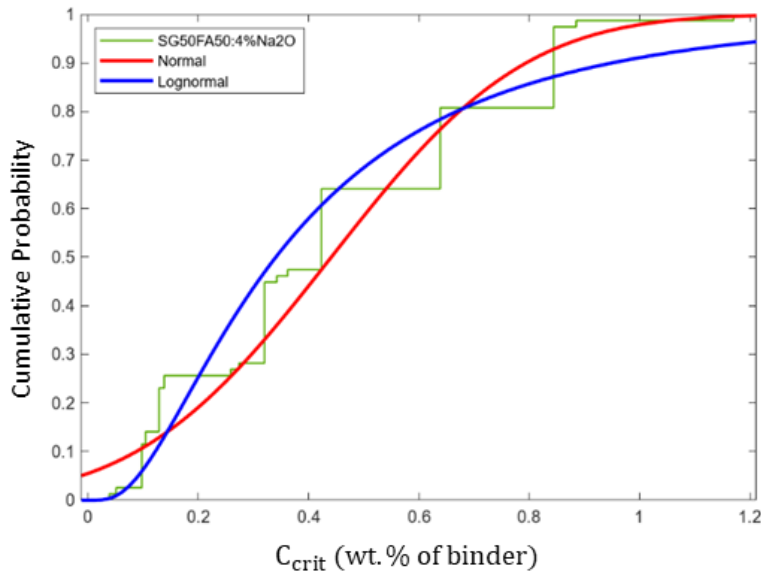


Figure 4.9 Cumulative probability plot for C_{crit} in 50SG50FA. Data are the set of possible C_{crit} values obtained for 50%FA/50%SG, containing Na_2O of 4 wt.% of binder, as shown in Figure 5-part B.

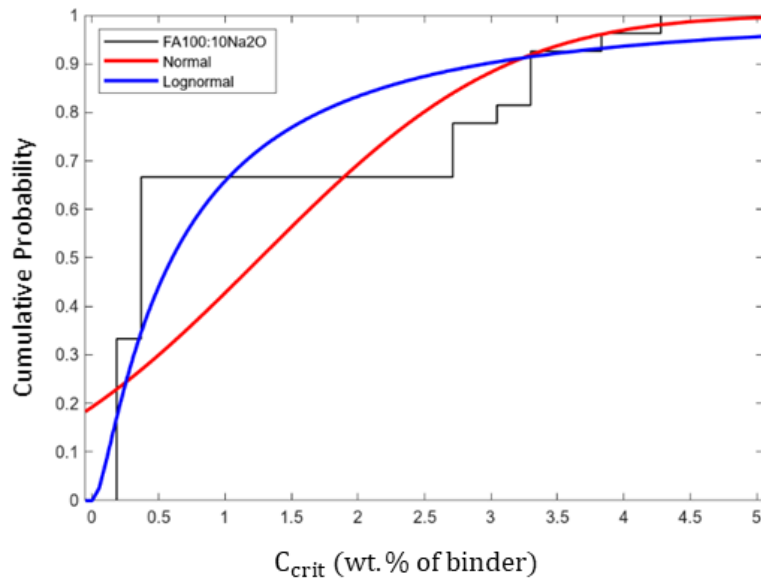


Figure 4.10 Cumulative probability plot for C_{crit} in FA100. Data are the set of possible C_{crit} values obtained for 100%FA, containing Na_2O of 10 wt.% of binder, as shown in Figure 6-part B.

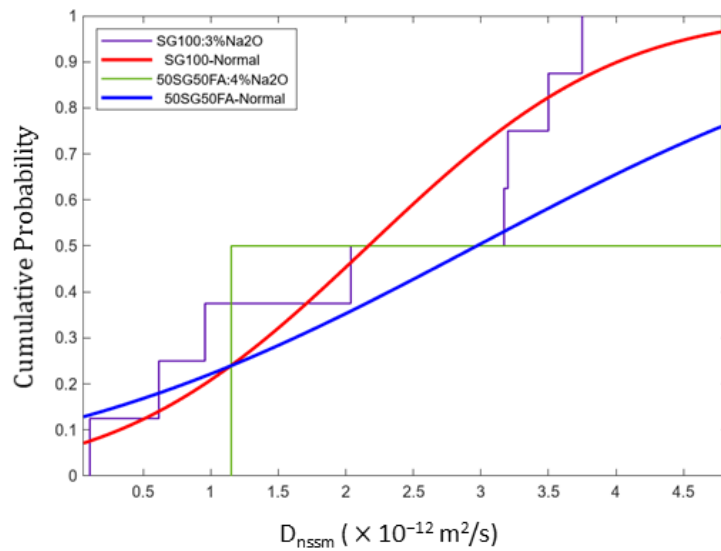


Figure 4.11 Cumulative probability plot for D_{nssm} . Data are the set of possible chloride migration values obtained for 100%SG and 50%FA/50%SG containing Na_2O of 3 and 4 wt.% of binder, respectively, as shown in Figure 4.2.

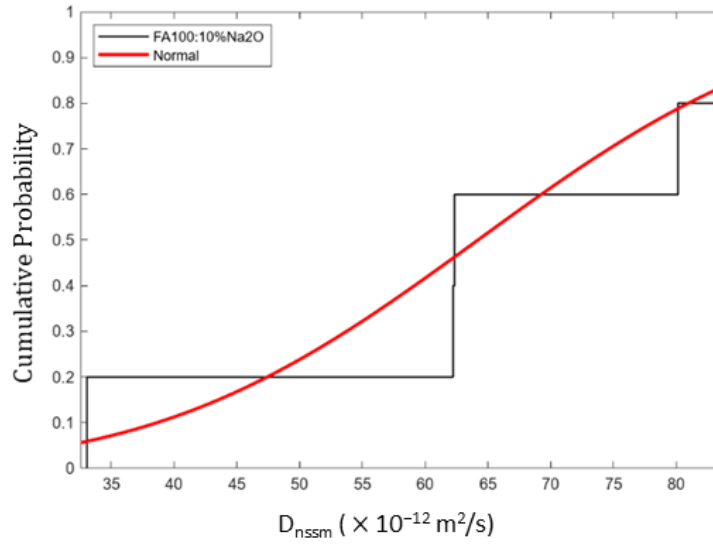


Figure 4.12 Cumulative probability plots for D_{nssm} in FA100. Data are the set of possible chloride migration values obtained for 100%FA, containing Na_2O of 10 wt.% of binder, as shown in Figure 4.3.

In summary, **Table 4.5** presents data distributions for environmental and material performance parameters, for use in the *fib* Bulletin 34 design code.

Table 4.5 *fib* Bulletin 34 code parameters used for service life prediction of alkali-activated concretes.

Parameter	Unit	Distribution	SG100	50SG50FA	FA100
C_{crit}	Wt.% of binder	Lognormal	Log mean; -0.58 Std; 0.65 Max; 2.38 Min; 0.22	Log mean; -1.08 Std; 0.80 Max; 1.17 Min; 0.0384	Log mean; -0.51 Std; 1.24 Max; 4.28 Min; 0.1854
C_0	Wt.% of binder	Deterministic	0.15	0.15	0.15
$C_{s,\Delta x}$	Wt.% of binder	Normal	Mean; 6 Std; 0.5	Mean; 6 Std; 0.5	Mean; 6 Std; 0.5
Δx	μm	Deterministic	0	0	0
d	mm	Deterministic	45	60	200
b_e	K	Normal	Mean; 4800 Std; 700	Mean; 4800 Std; 700	Mean; 4800 Std; 700
T_{ref}	K	Deterministic	293	293	293
T_{real}	K	Normal	Mean; 283 Std; 5	Mean; 283 Std; 5	Mean; 283 Std; 5
D_{RMC}	$mm^2/year$	Normal	Mean; 68.34 Std; 45.38 Max; 118.25 Min; 3.31	Mean; 93.64 Std; 81.08 Max; 150.97 Min; 36.31	Mean; 2024.62 Std; 629.05 Max; 2623.8 Min; 1043.01
k	-	Deterministic	1	1	1
n	-	Normal	Mean; 0.5 Std; 0.0313 Max; 0.5 Min; 0	Mean; 0.5 Std; 0.0313 Max; 0.5 Min; 0	Mean; 0.272 Std; 0.053 Max; 0.309 Min; 0

The *fib* Bulletin 34 code described in the above equations was coded in Matlab, and run 10^5 times per concrete formulation with parameters sampled from the distributions defined in Table 4.5, to simulate the service life via a Monte-Carlo approach. The histograms and cumulative distribution plots shown in **Figures 4.12-4.14** are the results obtained from this simulation. The required depassivation limit state in a XS2 environment [202] is set to a probability of failure (P_f) of 0.1, in compliance with the *fib* Bulletin 34 [161]. Thus, the service life is determined for each mix at the intersection between the probability failure level of 0.1 and the curve generated in the cumulative probability plots. In addition, the numerical code for the *fib* Bulletin 34 service life design can be found in Appendix 4.

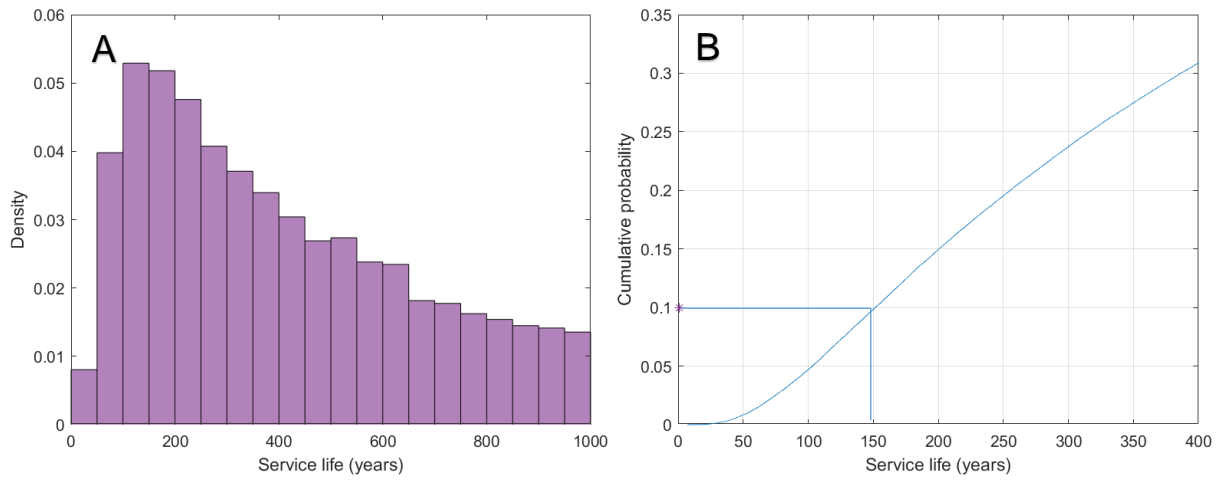


Figure 4.13 Simulated histogram (A) and cumulative distribution plot (B) for service life for SG100 concrete. $P_f = 0.1$ is indicated by a star and horizontal line in (B).

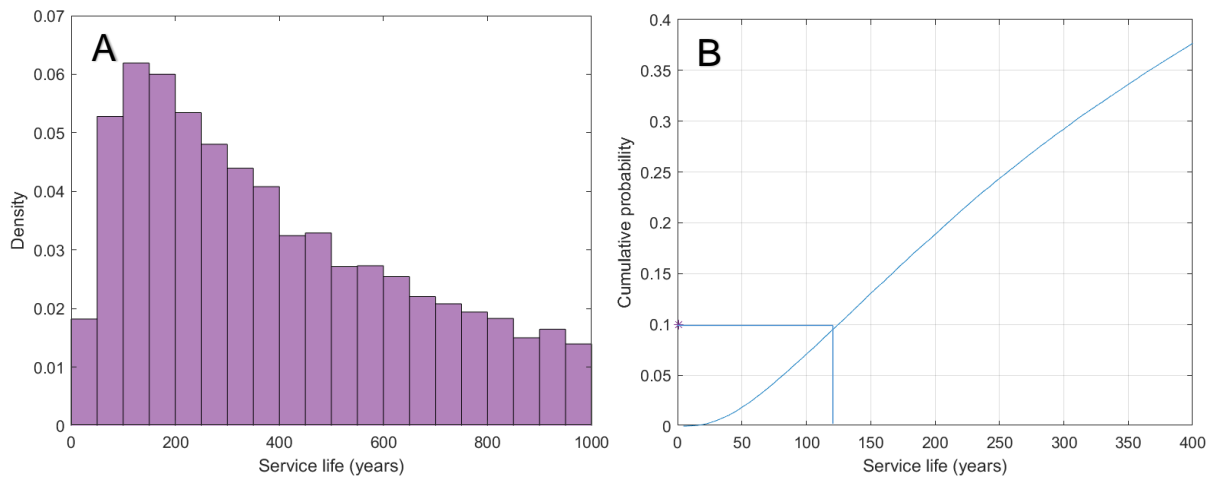


Figure 4.14 Simulated histogram (A) and cumulative distribution plot (B) for service life of SG50FA50 concrete. $P_f = 0.1$ is indicated by a star and horizontal line in (B).

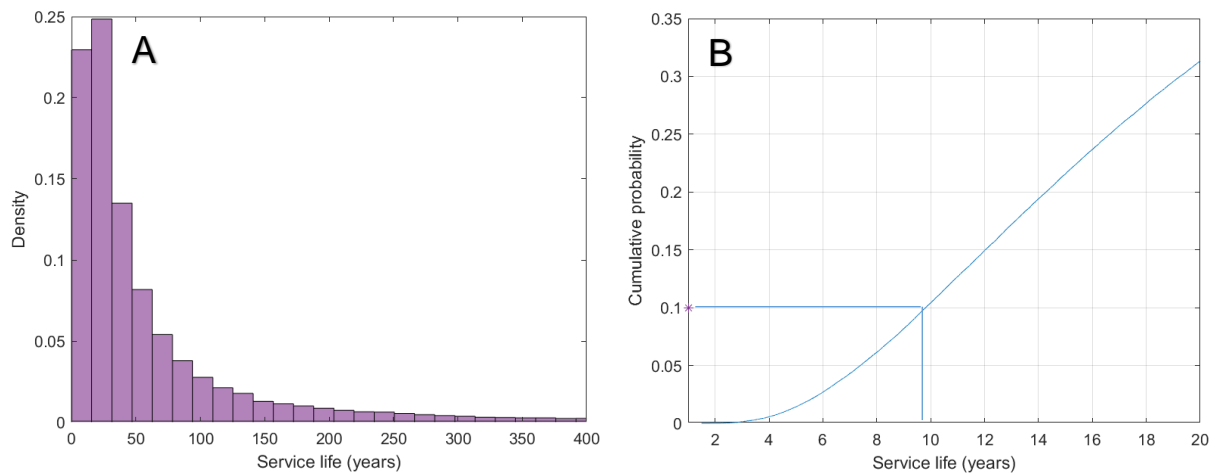


Figure 4.15 Simulated histogram (A) and cumulative distribution plot (B) for service life of FA100 concrete. $P_f = 0.1$ is indicated by a star and horizontal line in (B).

Lepech et al. [47] used the *fib* Bulletin 34 code, with Monte Carlo analysis (100,000 runs), to probabilistically predict the time to depassivation of steel reinforcement in two concrete cover replacements of 40 and 80 mm. They obtained histograms that follow a lognormal distribution similar to those obtained in Figures 4.12-4.14. However, the distributions of service life that they have obtained for the cover replacements of 40 mm and 80 mm were within 20 years and 50 years, respectively; less than half of the service life obtained in this research for SG100. Lepech et al. [47] implemented similar distribution values of critical chloride thresholds, via a beta function, as the values used here for SG100 in the lognormal function, and used higher values for the aging factor (beta distribution varying between 0 and 1 with a mean of 0.6 and std. of 0.15). Two important factors may have reduced the number of years in their computed service life calculations, which are: their high values of chloride migration coefficient (compared to the values used for SG100), being a normal distribution function with mean and std. of $6.9 \times 10^{-12} \text{ m}^2/\text{s}$ and $1.4 \times 10^{-12} \text{ m}^2/\text{s}$ respectively; and that their reference point of time, t_0 , was set at 0.767 years (280 days) instead of 0.0767 years (28 days) as usually used in the literature [46]. Testing our model here with the value of t_0 set to 0.767 showed a great reduction in service life; Figure 4.18 presents the computed service life of SG100 with $t_0 = 0.767$ years, where the service life obtained for SG100 of cover depth 45 mm is approximately 20 years, similar to the value obtained by [47]. It is likely that this provides an explanation for the difference in predicted service life between this study and that past study.

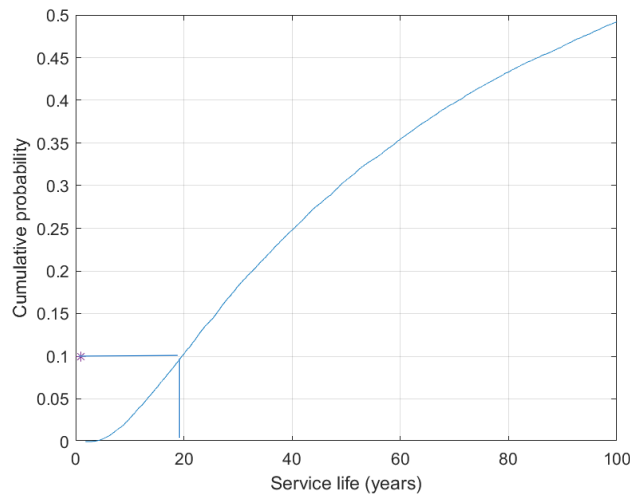


Figure 4.16 Service life of SG100 computed using 0.767 years as a reference point in time (t_0) to match the value of Lepech et al. [47].

Van den Heede et al. [46] have also computed service life data by using the *fib* Bulletin 34 code and by implementing similar distributions of critical chloride thresholds and aging factors, for concretes containing 50% CEM I and 50% slag (SG50) and others containing 30% CEM I and 70% slag (SG70). However, the range of values for chloride migration coefficients obtained for those two types of concretes, containing similar w/b of 0.45, were on the order of 380-400 mm²/year, or approximately 12×10^{-12} m²/s, which is significantly higher than the values obtained here for SG100 and SG50FA50. Also, Van den Heede et al. [46] used a surface chloride concentration approximately half of that which is used in this research. Their outcomes for SG50 and SG70, with cover thicknesses of 60 mm, are 100 years and >100 years respectively, which are comparable to the values obtained for SG100 and 50SG50FA in this study despite the differences in model parameterisation.

Finally, despite the very high concrete cover used here for FA100, the calculated service life is only 10 years, indicating that it is not likely to be a suitable construction material for structural application in marine splash zones. Although FA100 had a higher compressive strength than SG100, the average value of chloride migration obtained for FA100 is 30 times higher than the value obtained for SG100 because of the presence of a higher quantity of macro-pores in the microstructure of low calcium AAMs, which increases the permeability [189]. This further reinforces observations that the compressive strength is not the most important durability indicator for the prediction of service life of AAM structures in chloride-containing conditions[9].

4.4.3 Sensitivity Analysis

As described above, the performance properties of multiple elements made from any given AAC are likely to be statistically distributed, and the exact distributions are not yet well understood. So, in this section, sensitivity analysis is used to demonstrate the impact of variations in the input values for a given durability parameter. The parameters used in the Fib Bulletin 34 code (i.e. **Equation 4.3**) for sensitivity analysis are provided in **Table 4.6**.

Table 4.6 Sensitivity parameters for service life prediction of AAC.

Parameter	Description	SG100s	50SG50FA	FA100
x	Concrete cover, mm	35-55 mm	50-70 mm	100-300
T_{real}	real temperature, K	278-298	278-298	278-298
C_{crit}	Wt.% of cement	0.22-2.38	0.038-1.17	0.185-2.713
C_0	Wt.% of cement	0.15	0.15	0.15
$C_{s,\Delta x}$	Wt.% of cement	6	6	6
D_{RMC}	Chloride migration (mm^2/year)	3.31-118.25	36-151	1733-2552
t_0	Age of the concrete when the test is performed (years)	0.0767	0.0767	0.0767
n	Aging coefficient	0-0.5	0-0.5	0-0.309

Figures 4.16-4.18 show the results of sensitivity simulations where distributions of values are applied to each parameter to predict the service life as a function of cover depth. This approach is used to understand the overall uncertainty in the model, by considering the uncertainty associated with each parameter.

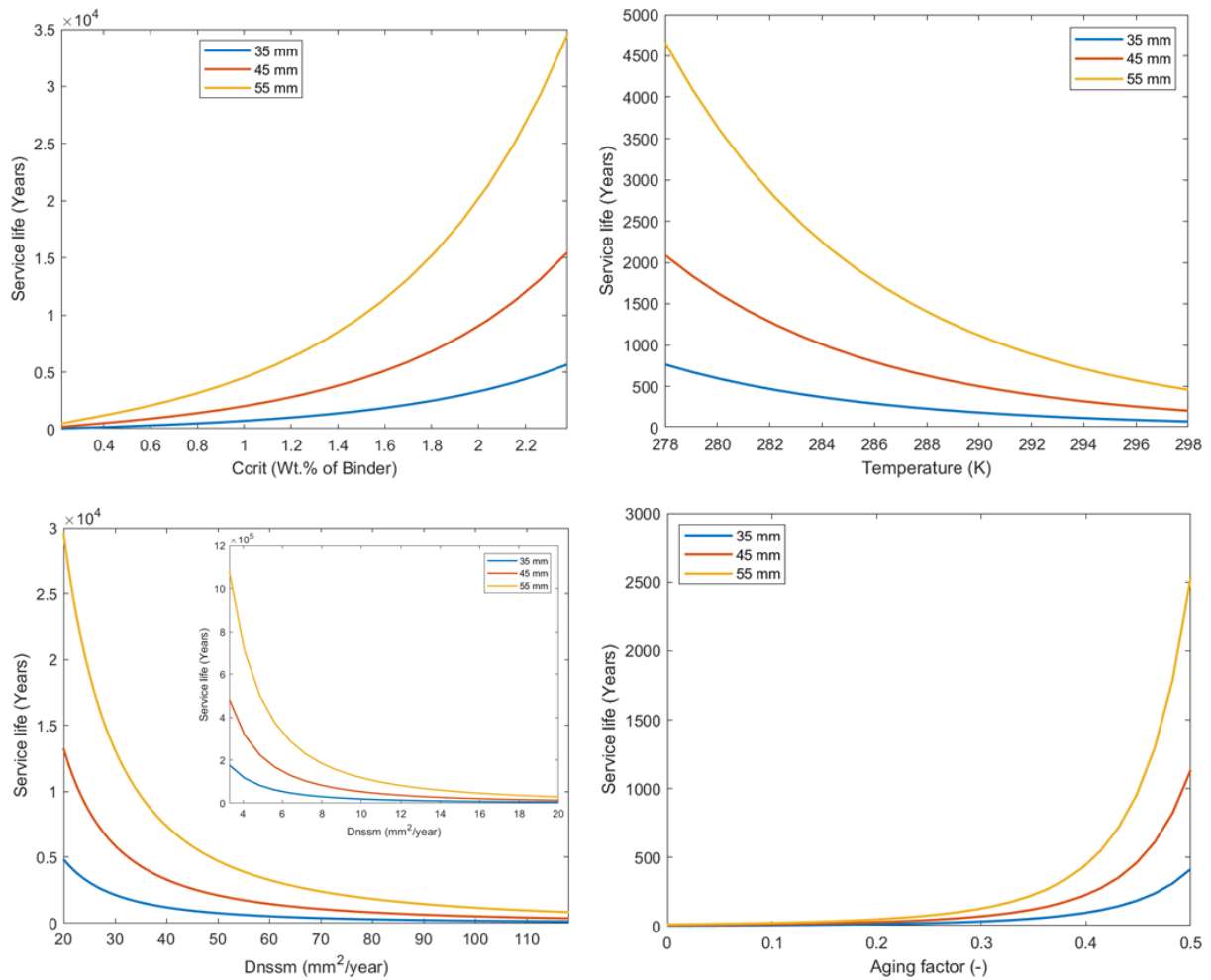


Figure 4.17 Sensitivity analysis in service life predictions for SG100 concretes of different cover depths (i.e. 35, 45 and 55 mm) as shown in the legend of each panel, showing the predicted service life as a function of C_{crit} , temperature, D_{nssm} , and aging factor. Note the differences in vertical scale between panels.

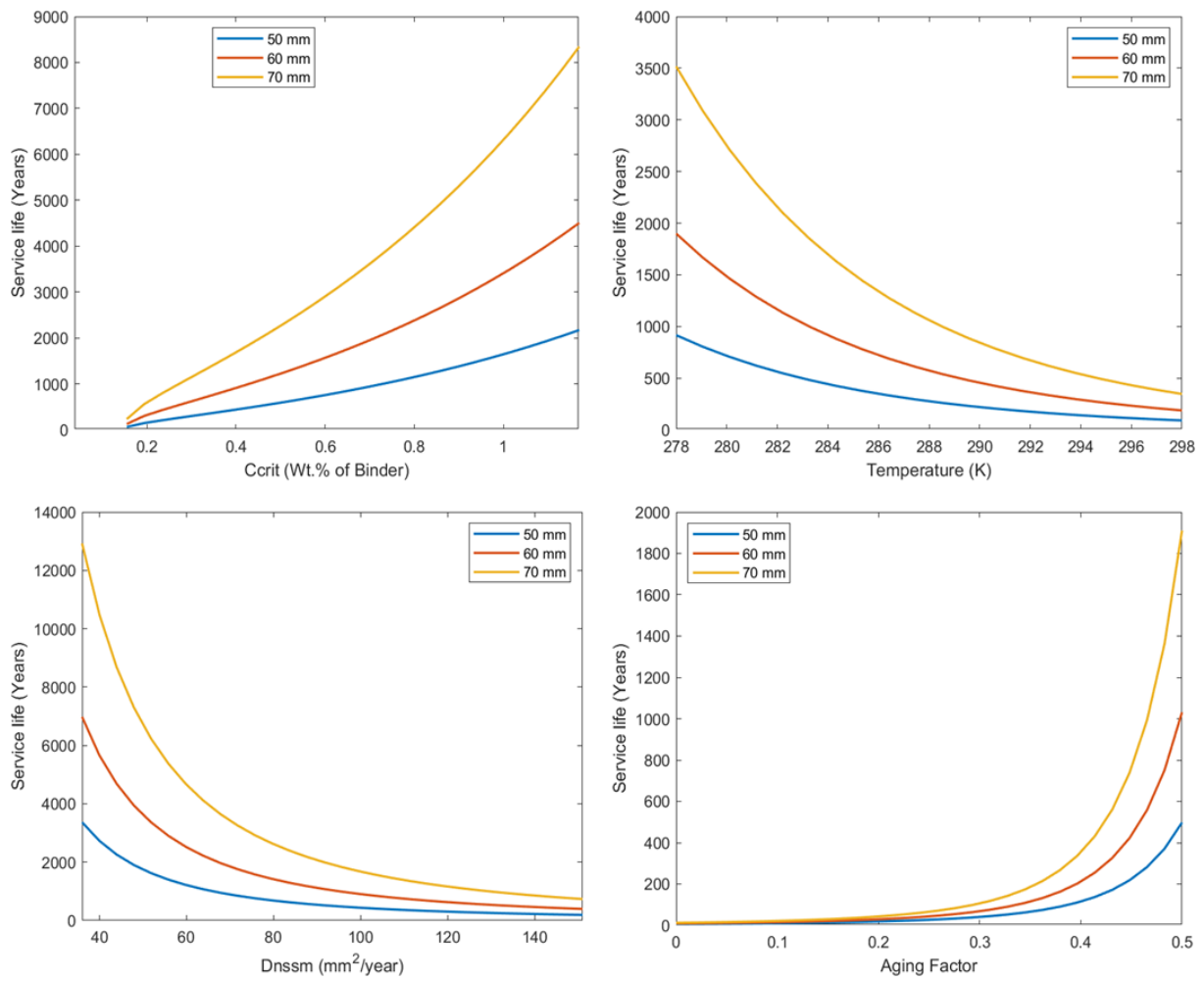


Figure 4.18 Sensitivity analysis in service life predictions for 50SG50FA concretes of different cover depths (i.e. 50, 60 and 70 mm) as shown in the legend of each panel, showing the predicted service life as a function of C_{crit} , temperature, D_{nssm} , and aging factor. Note the differences in vertical scale between panels.

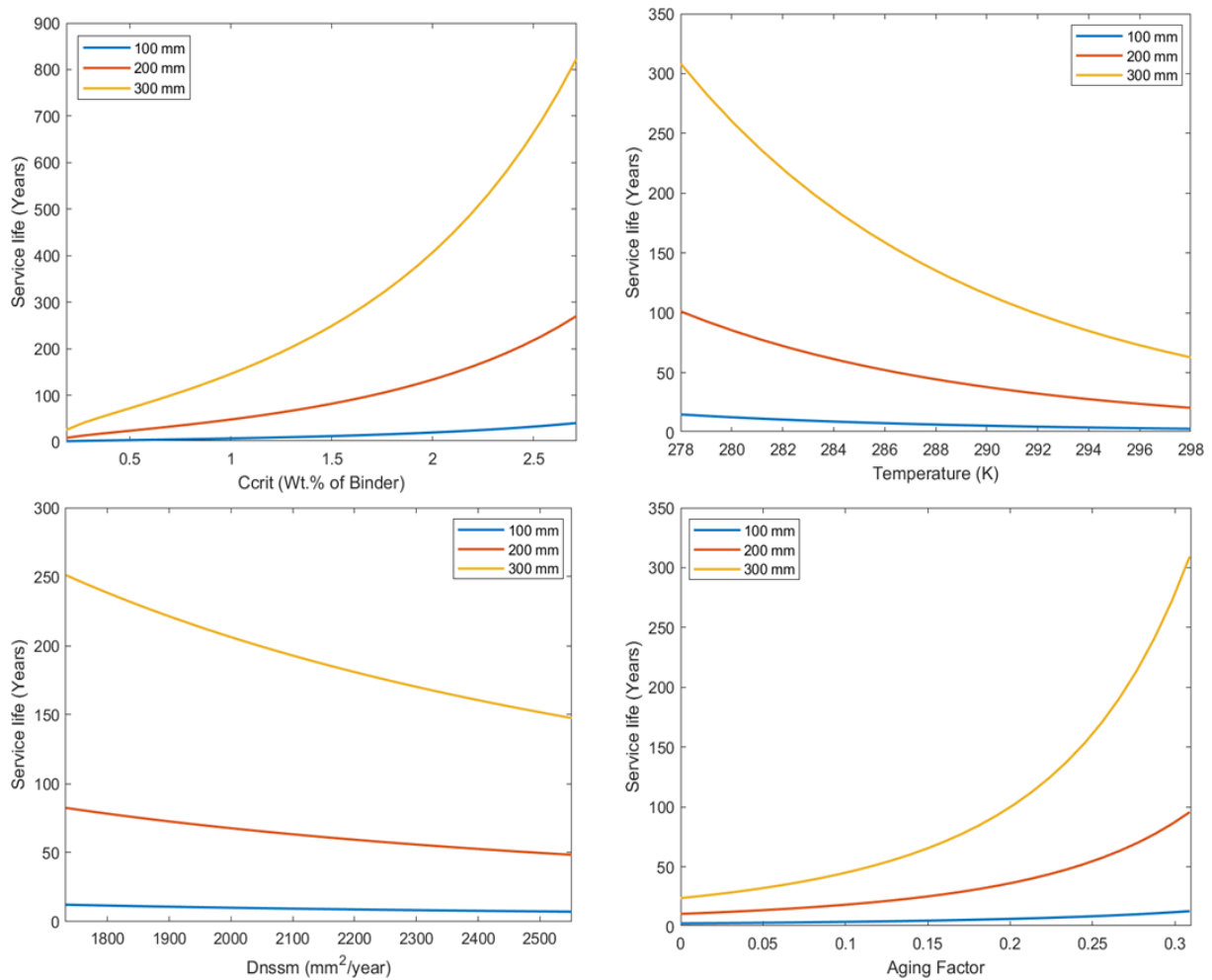


Figure 4.19 Sensitivity analysis in service life predictions for FA100 concretes of different cover depths (i.e. 100, 200 and 300 mm) as shown in the legend of each panel, showing the predicted service life as a function of C_{crit} , temperature, D_{nssm} , and aging factor. Note the differences in vertical scale between panels.

According to the sensitivity analysis, it is evident that the parameterisation of chloride transport (i.e. D_{nssm} and – in particular – the aging factor exponent) has the most impact on service life predictions for SG100 and SG50FA50. The range of variation in the rate of chloride transport is likely to be strongly influenced by the variation in the mineralogical composition and degree of reaction of the precursors, which define the cementitious binding phases responsible for the resistance of chloride migration (i.e. through pore refinement) into the AAC concrete cover [30]. As for the aging factor, its impact is most noticeable beyond a value of 0.25 for each of the three mixes. It is questionable whether the high aging factors sometimes applied in the literature (and codes) for PC concretes are considered valid over such extended periods of time; an argument may be made to set aging to zero after a particular age (years to decades) rather

than assuming that the material will continue to age and refine its pore structure indefinitely [203], but more information is needed on this topic. Additionally, the variability of temperature between 5-25°C is shown to accelerate the rate of transport of chloride ions in AAC due to the temperature dependence in **Equation 2.79**.

The pore solution alkalinity and potential leaching effects are two main factors that contribute to the extent of variation of C_{crit} , which defines the serviceability limit state. As can be seen in **Figures 4.16-4.18**, alkali-activated concretes with average performance properties (i.e. average values in **Table 4.6**) can have a short calculated service life span when the alkalinity of the pore solution drops below a certain level that makes C_{crit} approach 0; it is not clear whether this is in fact realistic. Hence, future improvements in the service life model should incorporate the effect of change in pore solution chemistry on C_{crit} , especially when the structure is in submerged conditions [204]. Moreover, considering the critical chloride thresholds obtained from the literature, Figure 4.1, the service life for SG100 at $C_{crit} = 0.21$ wt% of binder, can be 84 years with a concrete cover thickness of 35 mm; for SG50FA50 at $C_{crit} = 0.33$ wt% of binder, can be 314 years with a concrete cover thickness of 50 mm; and for FA100 at $C_{crit} = 0.52$ wt% of binder, the service life can be 25 years with a concrete cover thickness of 200 mm. This estimation is based on the assumption that the average critical chloride thresholds for the mortars in **Figure 4.1** are applicable for SG100, FA100 and 50SG50FA because of the similar mix designs.

Overall, critical chloride threshold and chloride migration are the most influential parameters for the service life, and based solely on variations in these two parameters within a relatively realistic range, the predicted service life values resulting from the model presented here can span from a few years to tens of thousands of years. There is a clear need to improve the understanding of these parameters and how they relate to each other, both in general application of this type of model but also specifically in its application to AAMs.

4.5 Conclusions

The *fib* Bulletin 34 code, incorporating transport properties and C_{crit} , can be used to provide a probabilistic prediction of the service life of alkali-activated concretes. The model includes the variation of composition and reactivity of the precursors by including the variability of performance in each durability parameter in the service life model. Based on the results of this study, the following conclusions and suggestions for future improvements can be drawn:

1. The distribution of critical chloride thresholds for different types of alkali-activated concrete mixes can be estimated by considering factors such as mineralogical composition, alkalinity of the pore solution, porosity, and potential leaching effects. The estimated thresholds align with values reported in the literature, but further data validation is necessary.
2. The probabilistic calculation simulated by the Monte Carlo approach shows that high calcium alkali-activated concretes may be suitable for structural applications in submerged marine environment.
3. There is a need for further characterization of field and laboratory samples for the development and refinement of C_{crit} parameters, to include the impact of change of pore solution chemistry.
4. Continued research and data collection are needed to enhance our understanding of the extent of refinement in the microstructure of AACs (i.e. aging factor) exposed to service conditions. Where, the impact of alkali leaching can disrupt the evolution of microstructure of the cement and cause an increase in permeability of the concrete.

Overall, including the effect of change in pore solution chemistry will enable more accurate predictions of service life and aid in the development of optimal mix designs for different environmental conditions and structural applications.

Chapter 5: Moisture Permeability in Alkali-Activated Materials

Abstract

Despite the potential environmental benefits of AAMs, there is still a need for a deeper understanding of their durability under the combined action of carbonation and chloride ingress, which can lead to the corrosion of the reinforcement embedded in alkali-activated concretes.

The moisture state and transport in these porous materials is an essential durability factor that should be accurately predicted in order to model the simultaneous ingress of chlorides and CO₂ in marine conditions. During wetting and drying cycles, the difference between adsorption and desorption isotherms, called hysteresis, could be related to the pore network geometry, mostly the pore interconnectivity, in the alkali-activated binder.

In this research, three moisture transport models, namely the single, dual, and mechanistic permeability models, are implemented to assess the moisture transport in AAMs during wetting and drying cycles. This enables study of the significance in each model, accounting for the complex porous microstructure of the material, on interpreting the main causes of the hysteresis effects.

In comparison with data for PC, it can be concluded that the dual permeability model is a suitable model to simulate and predict the degree of saturation in the pores of AAM binders. This is due to its better description of the transport of moisture in large and small pore regions of a cement along with the interconnectivity between the two pore regions. However, future refinement of this model may include the effect of pore solution chemistry, particularly the impact of high concentrations of alkali ions.

Keywords: Moisture transport; Permeability; Alkali-activated binders; Durability; Microstructure.

5.1 Introduction

In studies published to date, many alkali-activated cements have been found to have higher resistance to chloride-induced corrosion of embedded steel rebar [153]. Such corrosion studies are often conducted under saturated conditions; i.e., the samples are submerged in aqueous salt

solutions. This neglects the transport of gases such as oxygen and carbon dioxide into the capillary pores of the hydrated matrix where, if they coexist with chloride, they can influence the extent of corrosion [7]. Therefore, the likelihood of coupled degradation phenomena would increase if hydrated cements are in an unsaturated state (i.e. lack of free water filling the pores) resulting from a series of wetting and drying cycles which represents real conditions that the construction material is most likely to be exposed to during its service life [179].

Water vapour sorption isotherms (WVSIs) have been used to describe the relationship between the environmental relative humidity RH and evaporable or free water content in the pores of the cement [69]. The difference in evaporable water content at the same RHs between the adsorption and desorption curve of the WVSIs, as shown in Figure 5.11, is called hysteretic behaviour and it is caused by the wide range of magnitude of pore sizes existing in cement (i.e. interlayer to capillary pores). Consequently, this complex microstructure will slow down the transport of water vapour during desorption once it is adsorbed during adsorption [70].

Babae and Castel [69] and Ke et al.[168] have measured the full water vapour sorption (i.e. 0%-100% RH) isotherms of alkali-activated cements. Hence, it is useful to compare the WVSIs of Portland cement and AAMs obtained from the literature to compare the effect of the extra amount of alkali ions present in the pore solution of AAMs. **Table 5.1** and **Table 5.2** contains the mix design of the Portland cements and AAMs, respectively, studied in room temperature conditions whereas the MK200 sample is the alkali-activated metakaolin, MK200, that has been exposed to 200°C before sorption measurements.

Table 5.1 Mix designs of Portland cement pastes obtained from the literature.

Sample	Notation	CEM	w/b ^c	Curing Method	Ref
PC	PC-0.45	I	0.45	Ambient cured (sealed)	[62]
PC	PC-0.35	I	0.35	Ambient cured (sealed)	[70]
PC	PC-0.6	I	0.6	Ambient cured (sealed)	[62]
PC	PC-0.45 ^d	I	0.45	Ambient cured (sealed)	[205]

^cw/b; w includes water within the activating solution and extra free water added in the mix design and b includes total amount of solids (precursors + anhydrous activator)

^dPC-0.45* and PC-0.45 are the same type of cement, CEM I, with the same w/b. However, data on WVSI for each binder is obtained from a different source.

Table 5.2 Mix designs of AAMs obtained from the literature.

Sample	Notation	FA+SG+MK ^a (%)	CEM	M _r ^b	Na ₂ O%	w/b ^c	Curing Method	Ref
AAMs	90FA10SG*	90%FA+10%SG	-	1.17	9.25	0.28	Heat cured (18h @ 75°C)	[69]
AAMs	75SG25FA*	25%FA+75%SG	-	1.5	4	0.45	Ambient cured (sealed)	[69]
AAMs	50SG50FA*	50%FA+50%SG	-	1.5	8	0.3	Ambient cured (sealed)	[69]
AAMs	MK200	100%MK	-	1.3	18.5	0.44	Ambient cured(sealed)	[168]

^aFA+SG+MK (%); is the percentage of the amount of slag, fly ash and metakaolin precursors in alkali- activated binders.

^bM_r; silica modulus in the activating solution (ratio of moles of SiO₂ to moles of Na₂O)

^cw/b; w includes water within the activating solution and extra free water added in the mix design and b includes total amount of solids (precursors + anhydrous activator)

*Alkali-activated binders studied in [69]

According to **Figure 5.1** it is evident that a higher water/binder ratio gives faster desorption for Portland cement of type CEM I. It is also clear that 50SG50FA* and 75SG25FA* have higher evaporable water content than PC-0.35 during desorption in high relative humidity conditions.

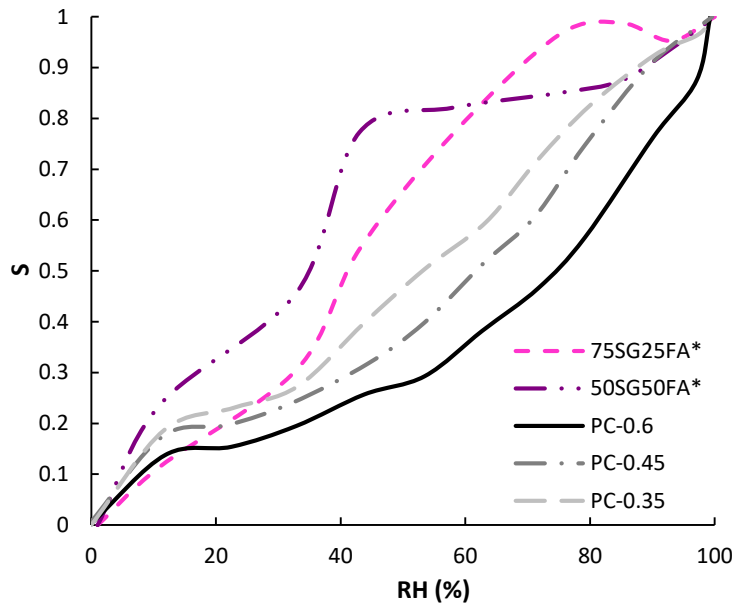


Figure 5.1 Desorption isotherms of various cements. Data obtained from [62, 69, 70] and replotted. Note that the drop in degree of saturation in the pink curve (i.e. 75SG25FA*) at 93% RH is in the original data set found in [69] and appears to be an analytical error.

The effect of alkali dosage, as a parameter in mix design of AAMs, on WVSIs could possibly play a role in preventing the water vapour from leaving the pores of the binder. As can be seen in **Figure 5.2**, MK200, despite being exposed to 200°C, showed a slower desorption process than 90FA10SG containing a lower water/binder and alkali dosage in its mix design and exposed to a temperature of 75°C for 18 hours as part of its curing condition. Therefore, it is possible that the free alkali ions in the pore solution prevented free evaporable water from leaving the pores because it may have induced, in the presence of moisture, hydration reactions that could further densify the microstructure by the blocking of the pores [62]. Additionally, the presence of high concentration of alkali ions in the pore solution can minimize the loss of the free water content [206]. Consequently, the amount of free water vaporized from the concentrated pore solution, as in the case of AAMs, during desorption is lower than in the case of PC with a less concentrated pore solution. Thus, the difference in ionic concentrations in the pore solution can explain the reason for AAMs retaining a higher content of evaporable water than PC during the stage of desorption.

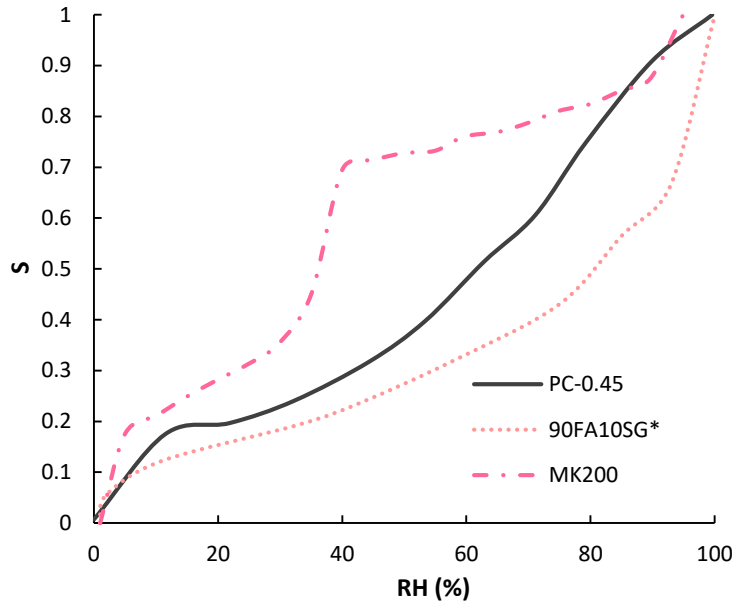


Figure 5.2 Desorption isotherms of geopolymer based cements and Portland cement [62, 69].

As for the case of adsorption and according to **Figure 5.3**, it is seen clearly that PC-0.45 has a higher evaporable water content along the adsorption curve compared to PC-0.35. The difference may be due to the ratio of water to binder used in the mix design where a higher w/b can increase the overall porosity of the material and allow the passage of more water vapour through the pores of the material [207]. The adsorption curve of 75SG25FA* is seen to be around the adsorption curve of PC-0.45. In the case of 50SG50FA* the adsorption curve is higher than the curve for PC-0.45. Although 50SG50FA* contains a lower w/b than PC-0.45, the microstructure of 50SG50FA* is more porous because of the presence of 50% of fly ash in its mix design increases the effective porosity and allows the passage of more water vapour into the pores of the material [207]. Note that the relationship in WVSIs between AAMs and PC can be used to compare simulated saturation profiles in AAMs with data obtained for PC at the end of wetting and drying experiments reported in the literature, due to lack of data for AAMs.

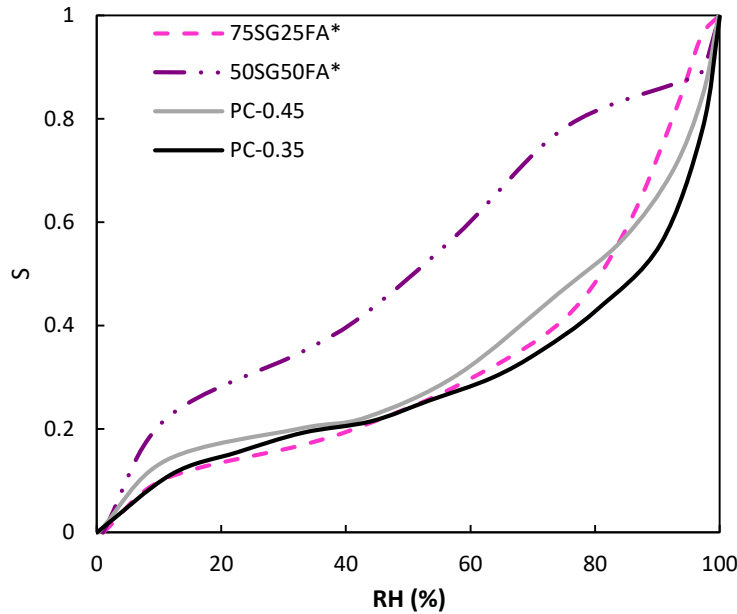


Figure 5.3 Adsorption isotherms of alkali-activated cements and Portland cement. Data obtained from [69, 70, 205].

Numerous studies have found that moisture transport, during drying and wetting cycles, follows an anomalous flow relationship: the transport for the first short time period follows Fick's second law of diffusion, then deviates from this law and slows down during a longer timescale. This deviation is also termed as a moisture hysteresis effect, caused by the complex microstructure and the free ions present in the pore solution of the cementitious material [62].

De Burgh and Foster [205] used the spinodal time-dependent microstructural change theory to explain the anomaly effect found in moisture transport, by interpreting the microstructural interaction of moisture with cement hydrates. In general, during the drying stage, that is the desorption process from complete saturation, the saturated spaces in the microstructure tend to contract and migrate under consolidation forces. The consolidation forces that occur at humidity levels below the cavitation point (i.e. spontaneous nucleation and evolution of gas bubbles in the metastable condensed water present in ink-bottle shaped pores of the cement) are caused by the increase in surface energy and disjoining pressure of cement hydrates, and the loss of water from the interlayer spaces of the C-S-H gel found in Portland cement. Conversely, during the wetting stage, that is the adsorption process starting from a dried state, capillary forces are the main causes of the microstructural rearrangement where the capillary pores tend to increase in pore size and gel pores, classified in the mesoporous range, tend to shrink. This can lead to a reduction in the retained water volume, especially when there is a delay in the mechanical response of the cement in the wetting cycle [69, 205]. Jennings et al.

[208] have used a similar interpretation to model the response of cementitious materials during sorption and desorption stages, through quantitatively linking the specific class of pores (i.e. the interlayer, gel or capillary spaces) that contribute to the irreversible changes in the microstructure according to **Figure 5.4**.

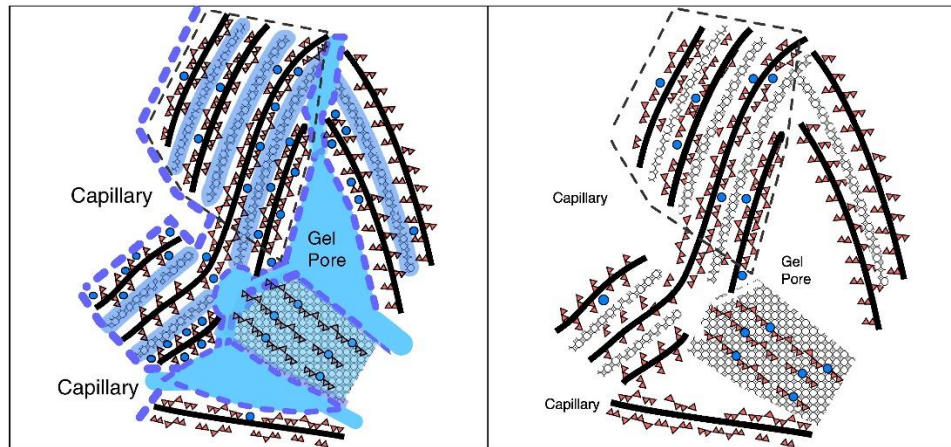


Figure 5.4 A diagram of the C-S-H structure containing the solid components (Ca-O sheets, with attached silicate tetrahedra) with chemisorbed/hydroxylated water, and physisorbed, or liquid water kept in the gel and capillary pores during the wetting stage (left) and drying stage (right). Figure obtained from [208].

They highlighted that the capillary and gel pores are the main transport and interaction media during both the sorption and desorption process, whereas the interlayer spaces only take part in the transport and volume change of the microstructure when cement is dried at RH below 25%.

It has also been noted that capillary pores do not undergo modification, and have minor contributions to irreversible pore volume changes upon drying whereas the gel pores contribute to the changes upon drying and aging which has been measured through the water vapour sorption isotherms [208]. The interlayer pores contribute to irreversible pore volume change only when the cement is exposed to high temperature and/or pressure, in such a way that water removed from these spaces cannot immediately re-enter during the sorption stage [208]. Jennings et al. [208] concluded that the capillary and gel pore manipulate the material behaviour and the interlayer pores control the material response where only under normal atmospheric conditions the water in this type of space is considered static [208, 209].

Furthermore, Zhang and Angst [62] described the morphological change of C-S-H gel, found in Portland cement, during drying and wetting stages through needle-like shaped structures as illustrated in **Figure 5.5**.

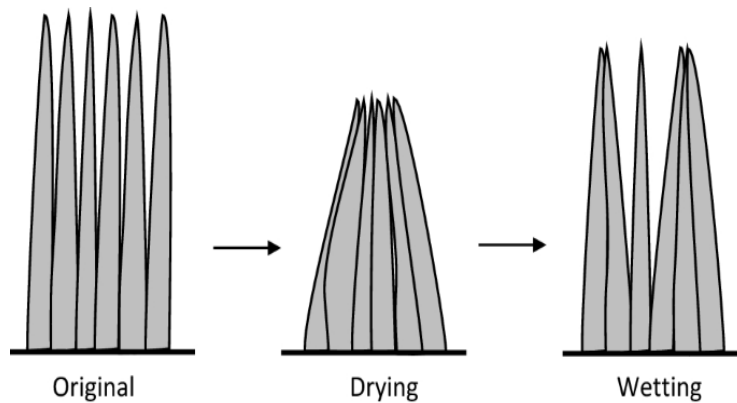


Figure 5.5 Effect of drying and wetting on the morphology of cement hydrates. Drying results in the collapse of the structure and only part of the structure can be recovered after wetting, Figure obtained from [62].

Figure 5.5 shows that after drying the original microstructure collapses which is partially recovered to a certain extent by rewetting, but will not return immediately to its original microstructural state. This has been proven at the macroscopic level through measured adsorption and desorption isotherms, where the re-saturated sample contains lower water content than the saturated sample before the next cycle, indicating the refinement of total porosity after multiple wetting and drying cycles [62]. The effect of pore refinement, that is lowering the total porosity of the material, can block the passage of water during a wetting cycle and can cause less water content to be adsorbed by the binder.

McDonald et al. [210] utilized proton NMR to probe the microstructural changes in C-S-H during drying and wetting phases. Figure 5.6 shows a representation of the structure of C-S-H, found in Portland cement, where three CaO backbones are in solid black with two interlayer and one gel pore such that this sequence is repeated four times, as indicated in the vertical dotted lines [210]. In addition, it is shown in figure 5.6 that the gel pore width is larger than the interlayer space, and porosity of the gel pore is higher than that of the interlayer. According to figure 5.6, the first stage in complete saturation, $S=1$, water (in dot pattern) fills the microstructure of the C-S-H completely, then following desorption at $S=0.33$ the water leaves the gel pores and some residual water manifests as interlayer water or can be regarded as chemisorbed water. At this stage the number of interlayers increases and reaches its maximum value. This is in contrast to the above discussion where the interlayer spaces in the C-S-H was identified to collapse upon drying. However, in continued drying across stages $S=0.31$ and 0 the gel and interlayer spaces do eventually collapse and densify the C-S-H gel. Then upon wetting the gel pores tend to fill first, as shown in stage $S=0.45$, and when left alone in saturated conditions, at $S=1$, for a long period time scale the interlayer spaces finally fill up and the

microstructure returns to its initial state shown in the final row of Figure 5.6 [210]. This result is in contrast with the above literature and this may be because before the proton NMR measurements have been conducted, the sample has undergone several sorption cycles where it was exposed to 60°C as drying condition and submerged in calcium hydroxide solution as wetting condition. These kind of conditions do not match with the test conditions used in the above literature and have the possibility to alter the microstructure of the cement and consequently its durability performance [205, 210]. Finally, it should be noted that there is a sign of pore coarsening (i.e. increase in total porosity of the material) in **Figures 5.5** and **5.6** during the exposure of the binder in a wetting stage before reaching complete saturation (i.e. $S=1$) where the material slowly returns to its initial microstructural state as shown in **Figure 5.6**.

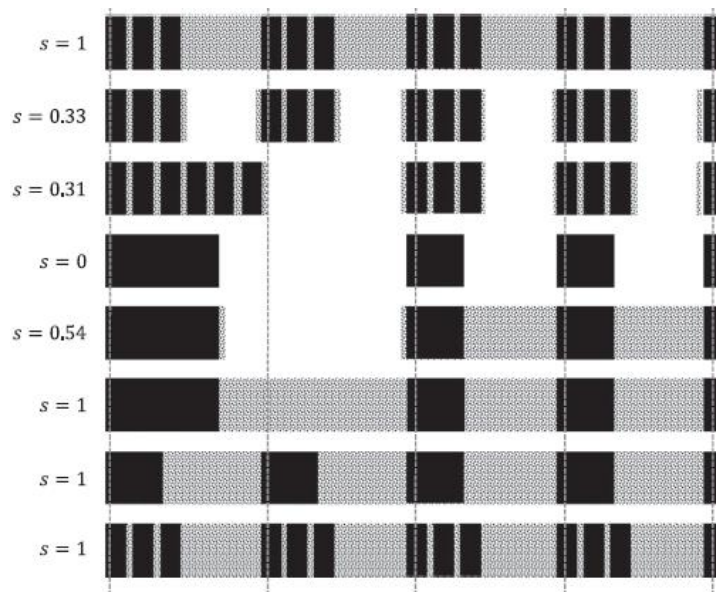


Figure 5.6. C-S-H in Portland cement, containing interlayers and gel pores, undergoing microstructural changes during a drying and then wetting cycle [210].

The importance of the cementitious pore network and interactions is that it governs the diffusion of moisture in the cement as a function of degree of liquid water saturation in the pores, which is controlled by the environmental relative humidity. In addition, several test methods have been conducted to assess the permeability of Portland cement and concrete such as the cup test, sorption kinetics, and data obtained from dynamic vapour sorption instrument [79, 81, 82]. However, the obtained moisture diffusion coefficients can range between 10^{-15} - 10^{-10} m^2/s as a function of the degree of liquid saturation, according to Figure 5.7. The reason for this scatter maybe due to the type of testing conditions, such as temperature and/or pressure that can induce micro/nanostructural damage to the binder, and moisture history which defines

the sample's degree of water saturation before undergoing a permeability test [82]. It is also shown in **Figure 5.7** that vapour dominates the moisture transport in pores that are nearly empty (i.e. degree of saturation < 0.5), and liquid transport occurs when the pores are nearly saturated (i.e. degree of saturation ≥ 0.5).

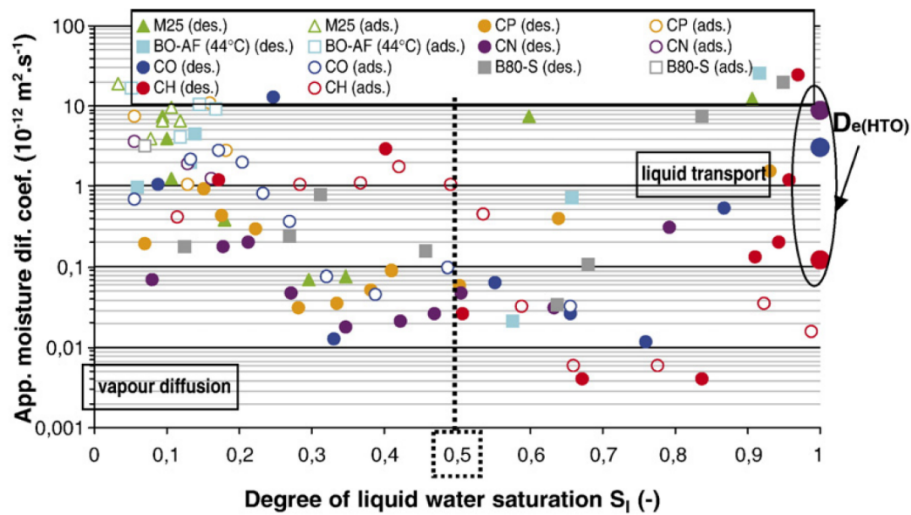


Figure 5.7. Apparent moisture diffusion coefficient D_a vs. degree of liquid water saturation S_l , assessed from sorption kinetics (under non-steady-state conditions for adsorption – “ads” – and desorption – “des”), on various samples of Portland cement pastes and concretes. Comparison with effective titrated water diffusion coefficient $D_{e(HTO)}$ (under steady-state conditions), Figure obtained from [82].

Zhang and Angst [62], have further, based on literature data, quantified the moisture diffusivity in the large and small pore regions in the cement, according to **Figure 5.8**, and predicted that the permeability in large pores, red dashed line, is greater than in small pores. In addition, the distinction between the liquid and vapour transport dominant regions in each type of pore is marked at 74% RH for the large pore region and 50% for the small pore region [62].

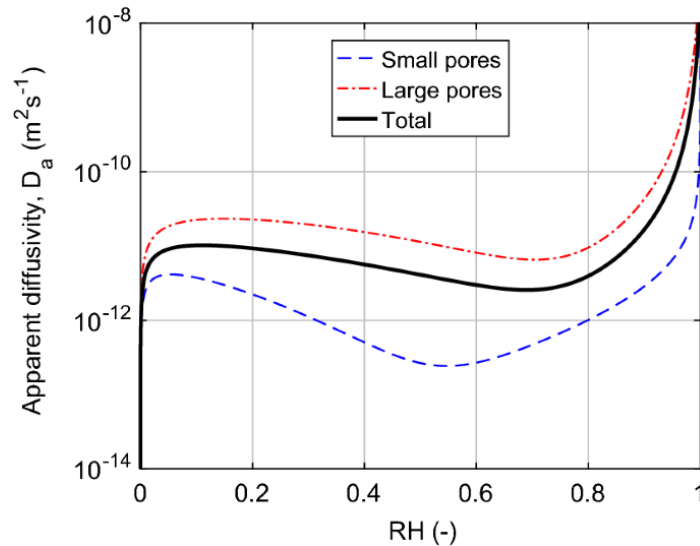


Figure 5.8. Apparent moisture diffusivity in the small and large pores during desorption state, Figure obtained from [62].

In comparison to Portland cement, alkali-activated binders could react differently in wetting and drying conditions. Babae and Castel [69] have measured the sorption kinetics of AAM between 0-100% RH. In their research, the moisture transport in high calcium based AAMs showed to have the highest anomaly effect or non-Fickian type of transport and this may be due to several reasons which are: microstructure containing fine pores, higher-calcium hydrates containing high moisture binding capacity, and hydrates swelling which can lead to a change in the microstructure [69]. In contrast, the geopolymers (with low calcium content) are less prone to microstructural changes, and moisture transport in these binders significantly follows the Fickian diffusion process. Finally, the diffusivities as a function of RH during the wetting process were calculated using the sorption kinetic data (i.e. the method used to calculate the moisture diffusivity values in cementitious materials can found in [69]) and the values obtained were in the range of 10^{-12} - 10^{-11} m^2/s [69].

This chapter focuses on calculating the permeability of moisture in alkali-activated binders using the apparent moisture diffusivity as a function of RH data obtained from the dynamic vapor sorption (DVS) instrument, which is the second method suggested in [79]. The first part (i.e. section 5.5.1) describes the characterization of the materials by the use of thermogravimetry (TGA) and mercury intrusion porosimetry (MIP) in order to identify possible carbonated phases and estimate the volumetric fraction of the large pore region of the binders, respectively. The second part (i.e. section 5.5.2 and 5.5.3) aims to predict the adsorption and desorption isotherms of AAMs with the current existing mathematical models, discussed in the literature review (i.e. **Chapter 1**), which determine the parameters that control the overall shape

of water vapor sorption isotherms (WVSIs). The third part (i.e. section 5.5.4 and 5.5.5) compares the predicted degree of saturation in the pores of alkali-activated binders as a function of sample thickness by the use of the three moisture permeability models discussed in Chapter 2. With the use of the difference of isotherms between PC and AAMs, the predicted saturation profiles for AAMs are compared with the data for PC with similar water/binder ratio. Finally, discussion is written in detail for each section followed by a proposed procedure for upscaling of moisture transport properties from cement to mortar and concrete as a final part of this chapter (i.e. section 5.5.6).

5.2 Methodology

5.2.1 Mix Design of Alkali-Activated Cements

Table 3.1 contains the average mineralogical composition of precursors used in this study where the data is obtained from [165]. **Table 5.3 and 5.4** contains the notations used for the alkali-activated binders studied in this chapter, with similar mix design composition of the binders studied in [69, 98, 168], but a slightly higher water content in the 100% slag based alkali-activated binders. The reason for the selection of the four types of binders in **Table 5.4** is to study the effect of calcium oxide content and alkali dosage (in **Table 5.3**) on durability properties.

Table 5.3 Mix designs of 100%SG alkali-activated cements discussed in this chapter.

Cement	Precursor	Activator	w/b	Na ₂ O (wt.% with respect to precursor)	Mr (moles SiO ₂ /moles Na ₂ O in activator)
100SG	100% Slag	NaOH- Na ₂ Si ₂ O ₅	0.5	4	1.5
100SG8	100% Slag	NaOH- Na ₂ Si ₂ O ₅	0.47	8	1.5

Table 5.4. Mix designs of blended alkali-activated cements discussed in this chapter.

Cement	Precursor	Activator	w/b	Na ₂ O (wt.% with respect to precursor)	Mr (moles SiO ₂ /moles Na ₂ O in activator)
75SG25FA	75% Slag and 25% Fly ash	NaOH- Na ₂ Si ₂ O ₅	0.45	4	1.5
50SG50FA	50% Slag and 50% Fly ash	NaOH- Na ₂ Si ₂ O ₅	0.4	4	1.5

5.2.2 Characterizations

5.2.2.1 Thermogravimetric Analysis

Methodology explained in “**Chapter 2: Materials and Methods**”

5.2.2.2 Mercury Intrusion Porosimetry

Methodology explained in “**Chapter 2: Materials and Methods**”

5.2.2.3 Dynamic Vapour Sorption

Dynamic vapour sorption, DVS, is used to study the moisture permeability in cement and the water vapour sorption isotherms, WVSIs, including adsorption and desorption, in order to estimate free water content, or degree of water saturation, in cement as a function of the RH in the external environment [79]. The methodology is already explained in “**Chapter 2: Materials and Methods**”

In this study, WVSIs of the cement samples were obtained by monitoring the mass changes from 50% to 95% relative humidity. In this case, the calculation of the degree of saturation, S , is according to **Equation 3.2**.

The degree of saturation obtained using **Equation 3.2** at 50% RH was calculated to be 0 because it was the reference point for the data acquisition. However, this is not a true value because after the completion of hydration reactions there is still free evaporable water present in the pores of the cement, and the moisture profile measured by the gamma-ray attenuation method for a Portland cement sample dried at 50% RH shows the presence of free water [30, 179]. Therefore the reference value for the degree of saturation at 50%RH, S_{ref} , used for 100SG, 75SG25FA and 100SG8 is the same value obtained for 75SG25FA*, from [69], when dried at 43%RH (i.e. from **Figure 5.1**, $S_{ref} = 0.54$) because of their similar mix designs. The reference value for the degree of saturation at 50%RH, S_{ref} , used for 50SG50FA is the same value obtained for 50SG50FA*, also from [69], when dried at 43%RH (i.e. from figure 5.1, $S_{ref} = 0.77$) because of their similar mix designs. Note that an assumption has been made in which value of the degree of saturation obtained at 43%RH is close to the value of 50%RH condition, used in the DVS, because data measurement at precisely 50%RH was not done in [69]. Accordingly, the WVSIs for AAMs have been adjusted according to **Equation 5.1**;

$$S = S_{meas.} \times (1 - S_{ref}) + S_{ref} \quad (5.1)$$

Where, $S_{meas.}$; measured degree of saturation and S_{ref} ; reference degree of saturation at 50% RH.

5.2.3 Moisture Permeability Transport Parameters

There are several important parameters that need to be determined for the prediction of moisture transport in cement. The first ones are the shape parameters of the WVSIs, m and n , then the entry flow pressure, a , which are all determined by fitting the VG and/ or dual porosity models (i.e. VG-Dual) to the adsorption and desorption isotherm data. Next, is the determination of the liquid permeability factor, K , and the vapour resistance factor x_d . The description of the moisture transport and isotherm models can be found in section 2.10 of **Chapter 2**.

Zhang et al. [79] have discussed two methods used to calculate these K and x_d parameters, which are fitting the apparent water vapour diffusivity curve as a function of degree of saturation, and an inverse analysis method [79, 168]. The former method is applied by measuring the mass change kinetics associated with each measured point of the sorption/desorption isotherm and fitting the apparent diffusion, D_a , factor from Richards' equation (**Equation 2.33**) with the assumption that the moisture transport in the material between two small RH steps is governed by diffusion. Then the liquid permeability and vapour resistance factors are obtained by fitting the plotted curve of D_a as a function of liquid water saturation (i.e. S). The latter method utilizes data of mass loss from a cement sample in a drying experiment and its saturation profile determined based on its density changes measured by gamma-ray attenuation. First, the liquid permeability factor is fitted through the measured drying kinetic data with x_d initially set to the value of 2.74 (i.e. 2.74 value is initially assumed by Zhang et al. [79] while fitting the mass loss in evaporable water from Portland cement during a drying experiment) which is then adjusted with the saturation profile. Then a new K factor is obtained by fitting the mass loss curve again by using the new obtained value for x_d . Moreover, Zhang et al. [79] highlighted that the K obtained by fitting the D_a vs. S curve. is 4-10 times smaller than the value calculated from the inverse analysis method, but have considered it to be acceptable due to the presence of scattered data of moisture permeability in the literature. In addition, they have noted that the values obtained for the x_d factor by the two methods are quite similar [79].

In this research the former method is applied where the DVS instrument measured apparent moisture diffusivity vs. RH data for the alkali-activated binders exposed to three wetting and drying cycles in 50%-95% RH range and did not undergo a pre-heating stage prior to the measurements. Then the liquid permeability and vapour resistance factors are obtained by fitting the plotted curve of D_a as a function of liquid water saturation (i.e. S).

5.2.4 Prediction of WVSIs

The use of mathematical models to estimate the WVSIs is necessary to predict the overall shape of the saturation profiles of the cement during wetting (i.e. adsorption) and/or drying (i.e. desorption) stages. Zhang et al. [70] have reviewed and adapted several empirical models, which some were initially used in studies of soil, to predict the equilibrium between liquid water and water vapour in the pores of the cement as a function of environmental RH. The models have already been discussed in section 2.10 of **Chapter 2**, and are applied here to predict the adsorption and desorption curves, that include the hysteretic behaviour of the cement, for the studied alkali-activated cements.

5.2.5 Moisture Permeability Models

Moisture permeability models are implemented to simulate saturation profiles in circular disk shape AAMs samples with thickness of 50 mm and exposed on opposite sides to wetting and drying conditions. The wetting conditions is set such that the samples are initially dried at 50%RH and the exposed to 100%RH. Whereas the drying condition is the inverse of the wetting. Furthermore, it is considered that mass transport is uni-directional by neglecting moisture transport from the circumferential surface and that moisture transport only occurs across the surfaces of the disk sample. This is based on the assumption that the moisture loss and gain is mainly from the disk surfaces rather than the circumferential surface because it is assumed that the diameter of the disk is relatively bigger than its thickness. This assumption has been made in [79, 168] for obtaining moisture transport properties of cements from DVS data (i.e. measured D_a vs. S curve) and simulating their saturation profiles at the end of drying and wetting experiments.

5.2.5.1 *Single permeability moisture transport model*

In summary, the Van Genuchten model (VG) is used in the single permeability model (i.e. single-porosity moisture transport model) to correlate the external relative humidity to amount of evaporable water in the pores of alkali-activated binders, at constant temperature, according to **Equation 2.24**.

Equation 2.33 represents the S -based form of Richards' equation and **Equations 2.34 and 2.35** are part of the apparent diffusivity parameter in the model that represent moisture-liquid phase diffusion and moisture-vapour phase diffusion, respectively, such that $D_a = D_l(S) + D_v(S)$. The models are from section 2.10 from Chapter: 2 where they are explained in more details.

Overall the set of **Equations 2.33-2.35** represent the single porosity moisture transport model studied in this section.

Equations 2.34 and **2.35** are used to fit the Da vs. S data, obtained from the DVS instrument, to obtain the liquid permeability factor (K) and vapour resistance factor (x_d), and are implemented in **Equation 2.33** to predict the diffusivity data at the end of desorption and adsorption of the alkali-activated binders. Additionally, the numerical code used to simulate moisture transport in cementitious material by the single permeability moisture transport model implemented the pdepe function described in section 3.4.2.1 of **Chapter 3**.

5.2.5.2 Dual permeability moisture transport model

In summary, the bimodal equation (i.e. VG- Dual) is used in the dual permeability model (i.e. dual-porosity moisture transport model) to correlate the external relative humidity to amount of evaporable water in the pores of alkali-activated binders, at constant temperature, according to **Equation 2.39a**. This equation also represents the sum of degree of saturation in large and small pore regions of the cement as interpreted by **Equation 2.39.b**.

In summary, **Equations 2.44** and **2.46** are implemented in **Equations 2.43** and **2.45** to simulate the moisture transport in large and small pore regions of the cement respectively. In addition, the moisture transport between two porosity regions is predicted by using **Equation 2.47** and is also included in the moisture transport in large and small pore regions. The moisture diffusivities in these two pore regions are combined with the contribution factor of the large pore region to the moisture transport (i.e. $w_{f,D}$) as shown in **Equation 2.42** to calculate the overall apparent moisture diffusivity parameter D_a used in **Equation 2.33**. Note that $w_{f,D}$ is not the same parameter as w_f (i.e. the volumetric fraction of the large pore region in cement) implemented in **Equation 2.39 a+b**. The models are from section 2.10 from Chapter: 2 where they are explained in more details.

In addition, the transport in the large pore region is predicted to be faster than in the small pore region, as similarly discussed in [62], because of the higher size in diameter of the large pore region compared to the small pore region.

Additionally, most of the free evaporable water content is predicted to be present in the small pore region of the binders. The reason for the small pores to have a higher degree of saturation than in the large pores is according to Laplace-Kelvin equation which describes that the menisci of the evaporable water formed in the partially saturated pores creates a capillary tension (i.e.

capillary pressure) on the pore solution and also impacts the internal relative humidity of the cementitious material as shown in **Equation 5.2** [211]. For example, when the capillary tension decreases, as a result of increase in pore radius, the internal relative humidity inside the pore of the cement will increase.

$$P_c = \frac{2\gamma\cos\theta}{r} = -\frac{\rho_l RT}{M_v} \ln RH \quad (5.2)$$

P_c ; capillary pressure, Pa

γ ; surface tension

θ ; contact angle between the menisci and capillary pore

r ; pore radius

ρ_l ; liquid water density 997 kg.m⁻³.

R ; gas constant, 8.314 Pa.m³.K⁻¹.mol⁻¹.

T ; absolute temperature, 293.15 K

M_v ; molar mass of the water molecule, 0.018 kg.mol⁻¹

RH; relative humidity, as a fraction

However, the pore radius will impact the degree of saturation in the small and large pore regions of the cement in a such a way that more moisture will condense on the walls of the small pore region and fill the pores with high amounts of free water as shown in **Figure 5.9**.

Whereas the pores of the large pore region are further apart which leads to less condensation of moisture on the walls and therefore less water will fill the pores as shown in Figure 5.9.

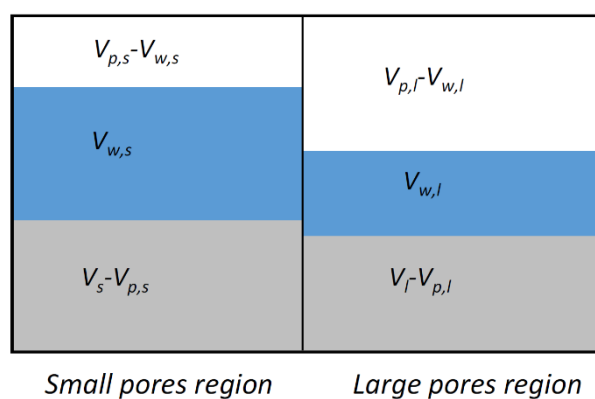


Figure 5.9 Degree of saturation in small and large pore regions of a cement. Abbreviations are s and l for small and large pores, respectively, w for evaporable water occupied volume and p for pore volume. Figure obtained from [62].

Furthermore, **Equations 2.44** and **2.46** implemented in **Equation 2.42** are used to fit the data of moisture diffusivity vs. the degree of saturation, to obtain the liquid permeability factor in the large and small pore regions (K_l and K_s), vapour resistance factor (x_d), and contribution factor of the large pore region to moisture transport ($w_{f,D}$) so that they are implemented in **Equations 2.43** and **2.45** to simulate the saturation profiles in the large and small pore regions of alkali-activated binders at the end of desorption and adsorption. Note that Zhang and Angst [62] implemented a single value of vapour resistance factor (x_d) for the large and small pore regions in their model. Consequently, in this study a single value for vapour resistance factor is also implemented. Additionally, the numerical code used to simulate moisture transport in cementitious material by the dual permeability moisture transport model implemented the pdepe function described in section 3.4.2.1 of **Chapter 3**.

5.2.5.3 Mechanistic permeability moisture transport model

In summary, the Van Genuchten model (VG) is used in the mechanistic permeability model (i.e. mechanistic moisture transport model) to correlate the external relative humidity to amount of evaporable water in the pores of alkali-activated binders, at constant temperature, according to **Equation 2.24**.

Equation 2.33 represents the S-based form of Richards' equation and **Equation 2.49** represents the equation for the apparent diffusivity parameter in the model that contains the moisture-liquid phase diffusion and moisture-vapour phase diffusion. The models used for vapour and liquid diffusivities in the mechanistic model are shown in **Equations 2.50** and **2.55** respectively. These models are different from the ones used in the single permeability model because the vapour diffusivity equation contains a different form of vapour resistance factor, **Equation 2.50**, and the liquid permeability factor is multiplied with a relative liquid permeability factor, **Equation 2.55**, that is different than the van Genuchten-Mualem model [74] used in the single and dual permeability models. Overall the set of **Equations 2.49-2.50**, **2.55-2.56** and **2.60** are the main equations of the mechanistic model used to calculate the apparent diffusivity parameter in Richards' equation to simulate saturation profile in 50SG50FA binder studied in this section. All these models are from section 2.10 in Chapter: 2 where they are explained in more details.

In the case of water vapour diffusion in cement, the value of $D_{v,air}(T)$ in **Equation 2.50** is set to $2.47 \times 10^{-5} \text{ m}^2 \cdot \text{s}^{-1}$, which is also used in the single and dual moisture permeability models, because this is the right value of water vapour diffusivity in air between 20°C and 25°C [82].

In the case of moisture-liquid phase diffusion, **Equation 2.55** describes the liquid permeability factor, $K_l(S)$, of the cementitious material and it is a function of the liquid permeability in hygroscopic conditions, $K_{l,hyg}(S)$, (i.e. extremely low RH condition) and the effective liquid permeability factor, K_{eff} . The effective liquid permeability factor is coupled with scaling parameter and function, n_{cap} and $f_l(S)$, used to adjust the liquid flow in cement exposed to high relative humidity environment, and relative conductivity function, $K_{l,rel}(S)$, that contains information on the pore structure of the porous media [18]. In this research the $K_{l,hyg}(S)$ is neglected because the studied binders are not exposed to severe drying conditions. The parameters needed for the calculation of $K_{l,rel}(S)$, as shown in **Equation 2.60**, are from the moisture storage curves obtained from the adsorption and desorption isotherms of 50SG50FA* that are replotted in terms of the degree of saturation as a function pC which is $\log(Pc/Pref)$ with $Pref = 1 \text{ Pa}$ [88]. The full WWSI, 0-100%RH, of 50SG50FA* is used to obtain parameters needed for the calculation of $K_{l,rel}(S)$ and is based on the assumption that 50SG50FA and 50SG50FA* have a similar porous microstructure. Some of these parameters are the pore maxima pC_i which are the inflection points within the moisture storage curves. The other parameters are the slopes, s_i , which are the slopes of straight lines drawn tangent to the moisture storage curves at the inflection points. The parameter ΔS_i represents the difference between the plateau levels in the moisture storage curves such that the sum of ΔS_i must equal to 1 according to **Equation 5.3**.

$$\Delta S_i = S_i - S_{i+1} \quad \text{for } i < N \quad \Delta S_N = 1 \quad (5.3)$$

In this research, the parameters n_{cap} , $f_l(S)$, and $K_{l,rel}(S)$ in **Equation 2.55** are coupled into one form of function called mechanistic relative permeability, $Kr_{Mechanistic}$. The output of this function is multiplied with the effective liquid permeability factor, K_{eff} , to calculate the liquid permeability factor as a function of degree of saturation according to **Equation 5.4**. In addition, the value of the liquid permeability factor obtained for the single permeability model is also used in effective liquid permeability factor, K_{eff} , for the mechanistic model to simulate the transport of moisture in 50SG50FA. This method is applied in this research because the effective liquid permeability factor was not measured with a permeameter or infiltrometer device on samples submerged in water as suggested by the authors of the mechanistic permeability model [88]. The purpose of this research is to exclusively study the transport

properties of unsaturated cement samples exposed in RH environment ranging from 50-100%RH.

$$K_l(S) = Kr_{\text{Mechanistic}}(S)K_{\text{eff}} \quad \text{if } S \leq 1 \quad (5.4)$$

Where $Kr_{\text{Mechanistic}} = n_{\text{cap}} \times f_l(S) \times K_{l,\text{rel}}(S)$.

Similar to the van Genuchten-Mualem model [74], for relative permeability shown in **Equation 2.32**, which is also multiplied with the liquid permeability factors in the single and dual permeability models, the $Kr_{\text{Mechanistic}}$ varies between 0-1 to account for the transport of moisture in unsaturated cementitious materials.

Consequently, the scaling factors n_{sp} and n_{cap} are determined by fitting the mechanistic relative permeability curve with the curve generated by the van Genuchten-Mualem model [74]. This approach is applied in this research because dry and wet cup tests were not conducted in this research to obtain the parameters n_{sp} and n_{cap} that adjust the liquid permeability factor when the cement is exposed to a low and high relative humidity environment. More information on the experimental set up for dry and wet cup tests can be found in [82]. In addition, the isotherm parameters a , m , and n used in the $K_{l,\text{rel}}(S)$ for the mechanistic relative permeability function are obtained by fitting the Van Genuchten model, **Equation 2.24**, the WVSIs of 50SG50FA*. Additionally, the numerical code used to simulate moisture transport in cementitious material by the mechanistic permeability moisture transport model implemented the pdepe function described in section 3.4.2.1 of **Chapter 3**.

5.3 Statistical Criterion for Curve Fitting

The curve fitting of the WVSIs and Da vs. (S) data is done by optimizing the parameters in the models to fit the experimental data using a non-linear squared optimization method that minimizes the sum of squares of the errors between the measured and predicted data. In addition, a statistical criterion known as the normalized mean error (NME) is used to assess the accuracy of the modelling results according to **Equation 5.5**. Where calculated values close to 0 indicate better prediction of the data computed by the models.

$$\text{NME} = \frac{1}{n} \sum_{i=1}^n \frac{|S_i^{\text{pr}} - S_i^{\text{ms}}|}{S_i^{\text{ms}}} \quad (5.5)$$

S_i^{ms} and S_i^{pr} ; measured and predicted values, respectively.

n; number of measured data

5.4 Comparison of Saturation Profile Data between PC and AAMs

Zhang et al. [179] have utilized saturation profile data of Portland cement samples, PC-0.45, first subjected to a drying state at 53.5% RH for 370 days and then exposed to a wetting state at 97% RH for 315 days at constant room temperature, 23°C. The data was obtained by Baroghel-Bouny [212] and Nguyen [213] where they implemented the gamma-ray attenuation method on cylindrical Portland samples of thickness of 100 mm. For each specimen the circumferential surface and one end of it were sealed with adhesive aluminium foil sheets and the other end was exposed to moisture exchanges with the ambient environment to ensure that the transport of moisture was in unidirectional manner.

In this section, the obtained data set was used to compare the predicted saturation profiles in the alkali-activated binders. Although the chemistry of the PC and alkali-activated binders are different, each binder shares a similar w/b in the mix designs which serves as an indication that the overall porosity (i.e. key parameter that directly affects the permeability property of concrete [214]) can be comparable in each system. In addition, with the difference in WVSIs between PC and AAMs discussed in section 5.1, the saturations profiles at the end of wetting and drying experiments can be nearly estimated qualitatively. In summary, for the case of adsorption, and according to Figure 5.3, the PC-0.45 and 75SG25FA binders (i.e. 75SG25FA* has the same mix design as 75SG25FA) have a similar adsorption curve because of the presence of C-S-H and C-A-S-H phase in each system respectively, that chemically bond to evaporable water. 100SG binder could have the adsorption curve just a little higher than PC-0.45 because 100SG has a slightly higher water binder ratio in its mix design (i.e. w/b in 100SG is 0.5 and w/b in PC-0.45) that can form more pores than in the case of PC-0.45 [207]. The 50SG50FA adsorption curve will be higher than that of PC-0.45, 100SG and 75SG25FA for two main reasons which are the presence of a big amount of N-A-S-H gel in 50SG50FA, that does not chemically bond to evaporable water, and because 50SG50FA is more porous in its microstructure due to the incomplete dissolution of the fly ash precursors responsible for the formation of hydrates that tend to fill up the pore spaces [69, 194]. Therefore, the moisture profiles of 100SG and 75SG25FA will have a similar saturation profile as the one obtained for PC-0.45 at the end of the wetting experiment. Conversely, 50SG50FA will have a higher moisture profile than the profile obtained for PC-0.45 because 50SG50FA has a low binding capacity to evaporable water and it has a high porous microstructure that can increase the

permeability of moisture. While in the case of desorption and according to Figure 5.1 the desorption curve of 75SG25FA* is higher than the curve for PC-0.45 which means that the saturation profiles of 100SG and 75SG25FA maybe be higher than the profile obtained for PC-0.45. This is because of the effect of high content of free alkali ions in the pore solution of AAMs, compared to PC binders, that can minimise the loss of evaporable water during the drying experiment. However, the desorption curve of 50SG50FA may be lower than the curve for PC-0.45 because 50SG50FA has a more porous microstructure that can increase rate of moisture transport during desorption [197, 214].

Furthermore, the numerical simulations are carried out by using the same values of the degree of saturation at the initial and boundary conditions that represent the moisture states at the inner and surface parts of the PC specimens when exposed to wetting/drying experiments. This is done in order to compare the saturation profiles of AAMs and PC binders containing the same degree of saturation at the initial and surface states. In addition, the same sample thickness of 100 mm is used for the alkali-activated binders with one-sided exposure and were all subjected to wetting/drying conditions for the same time duration used for the experiments on PC-0.45 samples.

Moreover, for the case of the wetting experiment, the initial condition has been set as the degree of saturation as a function of thickness of the sample, because the data reported in the literature shows that the pores at the surface of the cement are less filled with free water than the pores in the inner part of the sample even at the end of the experiment. **Table 5.5** presents the initial condition function, with the NME value, obtained by curve fitting the experimental data with a power law equation.

Table 5.5 Initial moisture condition functions, where $S(x)$ is the degree of saturation, S , as a function of distance, x , which is the thickness of the cement sample. Data obtained from [179].

Sample	$S(x)$	NME
PC-0.45	$0.7346x^{0.0369}$	0.015248

5.5 Results and Discussion

5.5.1 Characterization

5.5.1.1 Thermogravimetric Analysis

Figures 5.10 and 5.11 present the thermogravimetric analysis (TGA) data for the alkali-activated binders. In both figures, the mass loss around 100°C is associated with the free and/or loosely bound water from the C-A-S-H phase in the cementitious hydrates [215]. In **Figure**

5.10, 75SG25FA had a slightly higher mass loss compared to 100SG and 50SG50FA. The reasons could be due to the high intensity of pore refinement in case of 100SG, with its homogeneous phase, and due to the pore-blocking effect in the microstructure of 50SG50FA because of the incorporation of fly ash responsible for the formation of the N-A-S-H gel, with large pores, coexisting with the C-A-S-H gel, with very fine pore structure, obtained from the slag phase. Both of these factors make it difficult for the free water to be easily drawn out of the cementitious microstructure [137, 215].

According to literature, mass losses from 400°C to 800°C correspond to the decomposition of CaCO_3 , a primary carbonate phase found in carbonated cements. The reason for this broad temperature range is because CaCO_3 can vary in the extent of its crystallinity and structure [215]. In **Figure 5.10** a very minor peak, marked with a star, is shown at 600-700°C and is consistent with a highly crystalline calcite. This indicates that the samples have undergone a very slight carbonation reaction.

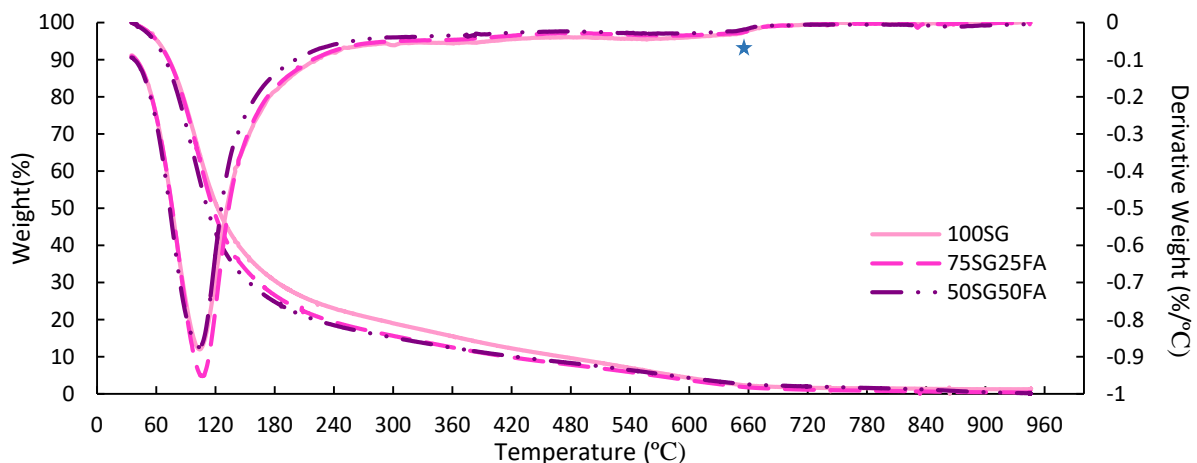


Figure 5.10 TGA of alkali-activated binders-effect of calcium oxide content in mineralogical composition.

In **Figure 5.11**, containing data for 100% slag alkali-activated binder with a higher alkali-dosage (i.e. 100SG8), the mass loss around 350°C up to 435°C is associated with the dehydration of the hydrotalcite-like phase [216] [215]. Which means there is more of this phase for 100% slag activated with a high alkali-dosage [216]. In the case of 100SG, water in the free state is released which easily evaporates at its normal boiling temperature, 100°C. Whereas in the case of 100SG8 containing a lower w/b content in the mix design, a greater loss of water, at around 116°C is noted in **Figure 5.11**. This difference has also been noted in [216] where

slag activated with a higher alkali-dosage released more water, at a similar temperature range, than slag activated with a lower amount of alkali-dosage. The reason for this difference can be due to the formation of more C-A-S-H phase, in slags activated with high alkali-dosage, and which chemically bonds to more water [216]. Consequently, more water is released in AAMs containing higher amounts of C-A-S-H gel during the dehydration reaction between 25 and 220°C [216].

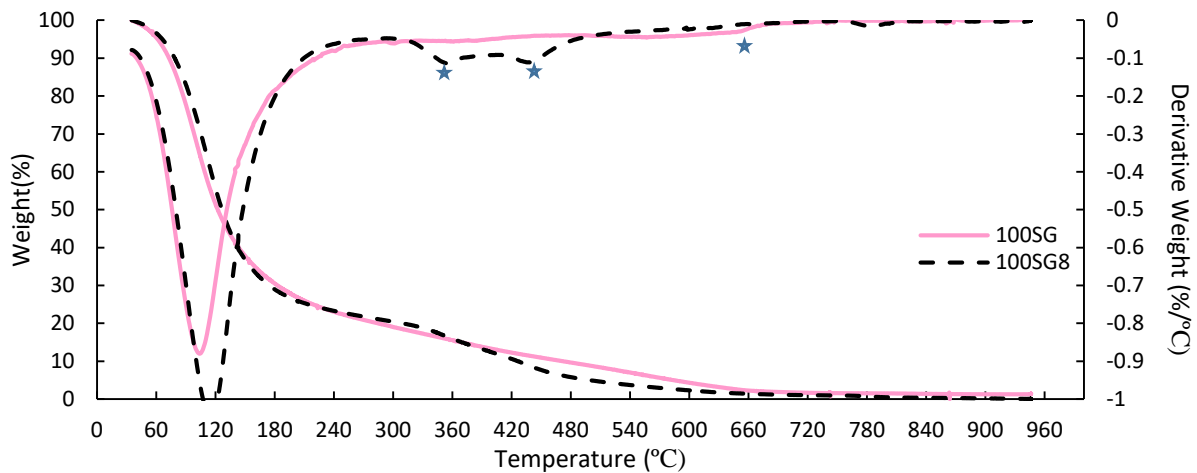


Figure 5.11 TGA of alkali-activated binders - effect of alkali dosage in mix design.

5.5.1.2 Mercury Intrusion Porosimetry Measurements

Figures 5.12 represent data on pore size distributions and cumulative pore volumes obtained by mercury intrusion Porosimetry (MIP).

According to **Figure 5.12 A**, the alkali-activated binders, especially 100SG and 75SG25FA, show a fine pore structure with a unimodal pore size distribution ranging in the mesoporous scale from 5 nm to 15 nm, whereas 50SG50FA contained small macro-pores ranging from 15 nm to 130 nm. In **Figure 5.12 B**, the data on cumulative pore volume indicate that 75SG25FA contains mostly small pores, followed by 100SG then 50SG50FA. Lastly, the pore size distribution and cumulative pore volume for 100SG and 100SG8 shown in **Figure 5.12 C + D**, indicates that 100SG8 has a more uniform pore size distribution and dense microstructure compared to 100SG.

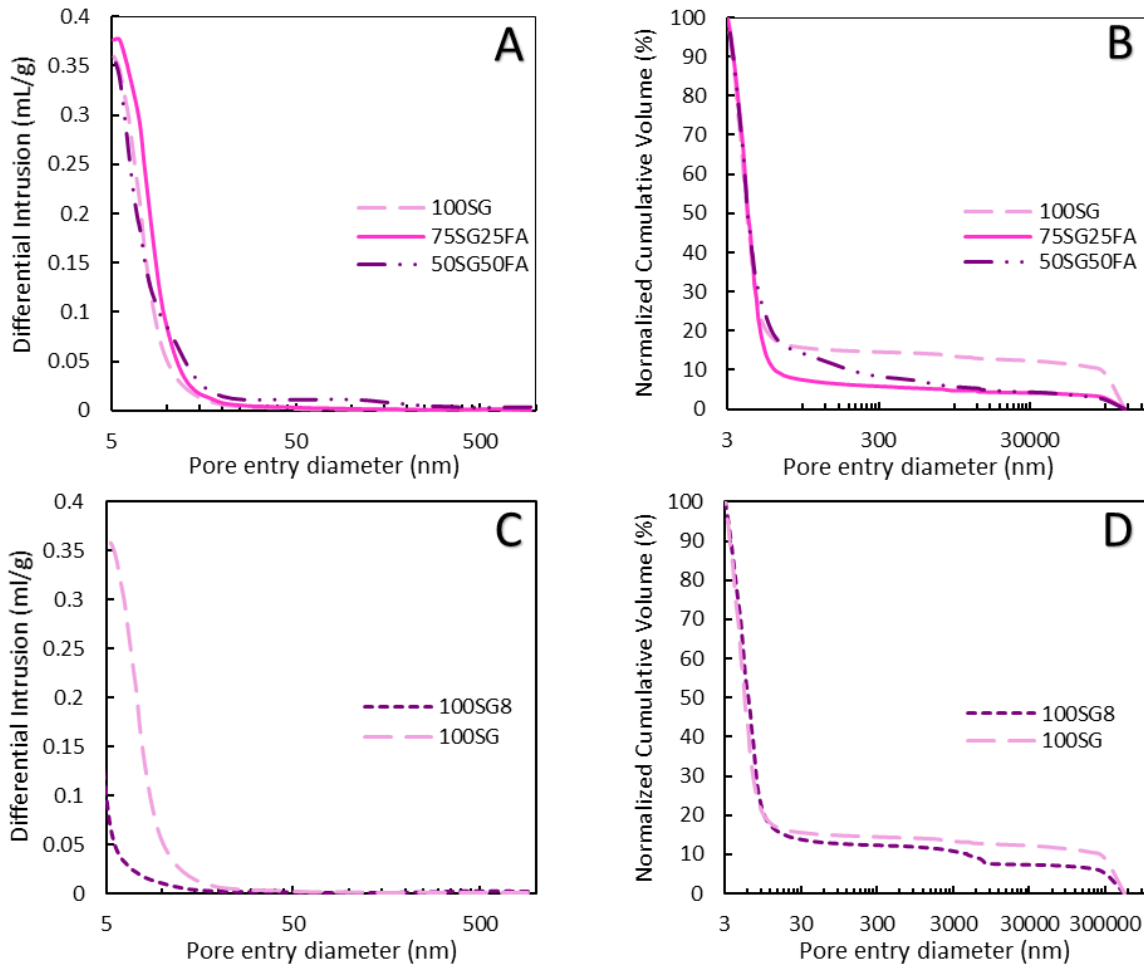


Figure 5.12. Pore size distribution (A and B) and cumulative pore volume (C and D) of alkali-activated cement pastes.

Based on MIP data on cumulative pore volume, in **Figure 5.12 C+D**, the volumetric fraction of the large pore region, w_f , of the binders is estimated from the point on the curve where it starts to plateau. The w_f parameter shown in **Table 5.6**, is used in the dual permeability model in following sections of this chapter, to describe the anomalous moisture transport in the binders. The method of obtaining w_f is different from the older technique of curve fitting water vapour sorption isotherms, but the estimated values in this study are in the same range of values that were obtained in [62].

The effective porosities of alkali-activated binders measured by MIP are also shown in **Table 5.6**. The effective porosity can be seen to be similar for all the alkali-activated binders, maybe because of the similar water/binder ratio used in their mix design that mainly impacts the overall microstructure [21].

Table 5.6 Volumetric fraction of large pore region, w_r , and effective porosity ϕ as measured by MIP.

Sample	w_r	ϕ
100SG	0.11	0.304
100SG8	0.09	0.183
75SG25FA	0.097	0.307
50SG50FA	0.14	0.297

The BJH technique (i.e. Barrett, Joyner, and Halenda method) [217] has also been used for similar alkali-activated binders in the literature to study the pore size distribution [69, 218, 219]. The technique is based on emptying and filling the pores of the cement as a stepwise function of partial pressure, P/P_0 , during the adsorption and desorption of nitrogen gas or water, where Kelvin's equation has been used as the numerical basis for the data analysis. **Figure 5.13** describes the cumulative volume as a function of pore size of a set of alkali-activated cements that were studied in [69], where AAP# is the type of alkali-activated cement and HCP is the Portland cement. However, it has been highlighted that the BJH method underestimates the pore size of the cement, where the degree of underestimation is bigger for the case of small pores [69].

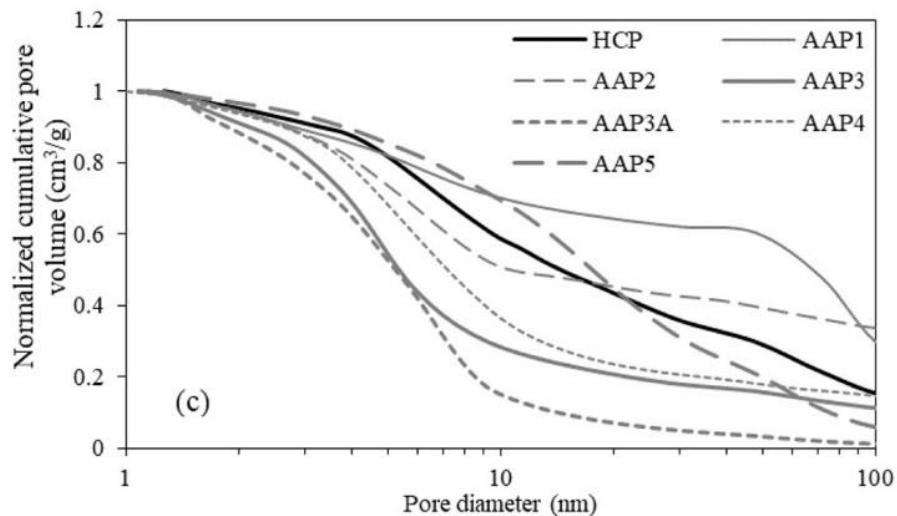


Figure 5.13. Cumulative pore volume of alkali-activated binders, denoted as AAP#, and Portland cement, noted as HCP, obtained from BJH analysis of the adsorption branch in water vapour sorption isotherms and normalized by the total pore volume. Graph obtained from [69].

The graph, shown in **Figure 5.13**, with the data of the pore structure plotted in the mesoporous range, was used to estimate the volumetric fraction of the large pore region, following the same method used with the MIP data. Only some alkali-activated binders with similar mix design of the studied binders are selected: AAP1, AAP3A and AAP5. AAP5 has the exact mix design and curing condition of 75SG25FA. Based on BJH data on normalized cumulative pore volume

the volumetric fraction of the large pore region for AAP5, estimated from the point on the curve where it starts to plateau, is 0.22, which is higher than the one determined from MIP data by 126%. However, BJH technique, only measures the pore size up to 100 nm and values measured by the MIP test beyond 100 nm could possibly be spaces between particles or air bubbles [217, 220]. Consequently, these two types of limitations could impact the quantification of volume fraction of the large pore region in cementitious materials. In order to account for data uncertainty, the moisture permeability factor of alkali-activated concrete is set as a variable to study the impact of rate of moisture transport on the overall service life as will be discussed in chapter 6. The following **Table 5.7** contains the selected alkali-activated binders, from the study in [69], along with their mix designs and estimated volumetric fractions of the large pore region from BJH analysis shown **Figure 5.13**. Note that the estimated volumetric fraction of the large pore region for each of these alkali-activated binders is used in Dual-Porosity Van Genuchten model to predict their WVSIs in the next section.

Table 5.7 Volumetric fraction of large pore region estimated through BJH analysis [69].

Sample	Notation	FA+SG (%)	Mr	Na ₂ O	w/b	Curing Method	w _f
AAP1	90FA10SG*	90%FA+10%SG	1.17	9.25	0.28	Heat cured (18h@75°C)	0.194
AAP5	75SG25FA*	25%FA+75%SG	1.5	4	0.45	Ambient cured (sealed)	0.22
AAP3A	50SG50FA*	50%FA+50%SG	1.5	8	0.3	Ambient cured (sealed)	0.182

5.5.2 Prediction of WVSIs

The obtained adsorption and desorption curves for 90FA10SG*, 75SG25FA* and 50SG50FA* binders predicted by the isotherm models, explained in section 2.10 of **Chapter 2**, are shown in **Figures 5.14-5.15**.

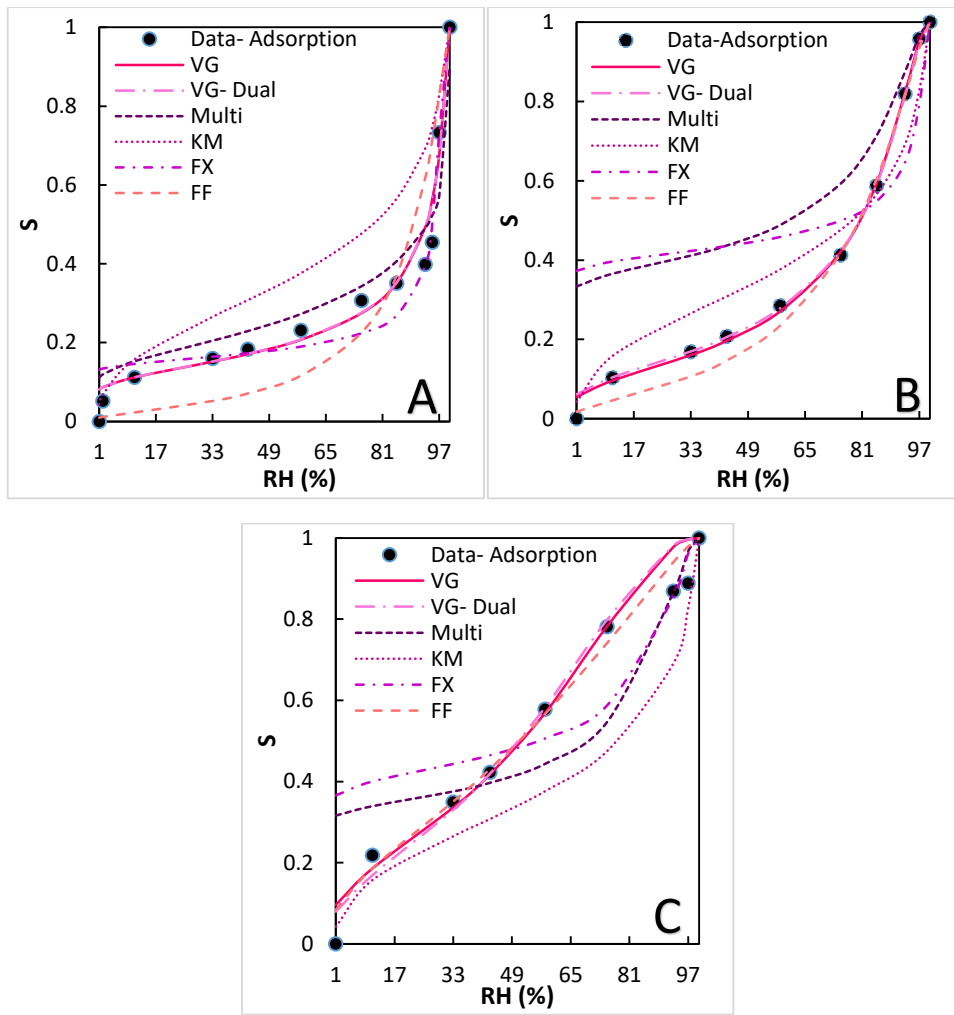
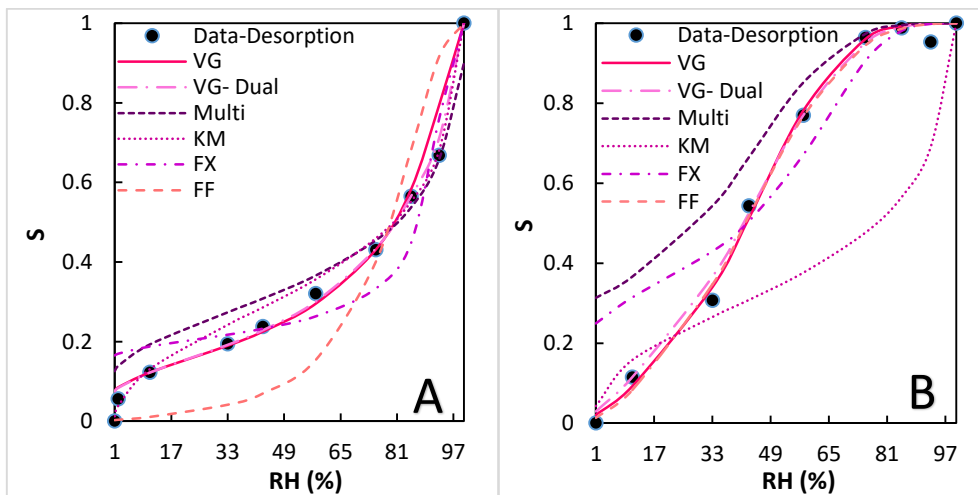


Figure 5.14 Water vapour adsorption isotherms of 90FA10SG* (A), 75SG25FA* (B), 50SG50FA* (C), with predictions from different models: VG, Van Genuchten model, VG-Dual, Dual-Porosity Van Genuchten model, Multi, multimodal model, KM, Kosugi model, FX, Fredlund and Xing's Model, and FF, Feng and Fredlund's model, according to the equations presented in chapter 2 section 2.10.



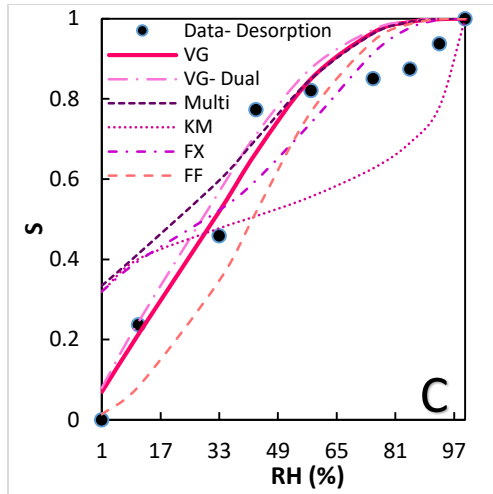


Figure 5.15 Water vapour desorption isotherms of 90FA10SG* (A), 75SG25FA* (B), 50SG50FA* (C), with predictions from different models: VG, Van Genuchten model, VG-Dual, Dual-Porosity Van Genuchten model, Multi, multimodal model, KM, Kosugi model ,FX, Fredlund and Xing’s Model, and FF, Feng and Fredlund’s model, according to the equations presented in Chapter 2 section 2.10.

NME values obtained from fitting of the desorption and sorption isotherms are shown in **Figures 5.16** and **5.17** where values close to 0 indicate better prediction of the data computed by the models.

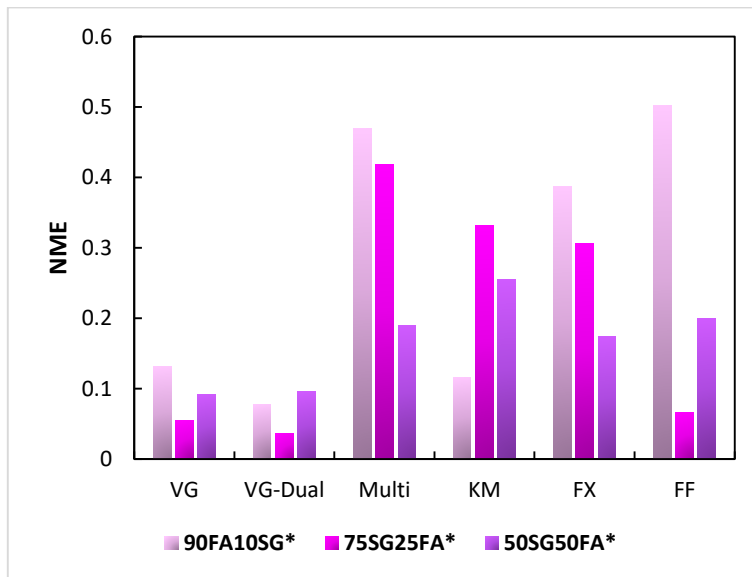


Figure 5.16 Comparison of NME for desorption isotherms. Each column in the figure stands for one type of binder according to the legend.

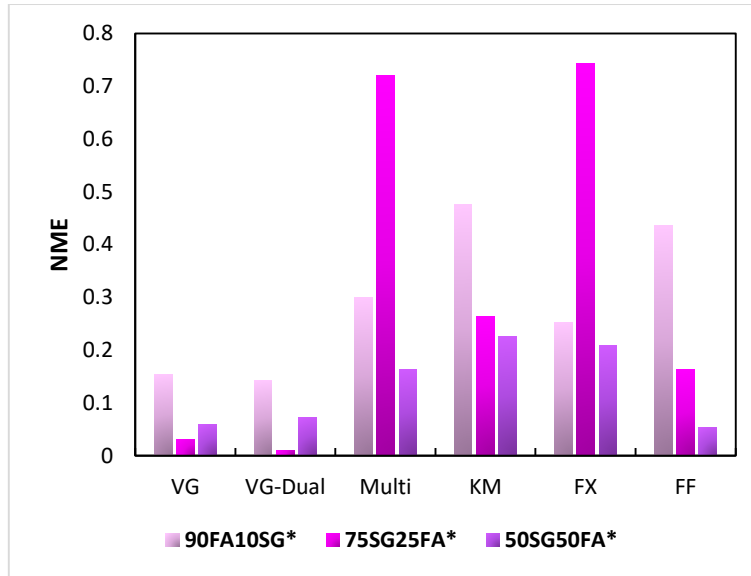


Figure 5.17 Comparison of NME for adsorption isotherms. Each column in the figure stands for one type of binder according to the legend.

For all the studied models, it can be seen in **Figures 5.17** and **5.18** that the fitting of the desorption isotherm is better than the fitting of the adsorption isotherm. The NME values obtained from VG and VG-Dual models are closest to zero which shows better fitting results than the rest of the models. In addition, the VG-Dual model, accounting for two pore sizes in 90FA10SG* and 75SG25FA* binders, fits the data better than the VG model, accounting for singular pore size in the cement. Although in the case of 50SG50FA binder, the VG model fits the data of the WVSIs better than VG-Dual model. Overall, the actual pore structure of the cements can be described by two discrete pore sizes that should be implemented in an isotherm model to obtain close approximations to the adsorption and desorption data.

5.5.3 Cyclic Water Vapour Sorption Isotherms

In normal environmental conditions, the structure is exposed to cyclic drying and wetting cycles in a relative humidity range of 50-100%. This could cause changes in the durability of the cementitious material manifested through changes in the degree of saturation exposed to the same RH. Zhang et al. [70] have explained these changes through a model that captures the scanning curves that represent the changes in the WVSIs or decrease in the hysteresis effect between the adsorption and desorption curve, as shown in **Figure 5.18**.

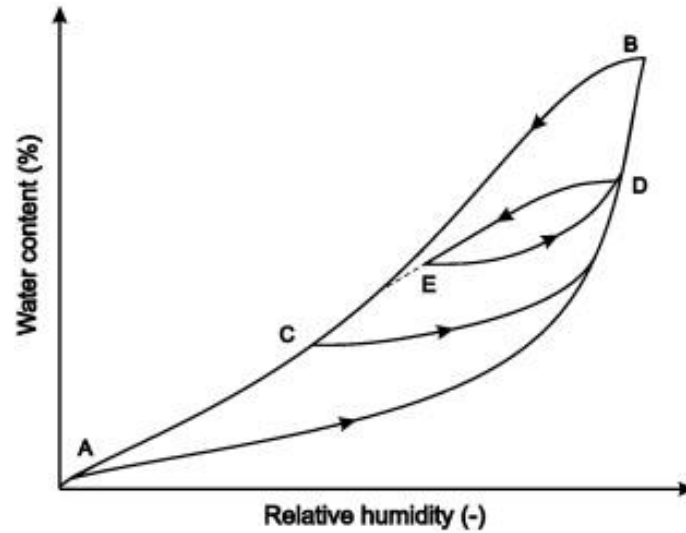


Figure 5.18 Scanning curves of water vapour sorption isotherms. AB and BA are the main adsorption and desorption curves respectively. CB and DE are the first scanning curves in wetting and drying respectively. EB is the second scanning curve in wetting. Figure from [70].

In this study, 100SG, 75SG25FA, 50SG20FA and 100SG8 binders were exposed to three cyclic wetting-drying cycles in 50-100%RH condition in a DVS instrument. The measured data is the change in mass percentage, due to the adsorption/desorption of moisture by the binders, as a function of RH as shown in **Figure 5.19**.

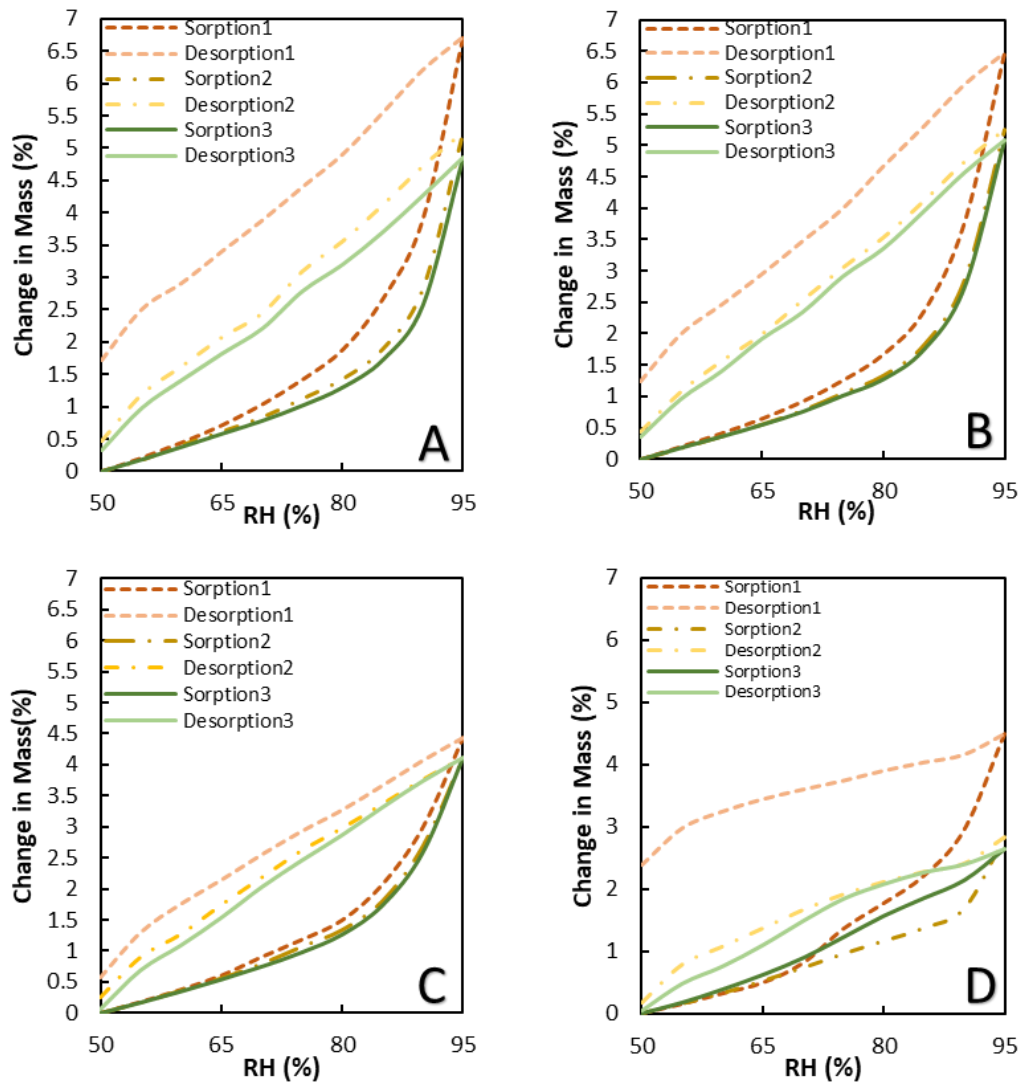


Figure 5.19 Change in mass of 100SG (A), 75SG25FA (B), 50SG50FA (C) and 100SG8 (D) during three sorption/desorption cycles.

According to the data shown in **Figure 5.19**, the change in mass loss along the first desorption curve between 95%RH and 50%RH is the highest in 75SG25FA followed by 100SG, 50SG50FA and 100SG8. The change in mass gain along the first adsorption curve between 50%RH and 95%RH is the highest in 100SG followed by 75SG25FA, 50SG50FA and 100SG8. Although the change in mass loss and gain is similar between 100SG and 75SG25FA may be due to similar w/b used in their mix designs that controls the effect porosity of the material. However, 100SG and 100SG8 have similar w/b in their mix designs but the change in mass loss and gain is greater for the case of 100SG. The difference maybe because of the extra alkali ions present in the pore solution of 100SG8 that contributes to hydration reactions that fill up the pores with reaction products during adsorption and also minimizes the loss of evaporable

water during desorption. Moreover, 50SG50FA showed the lowest change in mass loss and gain, maybe because it contained the lowest w/b in its mix design, compared to other binders, that lowers the porosity of the binder and slows down the transport of moisture during sorption and desorption.

During the second and third wetting and drying cycles the hysteresis between the adsorption and desorption curves is the lowest in 100SG8 followed by 50SG50FA, 75SG5FA and 100SG. This can serve as an evidence for the theory that cements, especially the ones containing a high content of alkali ions in the pore solution, can react with the moisture present during the wetting/ drying cycles and undergo further hydration reactions as proposed in [62]. The initiation of additional hydration reactions can densify the microstructure of the binder through filling up the pores with hydration products (i.e. hydrates). Furthermore, in comparison between 100SG,75SG25FA and 50SG50FA binders, all containing the same amount of alkali dosage in their mix designs, the extent of hysteresis between the adsorption and desorption curves was the highest for 100SG and the lowest for 50SG50FA because 100SG contained the highest w/b and 50SG50FA contained the lowest amount of w/b in their mix designs. Thus, the impact of w/b can further increase the intensity in complexity of the microstructure by inducing pores with various sizes that slow down the transport of moisture during wetting and drying cycles.

As can be seen in **Figure 5.20 A-C**, the WVSIs calculated for 100SG, 75SG25FA, and 50SG50FA show slight change in the amount of hysteresis between the main adsorption and desorption curves even after three wetting-drying cycles. This is in contrast for the case of 100SG8, as shown in **Figure 5.20 D**, where the amount of hysteresis between the two main curves decreased with the increase of cycles due to pore refinement as previously explained. Furthermore, the scanning loops of adsorption and desorption curves obtained after three cycles for 100SG,75SG25FA and 50SG50FA binders are within the first measured loop of adsorption and desorption curve as can be seen in **Figure 5.20 A-C**. This shows a certain small degree of pore refinement caused by hydration reactions when the binders react with moisture during wetting/drying cycle. The highest extent in pore refinement is shown in **Figure 5.20 D** for 100SG8 where the magnitude of hysteresis between adsorption and desorption curves decreases with the number of wetting and drying cycles.

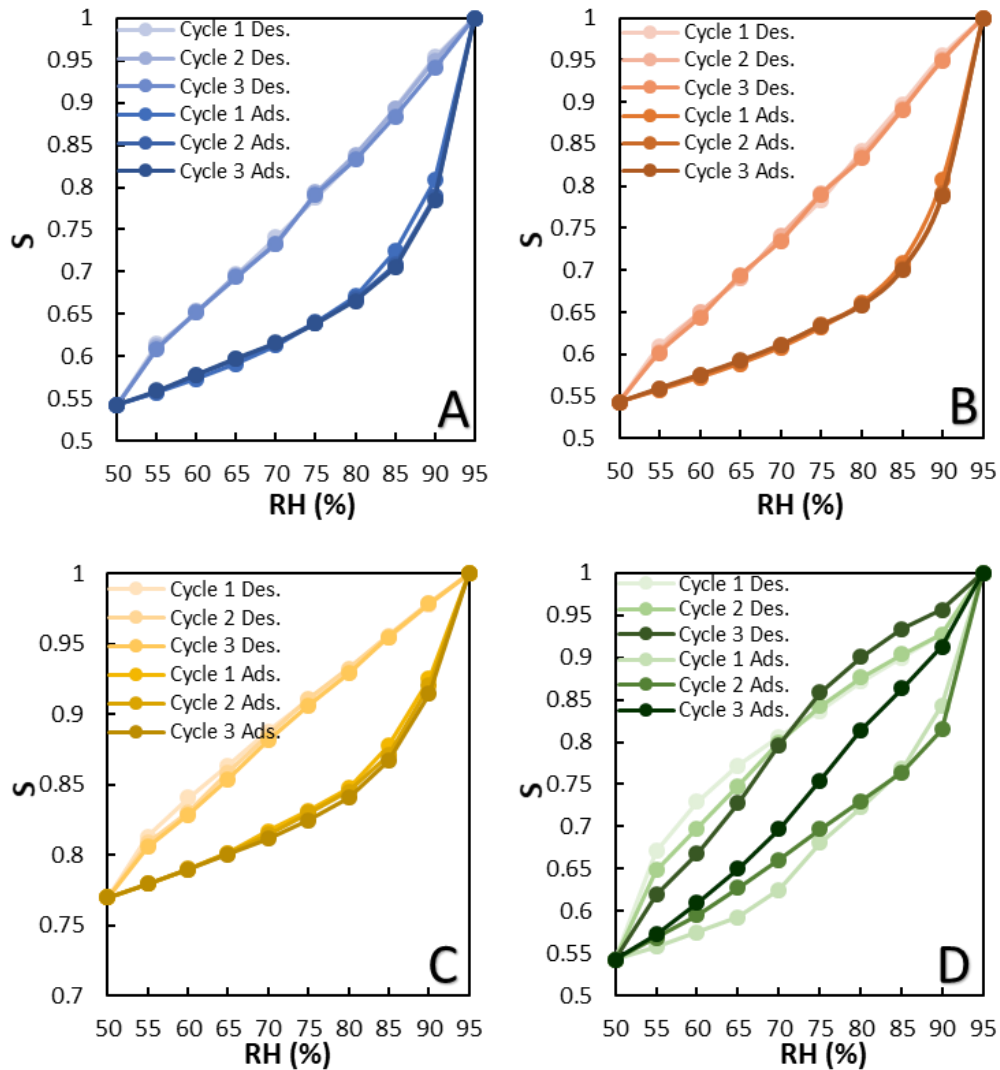


Figure 5.20 Water vapor sorption isotherms of 100SG (A), 75SG25FA (B), 50SG50FA (C) and 100SG8 during three sorption/desorption cycles.

The VG and dual porosity models are used to predict the data obtained in adsorption and desorption stages from the third cycle for 100SG, 75SG25FA, and 50SG50FA, as shown in **Figures 5.21-5.22**, and the calculated NME values are presented in **Figure 5.23**. The data from the third cycle has been chosen in this research because it describes the transport of moisture in binders which may have reached their possible extent in microstructural densification (i.e. pore refinement) due to effect of moisture in the previous wetting-drying cycles according to **Figure 5.20**. Thus, the transport of moisture in AAMs is modelled based on the assumption of negligible pore refinement during the adsorption and desorption stages.

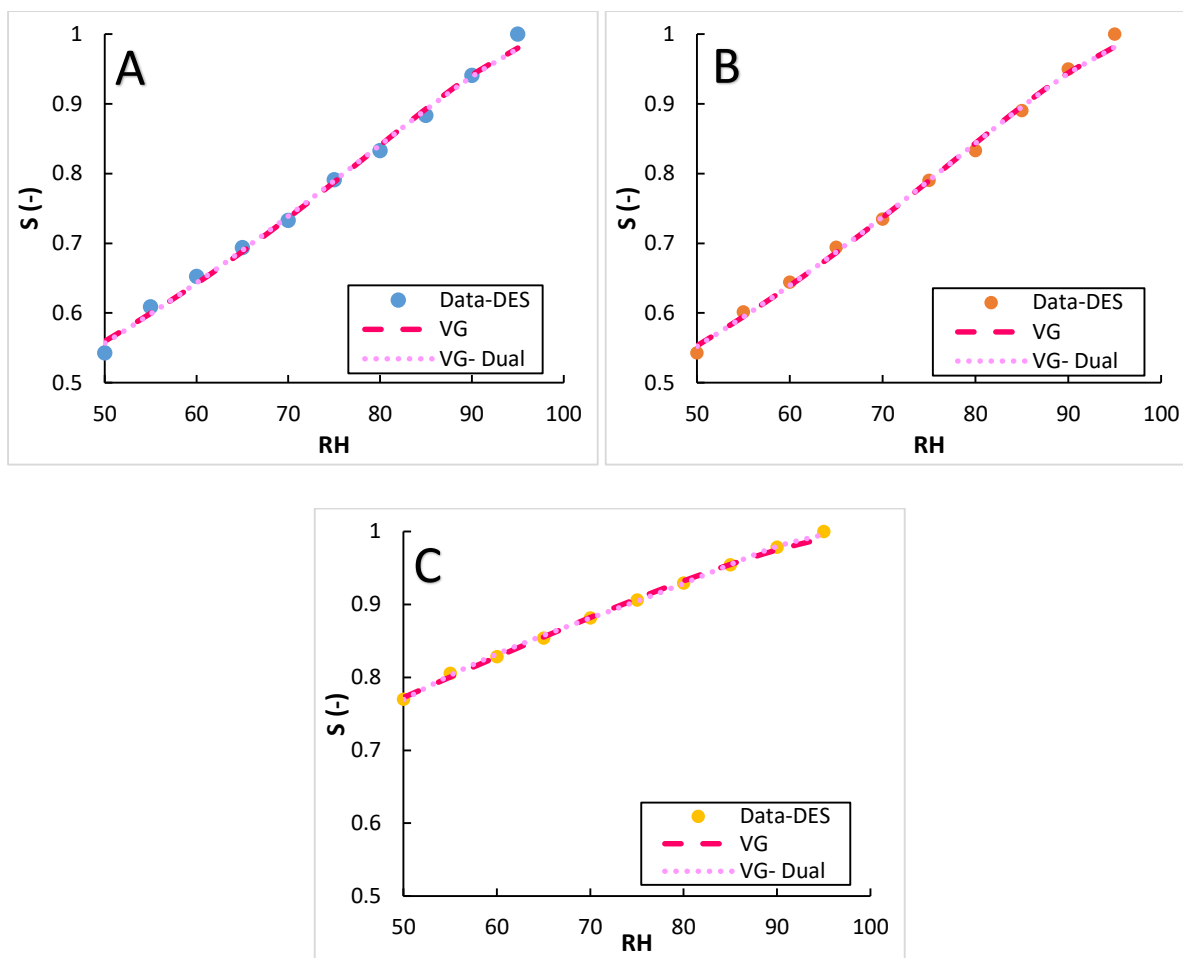


Figure 5.21 Water vapor desorption isotherms (DES) of 100SG (A), 75SG25FA (B), 50SG50FA (C), obtained from the third desorption cycle, and predictions from different isotherm models: VG, Van Genuchten model, and VG-Dual, Dual-Porosity Van Genuchten model.

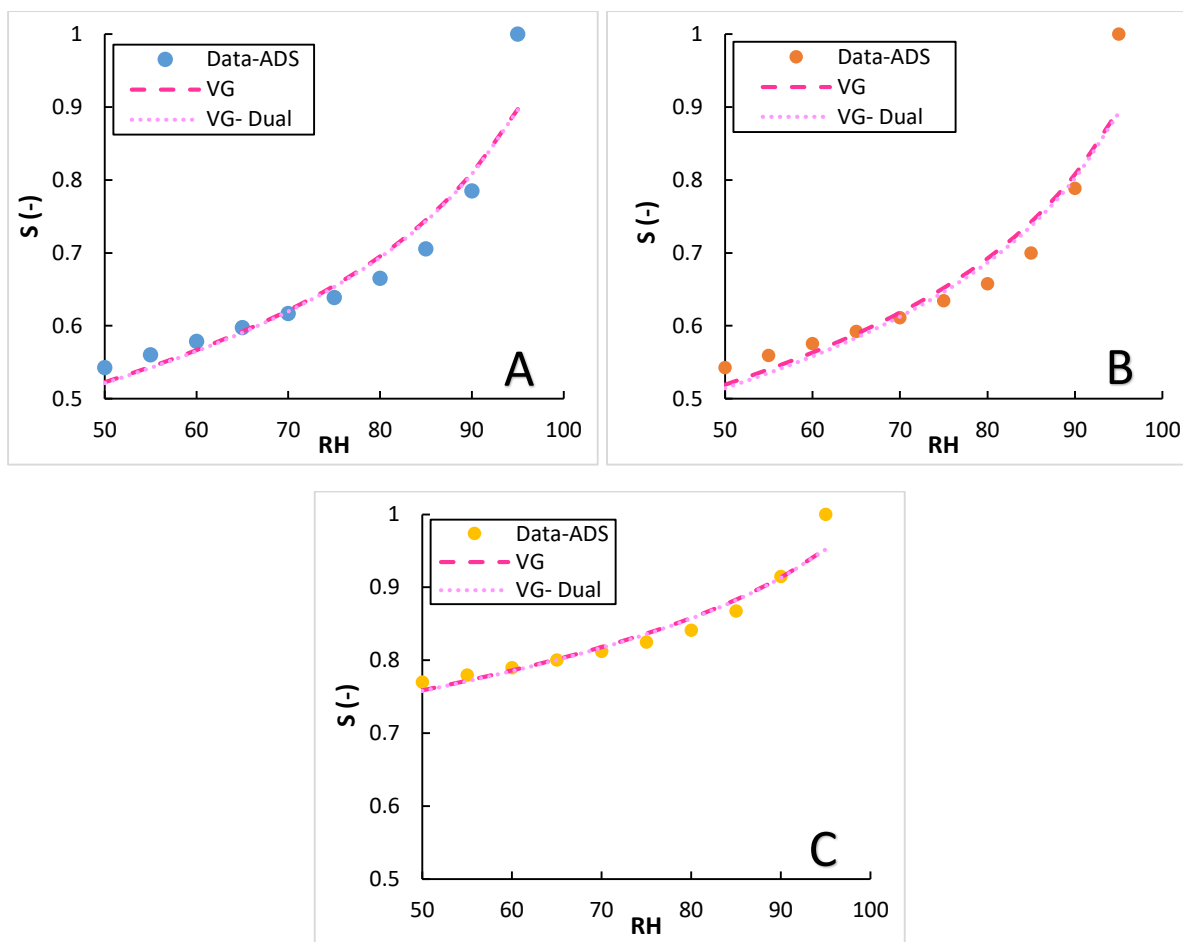
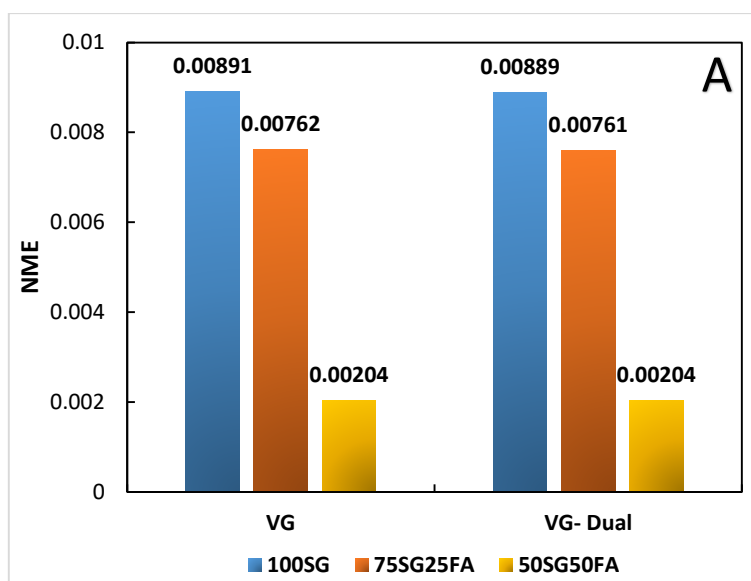


Figure 5.22 Water vapor sorption isotherms (ADS) of 100SG (A), 75SG25FA (B), 50SG50FA (C), obtained from the third adsorption cycle, and predictions from different isotherm models: VG, Van Genuchten model, and VG-Dual, Dual-Porosity Van Genuchten model.



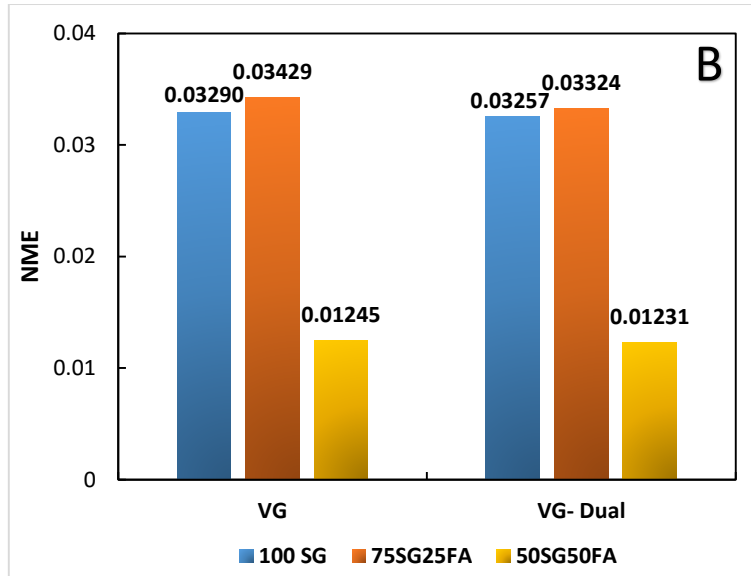


Figure 5.23 Fits for desorption isotherm (A) and adsorption isotherm (B) by VG and VG-Dual models.

Overall, the VG and VG-Dual models fit a lot better for the desorption data than adsorption data. The difference could be due to the moisture reacting with the binder during the wetting stage which may shift its transport from classical adsorption behaviour to anomalous adsorption. In the case of the drying stage, moisture seems to desorb from the surface of the hydrates through a classical desorption behaviour that is accurately predicted by the VG and VG-Dual models. Therefore, future isotherm models need to account for the effect of hydration reactions during the transport of moisture in cementitious materials. Furthermore, the fitted parameters for the VG and VG-Dual models are further discussed in the next section that describes the transport of moisture in AAMs during the wetting and drying stages.

5.5.4 Moisture Transport in Alkali-Activated Cements

The D_a values obtained are displayed in **Tables 5.8-5.11**. The measured samples were in crushed powder form so the average particle size was measured to calculate the apparent moisture diffusivity according to the method in section 3.2.1 of **Chapter 3**. The difference in the obtained average particle size between the 100SG, 75SG25FA and 50SG50FA binders is a maximum factor of 1.3-1.5 which does not have a great impact during the comparison of the measured apparent moisture diffusivities. This can be explained by calculating the moisture diffusivity using the minimum, maximum and average particle sizes, from these binders. The calculated difference in the moisture diffusivity only becomes noticeable when the factor between the average and minimum particle size is 10 and the factor between the maximum and

average particle size is 4, as demonstrated in Appendix 5 “Impact of particle size on moisture diffusivity”.

Table 5.8. Apparent moisture diffusivity during desorption process as determined from DVS instrument.

RH(%)	100SG (d_{avg} ; 59.3 μm) Da ($10^{-14}\text{m}^2/\text{s}$)			75SG25FA (d_{avg} ; 59.2 μm) Da ($10^{-14}\text{m}^2/\text{s}$)			50SG50FA (d_{avg} ; 78.9 μm) Da ($10^{-14}\text{m}^2/\text{s}$)		
	I	II	III	I	II	III	I	II	III
50	1.5	1.7	2.2	1.4	2	1.8	3	3.8	3.7
55	4.1	4.0	4.1	3	2.9	3.2	6.5	9.4	8.8
60	3.5	3.8	4.6	2.7	6.2	2.9	30.5	7.3	7.3
65	2.9	3.5	5.3	2.8	2.8	3.8	8	9	7.4
70	2.9	2.0	2.5	3.1	2.9	2.5	8.7	7.4	7.2
75	10.5	4.1	4.8	2.3	4.2	3.0	9.6	10	8.7
80	3.0	3.4	4	2.6	3.2	3.0	8.3	7.8	8.3
85	2.6	2.9	2.9	2.1	2.5	3.5	8.0	8.2	6.8
90	4.2	4.2	3.3	3.6	3.6	18.5	10	10.7	10.3
95	-	-	-	-	-	-	-	-	-

In comparison between 100SG and 75SG25FA, moisture diffusion in 100SG is faster than 75SG25FA during the drying stage, which may be because 100SG has a higher total porosity and pore size distribution than 75SG25FA according to the MIP data in **Figure 5.8**. Whereas, 50SG50FA has the highest apparent moisture diffusivity maybe because there is less chemical binding to the evaporable water because of the presence of a lower amount of C-A-S-H phase, responsible for chemical binding to the free water in the cement, compared to 100SG and 75SG25FA [108].

Table 5.9. Apparent moisture diffusivity during adsorption process as determined from DVS instrument.

RH(%)	100SG (d_{avg} ; 59.3 μm) Da ($10^{-14}\text{m}^2/\text{s}$)			75SG25FA (d_{avg} ; 59.2 μm) Da ($10^{-14}\text{m}^2/\text{s}$)			50SG50FA (d_{avg} ; 78.9 μm) Da ($10^{-14}\text{m}^2/\text{s}$)		
	I	II	III	I	II	III	I	II	III
50	-	-	-	-	-	-	-	-	-
55	10.5	41.5	17.7	12.4	12.2	23	34	31	30
60	9.6	10.1	9.3	12.0	12.3	19	21	30	29
65	8.6	6.1	10.0	12.8	12.2	9.2	21	12	21
70	17.3	12.5	7.6	7.9	8.3	10.6	9.1	20	18
75	4.6	7.2	6.5	5.7	6.0	14.4	13	12	16
80	3.6	6	6.4	4.5	5.8	10.3	8.5	19	11
85	2.0	3.2	4.0	2.5	3.3	3.9	4.8	5.7	6.2
90	1.3	1.5	1.6	1.1	1.4	2.1	3.2	3.1	3.4
95	0.65	0.69	0.7	0.7	0.7	0.7	2.2	2.2	2.3

In comparison between 100SG and 75SG25FA moisture transport in 100SG is slower than in 75SG25FA, during the adsorption stage, maybe due to the presence of more chemical binding

of the water, although both binders have similar diffusivities at high relative humidity between 85-95%. While, 50SG50FA binder still has the highest apparent moisture diffusivity.

The apparent moisture diffusivities for 100SG and 100SG8 are compared in **Tables 5.10-5.11**, where in the case of desorption and adsorption the 100SG8 binder is slower than the 100SG binder. The difference serves as an indication that the extra hydroxide and alkali ions took part in further dissolution of slag precursors and hydration reactions that fill up the pores with formed hydrates during the adsorption stage. Whereas, during the desorption stage the presence of alkali ions in the pore solution keeps it concentrated and minimizes the loss of evaporable water [206]. Consequently, moisture transport in 100SG8 is slower than in 100SG because of the extra alkali ions present in the pore solution which are obtained from the high amount of sodium hydroxide solution used in the mix design of 100SG8.

Table 5.10 Apparent moisture diffusivity during desorption process as determined from DVS experimental data.

RH(%)	100SG4%, w/b=0.5 (d_{avg} ; 59.3 μm) Da ($10^{-14}\text{m}^2/\text{s}$)			100SG8%, w/b=0.47 (d_{avg} ; 37.1 μm) Da ($10^{-14}\text{m}^2/\text{s}$)		
	I	II	III	I	II	III
50	1.5	1.7	2.2	0.7	0.8	1.3
55	4.1	4.0	4.1	2.0	2.4	2.7
60	3.5	3.8	4.6	2.4	2.4	1.3
65	2.9	3.5	5.3	3.9	2.1	1.9
70	2.9	2.0	2.5	4.8	1.9	2.2
75	10.5	4.1	4.8	8	3.7	2
80	3.0	3.4	4	3.1	3.8	4.2
85	2.6	2.9	2.9	9.5	4.6	3.1
90	4.2	4.2	3.3	2.4	2.1	4.4
95	-	-	-	-	-	-

Table 5.11 Apparent moisture diffusivity during adsorption process as determined from DVS experimental data.

RH(%)	100SG4%, w/b=0.5 (d_{avg} ;59.3 μm) Da ($10^{-14}\text{m}^2/\text{s}$)			100SG8%, w/b=0.47 (d_{avg} ;37.1 μm) Da ($10^{-14}\text{m}^2/\text{s}$)		
	I	II	III	I	II	III
50	-	-	-	-	-	-
55	10.5	41.5	17.7	4.34	4.6	4.7
60	9.6	10.1	9.3	4.11	4.5	3.5
65	8.6	6.1	10.0	4.78	3.8	4.1
70	17.3	12.5	7.6	1.17	3.1	3.1
75	4.6	7.2	6.5	0.337	2.7	3
80	3.6	6	6.4	0.547	2.9	5.3
85	2.0	3.2	4.0	0.528	2.4	27.1
90	1.3	1.5	1.6	0.219	1.0	2.3
95	0.65	0.69	0.7	0.0927	0.2	0.6

Babae et al. [69] have curved fitted the mass change adsorption kinetics to obtain the moisture diffusivity factor, from Richards' equation, and the range of values they determined is 10^{-11} - $10^{-12}\text{m}^2/\text{s}$ which is 1000 times bigger than the values obtained in **Table 5.9** for the 75SG25FA binder with similar mix design as 75SG25FA* binder studied in [69]. The reason for the large difference may be because the authors have fully dried, to 0% RH, their sample before exposure to saturation conditions, which can impact the microstructure of the binder. Another reason can be the method of apparent moisture diffusivity calculation because their values have been calculated in large RH steps, for example between 0-97% RH, and this is in contrast to the method of calculation of apparent moisture diffusivity with the data obtained from the DVS instrument as explained in section 3.2.1 of Chapter 3 where small RH steps are used instead.

However, for the apparent moisture diffusivities obtained for the current study to be in the range of values reported in **Figure 5.8**, the values for all the alkali-activated binders are recalibrated to the order of 10^{-11} - $10^{-12}\text{m}^2/\text{s}$ by multiplying them with a factor of 200. In addition, the impact of variation in apparent moisture diffusivity on transport of corrosive agents will be investigated through sensitivity analysis in Chapter 6.

5.5.5 Simulation of Moisture Transport in Alkali-activated Cements

The simulations of saturation profiles are done using the single, dual and mechanistic permeability models as explained in section 2.10 of **Chapter 2**. The predicted saturation profiles by each model, during drying and wetting cycle, is also compared with the data obtained for Portland cement from the literature.

5.5.5.1 Single-Porosity Moisture Transport Model

5.5.5.1.1 Desorption

Equations 2.34 and **2.35** are used to fit the D_a vs. S data, obtained from the DVS instrument, at the end of desorption of the alkali-activated binders according to **Figure 5.24**. It can be seen in this figure that the relationship between the model and experimental data is not in the right shape for 100SG, although it is better for 75SG25FA and 50SG50FA. The fitted permeability factors K and x_d are implemented in **Equations 2.34** and **2.35** and are applied in **Equation 2.33** to predict the saturation profile at the end of desorption for alkali-activated binders as shown in **Figure 5.25**.

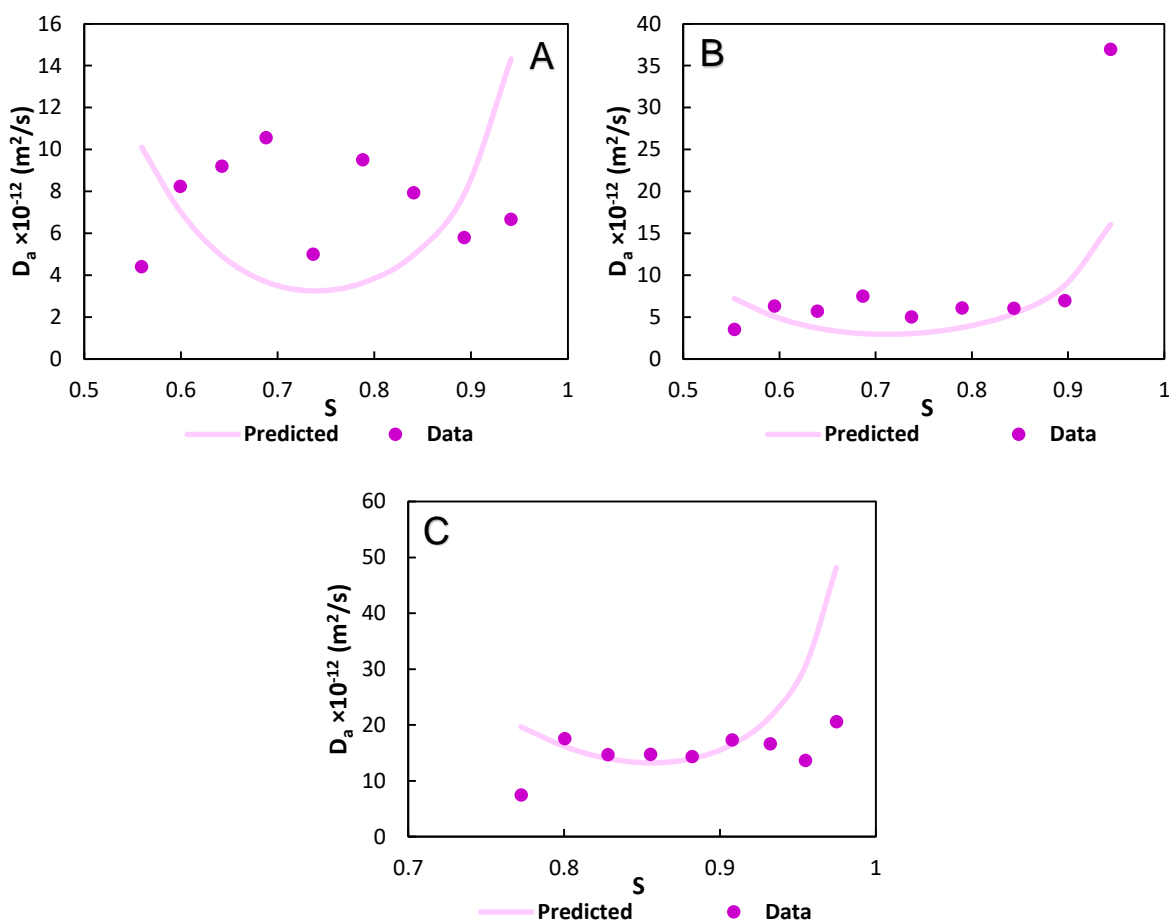


Figure 5.24 Circular symbols represent experimental D_a data obtained during the desorption of 100SG (A), 75SG25FA(B) and 50SG50FA (C) binders. The measured curves of D_a , lines, are fitted by means of implementing **Equations 2.34** and **2.35** in **Equation 2.33**.

Tables 5.12 and **5.13** present the fitted parameters of the VG isotherm model and single permeability model for moisture transport in alkali-activated cements during the desorption stage. According to **Table 5.13**, 50SG50FA has the highest permeability and lowest vapour

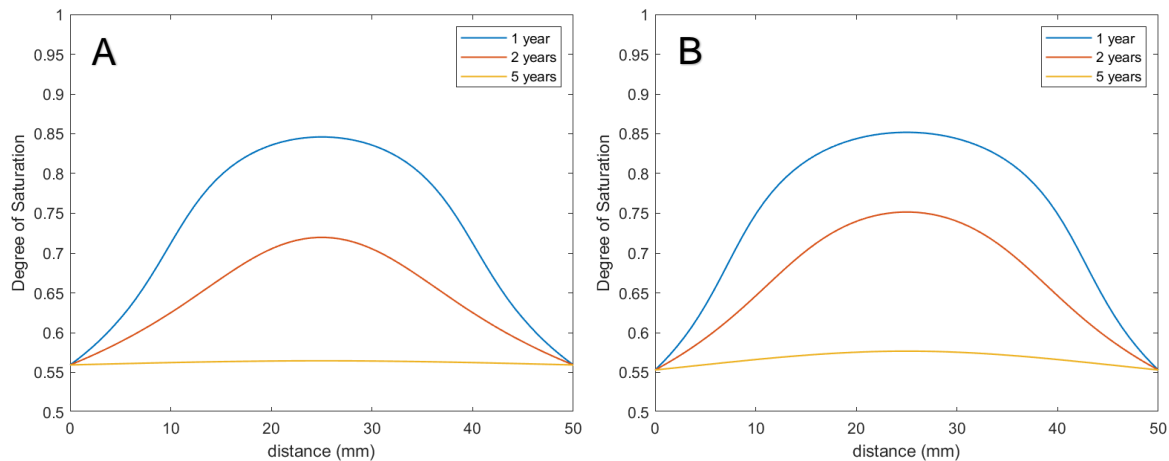
resistance factor compared to 100SG and 75SG25FA. 75SG25FA has a slightly higher vapour resistance value compared to 100SG and similar liquid permeability factor. It can be seen in **Figure 5.25** that 50SG50FA binder reaches the drying stage at 50%RH in less than two years followed by 100SG and 75SG25FA which both take 5 years to reach the drying stage at 50%RH. The alkali-activated binders have similar values in liquid permeability factor but 75SG25FA has the highest vapour resistance factor which slowed the moisture transport during the desorption process compared to 50SG50FA and 100SG. Hence, the vapour resistance factor of the cementitious materials plays an important part in slowing down and speeding up the desorption process.

Table 5.12 Parameters of the Van Genuchten model used to simulate desorption isotherms of alkali-activated binders.

Sample	a (Pa)	m	n	NME
100SG	422×10^5	0.38	1.61	0.01
75SG25FA	437×10^5	0.39	1.65	0.01
50SG50FA	774×10^5	0.30	1.44	0.003

Table 5.13. Parameters obtained from fitting D_a -S desorption data by means of implementing equations 2.34 and 2.35 in the single permeability moisture transport model.

Sample	K (m ²)	x_d	NME
100SG	1×10^{-22}	1.8	0.60
75SG25FA	1×10^{-22}	2	0.43
50SG50FA	1.2×10^{-22}	0.8	0.53



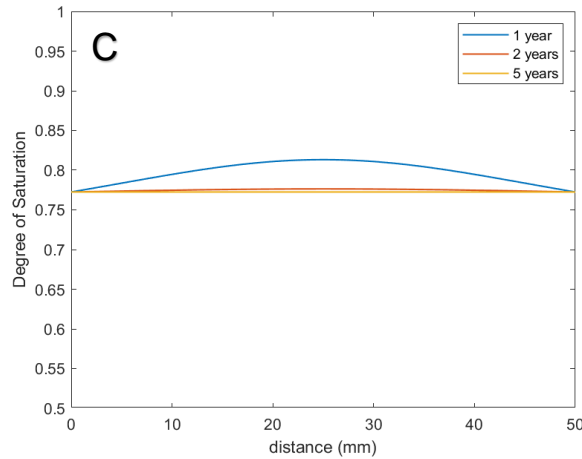
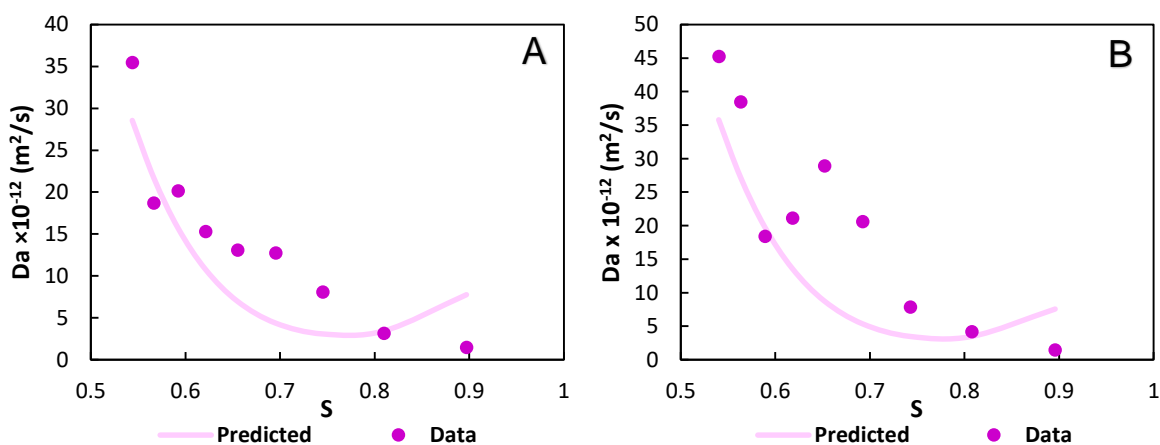


Figure 5.25. Saturation profile at the end of drying from 100% to 50% RH for 100SG(A), 75SG25FA (B), and 50SG50FA (C) binders simulated by implementing equations 2.34 and 2.35 in equation 2.33 and using the moisture transport parameters presented in **Tables 5.12-5.13**.

5.5.5.1.2 Adsorption

Equations 2.34 and **2.35** are used to fit the Da vs. S data, obtained from the DVS instrument, at the end of adsorption of the alkali-activated binders according to **Figure 5.26**. It can be seen in this figure that the model and experimental data is in good agreement for all the alkali-activated binders. The fitted permeability factors K and x_d are implemented in **Equations 2.34** and **2.35** and are applied in **Equation 2.33** to predict the saturation profile at the end of adsorption for alkali-activated binders as shown in **Figure 5.27**.



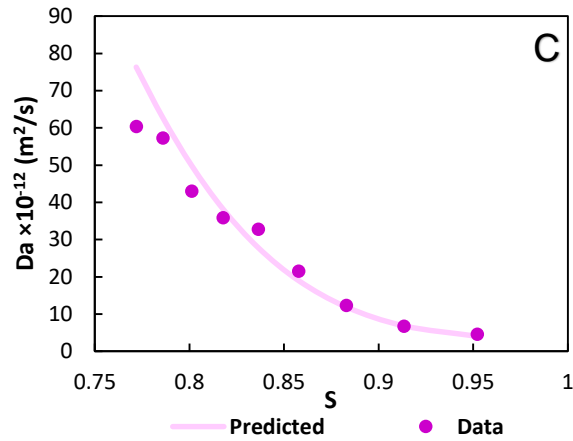


Figure 5.26 Circular symbols represent experimental Da data obtained during the adsorption of 100SG (A), 75SG25FA(B) and 50SG50FA (C) binders. The measured curves of Da, lines, are fitted by means of implementing **Equations 2.34** and **2.35** in **Equation 2.33**.

Tables 5.14 and **5.15** present the fitted parameters of the VG isotherm model and single permeability model for moisture transport in alkali-activated cements during the adsorption stage. Although the data in **Table 5.15** show that moisture transport in 75SG25FA is faster than 100SG, the estimated permeability parameters shown in **Table 5.15** are similar between these two binders. Data for moisture transport is the highest for 50SG50FA binder although the value of the fitted liquid permeability factor is slightly lower than the values obtained for 75SG25FA and 100SG. However, 50SG50FA binder has the lowest value of the vapour resistance factor, compared to the other binders, which explains the reason for 50SG50FA reaching its saturation state faster than 100SG and 75SG25FA as shown in **Figure 5.27**. Furthermore, it should be noted that the values of the vapour resistance factor for all the studied binders in both cases of adsorption and desorption are quite similar. However, values of the liquid permeability factor for all the binders are higher in the case of adsorption than in the case of desorption.

Table 5.14 Parameters of the Van Genuchten model used to simulate adsorption isotherms of alkali-activated binders.

Sample	a (Pa)	m	n	NME
100SG	98×10^5	0.22	1.28	0.03
75SG25FA	97×10^5	0.22	1.28	0.03
50SG50FA	121×10^5	0.11	1.13	0.01

Table 5.15 Parameters obtained from fitting D_a -S adsorption data by means of implementing equations 2.34 and 2.35 in the single permeability moisture transport model.

Sample	K (m^2)	x_d	NME
100SG	1×10^{-21}	1.6	0.79
75SG25FA	1×10^{-21}	1.5	0.83
50SG50FA	6×10^{-22}	0.55	0.11

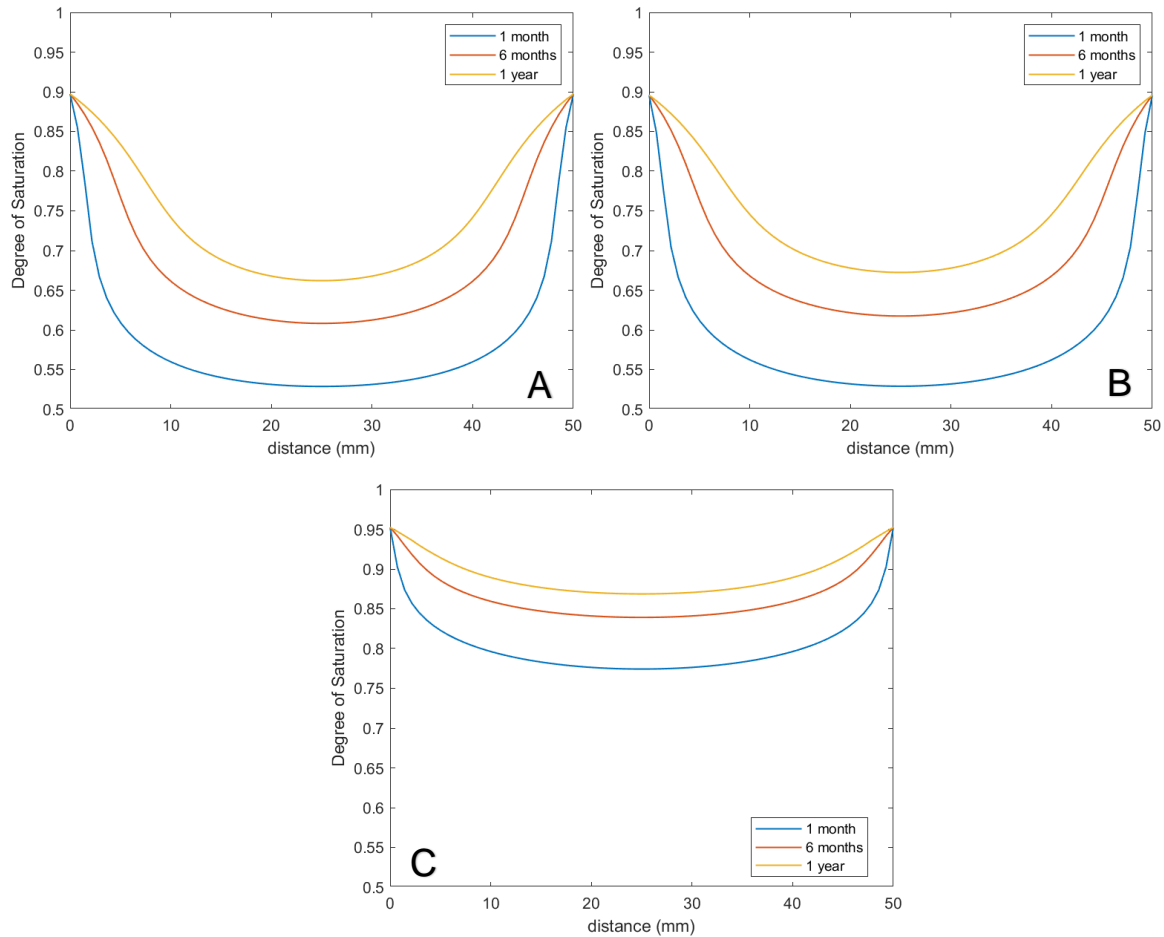


Figure 5.27 Saturation profile at the end of wetting from 50% to 100% RH for 100SG(A), 75SG25FA (B), and 50SG50FA (C) binders simulated by implementing equations 2.34 and 2.35 in the single permeability model and using the moisture transport parameters present in **Table 5.15**.

Moreover, **Figure 5.28** represents comparison of saturation profiles of AAMs during desorption after 5 years and wetting after 1 month. It can be seen in both drying and wetting conditions that 100SG and 75SG25FA have similar saturation profiles after 5 years and 1 month, respectively, because of their similar moisture transport properties (i.e. K and X_d). Whereas 50SG50FA has a higher saturation profile than 100SG and 75SG25FA binders mainly because 50SG50FA initially contained a higher content of evaporable water in the pores according to the WWSIs of the alkali-activated binders shown in **Figure 5.20**.

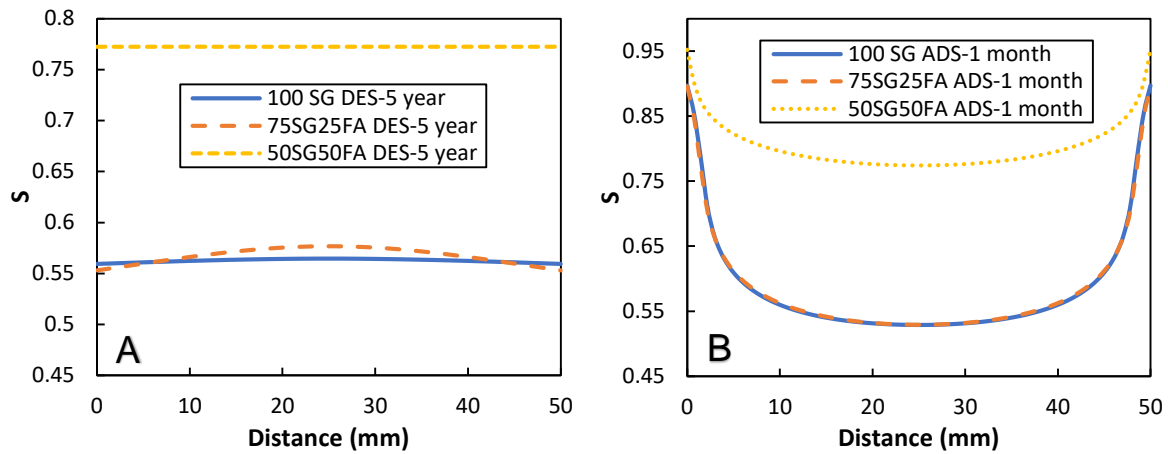


Figure 5.28 Saturation profile at the end of drying from 100% to 50% RH (A) and at the end of wetting from 50% to 100%RH (B) simulated by the single permeability model.

Figure 5.29 represents saturation profiles in 3D for 75SG25FA binder exposed to wetting condition for 1 year and drying condition for 5 years simulated by the single permeability moisture transport model.

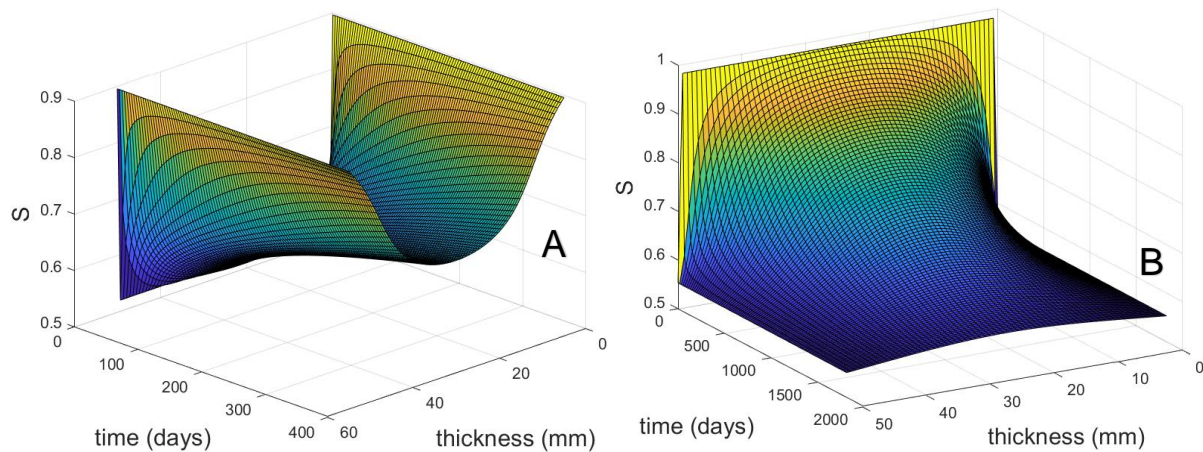


Figure 5.29 Saturation profiles in 3D for 75SG25FA binder as function of its thickness, in mm, during wetting for 1 year (A) (i.e. 365 days) and during drying for 5 years (B) (i.e. 1825 days) simulated by the single permeability moisture transport model.

5.5.5.1.3 Data Comparison with Single Permeability Model Predictions

In this section, **Figure 5.30 A+B** present the predicted moisture profiles from the single permeability model, compared with experimental data during wetting and drying conditions respectively. Note that the comparison of saturation profiles of AAMs and PC is based on the difference in the WVSIs as previously discussed in section 5.4.

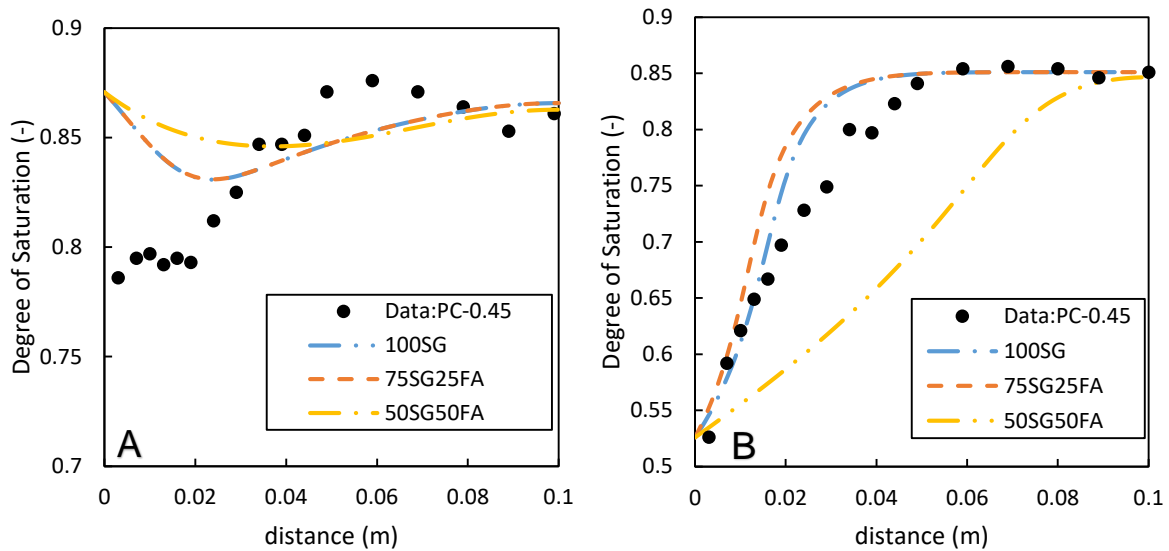


Figure 5.30 Simulated saturation profile, dashed line, for AAMs and data, circle symbol, of measured profiles for PC-0.45 at the end of wetting after 315 days, from 53.5% to 97% RH (A) and at the end of drying after 370 days from 89% to 53.5% RH (B). Data obtained from [179].

For the case of adsorption, in **Figure 5.30 A**, the single permeability model slightly overestimates the degree of saturation of 100SG and 75SG25FA which should have comparable moisture profiles as PC-0.45. The predicted saturation profile of 50SG50FA is a bit higher than the data points plotted which is initially expected according to the discussion in section 5.4. In the case of desorption in **Figure 5.30 B**, the simulated saturation profiles for 100SG and 75SG25FA are slightly higher the saturation profile of PC-0.45 although the difference should be more noticeable according to the water vapour desorption isotherms in **Figure 5.1**. The difference between the data and the predicted saturation profile for 50SG50FA is more obvious because the predicted profile for 50SG50FA is greatly lower than the data for PC-0.45 which is also expected. However, the simulated saturation profile for 50SG50FA is nearly linear throughout the thickness of the sample and without the presence of any deviation towards a plateau shape, compared to the profiles obtained for 100SG and 75SG25FA at the end of drying. The absence of this deviation indicates a missing effect of anomalous moisture transport property during the simulation of saturation profile for 50SG50FA [59, 60].

5.5.5.2 Dual-Porosity Moisture Transport Model

5.5.5.2.1 Desorption

Equations 2.44 and **2.46** are implemented in **Equation 2.42** which is used to fit the data of moisture diffusivity vs. the degree of saturation, according to **Figures 5.31-5.33**. Note that a

single value for vapour resistance factor is implemented to predict vapour diffusivity in the small and large pore regions of the cement simultaneously according to Zhang and Angst [62]. It can be seen in these Figures that the relationship between the model and experimental data is not in the right shape for 100SG and 50SG50FA, although it is better for 75SG25FA. The fitted moisture transport parameters, K_l , K_s and x_d , are implemented in **Equations 2.43** and **2.45** to simulate the saturation profiles in the large and small pore regions of alkali-activated binders at the end of drying as shown in **Figures 5.34-5.36**.

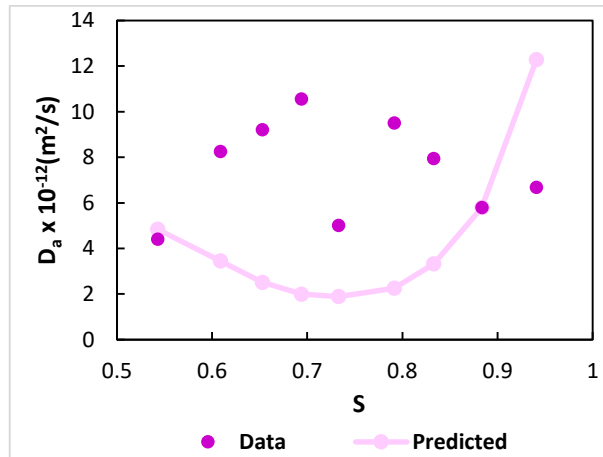


Figure 5.31 Circular symbols represent experimental D_a data obtained during the desorption of 100SG. The measured curves of D_a (lines) are obtained by means of fitting the overall moisture transport equation (Eq. 2.42) which includes moisture transport in the large pore region (Eq. 2.44) and small pore region (Eq.2.46) along with the transport contribution factor from the large pore region ($w_{f,D}$).

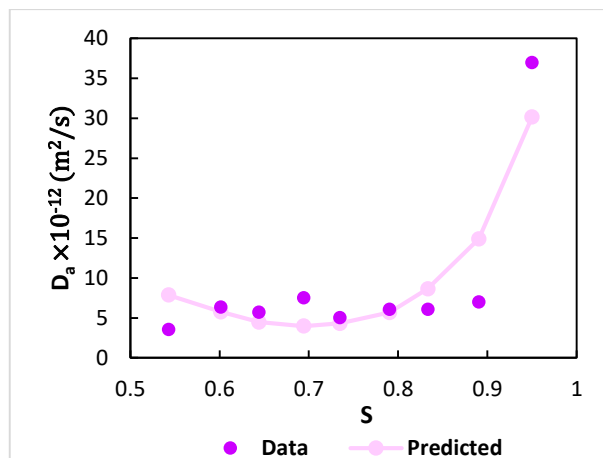


Figure 5.32 Circular symbols represent experimental D_a data calculated from the diffusivity data obtained during the desorption of 75SG25FA. The measured curves of D_a (lines) are obtained by means of fitting the overall moisture transport equation (Eq. 2.42) which includes moisture transport in the large pore region (Eq. 2.44) and small pore region (Eq.2.46) along with the transport contribution factor from the large pore region ($w_{f,D}$).

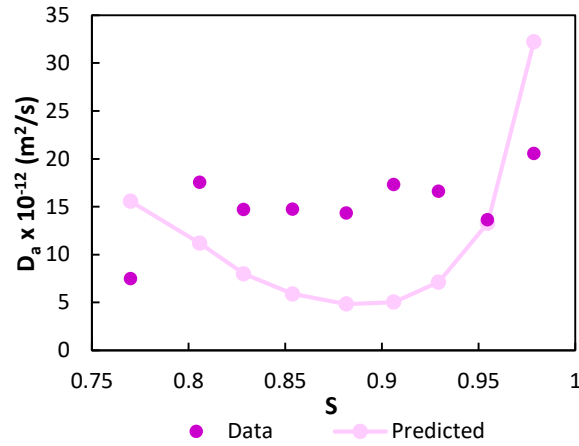


Figure 5.33 Circular symbols represent experimental D_a data calculated from the diffusivity data obtained during the desorption of 50SG50FA. The measured curves of D_a (lines) are obtained by means of fitting the overall moisture transport equation (Eq. 2.42) which includes moisture transport in the large pore region (Eq. 2.44) and small pore region (Eq.2.46) along with the transport contribution factor from the large pore region ($w_{f,D}$).

Tables 5.16 and 5.17 present the fitted parameters of the VG- Dual isotherm model and dual permeability model for moisture transport in alkali-activated cements during the desorption stage. Tables 5.17 present the moisture permeability factors for the transport of evaporable water in the large and small pore regions respectively. Similar to the single permeability results 50SG50FA has the lowest vapour resistance factor during the transport of moisture in the desorption stage. However, 50SG50FA has the lowest liquid permeability factor in the small pore region. 100SG and 75SG25FA have similar values for vapour resistance factor although 75SG25FA has higher liquid permeability factor for both pore regions compared to 100SG.

Table 5.16 Parameters of the VG-Dual model used to simulate desorption isotherms for alkali-activated binders.

Sample	w_f	a_l (Pa)	a_s (Pa)	m	n	NME
100SG	0.11	160×10^5	524×10^5	0.41	1.69	0.01
75SG25FA	0.097	215×10^5	492×10^5	0.41	1.68	0.01
50SG50FA	0.14	238×10^5	1621×10^5	0.59	2.43	0.002

Table 5.17 Parameters obtained from fitting D_a -S desorption data by means of implementing equation 2.44 for moisture transport in large pore region.

Sample	K_l (m ²)	K_s (m ²)	x_d	$w_{f,D}$	NME
100SG	2.00×10^{-22}	1.00×10^{-23}	1.6	0.45	0.56
75SG25FA	8.00×10^{-22}	3.00×10^{-23}	1.6	0.1	0.44
50SG50FA	5.00×10^{-22}	1.00×10^{-24}	0.6	0.1	0.56

Figures 5.34-5.36 present the moisture profiles in the small and large pore regions of the alkali-activated binders. The simulated saturation profiles in the large and small pore regions for 100SG and 75SG25FA in Figures 5.34 and 5.35 show that the desorption in 75SG25FA is faster than in 100SG. The reason could be because the fitted values for K_l and K_s for 75SG25FA are higher than the values obtained for 100SG which may cause the difference in transport during desorption.

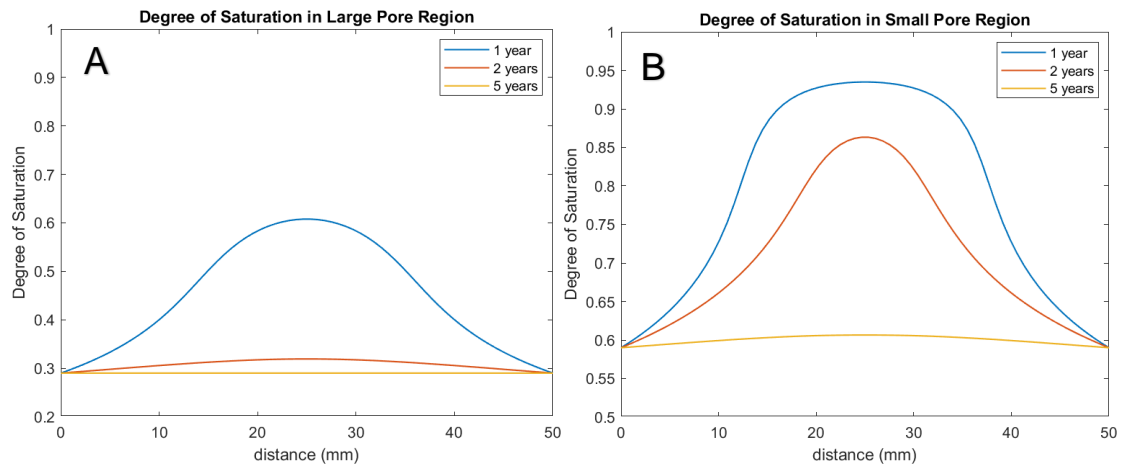


Figure 5.34 Saturation profile at the end of drying from 100% to 50% RH for 100SG in the large pore region (A) and in the small pore region (B). Profiles are simulated by implementing equations 2.43 and 2.45 in the dual permeability model and using the moisture transport parameters present in Tables 5.16-5.17.

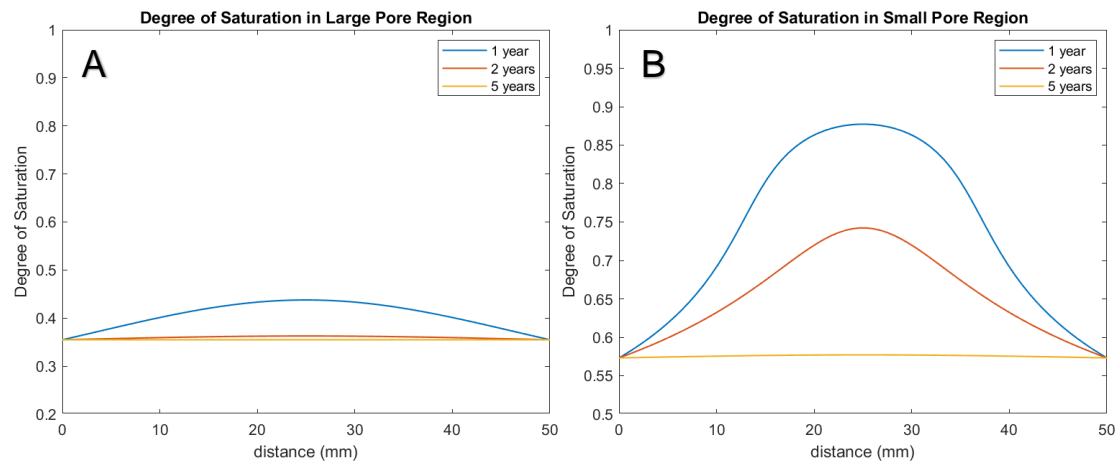


Figure 5.35 Saturation profile at the end of drying from 100% to 50% RH for 75SG25FA in the large pore region (A) and in the small pore region (B). Profiles are simulated by implementing equations 2.43 and 2.45 in the dual permeability model and using the moisture transport parameters present in Tables 5.16-5.17.

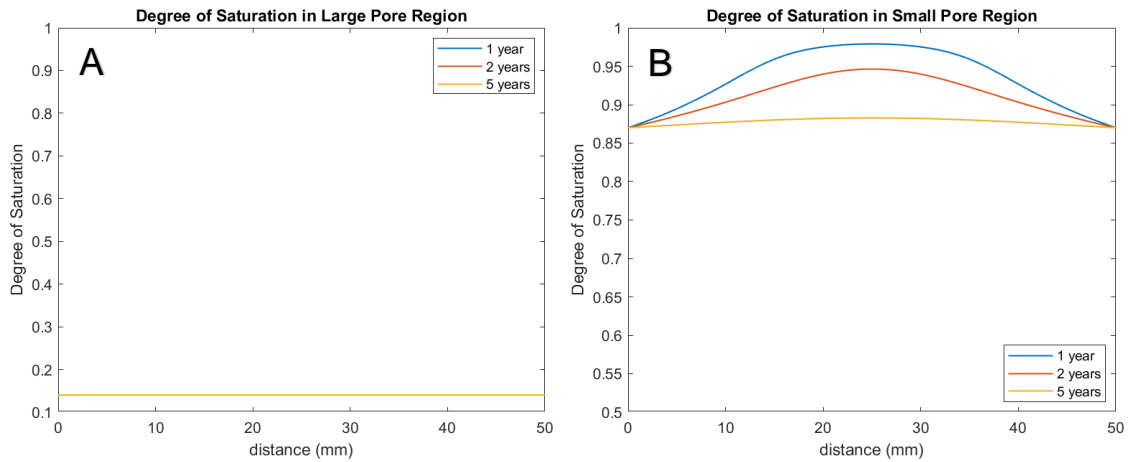


Figure 5.36 Saturation profile at the end of drying from 100% to 50% RH for 50SG50FA in the large pore region (A) and in the small pore region (B). Profiles are simulated by implementing equations 2.43 and 2.45 in the dual permeability model and using the moisture transport parameters present in **Tables 5.16-5.17**.

5.5.5.2.2 Adsorption

Equations 2.44 and **2.46** are implemented in **Equation 2.42** which is used to fit the data of moisture diffusivity vs. the degree of saturation, according to **Figures 5.37-5.39**. It can be seen in these figures that the model and experimental data is in good agreement for moisture transport in alkali-activated binders exposed to wetting cycle. Note that a single value for vapour resistance factor is implemented to predict the moisture diffusivity data of the cement according to Zhang and Angst [62]. The fitted moisture transport parameters, K_l , K_s and x_d , are implemented in **Equations 2.43** and **2.45** to simulate the saturation profiles in the large and small pore regions of alkali-activated binders at the end of adsorption stage.

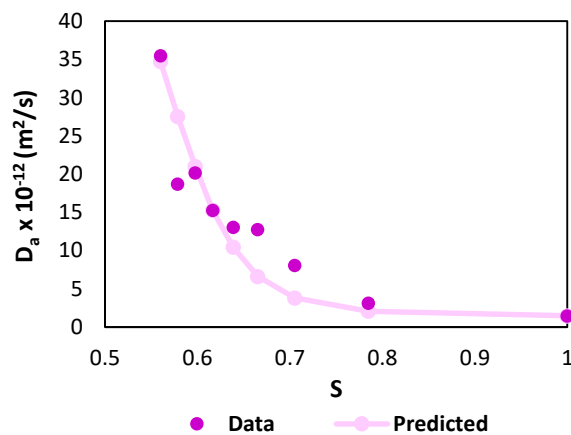


Figure 5.37 Circular symbols represent experimental D_a data obtained during the adsorption of 100SG. The measured curves of D_a (lines) are obtained by means of fitting the overall moisture transport equation (Eq.

2.42) which includes moisture transport in the large pore region (Eq. 2.44) and small pore region (Eq.2.46) along with the transport contribution factor from the large pore region ($w_{f,D}$).

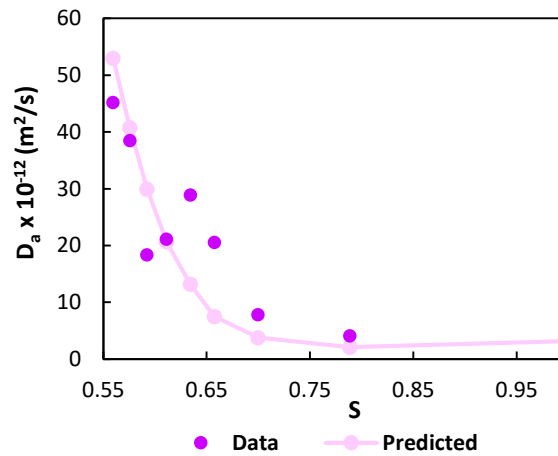


Figure 5.38 Circular symbols represent experimental D_a data obtained during the adsorption of 75SG25FA. The measured curves of D_a (lines) are obtained by means of fitting the overall moisture transport equation (Eq. 2.42) which includes moisture transport in the large pore region (Eq. 2.44) and small pore region (Eq.2.46) along with the transport contribution factor from the large pore region ($w_{f,D}$).

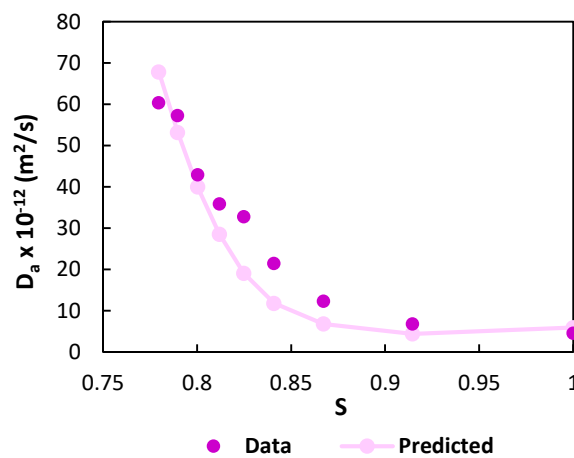


Figure 5.39 Circular symbols represent experimental D_a data obtained during the adsorption of 50SG50FA. The measured curves of D_a (lines) are obtained by means of fitting the overall moisture transport equation (Eq. 2.42) which includes moisture transport in the large pore region (Eq. 2.44) and small pore region (Eq. 2.46) along with the transport contribution factor from the large pore region ($w_{f,D}$).

Tables 5.18 and 5.19 present the fitted parameters of the VG- Dual isotherm model and dual permeability model for moisture transport in alkali-activated cements during the adsorption stage. Table 5.19 show that the moisture transport in 75SF25FA is faster than in 100SG which is in agreement with the obtained moisture diffusivity values in Table 5.9. The fitted liquid

permeability for moisture transport in the large pore region of 50SG50FA has the highest value compared to 100SG and 75SG25FA. However, the liquid permeability values of moisture transport in the small pore region for 50SG50FA is similar to 75SG25FA even though the obtained apparent diffusivity values shown in **Table 5.9** show that moisture transport during adsorption is faster in 50SG50FA than in 75SG25FA.

Table 5.18 Parameters of the VG-Dual model used to simulate adsorption isotherms for alkali-activated binders.

Sample	w	a_l (Pa)	a_s (Pa)	m	n	NME
100SG	0.11	88×10^5	98×10^5	0.22	1.29	0.03
75SG25FA	0.097	67×10^5	98×10^5	0.22	1.32	0.04
50SG50FA	0.14	111×10^5	121×10^5	0.11	1.13	0.01

Table 5.19 Parameters obtained from fitting D_a -S adsorption data by means of implementing equation 2.44 for moisture transport in large pore region.

Sample	K_l (m ²)	K_s (m ²)	x_d	$w_{f,D}$	NME
100SG	1×10^{-22}	1×10^{-23}	1.4	0.47	0.23
75SG25FA	5×10^{-22}	2×10^{-22}	1.3	0.1	0.48
50SG50FA	1×10^{-21}	2×10^{-22}	0.8	0.1	0.27

Figures 5.40-5.42 present the simulated saturation profiles in the small and large pore regions in alkali-activated binders where it is shown that 50SG50FA reaches saturation the fastest followed by 75SG25FA and 100SG. In the case of moisture transport in the small and large pore regions, 75SG25FA has a similar value of vapour resistance factor but higher liquid permeability factor compared to 100SG which explains the reason for 75SG25FA reaching saturation faster than 100SG according to **Figures 5.40 B** and **5.41 B**. Hence, the liquid permeability factor of the cementitious materials plays a more important role than the vapour resistance factor in slowing down and speeding up the adsorption process of cementitious materials.

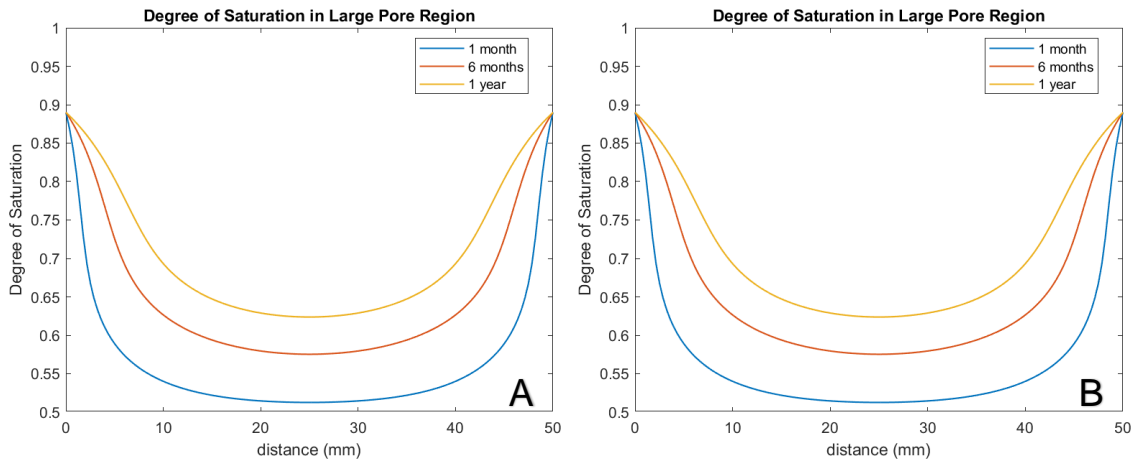


Figure 5.40 Saturation profile at the end of wetting from 50% to 100% RH for 100SG in the large pore region (A) and in the small pore region (B). Profiles are simulated by implementing equations 2.43 and 2.45 in the dual permeability model and using the moisture transport parameters present in table 5.18-5.19.

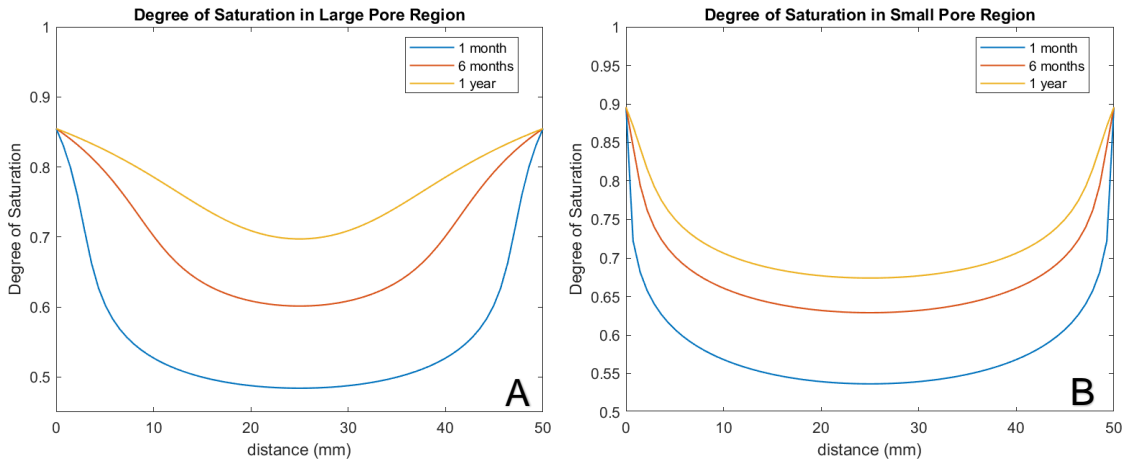


Figure 5.41 Saturation profile at the end of wetting from 50% to 100% RH for 75SG25FA in the large pore region (A) and in the small pore region (B). Profiles are simulated by implementing equations 2.43 and 2.45 in the dual permeability model and using the moisture transport parameters present in table 5.18-5.19.

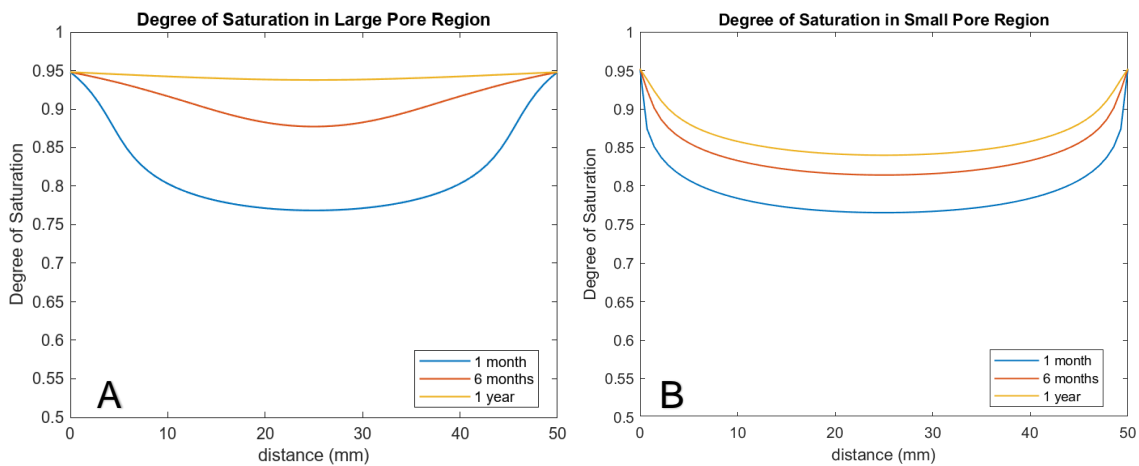


Figure 5.42 Saturation profile at the end of wetting from 50% to 100% RH for 50SG50FA in the large pore region (A) and in the small pore region (B). Profiles are simulated by implementing equations 2.43 and 2.45 in the dual permeability model and using the moisture transport parameters present in table 5.18-5.19.

Figures 5.43 and 5.44 present saturation profiles in 3D in the large and small pore regions for 100SG binder exposed to wetting conditions for 1 year and drying conditions for 5 years, simulated by the dual permeability moisture transport model.

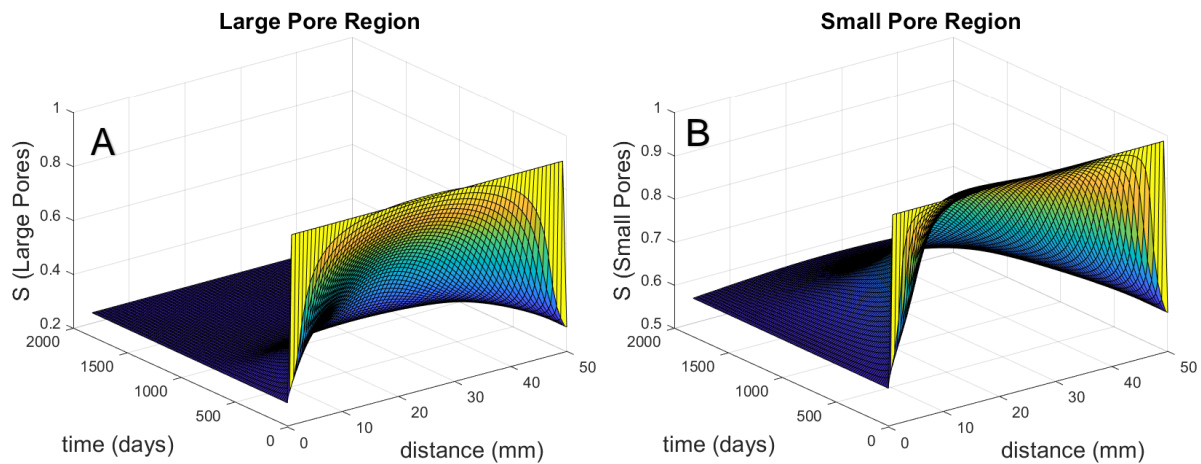


Figure 5.43 100SG Saturation profiles in 3D for 100SG binder as a function of its thickness, in mm, during drying for 5 years (i.e. 1825 days) in the large and small pore regions simulated by implementing **Equations 2.43 and 2.45** in the dual permeability model.

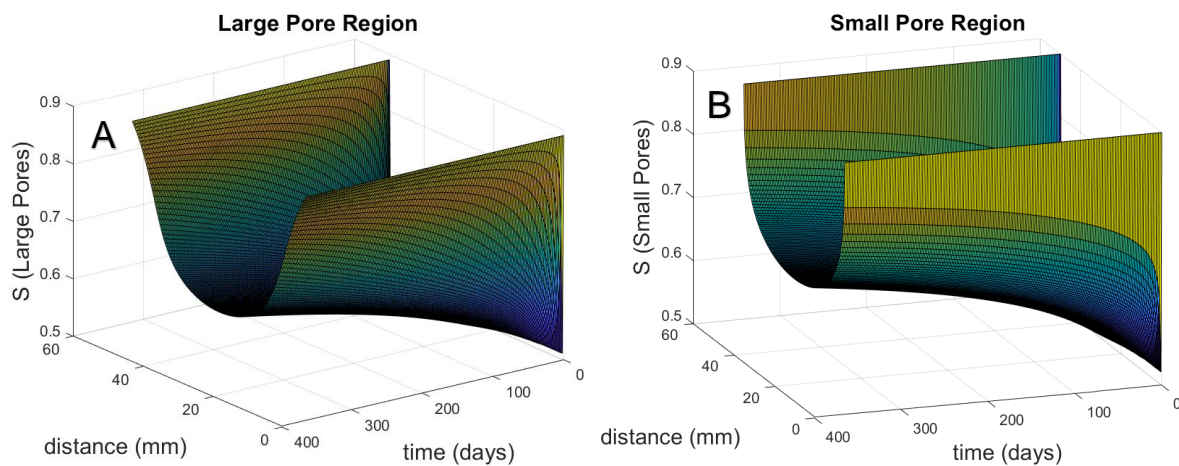


Figure 5.44 100SG Saturation profiles in 3D for 100SG binder as a function of its thickness, in mm, during wetting for 1 years (i.e. 365 days) in the large (A) and small pore regions (B) simulated by implementing **Equations 2.43 and 2.45** in the dual permeability model.

Moreover, **Figure 5.45** represents comparison of saturation profiles of AAMs during desorption after 5 years and wetting after 1 month estimated by implementing equation 2.39.b to include the degree of saturation in the large and small pore regions of the cement.

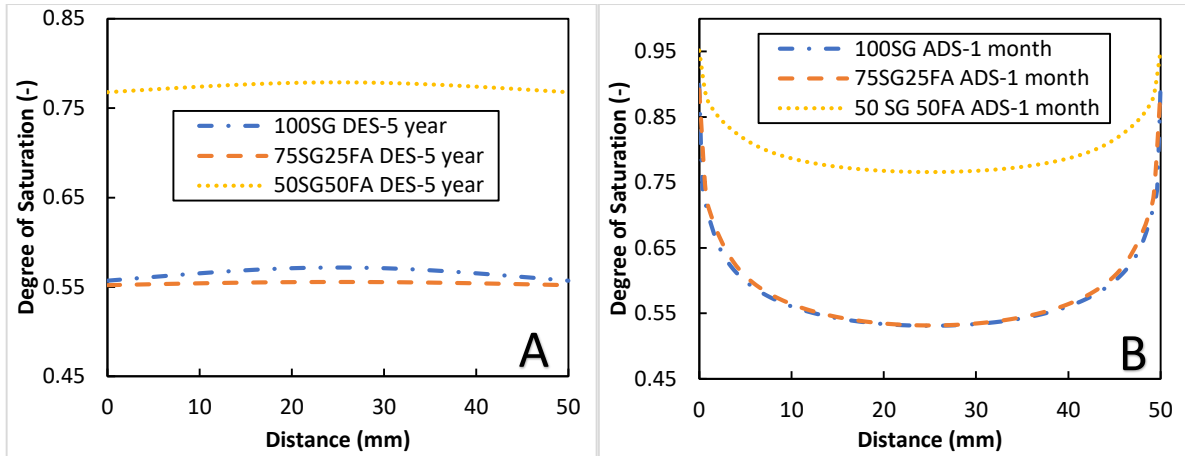


Figure 5.45 Saturation profile at the end of drying from 100% to 50% RH (A) and at the end of wetting from 50% to 100% RH (B) for 100SG, 75SG25FA and 50SG50FA of the alkali-activated binder simulated by the dual permeability model.

In the case of wetting, the moisture transport simulated by the dual permeability model is slower than the transport simulated by the single permeability model in comparison between the saturation profiles shown in **Figures 5.45 B** and **5.28 B**. Whereas in the case of drying, the simulated moisture profiles by the single and dual permeability models are nearly the same for 100SG and 50SG50FA. However, in the case of 75SG25FA binder the moisture transport predicted by the single permeability model is slightly slower than the transport predicted by the dual permeability model.

5.5.5.2.3 Data Comparison with Dual Permeability Model Predictions

In this section, **Figure 5.46** present the predicted moisture profiles from the dual permeability model, compared with experimental data during wetting and drying conditions respectively. Note that the comparison of saturation profiles of AAMs and PC is based on the difference in the WVSI as previously discussed in section 5.4.

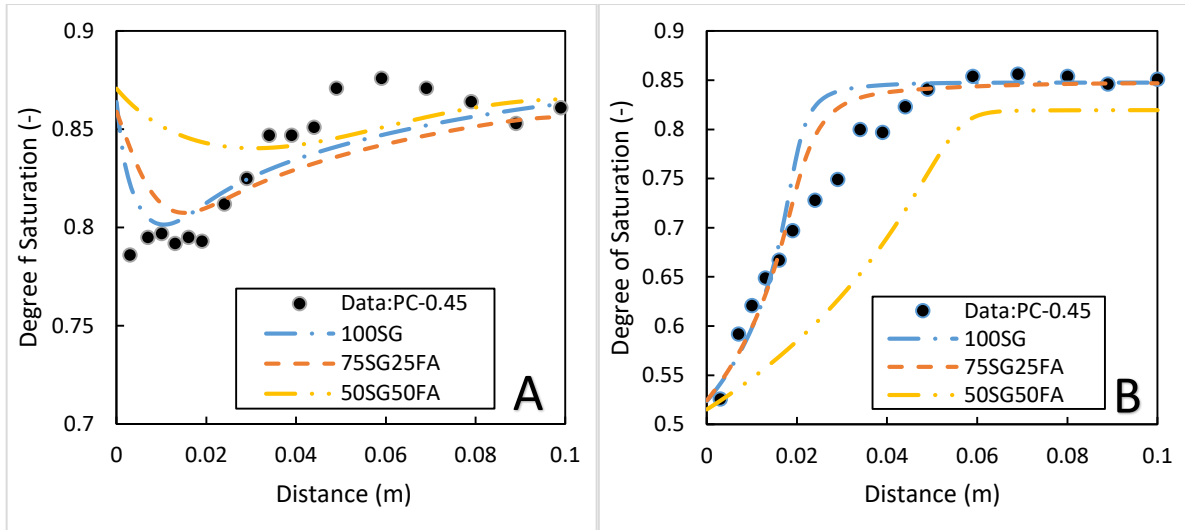


Figure 5.46. Simulated saturation profile, dashed line, for AAMs 100SG, 75SG25FA, 50SG50FA and data, circle symbol, of measured profiles for PC-0.45 at the end of wetting after 315 days, from 53.5% to 97% RH (A) and at the end of drying after 370 days from 89% to 53.5% RH (B). Data obtained from [179].

In the case of wetting, the dual permeability model performed better than the single permeability model because the simulated saturation profiles for 100SG and 75SG25FA binders are closer to the data set than the profiles obtained by the single permeability model, according to **Figure 5.30 A**. In the case of drying the single permeability model performed better than the dual permeability model because the simulated saturation profiles by the single permeability model for 100SG and 75SG25FA binders, shown in **Figure 5.30 B**, are more above the data set of PC-0.45. This should be the case due to the effect of high content of alkali ions present in pore solution on minimizing the evaporation of free water during the stage of desorption [206]. Finally, in comparison of the shape of the saturation profile at the end of drying for 50SG50FA simulated by the single and dual permeability models, the profile obtained by the dual permeability model includes the knee effect, the point of deviation where the curve goes into plateau shape, which represents the anomaly property of moisture transport in cementitious materials [60].

5.5.5.3 Mechanistic Permeability Model

The full WVSI, 0-100%RH, of 50SG50FA* is used to obtain parameters needed for the calculation of $K_{l,rel}(S)$ and is based on the assumption that 50SG50FA and 50SG50FA* have a similar porous microstructure. Some of these parameters are the pore maxima pC_i which are the inflection points within the moisture storage curves indicated by vertical dashed lines in **Figures 5.47** and **5.48**. The other parameters are the slopes, s_i , which are the slopes of straight

lines drawn tangent to the moisture storage curves at the inflections points shown in **Figures 5.47** and **5.48**. The parameter ΔS_i represents the difference between the plateau levels in the moisture storage curves such that the sum of ΔS_i (where “i” is the number of plateau levels) must equal to 1 according to **Equation 5.3**.

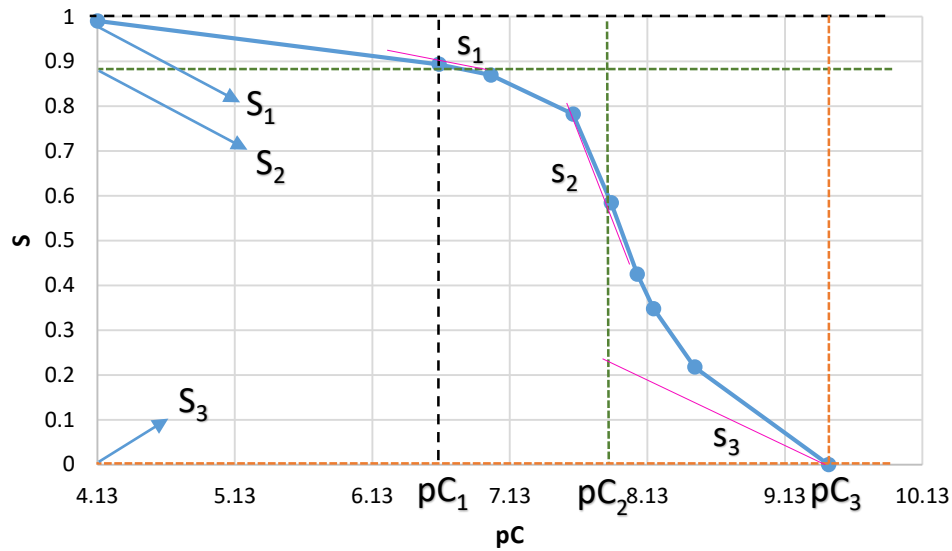


Figure 5.47 The moisture storage curves obtained from the adsorption isotherm of 50SG50FA* that is replotted in terms of the degree of saturation as a function of pC which is $\log(P_c/P_{ref})$ with $P_{ref} = 1 \text{ Pa}$ [88]. The parameters shown in this graph are the pore maxima pC_i which are the inflection points within the moisture storage curves indicated by vertical dashed lines. The other parameters are the slopes, s_i , of the moisture storage curve at the inflection points and are equal to the slope of straight lines drawn tangent to the curve at those points. The parameter ΔS_i represents the difference between the plateau levels, which are indicated by horizontal dashed line, in the moisture storage curves. Note that the subscript “i” is a number ranging from 1 to 3.

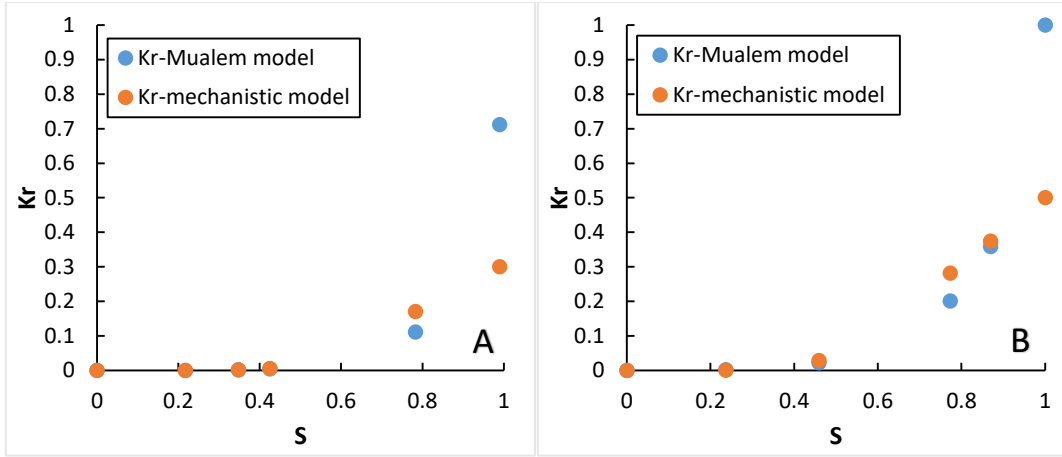


Figure 5.49 Relative permeability curves obtained from the mechanistic relative permeability function and the van Genuchten-Mualem model in the case of adsorption (A) and desorption (B) for 50SG50FA*.

In addition, the values obtained for n_{cap} and n_{sp} shown in **Table 5.21** for both cases of adsorption and desorption are similar to the values found in [88] which are 0.38 and 2.8 for n_{cap} and n_{sp} , respectively.

Table 5.21 The scaling factors n_{sp} and n_{cap} determined by fitting the mechanistic relative permeability curve with the curve generated by the van Genuchten-Mualem model. The normalized mean error (NME) is used to assess the accuracy of the curve fitting results in Figure 5.49.

	n_{sp}	n_{cap}	NME
Adsorption	4	0.3	0.45
Desorption	3	0.5	0.37

After obtaining the scaling factors for the mechanistic relative permeability function, the saturation profiles for 50SG50FA at end of drying and wetting are simulated by the mechanistic permeability model and are shown in **Figure 5.50**. In addition, the values for the effective liquid permeability factors for moisture transport during desorption and adsorption are $1.2 \times 10^{-22} \text{ m}^2$ and $6 \times 10^{-22} \text{ m}^2$, respectively, which are the values initially obtained for the single permeability model. The Van Genuchten model, **Equation 2.24**, is also applied in the mechanistic permeability model to predict the WVSIs of 50SG50FA. The parameters for the VG model are shown in **Table 5.22** with the accuracy of curve fitting the model with data of WVSIs obtained for 50SG50FA from the DVS.

Table 5.22 Parameters of the Van Genuchten model used to simulate WVSIs of 50SG50FA and implemented in the mechanistic permeability model.

	a (Pa)	m	n	NME
Adsorption	121×10^5	0.11	1.13	0.01
Desorption	774×10^5	0.31	1.44	0.003

Figure 5.50 shows that the saturation profiles, simulated by the mechanistic permeability model, reaches the full dried and wet conditions in two years and one year, respectively. In comparison with the saturation profiles obtained by the single permeability, **Figures 5.25 C** and **5.27 C**, the moisture transport simulated by the mechanistic model is predicted to be faster even though the same values for liquid permeability factor in case of desorption and adsorption have been used in both models. The difference between the two permeability models is in the form of the relative permeability function and the vapour resistance factor that may have caused the great difference in the simulated saturation profiles.

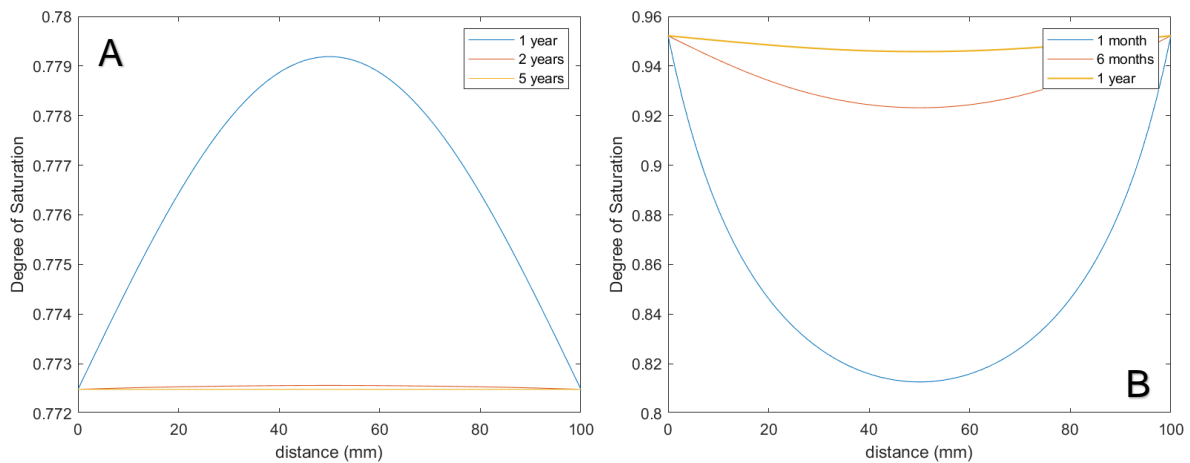


Figure 5.50 Saturation profile at the end of drying from 100% to 50% RH (A) and wetting from 50% to 100% RH (B) for 50SG50FA binder. Profiles are simulated by **Equation 2.33** where the apparent moisture diffusivity parameter is obtained implementing **Equations 2.50** and **2.55** in **Equation 2.49**. The moisture transport parameters are presented in **Table 5.19** with liquid permeability factors of $1.2 \times 10^{-22} \text{ m}^2$ and $6 \times 10^{-22} \text{ m}^2$ implemented in the transport of moisture during desorption (A) and adsorption (B), respectively.

Figure 5.51 presents saturation profiles in 3D for 50SG50FA binder exposed to wetting condition for 1 year and drying condition for 5 years simulated by the mechanistic permeability moisture transport model.

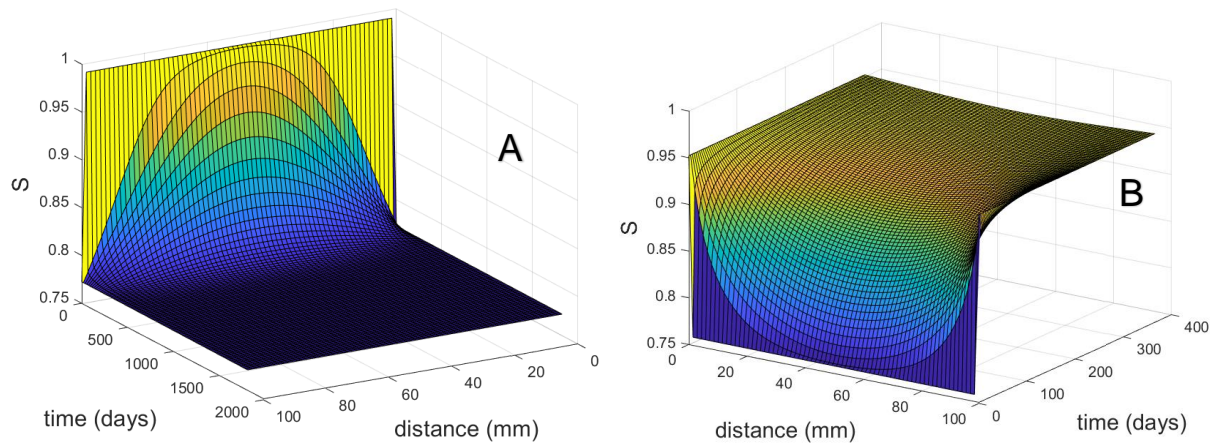


Figure 5.51 Saturation profiles in 3D for 50SG50FA binder as a function of its thickness, in mm, during wetting for 1 year (A) (i.e. 365 days) and during drying for 5 years (B) (i.e. 1825 days) simulated by the single permeability moisture transport model.

5.5.5.3.1 Data Comparison with Mechanistic Permeability Model Predictions

In this section the saturation profiles for 50SG50FA binder simulated by single, dual and mechanistic permeability moisture transport models are compared to each other with the data set obtained for PC-0.45 at the end of the wetting and drying experiments. It can be seen in both cases of wetting and drying, as shown in **Figure 5.52**, the moisture transport simulated by the mechanistic model is predicted to be faster in comparison with the single and dual permeability models. The reason can be that the mechanistic model does not accurately account for the anomaly effect (presented as a knee point in the shape of the saturation profile) in moisture transport, during desorption and adsorption, as much as the single and dual permeability models. It can also be seen that the simulated moisture transport predicted by the dual permeability model is the slowest because it accounts for the moisture hysteresis effect more than the single and mechanistic models in both cases of adsorption and desorption. Hence, the dual porosity moisture transport model can be a suitable tool for the prediction of the amount of evaporable water content in the pores of the alkali-activated binder, made of a mixed composition, as a function of the relative humidity of exposure environment.

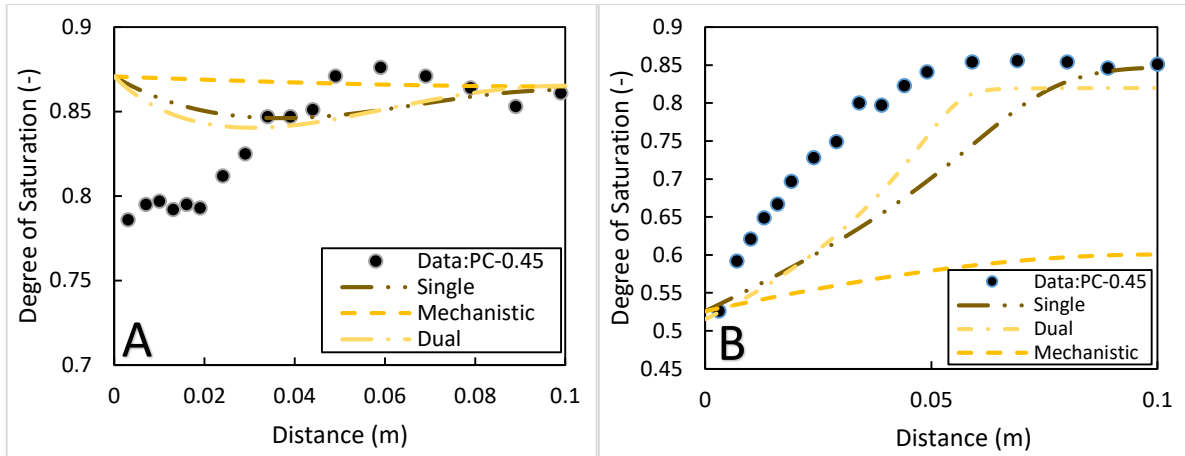


Figure 5.52 Simulated saturation profile, dashed line, for 50SG50FA and data, circle symbol, of measured profiles for PC-0.45 at the end of wetting after 315 days, from 53.5% to 97% RH (A) and at the end of drying after 370 days from 89% to 53.5% RH (B). Data obtained from [179].

5.5.6 Upscaling of Moisture Transport Properties from Cement to Mortar and Concrete

The layer that forms within the concrete structure when the material is cast during the construction stage in service conditions is shown in **Figure 5.53**. As can be seen in this Figure, the surface of the concrete cover, next to the formwork, is mostly composed of a cement skin with about 0.1 mm thickness. After this layer, the first 5 mm is composed of a mortar phase containing less aggregate and more sand than the remaining cover which is the bulk concrete phase containing some air voids. Consequently, modelling moisture transport in concrete should be done mainly into two phases; mortar and concrete phases. As has already been discussed in section 2.14.2 of Chapter 2, the chloride content in the vicinity of the surface layer tends to increase to a maximum and then decrease along the depth of the concrete cover [7]. This has been explained by the combined effect of capillary suction and moisture evaporation at the surface of the concrete [164]. Consequently, for this research the moisture transport in the first 5 mm thickness of the concrete is simulated by the single permeability model. This is to account for the faster mode of transport of evaporable water, that carries the corroding agents, in the mortar skin layer of the concrete during wetting and drying cycles. Whereas, for the remaining concrete cover the moisture transport is simulated by the dual permeability model which accounts more for anomaly effect through the reduction in speed of moisture transport in the bulk concrete phase. The following sections 5.5.6.1 and 5.5.6.2 describe the upscaling of moisture transport properties from cement to mortar and concrete.

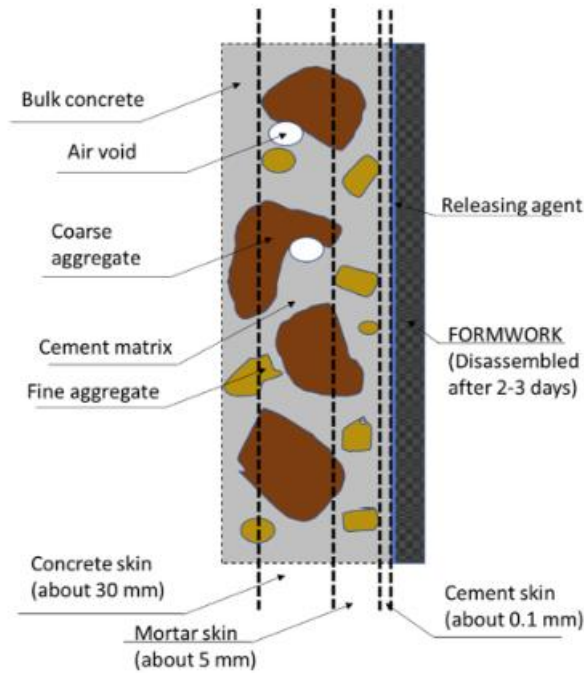


Figure 5.53 The cement and mortar skin of the concrete cover affected by the contact with formwork during the process of concrete casting. Figure obtained from [221].

5.5.6.1 Mortar and Concrete Isotherms

The first step is the determination of the isotherms of alkali-activated mortars and concretes. Figure 5.54 represents data obtained from literature, [205] [69] [222], of desorption isotherms for the same type of cement, CEM I, at cement, mortar and concrete level, although the mortar had a lower water content than cement and concrete.

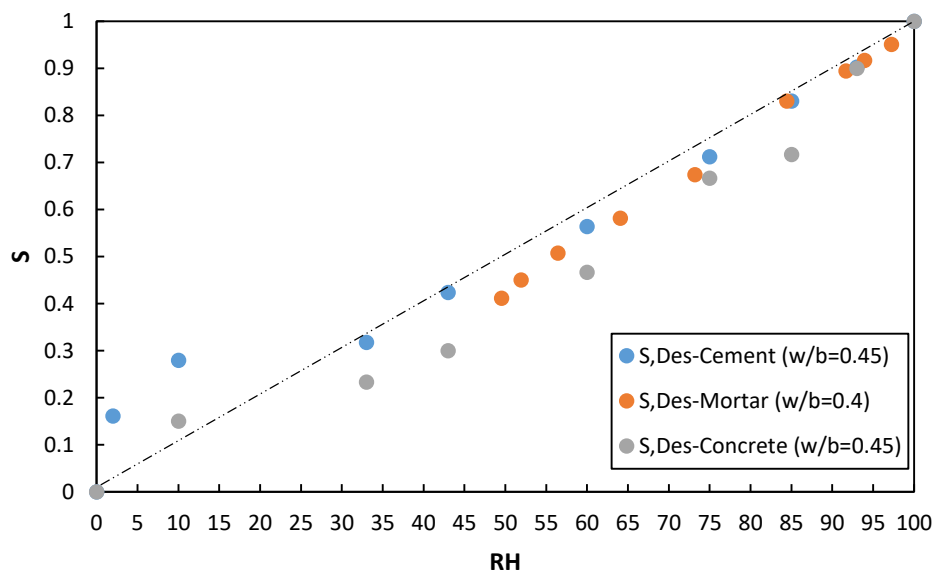


Figure 5.54 Water vapour desorption isotherms for Portland cement at cement, mortar and concrete scale. Data obtained from [69, 205, 222].

According to **Figure 5.54**, it is assumed that the water vapour sorption isotherms of alkali-activated binders have the same set of values of degree of saturation as a function of relative humidity, during adsorption and desorption, when the binders are placed in mortar and concrete mix designs. This assumption is based on the close values of degree of saturation of Portland cement, mortar and concrete exposed to desorption as shown in **Figure 5.54**.

The following section describes the simulation of moisture transport in alkali-activated mortar and concrete by the single permeability model and the dual permeability model, respectively.

5.5.6.2 *Moisture Transport in Alkali-Activated Mortars and Concretes*

The next step is the determination of the moisture permeability properties of mortar and concrete. Wang et al. [223] have considered the diffusivity of moisture in cement is faster than in aggregate. Based on their statement, the moisture diffusivity in concrete, mostly made of binder and aggregate, can be predicted using **Equation 5.8** developed by Xi et al. [224].

$$D_{H-H} = D_{H_{cp}} \left(1 + \frac{g_i}{\left(\frac{1-g_i}{3} - 1\right)} \right) \quad (5.8)$$

$D_{H_{cp}}$; Moisture diffusivity in cement phase

g_i ; Volume fraction of aggregates

For this research the volume fraction of aggregates, g_i , used in **Equation 5.8** is set to 0.66, which is similar to the value of 0.65 used by Wang et al. [223], to determine moisture diffusivity in concrete (D_{H-H}). The parameter g_i is also set as the ratio of binder to sand for the determination of moisture diffusivity in mortar. The value for binder to sand ratio used in alkali-activated mortar is 0.33. **Figures 5.55-5.56** present the upscale moisture diffusivity data from the desorption and adsorption of 100SG, 75SG25FA and 50SG50FA from cement to mortar and concrete. However, it should be noted that Xi et al. [224] have developed Equation 5.8 based on the mechanism of microstructural evolution of interfacial transition zone (ITZ) formed in Portland cement concrete. The interfacial transition zone is an area between the aggregate and cement paste, in the concrete, formed during casting and has a different microstructure compared to the surrounding hydrated cement paste. The difference in microstructure is caused by higher w/b content in the ITZ compared to the paste matrix which leads to a higher proportion of pores in the ITZ region [225, 226]. This is not the case for alkali-

activated slag and alkali-activated fly ash-slag concretes. The ITZ formed in the case of alkali-activated slag concrete has a more uniform microstructure (i.e. containing less pores) as a result of the filling of reaction products known to be the C-A-S-H gels [227] [228, 229]. Whereas in the case of alkali-activated fly ash- slag concrete, the ITZ region contains a higher effective alkaline activator/precursor ratio compared to the paste matrix which accelerates the hydration reaction which induces the formation of C-(N)-A-S-H gels that fill up the empty spaces in the ITZ [230]. Hence, the main limitation of this approach in upscaling the moisture transport properties from alkali-activated cement to mortar and concrete is not accounting for the difference in pore solution chemistry between alkali-activated concrete and Portland cement concrete leading to their ITZ regions to possess different chemical and physical properties [230].

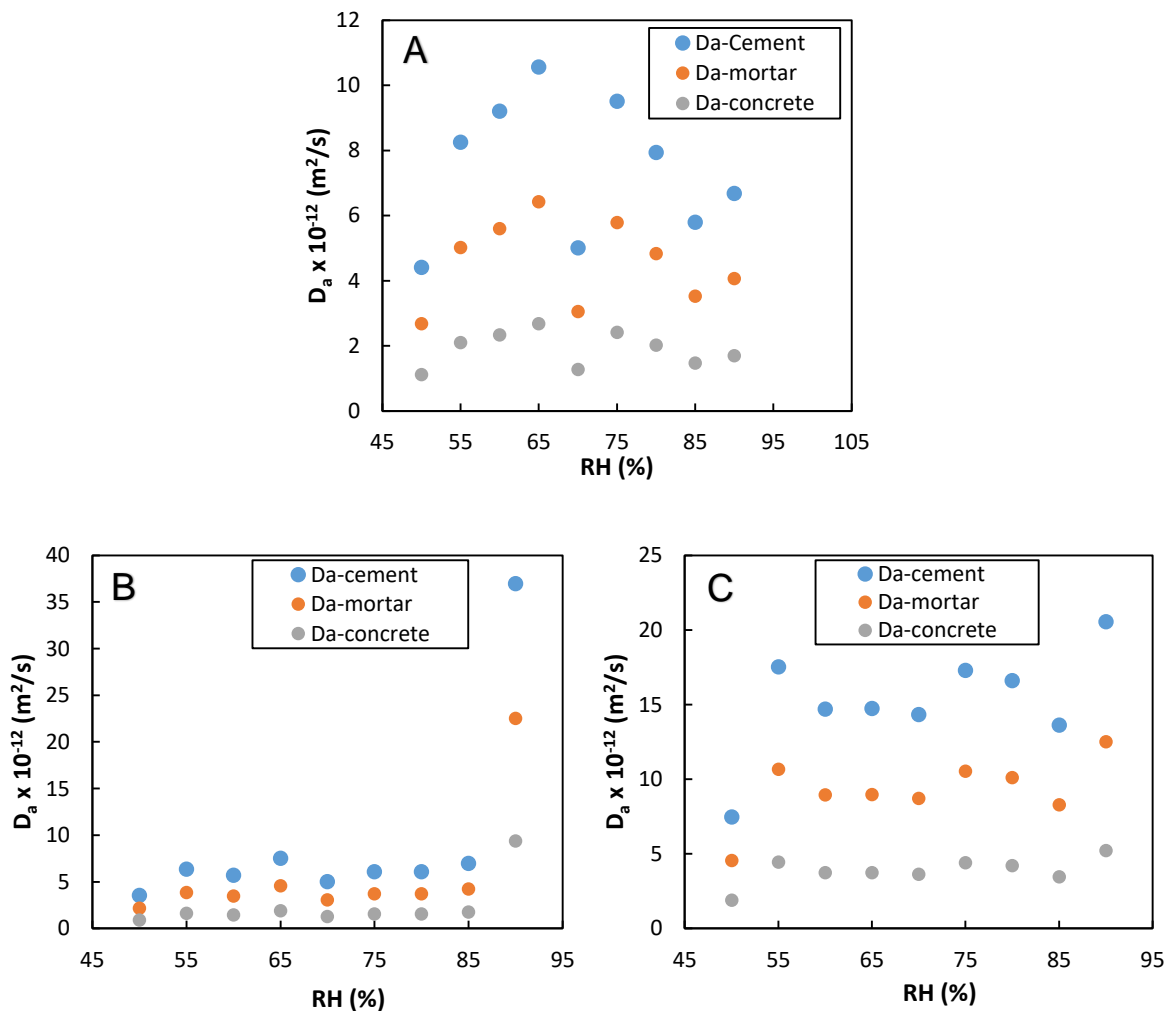


Figure 5.55 D_a vs. RH data from the desorption of 100SG (A) 75SG25FA(B) 50SG50FA(C) from cement to mortar and concrete resulting from the upscaling procedure.

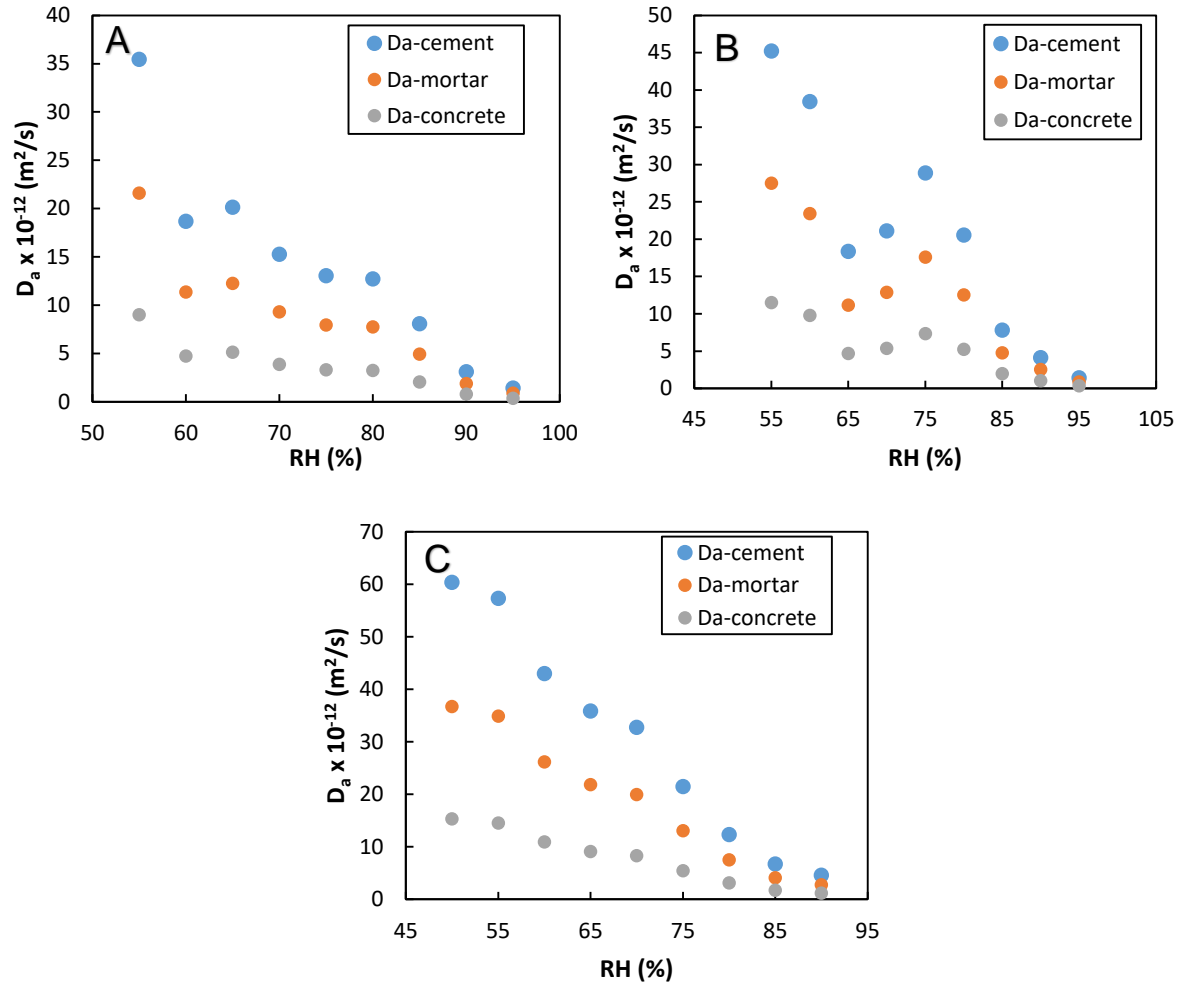


Figure 5.56 D_a vs. RH data from the adsorption of 100SG (A) 75SG25FA(B) 50SG50FA(C) from cement to mortar and concrete resulting from the upscaling procedure.

Moreover, Ismail et al. [152] have reported values of porosity of alkali-activated mortars and concretes with similar mix designs to the studied alkali-activated binders in this research, as presented in **Table 5.23**. These values are implemented in the single and dual moisture transport models to simulate the saturation profiles in alkali-activated mortars and concretes.

Table 5.23 values of porosity of alkali-activated mortars and concretes obtained from literature [152].

	100SG	75SG25FA	50SG50FA	Ref.
Mortar	0.0798	0.0833	0.079	[152]
Concrete	0.156	0.148	0.136	[152]

5.5.6.2.1 Single Permeability Moisture Transport in Alkali-activated Mortar

This section describes the simulated saturation profiles, by the single permeability moisture transport model, in alkali-activated mortars exposed to drying and wetting conditions for 5 years and 1 year respectively.

Desorption

Equations 2.34 and 2.35 are used to fit the D_a vs. S data for alkali-activated mortars, obtained from upscaling the data of moisture diffusivities of alkali-activated binders, as shown in **Figure 5.57**. It can be seen in this figure that the relationship between the model and experimental data is not in the right shape for 100SG, although it is better for 75SG25FA and 50SG50FA. The fitted moisture transport parameters, K and x_d , are implemented in Equation 2.33 to predict the saturation profile at the end of desorption of alkali-activated mortars according to **Figure 5.58**.

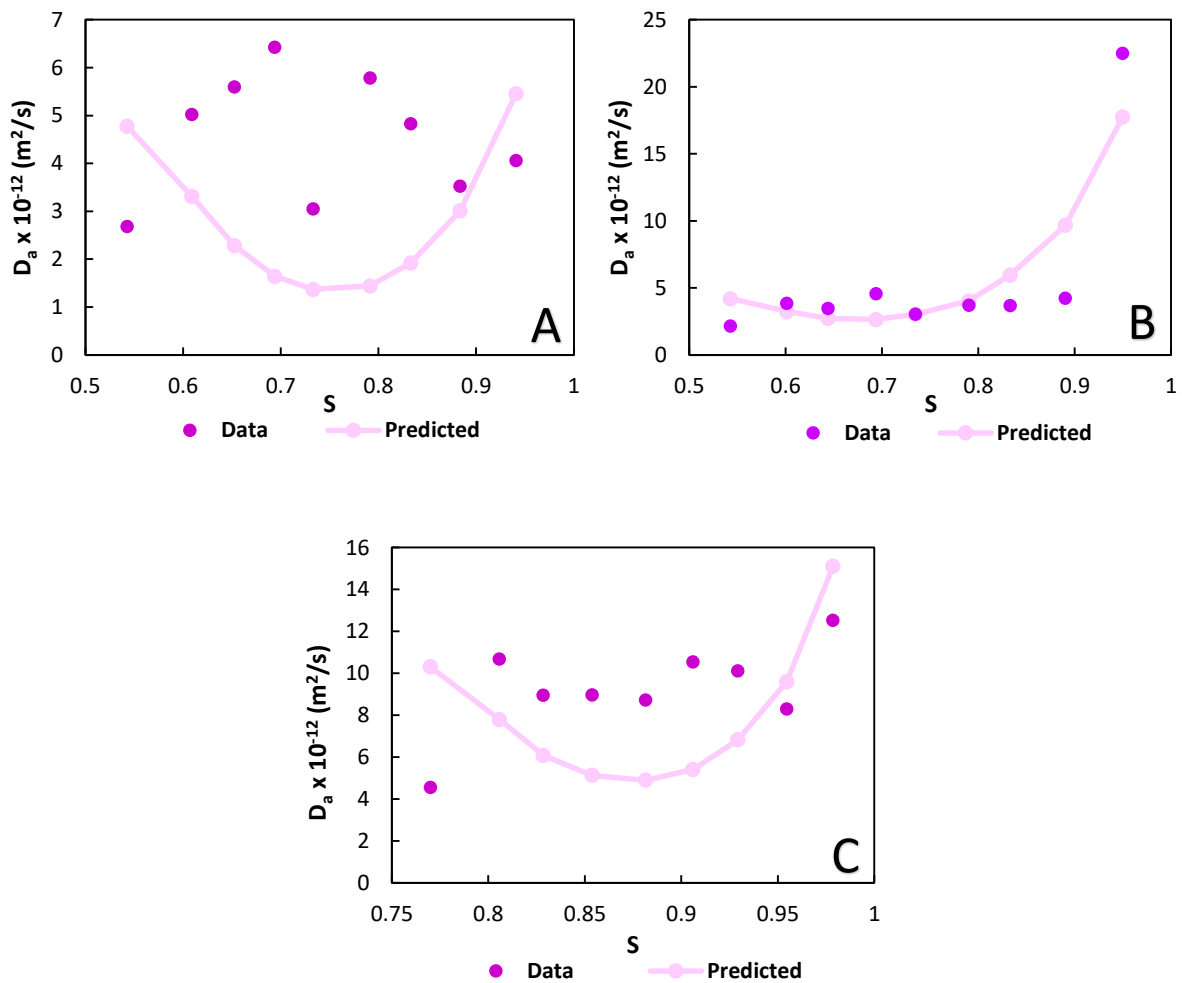


Figure 5.57 Circular symbols represent experimental Da data obtained during the desorption of 100SG (A), 75SG25FA(B) and 50SG50FA (C) mortars. The measured curves of Da , lines, are fitted by means of implementing equations 2.34 and 2.35 in equation 2.33.

Tables 5.24 and **5.25** present the fitted parameters of the VG isotherm model and single permeability model for moisture transport in alkali-activated mortars during the desorption stage. According to Table 5.25, 50SG50FA has the lowest vapour resistance factor compared to 100SG and 75SG25FA. Whereas, 75SG25FA has slightly higher vapour resistance and liquid permeability values compared to 100SG. It can be seen in **Figure 5.58** that 50SG50FA binder reaches the drying stage at 50%RH faster than 75SG25FA followed by 100SG.

Table 5.24 Parameters of the Van Genuchten model used to simulate desorption isotherms of alkali-activated mortars.

Sample	a (Pa)	m	n	NME
100SG	422×10^5	0.38	1.61	0.01
75SG25FA	437×10^5	0.4	1.65	0.01
50SG50FA	774×10^5	0.31	1.44	0.003

Table 5.25 Parameters obtained from fitting D_a -S desorption data of alkali-activated mortars by means of implementing equations 2.34 and 2.35 in the single permeability moisture transport model.

Sample	K (m ²)	x_d	NME
100SG	1×10^{-23}	1.7	0.54
75SG25FA	3×10^{-23}	1.8	0.44
50SG50FA	1×10^{-23}	1	0.43

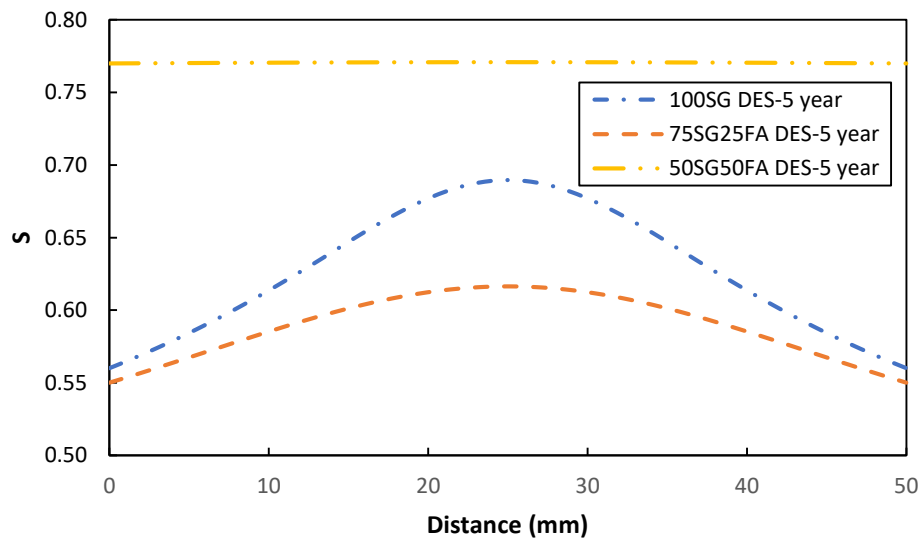


Figure 5.58 Saturation profile at the end of drying from 100% to 50% RH for 100SG(A), 75SG25FA (B), and 50SG50FA (C) binders simulated by implementing Equations 2.34 and 2.35 in **Equation 2.33** and using the moisture transport parameters present in **Tables 5.24-5.25**.

Adsorption

Equations 2.34 and 2.35 are used to fit the D_a vs. S data for alkali-activated mortars, obtained from upscaling the data of moisture diffusivities of alkali-activated binders, as shown in **Figure 5.59**. It can be seen in this Figure that the model and experimental data is in good agreement for all the alkali-activated mortars. The fitted moisture transport parameters, K and x_d , are implemented in Equation 2.33 to predict the saturation profile at the end of adsorption of alkali-activated mortars according to **Figure 5.60**.

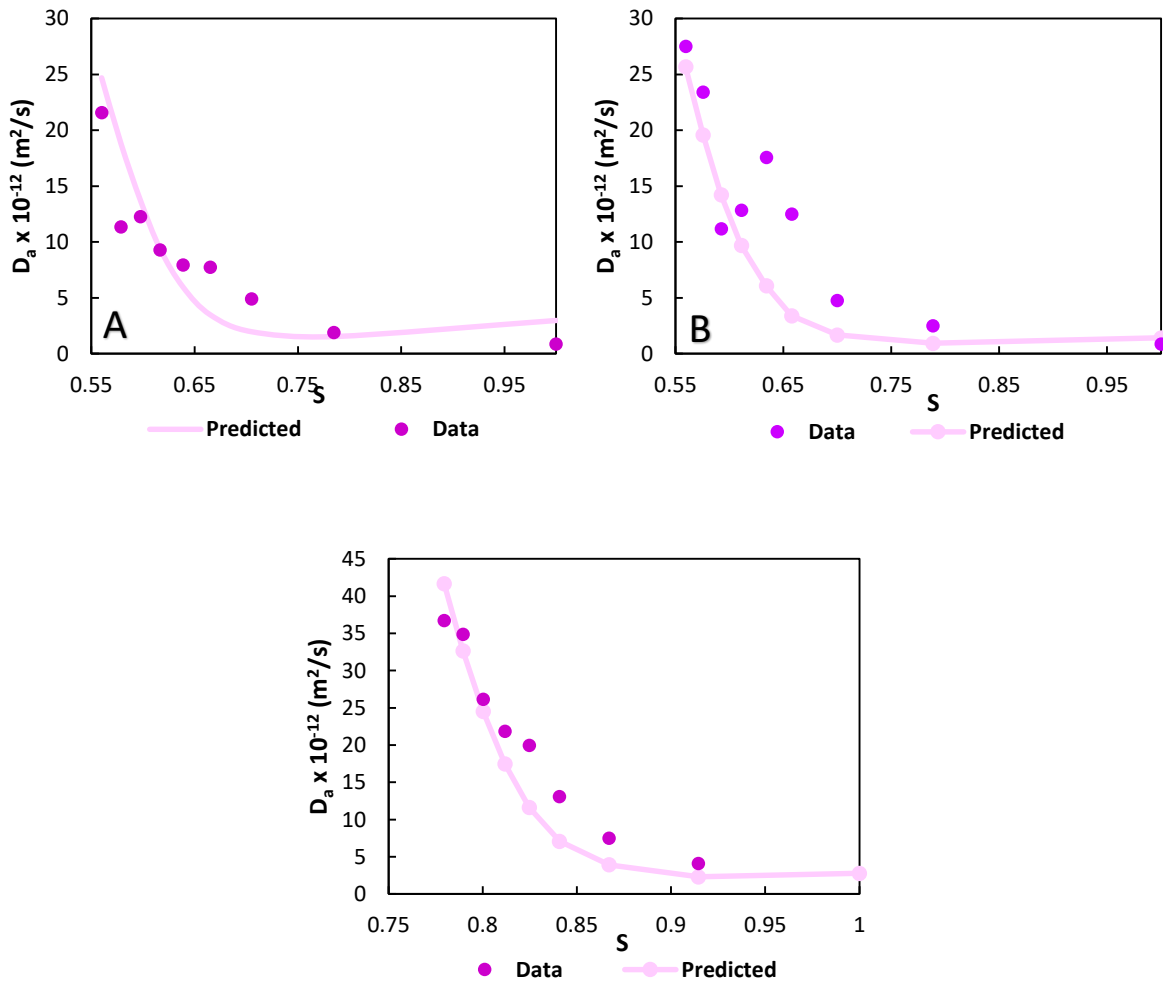


Figure 5.59 Circular symbols represent experimental D_a data obtained during the adsorption of 100SG (A), 75SG25FA(B) and 50SG50FA (C) mortars. The measured curves of D_a , lines, are fitted by means of implementing **Equations 2.34** and **2.35** in **Equation 2.33**.

Tables 5.26 and **5.27** present the fitted parameters of the VG isotherm model and single permeability model for moisture transport in alkali-activated mortars during the adsorption stage. According to **Table 5.27**, 50SG50FA has the lowest vapour resistance factor compared to 100SG and 75SG25FA. 75SG25FA has the lowest liquid permeability factor compared to 100SG. 100SG and 75SG25FA have the exact value for the vapour factor which explains the reason for both mortars to contain similar saturation profiles at the end of wetting as shown in **Figure 5.60**.

Table 5.26 Parameters of the Van Genuchten model used to simulate adsorption isotherms of alkali-activated mortars.

Sample	a (Pa)	m	n	NME
100SG	98×10^5	0.22	1.28	0.04
75SG25FA	97×10^5	0.22	1.28	0.03
50SG50FA	121×10^5	0.11	1.13	0.01

Table 5.27 Parameters obtained from fitting D_a -S adsorption data, of alkali-activated mortars, by means of implementing equations 2.34 and 2.35 in the single permeability moisture transport model.

Sample	K	X_d	NME
100SG	1×10^{-22}	1.4	0.28
75SG25FA	5×10^{-23}	1.4	0.45
50SG50FA	1×10^{-22}	0.8	0.25

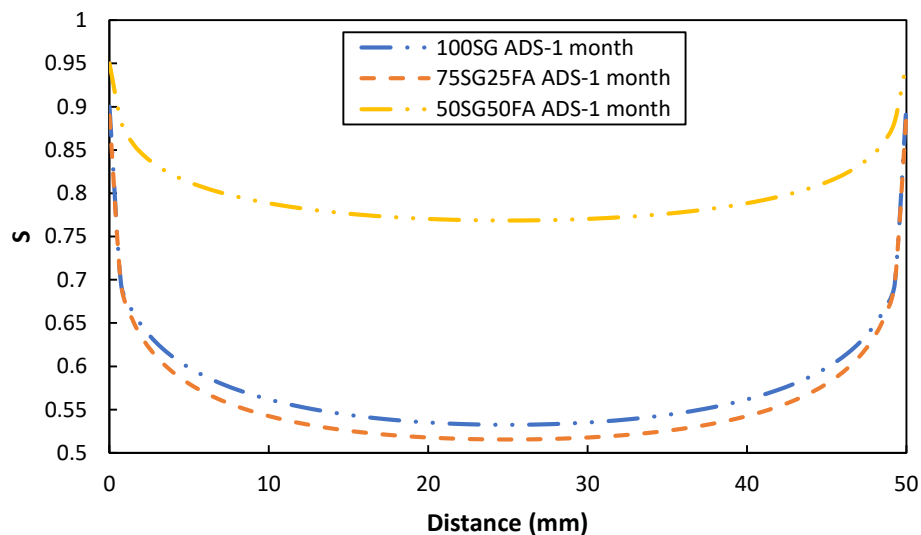


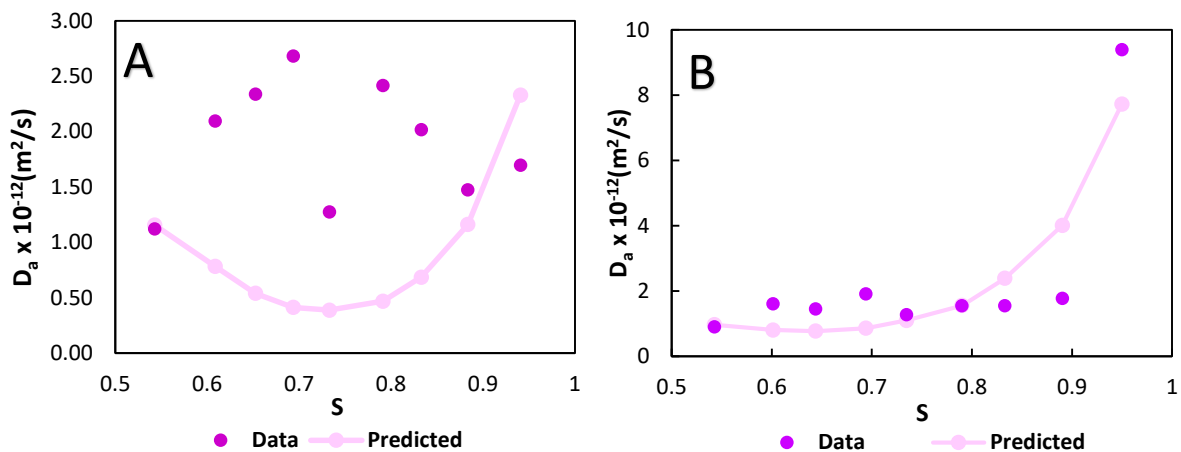
Figure 5.60 Saturation profile at the end of wetting from 50% to 100% RH for 100SG(A), 75SG25FA (B), and 50SG50FA (C) binders simulated by implementing equations 2.34 and 2.35 in the single permeability model and using the moisture transport parameters present in **Tables 5.26** and **5.27**.

5.5.6.2.2 Dual Permeability Moisture Transport in Alkali-Activated Concrete

This section describes the simulated saturation profiles, by the dual permeability moisture transport model, in the large and small pore regions of the binder phase in alkali-activated concretes exposed to drying and wetting conditions for 5 years and 1 year respectively. In addition, the values of the volumetric fraction of the large pore region and the contribution factor of the large pore region to moisture transport are also applied to model the transport of moisture in the large and small pore regions of the binder phase in the alkali-activated concrete.

Desorption

Equations 2.44 and **2.46** are implemented in **Equation 2.42** to fit the data of moisture diffusivity vs. the degree of saturation (i.e. D_a vs S data) for alkali-activated concretes, obtained from upscaling the data of moisture diffusivities of alkali-activated binders to concrete level as shown in **Figure 5.61**. It can be seen in these Figures that the model trend is not the same as the experimental data for 100SG and 50SG50FA, although it is better for 75SG25FA.



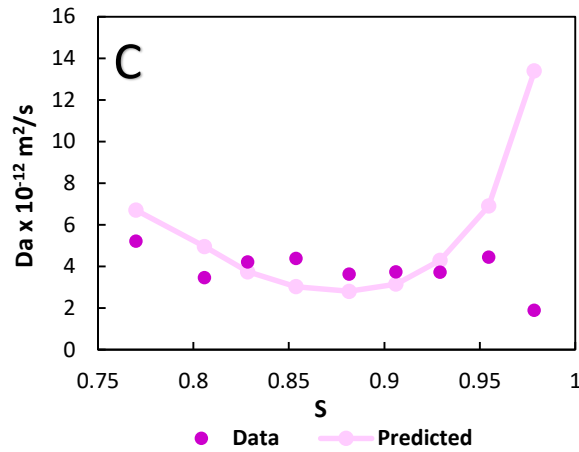


Figure 5.61 Circular symbols represent experimental D_a data obtained during the desorption of 100SG (A), 75SG25FA (B) and 50SG50FA (C). The measured curves of D_a (lines) are obtained by means of fitting the overall moisture transport equation (Eq. 2.42) which includes moisture transport in the large pore region (Eq. 2.44) and small pore region (Eq.2.46) along with the transport contribution factor from the large pore region ($w_{f,D}$).

Table 5.28 and **Table 5.29** present the fitted parameters of the VG-Dual isotherm model and dual permeability model for moisture transport in alkali-activated concretes during the desorption stage. **Equation 2.44** and **2.46** are implemented in **Equations 2.43** and **2.45** to simulate the saturation profiles in the large and small pore regions of the binder phase in alkali-activated concrete at the end of drying by using parameters presented in **Table 5.29**. The saturation profiles for alkali-activated concretes are shown in **Figure 5.62**. According to the fitted moisture permeability factor for the transport in small pore region, as shown in Table 5.29, 75SG25FA concrete has a higher vapour resistance factor and liquid permeability factor than 100SG concrete. According to **Figure 5.62 A** the desorption process in 75SG25FA is slower than in 100SG even though the liquid permeability factor for moisture transport in large pore region of 75SG25FA is 1.25 times higher than in 100SG. Thus, the vapor resistance factor also plays a dominant role in the transport of moisture during the desorption process of alkali-activated concrete. Although 50SG50FA concrete has the lowest vapor resistance factor and liquid permeability factor compared to 100SG and 75SG25FA, it is shown in **Figure 5.62 C** that 50SG50FA reaches the drying stage at 50%RH the fastest. The reason can be because 50SG50FA has the lowest vapor resistance factor which dominates the transport of moisture during the desorption stage.

Table 5.28 Parameters of the VG-Dual model used to simulate desorption isotherms for alkali-activated concretes.

Sample	w	a_l (Pa)	a_s (Pa)	m	n	NME
100SG	0.11	160×10^5	524×10^5	0.41	1.69	0.01
75SG25FA	0.097	215×10^5	492×10^5	0.41	1.68	0.01
50SG50FA	0.14	238×10^5	1621×10^5	0.59	2.43	0.002

Table 5.29 Parameters obtained from fitting $D_a(l)$ desorption data, of alkali-activated concretes, by means of implementing equation 2.44 for moisture transport in the large pore region.

Sample	K_l (m ²)	K_s (m ²)	x_d	$w_{t,D}$	NME
100SG	4×10^{-23}	2×10^{-24}	1.8	0.15	0.56
75SG25FA	5×10^{-23}	1×10^{-23}	2	0.11	0.41
50SG50FA	1×10^{-24}	5×10^{-25}	0.7	0.1	0.92

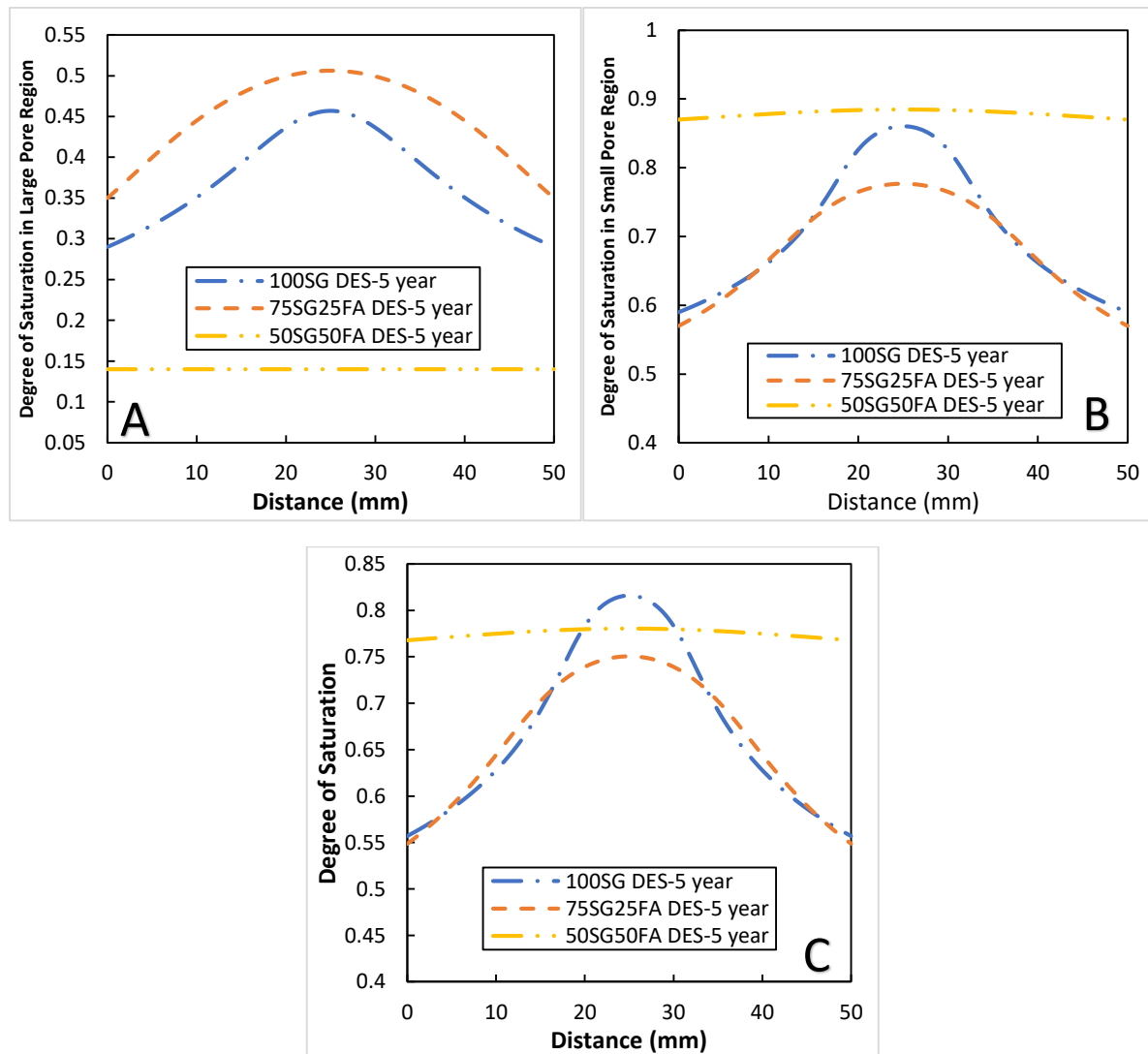


Figure 5.62 Saturation profile at the end of drying from 100% to 50% RH for alkali-activated concretes in the large pore region (A), in the small pore region (B) and total saturation (C). Profiles are simulated for

100SG, 75SG25FA and 50SG50FA by implementing **Equations 2.43** and **2.45** in the dual permeability model and using the moisture transport parameters presented in **Tables 5.28-5.29**.

Adsorption

Equations 2.44 and **2.46** are implemented in **Equation 2.42** to fit the data of moisture diffusivity vs. the degree of saturation (i.e. D_a vs S data) for alkali-activated concretes, obtained from upscaling the data of moisture diffusivities of alkali-activated binders to concrete level as shown in **Figure 5.63**. It can be seen in this Figure that the model and experimental data is in good agreement for moisture transport in alkali-activated concretes.

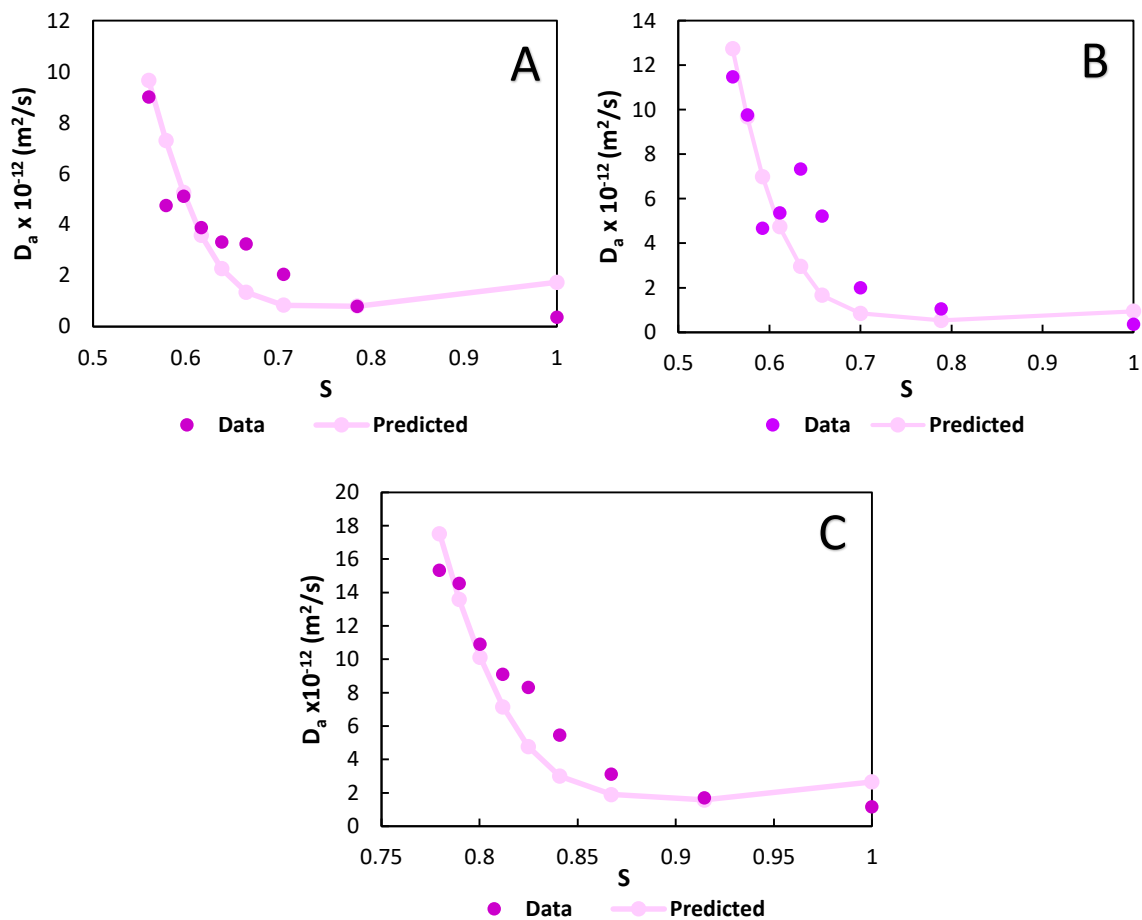


Figure 5.63 Circular symbols represent experimental D_a data obtained during the desorption of 100SG (A), 75SG25FA (B) and 50SG50FA (C). The measured curves of D_a (lines) are obtained by means of fitting the overall moisture transport equation (Eq. 2.42) which includes moisture transport in the large pore region (Eq. 2.44) and small pore region (Eq.2.46) along with the transport contribution factor from the large pore region ($w_{l,D}$).

Table 5.30 and **Table 5.31** present the fitted parameters of the VG-Dual isotherm model and dual permeability model for moisture transport in alkali-activated concretes during the adsorption stage. **Equations 2.44** and **2.46** are implemented in **Equations 2.43** and **2.45** to

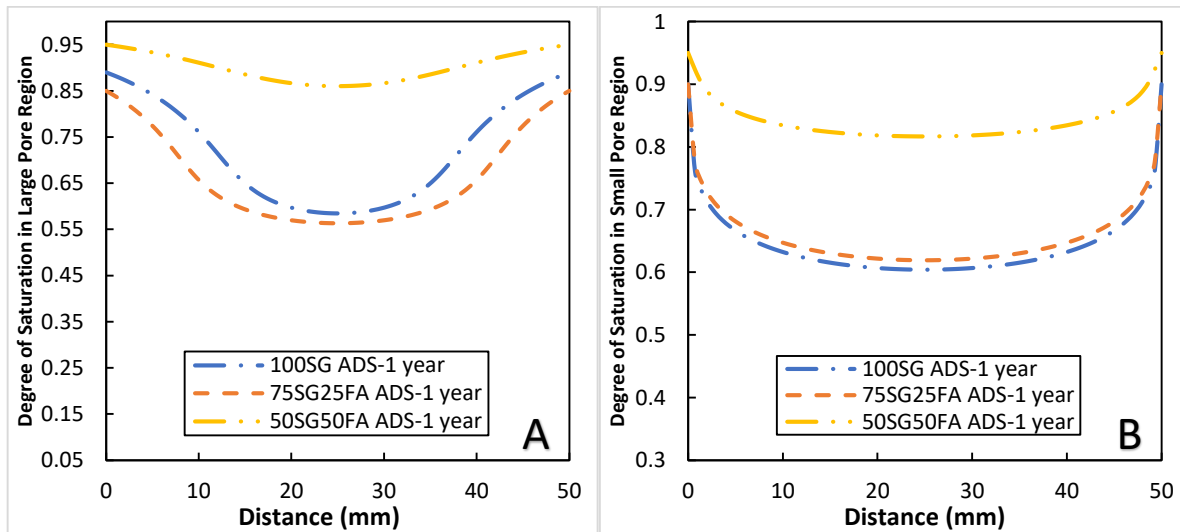
simulate the saturation profiles in the large and small pore regions of the binder phase in alkali-activated concrete at the end of wetting by using parameters presented in **Tables 5.30-5.31**. The saturation profiles for alkali-activated concretes are presented in **Figure 5.64**.

Table 5.30 Parameters of the VG-Dual model used to simulate adsorption isotherms for alkali-activated concretes.

Sample	w	a_l (Pa)	a_s (Pa)	m	n	NME
100SG	0.11	88×10^5	98×10^5	0.22	1.28	0.03
75SG25FA	0.097	67×10^5	98×10^5	0.22	1.28	0.04
50SG50FA	0.14	111×10^5	121×10^5	0.11	1.13	0.01

Table 5.31 Parameters obtained from fitting $D_a(S)_l$ adsorption data, of alkali-activated concretes, by means of implementing equation 2.44 for moisture transport in the large pore region.

Sample	K_l (m ²)	K_s (m ²)	x_d	$w_{t,D}$	NME
100SG	1×10^{-22}	1×10^{-23}	1.6	0.15	0.25
75SG25FA	1×10^{-22}	1×10^{-23}	1.5	0.11	0.52
50SG50FA	2×10^{-22}	5×10^{-23}	1	0.1	0.35



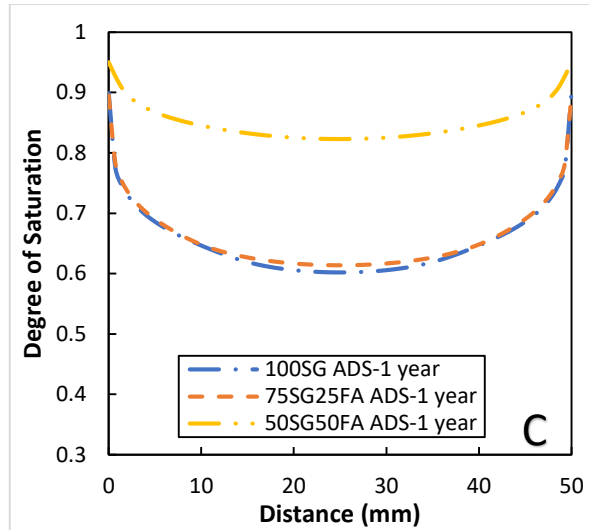


Figure 5.64 Saturation profile at the end of wetting from 50% to 100% RH for 100SG, 75SG25FA, 50SG50FA in the large pore region (A), in the small pore region (B) and total saturation (C). Profiles are simulated by implementing **Equations 2.43** and **2.45** in the dual permeability model and using the moisture transport parameters presented in **Tables 5.30-5.31**.

Overall, the studied moisture permeability models have been attained from studies on moisture transport properties of Portland cement solely at binder level [62, 70, 79, 88]. The studied models neglect the fine and/or coarse aggregate effect that blocks the propagation of moisture through the pores of the binder. In addition, the effect of the interfacial transition zone – ITZ – in concrete which is the region of the cement paste around the aggregate particles [231], can induce pores that are bigger than the pores present in the bulk binder phase of Portland cement concrete as previously discussed in section 5.5.6.2. This can further increase the complexity of the pore network of the concrete. However, in this study an approach has been taken to simulate moisture transport in alkali-activated mortar and concrete by implementing Equation 5.8 to estimate the apparent moisture diffusivity at mortar and concrete levels. This approach includes the effect of aggregate, according to Equation 5.8, which lowers the value of moisture transport throughout the pores of the binder phase but does not include the impact of pore solution chemistry of AAMs that condenses the microstructure of ITZ in alkali-activated concrete. Moreover, it should be noted that the values for the moisture permeability factor, K , obtained for alkali-activated concretes in this study are lower than the range of $0.98 - 8.88 \times 10^{-21}$ obtained for PC based concretes by different experimental methods reported in [79].

5.6 Conclusions

Based on the results of this study, the following conclusions can be drawn:

1. The effect of the high content of alkali ions present in the pore solution of AAMs can minimize the evaporation of free water during the stage of desorption. The same effect has been reported for the presence of dissolved sodium hydroxide that lowers the extent of evaporation of water from the aqueous solution [206]. Whereas in the case of adsorption, the free alkali ions induce further hydration reactions with the remaining unreacted precursors due to the presence of moisture condensing on the pore walls and forming into liquid water. This results in pore refinement because of the formation of hydrates that fill up the pores of the binder. Consequently, the degree of hysteresis between the adsorption and desorption curves lowers because of the development of the binder with a more uniform pore size and dense microstructure.
2. During moisture transport, the vapour resistance factor of the cementitious materials plays an important part in slowing down and speeding up the desorption process. Whereas, the liquid permeability factor of the cementitious materials plays a more important role in slowing down and speeding up the adsorption process.
3. The values of the vapour resistance factor for all the studied cementitious materials in both cases of adsorption and desorption are quite similar. However, values of the liquid permeability factor for all the materials are higher in the case of adsorption than in the case of desorption.
4. The single porosity moisture transport model predicted the estimated saturations profiles of AAMs during the wetting experiment but not during the drying experiment for the case of blended alkali-activated binder (i.e. 50SG50FA). The model falls short on predicting the saturation profile for blended cements due to the presence of complex microstructure containing more than one type of pore size.
5. The mechanistic model does not accurately account for the anomaly effect (presented as a knee in the shape of the saturation profile) in moisture transport, during desorption and adsorption stages.
6. The dual permeability model predicts the saturation profile better than the single permeability model because it includes the anomaly effect of moisture transport by accounting the fast and slow transport of moisture in two different pore size regions of a material with a complex microstructure such as the case of blended cements [60, 62]. It also includes an interconnectivity factor that represents the transport of moisture between the large and small pore regions of the cement during adsorption and desorption stages [62].

7. An approach has been taken to simulate moisture transport in mortar and concrete by accounting the effect of sand and aggregate in lowering the moisture diffusivity through the pores of the binder phase.

Overall the current existing mathematical descriptions to model sorption isotherms and moisture transport are largely formulated for Portland cement-based binders, and so they fall short in dealing with alkali-activated cements as these are quite different in their chemistries, especially in relation to their highly alkaline pore solutions. Hence, a model that accounts for the microstructure and effect of pore solution during moisture transport needs to be developed. The moisture transport calculations in mortar and concrete layer in the concrete cover will be used to estimate the degree of water saturation in the concrete cover as a function of time and thickness of the cover to model the chloride transport in the aqueous phase and carbonation reaction in the gaseous phase of the pores of the binder as will be discussed in **Chapter 6**.

Chapter 6: Coupling Chloride Ingress and Carbonation for Service Life Prediction of Alkali-Activated Concrete

Abstract

The serviceability limit state of a concrete structure exposed to a corrosive environment has often been calculated by service life models (SLM) solely based on Fick's second law for chloride diffusion [159]. The main limitation of this type of model is that it does not account for various modes of transport and reactions that occur when the concrete is exposed to unsaturated conditions; moisture transport, chloride ingress and carbonation reactions can occur at the same time and influence the durability of the structure. Hence, a numerical model has been developed and validated for service life prediction of alkali-activated concrete (AAC) in marine splash zone conditions. However, one major drawback of this model is that it is deterministic, with a single output value in service life calculations. This is a disadvantage because the performance properties of multiple elements made from any given concrete are intrinsically scattered, leading to a variation in the serviceability limit state of the overall structure.

Therefore, the focus of this research is to probabilistically calculate the service life of AAC by using the developed model. The sensitivity analysis will incorporate consideration of the mix design of AAC as well as carbonation kinetics, chloride binding, ageing and moisture permeability values, which are systematically varied in the model in order to provide a range of values for service life. Thus, uncertainty values are estimated for the service life calculation of AAC. This also enables the assessment of the main mix variables and durability parameters that have the most impact on the calculated service life of AAC. This is important for efficient decision-making in material design of concrete for suitable structural applications and with low environmental impact.

Keywords: Alkali-activated concrete, Reactive transport, Probabilistic Service Life Prediction

6.1 Introduction and aim

The entry of chloride ions from the environment into concrete can occur through several modes of transport, such as advection due to a pore capillary pressure gradient, diffusion caused by a concentration gradient, and migration from a potential gradient in the ionic pore solution [162]. There are various analytical models, based on modified versions of the classical error function solution of Fick's second law, used to solely model the diffusional transport of chloride ions. The HETEK model [184] implements a variable surface chloride boundary condition in modelling the chloride diffusion in concrete. The ClinConc model [160] simulates the chloride diffusion by taking into account the non-linear chloride binding along the concrete cover [159, 160]. The DuraCrete model [232] is a probabilistic model that predicts the service life based on the distribution values of its durability parameters in the error function solution to Fickian diffusion [47]. All these models have been developed but none have included the effect of changes in the phase assemblage of cement hydrates, during a deterioration reaction, on the mass transport. This is a deterioration mode that occurs when the structure is exposed in unsaturated service conditions favouring the impact of carbonation reactions on chloride ingress. These conditions occur most likely in marine splash zone environments where aerosol chlorides, from the sea, and atmospheric CO₂ dissolve and propagate through the capillary pores of the concrete and begin corrosion reactions.

Reactive transport modelling is a multi-physics tool used to model the transport of ions, in a reactive porous media such as concrete, by the use of various modes of transport equations included in the Poisson-Nernst-Planck equation [18]. In addition, it models the transport of free ions in the pore solution by including a reaction term in the transport equation to account for the reaction between the aqueous species and solid hydrates. Some recent literature has used reactive transport to model solute transport in concrete exposed to carbonation and/or chloride ingress [17]. For example, Xie et al. [5] have modelled the concurrent effects of carbonation on chloride ingress in Portland cement based concrete by a reactive transport model developed by them. However, those authors have highlighted the fact that their model is solely based on Portland cement, whereas incorporating supplementary cementitious materials (SCMs) along with PC would change the reactants for carbonation and chloride binding isotherms because of the formation of complex hydrates. In addition, they have pointed out that the moisture and ionic model, used as sub-models in their reactive transport model, need further justification in order to improve the description of mass transport in cements.

In this paper, a numerical model accounting for carbonation-chloride induced reactions is proposed and validated against chloride profile data for a structure exposed in unsaturated conditions. With this validation and basic model refinement implemented, the model has been used to probabilistically predict the service of AAC based on carbonation-chloride induced corrosion thresholds. Finally, sensitivity analysis has been conducted for the assessment of the main mix variables and durability parameters that have the most impact on the calculated service life of AAC.

6.2 Materials and Methodology

6.2.1 Raw Materials and Mix Designs:

Table 6.1 describes the mix designs of the alkali-activated mortars studied in this research.

Table 6.1 Mix design of alkali-activated mortars.

Sample	Na ₂ O (Wt.% of Binder)	Mr (nSiO ₂ /nNa ₂ O)	water/binder	Sand/binder
100SG	4	1.5	0.5	3
75SG25FA	4	1.5	0.45	3
50SG50FA	4	1.5	0.4	3
CEMII	-	-	0.5	3

6.2.2 Test Methods

6.2.2.1 Bulk Resistivity Measurements

The embedded electrode method (EEM) is used to measure the resistivity of the alkali-activated mortars. The methodology is explained in “**Chapter 2: Materials and Methods**”.

6.2.2.2 Calculation of concentration of pore solution ions in Alkali-activated binders

The open source software GEM-Selektor v.3 (<https://gems.web.psi.ch/> [233]) was utilised, where the mineralogical composition, extent of degree of reaction for the precursors, and mix design of the alkali-activated binders were set as inputs in order to obtain the concentrations of ions present in the aqueous phase of the binders. The methodology is explained in “**Chapter 3 Materials and Methods**”.

6.2.3 Estimation of Chloride Profile of Alkali-Activated Concrete in Real Service Conditions

In this research, a link between chloride data in laboratory and service conditions is made, to predict the chloride profiles in AAMs for the same number of years that a PC based structure is exposed in a real marine environment. For this outcome to be estimated, the following steps

have been implemented. First, periodic resistivity measurements, through the embedded electrode method [173], have been performed on alkali-activated and Portland cement-based mortars submerged in water for 288 days at three different testing temperature conditions: 10, 20 and 30°C.

Next, the data obtained are used to estimate the time evolution of formation factor of the mortars, that is needed to calculate the aging factor and be included in the effective diffusion of chloride ions. This aging factor represents the extent of cement hydration resulting from pozzolanic activity. The third step is comparison between the chloride profile of laboratory PC concrete extrapolated to 25 years and the chloride profile, obtained from literature, of a PC structure exposed for the same number of years [163]. Based on differences between these results, the chloride aging model for PC has been readjusted to incorporate effects of real service conditions on the durability of the concrete. Finally, combining the real service chloride profile of PC-based concrete and the scaling factors of the chloride profiles between AAM and PC-based mortars, obtained in laboratory conditions, the chloride profile of AAM-concrete in real conditions after 25 years is predicted. The data will be used to validate the proposed numerical model.

6.3 Fundamental Relations

Concrete is described as a reactive porous medium with a variable moisture state that is dependent on the environmental relative humidity. The pore saturation degree governs the effect of carbonation on chloride ingress when its value is in the low and medium ranges, whereas under complete saturation, only chloride ingress would take place [62]. The relationship between the degree of water saturation, S , and pore volume of the material is introduced in **Equation 2.18**. Equivalently, the degree of saturation can be defined in terms of effective porosity according to **Equation 2.19**.

6.3.1 Coupled Reactive Mass Transport Model

The concrete is made of solid phases consisting of cement hydrates, residual precursors, and inert phases. Carbonation and chloride ingress could induce modifications in terms of changes in the microstructure, alkalinity and ionic strength of the pore solution. These changes can either enhance or limit the transport rate of corrosive agents towards the rebar. Therefore, coupling moisture transport, that determines the degree of saturation, ϵ , diffusion of chloride

with minimal chloride binding in the liquid phase, and flow of carbon dioxide in the gas phase, has been implemented to account for the presence of several corrosive agents from the environment [5, 106].

Michel et al. [18] have proposed a modelling framework to describe leaching and carbonation reactions in a saturated concrete by accounting for the changes in pore structure, that is separately induced by these reactions, on mass transport of ions in the pore solution. They have described the mass transport in cement based materials along with chemical equilibrium between ions in the pore solution and solid hydrates through an extended version of the Poisson-Nernst-Planck (PNP) system of equations. The model of mass transport is coupled with a thermodynamic modelling program in which results of the transport of ions serve as input for the dissolution and precipitation reactions of the solid hydrates. Then the results obtained from the chemical equilibrium equations are used as initial value for the subsequent mass transport equations, as a function of space and time. Further information on coupling these two models (i.e. mass transport and thermodynamic model) can be found in [18]. The mass transport equation coupled with the chemical equilibrium term, q_i , is described in **Equation 6.1**.

$$\varepsilon \frac{\partial C_i}{\partial t} + c_i \frac{\partial \varepsilon}{\partial t} = \nabla(D_i \varepsilon \nabla C_i + D_i C_i \nabla \varepsilon - A_i z_i \varepsilon c_i \nabla \phi) + v \varepsilon \nabla C_i + v C_i \nabla \varepsilon + q_i \quad (6.1)$$

ε ; degree of saturation

C_i ; ionic concentration of species i in the liquid phase

D_i ; diffusion coefficient of the i^{th} ionic species.

z_i ; valence of the i^{th} ionic species.

ϕ ; electric potential

v ; velocity of the liquid phase

A_i ; ion mobility of the i^{th} ionic species

q_i ; chemical equilibrium term that accounts for the reactions among ions present in the pore solution. The term also accounts for the equilibrium between the aqueous ionic species and the cement hydrates, and between the aqueous ionic species and the gaseous components in the air-filled space of the pore.

The first and second terms of **Equation 6.1** describe the diffusion and effect of moisture gradient changes on the ion concentrations, respectively, and the third term accounts for the effect of diffusion of the i^{th} ionic species due to the development of electrical potential gradient

caused by the difference in concentration of pore solution ions, with different valences, across the concrete. Finally, the fourth and fifth terms account for the advective motion due to moisture gradients.

However, in this research the proposed model in **Equation 6.1** is utilized with the assumption that the ionic movement is caused by moisture and concentration gradients, excluding the electrical potential gradient in the third term on the right hand side. The electrical potential gradient is set to zero based on the assumption that the electro-neutrality of the pore solution is maintained.

In addition, the thermodynamic software is not directly coupled with the mass transport equations, but rather the chemical equilibrium term that accounts for chloride binding and carbonation reactions is implemented through empirical relationships.

In this research, the following system of partial differential equations (PDEs), **6.2**, is used to describe the physical-chemical phenomena taking place inside unsaturated concrete exposed to simultaneous chloride ingress and carbonation reactions. Each PDE is discussed in the following sections.

$$\left\{ \begin{array}{l} (C_{Cl} + C_{CO_3^{2-}}) \frac{\partial \varepsilon}{\partial t} = (D_{eff,Cl} C_{Cl} + D_{eff,CO_3^{2-}} C_{CO_3^{2-}}) \frac{\partial^2 \varepsilon}{\partial x^2} + v(C_{Cl} + C_{CO_3^{2-}}) \frac{\partial \varepsilon}{\partial x} + (C_{Cl} + C_{CO_3^{2-}}) \Gamma_w \quad (6.2. a) \\ \varepsilon \phi \frac{\partial C_{Cl}}{\partial t} = \varepsilon \phi D_{eff,Cl} \frac{\partial^2 C_{Cl}}{\partial x^2} + \varepsilon \phi v \frac{\partial C_{Cl}}{\partial x} - \frac{\partial C_{Cl,B}}{\partial t} \quad (6.2. b) \\ (1 - \varepsilon) \phi \frac{\partial C_{CO_2}}{\partial t} = (1 - \varepsilon) \phi D_{eff,CO_2} \frac{\partial^2 C_{CO_2}}{\partial x^2} + (1 - \varepsilon) \phi g \frac{\partial C_{CO_2}}{\partial x} - rCO_{2(aq)} \quad (6.2. c) \\ \varepsilon \phi \frac{\partial C_{CO_3^{2-}}}{\partial t} = \varepsilon \phi D_{eff,CO_3^{2-}} \frac{\partial^2 C_{CO_3^{2-}}}{\partial x^2} + \varepsilon \phi v \frac{\partial C_{CO_3^{2-}}}{\partial x} + rCO_3^{2-} - rC \quad (6.2. d) \\ \frac{\partial n_{CaCO_3}}{\partial t} = Ak (\Omega^n - 1)^m \quad (6.2. e) \\ \frac{\partial T}{\partial t} = \frac{k}{\rho C_p} \frac{\partial^2 T}{\partial x^2} \quad (6.2. f) \end{array} \right.$$

Eq.6.2.a; couples the degree of water saturation in pores, ε , via anomalous transport due to the moisture hysteresis effect present in the cementitious system, with dissolved ions, chlorides and carbonates, that result from chloride ingress and carbonation reactions.

Eq.6.2.b; defines the ingress of chloride ions, Cl^- , in the aqueous state, along with chloride binding by the formed cement hydrates.

Eq.6.2.c; describes the diffusion of carbon dioxide in the gaseous phase of the capillary pores of the concrete and its dissolution into the pore solution in the form of carbonate ions, CO_3^{2-} .

Eq.6.2.d; links the transport of formed carbonate ions with their consumption via the formation

of the carbonate phase calcite, CaCO_3 .

Eq.6.2.e; Rate of calcium carbonate formation, dependent on the concentration of free carbonate ions in the pore solution. Pseudo-steady state assumption is implemented in this research with rate limitation by the dissolution step of calcium-containing cement hydrates. This means that once the dissolution of calcium-containing cement hydrates (i.e. C-A-S-H) occurs then the precipitation of calcium carbonate takes place, leaving a very low dissolved concentration of C-A-S-H phase. Consequently, the change in the porosity is coded in the numerical model such that the amount of calcium carbonate formed is equal to the amount of calcium-containing cement hydrate dissolved until the maximum change in porosity has been reached (i.e. cement phase in concrete is fully carbonated) then the porosity, with the updated value, is set to remain constant throughout the remaining service life of the concrete.

Eq.6.2.f: Heat transfer through concrete due to the difference in temperature between the concrete and the environment. The effect of heat is taken into account in the calculation of the effective diffusion of the ionic species, Cl^- and CO_3^{2-} , in the aqueous phases of the capillary pores of the concrete.

6.3.2 Aging Factor of Concrete

Conductivity, which is the reciprocal of resistivity, has been used for the estimation of the mobility of ions in the pore solution of the concrete to estimate the rate of its deterioration in exposure conditions [234]. It has also been applied to measure the extent of the refinement of the pore structure in the cementitious matrix of the concrete as it ages with time [106]. This effect of aging slows down the transport of corrosive ions because it is highly dependent on the overall porosity and the interconnectivity of the pores inside the binder. The change in diffusional transport can be captured by **Equation 6.3** with updated values of the formation factor, F , at various ages [106]. The diffusion coefficient of ionic species “i” in concrete $D_{\text{eff},i}$ ($\text{m}^2 \cdot \text{year}^{-1}$), is calculated using the diffusion coefficient of ionic species in water, D_i ($\text{m}^2 \cdot \text{year}^{-1}$), and the formation factor of the concrete determined in saturated conditions [106]. The parameter $D_{\text{eff},i}$ multiplied by the degree of saturation in the concrete, as shown in **Equations 6.2.b** and **6.2.d**, is a method suggested by Isgor et al. [106] to model the ionic transport in saturated and unsaturated concrete. However, ionic transport models for concrete in unsaturated conditions can be used for more accurate representation of the service life of concretes in unsubmerged conditions such as the model developed in [235] which requires the degree of saturation and the average pore diameter of the cementitious material. Nevertheless, for this research the simplified version of ionic transport in saturated and unsaturated concrete is

implemented as a first step in coupling the effect of moisture transport, chloride ingress and carbonation on the service life of alkali-activated concretes. Still, future research is needed to improve the ionic and gaseous transport models in unsaturated alkali-activated concrete.

$$D_{\text{eff},i} = \frac{D_i}{F} \quad (6.3)$$

$D_{\text{eff},i}$; effective diffusion of ionic species in concrete

D_i ; diffusion of ionic species in water

F; formation factor

In this research the transport processes of two ionic species, Cl^- and CO_3^{2-} , are being modelled as a function of time and distance across the thickness of the concrete cover. One is the chloride ion with its diffusion value in water of $2.03 \times 10^{-9} \text{ m}^2 \cdot \text{s}^{-1}$, and the other is the carbonate ion with its diffusion value in water of $5.4468 \times 10^{-9} \text{ m}^2 \cdot \text{s}^{-1}$ [106, 236].

6.3.2.1 Formation Factor

The formation factor of concrete at a given age can be determined, as the ratio of the resistivity of the concrete, ρ_c , to the resistivity of the pore solution, ρ_s , according to **Equation 6.4** [106].

$$F = \frac{\rho_c}{\rho_s} \quad (6.4)$$

F; formation factor in saturated conditions

ρ_c ; resistivity of concrete ($\Omega \cdot \text{cm}$)

ρ_s ; resistivity of pore solution ($\Omega \cdot \text{cm}$)

In this research, the resistivity of the alkali-activated mortar is measured by the embedded electrode method. Next, the calculated ionic diffusion coefficients for the alkali-activated mortars is scaled to concrete with a scaling factor of 0.773. This value is calculated based on the difference between chloride migration values obtained for mortar and concrete, with similar mix designs (e.g. w/b=0.4), found in [152, 237]. This step is required to incorporate the effect of aggregates, that are absent in the mix design of alkali-activated mortars, on slowing down the transport of ionic species throughout the concrete cover [223]. Consequently, the results obtained from the NTBUILD 492 [11] (i.e. chloride migration test) is used to obtain the scaling factor because this test method incorporates the effect of the microstructure of concrete on the transport of ionic species throughout concrete and mortar sample [238, 239].

The resistivity of the pore solution has been calculated theoretically by obtaining the ionic composition of the pore solution by thermodynamic modelling, at a given degree of reactivity of the precursors, and by applying the NIST model [240] according to the set of **Equations 6.5-6.7**. The assumed reactivity for slag is 70% and for fly ash is 35%, which are the extreme values found for the reactivity of supplementary cementitious materials in blended cements reported in [194, 241], but given the variability found in [194] the selected values are suitable.

$$\rho_s = \left(\sum_i z_i c_i \lambda_i \right)^{-1} \quad (6.5)$$

$$\lambda_i = \frac{\lambda_i^0}{1 + G_i I^{0.5}} \quad (6.6)$$

$$I = 0.5 \sum_{i=1}^{n_s} c_i z_i^2 \quad (6.7)$$

λ_i^0 ; equivalent conductivity of the ionic species, in the pore solution, at infinite dilution ($\text{cm}^2 \cdot \text{S} \cdot \text{mol}^{-1}$)

G_i ; empirical coefficient for each ionic species at a given temperature ($\text{mol} \cdot \text{L}^{-1}$)^{-0.5}

I ; molar ionic strength ($\text{mol} \cdot \text{L}^{-1}$), that is the measure of the concentration of electrically charged ionic species in the pore solution [242].

The values of the coefficients, λ_i^0 and G_i , in **Equations 6.6** and **6.7** are given in **Table 6.2**.

Table 6.2 Properties of ionic species in concrete pore solution [106].

Species	$z_i \lambda_i^0$ at 25°C ($\text{cm}^2 \cdot \text{S} \cdot \text{mol}^{-1}$)	$G_i (\text{mol} \cdot \text{L}^{-1})^{-0.5}$
OH⁻	198	0.353
Ca²⁺	59	0.771
Cl⁻	76.4	0.548
Na⁺	50.1	0.733
K⁺	73.5	0.548
SO₄²⁻	79	0.877

6.3.2.2 Pore Solution Chemistry

A thermodynamic modelling programme was used to predict the concentration of dominant ions of the pore solution in AAMs and CEM III. As well as the alkalinity and ionic strength of the pore solution in AAMs and CEM III. The open source software GEM-Selektor v.3 (<https://gems.web.psi.ch/> [193]) was utilised, where the mineralogical composition, extent of degree of reaction for the precursors, and mix design of the alkali-activated binders were set as inputs in order to obtain the concentrations of ions present in the aqueous phase of the cements. The inputs to the software account for the extent of reactivity of the precursors used in AAMs and for the extent of reactivity of CEM III; these are provided in appendix 4 and 6, respectively. Details on the method of application of the open source software GEM-Selektor v.3 are explained in “**Chapter 3: Materials and Methods**”.

6.3.2.3 Aging with change in temperature

It is also useful to measure the changes in resistivity of the concrete as a function of temperature, since concrete is exposed to fluctuating ambient temperatures. The effect of temperature on the conductivity measurements has been applied through the Arrhenius equation according to **Equation 6.8** [234].

$$\sigma_x = \sigma_y e^{\frac{-E_a}{R} \left[\frac{1}{T_x} - \frac{1}{T_y} \right]} \quad (6.8)$$

σ_y ; conductivity recorded at temperature T_y

σ_x ; conductivity at reference temperature T_x

E_a ; activation energy of the conduction process

R ; universal gas constant ($8.314 \text{ J} \cdot \text{mol}^{-1} \cdot \text{K}^{-1}$)

Equation 6.8 is modified into resistivity measurements to calculate the effective diffusivity of ions as a function of temperature. The ionic diffusion coefficient obtained at the time where the mortars have been cured in ambient conditions (e.g. temperature 20°C and relative humidity 60%) for 28 days is considered as an initial value which will change with time and varying temperature, according to **Equation 6.9**.

$$D_e = D_0 \times t^m \times e^{\frac{E_a}{R} \times \left(\frac{1}{T_e} - \frac{1}{T_0} \right)} \quad (6.9)$$

D_0 ; initial effective chloride diffusion coefficient obtained on the 28th day.

m ; aging factor, can vary between 0 and 1, dimensionless.

E_a ; activation energy, J.mol⁻¹.

$T_{0,e}$; initial and final temperature

6.3.3 Moisture Permeability Models

The prediction of the degree of saturation of the pores in the concrete and moisture permeability is essential because the transport of ionic species is through the aqueous phase of the pores. The moisture propagates through the concrete and partly condenses on the walls of the pores, fills the pores with free water (i.e. evaporable water) and carries the ions by a bulk fluid motion known as liquid flow. The remaining part of the moisture remains as vapour phase in the empty space of the pore and transfers the gaseous components. This transport is known as vapour flow [5].

In this research, the dual moisture permeability model [62], discussed in **Chapter 5**: “Moisture Permeability in Alkali-activated materials”, has been implemented to predict the degree of water saturation by including the presence of the large and small porosity regions, along with their interconnection, present in the cement phase of the concrete. Conversely, the single moisture permeability model [79], discussed in Chapter 5: “Moisture Permeability in Alkali-activated materials”, has been implemented to predict the degree of saturation in the cement phase of the concrete’s skin layer (i.e. a mortar phase). The spatial discretization is further explained in section 6.4. **Equation 6.2.a** describes the transport of ionic species through the aqueous phase of the pores as a function of degree of saturation ε , their effective diffusional transport D , the flow velocity of the evaporable water v , and the flow of evaporable water in the interconnectivity region between the small and large pore regions Γ_w , in the concrete phase.

$$(c_{Cl^-} + c_{CO_3^{2-}}) \frac{\partial \varepsilon}{\partial t} = (D_{eff,Cl^-} c_{Cl^-} + D_{eff,CO_3^{2-}} c_{CO_3^{2-}}) \frac{\partial^2 \varepsilon}{\partial x^2} + v(c_{Cl^-} + c_{CO_3^{2-}}) \frac{\partial \varepsilon}{\partial x} + (c_{Cl^-} + c_{CO_3^{2-}}) \Gamma_w \quad (6.2.a)$$

$c_{Cl^-,CO_3^{2-}}$; concentration of chloride and carbonate ions, mol.L⁻¹

$D_{Cl^-,CO_3^{2-}}$; diffusion coefficient of chloride and carbonate ions, m².year⁻¹

ε ; degree of saturation

v ; liquid flow velocity, m.year⁻¹

Γ_w ; flow of evaporable water in the interconnectivity region between the small and large pore regions in the concrete, 1.year⁻¹

In addition, the velocity component of the liquid phase from the moisture is implemented to model the transfer of ions in the aqueous phase, and the velocity component of the vapour phase is used to model the transfer of gaseous components across the empty space of the pores. The flow velocity components (i.e. in m.year⁻¹) for evaporable water and vapour, v and g respectively, are both calculated according to **Equations 6.10** and **6.11** that are obtained from the moisture permeability model (i.e. single and dual permeability moisture transport models [62, 79]).

$$v = -k_{rl} \frac{K_l}{\phi \eta} \frac{\partial P_c}{\partial S} \frac{\partial S}{\partial x} \quad (6.10)$$

$$g = -\left(\frac{M_v}{\rho_l RT}\right)^2 D_{v0} f(S, \phi) \frac{P_{vs} \phi}{\phi} \frac{\partial P_c}{\partial S} \frac{\partial S}{\partial x} \quad (6.11)$$

It should be noted that Equation 6.13 is similar to Darcy's law [243], that describes the flow of a fluid (i.e. free water in this research) through a porous medium as a function of liquid pressure gradient, ∇P_L , according to **Equation 6.12**. Instead, Equation 6.13 utilizes the liquid water saturation gradient, ∇S , which is related to the liquid pressure gradient [5, 79]. Moreover, the porosity parameter, that is already included in **Equation 6.10**, accounts for the change of intrinsic permeability factor, K , as a function of changes in the porosity of the concrete as a result of carbonation reaction. A similar approach was implemented by Xie et al. [5] in their research where they have used Darcy's law to model the transport of free water through the pores of the concrete and the change of the intrinsic permeability factor was calculated through a relationship, found in [244], that accounts for the changes in the porosity of the concrete.

$$v = -\frac{K_l}{\eta} \frac{\partial P_L}{\partial x} \quad (6.12)$$

6.3.4 Transport of Ions and Carbonation Reaction

6.3.4.1 Chloride Ingress Model

Equation 6.2.b describes the transport of free chloride ions in the aqueous phase of the concrete through diffusion, driven by the concentration gradient and by the flow of pore solution (i.e. containing the evaporable water). Along with the diffusion of chloride ions in concrete, the hydrates tend to bind to some of the ions and form reaction products. This chloride binding in concrete is a durability factor because it removes chloride ions from the pore solution and reduces the concentration of free chloride ions from accumulating at the surface of the steel reinforcement [52]. Therefore, the chloride binding capacity of a concrete is an important parameter for service life prediction of reinforced concrete structures. Furthermore, Equation 6.2.b is further arranged as shown in Equations **6.13.a-6.13.e**.

$$\phi\varepsilon \frac{\partial C_{Cl}}{\partial t} = \phi\varepsilon D_{\text{eff,Cl}} \frac{\partial^2 C_{Cl}}{\partial x^2} + \phi\varepsilon v \frac{\partial C_{Cl}}{\partial x} - \frac{\partial C_{cl,B}}{\partial t} \quad (6.2.b)$$

$$\frac{\partial C_{Cl}}{\partial t} = D_{\text{eff,Cl}} \frac{\partial^2 C_{Cl}}{\partial x^2} + v \frac{\partial C_{Cl}}{\partial x} - \frac{1}{\phi\varepsilon} \frac{\partial C_{cl,B}}{\partial t} \quad (6.13.a)$$

$$\frac{\partial C_{Cl}}{\partial t} + \frac{1}{\phi\varepsilon} \frac{\partial C_{cl,B}}{\partial t} = D_{\text{eff,Cl}} \frac{\partial^2 C_{Cl}}{\partial x^2} + v \frac{\partial C_{Cl}}{\partial x} \quad (6.13.b)$$

$$\frac{\partial C_{Cl}}{\partial t} + \frac{1}{\phi\varepsilon} \left(\frac{\partial C_{cl,B}}{\partial C_{cl}} \frac{\partial C_{cl}}{\partial t} \right) = D_{\text{eff,Cl}} \frac{\partial^2 C_{Cl}}{\partial x^2} + v \frac{\partial C_{Cl}}{\partial x} \quad (6.13.c)$$

$$\frac{\partial C_{Cl}}{\partial t} \left(1 + \frac{1}{\phi\varepsilon} \frac{\partial C_{cl,B}}{\partial C_{cl}} \right) = D_{\text{eff,Cl}} \frac{\partial^2 C_{Cl}}{\partial x^2} + v \frac{\partial C_{Cl}}{\partial x} \quad (6.13.d)$$

$$\frac{\partial C_{Cl}}{\partial t} = \frac{D_{Cl}}{\left(1 + \frac{1}{\phi\varepsilon} \frac{\partial C_{cl,B}}{\partial C_{cl}} \right)} \frac{\partial^2 C_{Cl}}{\partial x^2} + \frac{v}{\left(1 + \frac{1}{\phi\varepsilon} \frac{\partial C_{cl,B}}{\partial C_{cl}} \right)} \frac{\partial C_{Cl}}{\partial x} \quad (6.13.e)$$

C_{Cl} ; free chloride concentration (mol.L^{-1})

D_{Cl} ; effective chloride diffusion coefficient ($\text{m}^2.\text{year}^{-1}$)

$\frac{\partial C_{Cl,B}}{\partial t}$; rate of chloride to be adsorbed or bound to the cement hydrates (mol.L⁻¹.year⁻¹)

v; liquid flow velocity (m.year⁻¹)

In Equation (6.13.e) the $\frac{\partial C_{Cl,B}}{\partial C_{Cl}}$ term is the derivative form of the Langmuir binding isotherm, with respect to C_{Cl} , and the unit is ((mg Cl. L)/(g binder. mol Cl)) [113]. This term needs to become dimensionless to have the same units on both sides of Equation 6.16.f. Consequently, **Equation 6.13.e** is modified into **Equation 6.14**.

$$\frac{\partial C_{Cl}}{\partial t} = \frac{D_{eff,Cl}}{\left(1 + \left(\frac{\rho_b}{\theta}\right) \left(\frac{1}{M_{Cl}}\right) (f_b) \left(\frac{\alpha(1+\beta C_{Cl}) - \alpha\beta C_{Cl}}{(1+\beta C_{Cl})^2}\right)\right)} \frac{\partial^2 C_{Cl}}{\partial x^2} + \frac{v}{\left(1 + \left(\frac{\rho_b}{\theta}\right) \left(\frac{1}{M_{Cl}}\right) (f_b) \left(\frac{\alpha(1+\beta C_{Cl}) - \alpha\beta C_{Cl}}{(1+\beta C_{Cl})^2}\right)\right)} \frac{\partial C_{Cl}}{\partial x} \quad (6.14)$$

ρ_b ; binder density (kg of cement per L of cement, 1.96 [245]).

θ ; evaporable water content (volume of the liquid pore solution (in L) per pore volume of the concrete (in L), obtained by multiplying the degree of saturation, ε , by the porosity of the concrete, ϕ).

M_{Cl} ; Molar mass of chloride (g/mol).

f_b ; volumetric fraction of the binder in concrete (L/L)

$\frac{\partial C_{Cl,B}}{\partial C_{Cl}}$; Langmuir binding isotherm for alkali-activated cements ((mg Cl. L)/(g binder. mol Cl)), obtained from [113].

The volumetric fraction of the binder is obtained by using the density of the binder, 1.96 [245], and the density of the concrete, 2540 kg.m⁻³, with the mass of binder used to produce 1 m³ of alkali-activated concrete, 410 kg.m⁻³. The binder content of the alkali-activated concretes is obtained from [98] because the mix design of the alkali-activated binders in these concretes is similar to the mix design of the 100SG, 75SG25FA and 50SG50FA binders used in the studied alkali-activated mortars according to Table 6.1. Additionally, the volumetric fraction of the binder in concrete is implemented in Equation 6.17 because the boundary and initial conditions of chloride content, C_{Cl} , are defined in mol of chloride per L of concrete. The boundary and initial conditions are further explained in section 6.4.2.3.

6.3.4.2 Carbonation Model

6.3.4.2.1 CO₂ transport and dissolution in pore solution

The first step in carbonation is the diffusion of CO₂ gas molecules into the empty space of the capillary pores of the concrete and its dissolution into the alkaline pore solution, according to **Equation 6.15**.



Equation 6.2.c describes the transport process of CO₂ through diffusion and vapour flow, as well as mass transfer of CO₂ from the gas phase into the liquid phase. The diffusional transport is caused by a concentration gradient, vapour flow is induced by a moisture gradient, and the mass transfer of CO₂ to the pore aqueous phase is caused by the chemical potential gradient between the gas and liquid phases in the pore. **Equation 6.2.c** is rearranged to give **Equation 6.16**.

$$\phi(1 - \varepsilon) \frac{\partial C_{\text{CO}_2}}{\partial t} = \phi(1 - \varepsilon) D_{\text{eff,CO}_2} \frac{\partial^2 C_{\text{CO}_2}}{\partial x^2} + \phi(1 - \varepsilon) g \frac{\partial C_{\text{CO}_2}}{\partial x} - r\text{CO}_{2(\text{aq})} \quad (6.2.c)$$

$$(1 - \varepsilon) \frac{\partial C_{\text{CO}_2}}{\partial t} = (1 - \varepsilon) D_{\text{eff,CO}_2} \frac{\partial^2 C_{\text{CO}_2}}{\partial x^2} + (1 - \varepsilon) g \frac{\partial C_{\text{CO}_2}}{\partial x} - \frac{r\text{CO}_{2(\text{aq})}}{\phi} \quad (6.16)$$

$D_{\text{eff,CO}_2}$; effective diffusion of CO₂, m².year⁻¹

g ; vapour flow rate, m.year⁻¹

$r\text{CO}_{2(\text{aq})}$; rate of CO₂ dissolution into pore solution, (mol.L⁻¹.year⁻¹)

Equation 6.17 describes the diffusion of CO₂ by accounting for the tortuosity and porosity of the cementitious material. This equation has been formulated from an accelerated carbonation experiment where a granular bed of cement paste particles was exposed to a 10% CO₂ environment [246].

$$D_{\text{CO}_2} = D_{\text{CO}_2}^0 \times \phi^{2.7} \times (1 - \varepsilon)^{4.2} \quad (6.17)$$

$D_{\text{CO}_2}^0$; CO₂ diffusion coefficient in air, 1.6×10^{-5} m²/s, at T = 293 K and P_{atm} = 101.325 kPa

The rate of gas-liquid mass transfer for CO₂ from the gas phase, CO_{2(g)}, into the dissolved phase, CO_{2(aq)}, is determined by the gas/liquid exchange surface, its partial pressure in the gas phase, and its concentration in the pore solution [247]. **Equation 6.18** describes the rate of formation of CO_{2(aq)} as being proportional to the deviation of the actual dissolved CO₂ concentration at any point in time from equilibrium [118], where the repartition of CO_{2(g)} to water at equilibrium is governed by Henry's law [118].

$$r\text{CO}_{2(\text{aq})} = k_t(k_{\text{henry}}C_{\text{CO}_{2(\text{g})}} - C_{\text{CO}_{2(\text{aq})}}) \quad (6.18)$$

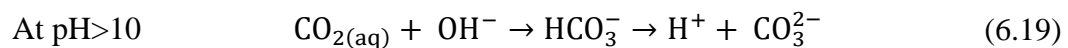
$r\text{CO}_{2(\text{aq})}$; rate of CO₂ dissolution into pore solution, (mol.L⁻¹.year⁻¹)

k_t ; interfacial gas-liquid mass transfer coefficient for CO₂ , (year⁻¹)

k_{henry} ; 0.8317 (dimensionless) is Henry's Law constant for equilibrium partitioning of CO₂ gas to water [248].

6.3.4.2.2 Formation and transport of carbonate ion

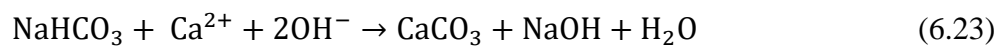
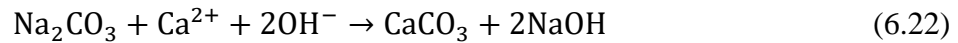
Kashef-Haghighi et al. [118] described the overall dominant reaction of CO_{2(aq)} in the pore solution to be hydrolysis, as shown in **Equation 6.19**. This is for the case when the pore solution alkalinity remains above 10.



This is also the condition of pore solution in fresh and carbonated high and low calcium AAMs, where the pore solutions of these materials remain above 10 even under accelerated conditions at 1% CO₂ when cured under sealed conditions and at RH = 55% as reported in [138]. Thus, it can be considered that the reaction described in equation 6.23 is the dominant first step of reaction of CO_{2(aq)} in the pore solution of AAMs.

The next step in carbonation of pore solution is the reaction of the formed carbonate ions with NaOH, that is dominantly present in the pore solution of AAMs as reported in [249]. The reaction products are sodium carbonates and bicarbonates as shown in **Equations 6.20-6.21**. Generally, the alkali (bi)carbonates are highly mobile and soluble in water, resulting in a dissociation reaction and the release of carbonate ions back into the solution [250]. Then these carbonate ions react with calcium ions that have been released during the dissociation of C-A-

S-H (the dominant hydrate in high calcium AAMs), as a result of the drop of the alkalinity of the pore solution during carbonation, to form insoluble calcium carbonates as shown in **Equations 6.22** and **6.23** [129, 247].



Equation 6.2.d describes the transport of dissolved $\text{CO}_{2(\text{aq})}$ in the pore solution. This equation is furthermore modified to obtain **Equation 6.24**. However, it is assumed in this research that $\text{CO}_{2(\text{aq})}$ immediately forms into carbonate ions according to **Equation 6.19**. Hence, **Equation 6.25** is implemented to model the transport of free carbonate ions through the aqueous phase of the pores by the diffusion term followed by the flow of pore solution, the rate of formation of CO_3^{2-} ions from $\text{CO}_{2(\text{aq})}$ and then the rate of consumption of carbonate ions during the formation of carbonate phases.

$$\phi\varepsilon \frac{\partial C_{\text{CO}_2(\text{aq})}}{\partial t} = \phi\varepsilon D_{\text{CO}_2(\text{aq})} \frac{\partial^2 C_{\text{CO}_2(\text{aq})}}{\partial x^2} + \phi\varepsilon v \frac{\partial C_{\text{CO}_2(\text{aq})}}{\partial x} + r_{\text{CO}_2(\text{aq})} - r_{\text{C}} \quad (6.2.d)$$

$$\varepsilon \frac{\partial C_{\text{CO}_2(\text{aq})}}{\partial t} = \varepsilon D_{\text{CO}_3^{2-}} \frac{\partial^2 C_{\text{CO}_2(\text{aq})}}{\partial x^2} + \varepsilon v \frac{\partial C_{\text{CO}_2(\text{aq})}}{\partial x} + \frac{r_{\text{CO}_2(\text{aq})}}{\phi} - \frac{r_{\text{C}}}{\phi} \quad (6.24)$$

$$\varepsilon \frac{\partial C_{\text{CO}_3^{2-}}}{\partial t} = \varepsilon D_{\text{CO}_3^{2-}} \frac{\partial^2 C_{\text{CO}_3^{2-}}}{\partial x^2} + \varepsilon v \frac{\partial C_{\text{CO}_3^{2-}}}{\partial x} + \frac{r_{\text{CO}_3^{2-}}}{\phi} - \frac{r_{\text{C}}}{\phi} \quad (6.25)$$

$D_{\text{CO}_3^{2-}}$; effective diffusivity of carbonate ions, $\text{m}^2 \cdot \text{year}^{-1}$

$r_{\text{CO}_3^{2-}}$; rate of production of carbonate from dissolved $\text{CO}_{2(\text{aq})}$, $\text{mol} \cdot \text{L}^{-1} \cdot \text{year}^{-1}$

r_{C} ; rate of consumption of carbonate ions (i.e. $\text{CO}_{2(\text{aq})}$ transformed to CO_3^{2-} , as shown in equation 6.23) to form carbonate phases, $(\text{mol} \cdot \text{L}^{-1} \cdot \text{year}^{-1})$

Where the rate of formation of bicarbonate, HCO_3^- , and carbonate ions, CO_3^{2-} , is calculated according to **Equation 6.26**, adapted from [251].

$$r\text{CO}_3^{2-} = k[\text{OH}^-][\text{CO}_{2(\text{aq})}] \quad (6.26)$$

Kashef-Haghighi et al. [118] have implemented the kinetic **Equations (e.g. 6.18 and 6.26)** for the dissolution of $\text{CO}_{2(\text{g})}$, the formation of carbonate and bicarbonate ions, and the consumption of these ions in their model for the uptake of CO_2 by Portland cement based mortar exposed to accelerated carbonation of 20-40% CO_2 condition. The kinetic rate values implemented by Kashef-Haghighi et al. [118] are extremely high, and cannot be transferable for the case of concrete exposed to natural carbonation conditions of 0.04% CO_2 in the environment.

Consequently, several modifications and assumptions for the reaction kinetics of natural carbonation reaction have been made in this research. The first assumption is that the interfacial gas-liquid mass transfer coefficient for CO_2 in **Equation 6.18**, k_t , is set to 1 such that the dissolution rate of $\text{CO}_{2(\text{g})}$ is only dependent on the concentration of the dissolved CO_2 gas (i.e. calculated through Henry's law [248]: $C_{\text{CO}_{2(\text{aq})}} = k_{\text{henry}}C_{\text{CO}_{2(\text{g})}}$) in the liquid phase. The second assumption is that 100% of the dissolved $\text{CO}_{2(\text{aq})}$ is converted to carbonate ions in each time step, as shown in **Equation 6.27**, which means that the impact of changes in the alkalinity of the pore solution, in **Equation 6.26**, is omitted. Finally, 95% of carbonate ions are assumed to be consumed to form calcium carbonate phases, as shown in **Equation 6.28**, which means that the impact of the formation of calcium carbonate on the reduction of the exposed surface area of the reactive solids for carbonation reactions is also omitted. Additionally, percentage values of 100% and 95% for the conversion rate of carbonate ions and the formation rate of calcium carbonate, respectively, are selected because of the high alkalinity of pore solution that accelerates the formation of calcium carbonate [138, 252].

$$\frac{r\text{CO}_3^{2-}}{\phi} = \frac{r\text{CO}_{2(\text{aq})}}{\phi} \quad (6.27)$$

$$\frac{r\text{C}}{\phi} = 0.95 \times \frac{r\text{CO}_3^{2-}}{\phi} \quad (6.28)$$

Overall, the impact of carbonation is the change in the morphology of cement by the dissolution of calcium-containing cement hydrates (i.e. C-A-S-H) and precipitation of calcium carbonate phases [147]. Therefore, the change in porosity, as a durability factor, should be estimated for each time step in the numerical model because the ionic transport is generally very sensitive to porosity values. Additionally, all the kinetic parameters for the carbonation reaction will be varied in the sensitivity analysis to assess their effects in service life predictions through changes in overall porosity of the concrete. The next section describes the kinetic model used to calculate the change in porosity at each time step.

6.3.4.2.3 *Precipitation kinetic model*

The rate law used to calculate the precipitation of calcite in the numerical model is similar to the one used by Gebrehiwet et. al [253] where the affinity-based rate law, **Equation 6.29**, is applied. In this research, congruent dissolution of the C-A-S-H phase in AAMs and precipitation of CaCO₃ is assumed. This assumption of identical dissolution and precipitation law is based on an assumption of pseudo-steady-state for dissolved calcium concentration in the pore solution, and has also been considered in [17] .

$$R = kA_T(\Omega^n - 1)^m \quad (6.29)$$

R; precipitation rate, mol. year⁻¹

k; rate constant, mol.m⁻².year⁻¹

A_T; total surface area, m²

n and m; exponents, both assumed to be 1.0 according to [17]

The mineral saturation index (SI), Ω , is a tool used to assess the saturation state of a mineral in a solution by calculating the ratio of the activity product of its ions (IAP), in the solution, to its solubility product constant, K_{sp} [254]. **Equation 6.30** shows that the equilibrium between the mineral and the solution ions is reached when SI is equal to 0. The mineral starts to precipitate when the SI > 0 and dissolves when the SI < 0, until equilibrium is reached in these two cases. **Equation 6.30** describes the mineral saturation state for calcite as a function of the ion activity product of its ions and the solubility product constant.

$$\Omega = \left(\frac{\gamma_{\text{Ca}^{2+}} [\text{Ca}^{2+}] \times \gamma_{\text{CO}_3^{2-}} [\text{CO}_3^{2-}]}{K_{\text{sp, CaCO}_3}} \right) \quad (6.30)$$

$\gamma_{\text{Ca}^{2+}} [\text{Ca}^{2+}] \times \gamma_{\text{CO}_3^{2-}} [\text{CO}_3^{2-}]$; ion activity product for CaCO_3 , that is the product of the concentration of each ion with their activity coefficient, γ .

$K_{\text{sp, CaCO}_3}$; solubility product constant, $3.3 \times 10^{-9} \text{ mol}^2 \text{L}^{-2}$ [255].

In this research the calculation of saturation index is implemented as a function of the free carbonate ions in the pore solution calculated from **Equation 6.25**. However, the concentration of calcium ions is kept constant, and the details for the estimation of its fixed value in naturally carbonated pore solution of AAMs are explained in the next section.

6.3.4.2.4 *Concentration of calcium ions in carbonated pore solution of AAMs*

The concentration of calcium ions in carbonated pore solution of AAMs is calculated using **Equation 6.30** by implementing the maximum concentration of carbonate ion that can be reached from the dissolution of $\text{CO}_{2(\text{g})}$. The maximum concentration of carbonate ion is calculated using **Equation 6.18** with the initial concentration of $\text{CO}_{2(\text{aq})}$ (i.e. CO_3^{2-}) set to 0 mol/L and concentration of $\text{CO}_{2(\text{g})}$ set to 0.0096 mol/L \equiv 421 ppm, that is the concentration of $\text{CO}_{2(\text{g})}$ in ambient air [256]. Thus, the highest concentration for carbonate ion in the pore solution of the binder is calculated to be 0.00796 mol.L⁻¹. Next, the activity coefficients of Ca^{2+} and CO_3^{2-} are initially assumed to be 1 and the saturation index, Ω , is set to 1.5. The value of 1.5 is selected to have a positive rate of formation of calcium carbonate, according to **Equation 6.31**, and because the concentration of carbonate ion is low compared to the concentration of 0.45 mol.L⁻¹ for carbonate ions used in aqueous solution to obtain a saturation index between 9 and 10 as reported in [253]. Subsequently, the new activity coefficients of Ca^{2+} and CO_3^{2-} are obtained from the output of the Pitzer model [257] as implemented in the PitzerXXL spreadsheet [258] by inputting the concentration of the dominant ions present in the pore solution of AAMs, the concentration of carbonate ion (0.00796 mol.L⁻¹) and the calculated concentration of calcium ion. In addition, the concentration of hydroxide ion is slightly modified from its original value in the pore solution of AAMs to maintain the charge balance of the carbonated pore solution. Finally, the calcium concentration is recalculated by using **Equation 6.30** with the new values for the activity coefficients of Ca^{2+} and CO_3^{2-} . The concentration of calcium ions in the carbonated pore solution of AAMs, and activity

coefficients of calcium and carbonate ions in the carbonated pore solution for all the alkali-activated binders are shown in **Table 6.8**. Further details, and outputs from the PitzerXXL spreadsheet containing the concentration of pore solution ions with their activity coefficients for carbonated alkali-activated binders and calculation of calcium ion concentration in carbonated pore solution of AAMs, are shown in appendices 6.B and 6.C.

6.3.4.2.5 Formation of Calcium Carbonate

Equation 6.31 is used to calculate the amount of calcium carbonate formed, in moles. year⁻¹, as a function of the concentration of free carbonate ions in the pore solution, calculated from **Equation 6.25**, with the concentration of calcium ion kept constant in carbonated pore solution of AAMs. The calculated concentration of calcium ion in the carbonated pore solution for each alkali-activated binder is presented in **Table 6.8**. The rate constant (k_c), which is the combination of $k \times A_T$, is empirically calculated, based on the change in porosity of alkali-activated pastes exposed to natural laboratory carbonation conditions (55% RH and 20°C) for a period of 1 year, as shown in **Table 6.3**. The calculation of k_c is obtained by implementing the maximum concentration of calcium and carbonate ions that can be reached in naturally carbonated pore solution of AAMs. The values of the rate constant, k_c , are also shown in **Table 6.8**.

$$R = k_c \left(\frac{\gamma_{Ca^{2+}} [Ca^{2+}] \times \gamma_{CO_3^{2-}} [CO_3^{2-}]}{K_{sp,CaCO_3}} - 1 \right) \quad (6.31)$$

k_c ; rate constant, mol. year⁻¹

$K_{sp,CaCO_3}$; solubility product constant, 3.3×10^{-9} mol²L⁻² [255].

Table 6.3 Change in porosity of naturally carbonated alkali-activated fly ash and slag based cements. MIP data obtained from [147].

Binder	Total porosity (vol.%) - uncarbonated	Total porosity (vol. %) - carbonated	Porosity change (%)
100%SG	3.57	3.38	-5.3%
70%SG30%FA	6.54	9.66	+48%
50%SG50%FA	9.40	17.09	+82%

In this research the rate law is assumed identical for the C-A-S-H and CaCO_3 phases based on the assumption of congruent dissolution of the C-A-S-H phase and precipitation of the CaCO_3 phase. This means that the amount of calcite formed is set equal to the amount of C-A-S-H phase dissolved while calculating the change in porosity in the numerical model. Equation 6.37 is implemented to calculate the change in porosity at each time step in the numerical model.

Finally, according to the porosity change in **Table 6.3** the overall porosity, dependent on the type of binder, can either decrease or increase. Consequently, **Equation 6.32** is set as “+” for an increase in porosity and “-” for decrease in the overall porosity of the concrete.

$$\varphi_u = \varphi_0 \pm \sum_j V_j \Delta n \quad (6.32)$$

φ_u ; updated porosity of the concrete

φ_0 ; initial porosity of the concrete

V_j ; molar volume of the solid phase j (m^3/mol)

Δn ; change in the molar amount of the solid phase (mol)

V_{CASH} ; molar volume of the C-A-S-H phase, 64.5×10^{-6} (m^3/mol) [123]

V_{CaCO_3} ; molar volume of the CaCO_3 phase, 36.943×10^{-6} (m^3/mol) [123]

The molar change in the solid phase, Δn , is set to be equal to the amount of formed calcium carbonate with its initial amount set to zero based on the assumption that the alkali-activated binders did not undergo a carbonation reaction during the period of curing.

6.3.5 Transport of Heat in Concrete

In this research the heat transfer model for conduction across the thickness of the concrete cover is chosen to predict the temperature profile in the construction material when exposed to higher or lower temperature environmental condition with respect to its internal cover temperature. The basic equation of the heat transfer model with respect to the thickness of the concrete cover, x , and time, t , is **Equation 6.33**, adapted from [259] .

$$\frac{\partial T}{\partial t} = \frac{k}{\rho C_p} \frac{\partial^2 T}{\partial x^2} \quad (6.33)$$

k ; thermal conductivity of concrete, $1.628 \text{ W.m}^{-1}.\text{K}^{-1}$ [260].

ρ ; density of the concrete, 2500 kg.m^{-3} [260].

C_p ; Heat capacity of concrete, $837 \text{ J.Kg}^{-1}.\text{K}^{-1}$ [260].

The change in temperature across the concrete cover is implemented in the effective diffusion coefficients, as shown in **Equation 6.9**, for the transport of chloride and carbonate ions throughout the aqueous phase of the pores of the concrete.

6.4 Spatial Discretization, Boundary and Initial Conditions

6.4.1 Spatial Discretization

Modelling transport of ionic species in the liquid phase and CO_2 in the gas phase of the pores in concrete should be done mainly in two phases, according to **Figure 5.53**, as was discussed in Chapter 5. In this research, the spatial discretization contains an interface such that the first 5 mm of thickness is mortar phase and the remaining cover is concrete phase. In the mortar skin layer, the liquid phase transport is simulated by the single permeability model based on the assumption that the mortar phase has a more uniform pore size distribution than the bulk concrete. In the remaining concrete cover, 45 mm, the liquid phase transport is simulated by the dual permeability model to account for the presence of large and small pore regions present in the cement phase of the concrete. The porosities of alkali-activated concretes and mortars with similar mix designs to the studied alkali-activated mortars are obtained from [152, 261]. These porosities in each layer are implemented in the numerical model as initial conditions and are subjected to changes caused by the carbonation reaction, as explained in section 6.3.4.2. Also, the effective diffusion of ionic and gaseous transports is set to be slightly slower in the concrete phase than in the mortar phase. The upscaling of diffusion coefficients for the alkali-activated mortars to concrete with a scaling factor of 0.773 has already been discussed in section 6.3.2.1, and it is also applied in the skin layer and concrete phase of the concrete cover. Finally, the thickness of the concrete cover and skin layer will be varied in the sensitivity analysis to check the impact on service life calculation for alkali-activated mortars.

6.4.2 Boundary and Initial Conditions

6.4.2.1 Relative Humidity

The boundary condition is set based on type of exposure states that are: 50% RH for drying and 100% RH for wetting conditions. Also the values of the initial conditions are set by whether the concrete is initially dried, 50% RH, or wet, 100%RH.

6.4.2.2 Temperature

The boundary conditions can be set to vary between 10-40°C, whereas the initial condition is set at ambient temperature 20°C.

6.4.2.3 Carbon dioxide concentration

It is assumed that the gas phases in the empty space of the pores of the concrete are constantly connected to the atmosphere and the pressure equilibrium is always conserved. This assumption has also been stated in [5] for modelling simultaneous ingress of chloride and carbonation in concrete. Hence, for natural carbonation conditions, the boundary concentration is set to 0.0096 mol.L⁻¹ \equiv 421 ppm which is the concentration of CO_{2(g)} in ambient air [256]. The initial concentration is taken as 0 mol.L⁻¹.

6.4.2.4 Carbonate concentration

The carbonate concentration at the boundary condition is taken from the value obtained from Henry's law that depicts the repartition of gaseous CO₂ and its dissolved form CO_{2(aq)} (assumed instantaneously converted to CO₃²⁻), in the pore solution of the concrete, according to **Equation 6.34** [118, 248].

$$H_s^{cc} = \frac{c_{aq}}{c_{gas}} \quad (6.34)$$

H_s^{cc} ; Henry's constant, 0.8317 at 25°C, unitless.

c_{aq} ; concentration of CO₂ in the aqueous phase, mol.L⁻¹

c_{gas} ; concentration of CO₂ in the gaseous phase, mol.L⁻¹

Therefore, the carbonate concentration at the boundary condition is set to 0.00796 mol.L⁻¹ and the initial concentration is taken as 0 mol.L⁻¹.

6.4.2.5 Chloride Concentration

The boundary condition of surface chloride concentration can vary depending on the type of structure, its geographic location, and zone of exposure as shown in **Table 6.4** obtained from [262]. The surface concentration can be a constant, in the case of a marine splash zone, and/or can go through a linear build-up rate during the first couple of service years, and then stabilize, dependent on the type of exposure condition. This can indicate that the maximum time to reach the maximum surface chloride concentration can vary from instantaneous (Inst.) to about 31 years in the case of a structure within 1.5 km of the ocean. Note that the application of de-icing salts is not included because the effect of freezing-thawing on the durability of concrete is excluded in this research. Furthermore, the values obtained for chloride in wt.% of the concrete, shown Table 6.4, are multiplied by the density of the concrete (2.540 kg.L^{-1}) then divided by the molar mass of chloride, $35.453 \text{ g.mol}^{-1}$, to obtain the chloride concentration in concrete in mol.L^{-1} .

Table 6.4 Build-up rates and maximum surface concentration, dependent on various zones. Data obtained from [262].

	Build-up Rate (% wt.conc .year⁻¹)	Maximum (% wt.conc.)	Build-up Rate (mol.L⁻¹.year⁻¹)	Maximum (mol.L⁻¹)
Marine splash zone	Inst.	0.8	Inst.	0.57
Marine spray zone	0.1	1.0	0.07	0.72
Within 800 m of the ocean	0.04	0.6	0.03	0.43
Within 1.5 km of the ocean	0.02	0.6	0.014	0.43

As for the initial condition, the maximum allowed chloride content in concrete containing steel reinforcement, according to BS EN 206 standard [191], is 0.2 wt.% of cement. This wt.% of cement is converted to wt.% of the concrete, by multiplying the ratio of the total weight of the binder (i.e. 410 Kg.m^{-3}) used in concrete to the total weight of the concrete (i.e. 2540 kg.m^{-3}). Finally, the initial chloride content in wt.% of the concrete is multiplied by the density of the concrete (2.540 kg.L^{-1}) and then divided by the molar mass of chloride to obtain the chloride concentration in concrete in mol.L^{-1} . The value obtained for the initial chloride content in concrete is 0.02 mol.L^{-1} .

6.5 Critical Chloride Threshold

The critical chloride threshold for the alkali-activated concretes is described using a lognormal distribution according to **Equation 4.5**, based on the distribution of data, in wt.% of the binder, shown in **Figure 6.1**. The values of the distribution of critical chloride thresholds have been

previously calculated in section 4.1 of Chapter 4 “Probabilistic Service Life Prediction of Alkali-Activated Concrete”. However, the outliers and data along the whiskers of the box plots for C_{crit} in section 4.1 are excluded in order to have the distribution around the median value for 100SG and 50SG50FA concretes. In the absence of specific information, the distribution of critical chloride threshold, C_{crit} , for 75SG25FA concrete is set equal to the distribution of C_{crit} for 100SG concrete in this research.

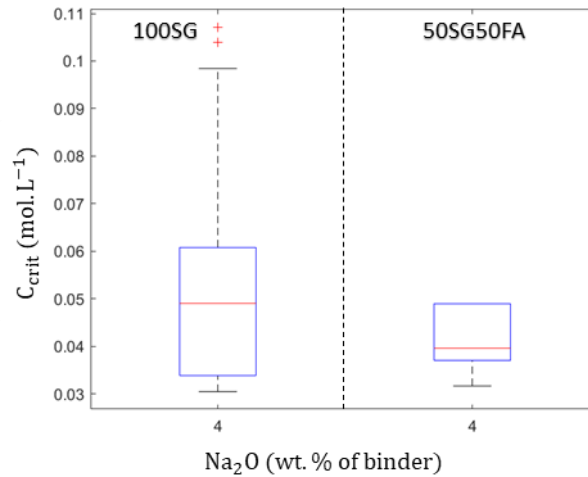


Figure 6.1 C_{crit} (mol.L⁻¹) of high calcium AAMs, 100%SG and 50%SG50%FA, as a function of alkali dosage (wt.% of binder).

6.6 Modelling Summary

The system of PDEs defined in Equation 6.42 describes the physical-chemical phenomena taking place inside unsaturated concrete exposed to simultaneous chloride ingress and carbonation reactions. This system of PDEs is solved using a dedicated Matlab code.

In summary, the moisture transport model, **Equation 6.2.a** simulates the transport of ionic species in the aqueous phase of the pores of the concrete. However, the unit of chloride concentration is set as mol of Cl per litre of the solid concrete. Consequently, the unit of chloride concentration in **Equation 6.2.a** should change to mol per litre of the pore solution. Hence, **Equation 6.2.a*** is implemented to calculate the concentration of chloride in the pore solution of concrete and it is denoted as C_{Cl}^* .

$$C_{Cl}^* = \frac{C_{Cl}}{\theta} \quad (6.35)$$

C_{Cl} ; mol of Cl per L of concrete

θ ; evaporable water content (volume of the liquid pore solution (in L) per pore volume of the concrete (in L)), obtained by multiplying the degree of saturation, ε , by the porosity of the concrete, ϕ .

Next, the chloride transport model **Equation 6.14** simulates the transport of chloride through the aqueous phase of the pores of the concrete along with possible chloride binding reaction. The unit for chloride concentration is defined in terms of mol of Cl per L of the concrete because infield practice the concentration of chloride across the concrete cover of a structure exposed to a marine environment is determined in terms of wt.% of the binder or wt.% of the concrete [12, 13, 163]. The transport of $CO_{2(g)}$ in the empty space of the pore of the concrete, **Equation 6.16**, and transport of CO_3^{2-} in the pore solution, **Equation 6.25**, describe the carbonation reaction by accounting for the change in pore structure, **Equation 6.31**, and its impact on mass transport of ions in the pore solution. Finally, heat transport, **Equation 6.33**, is included in the numerical model to account for the effect of temperature on the aging factor of the concrete. **Figure 6.2** describes the algorithm implemented in the numerical model. The system of PDEs (6.36) is solved using a dedicated Matlab code, which implemented the pdepe function described in section 3.4.2.1 of **Chapter 3**.

$$\left\{ \begin{array}{l} (C_{Cl}^* + C_{CO_3^{2-}}) \frac{\partial \varepsilon}{\partial t} = (D_{eff,Cl} C_{Cl}^* + D_{eff,CO_3^{2-}} C_{CO_3^{2-}}) \frac{\partial^2 \varepsilon}{\partial x^2} + v(C_{Cl}^* + C_{CO_3^{2-}}) \frac{\partial \varepsilon}{\partial x} + (C_{Cl}^* + C_{CO_3^{2-}}) \Gamma_w \quad (6.2.a^*) \\ \frac{\partial C_{Cl}}{\partial t} = \frac{D_{eff,Cl}}{\left(1 + \left(\frac{\rho_b}{\theta}\right) \left(\frac{1}{M_{Cl}}\right) (f_b) \left(\frac{\alpha(1 + \beta C_{Cl}) - \alpha \beta C_{Cl}}{(1 + \beta C_{Cl})^2}\right)\right)} \frac{\partial^2 C_{Cl}}{\partial x^2} + \frac{v}{\left(1 + \left(\frac{\rho_b}{\theta}\right) \left(\frac{1}{M_{Cl}}\right) (f_b) \left(\frac{\alpha(1 + \beta C_{Cl}) - \alpha \beta C_{Cl}}{(1 + \beta C_{Cl})^2}\right)\right)} \frac{\partial C_{Cl}}{\partial x} \quad (6.14) \\ (1 - \varepsilon) \frac{\partial C_{CO_2}}{\partial t} = (1 - \varepsilon) D_{eff,CO_2} \frac{\partial^2 C_{CO_2}}{\partial x^2} + (1 - \varepsilon) g \frac{\partial C_{CO_2}}{\partial x} - \frac{rCO_{2(aq)}}{\phi} \quad (6.16) \\ \varepsilon \frac{\partial C_{CO_3^{2-}}}{\partial t} = \varepsilon D_{CO_3^{2-}} \frac{\partial^2 C_{CO_3^{2-}}}{\partial x^2} + \varepsilon v \frac{\partial C_{CO_3^{2-}}}{\partial x} + \frac{rCO_3^{2-}}{\phi} - \frac{rC}{\phi} \quad (6.25) \\ \frac{\partial n_{CaCO_3}}{\partial t} = R = k_c \left(\frac{\gamma_{Ca^{2+}} [Ca^{2+}] \times \gamma_{CO_3^{2-}} [CO_3^{2-}]}{K_{sp,CaCO_3}} - 1 \right) \quad (6.31) \\ \frac{\partial T}{\partial t} = \frac{k}{\rho C_p} \frac{\partial^2 T}{\partial x^2} \quad (6.33) \end{array} \right.$$

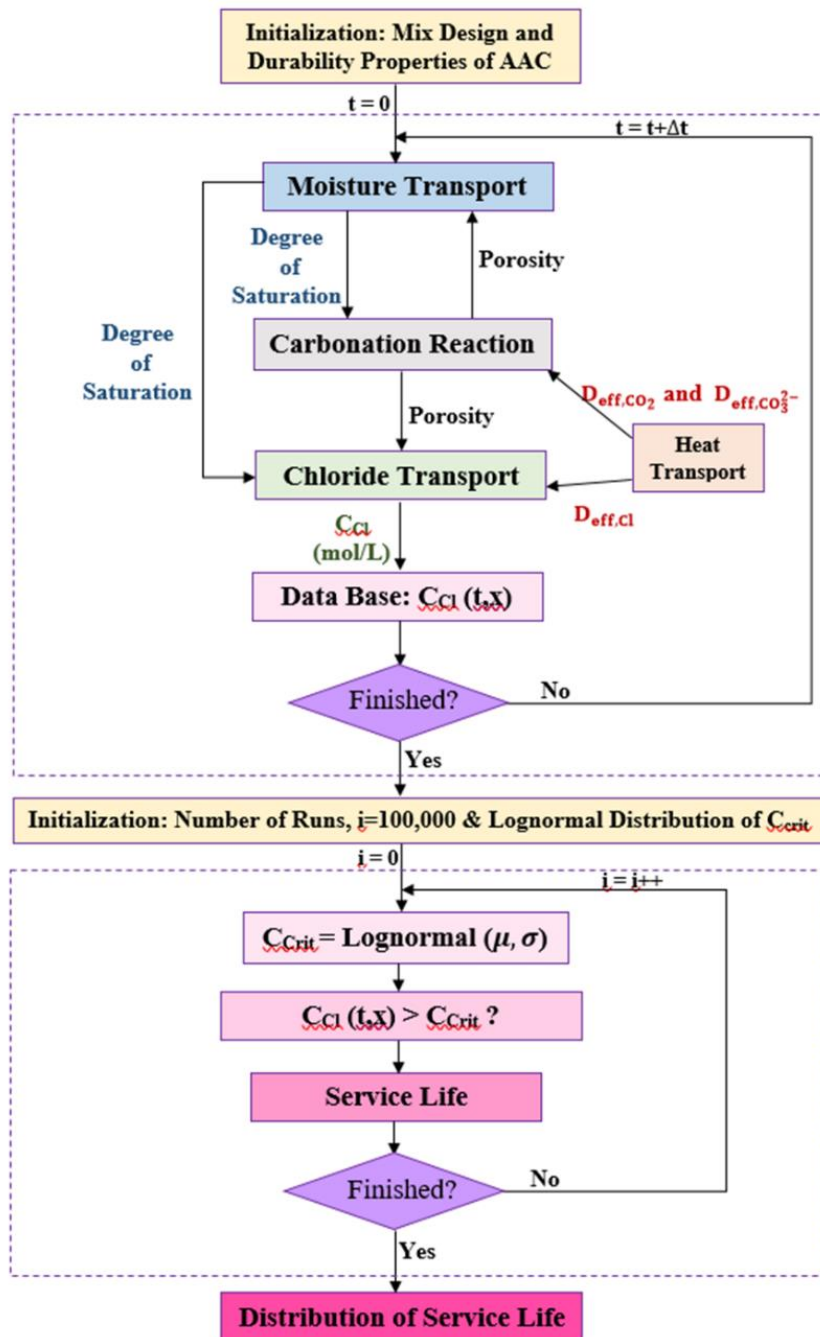


Figure 6.2 Algorithm of the developed numerical service life model. Where “x” in $C_{Cl}(t,x)$ is the location of the rebar in reinforced alkali-activated concrete and “t” is time in years.

6.7 Results and Discussion

6.7.1 Aging Factor of Alkali-Activated Concrete

Van Belleghem et al. [173] have studied the suitability of mortars as local repairs for delaminated concrete by resistivity tests. This type of test method is used to check the compatibility of the repair mortar to the parent concrete prior to the application of cathodic protection that reduces the corrosion of steel in reinforced concrete. Van Belleghem et al. [173] measured the resistivity of their repair materials under the same temperature, 20°C, and at three relative humidity conditions, 60, 80 and 100%, and with three different test methods. They concluded that the embedded electrodes method (EEM) bulk resistivity test is the most suitable technique for resistivity measurement in unsaturated and saturated conditions, which is at 60% and 100% RH, respectively.

The embedded electrodes method (EEM) bulk resistivity test has been implemented in this research to measure the resistivity of alkali-activated and Portland cement, type CEM III/B, mortars to obtain their aging or formation factor. First the resistivity of the samples in the fresh state (i.e. after being cured for 28 days) is measured and is noted as “Ref samples_28 days” as shown in **Figures 6.4-6.11**. Then measurements are taken in submerged conditions (i.e. under water) at three different temperatures, 10, 20 and 30°C, and in unsaturated conditions, 60% RH, at two different temperatures, 10 and 20°C. The results obtained are shown in **Figures 6.4-6.9** for alkali-activated mortars, and in **Figures 6.10-6.11** for Portland cement mortars. Overall, the measurements obtained for all the mortars, except for the CEM III based mortar, in submerged conditions for 1 week are slightly lower, by a factor of 1.22-1.88, than the value measured for Portland cement repair mortar stored at 100% RH and at 20°C for 91 days as reported in [173], and shown in **Figure 6.3**.

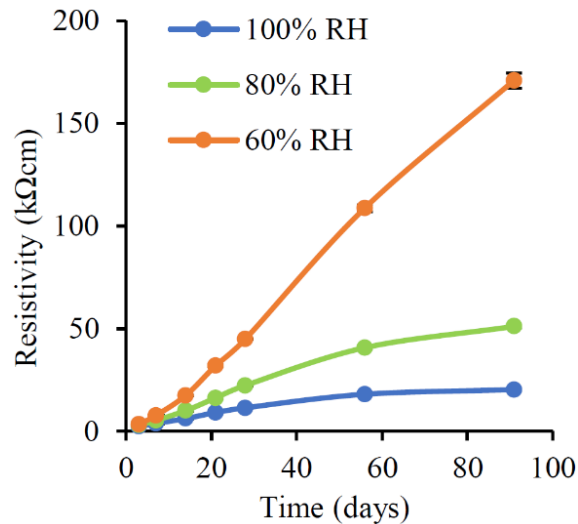


Figure 6.3 Measured resistivity of Portland cement (PC) mortar, by EEM test, as a function of time and relative humidity. Figure obtained from [173].

According to **Figure 6.3**, the PC mortar exposed to 100%RH has a resistivity value of approximately 20,000 Ωcm which is similar to the value obtained for the studied CEM III mortar in submerged conditions for 1 week. Portland cement mortar stored at 60%RH and 20°C for 91 days, shown in **Figure 6.3**, had a higher value of resistivity by a factor of 2.6 to 3.2 than alkali-activated mortars stored in the same conditions for 98 days according to **Figures 6.5, 6.7 and 6.9**. The PC mortar exposed to 60%RH in figure 6.4 has a resistivity of approximately 170,000 Ωcm , that is similar to the value obtained for the studied CEM III mortar under the same conditions, Figure 6.12. Overall, the trend of results in resistivity measurements in **Figure 6.4-6.11** is similar to the set of data obtained in **Figure 6.3**, where in both saturated (i.e. 100%RH condition, shown by the blue curve in **Figure 6.3**) and submerged conditions (i.e. under water) the resistivity nearly reaches a stable value after a testing period of 98 days for AAM mortars. However, for CEM III mortars in submerged conditions at 20 and 10°C the resistivity has slightly decreased by an average factor of 1.2 from 98 days to 251 days, as shown in **Figure 6.10**. Furthermore, in unsaturated conditions, at 60% RH and 20°C, the resistivity values for all the alkali-activated mortars and CEM III continue to increase, even after 98 days, and with a similar rate to the literature data reported in **Figure 6.3**.

In the case of 100SG mortar, the resistivity of the sample continued to increase in submerged and in unsaturated conditions after being cured for 28 days. The resistivity is also impacted more by the presence of water than humidity, according to **Figures 6.4 and 6.5**, where the resistivity is higher in an unsaturated state. The effect of temperature in both cases should also

be noted, where the samples stored at low temperature, at 10°C, have a higher resistivity than the samples stored at higher temperature, at 30°C. Hence, an increase in temperature has an effect on the microstructure of the mortar such that it increases the interconnectivity of the pores which makes the material more permeable (i.e. less resistant) to corroding agents (i.e. chloride ions) propagating from the external environment [263, 264]. Except in the last testing period of 288 days in unsaturated condition, the measured resistivity at 20°C was higher than at 10°C.

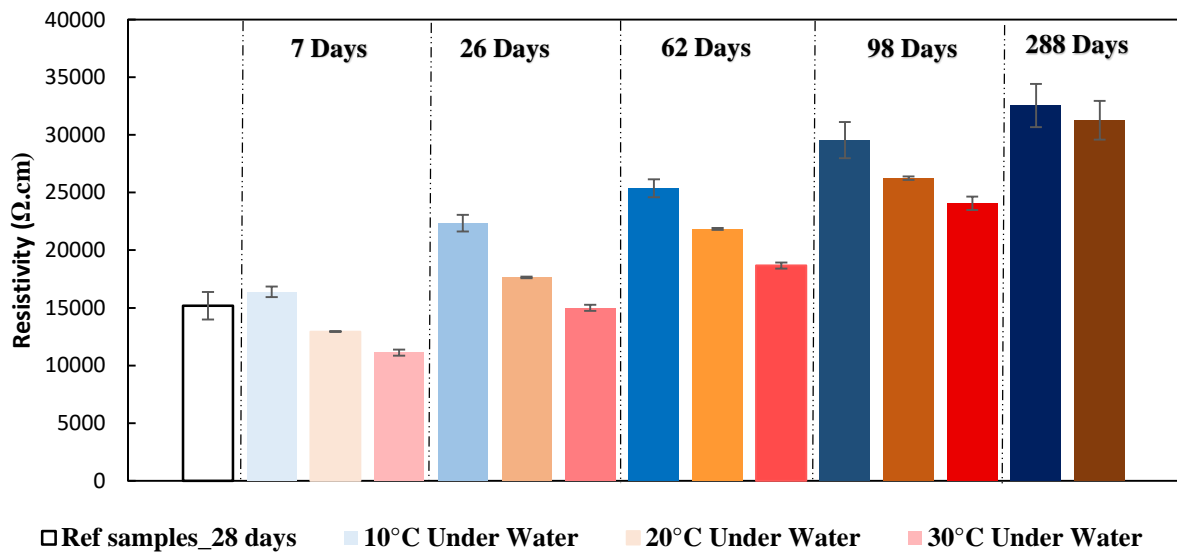


Figure 6.4 Resistivity measurements of 100SG in submerged conditions as a function of time and temperature.

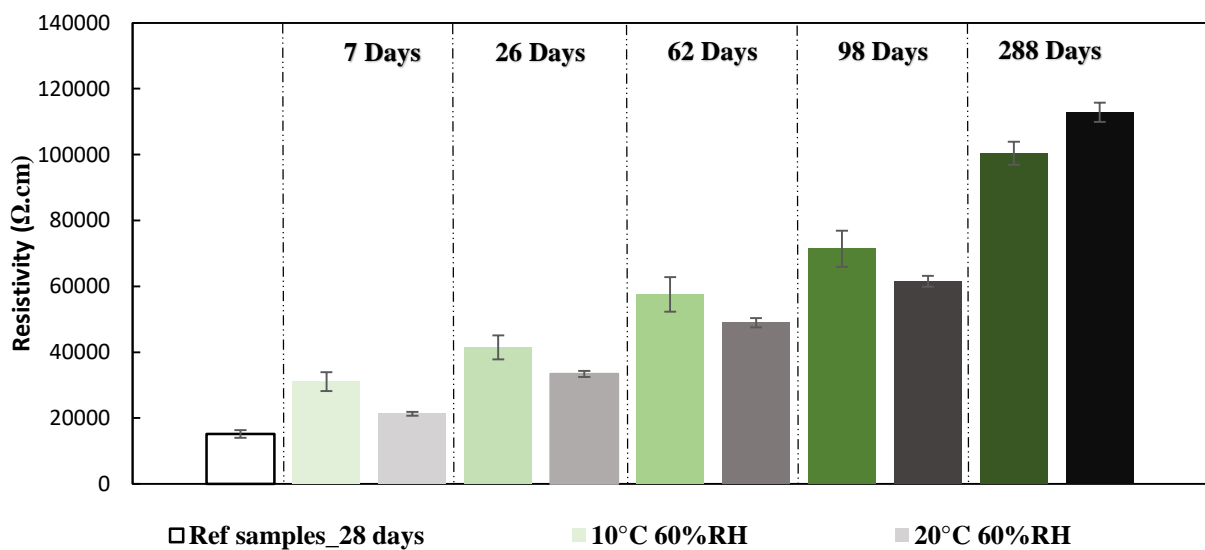


Figure 6.5 Resistivity measurements of 100SG in unsaturated conditions, 60% RH, as a function of time and temperature.

In the case of 75SG25FA, according to **Figures 6.6 and 6.7**, a similar trend in resistivity measurements as seen for 100SG is observed. Although 75SG25FA has a lower water content in its mix design, the measured resistivity is slightly lower than 100SG, indicating that 75SG25FA is more porous than 100SG. In addition, there is a greater jump in resistivity from 98 days to 288 days in unsaturated conditions, compared to 100SG, signifying that fly ash in the mix design has further reacted after a long period of time.

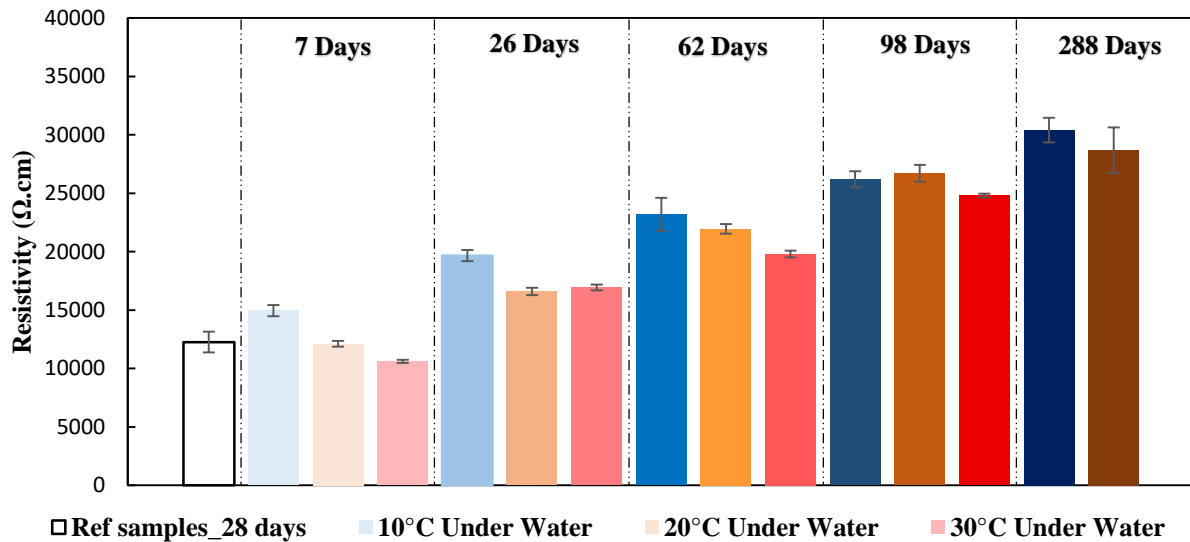


Figure 6.6 Resistivity measurements of 75SG25FA in submerged conditions as a function of time and temperature.

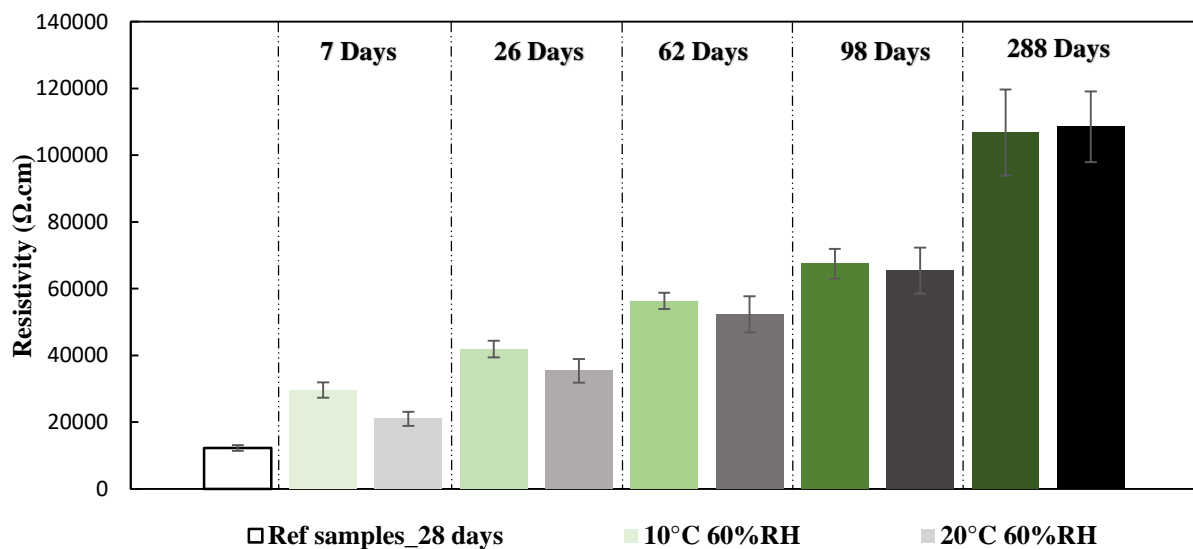


Figure 6.7 Resistivity measurements of 75SG25FA in unsaturated conditions, 60%RH, as a function of time and temperature.

In the case of 50SG50FA, according to **Figures 6.8 and 6.9**, a similar trend in resistivity measurements as in 100SG and 75SG25FA is observed. Although 50SG50FA has the lowest water content in its mix design, the measured resistivity is greatly lower than 100SG and 75SG25FA, indicating that 50SG50FA has the most porous microstructure.

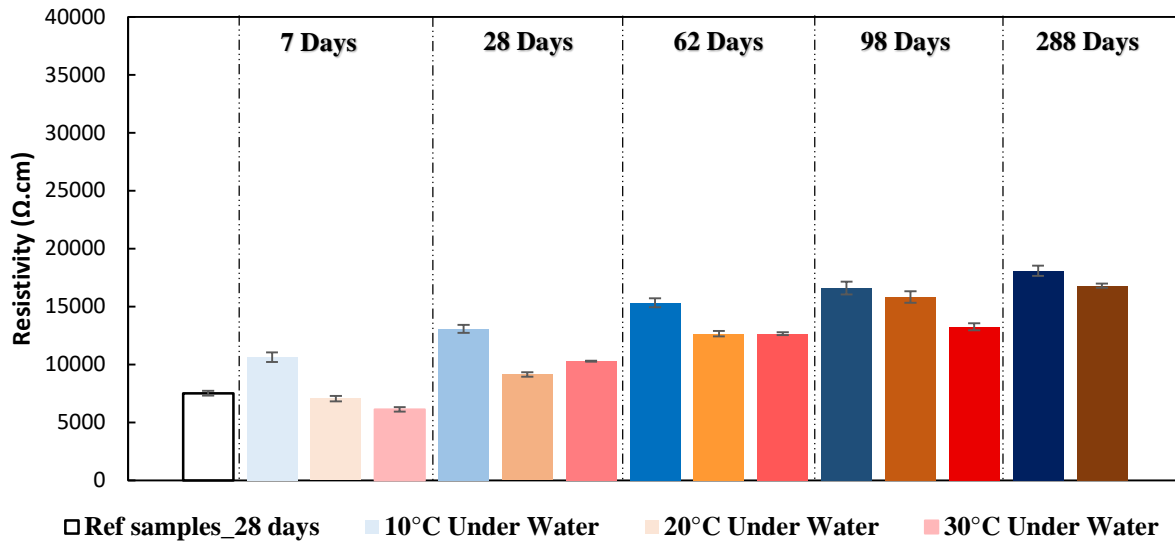


Figure 6.8 Resistivity measurements of SG50FA50 in submerged conditions as a function of time and temperature.

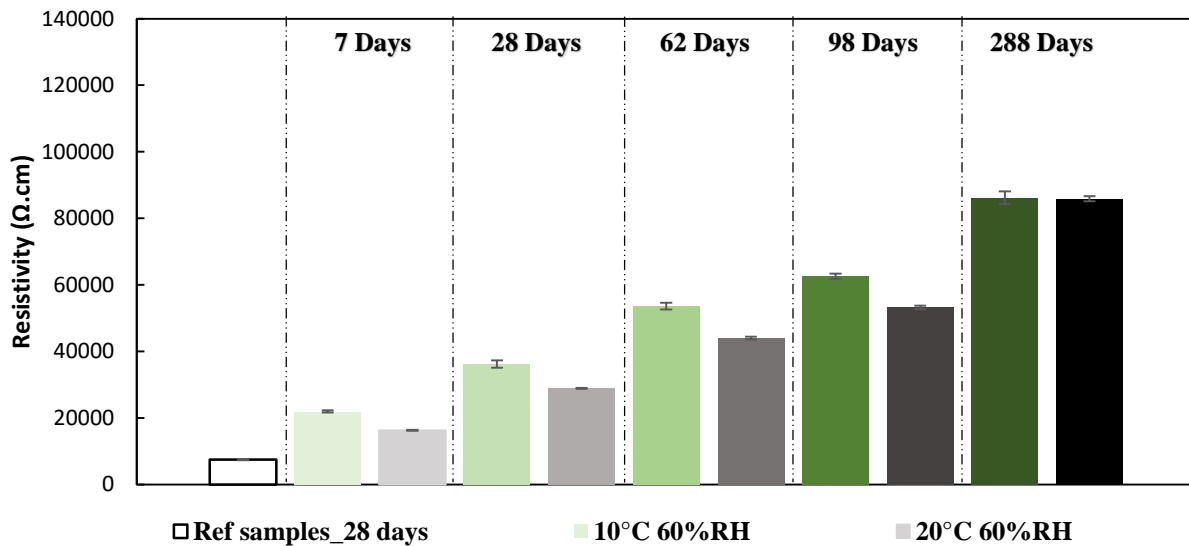


Figure 6.9 Resistivity measurements of SG50FA50 in unsaturated conditions, 60% RH, as a function of time and temperature.

In the case of CEM III mortar, according to **Figures 6.10 and 6.11**, the resistivity of the sample in submerged conditions dropped by a factor of 2.3, after being cured for 28 days. Although the resistivity continued to increase with time, it does not reach its initial value, measured after 28 days of curing, even after a long period of time. In addition, the impact of temperature on

resistivity of the samples in submerged conditions is not as significant as in the case of alkali-activated mortars.

It should also be noted that the resistivity obtained on the 251st day for the CEM III sample in unsaturated condition is higher at 20°C than at 10°C. This is also evident in the case of 100SG. Thus, high calcium cementitious materials may favour room temperature conditions to reach the highest extent of reactivity of slag precursors, that can further densify the microstructure and increase the resistance of the material against propagating corroding agents.

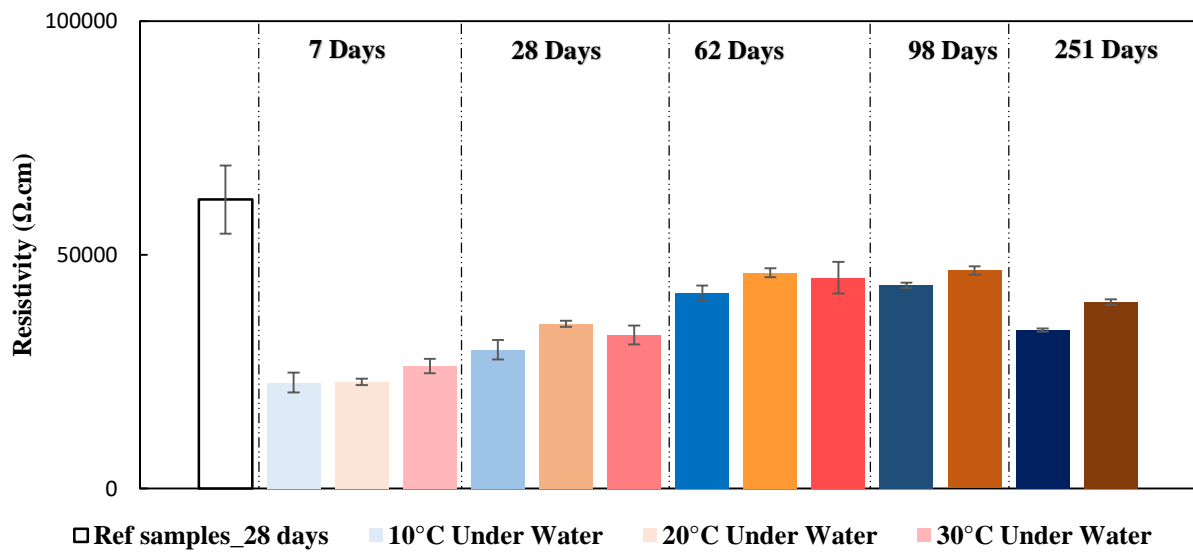


Figure 6.10 Resistivity measurements of CEM III in submerged conditions as a function of time and temperature.

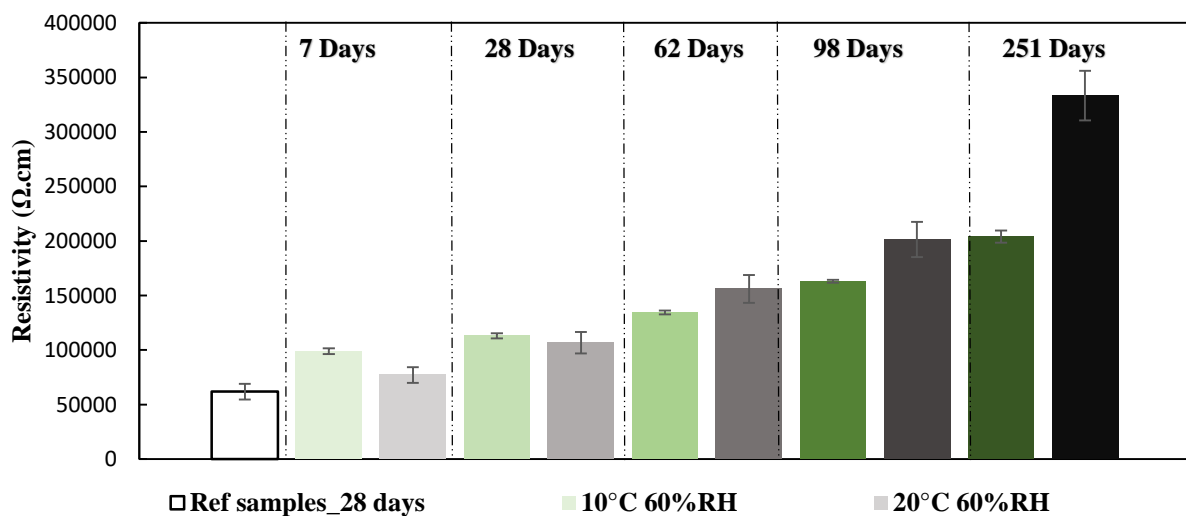


Figure 6.11 Resistivity measurements of CEM III in unsaturated conditions, 60%RH, as a function of time and temperature.

After measuring the resistivity of the mortars in submerged conditions, the next step in obtaining the aging factor is to theoretically calculate the pore solution resistivity using the NIST model [240]. GEM-Selektor v.3 [193] is used in this research to calculate the phase assemblage and pore solution composition of the alkali-activated binders and CEM III cement. **Figure 6.12** represents the phase assemblage, containing the reaction products or hydrates of these binders where only 70% of the slag and 35% of the fly ash is assumed to be reacted. Additionally, 70% of CEM III cement is assumed to have been reacted, based on the high amount of composition of slag in CEM III/B cement, between 66 and 80 wt.% [166]. According to **Figure 6.12**, The predicted phase assemblage, by GEM-Selektor v.3, for AAMs shows that the main reaction product is C-(N)-A-S-H gel and the secondary reaction products are MgAl-OH-LDH (i.e. hydrotalcite-like phases), strätlingite (i.e. AFm phase) and natrolite (i.e. zeolite phase or N-A-S-H gel). This kind of phase assemblage for high calcium based AAMs (i.e. 100%SG and 50%SG + 50%FA AAMs) as experimental data has already been reported by Myers et al. [265]. It should be noted in **Figure 6.12** that an increase in fly ash replacement (i.e. from 0% to 50% of the total amount of precursors) led to the formation of more N-A-S-H gel and less C-(N)-A-S-H gel in the phase assemblages of the hydrated alkali-activated cements. This can be explained by the increase in the bulk Alumina content, coming from the fly ash precursors, leading to an increase in the formation of additional disordered N-A-S-H gel with high Al and sodium (Na) contents [31]. Whereas, a decrease in the bulk Calcium content, as in the case of 50SG50FA, leads to a decrease in the amount of C-(N)-A-S-H gel formed compared to 100SG [69].

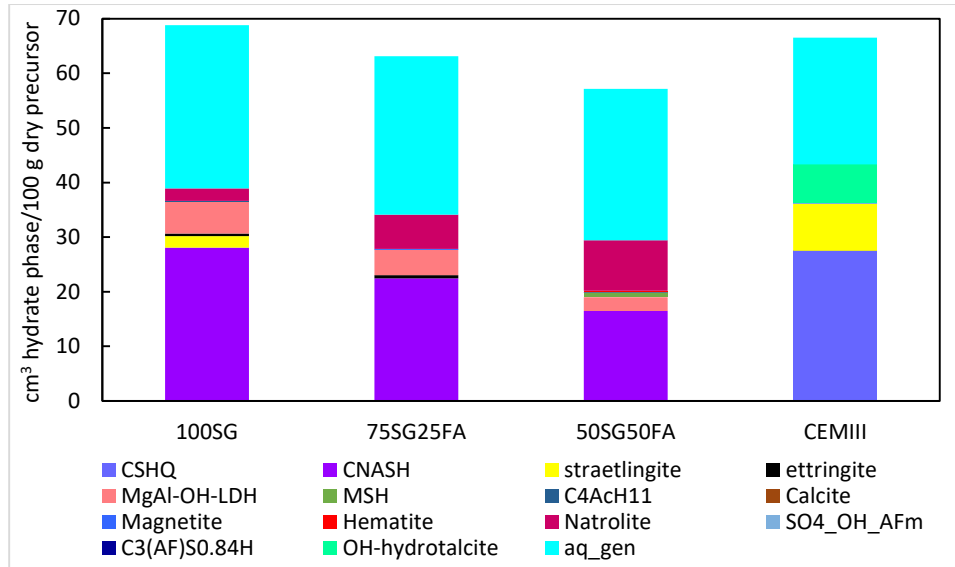


Figure 6.12 Phase assemblages of alkali-activated binders and CEM III, as calculated by thermodynamic simulations in GEM-Selektor. Note that aq_gen is the pore fluid (evaporable/free water with dissolved ions) present in the binders.

Table 6.5 contains the calculated pore solution compositions in terms of the dominant ions present in the pore solution of the binders. It can be noted that the pore solution alkalinity is the highest for 100SG and the lowest for 50SG50FA. The concentration of the alkali-ions (i.e. sodium and potassium ions) and ionic strength in AAMs is higher than for CEM III because of the presence of extra alkali ions in the alkali-activator for the mix design of AAMs.

Table 6.5 Pore solution chemistry of alkali-activated binders and CEM III binder.

Ionic Concentration, mol/l	100SG	75SG25FA	50SG50FA	CEM III
OH⁻	0.67	0.34	0.07	0.14
Ca²⁺	0.000043	0.000051	0.00012	0.002
Na⁺	0.57	0.2	0.03	0.046
K⁺	0.18	0.28	0.4	0.09
SO₄²⁻	0.03	0.06	0.18	0.000029
IS	0.76	0.5	0.5	0.14
pH	13.7	13.4	12.7	13

Figure 6.13 shows the calculated pore solution resistivity of AAMs and CEM III based on the concentrations of pore solution ions in **Table 6.5**. It can be noted that 100SG had the lowest calculated pore solution resistivity, followed by 75SG25FA, 50SG50FA and CEM III. Although the pore solution alkalinity in 50SG50FA is lower than in CEM III, it contained a higher concentration of alkali metal cations, making the pore solution more conductive [14].

Hu et al. [14] have theoretically calculated the pore solution conductivity of their alkali-activated paste sample with a similar mix design to the studied 100SG in this research. They estimated the conductivity of the cement paste pore solution from the dominant OH^- , K^+ and Na^+ ion concentrations, according to the method found in [240], and obtained a value of $18.598 \Omega^{-1} \cdot \text{m}^{-1}$. This outcome is re-calculated to a resistivity value, given that resistivity is the inverse of conductivity, and the value obtained is $5.38 \Omega \cdot \text{cm}$ which is lower than the value estimated for 100SG that is $7.7 \Omega \cdot \text{cm}$ as shown in **Figure 6.13**. However, the difference in both results is reasonable since the studied 100SG contains a higher w/b content in its mix design compared to the alkali-activate slag paste studied by Hu et al. [14], with a w/b of 0.35, which make the pore solution in 100SG binder to have a higher resistivity value [106].

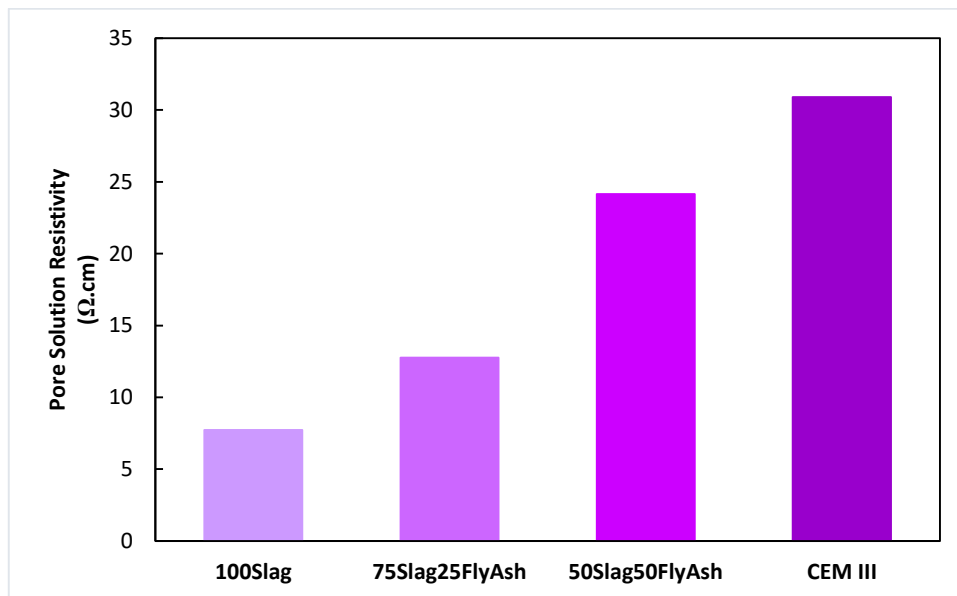


Figure 6.13 Pore solution resistivity measurements calculated theoretically using the NIST model [240] based on thermodynamic calculations of pore fluid compositions.

Based on the measured resistivity and calculated pore solution resistivity for the alkali-activated mortars, the chloride and carbonate aging transport models (diffusion coefficients and aging factors) are shown in **Table 6.6**. It should be noted that the $D_{\text{eff,Cl}}$ data for alkali-activated mortars and concretes are fitted by a power law model, with the aging factor as the exponent, and the graphs containing the curve fitting for alkali-activated mortars can be found in appendix 6.D “Chloride diffusion transport models in alkali-activated mortars”. It should also be noted that the values of effective chloride diffusion obtained for alkali-activated mortars, cured for 28 days and then submerged in water for 7 days at 20°C , match the values of chloride migration

obtained for alkali-activated concretes, aged for 28 days before the test, according to **Figure 4.2** in **Chapter 4**.

Table 6.6 Chloride and carbonate ion transport models for alkali-activated mortars.

Sample	$D_{\text{eff,Cl}} \times 10^{-5} \text{ (m}^2\text{/year)}$			$D_{\text{eff,CO}_3^{2-}} \times 10^{-5} \text{ (m}^2\text{/year)}$		
	10°C	20 °C	30°C	10°C	20 °C	30°C
100SG	$1.38 \times t^{-0.19}$	$1.45 \times t^{-0.246}$	$1.53 \times t^{-0.279}$	$3.72 \times t^{-0.19}$	$3.89 \times t^{-0.246}$	$4.11 \times t^{-0.279}$
75SG25FA	$2.5 \times t^{-0.196}$	$2.47 \times t^{-0.25}$	$2.26 \times t^{-0.308}$	$6.71 \times t^{-0.196}$	$6.63 \times t^{-0.25}$	$6.07 \times t^{-0.308}$
50SG50FA	$7.95 \times t^{-0.149}$	$7.99 \times t^{-0.256}$	$7.8 \times t^{-0.288}$	$21.33 \times t^{-0.149}$	$21.45 \times t^{-0.256}$	$20.94 \times t^{-0.288}$

Including the scaling factor of 0.773 (i.e. from mortar to concrete), the ionic transport models are shown in Table 6.7.

Table 6.7 Chloride and carbonate ion transport models, in $\text{m}^2\text{/year}$, in alkali-activated concretes.

Sample	$D_{\text{eff,Cl}} \times 10^{-5} \text{ (m}^2\text{/year)}$			$D_{\text{eff,CO}_3^{2-}} \times 10^{-5} \text{ (m}^2\text{/year)}$		
	10°C	20 °C	30°C	10°C	20 °C	30°C
100SG	$1.07 \times t^{-0.19}$	$1.12 \times t^{-0.246}$	$1.18 \times t^{-0.279}$	$2.87 \times t^{-0.19}$	$3.01 \times t^{-0.246}$	$3.18 \times t^{-0.279}$
75SG25FA	$1.93 \times t^{-0.196}$	$1.91 \times t^{-0.25}$	$1.75 \times t^{-0.308}$	$5.19 \times t^{-0.196}$	$5.13 \times t^{-0.25}$	$4.69 \times t^{-0.308}$
50SG50FA	$6.14 \times t^{-0.149}$	$6.18 \times t^{-0.256}$	$6.03 \times t^{-0.288}$	$16.48 \times t^{-0.149}$	$16.58 \times t^{-0.256}$	$16.19 \times t^{-0.288}$

The effect of temperature is also included in the chloride and carbonate transport through Equation 6.11, where the activation energy, E_a , is obtained by fitting the effective chloride diffusion coefficients through the Arrhenius equation, **Equation 6.9**. The obtained activation energy is $10 \text{ kJ}\cdot\text{mol}^{-1}$ as it closely predicts the chloride diffusion as a function of temperature and for each period of testing for alkali-activated mortars and CEM III mortar as shown in **Figures 6.14 and 6.15**, although this value of activation energy is lower than the value of $35 \text{ kJ}\cdot\text{mol}^{-1}$ used in the Life-365 service life model [262].

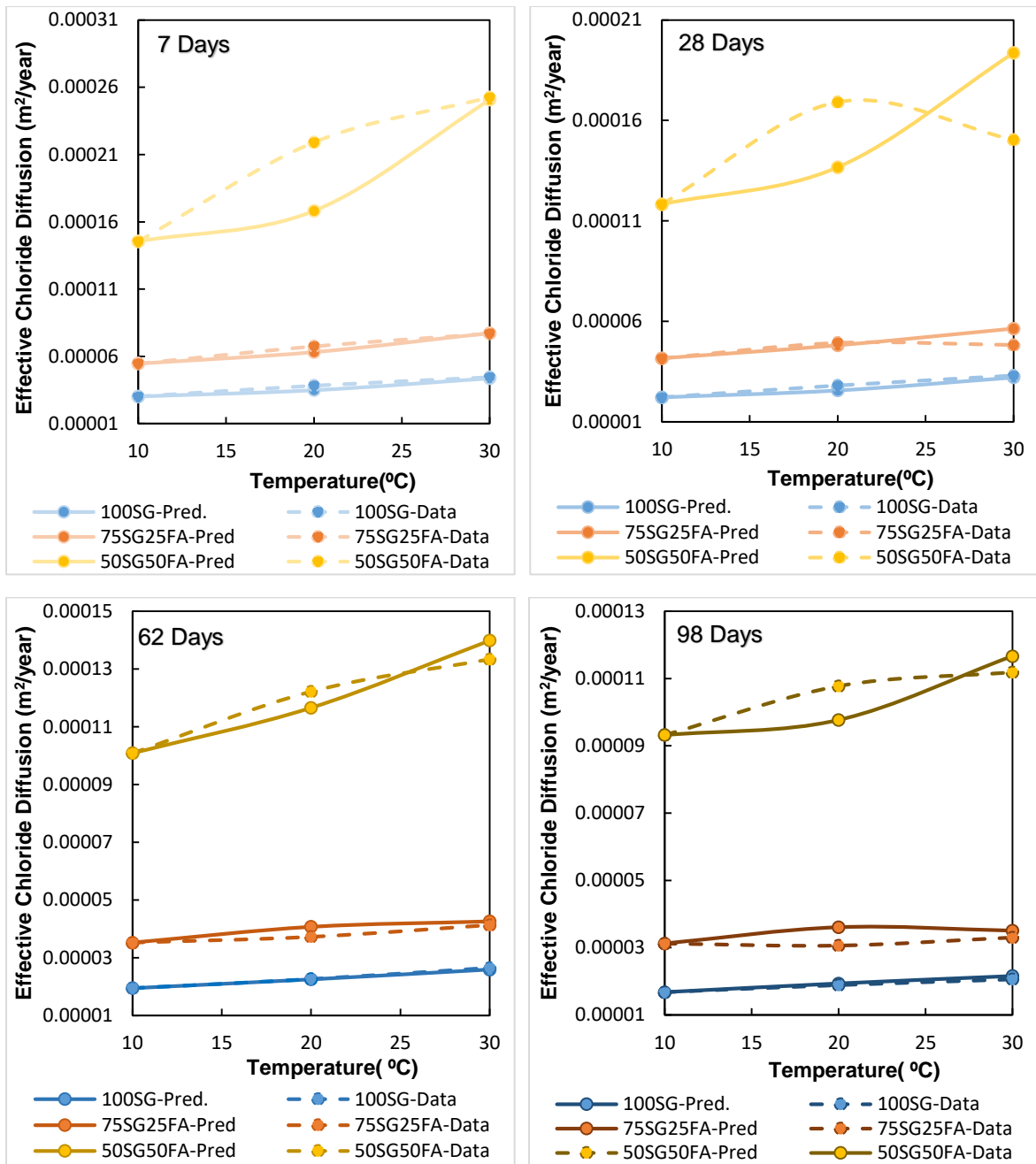


Figure 6.14 Effective chloride diffusion in alkali-activated mortars, in submerged condition, as a function of time and temperature.

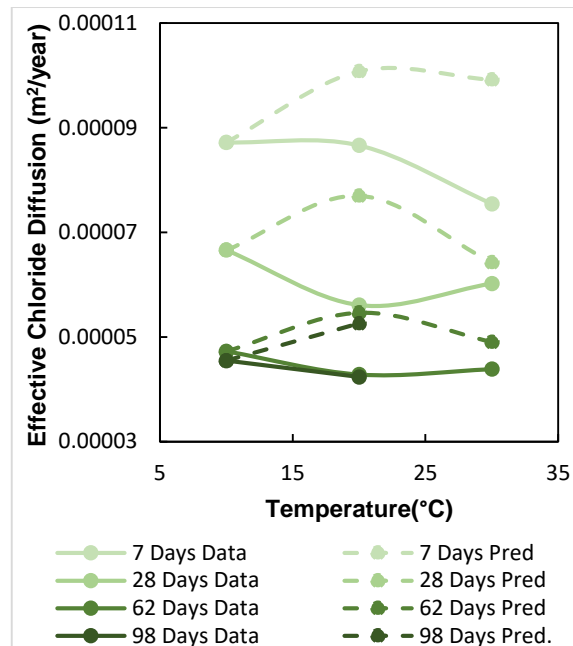


Figure 6.15 Effective chloride diffusion in CEM III mortars, in submerged condition, as a function of time and temperature.

6.7.2 Calcium Carbonate Precipitation Rates

The calculated precipitation rate constants for AAMs are shown in **Table 6.8**. The values are different because of the difference in concentrations of free calcium ions in the pore solutions of these cements, along with the calculated activity coefficients, γ , and the total change in porosity of these binders when carbonated (**Table 6.3**).

Table 6.8 Calculated calcium concentration, activity coefficients and precipitation rate constants for CaCO_3 for carbonated AAMs.

Binders	$[\text{Ca}^{2+}]$ (mol.L^{-1})	$\gamma_{\text{Ca}^{2+}}$	$\gamma_{\text{CO}_3^{2-}}$	Calculated precipitation rate (mol. s^{-1})
100SG	0.0001	0.043	0.137	4.38×10^{-6}
75SG25FA	4.88×10^{-5}	0.073	0.174	7.22×10^{-5}
50SG50FA	4.05×10^{-5}	0.093	0.165	1.78×10^{-4}

6.7.3 Estimation of Total Chloride Profile of a Structure in Real Service Conditions

In this section the chloride profile obtained from a bridge structure exposed to a marine environment for over 25 years, reported in [163], is used to qualitatively estimate the chloride profile of AAMs in real conditions. The structure contains Portland cement with 20% slag and a ratio of water to cement of 0.36 in its mix design. This design is different from the Portland cement mix used in this research in which CEM III/B 42.5N contained at least 66% slag by

mass, according to the EN 197-1 standard [266], and a water to binder ratio of 0.5. However, the data set obtained under real service conditions is utilized to validate, as far as is possible, the proposed numerical model for AAMs under both mechanical and environmental loadings. The methodology has been explained in section 6.2, and the chloride profiles for AAMs qualitatively estimated after 25 years are shown in **Figure 6.16**, along with the real service chloride profile obtained from the structural element, inside the column of the bridge, located 40 mm above sea level. Each service data point is shown with upper and lower error bounds of $\pm 10\%$ to obtain the minimum and maximum chloride profiles for AAMs, to account for the variability in the initial service data set obtained from [163].

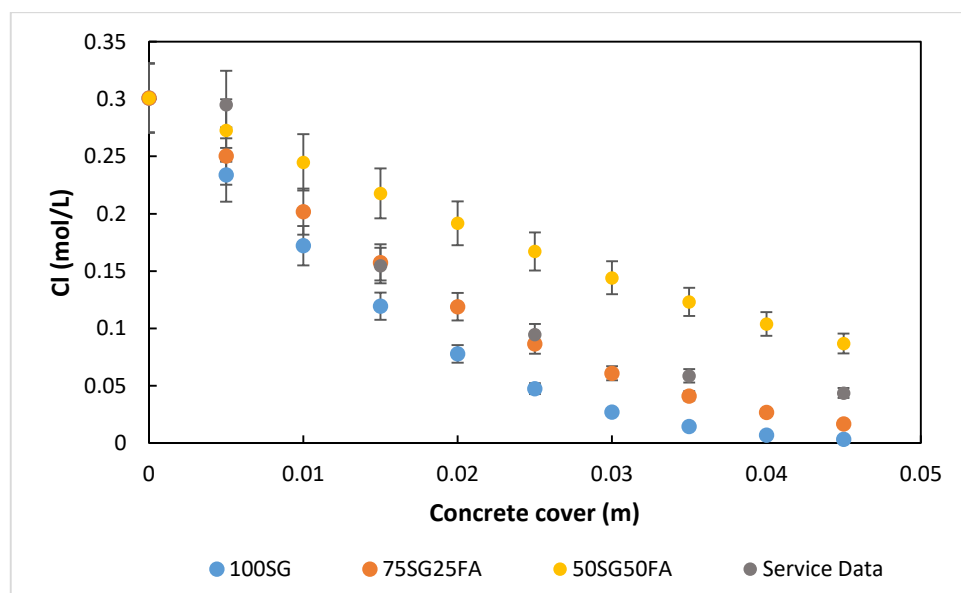


Figure 6.16 Total chloride profile (mol/L) of a structure, made of CEM II cement, in service conditions for more than 25 years at 40 mm above sea level [163], compared to the profiles modelled in this study for the AAM concretes as indicated.

6.7.4 Extent of Aging Factor

Effective chloride diffusion coefficients of AAMs obtained in laboratory conditions, during a testing period of 288 days and in different temperature conditions, are fitted by a power function passing through the diffusion point estimated after 25 years, as shown in **Figure 6.17-6.19**. This diffusion is calculated by fitting the error function solution to Fick's second law of diffusion through the data of AAMs shown in **Figure 6.16**. It should be noted that the erf solution is only technically valid without the time-dependence from the aging, but it is a useful approximation to estimate the instantaneous diffusion coefficient for concrete at a specific point in time [159]. The power law model, with the coefficient as aging factor, for each alkali-

activated concrete shows that there is only a slight change in chloride diffusion after a period of 1 year, which signifies that nearly all the precursors present in the binder have reacted by this time. Hence, the hydration reaction in these cementitious material has been nearly completed, leading to a fully developed overall microstructure for each concrete. Thus, the aging effects that cause each ionic transport process to decrease as a function of time are set to continue only up to one year in the numerical model. After this point, the model utilizes the same value of ionic diffusion coefficients achieved at 1 year, as a constant throughout the remaining service life.

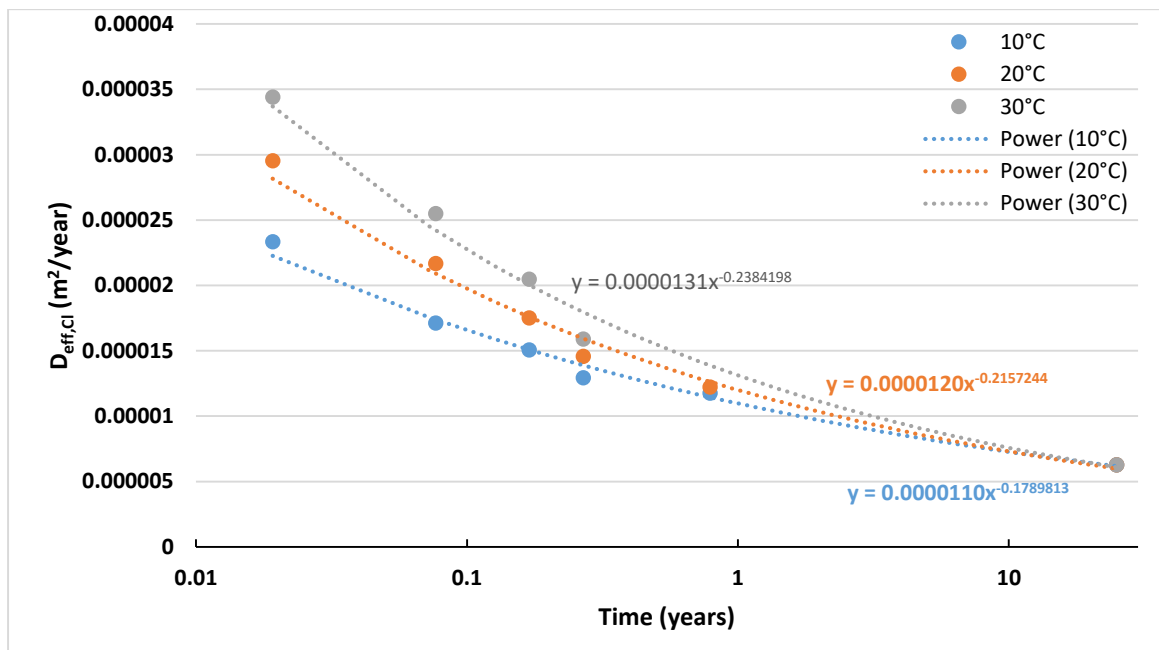


Figure 6.17 Time-dependence of chloride diffusion coefficients of 100SG concrete.

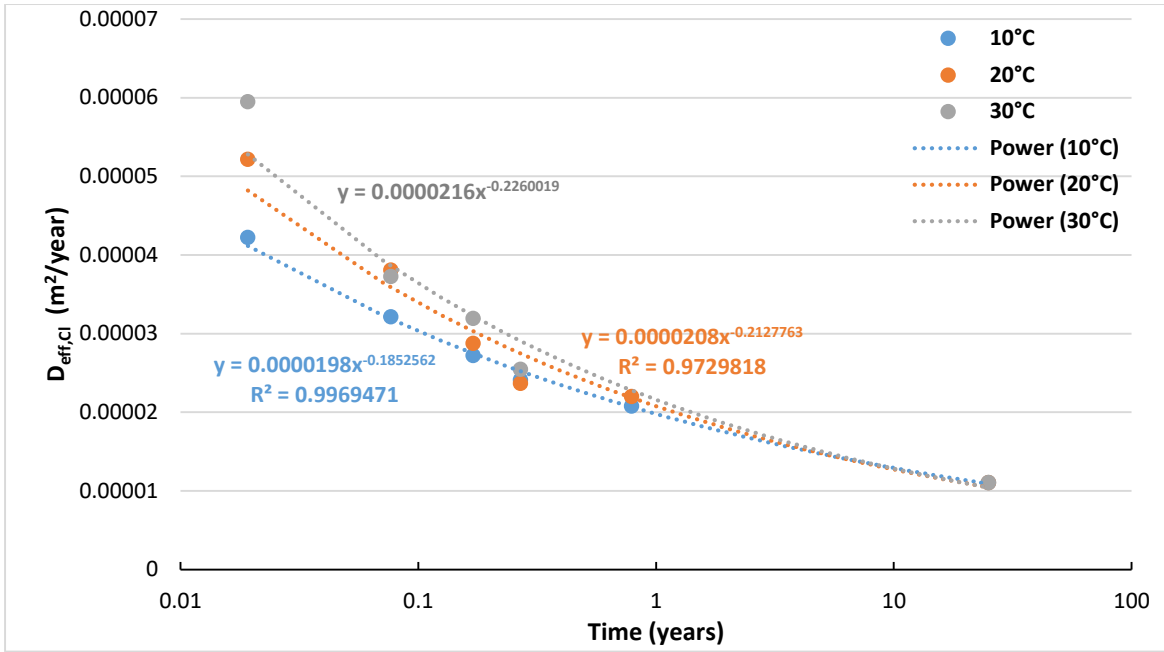


Figure 6.18 Time-dependence of chloride diffusion coefficients of 75SG25FA concrete.

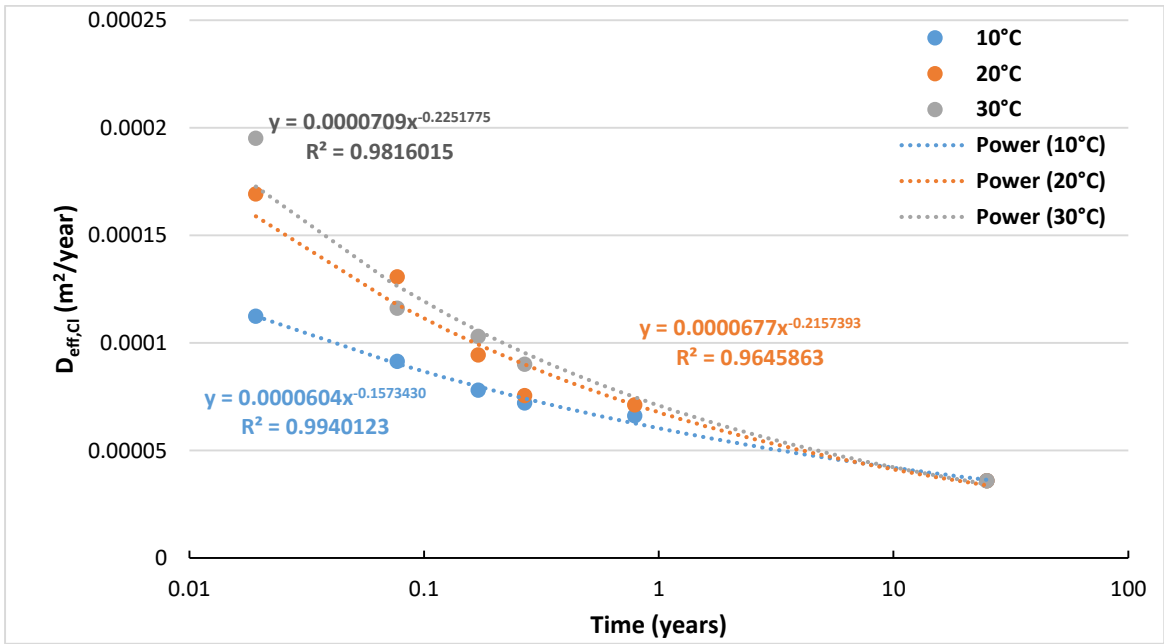


Figure 6.19 Time-dependence of chloride diffusion coefficients of alkali-activated 50SG50FA concrete.

6.8 Service Life Prediction of Alkali-Activated Concretes

In this section the service life of alkali-activated concretes, with mix design shown in **Table 6.9**, is estimated by using the proposed numerical model. The mix design of the binder in each concrete is the same as the mixes used in the alkali-activated mortars studied in this research, to use the obtained ionic transport models.

Table 6.9 Mix designs of alkali-activated concretes

Mix	Precursor (kg/m ³)	Sand (kg/m ³)	Aggregate (kg/m ³)	Water (kg/m ³)	NaOH (kg/m ³)	Na ₂ SiO ₅ (kg/m ³)
100SG	410	720	1080	175	5.7	90
75SG25FA	410	720	1080	150	5.7	90
50SG50FA	410	720	1080	125	5.7	90

6.8.1 Summary of Inputs for Numerical Model

The list of parameters used in the proposed numerical model are listed in **Tables 6.10-6.13**. Each of the durability parameters defined for the microstructure, carbonation reaction, ionic transport, and permeability can be altered to check its overall impact on the predicted service life. Additionally, the mix design can be directly modified, which in turn affects the durability parameters. According to the sub-models used in the numerical model, the sand to aggregate ratio has an effect on moisture permeability, and the cement content determines the amount of chloride binding. Also, the water to binder ratio affects the overall porosity of the microstructure of the material, but this parameter is an input based on the data available in the literature. Finally, model refinement for CO₂ transport is also implemented, through a reduction factor, prior the calculation of service life. This step is discussed in the following section of sensitivity analysis.

Table 6.10 Parameters used in the numerical model for transport in the mortar phase (i.e. skin layer) and concrete phase for the studied alkali-activated concretes.

Parameters	100SG	75SG25FA	50SG50FA			
Microstructure						
Porosity – Concrete ^a	0.16	0.15	0.14			
Porosity – Mortar ^a	0.08	0.08	0.08			
Carbonation						
Change in porosity (%) ^b	-5.3%	+47.75%	+81.73%			
k_c (mol.s ⁻¹)	4.38×10^{-6}	7.22×10^{-5}	1.78×10^{-4}			
[Ca ²⁺] (mol.L ⁻¹)	0.0001	4.88×10^{-5}	4.05×10^{-5}			
$\gamma_{Ca^{2+}}$	0.043	0.073	0.093			
$\gamma_{CO_3^{2-}}$	0.137	0.174	0.165			
Carbonate Transport						
Carbonate transport model – Mortar ^a : $D_{eff,CO_3^{2-}}$ (m ² /year)	$3.89 \times 10^{-5} t^{-0.246}$	$6.63 \times 10^{-5} t^{-0.25}$	$21.45 \times 10^{-5} t^{-0.256}$			
Carbonate transport model – Concrete ^a : $D_{eff,CO_3^{2-}}$ (m ² /year)	$3.01 \times 10^{-5} t^{-0.246}$	$5.13 \times 10^{-5} t^{-0.25}$	$16.58 \times 10^{-5} t^{-0.256}$			
Effect of Temperature						
Activation Energy (kJ/mol)	10	10	10			
Chloride Transport						
Langmuir Binding isotherm: α ; β for alkali-activated cement ^{**}	17.5	0.07	23.7	0.08	11.7	0.06
Chloride transport model - Mortar: $D_{eff,Cl}$ (m ² /year)	$1.45 \times 10^{-5} t^{-0.246}$		$2.47 \times 10^{-5} t^{-0.25}$		$7.99 \times 10^{-5} t^{-0.256}$	
Chloride transport model ^a - Concrete: $D_{eff,Cl}$ (m ² /year)	$1.12 \times 10^{-5} t^{-0.246}$		$1.91 \times 10^{-5} t^{-0.25}$		$6.18 \times 10^{-5} t^{-0.256}$	
Mix Design						
Binder content, kg, in 1 m ³ of concrete	410	410	410			
Concrete Density (kg/dm ³)	2.540	2.540	2.540			

*The precipitation rate for calcium carbonate, k_c , is converted to mol/year in the numerical model.

**The parameters, α and β , used in the Langmuir binding isotherm for chloride ions is obtained from [113]

^a Porosity of alkali-activated mortar and concrete obtained from [152].

^b Change in porosity, by %, of alkali-activated cements after carbonation obtained from [147].

Table 6.11 Moisture permeability parameters for 100SG concrete with 5 mm skin layer of mortar phase. The moisture transport parameters have been already calculated in in “Chapter 5: Moisture Permeability in Alkali-Activated Materials”.

Desorption	Permeability-Single: K^{**} ; x_d	1×10^{-23}		1.7	Adsorption	Permeability-Single: K^{**} ; x_d	1×10^{-22}		1.4
	Desorption Isotherm-Single: a^* ; m	422×10^5		0.38		Adsorption Isotherm-Single: a^* ; m	98×10^5		0.22
	Permeability-Dual-Large Pore: K_L^{**} ; x_d	4×10^{-23}		1.8		Permeability-Dual-Large Pore: K_L^{**} ; x_d	1×10^{-22}		1.6
	Permeability-Dual-Small Pore: K_s^{**} ; x_d	2×10^{-24}		1.8		Permeability-Dual-Small Pore: K_s^{**} ; x_d	1×10^{-23}		1.6
	Desorption Isotherm-Dual: a_L^* ; S_L/S^{***}	159×10^5		0.66		Adsorption Isotherm-Dual: a_L^* ; S_L/S^{***}	88×10^5		0.98
	w_f ; $w_{f,D}$; m	0.11	0.15	0.4		w_f ; $w_{f,D}$; m	0.11	0.15	0.22
	Desorption Isotherm-Dual: a_s^* ; S_s/S^{***}	524×10^5		1		Adsorption Isotherm-Dual: a_s^* ; S_s/S^{***}	98×10^5		1

*The overall air entry pressure, a , and for the large and small pores, a_L and a_s respectively, are in Pa in the numerical model.

**The overall moisture permeability factor, K , and for the large and small pores, K_L and K_s , are in m^2 . The apparent moisture diffusivity is converted from m^2/s to $m^2/year$ in the numerical model.

***Average fraction of degree of saturation in large and small pores, S_L/S and S_s/S , in the concrete cover.

Table 6.12 Moisture permeability parameters for 75SG25FA concrete with 5 mm skin layer of mortar phase. The moisture transport parameters have been already calculated in in “Chapter 5: Moisture Permeability in Alkali-Activated Materials”.

Desorption	Permeability-Single: K^{**} ; x_d	3×10^{-23}		1.8	Adsorption	Permeability-Single: K^{**} ; x_d	5×10^{-23}		1.4
	Desorption Isotherm-Single: a^* ; m	437×10^5		0.4		Adsorption Isotherm-Single: a^* ; m	97×10^5		0.22
	Permeability-Dual-Large Pore: K_L^{**} ; x_d	5×10^{-23}		2		Permeability-Dual-Large Pore: K_L^{**} ; x_d	1×10^{-22}		1.5
	Permeability-Dual-Small Pore: K_S^{**} ; x_d	1×10^{-23}		2		Permeability-Dual-Small Pore: K_S^{**} ; x_d	1×10^{-23}		1.5
	Desorption Isotherm-Dual: a_L^* ; S_L/S^{***}	215×10^5		0.76		Adsorption Isotherm-Dual: a_L^* ; S_L/S^{***}	67×10^5		0.92
	w_f; $w_{f,D}$; m	0.097	0.11	0.41		w_f; $w_{f,D}$; m	0.097	0.11	0.22
	Desorption Isotherm-Dual: a_s^* ; S_s/S^{***}	492×10^5		1		Adsorption Isotherm-Dual: a_s^* ; S_s/S^{***}	98×10^5		1

*The overall air entry pressure, a , and for the large and small pores, a_L and a_s respectively, are in Pa in the numerical model.

**The overall moisture permeability factor, K , and for the large and small pores, K_L and K_S , are in m^2 . The apparent moisture diffusivity is converted from m^2/s to $m^2/year$ in the numerical model.

***Average fraction of degree of saturation in large and small pores, S_L/S and S_s/S , in the concrete cover.

Table 6.13 Moisture permeability parameters for 50SG50FA concrete with 5 mm skin layer of mortar phase. The moisture transport parameters have been already calculated in in “Chapter 5: Moisture Permeability in Alkali-Activated Materials”.

Desorption	Permeability- Single: $K^{**}; x_d$	1×10^{-23}		1	Adsorption	Permeability- Single: $K^{**}; x_d$	1×10^{-22}		0.8
	Desorption Isotherm- Single: $a^*; m$	774×10^5		0.31		Adsorption Isotherm- Single: $a^*; m$	121×10^5		0.11
	Permeability- Dual-Large Pore: $K_L^{**}; x_d$	1×10^{-22}		0.7		Permeability- Dual-Large Pore: $K_L^{**}; x_d$	2×10^{-22}		1
	Permeability- Dual-Small Pore: $K_S^{**}; x_d$	1×10^{-25}		0.7		Permeability- Dual-Small Pore: $K_S^{**}; x_d$	5×10^{-23}		1
	Desorption Isotherm- Dual: $a_L^*; S_L/S$	238×10^5		0.5		Adsorption Isotherm- Dual: $a_L^*; S_L/S$	111×10^5		0.99
	$w_f; w_{f,D}; m$	0.14	0.1	0.59		$w_f; w_{f,D}; m$	0.14	0.1	0.11
	Desorption Isotherm- Dual: $a_s^*; S_s/S^{***}$	1621×10^5		1		Adsorption Isotherm- Dual: $a_s^*; S_s/S^{***}$	121×10^5		1

*The overall air entry pressure, a , and for the large and small pores, a_L and a_s respectively, are in Pa in the numerical model.

**The overall moisture permeability factor, K , and for the large and small pores, K_L and K_S , are in m^2 . The apparent moisture diffusivity is converted from m^2/s to $m^2/year$ in the numerical model.

***Average fraction of degree of saturation in large and small pores, S_L/S and S_s/S , in the concrete cover.

6.8.2 Computational Study

In this section, computational experiments are first conducted to check the validity of each equation, with numerous variables, used in the numerical model to calculate the service life of alkali-activated concretes. In addition, two environmental conditions can be selected in the numerical model which are the drying and wetting conditions. The drying condition is set so that the concrete is initially saturated at 100% RH and 20°C then exposed to 50% RH and 30°C environment. Whereas, the wetting condition is set so that the concrete is initially dried at 50% RH and 20°C then exposed to 100% RH and 30°C environment. So in the case of drying, the mode of transport of moisture and corroding agents (i.e. Cl^- and CO_3^{2-}) is in countercurrent flow with moisture transporting out of the concrete. Whereas in the case of wetting, the mode of transport of moisture and corroding agents is in cocurrent flow into the concrete. Furthermore, model refinement may be proposed but then will be based on data from the literature. Next, the numerical model, including possible refinements, is qualitatively tested on chloride profiles estimated for alkali-activated activated concretes exposed to marine environment for at least 25 years.

6.8.2.1 Sensitivity in Chloride Binding

Zhang et al. [113] and Mangat et al. [104] have conducted experiments to quantify chloride binding by AAMs. Zhang et al. [113] have performed their experiments at the level of the binder whereas Mangat et al. [104] at the level of the concrete but both sample types have been exposed in the same experimental condition which is in a solution with a certain concentration of NaCl. The two studies have also implemented the Langmuir binding isotherm to relate the amount of bound and free chloride ions in AAMs. However, the fitted parameters of the Langmuir isotherm have shown different values in both studies even for the same type of alkali-activated binder (i.e. same mix design containing 100% slag as precursor) used in the concrete as shown in **Table 6.14**.

Table 6.14 Fitted parameters, α and β , for Langmuir isotherms for AAMs obtained at the cement level from [113] and at concrete level [104].

	Langmuir Binding Isotherm	
	α	β
Cement Mix design: 100% Slag - Na ₂ O; 4 wt.% binder – Ms; 1.5 - w/b; 0.5	17.5	0.07
Concrete Mix design: 100% Slag - Na ₂ O; 4 wt.% binder – Ms; 2 - w/b; 0.47 and sand/aggregate; 0.4	1.2	7

To test the impact in the difference of values for the parameters of the Langmuir binding isotherm, each set of fitted α and β shown in **Table 6.14** is implement in the numerical model to predict chloride transport in 100SG concrete because it has a similar mix design to the reported AAMs in **Table 6.14**. The concrete, with a cover of 50 mm, is set to be located in a marine splash zone with its initial moisture state set at 50%RH and 20°C, and exposed to 100% RH and 30°C environment (i.e. wetting condition) to predict the extent of chloride transport in alkali-activated concrete. **Figure 6.20** presents the chloride profiles in 100SG concrete predicted by implementing the Langmuir isotherm with the coefficients determined at the level of the cement (**A**) and at the level of the concrete (**B**) in the numerical model. It can be seen in **Figure 6.20** that there is less chloride binding at the level of the concrete than at the level of the cement. Hence, the amount of bonded chloride in cement predicted by the Langmuir isotherm should have a reduction factor that can account for the percentage of the hydrated products that can be available for chloride binding in the level of the concrete [106].

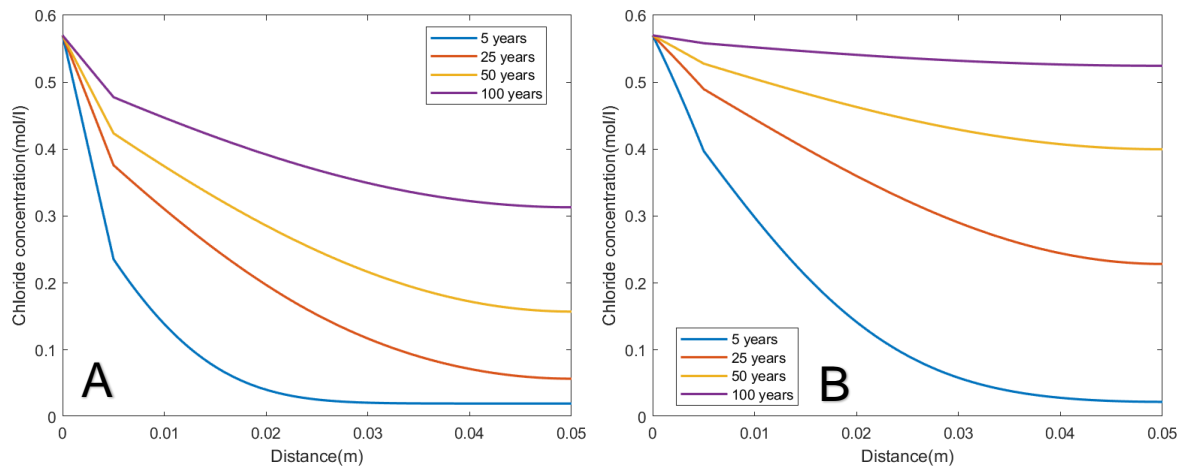


Figure 6.20 Chloride profiles for 100SG concrete in marine splash zone environment at 100% RH and 30°C. The chloride profiles in 100SG concrete are predicted by implementing the Langmuir isotherm with the coefficients determined at the level of the cement (A) and at the level of the concrete (B).

In addition, Babae and Castel [55] have also conducted experiments on alkali-activated mortars exposed to aqueous chloride solutions and have not found evidence of chloride binding in their studied samples. Consequently, the reduction factor for the amount of chloride binding, predicted by the Langmuir binding isotherm for alkali-activated cements, is set in the numerical model to vary between 0% and 100% to assess the impact of chloride binding on chloride transport in alkali-activated concretes exposed to drying and wetting condition. **Figures 6.21** and **6.22** present the chloride profiles in 100SG concrete, with cover of 50 mm, located within 1.5 km of the ocean and exposed to drying and wetting conditions respectively. It should be noted that chloride profiles predicted for 100SG concrete, with negligible chloride binding, exposed to drying condition within 1.5 km of the ocean, **Figure 6.21 B**, is still slightly lower than the chloride profiles in 100SG concrete exposed to wetting condition, **Figure 6.22 B**. The effect of environmental RH is more evident in **Figures 6.21A** and **6.22A** where the chloride profiles predicted for 100SG concrete, with total chloride binding, exposed to drying condition within 1.5 km of the ocean are lower than the chloride profiles in 100SG concrete exposed to wetting condition. Hence, environmental RH plays a crucial role in the durability of concrete because not only it can increase the flow rate of chloride ion, when its value is higher than the internal RH in the pores of the concrete, but it can also drive out the corroding agents from the concrete when its value is lower than the internal RH in the pores of the concrete.

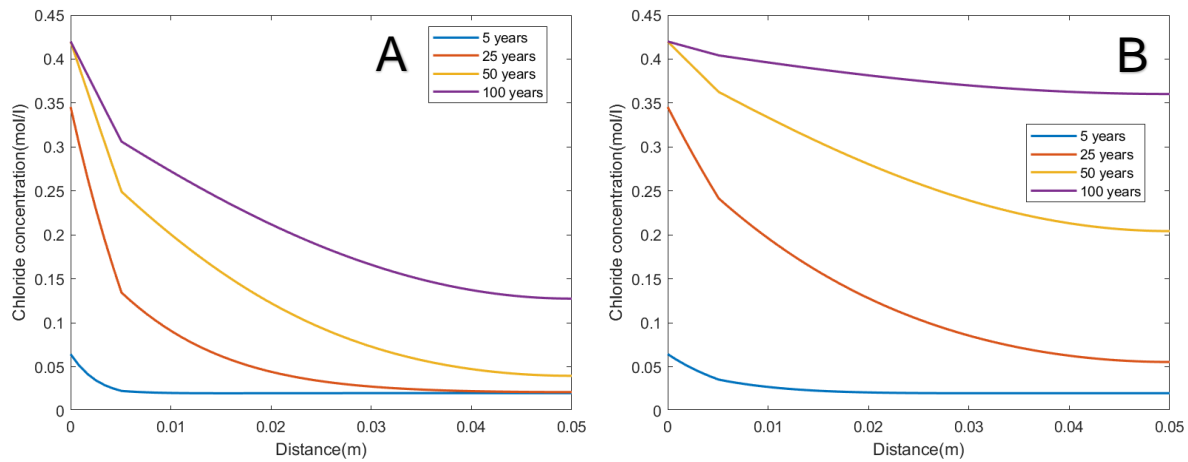


Figure 6.21 Chloride profiles for 100SG concrete within 1.5 km of the ocean at 50% RH and 30°C. The chloride profiles in 100SG concrete are predicted by reducing the total amount of bonded chloride predicted by the Langmuir isotherm for 100SG binder by 0% **A** and 100% **B**.

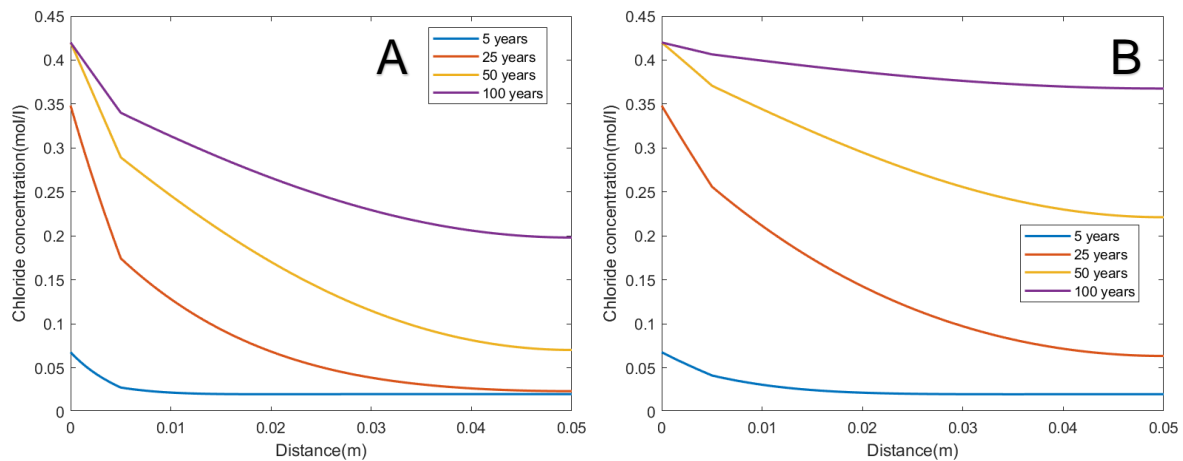


Figure 6.22 Chloride profiles for 100SG concrete within 1.5 km of the ocean at 100% RH and 30°C. The chloride profiles in 100SG concrete are predicted by accounting for the total amount of bonded chloride predicted by the Langmuir isotherm for 100SG binder (**A**) and by reducing the total amount of bonded chloride predicted by the Langmuir isotherm for 100SG binder by 100% (**B**).

Furthermore, **Figure 6.23** represents chloride profiles for 100SG concrete in various locations at 100% RH and 30°C and the profiles are predicted by accounting for the total amount of bonded chloride predicted by the Langmuir isotherm for 100SG binder. The purpose of this figure is to represent the chloride build up at the surface of the concrete when it is not in direct contact to salt water (i.e. marine splash zone). Once the maximum chloride concentration has been reached, it is set in the numerical model to remain constant throughout the remaining service life of the concrete.

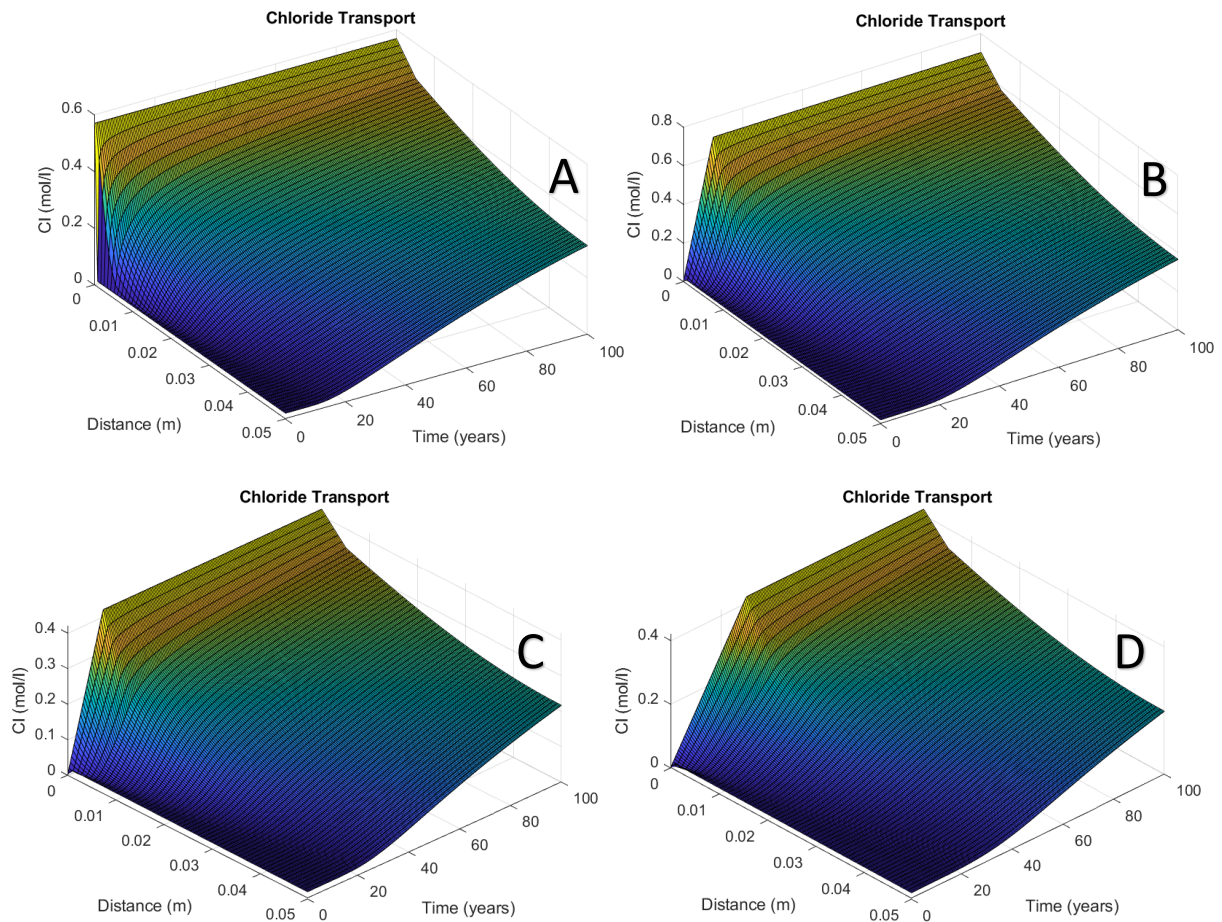


Figure 6.23 Chloride profiles for 100SG concrete in marine splash zone environment (A), marine spray zone (B), within 800 m of the ocean (C), and within 1.5 km of the ocean (D), at 100% RH and 30°C. The chloride profiles in 100SG concrete are predicted by accounting for the total amount of bonded chloride predicted by the Langmuir isotherm for 100SG binder.

In the application of the numerical model for all the studied alkali-activated concretes, the chloride profiles in reinforced concretes located in various zones and exposed to different environmental conditions are predicted by accounting 100% of the total amount of bonded chloride predicted by the Langmuir isotherm for alkali-activated cements. In addition, sensitivity analysis is conducted to assess the impact of chloride binding on service life of alkali-activated concretes to account for the variability in amount of bonded chloride in concrete which is always subjected to cyclic drying and wetting cycles in real service condition [179].

6.8.2.2 Sensitivity in CO₂ transport

The transport of CO₂ in concrete needs to be refined in the numerical model because the effective diffusion model for CO₂ was obtained from an accelerated carbonation experiment as reported in [246]. Consequently, a computational experiment is conducted for 100SG concrete, with cover of 50 mm, and located at a distance of 1.5 km from the ocean. In addition, the concrete is set to be initially saturated, at 100% RH and 20°C, and exposed to 50% RH and 30°C environment (i.e. drying condition) to predict the extent of CO₂ transport in alkali-activated concrete. **Figure 6.24 A** and **B** represent the CO₂ transport profile in 3D and CO₂ with CO₃²⁻ transport profiles in 2D as a function of distance (i.e. thickness of the concrete cover) and time. According to **Figure 6.24** and based on the concentration of carbonate ions in the pore solution, it can be seen that alkali-activated concrete will be carbonated in 20 years which means that the rate of carbonation is 2.5 mm per year. This rate seems to be very high compared to maximum rate of carbonation to be 1 mm/year for alkali-activated concretes in service conditions reported in [267]. Thus, a reduction factor for the transport of CO₂ should be included to obtain a carbonation rate of 1 mm/year. Consequently, the diffusion of CO₂ in the skin layer is reduced by a factor of 0.05 and in the concrete cover is reduced by a factor of 0.04. The reason for the lower reduction in the concrete cover is to utilize the same factor of difference between mortar and concrete (i.e.0.773 previously discussed in section 6.3.2.1) already implemented to model the transport of chloride and carbonate ions in the two phases of the concrete cover. **Figure 6.25** represents the updated CO₂ and CO₃²⁻ profiles, as results from the model refinement, and it can be seen that the rate of carbonation of 1 mm/year has been attained because the concentration of carbonate ions in the pore solution has reached its maximum value in 50 years. Therefore, the method of refinement for CO₂ transport in the skin layer and concrete cover is implemented in the numerical model to predict the service of alkali-activated concretes.

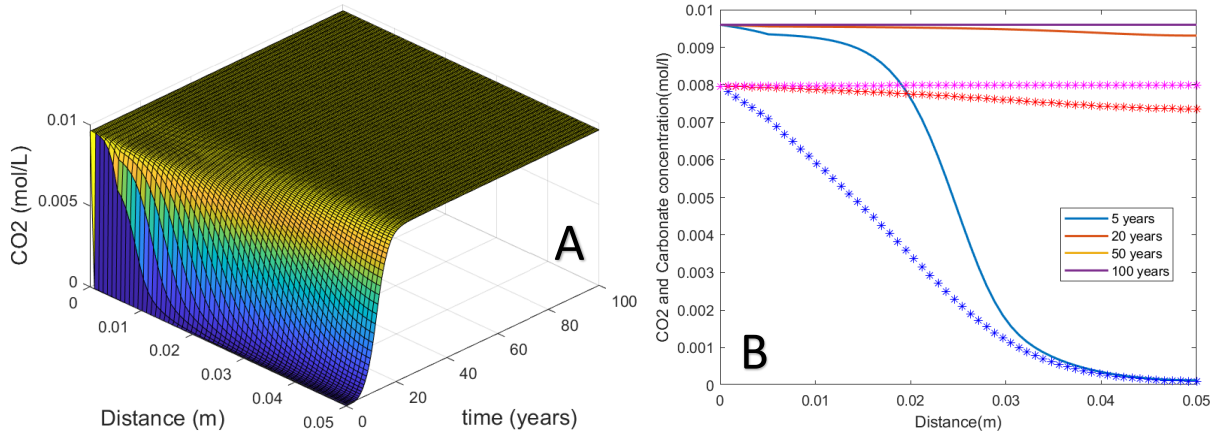


Figure 6.24 3D profile for CO_2 transport (A) and CO_2 with CO_3^{2-} transports, represented as solid line (-) and star sign (*) respectively, (B) in 100SG concrete, with cover of 50 mm, within 1.5 km of the ocean at 50% RH and 30°C. These are initial outputs from the proposed numerical model.

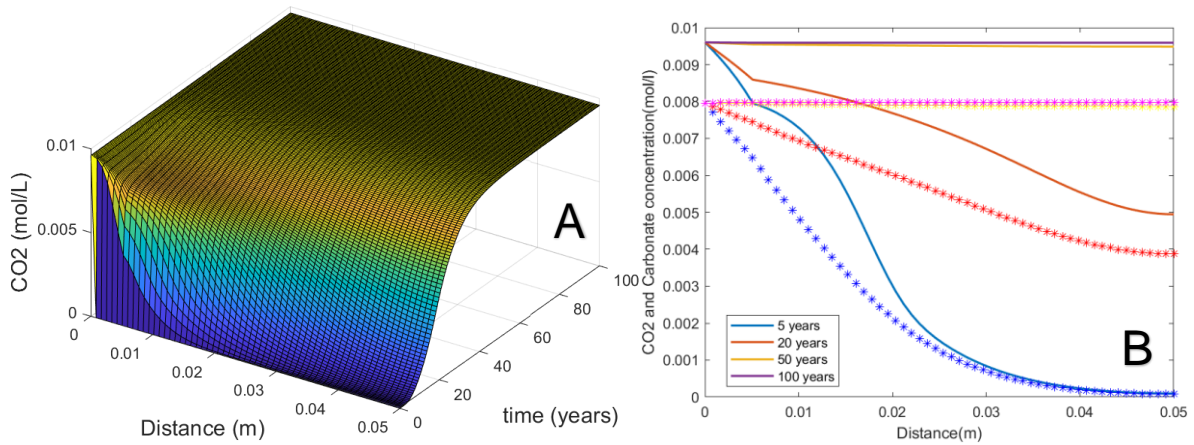


Figure 6.25 Updated 3D profile for CO_2 transport (A) and CO_2 with CO_3^{2-} transports, represented as solid line (-) and star sign (*) respectively, (B) in 100SG concrete, with cover of 50 mm, within 1.5 km of the ocean at 50% RH and 30°C. These outputs are from the updated numerical model that has included the reduction factor of values 0.05 and 0.04 for CO_2 transport in the skin layer and concrete cover, respectively.

6.8.2.3 Sensitivity in carbonation kinetics and effect of change in porosity on chloride transport

The overall profile of CO_2 and CO_3^{2-} concentrations in 100SG concrete including and excluding carbonation kinetics is shown in **Figure 6.26** where it is evident that carbonation kinetics includes the dissolution of CO_2 into the pore solution which increases the concentration of carbonate ions in the pore solution.

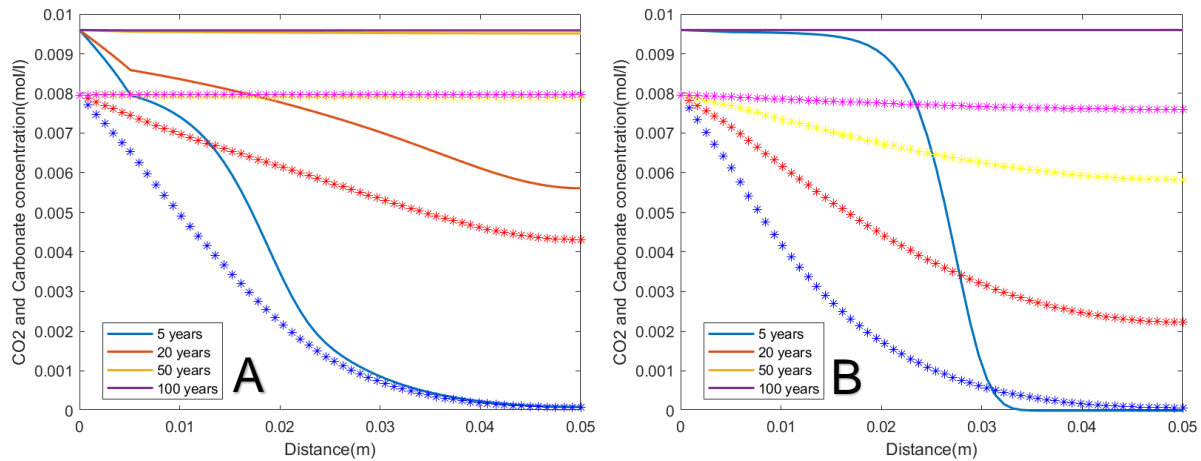


Figure 6.26 CO_2 with CO_3^{2-} profiles, represented as solid line and star sign respectively, in 100SG concrete, with cover within 800 m of the ocean at 50% RH and 30°C with carbonation kinetics (**A**) and without carbonation kinetics (**B**).

It is also useful to study the effect of change in porosity, as a result of carbonation reactions, on chloride transport in alkali-activated concrete. The computational experiment is conducted on 75SG25FA and 50SG50FA concretes initially saturated at 100%RH and located within 800 mm of the ocean at 50%RH and 30°C. **Figures 6.27** and **6.28** present the chloride profiles for 75SG25FA and 50SG50FA concretes with and without including the change in porosity in the numerical model. It can be seen that the change in porosity in 75SG25FA concrete has more impact on chloride transport than 50SG50FA although the percentage of change in porosity is lower in 75SG25FA than in 50SG50FA as reported in [147].

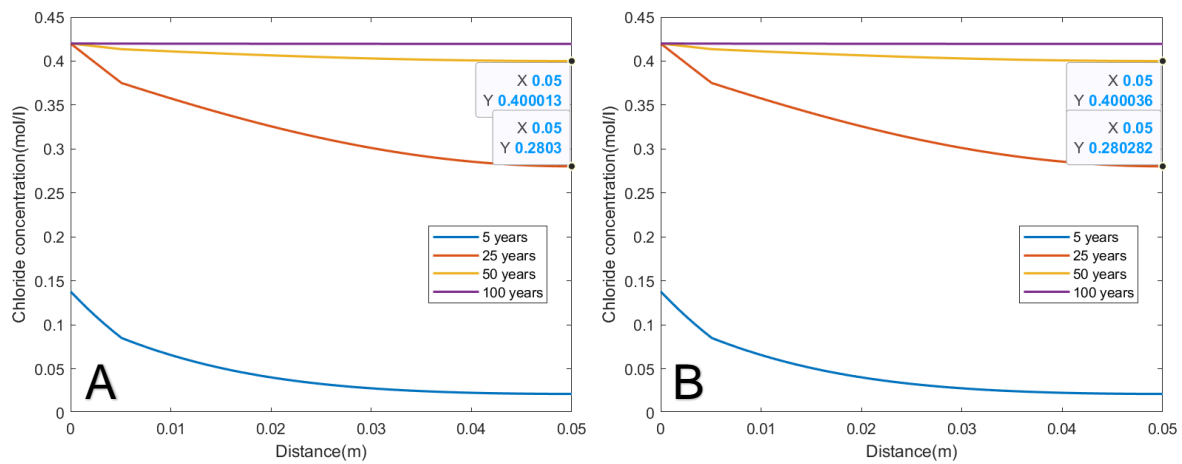


Figure 6.27 Chloride profile for 50SG50FA concrete within 800 m of the ocean at 50% RH and 30°C with carbonation kinetics (A) and without carbonation kinetics (B).

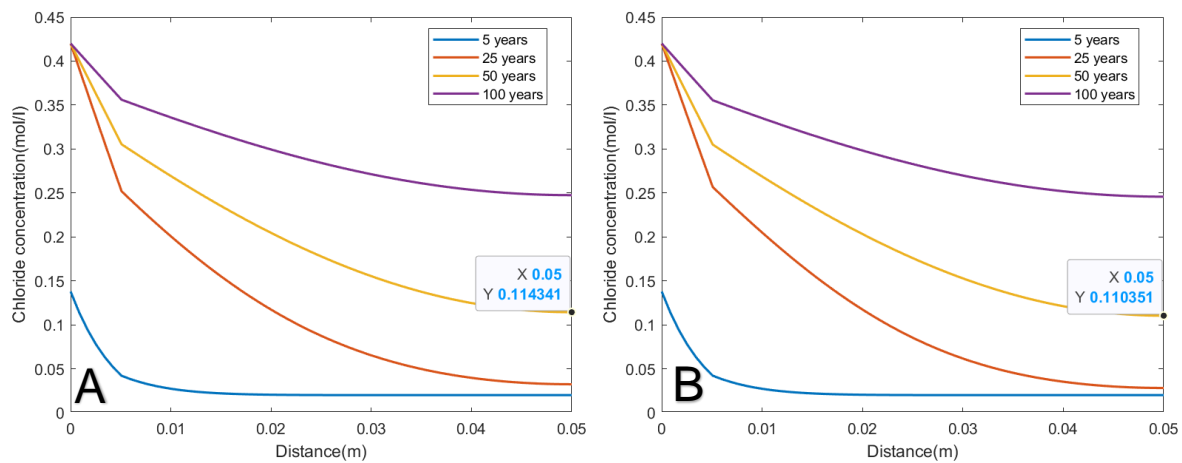


Figure 6.28 Chloride profile for 75SG25FA concrete within 800 m of the ocean at 50% RH and 30°C with carbonation kinetics (A) and without carbonation kinetics (B).

Unfortunately, the rate of precipitation of calcium carbonate (i.e. k parameter as calculated and presented in **Table 6.8**) in the concrete phase of 75SG25FA and 50SG50FA concretes had to be reduced by a factor of 10 in order for the numerical code to run and generate the outputs. Consequently, this refinement step is included in the numerical model to estimate the service life of 75SG25FA and 50SG50FA concretes. Initially, the numerical code was not able to meet the integration tolerance already installed in the pdepe function according to the output messages obtained while running the codes for 75SG25FA and 50SG50FA concretes as shown in **Figure 6.29**. This is a numerical problem which can be solved in the future through modification of the function by increasing the error tolerance so that the code could run and generate results in a convenient time frame.

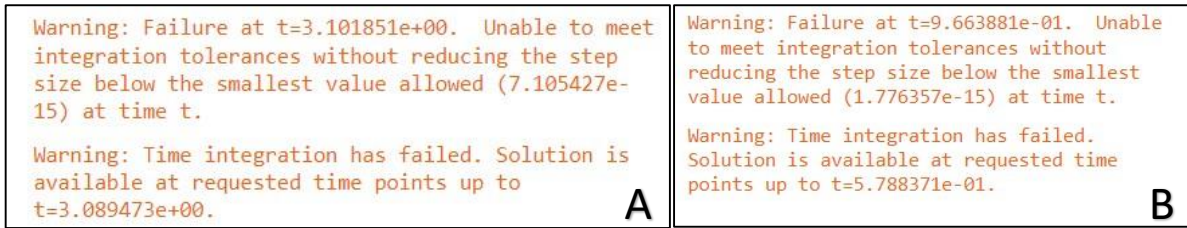


Figure 6.29 Output messages obtained while initially running the codes for 75SG25FA (A) and 50SG50FA (B) containing the initial rates of precipitation of calcium carbonate (i.e. k parameter as presented in Table 6.8).

6.8.2.4 Sensitivity in the effect of chloride binding on CO₂ and moisture transport

In this section the effect of chloride binding is tested on chloride, CO₂ and moisture transport in alkali-activated concrete. The computational experiment is conducted on 75SG25FA concrete initially dried at 50%RH and located in marine spray zone at 100%RH and 30°C. **Figures 6.30-6.33** present CO₂ with CO₃²⁻, and saturation profiles for 75SG25FA concrete with and without including the effect of change in porosity. It can be seen in **Figure 6.31** that the effect of chloride binding slows down the transport of moisture which increases CO₂ transport in the gas phase of the pore and increases production of carbonate ions in the pore solution as shown in **Figure 6.30**. The reason maybe because the chloride binding reduces the diffusion of chloride ions into the concrete and this diffusion coefficient is a parameter in the moisture transport model according to **Equation 6.2.a***. Hence, in the case of wetting condition the effect of chloride binding increases carbonation reaction in concrete.

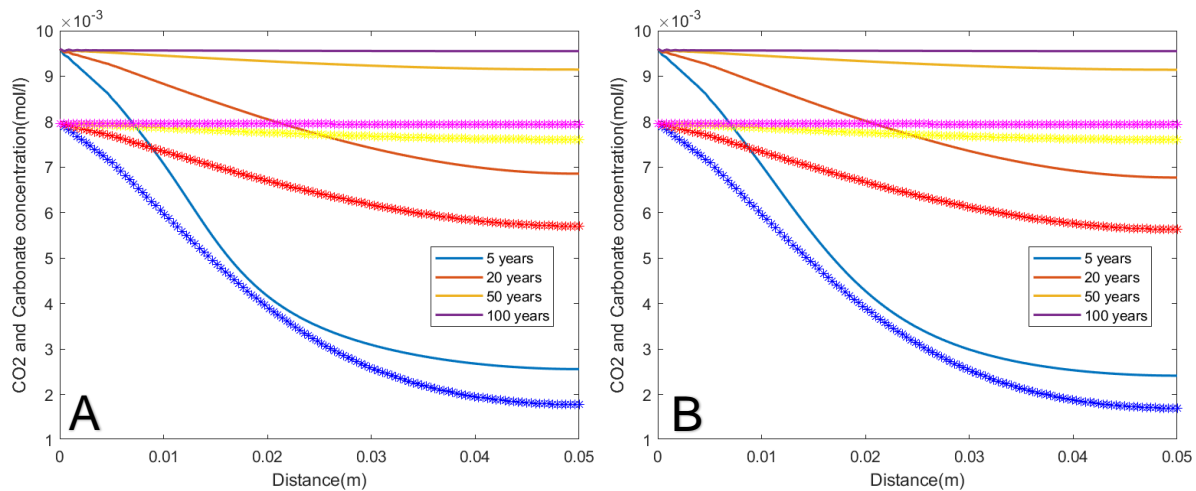


Figure 6.30 CO₂ with CO₃²⁻ profiles in 75SG25FA concrete, with cover of 50 mm, in marine spray zone environment at 100% RH and 30°C. with chloride binding (A) and without chloride binding (B).

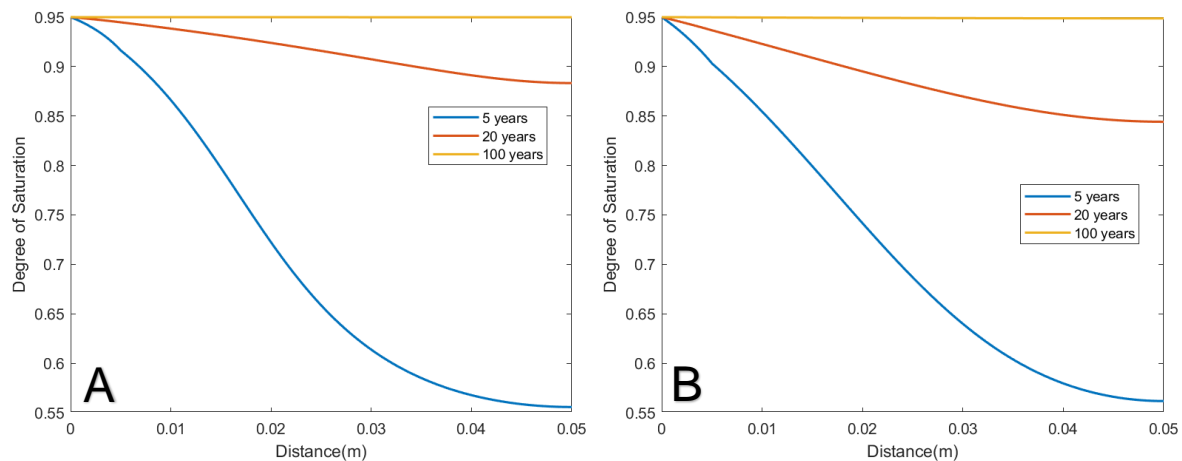


Figure 6.31 saturation profiles for 75SG25FA concrete, with cover of 50 mm, in marine spray zone environment at 100% RH and 30°C with chloride binding (A) and without chloride binding (B).

Another computational experiment is conducted on 75SG25FA concrete initially saturated at 100%RH and located in marine spray zone at 50%RH and 30°C. **Figures 6.32-6.33** present the CO₂ with CO₃²⁻, and saturation profiles for 75SG25FA concrete with and without including the effect of chloride binding. It is evident that in the case of drying condition the effect of chloride binding lowers the rate of moisture transport, as shown in Figure 6.34, which lowers the rate of carbonation reaction as shown in **Figure 6.32**. Therefore, the effect of chloride binding shows opposite effects when the concrete is exposed to opposite environmental conditions (i.e. wetting and drying conditions) and this is because the moisture transport is a function of the ionic concentrations in the pore solution along with their diffusion coefficients, according to **Equation 6.2.a***.

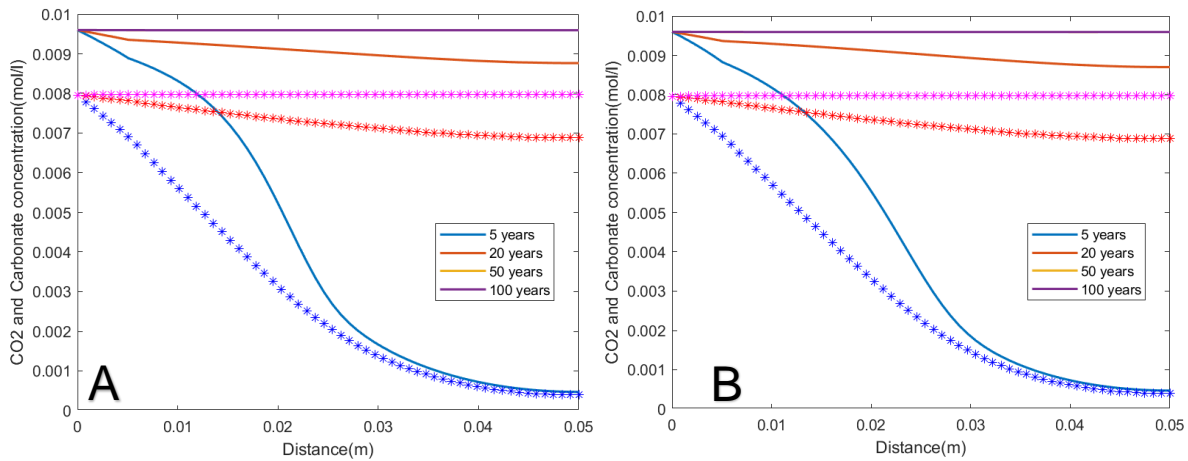


Figure 6.32 CO₂ with CO₃²⁻ profiles in 75SG25FA concrete, with cover of 50 mm, in marine spray zone environment at 50% RH and 30°C. with chloride binding (A) and without chloride binding (B).

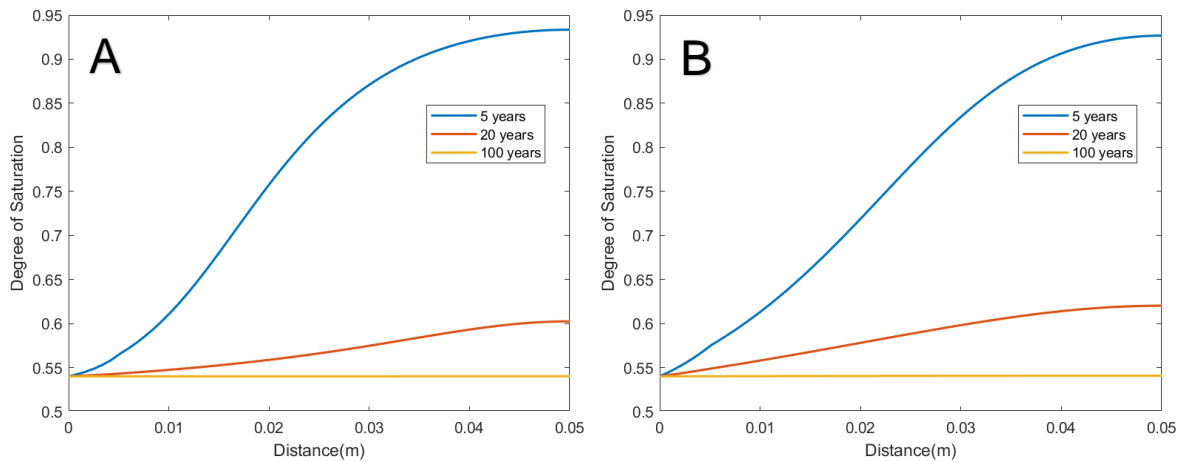


Figure 6.33 saturation profiles for 75SG25FA concrete, with cover of 50 mm, in marine spray zone environment at 50% RH and 30°C with chloride binding (A) and without chloride binding (B).

6.8.2.5 Model Validation

The validation of the numerical model is done by comparing the chloride profile estimated for AAMs exposed for at least 25 years in marine splash zone environment with the profile predicted by the numerical model, as shown in **Figures 6.34-6.36**. The methodology for the estimation of the chloride profile for AAMs has already been explained in section 6.2.3 where the data set for PC concrete is originally obtained from a part of the bridge column in service for at least 25 years in marine splash zone environment as reported in [163]. In addition, the difference between the effective chloride diffusion coefficients obtained for alkali-activated mortars and CEMIII mortars in the laboratory experiment, according to section 6.7.1, has been implemented to estimate the chloride profiles for AAMs in real service marine environment.

Note that this is not an accurate approach to estimate the profiles of AAMs in service conditions but it is only applied to qualitatively validate the proposed numerical model. **Figures 6.34-6.36** present validation of the numerical model by comparing the estimated chloride profile for AAMs with the predicted profile by the model in case when alkali-activated concrete is subjected to drying and wetting conditions.

According to **Figures 6.34-6.36** the proposed numerical model predicts quite well the profile for 100SG and 75SG25FA concretes. Whereas for the case of 50SG50FA concrete, the numerical model overestimates the chloride profile for this concrete exposed to marine splash zone environment for 25 years. However, no further model refinement is done at this stage of the research and the model is implemented to predict the service life of alkali-activated concretes.

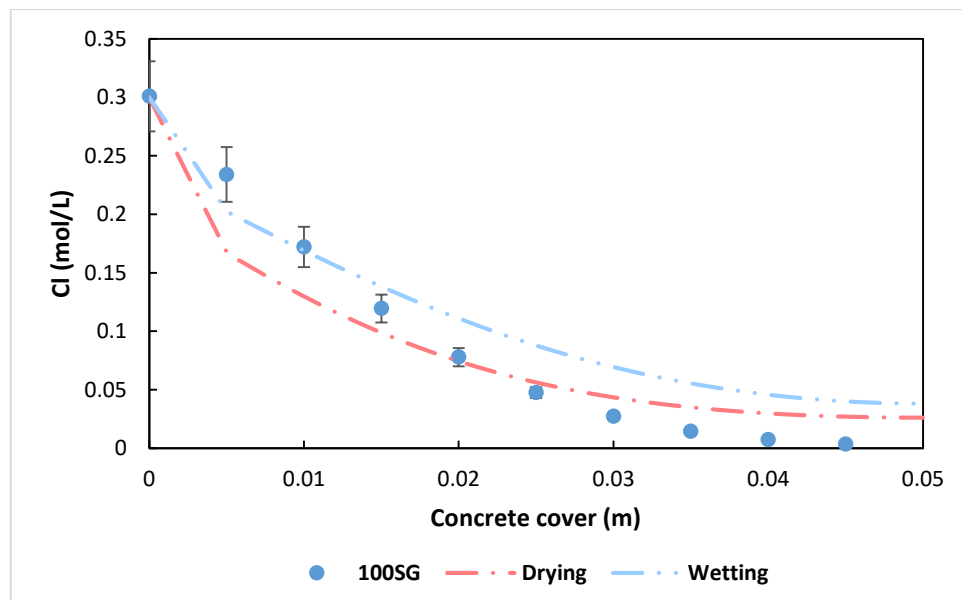


Figure 6.34 Model validation for 100SG concrete, with cover 50 mm, located in a marine splash zone. The circular symbols are the data set and the dashed lines are the predicted curves by the model in case when the concrete is exposed to wetting and drying conditions at 30°C.

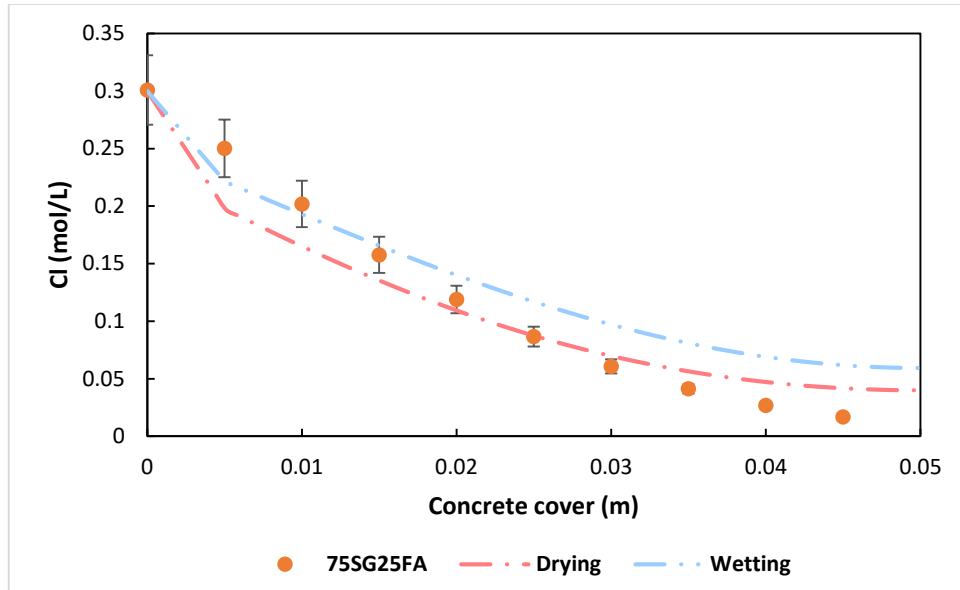


Figure 6.35 Model validation for 75SG25FA concrete, with cover 50 mm, located in a marine splash zone. The circular symbols are the data set and the dashed lines are the predicted curves by the model in case when the concrete is exposed to wetting and drying conditions at 30°C.

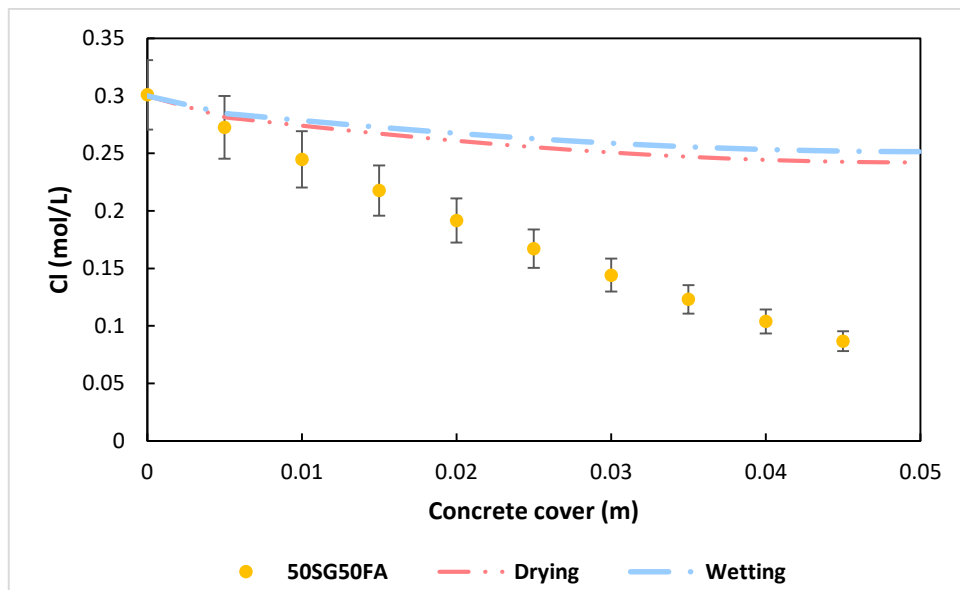


Figure 6.36 Model validation for 50SG50FA concrete, with cover 50 mm, located in a marine splash zone. The circular symbols are the data set and the dashed lines are the predicted curves by the model in case when the concrete is exposed to wetting and drying conditions at 30°C.

6.8.3 Probabilistic service life prediction

6.8.3.1 Critical Chloride Thresholds

The service is probabilistically calculated based on the distribution of critical chloride threshold initially obtained from **Chapter 4**. The distribution of critical chloride thresholds, in terms of mol/L (i.e. L of the solid), is fitted by a lognormal distribution function as shown in **Figure**

6.37 where the fitted log mean, μ , and standard deviation, σ , are shown in **Table 6.15**. Note that the chloride distribution obtained for 100SG is also implemented for 75SG25FA based on the assumption that these materials have similar pore solution chemistry [249].

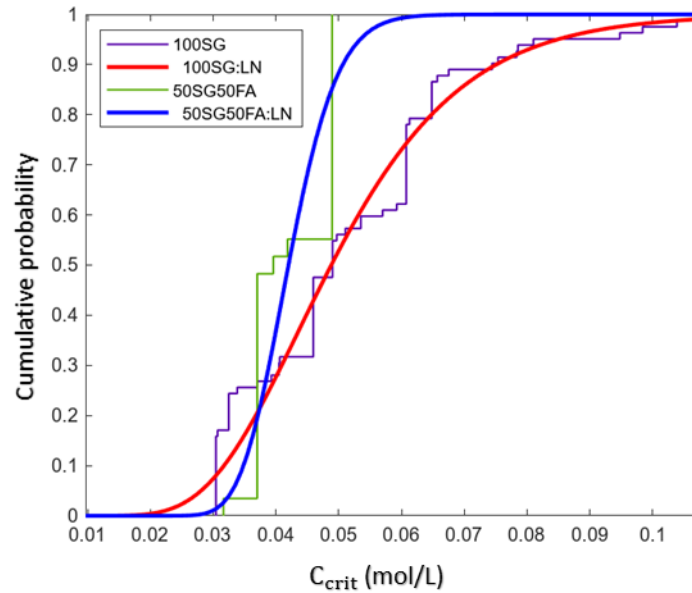


Figure 6.37 Distribution of critical chloride thresholds for 100SG and 50SG50FA concretes.

Table 6.15 Lognormal distributions fit of critical chloride thresholds for 100SG and 50SG50FA concretes.

	Lognormal distribution function	
	μ	σ
100SG	-3.01974	0.33586
50SG50FA	-3.16993	0.145826

Finally, the distribution of the service life of alkali-activated concrete is fitted by a normal distribution function. In addition, sensitivity analysis is conducted to test the impact of environmental condition and durability parameters on the service life of alkali-activated concretes.

6.8.3.2 Service life of Alkali-activated concretes

The service life is determined for 100SG and 75SG25FA concretes, with cover of 65 mm, located in various zones and exposed to different environmental conditions (i.e. drying and wetting conditions) and the distributions are shown in **Figures 6.38-6.41**.

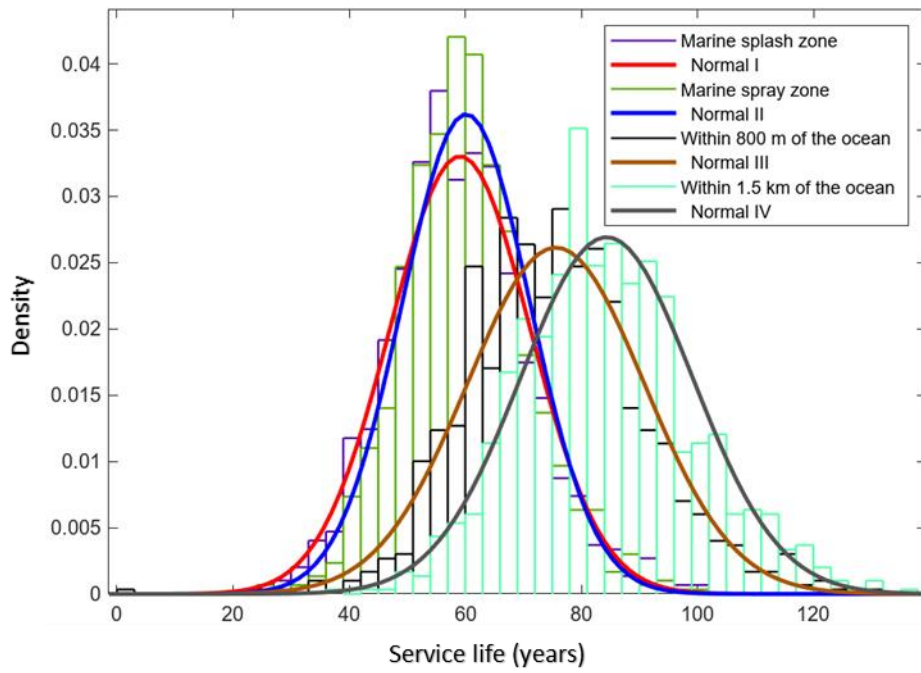


Figure 6.38 Probability service life distribution of 100SG concrete, with cover of 65 mm, in various zones at 50% RH and 30°C.

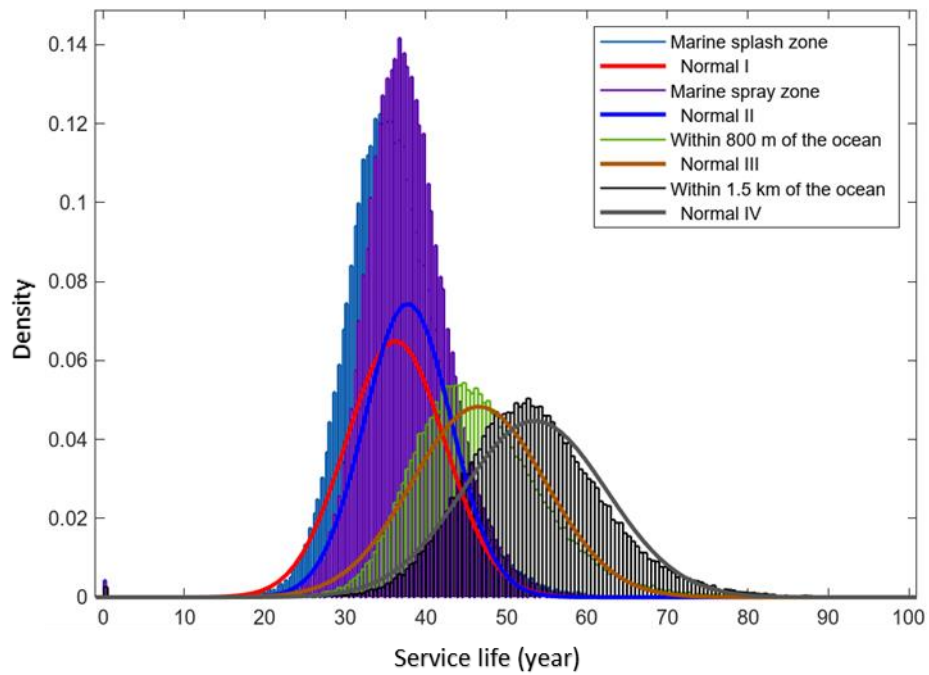


Figure 6.39 Probability service life distribution of 75SG25FA concrete, with cover of 65 mm, in various zones at 50% RH and 30°C.

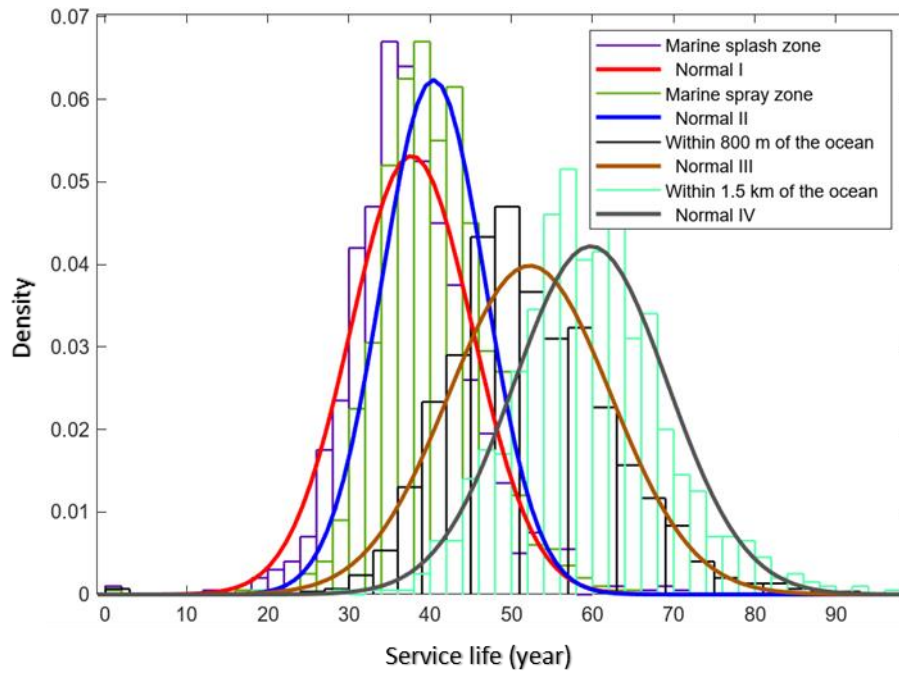


Figure 6.40 Probability service life distribution of 100SG concrete, with cover of 65 mm, in various zones at 100% RH and 30°C.

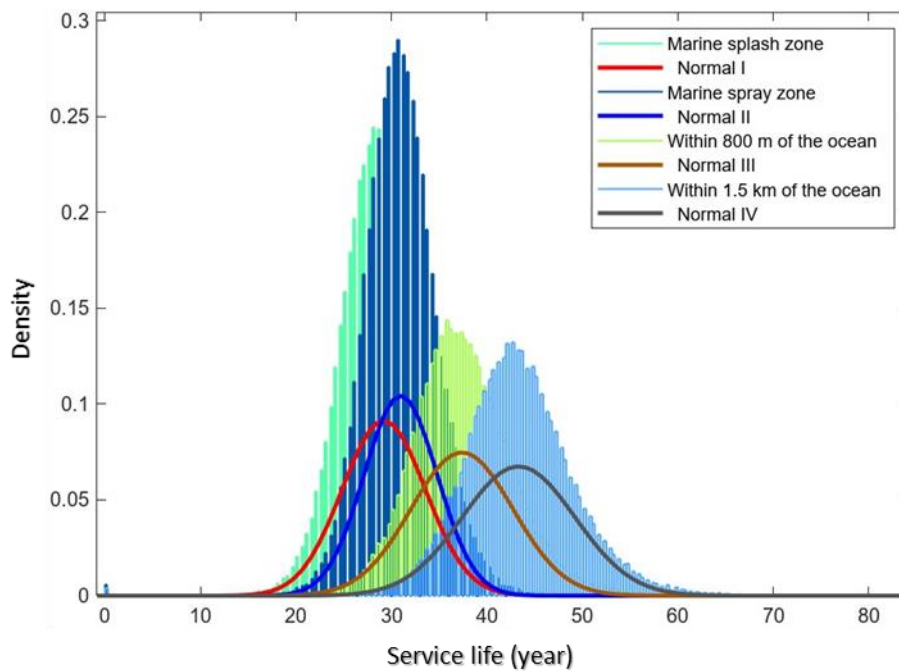


Figure 6.41 Probability service life distribution of 75SG25FA concrete, with cover of 65 mm, in various zones at 100% RH and 30°C.

On average, the minimum service life of high calcium based alkali-activated concretes is 39 years and the maximum is 86 years based on the predictions from the proposed numerical model as shown in **Tables 6.16** and **6.17**. In addition, the impact of environmental RH is most

evident for 100SG concrete than for 75SG25FA concrete because the service life for 100SG concrete has dropped by at least 15 years when the concrete is exposed to wetting condition in the same zone located 1.5 km away from the ocean. Whereas for the case of 75SG25FA concrete the service life got reduced by only 7 years. It should be noted that the small probability fraction at year zero shown in **Figures 6.38-6.41** occurred because the distribution of critical chloride threshold may have provided (for a few times during 100,000 runs) values that are similar to the initial chloride content in concrete (i.e. 0.02 mol.L⁻¹).

Table 6.16 Normal distribution fit of service life for 100SG and 75SG25FA concretes, with cover of 65 mm, in various zones and exposed to drying condition.

	100SG		75SG25FA	
	Mean	Std.	Mean	Std.
Marine splash zone	59	12	36	6
Marine spray zone	60	11	38	5
Within 800 m of the ocean	76	15	47	8
Within 1.5 km of the ocean	84	15	54	9

Table 6.17 Normal distribution fit of service life for 100SG and 75SG25FA concretes, with cover of 65 mm, in various zones and exposed to wetting condition.

	100SG		75SG25FA	
	Mean	Std.	Mean	Std.
Marine splash zone	38	8	29	4
Marine spray zone	40	6	31	4
Within 800 m of the ocean	52	10	37	5
Within 1.5 km of the ocean	60	9	43	6

Next, the service life distribution for 50SG50FA concrete is also determined but the thickness of the concrete cover for this type of material is set to 100 mm because the transport of the ionic species in 50SG50FA concrete is at least 3 times faster than the ionic transport in high calcium based alkali-activated concretes according to **Table 6.7**. The cumulative probability distribution of service life for 50SG50FA concrete in various zones and exposed to different environmental condition is shown in **Figure 6.42**. Furthermore, the estimated average of service life for 50SG50FA concrete in both drying and wetting conditions, shown in **Table 6.18**, is approximately half the service life of 75SG25FA concrete with cover thickness of only 65 mm. It should also be noted that the effect of environmental RH has the minimal effect for 50SG50FA concrete compared to 100SG concrete.

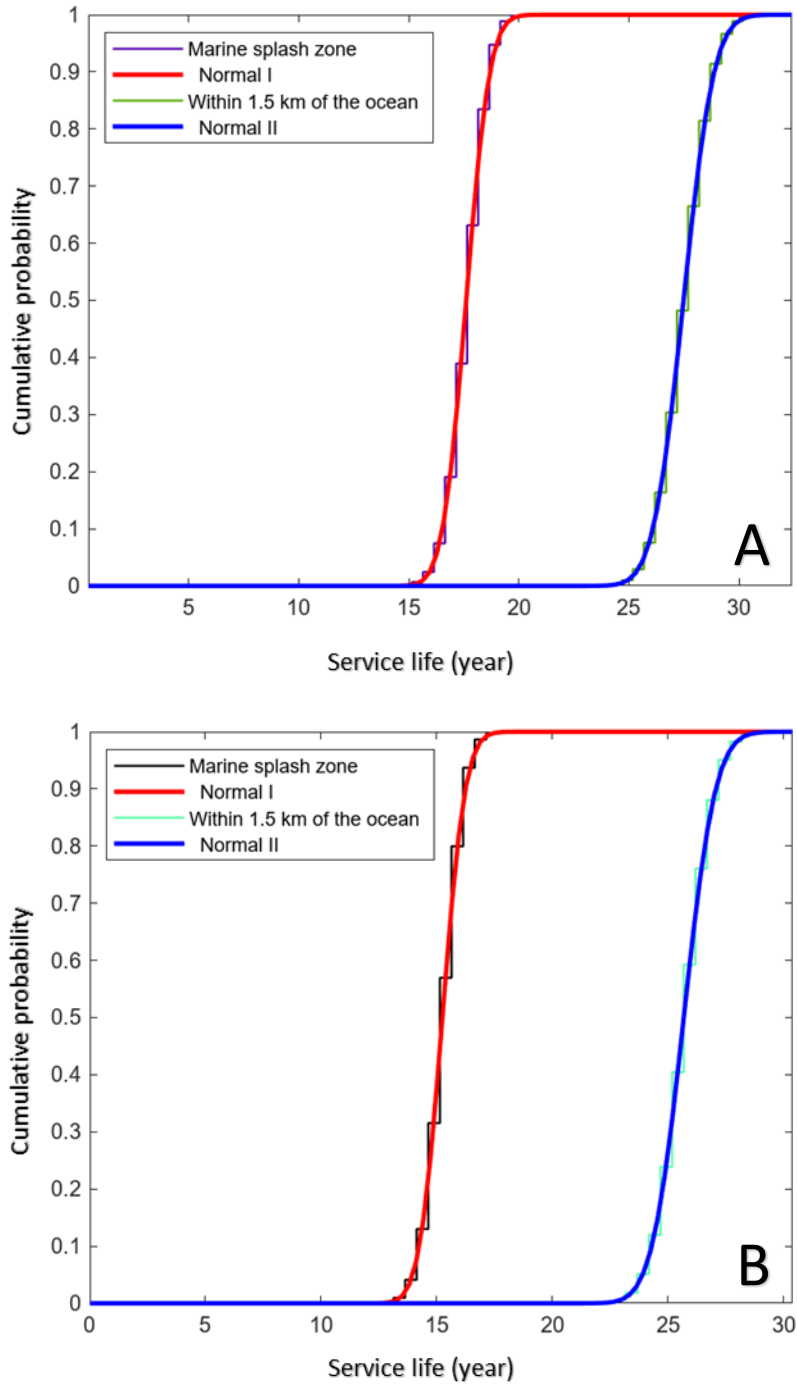


Figure 6.42 Cumulative probability service life prediction of 50SG50FA concrete, with cover of 100 mm, in various zones at 50% RH and 30°C (A) and at 50% RH and 30°C (B).

Table 6.18 Normal distribution fit of service life for 50SG50FA concrete, with cover of 100 mm, in various zones and exposed to drying and wetting condition.

	Drying		Wetting	
	Mean	Std.	Mean	Std.
Marine splash zone	17	1	15	1
Within 1.5 km of the ocean	27	1	26	1

6.8.3.3 Effect of change in porosity

The impact of change in porosity is mainly contributed by the mineralogical composition of alkali-activated cements. For example, and according to literature, high calcium alkali-activated binders containing a high content of magnesium oxide, around 7.44 wt.%, showed to have more resistance to carbonation reaction than the binder containing a low content of magnesium oxide, around 1.17 wt.% [134]. Hence, in this section the impact of change in porosity, caused by carbonation, on service life of 50SG50FA and 75SG25FA concretes is tested by setting the change in porosity to 1 and 0 in the numerical code to account for the variability in the mineralogical composition of the binders containing high and low magnesium oxide content in their composition, respectively. 50SG50FA, with cover of 100 mm, and 75SG25FA, with cover of 65 mm, are set to be located within 800 m of the ocean and exposed to different environmental conditions (i.e. drying and wetting conditions). The cumulative probability distribution of service life for 50SG50FA and 75SG25FA concretes are shown in **Figures 6.43 and 6.44**. According to **Figure 6.43**, the impact of change in porosity seems to have a negligible effect in the case of 50SG50FA exposed to a wetting environment and with a change in the porosity having a negative impact on the service life. Whereas in the case of exposure to drying condition, the change in porosity has a positive impact on the service life in increasing it by 1-2 years for 50SG50FA concrete. The reason could be because during drying the liquid water drives out the corrosive agents through the pores of the concrete, that are increasing in size due to carbonation reaction in Low-Ca AAMs, to the external environment. In the case of 75SG25FA concrete, according to **Figure 6.44**, the change in porosity has a negative impact when the concrete is exposed to both environmental conditions and it is more evident than in the case of 50SG50FA concrete. According to **Figure 6.44** and in the case of drying condition, the service life of 75SG25FA concrete decrease by a maximum of 15 years when the effect of change in porosity was included in the numerical model because in the case of 75SG25FA concrete the increase in porosity favoured the ingress of more chloride ions into the concrete cover. Whereas in the case of wetting condition, the impact of change in porosity has a less negative impact on service life of 75SG25FA concrete because the total service life has only been reduced by 7 years compare to drying condition. The reason is because CO₂ gets slowly transported into a concrete cover with pores nearly saturated with evaporable water, which makes the extent of carbonation reaction in a wet environment to be minimal.

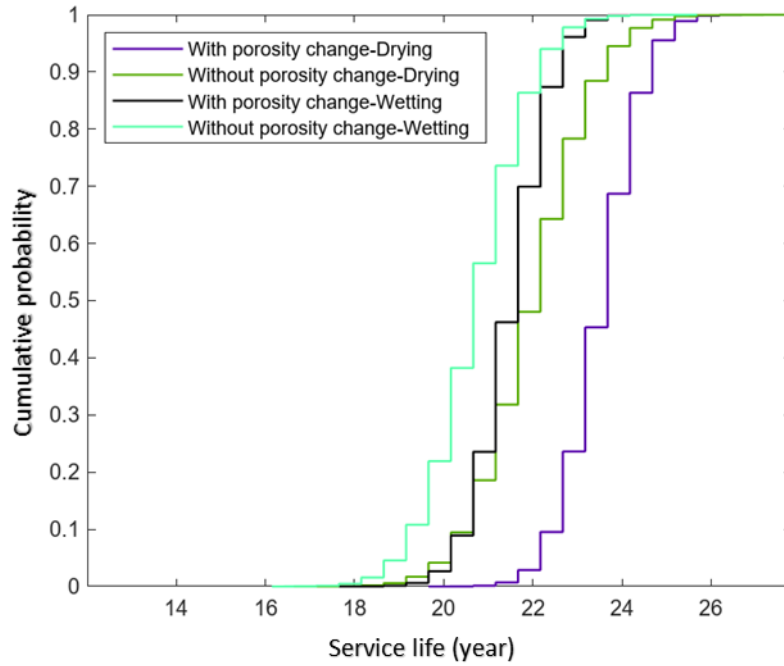


Figure 6.43 Cumulative probability service life prediction of 50SG50FA concrete, with cover of 100 mm, within 800 m of the ocean and exposed to drying and wetting conditions at 30°C . The prediction of service life is set with and without change in porosity of 50SG50FA concrete.

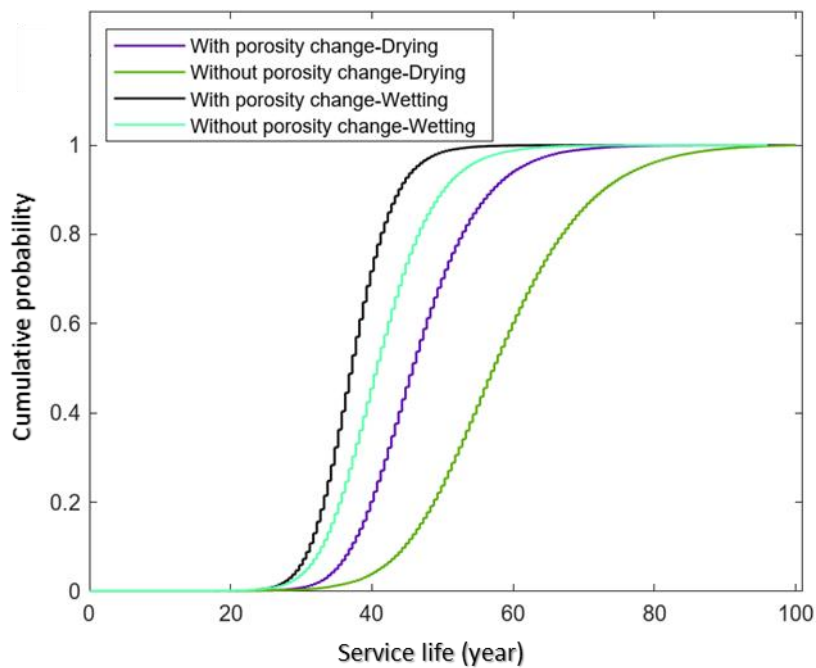


Figure 6.44 Cumulative probability service life prediction of 75SG25FA concrete, with cover of 65 mm, within 800 m of the ocean and exposed to drying and wetting conditions 30°C. The prediction of service life is set with and without change in porosity of 75SG25FA concrete.

6.8.3.4 Effect of moisture permeability

The change in the moisture permeability can be manifested through the change in amount of binder or aggregate used in the mix design of concrete [223]. For example, a decrease and/or increase in the binder content can increase the permeability and vice versa because the binder phase is mainly the transport media in the concrete since it forms pores with various sizes as it glues all the other non-porous components (i.e. sand and aggregate) of the concrete together. Hence, in this section the change in moisture permeability, caused by lowering the amount of aggregate or increasing the binder content in the mix design, on service life of 50SG50FA and 75SG25FA concretes is tested by setting the flow velocity of the evaporable water, v , to increase by a factor of 60 in the numerical code. 75SG25FA concrete, with cover of 65 mm, is set to be located in marine splash zone and exposed to different environmental conditions (i.e. drying and wetting conditions). In addition, the different environmental conditions are also set to be in severe states where in the case of severe drying condition the concrete is set to be initially dried at 55% at 20°C then exposed to a 50% RH at 30°C environment whereas in the case of severe wetting the concrete is set to be initially wet at 90% RH at 20°C then exposed to 100%RH at 30°C. The probability distribution of service life for 75SG25FA concrete in the case of wetting and drying condition is shown in **Figures 6.45 A and B**, respectively. In the case of wetting condition, **Figure 6.45 A**, the service life of 75SG25FA concrete reduced by 10 years when exposed to severe wetting condition. Whereas in the case of drying condition, **Figure 6.45 B**, the impact of severe drying state showed to have negligible effect on the service life only when the change in porosity is excluded in the numerical model. The reason can be because severe drying causes the pores of the cement phase to quickly become less saturated with liquid water which increases diffusion of $\text{CO}_{2(g)}$ into the concrete cover. Consequently, a rapid change in the porosity from carbonation reaction will result that increases the ingress of chloride ions into the concrete.

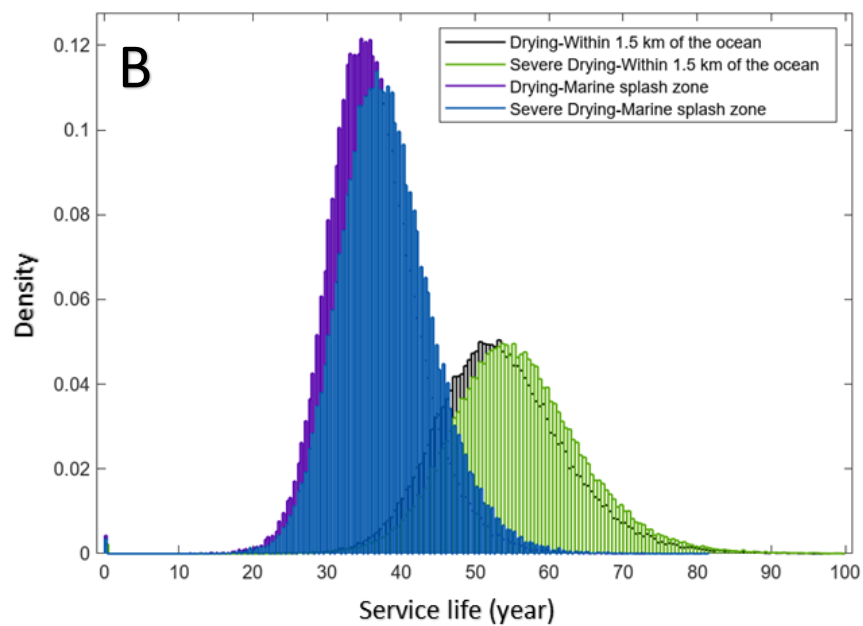
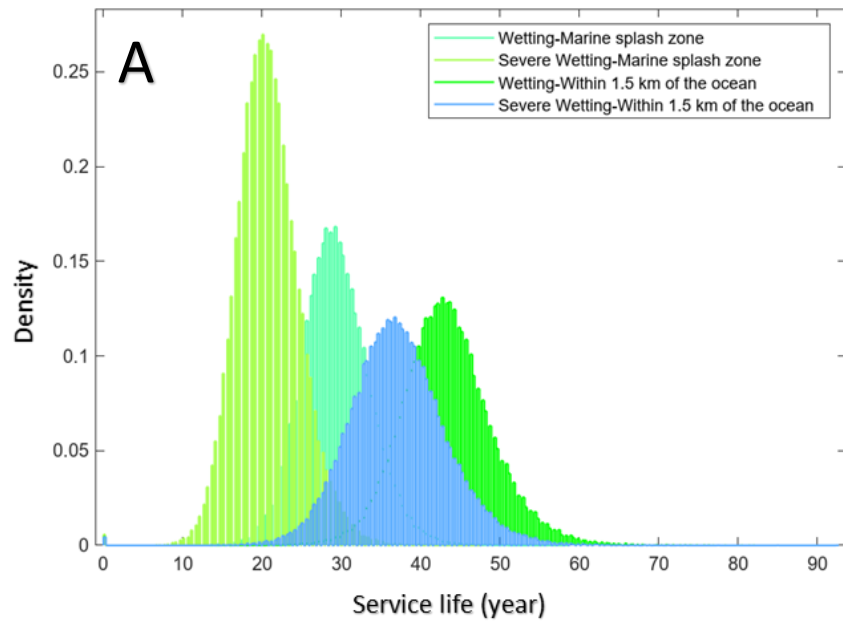


Figure 6.45 Probability service life distribution of 75SG25FA concrete, with cover of 65 mm, located in marine splash zone exposed to wetting with severe wetting condition A and drying with severe drying condition B at 30°C. In the case of severe drying condition, the impact of change in porosity is also included.

6.8.3.5 Effect of Chloride binding

In this section the variability of amount of bonded chloride, predicted by Langmuir binding isotherm, in alkali-activated materials is set to range from 0 to 100% to account for the case of complete absence and presence of chloride binding found in experiments from literature. The probability distribution of service life for 100SG concrete in the case of wetting and drying

condition with and without chloride binding is shown in **Figure 6.46**. It can be seen in this figure that the extent in amount of chloride binding plays the most crucial role in the service life of alkali-activated concrete because it can be reduced by a maximum of 40 years when chloride binding does not occur at the level of the cement in concrete.

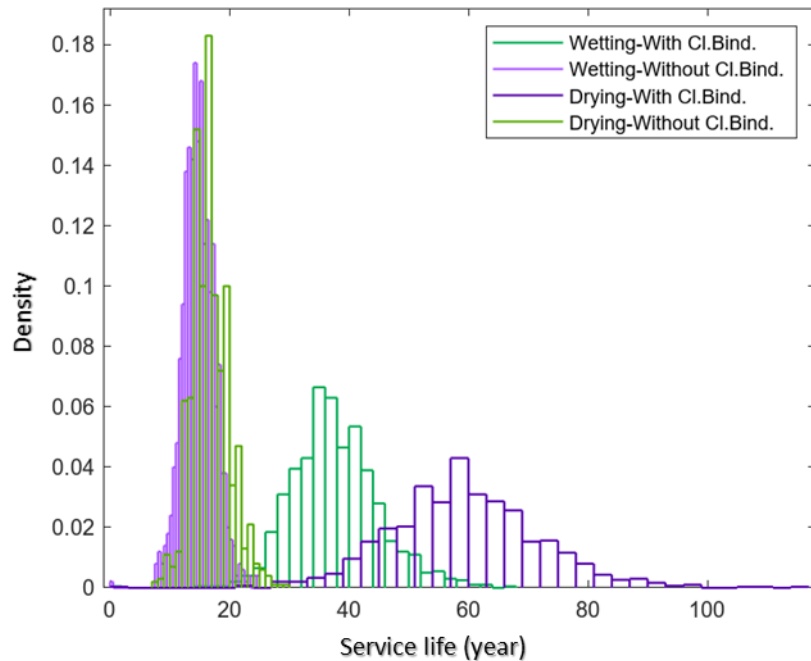


Figure 6.46 Probability service life distribution of 100SG concrete, with cover of 65 mm, located in marine splash zone exposed to drying and wetting conditions with and without chloride binding at level of the cement.

6.8.3.6 Effect of Exposure Temperature

In this section the impact of temperature on the service life of 100SG, located in marine splash zone, is analysed according to the cumulative probability plot shown in **Figure 6.47**. Where the alkali-activated concrete (i.e. 100SG) is exposed to drying and wetting conditions and at different exposure temperatures of 5°C, 20 °C and 50°C. It can be seen in **Figure 6.47** that the service life of 100SG increases as a function of decrease in temperature with the impact of change in temperature being more evident in the case of drying condition. The reason could be that when the construction material is initially saturated (i.e. at 100% RH) and exposed to high temperature condition then the microstructure of the material becomes more permeable to corroding agents (i.e. chloride ions) as has been previously explained in section 6.7.1.

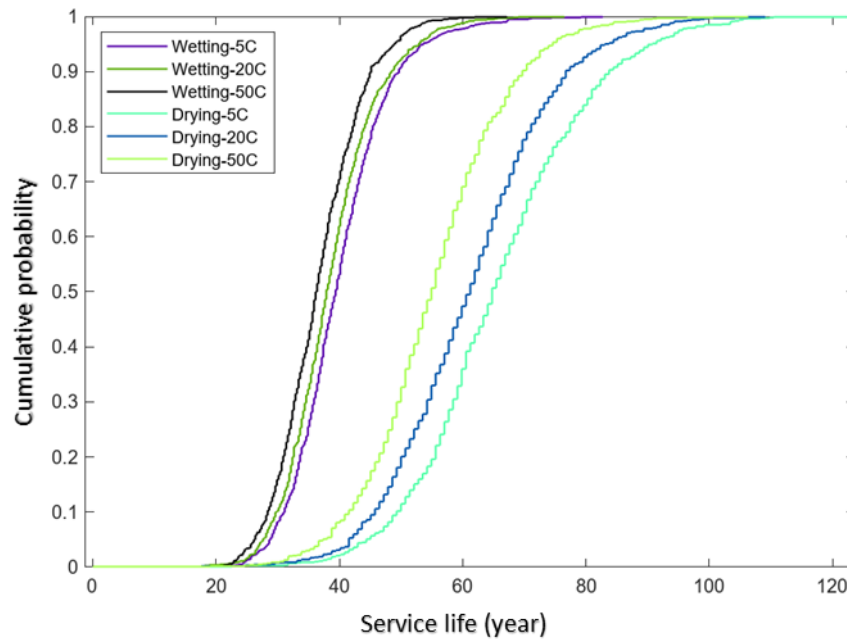


Figure 6.47 Cumulative probability service life prediction of 100SG concrete, with cover of 65 mm, located in marine splash zone and exposed to drying and wetting conditions also at different exposure temperatures of 5°C, 20 °C and 50°C.

6.9 Conclusion

Based on the results of this study, the usefulness of the developed model can be drawn:

1. It is a useful numerical tool to model the interplay of chloride ingress and carbonation reaction because of the incorporation of moisture permeability models that account for anomalous moisture transport in cement and predict the degree of saturation in the pores of the concrete cover as a function of environmental relative humidity. It also includes transport and reaction in the skin layer of the concrete (i.e. that is mortar phase) which is ignored in the service life models found in the literature.
2. The numerical model can also be used as an efficient decision-making tool in material design of concrete for the suitable structural application. It also provides estimated uncertainty values for the calculated service life of AAC and the assessment of the main mix variable and durability parameters that have the most impact on the serviceability limit state.

Overall, the important mix variable is the cement content and water to binder ratio. The mineralogical composition of the cement content yields estimates of the extent in binding of

the chloride and carbonation reactions. It also influences the alkalinity of pore solution that only impacts the extent of $\text{CO}_{2(g)}$ dissolution but also estimates the distribution of critical chloride threshold which is set as a serviceability limit state in the numerical model. The water/binder ratio defines the porosity and it is the most influencing durability parameter used in the moisture permeability models, which control the extent of reaction in gaseous and liquid phases of the pore. Finally, the variability in the relative humidity of the exposure environment is a vital parameter to have in numerical service life models because of its equal impact to carbonation reaction in reinforced concrete exposed in dried and wet environments.

Chapter 7: Conclusion and Future Research

The key outcome of this thesis is the implementation of numerical models to visualize the durability of AAMs and make predictions regarding the service life of Alkali-activated concretes for structural application in marine exposure environment. The primary focus of this thesis has been to develop, implement and disseminate an advanced mathematical model that will enable the service life of steel-reinforced concrete to be probabilistically predicted with value related to structural design using AAMs. As such, every chapter is presented as steps towards building the proposed service life model discussed in the final chapter of results. Although, like every existing model, the models implemented from the literature and the proposed service life model have limitations and assumptions which have been made to simplify the complex system of cementitious material. Hence, this chapter not only includes discussion of the main outcomes reached in each chapter but also highlights recommendations for future developments in the field of comprehending the durability of AAMs and interpreting it in models that can simulate the degradation and or reliability of AAMs in corrosive environment over time.

Chapter 2 of the thesis is a literature review of research done in the field of durability of AAMs, from binder to concrete scale, in corrosive environment where carbonation or chloride ingress is present as a single mode of deterioration or combined. This chapter also reviews numerical models that predict the water vapour sorption isotherms and moisture transport which have been formulated for durability studies on Portland cement. The final part of this chapter describe a numerical service life model that has been implemented to probabilistically predict the service life of PC concrete solely exposed to chloride ingress in submerged conditions. Based on the comparison in durability between PC and AAMs, it can be deduced that AAMs is an alternative low-carbon binder that can utilized in the production of concrete for structural application. However, numerical models have not been extensively applied in the literature to predict the durability and service life of AAMs over time. This then leads into the work presented in **Chapters 4, 5** and **6** where the existing service life model is implemented for AAMs and the missing features of the model to include moisture transport and carbonation reaction with chloride binding are developed and presented in chapters 5 and

6 respectively. The numerical model developed in this research provides a basis for future development of model factors that control reactions kinetics between the binder phase of the concrete and corroding agents when the concrete is exposed to different environmental conditions. The application of the model will not only be used to probabilistically calculate the service of reinforced concrete until the point of corrosion initiation but can also be a potential tool to predict the fate of toxic agents for immobilization application.

The *fib* Bulletin 34 code is applied to probabilistically predict the service life of Alkali-activated concretes in **Chapter 4**. The service life model incorporated three durability factors that are critical chloride threshold, chloride migration and aging factor of AAMs. The distribution of critical chloride threshold for different types of alkali-activated concretes was estimated based on the mineralogical composition, alkalinity of the pore solution, porosity and potential leaching effects and the thresholds aligned with values reported in the literature. However, more research is needed to validate the distribution of critical chloride threshold for AAMs. The values for chloride migration and aging factor were obtained from the literature where the migration test provided similar values only for high calcium based AAMs compared to PC. The test indicated that low calcium based AAMs is not a suitable construction material in a corrosive environment. However, experiments should be done to estimate the aging factor for various alkali-activated concretes by implementing a reliable test such as NTBUILD 492 on the concretes aged at different times. The main result will be the estimation of the extent of hydration reaction that controls the final state of the microstructure of the concrete which is the key factor in transport property of a service life model.

Two main outcomes have been attained in **Chapter 5** which are the application of a suitable moisture permeability model to predict the degree of saturation in AAMs and a method to simulate moisture transport in mortar and concrete by accounting the effect of sand and aggregate in lowering the moisture diffusivity through the pores of the binder phase. The dual permeability model predicts the saturation profile by including the anomaly effect during the transport of moisture in the cementitious material. The dual permeability captures the anomaly effect (i.e. the bending point in the shape of the saturation profile) by accounting the microstructure of cements with two distinct pore sizes (i.e. classified as large and small pores) which is usually a microstructural property of blended cements. However, the model does not include the effect of high content of alkali ions present in the pore solution of AAMs that can not only minimize the evaporation rate of free water during a drying cycle but can also induce pore refinement when free alkali ions react with unreacted precursors in the presence of

moisture during a wetting cycle. Therefore, further development in the moisture permeability model should include the chemistry of the pore solution with the microstructural aspect of alkali-activated binders. In addition, data on saturation profiles for AAMs exposed to a wetting and drying cycle need to be obtained to further validate the moisture permeability model including any model refinements.

A probabilistic service life model in **Chapter 6** has been developed that includes simultaneous transport of chloride and CO₂ in the aqueous and gaseous phase of the pore due to the implementation of a moisture permeability model. The importance of the moisture permeability model is its prediction of the degree of saturation in the pores of the binder phase in the concrete cover which interplays the extent of transport and reaction of chloride ingress and carbonation in concrete exposed to different environmental conditions. Furthermore, the service life model has been validated against chloride profile data obtained from bridge column exposed to a marine environment. The reaction kinetics models were included in the service life model through empirical equation that describe the adsorption of chloride ions, dissolution of CO₂ into the pore solution, and the rate of formation of CaCO₃. These are the areas for further research and can be broadly categorized as:

- Chloride binding – The amount of chloride binding needs to be quantified at the concrete scale by taking into account the amount of hydrated phases available for the reaction. The binding kinetics should include the effect of sand and aggregate in the concrete because according to literature the amount of bonded chloride is the highest at binder level followed by concrete and mortar. In addition, the amount of chloride binding should also be quantified when the concrete is exposed to a drying condition because the predicted amount of bonded chloride may be overestimated compared to the amount of chloride ions remaining after the ingress of evaporable water, that carries these corroding agents, towards the external environment which is seen in the case of 75SG25FA concrete exposed to a drying condition.
- Dissolution of CO₂ into pore solution – The rate of dissolution in the developed service life model did not account for the effect of change in pore solution alkalinity nor in interfacial gas-liquid mass transfer coefficient for CO₂. Further research is required in this area to develop a kinetic model that predicts the extent of carbonation reaction as a function of change in pore solution alkalinity of the concrete.

- Change in porosity – The carbonation reaction, as a deterioration process, should be implemented in a service life model as a kinetic model that inputs the dissolution and precipitation of hydrate phases that are the reactants and products of the carbonation reaction while maintaining equilibrium with the rest of the formed hydrates. In the proposed service life model, the rate of formation of CaCO_3 and dissolution of C-A-S-H is set equal where the formation rate is determined based on the data (i.e. obtained from the literature) of change in porosity of alkali-activated binders exposed to natural carbonation over a year in laboratory conditions. The rates determined for the studied 100SG, 75SG25FA, and 50SG50FA binders were $4.38 \times 10^{-6} \text{ mol. s}^{-1}$, $7.22 \times 10^{-5} \text{ mol. s}^{-1}$, $1.78 \times 10^{-4} \text{ mol. s}^{-1}$ respectively. However, the rate constants for 75SG25FA and 50SG50FA in the concrete cover have been lowered by a factor of 10 because the numerical code was not able to meet the integration tolerance already installed in the pdepe function. This is a numerical problem which can be solved in the future through modification of the function by increasing the error tolerance so that the code could run and generate results in a convenient time frame.

In summary, the conclusion of this research is that mathematical models, with durability data obtained from literature and some experiments, is applied to predict the service life of AAMs for structural application in marine environment. The proposed numerical model is a foundation for future work to be done in the field of research on the durability of AAMs to predict its serviceability limit state for various structural applications. Also, the serviceability should always be estimated probabilistically because the performance properties of multiple elements made from one type of concrete are intrinsically scattered, leading to the serviceability limit state to have a distribution set of values.

Appendix

Appendix 4 Supporting Information File for Chapter 4

Table 4.A.1 contains the variation in calculated critical chloride threshold, in terms of wt.% of binder, of SG100 concrete based on the pore solution alkalinity, concrete porosity and mix design (i.e. Precursor and concrete content reported in g/cm^3) presented **Table 4.4**. Note that the precursor content is considered to be the total binder content in alkali-activated concrete and excludes the minor amount of solid components present in the alkaline activating solution. The distribution of critical chloride threshold for SG100 is also estimated by implementing the ratio of chloride concentration to pore solution alkalinity (i.e. $[\text{Cl}^-/\text{OH}^-]$), which serves as corrosion indicating factor in high Ca-AAMs presented in **Table 2.1**, such as the ratio is strictly greater than 2.1 and strictly lower than 2.8. Consequently, the minimum and maximum values for the corrosion indicating factor is set to 2.11 and 2.79 respectively. Additionally, **Tables 4.A.2 - 4.A.3** also contain the variation in calculated critical chloride threshold, in terms of wt.% of binder, of SG100 concrete but based on fixed pore solution alkalinity values of 13.5 and 13.2, respectively. In summary, **Tables 4.A.1 - 4.A.3** contain values of parameters used for the calculation of critical chloride threshold values (i.e. **Equation 4.1**) for SG100 concrete.

Table 4.A.1 Calculation of critical chloride threshold (CT_{cement}, in wt.% of binder) by implementation of **Equations 4.1-4.2** based on variability of pore solution alkalinity along with other parameters including porosity, mix design and saturation state of SG100 concrete.

Mix nb	SG(kg/m3)	Cement(g/cm3)	Concrete(g/cm3)	Concrete Porosity	Saturation	Mr	Na2O,wt%Binder	pH	pKw	[Cl-]/[OH-] (Min)	CTcement	[Cl-]/[OH-] (Max)	CTcement
1	400	0.4	2.439	0.084	0.8	1	4	13.93621	14	2.11	1.08506243	2.79	1.4347508
2	400	0.4	2.421	0.084	0.8	1.45	4	13.28514	14		0.24231747		0.32041031
3	600	0.6	2.4	0.111	0.8	1.2	7	14.27777	14		2.09879085		2.77517842
4	600	0.6	2.4	0.111	0.8	1.2	5	14.15715	14		1.58982441		2.10218489
5	600	0.6	2.4	0.111	0.8	1.2	4	14.07551	14		1.31735906		1.74191079
6	400	0.4	2.448	0.084	0.8	0.75	4	13.93754	14		1.08839548		1.439158
7	400	0.4	2.448	0.084	0.8	1	4	13.86749	14		0.92626174		1.22477264
8	400	0.4	2.448	0.084	0.8	1.5	4	13.70939	14		0.64362474		0.85104882
9	400	0.4	2.448	0.084	0.8	2	4	13.53387	14		0.42964497		0.56810875
10	400	0.4	2.448	0.084	0.8	0.75	6	14.14176	14		1.74182182		2.30316725
11	400	0.4	2.448	0.084	0.8	1	6	14.11099	14		1.62267195		2.14561835
12	400	0.4	2.448	0.084	0.8	1.5	6	13.93411	14		1.0798383		1.42784306
13	400	0.4	2.448	0.084	0.8	2	6	13.71915	14		0.65824979		0.87038716
14	400	0.4	2.448	0.15601	0.8	0.75	8	14.28576	14		4.50689955		5.95936007
15	400	0.4	2.448	0.15601	0.8	1	8	14.22897	14		3.9544754		5.22890349
16	400	0.4	2.448	0.15601	0.8	1.5	8	14.09616	14		2.91255328		3.85119604
17	400	0.4	2.448	0.15601	0.8	2	8	13.84536	14		1.6348574		2.16173088
18	400	0.4	2.448	0.084	0.8	0.75	4	13.96612	14		1.16243246		1.53705524
19	400	0.4	2.448	0.084	0.8	1	4	13.88141	14		0.95643779		1.26467367
20	400	0.4	2.448	0.084	0.8	1.5	4	13.7328	14		0.67927046		0.89818227
21	400	0.4	2.448	0.084	0.8	2	4	13.59351	14		0.49289309		0.65174015
22	400	0.4	2.448	0.084	0.8	0.75	6	14.13786	14		1.72625412		2.28258246
23	400	0.4	2.448	0.084	0.8	1	6	14.101	14		1.58579384		2.09685537
24	400	0.4	2.448	0.084	0.8	1.5	6	13.9368	14		1.08654753		1.4367145
25	400	0.4	2.448	0.084	0.8	2	6	13.69078	14		0.61663437		0.81536014
26	400	0.4	2.448	0.15601	0.8	0.75	8	14.29947	14		4.65148772		6.15054537
27	400	0.4	2.448	0.15601	0.8	1	8	14.24914	14		4.14245576		5.47746519
28	400	0.4	2.448	0.15601	0.8	1.5	8	14.07763	14		2.79909387		3.69034209
29	400	0.4	2.448	0.15601	0.8	2	8	13.82099	14		1.54563833		2.04375874
30	300	0.3	2.41	0.084	0.8	0.45	4	13.91418	14		1.37520507		1.81839912
31	360	0.36	2.29	0.084	0.8	0.45	4	13.8697	14		1.03442074		1.36778856
32	400	0.4	2.313	0.084	0.8	0.45	4	13.91418	14		1.0314038		1.36379934
33	400	0.4	2.372	0.084	0.8	0.45	4	13.93915	14		1.09243279		1.44449644
34	400	0.4	2.313	0.084	0.8	0.45	6	14.0831	14		1.52175497		2.01217837
35	400	0.4	2.372	0.084	0.8	0.45	6	14.10985	14		1.6184181		2.13999361
36	400	0.4	2.372	0.15601	0.8	0.45	8	14.27611	14		4.40783043		5.82836346
37	400	0.4	2.372	0.084	0.8	1	4	13.81441	14		0.81970716		1.08387819
38	400	0.4	2.372	0.084	0.8	1	6	14.02874	14		1.34273011		1.7754583
39	400	0.4	2.372	0.15601	0.8	1	8	14.1759	14		3.49958768		4.62741688
40	357	0.357	2.424	0.084	0.8	0.33	3	13.91527	14		1.15853859		1.53190647
41	375	0.375	2.43	0.084	0.8	0.46	4	14.05121	14		1.50827124		1.99434918
42	357	0.357	2.428	0.084	0.8	0.33	3	13.65076	14		0.63007827		0.83313667
43	375	0.375	2.435	0.084	0.8	0.46	4	13.90119	14		1.06773001		1.41183258
44	375	0.375	2.43	0.084	0.8	0.46	4	14.03477	14		1.45224353		1.92026515
45	375	0.375	2.43	0.084	0.8	0.46	4	14.03477	14		1.45224353		1.92026515
46	375	0.375	2.43	0.084	0.8	0.46	4	14.03477	14		1.45224353		1.92026515
47	375	0.375	2.43	0.084	0.8	0.46	4	14.03477	14		1.45224353		1.92026515
48	357	0.357	2.424	0.084	0.8	0.33	3	13.84376	14		0.98263788		1.29931739
49	357	0.357	2.424	0.084	0.8	0.33	3	13.84376	14		0.98263788		1.29931739
50	357	0.357	2.424	0.084	0.8	0.33	3	13.84376	14		0.98263788		1.29931739
51	357	0.357	2.424	0.084	0.8	0.33	3	13.84376	14		0.98263788		1.29931739
52	357	0.357	2.424	0.084	0.8	0.33	3	13.84376	14		0.98263788		1.29931739
53	320	0.32	2.374	0.13	0.8	0.32	3	13.86996	14		1.80207892		2.38284369
54	600	0.6	2.4	0.111	0.8	1.2	7	14.27777	14		2.09879085		2.77517842
55	600	0.6	2.4	0.111	0.8	1.2	5	14.15715	14		1.58982441		2.10218489
56	600	0.6	2.4	0.111	0.8	1.2	4	14.07551	14		1.31735906		1.74191079
57	410	0.41	2.54	0.111	0.8	1.5	4	13.94776	14		1.43655598		1.89952189
58	570	0.57	2.236	0.11	0.8	1.5	5	13.64033	14		0.50451405		0.66710625
59	570	0.57	2.236	0.11	0.8	0.75	5	13.99005	14		1.12873051		1.49249199
60	400	0.4	2.382	0.15601	0.8	1.9	8	13.98632	14		2.26170459		2.99059516

Table 4.A.2 Calculation of critical chloride threshold (CT_{cement}, in wt.% of binder) by implementation of **Equations 4.1-4.2** based on fixed pore solution alkalinity of 13.5 along with other parameters including porosity, mix design and saturation state of SG100 concrete.

Mix nb	SG(kg/m3)	Cement(g/cm3)	Concrete(g/cm3)	Concrete Porosity	Saturation	Mr	Na ₂ O _{wt%Binder}	pH	pKw	[Cl-]/[OH-] (Min)	CT _{cement}	[Cl-]/[OH-] (Max)	CT _{cement}
1	400	0.4	2.439	0.084	0.8	1	4	13.5	14	2.11	0.39741543	2.79	0.52549244
2	400	0.4	2.421	0.084	0.8	1.45	4	13.5	14		0.39741543		0.52549244
3	600	0.6	2.4	0.111	0.8	1.2	7	13.5	14		0.35010407		0.46293382
4	600	0.6	2.4	0.111	0.8	1.2	5	13.5	14		0.35010407		0.46293382
5	600	0.6	2.4	0.111	0.8	1.2	4	13.5	14		0.35010407		0.46293382
6	400	0.4	2.448	0.084	0.8	0.75	4	13.5	14		0.39741543		0.52549244
7	400	0.4	2.448	0.084	0.8	1	4	13.5	14		0.39741543		0.52549244
8	400	0.4	2.448	0.084	0.8	1.5	4	13.5	14		0.39741543		0.52549244
9	400	0.4	2.448	0.084	0.8	2	4	13.5	14		0.39741543		0.52549244
10	400	0.4	2.448	0.084	0.8	0.75	6	13.5	14		0.39741543		0.52549244
11	400	0.4	2.448	0.084	0.8	1	6	13.5	14		0.39741543		0.52549244
12	400	0.4	2.448	0.084	0.8	1.5	6	13.5	14		0.39741543		0.52549244
13	400	0.4	2.448	0.084	0.8	2	6	13.5	14		0.39741543		0.52549244
14	400	0.4	2.448	0.15601	0.8	0.75	8	13.5	14		0.73810454		0.9759771
15	400	0.4	2.448	0.15601	0.8	1	8	13.5	14		0.73810454		0.9759771
16	400	0.4	2.448	0.15601	0.8	1.5	8	13.5	14		0.73810454		0.9759771
17	400	0.4	2.448	0.15601	0.8	2	8	13.5	14		0.73810454		0.9759771
18	400	0.4	2.448	0.084	0.8	0.75	4	13.5	14		0.39741543		0.52549244
19	400	0.4	2.448	0.084	0.8	1	4	13.5	14		0.39741543		0.52549244
20	400	0.4	2.448	0.084	0.8	1.5	4	13.5	14		0.39741543		0.52549244
21	400	0.4	2.448	0.084	0.8	2	4	13.5	14		0.39741543		0.52549244
22	400	0.4	2.448	0.084	0.8	0.75	6	13.5	14		0.39741543		0.52549244
23	400	0.4	2.448	0.084	0.8	1	6	13.5	14		0.39741543		0.52549244
24	400	0.4	2.448	0.084	0.8	1.5	6	13.5	14		0.39741543		0.52549244
25	400	0.4	2.448	0.084	0.8	2	6	13.5	14		0.39741543		0.52549244
26	400	0.4	2.448	0.15601	0.8	0.75	8	13.5	14		0.73810454		0.9759771
27	400	0.4	2.448	0.15601	0.8	1	8	13.5	14		0.73810454		0.9759771
28	400	0.4	2.448	0.15601	0.8	1.5	8	13.5	14		0.73810454		0.9759771
29	400	0.4	2.448	0.15601	0.8	2	8	13.5	14		0.73810454		0.9759771
30	300	0.3	2.41	0.084	0.8	0.45	4	13.5	14		0.52988724		0.70065659
31	360	0.36	2.29	0.084	0.8	0.45	4	13.5	14		0.4415727		0.5888049
32	400	0.4	2.313	0.084	0.8	0.45	4	13.5	14		0.39741543		0.52549244
33	400	0.4	2.372	0.084	0.8	0.45	4	13.5	14		0.39741543		0.52549244
34	400	0.4	2.313	0.084	0.8	0.45	6	13.5	14		0.39741543		0.52549244
35	400	0.4	2.372	0.084	0.8	0.45	6	13.5	14		0.39741543		0.52549244
36	400	0.4	2.372	0.15601	0.8	0.45	8	13.5	14		0.73810454		0.9759771
37	400	0.4	2.372	0.084	0.8	1	4	13.5	14		0.39741543		0.52549244
38	400	0.4	2.372	0.084	0.8	1	6	13.5	14		0.39741543		0.52549244
39	400	0.4	2.372	0.15601	0.8	1	8	13.5	14		0.73810454		0.9759771
40	357	0.357	2.424	0.084	0.8	0.33	3	13.5	14		0.4452834		0.58878705
41	375	0.375	2.43	0.084	0.8	0.46	4	13.5	14		0.42390979		0.56052527
42	357	0.357	2.428	0.084	0.8	0.33	3	13.5	14		0.4452834		0.58878705
43	375	0.375	2.435	0.084	0.8	0.46	4	13.5	14		0.42390979		0.56052527
44	375	0.375	2.43	0.084	0.8	0.46	4	13.5	14		0.42390979		0.56052527
45	375	0.375	2.43	0.084	0.8	0.46	4	13.5	14		0.42390979		0.56052527
46	375	0.375	2.43	0.084	0.8	0.46	4	13.5	14		0.42390979		0.56052527
47	375	0.375	2.43	0.084	0.8	0.46	4	13.5	14		0.42390979		0.56052527
48	357	0.357	2.424	0.084	0.8	0.33	3	13.5	14		0.4452834		0.58878705
49	357	0.357	2.424	0.084	0.8	0.33	3	13.5	14		0.4452834		0.58878705
50	357	0.357	2.424	0.084	0.8	0.33	3	13.5	14		0.4452834		0.58878705
51	357	0.357	2.424	0.084	0.8	0.33	3	13.5	14		0.4452834		0.58878705
52	357	0.357	2.424	0.084	0.8	0.33	3	13.5	14		0.4452834		0.58878705
53	320	0.32	2.374	0.13	0.8	0.32	3	13.5	14		0.76880962		1.01657764
54	600	0.6	2.4	0.111	0.8	1.2	7	13.5	14		0.35010407		0.46293382
55	600	0.6	2.4	0.111	0.8	1.2	5	13.5	14		0.35010407		0.46293382
56	600	0.6	2.4	0.111	0.8	1.2	4	13.5	14		0.35010407		0.46293382
57	410	0.41	2.54	0.111	0.8	1.5	4	13.5	14		0.51234742		0.67746413
58	570	0.57	2.236	0.11	0.8	1.5	5	13.5	14		0.36521051		0.48290868
59	570	0.57	2.236	0.11	0.8	0.75	5	13.5	14		0.36521051		0.48290868
60	400	0.4	2.382	0.15601	0.8	1.9	8	13.5	14		0.73810454		0.9759771

Table 4.A.3 Calculation of critical chloride threshold (CT_{cement}, , in wt.% of binder) by implementation of **Equations 4.1-4.2** based on fixed pore solution alkalinity of 13.2 along with other parameters including porosity, mix design and saturation state of SG100 concrete.

Mix nb	SG(kg/m3)	Cement(g/cm3)	Concrete(g/cm3)	Concrete Porosity	Saturation	Mr	Na2O,wt%Binder	pH	pKw	[Cl-]/[OH-] (Min)	CT _{cement}	[Cl-]/[OH-] (Max)	CT _{cement}
1	400	0.4	2.439	0.084	0.8	1	4	13.2	14	2.11	0.19917954	2.79	0.2633701
2	400	0.4	2.421	0.084	0.8	1.45	4	13.2	14		0.19917954		0.2633701
3	600	0.6	2.4	0.111	0.8	1.2	7	13.2	14		0.17546769		0.23201652
4	600	0.6	2.4	0.111	0.8	1.2	5	13.2	14		0.17546769		0.23201652
5	600	0.6	2.4	0.111	0.8	1.2	4	13.2	14		0.17546769		0.23201652
6	400	0.4	2.448	0.084	0.8	0.75	4	13.2	14		0.19917954		0.2633701
7	400	0.4	2.448	0.084	0.8	1	4	13.2	14		0.19917954		0.2633701
8	400	0.4	2.448	0.084	0.8	1.5	4	13.2	14		0.19917954		0.2633701
9	400	0.4	2.448	0.084	0.8	2	4	13.2	14		0.19917954		0.2633701
10	400	0.4	2.448	0.084	0.8	0.75	6	13.2	14		0.19917954		0.2633701
11	400	0.4	2.448	0.084	0.8	1	6	13.2	14		0.19917954		0.2633701
12	400	0.4	2.448	0.084	0.8	1.5	6	13.2	14		0.19917954		0.2633701
13	400	0.4	2.448	0.084	0.8	2	6	13.2	14		0.19917954		0.2633701
14	400	0.4	2.448	0.15601	0.8	0.75	8	13.2	14		0.36992857		0.48914726
15	400	0.4	2.448	0.15601	0.8	1	8	13.2	14		0.36992857		0.48914726
16	400	0.4	2.448	0.15601	0.8	1.5	8	13.2	14		0.36992857		0.48914726
17	400	0.4	2.448	0.15601	0.8	2	8	13.2	14		0.36992857		0.48914726
18	400	0.4	2.448	0.084	0.8	0.75	4	13.2	14		0.19917954		0.2633701
19	400	0.4	2.448	0.084	0.8	1	4	13.2	14		0.19917954		0.2633701
20	400	0.4	2.448	0.084	0.8	1.5	4	13.2	14		0.19917954		0.2633701
21	400	0.4	2.448	0.084	0.8	2	4	13.2	14		0.19917954		0.2633701
22	400	0.4	2.448	0.084	0.8	0.75	6	13.2	14		0.19917954		0.2633701
23	400	0.4	2.448	0.084	0.8	1	6	13.2	14		0.19917954		0.2633701
24	400	0.4	2.448	0.084	0.8	1.5	6	13.2	14		0.19917954		0.2633701
25	400	0.4	2.448	0.084	0.8	2	6	13.2	14		0.19917954		0.2633701
26	400	0.4	2.448	0.15601	0.8	0.75	8	13.2	14		0.36992857		0.48914726
27	400	0.4	2.448	0.15601	0.8	1	8	13.2	14		0.36992857		0.48914726
28	400	0.4	2.448	0.15601	0.8	1.5	8	13.2	14		0.36992857		0.48914726
29	400	0.4	2.448	0.15601	0.8	2	8	13.2	14		0.36992857		0.48914726
30	300	0.3	2.41	0.084	0.8	0.45	4	13.2	14		0.26557272		0.35116014
31	360	0.36	2.29	0.084	0.8	0.45	4	13.2	14		0.2213106		0.29263345
32	400	0.4	2.313	0.084	0.8	0.45	4	13.2	14		0.19917954		0.2633701
33	400	0.4	2.372	0.084	0.8	0.45	4	13.2	14		0.19917954		0.2633701
34	400	0.4	2.313	0.084	0.8	0.45	6	13.2	14		0.19917954		0.2633701
35	400	0.4	2.372	0.084	0.8	0.45	6	13.2	14		0.19917954		0.2633701
36	400	0.4	2.372	0.15601	0.8	0.45	8	13.2	14		0.36992857		0.48914726
37	400	0.4	2.372	0.084	0.8	1	4	13.2	14		0.19917954		0.2633701
38	400	0.4	2.372	0.084	0.8	1	6	13.2	14		0.19917954		0.2633701
39	400	0.4	2.372	0.15601	0.8	1	8	13.2	14		0.36992857		0.48914726
40	357	0.357	2.424	0.084	0.8	0.33	3	13.2	14		0.22317035		0.29509255
41	375	0.375	2.43	0.084	0.8	0.46	4	13.2	14		0.21245818		0.28092811
42	357	0.357	2.428	0.084	0.8	0.33	3	13.2	14		0.22317035		0.29509255
43	375	0.375	2.435	0.084	0.8	0.46	4	13.2	14		0.21245818		0.28092811
44	375	0.375	2.43	0.084	0.8	0.46	4	13.2	14		0.21245818		0.28092811
45	375	0.375	2.43	0.084	0.8	0.46	4	13.2	14		0.21245818		0.28092811
46	375	0.375	2.43	0.084	0.8	0.46	4	13.2	14		0.21245818		0.28092811
47	375	0.375	2.43	0.084	0.8	0.46	4	13.2	14		0.21245818		0.28092811
48	357	0.357	2.424	0.084	0.8	0.33	3	13.2	14		0.22317035		0.29509255
49	357	0.357	2.424	0.084	0.8	0.33	3	13.2	14		0.22317035		0.29509255
50	357	0.357	2.424	0.084	0.8	0.33	3	13.2	14		0.22317035		0.29509255
51	357	0.357	2.424	0.084	0.8	0.33	3	13.2	14		0.22317035		0.29509255
52	357	0.357	2.424	0.084	0.8	0.33	3	13.2	14		0.22317035		0.29509255
53	320	0.32	2.374	0.13	0.8	0.32	3	13.2	14		0.38531756		0.50949574
54	600	0.6	2.4	0.111	0.8	1.2	7	13.2	14		0.17546769		0.23201652
55	600	0.6	2.4	0.111	0.8	1.2	5	13.2	14		0.17546769		0.23201652
56	600	0.6	2.4	0.111	0.8	1.2	4	13.2	14		0.17546769		0.23201652
57	410	0.41	2.54	0.111	0.8	1.5	4	13.2	14		0.25678199		0.33953637
58	570	0.57	2.236	0.11	0.8	1.5	5	13.2	14		0.18303884		0.24202766
59	570	0.57	2.236	0.11	0.8	0.75	5	13.2	14		0.18303884		0.24202766
60	400	0.4	2.382	0.15601	0.8	1.9	8	13.2	14		0.36992857		0.48914726

The following code is typed in the GEM-Selektor v.3 software to account for the extent of reactivity for slag precursors at 70% and for fly ash precursors, at 35% used in AAMs. The code also accounts for the composition of the activating solution and amount of water used in the mix design to produce 100 g of alkali-activated binder.

\$Degree of reaction

modC[J][0]=: cNu; \$slag

modC[J][3]=:modC[J][0]*0.5; \$ fly ash

\$Mineralogical composition

xa_{Aqua} =: modC[0][2];

xa_{SiO2} =:

modC[0][1]*modC[J][0]*modC[1][2]+modC[0][4]*modC[J][3]*modC[2][2]+modC[7][1];

xa_{Al2O3} =:

modC[1][1]*modC[J][0]*modC[1][2]+modC[1][4]*modC[J][3]*modC[2][2];

xa_{CaO} =: modC[2][1]*modC[J][0]*modC[1][2]+modC[2][4]*modC[J][3]*modC[2][2];

xa_{Fe2O3} =:

modC[3][1]*modC[J][0]*modC[1][2]+modC[3][4]*modC[J][3]*modC[2][2];

xa_{Na2O} =:

modC[4][1]*modC[J][0]*modC[1][2]+modC[4][4]*modC[J][3]*modC[2][2]+modC[6][1];

xa_{MgO} =:

modC[5][1]*modC[J][0]*modC[1][2]+modC[5][4]*modC[J][3]*modC[2][2];

\$Sulfur from slag

xa_{H2S} =: modC[8][1]*modC[J][0]*modC[1][2];

\$Sulfur from fly ash

xa_{SO3} =: modC[8][4]*modC[J][3]*modC[2][2];

xa_{K2O} =: modC[9][1]*modC[J][0]*modC[1][2]+modC[9][4]*modC[J][3]*modC[2][2];

\$Alkali-activating solution

\$Na2O and SiO2 activator

\$modC[6][1]=Na2O=4g/100 g binder

\$SiO2/Na2O=1.5

\$modC[7][1]=SiO2=5.81 g/100g binder

Appendix 5 Supporting Information File for Chapter 5

DVS Diffusion Analysis Report		DVS Diffusion Analysis Report		DVS Diffusion Analysis Report																																																																																																																																																																									
Impact of particle size on moisture diffusivity		Average particle size 39		Maximum particle size 62 Ratio of Maximum particle size to Average particle size 3.8403042																																																																																																																																																																									
Minimum particle size 3.74 Sample: Sample 4 Temp: 23.1°C MRef: 25.8607 from Mass at end of first stage	Ratio of Average particle size to Minimum particle size 10.95	Average particle size 39 Sam Sample 4 Tem 23.1°C MRef 25.8607 from Mass at end of first stage	Target Diffusion % PFI Coeff. (cm²/s)	Prev Target % PFI Coeff. (cm²/s)	Diffusion Coeff. (cm²/s)																																																																																																																																																																								
<table border="1"> <thead> <tr> <th>Previous % PFI</th> <th>Target Diffusion % PFI Coeff. (cm²/s)</th> <th>R-sq. (%)</th> </tr> </thead> <tbody> <tr><td>50</td><td>2.71E-11</td><td>99</td></tr> <tr><td>55</td><td>2.59E-11</td><td>99.03</td></tr> <tr><td>60</td><td>1.93E-11</td><td>99.05</td></tr> <tr><td>65</td><td>1.61E-11</td><td>99.04</td></tr> <tr><td>70</td><td>1.47E-11</td><td>99.03</td></tr> <tr><td>75</td><td>9.65E-12</td><td>99.02</td></tr> <tr><td>80</td><td>5.53E-12</td><td>99.02</td></tr> <tr><td>85</td><td>3.04E-12</td><td>99</td></tr> <tr><td>90</td><td>3.24E-12</td><td>99.01</td></tr> <tr><td>95</td><td>5.12E-12</td><td>99.01</td></tr> <tr><td>99</td><td>7.28E-12</td><td>99.01</td></tr> <tr><td>99</td><td>7.28E-12</td><td>99.01</td></tr> <tr><td>75</td><td>6.44E-12</td><td>99.01</td></tr> <tr><td>70</td><td>6.62E-12</td><td>99.02</td></tr> <tr><td>65</td><td>6.60E-12</td><td>99.02</td></tr> <tr><td>60</td><td>7.88E-12</td><td>99.04</td></tr> <tr><td>55</td><td>3.38E-12</td><td>99.01</td></tr> </tbody> </table>	Previous % PFI	Target Diffusion % PFI Coeff. (cm ² /s)	R-sq. (%)	50	2.71E-11	99	55	2.59E-11	99.03	60	1.93E-11	99.05	65	1.61E-11	99.04	70	1.47E-11	99.03	75	9.65E-12	99.02	80	5.53E-12	99.02	85	3.04E-12	99	90	3.24E-12	99.01	95	5.12E-12	99.01	99	7.28E-12	99.01	99	7.28E-12	99.01	75	6.44E-12	99.01	70	6.62E-12	99.02	65	6.60E-12	99.02	60	7.88E-12	99.04	55	3.38E-12	99.01	<table border="1"> <thead> <tr> <th>Previous % PFI</th> <th>Target Diffusion % PFI Coeff. (cm²/s)</th> <th>R-sq. (%)</th> </tr> </thead> <tbody> <tr><td>50</td><td>3.02E-09</td><td>99</td></tr> <tr><td>55</td><td>2.87E-09</td><td>99</td></tr> <tr><td>60</td><td>2.15E-09</td><td>99</td></tr> <tr><td>65</td><td>1.79E-09</td><td>99</td></tr> <tr><td>70</td><td>1.64E-09</td><td>99</td></tr> <tr><td>75</td><td>1.07E-09</td><td>99</td></tr> <tr><td>80</td><td>6.16E-10</td><td>99</td></tr> <tr><td>85</td><td>3.38E-10</td><td>99</td></tr> <tr><td>90</td><td>2.29E-10</td><td>99</td></tr> <tr><td>95</td><td>1.03E-09</td><td>99</td></tr> <tr><td>99</td><td>6.91E-10</td><td>99</td></tr> <tr><td>99</td><td>6.91E-10</td><td>99</td></tr> <tr><td>80</td><td>8.35E-10</td><td>99</td></tr> <tr><td>75</td><td>9.65E-10</td><td>99</td></tr> <tr><td>70</td><td>7.19E-10</td><td>99</td></tr> <tr><td>65</td><td>7.37E-10</td><td>99</td></tr> <tr><td>60</td><td>7.35E-10</td><td>99</td></tr> <tr><td>55</td><td>8.77E-10</td><td>99</td></tr> <tr><td>50</td><td>3.74E-10</td><td>99</td></tr> </tbody> </table>	Previous % PFI	Target Diffusion % PFI Coeff. (cm ² /s)	R-sq. (%)	50	3.02E-09	99	55	2.87E-09	99	60	2.15E-09	99	65	1.79E-09	99	70	1.64E-09	99	75	1.07E-09	99	80	6.16E-10	99	85	3.38E-10	99	90	2.29E-10	99	95	1.03E-09	99	99	6.91E-10	99	99	6.91E-10	99	80	8.35E-10	99	75	9.65E-10	99	70	7.19E-10	99	65	7.37E-10	99	60	7.35E-10	99	55	8.77E-10	99	50	3.74E-10	99	<table border="1"> <thead> <tr> <th>Prev Target % PFI</th> <th>Diffusion Coeff. (cm²/s)</th> <th>R-sq. (%)</th> </tr> </thead> <tbody> <tr><td>50</td><td>4.45E-08</td><td>99</td></tr> <tr><td>55</td><td>4.23E-08</td><td>99</td></tr> <tr><td>60</td><td>3.17E-08</td><td>99</td></tr> <tr><td>65</td><td>2.65E-08</td><td>99</td></tr> <tr><td>70</td><td>2.42E-08</td><td>99</td></tr> <tr><td>75</td><td>1.58E-08</td><td>99</td></tr> <tr><td>80</td><td>9.08E-09</td><td>99</td></tr> <tr><td>85</td><td>4.39E-09</td><td>99</td></tr> <tr><td>90</td><td>3.37E-09</td><td>99</td></tr> <tr><td>95</td><td>1.32E-08</td><td>99</td></tr> <tr><td>99</td><td>1.00E-08</td><td>99</td></tr> <tr><td>99</td><td>1.25E-08</td><td>99</td></tr> <tr><td>80</td><td>1.26E-08</td><td>99</td></tr> <tr><td>75</td><td>1.09E-08</td><td>99</td></tr> <tr><td>70</td><td>1.09E-08</td><td>99</td></tr> <tr><td>65</td><td>1.09E-08</td><td>99</td></tr> <tr><td>60</td><td>1.29E-08</td><td>99</td></tr> <tr><td>55</td><td>5.51E-09</td><td>99</td></tr> </tbody> </table>	Prev Target % PFI	Diffusion Coeff. (cm ² /s)	R-sq. (%)	50	4.45E-08	99	55	4.23E-08	99	60	3.17E-08	99	65	2.65E-08	99	70	2.42E-08	99	75	1.58E-08	99	80	9.08E-09	99	85	4.39E-09	99	90	3.37E-09	99	95	1.32E-08	99	99	1.00E-08	99	99	1.25E-08	99	80	1.26E-08	99	75	1.09E-08	99	70	1.09E-08	99	65	1.09E-08	99	60	1.29E-08	99	55	5.51E-09	99
Previous % PFI	Target Diffusion % PFI Coeff. (cm ² /s)	R-sq. (%)																																																																																																																																																																											
50	2.71E-11	99																																																																																																																																																																											
55	2.59E-11	99.03																																																																																																																																																																											
60	1.93E-11	99.05																																																																																																																																																																											
65	1.61E-11	99.04																																																																																																																																																																											
70	1.47E-11	99.03																																																																																																																																																																											
75	9.65E-12	99.02																																																																																																																																																																											
80	5.53E-12	99.02																																																																																																																																																																											
85	3.04E-12	99																																																																																																																																																																											
90	3.24E-12	99.01																																																																																																																																																																											
95	5.12E-12	99.01																																																																																																																																																																											
99	7.28E-12	99.01																																																																																																																																																																											
99	7.28E-12	99.01																																																																																																																																																																											
75	6.44E-12	99.01																																																																																																																																																																											
70	6.62E-12	99.02																																																																																																																																																																											
65	6.60E-12	99.02																																																																																																																																																																											
60	7.88E-12	99.04																																																																																																																																																																											
55	3.38E-12	99.01																																																																																																																																																																											
Previous % PFI	Target Diffusion % PFI Coeff. (cm ² /s)	R-sq. (%)																																																																																																																																																																											
50	3.02E-09	99																																																																																																																																																																											
55	2.87E-09	99																																																																																																																																																																											
60	2.15E-09	99																																																																																																																																																																											
65	1.79E-09	99																																																																																																																																																																											
70	1.64E-09	99																																																																																																																																																																											
75	1.07E-09	99																																																																																																																																																																											
80	6.16E-10	99																																																																																																																																																																											
85	3.38E-10	99																																																																																																																																																																											
90	2.29E-10	99																																																																																																																																																																											
95	1.03E-09	99																																																																																																																																																																											
99	6.91E-10	99																																																																																																																																																																											
99	6.91E-10	99																																																																																																																																																																											
80	8.35E-10	99																																																																																																																																																																											
75	9.65E-10	99																																																																																																																																																																											
70	7.19E-10	99																																																																																																																																																																											
65	7.37E-10	99																																																																																																																																																																											
60	7.35E-10	99																																																																																																																																																																											
55	8.77E-10	99																																																																																																																																																																											
50	3.74E-10	99																																																																																																																																																																											
Prev Target % PFI	Diffusion Coeff. (cm ² /s)	R-sq. (%)																																																																																																																																																																											
50	4.45E-08	99																																																																																																																																																																											
55	4.23E-08	99																																																																																																																																																																											
60	3.17E-08	99																																																																																																																																																																											
65	2.65E-08	99																																																																																																																																																																											
70	2.42E-08	99																																																																																																																																																																											
75	1.58E-08	99																																																																																																																																																																											
80	9.08E-09	99																																																																																																																																																																											
85	4.39E-09	99																																																																																																																																																																											
90	3.37E-09	99																																																																																																																																																																											
95	1.32E-08	99																																																																																																																																																																											
99	1.00E-08	99																																																																																																																																																																											
99	1.25E-08	99																																																																																																																																																																											
80	1.26E-08	99																																																																																																																																																																											
75	1.09E-08	99																																																																																																																																																																											
70	1.09E-08	99																																																																																																																																																																											
65	1.09E-08	99																																																																																																																																																																											
60	1.29E-08	99																																																																																																																																																																											
55	5.51E-09	99																																																																																																																																																																											
Parameter Value Sample radius (microns) 3.74 DVS from SMS - The Sorption S Minimum P-squared (%) 0.99 MMinF Linear Limit 0.2 Linear calc Yes	Parameter Value Sample radius (microns) 39.45 DVS from SMS - The Sorption S Minimum P-squared (%) 0.99 MMinF Linear Limit 0.2 Linear calc Yes	Parameter Value Sample radius (microns) 151.5 DVS from SMS - The Sorption S Minimum P-squared (%) 0.99 MMinF Linear Limit 0.2 Linear calc Yes																																																																																																																																																																											

Appendix 6 Supporting Information File for Chapter 6

6.A Codes implemented in the open source software GEM-Selektor v.3

%% This code is typed in the GEM-Selektor v.3 software to account for the extent of reactivity for 70% of CEM III binder. The code also accounts for the amount of water used in the mix design to produce 100 g of CEM III binder.

```
$Degree of reaction
modC[J] =: cNu;
$composition
xa_{{Aqua}} =: 50 * 1;
xa_{{SiO2}} =: 30.61 * cNu;
xa_{{Al2O3}} =: 10.58 * cNu;
xa_{{CaO}} =: 45.52 * cNu;
xa_{{Fe2O3}} =: 1.42 * cNu;
xa_{{Na2O}} =: 0.31 * cNu;
xa_{{MgO}} =: 7.33 * cNu;
xa_{{H2S}} =: 1.13 * cNu;
xa_{{K2O}} =: 0.58 * cNu;
```

6.B Calculation of activity coefficients of calcium and carbonate ions in carbonated pore solution of AAMs

	A	E	F	G	H	I	M	N	O	P
1	**All concentrations in molality please!					**Inputs go in the yellow boxes only - output is in the green on				
2	Cation	Concentration	γ	Activity		Anion	Concentration	γ	Activity	
3	H(+)		1	0		Cl(-)		1	0	0
4	Li(+)		1	0		NO3(-)		1	0	0
5	Na(+)	0.566850519	0.664736	0.376805946	-56.01338378	SO4(2-)	0.033587654	0.090071196	0.00302528	-10.3191
6	K(+)	0.181925872	0.682616147	0.124185537	-21.34741575	HSO4(-)		1	0	0
7	Rb(+)		1	0		Br(-)		1	0	0
8	Cs(+)		1	0		ClO4(-)		1	0	0
9	Ag(+)		1	0		F(-)		1	0	0
10	Tl(+)		1	0		I(-)		1	0	0
11	Ca(2+)	6.21859E-07	0.043324313	2.69416E-08	-0.000150358	BrO3(-)		1	0	0
12	Mg(2+)		1	0		ClO3(-)		1	0	0
13	Cu(2+)		1	0		NO2(-)		1	0	0
14	Sr(2+)		1	0		CH3COO(-)		1	0	0
15	Ba(2+)		1	0		OH(-)	0.665682327	0.664396088	0.442276734	-43.4054
16	Ni(2+)		1	0		SO3(2-)		1	0	0
17	NH4(+)		1	0		H2PO4(-)		1	0	0
18	Cr(3+)		1	0		CO3(2-)	0.00796	0.137101328	0.001091327	-1.75739
19	Pb(2+)		1	0		HCO3(-)		1	0	0
20	Co(2+)		1	0		SiO(OH)3(-)		1	0	0
21	Fe(2+)		1	0		HPO4(2-)		1	0	0
22	Zn(2+)		1	0		CrO4(2-)		1	0	0
23	Al(3+)		1	0		Fe(CN)6(3-)		1	0	0
24	Me4N(+)		1	0		SCN(-)		1	0	0
25	Et4N(+)		1	0		S2O3(2-)		1	0	0
26	n-Pr4N(+)		1	0		PO4(3-)		1	0	0
27	n-Bu4N(+)		1	0		TcO4(-)		1	0	0
28	UO2(2+)		1	0		ReO4(-)		1	0	0
29	Cd(2+)		1	0		IO3(-)		1	0	0
30	Eu(3+)		1	0		Al(OH)4(-)		1	0	0
31	La(3+)		1	0		A29		1	0	0
32	Y(3+)		1	0		A30		1	0	0
33										
34	Ionic strength	0.79032591								
36	Osmotic coefficient	0.921596878			pH from a(OH-)	13.64569409				
37	Water activity	0.974098473								
38	Input component row #'s for γ_{MX} calculation									
39	M	X	vM	vX	ln(γ_{MX})					
40		5	15	1	-0.40862105					

Figure 6.49 Carbonated pore solution of 100SG

**All concentrations in molality please!				**Inputs go in the yellow boxes only - output is in the green one				
Cation	Concentration	γ	Activity	Anion	Concentration	γ	Activity	
H(+)		1	0	0 Cl(-)		1	0	
Li(+)		1	0	0 NO3(-)		1	0	
Na(+)	0.198433887	0.670520632	0.133054016	-19.80697045 SO4(2-)	0.064513329	0.11661582	0.007523275	
K(+)	0.280727853	0.67157532	0.188529898	-32.81265462 HSO4(-)		1	0	
Rb(+)		1	0	0 Br(-)		1	0	
Cs(+)		1	0	0 ClO4(-)		1	0	
Ag(+)		1	0	0 F(-)		1	0	
Tl(+)		1	0	0 I(-)		1	0	
Ca(2+)	6.21859E-07	0.073286725	4.5574E-08	-0.000150006 BrO3(-)		1	0	
Mg(2+)		1	0	0 ClO3(-)		1	0	
Cu(2+)		1	0	0 NO2(-)		1	0	
Sr(2+)		1	0	0 CH3COO(-)		1	0	
Ba(2+)		1	0	0 OH(-)	0.334215705	0.658973546	0.220239308	
Ni(2+)		1	0	0 SO3(2-)		1	0	
NH4(+)		1	0	0 H2PO4(-)		1	0	
Cr(3+)		1	0	0 CO3(2-)	0.00796	0.174028451	0.001385266	
Pb(2+)		1	0	0 HCO3(-)		1	0	
Co(2+)		1	0	0 Si(OH)3(-)		1	0	
Fe(2+)		1	0	0 HPO4(2-)		1	0	
Zn(2+)		1	0	0 CrO4(2-)		1	0	
Al(3+)		1	0	0 Fe(CN)6(3-)		1	0	
Me4N(+)		1	0	0 SCN(-)		1	0	
Et4N(+)		1	0	0 S2O3(2-)		1	0	
n-Pr4N(+)		1	0	0 PO4(3-)		1	0	
n-Bu4N(+)		1	0	0 TcO4(-)		1	0	
UO2(2+)		1	0	0 ReO4(-)		1	0	
Cd(2+)		1	0	0 IO3(-)		1	0	
Eu(3+)		1	0	0 Al(OH)4(-)		1	0	
La(3+)		1	0	0 A29		1	0	
Y(3+)		1	0	0 A30		1	0	
Ionic strength				0.551636624				
Osmotic coefficient				0.882005369	pH from a(OH-) 13.34289483			
Water activity				0.982622492				
Input component row #'s for γ MX calculation								
M	X	vM	vX	ln(γ MX)				
5	15	1	1	-0.408386347				

Figure 6.50 Carbonated pore solution of 75SG25FA

	A	E	F	G	H	I	M	N	O	P
1	**All concentrations in molality please!					**Inputs go in the yellow boxes only - output is in the green ones				
2	Cation	Concentration	γ	Activity		Anion	Concentration	γ	Activity	
3	H(+)		1	0		0 Cl(-)		1	0	0
4	Li(+)		1	0		0 NO3(-)		1	0	0
5	Na(+)	0.02869937	0.645908705	0.018537173		-2.917867543 SO4(2-)	0.178251827	0.110844031	0.019758151	-54.4019
6	K(+)	0.398312291	0.622238917	0.247845409		-46.40071705 HSO4(-)		1	0	0
7	Rb(+)		1	0		0 Br(-)		1	0	0
8	Cs(+)		1	0		0 ClO4(-)		1	0	0
9	Ag(+)		1	0		0 F(-)		1	0	0
10	Tl(+)		1	0		0 I(-)		1	0	0
11	Ca(2+)	6.21859E-07	0.092880622	5.77587E-08		-0.000149786 BrO3(-)		1	0	0
12	Mg(2+)		1	0		0 ClO3(-)		1	0	0
13	Cu(2+)		1	0		0 NO2(-)		1	0	0
14	Sr(2+)		1	0		0 CH3COO(-)		1	0	0
15	Ba(2+)		1	0		0 OH(-)	0.054589251	0.607439864	0.033159687	-3.69231
16	Ni(2+)		1	0		0 SO3(2-)		1	0	0
17	NH4(+)		1	0		0 H2PO4(-)		1	0	0
18	Cr(3+)		1	0		0 CO3(2-)	0.00796	0.165282617	0.00131565	-1.75465
19	Pb(2+)		1	0		0 HCO3(-)		1	0	0
20	Co(2+)		1	0		0 SiO(OH)3(-)		1	0	0
21	Fe(2+)		1	0		0 HPO4(2-)		1	0	0
22	Zn(2+)		1	0		0 CrO4(2-)		1	0	0
23	Al(3+)		1	0		0 Fe(CN)6(3-)		1	0	0
24	Me4N(+)		1	0		0 SCN(-)		1	0	0
25	Et4N(+)		1	0		0 S2O3(2-)		1	0	0
26	n-Pr4N(+)		1	0		0 PO4(3-)		1	0	0
27	n-Bu4N(+)		1	0		0 TcO4(-)		1	0	0
28	UO2(2+)		1	0		0 ReO4(-)		1	0	0
29	Cd(2+)		1	0		0 IO3(-)		1	0	0
30	Eu(3+)		1	0		0 Al(OH)4(-)		1	0	0
31	La(3+)		1	0		0 A29		1	0	0
32	Y(3+)		1	0		0 A30		1	0	0
33										
34	Ionic strength	0.613225353								
36	Osmotic coefficient	0.764648976			pH from a(OH-)	12.52061043				
37	Water activity	0.983247368								
38	Input component row #'s for γ_{MX} calculation									
39	M	X	vM	vX	ln(γ_{MX})					
40		5	15	1	1	-0.467799604				

Figure 6.51 Carbonated pore solution of 50SG50FA

6.C Calculation of calcium ions in carbonated pore solution of AAMs

		First Step	Final Step
omega (SI)	100SG	Calcium ion, [Ca2+] (mol/L)	Caclium ion, [Ca2+] (mol/L)
	1.5	6.21859E-07	0.000104693
K (Solubility Product Constant)			
	3.3E-09		
Carbonate ion, [CO32-] (mol/L)			
	0.007957857		
Carbonate ion, Rounded CO32- (mol/L)			
	0.00796		
		Gamma Ca2+ (Initial value)	Gamma Ca2+ (PitzerXXL Spreadsheet)
		1	0.043324313
		Gamma CO32- (Initial value)	Gamma CO32- (PitzerXXL Spreadsheet)
		1	0.137101328
		First Step	Final Step
omega	50SG50FA	Calcium ion, [Ca2+]	Calcium ion, [Ca2+]
	1.5	6.21859E-07	4.05079E-05
K (Solubility Product Constant)			
	3.3E-09		
CO32-			
	0.007957857		
Rounded CO32-			
	0.00796		
		Gamma Ca2+ (Initial value)	Gamma Ca2+ (PitzerXXL Spreadsheet)
		1	0.092880622
		Gamma CO32- (Initial value)	Gamma CO32- (PitzerXXL Spreadsheet)
		1	0.165282617
		First Step	Final Step
omega (SI)	75SG25FA	Calcium ion, [Ca2+]	Calcium ion, [Ca2+]
	1.5	6.21859E-07	4.87581E-05
K (Solubility Product Constant)			
	3.3E-09		
[CO32-] (mol/L)			
	0.007957857		
Rounded CO32- (mol/L)			
	0.00796		
		Gamma Ca2+ (Initial value)	Gamma Ca2+ (PitzerXXL Spreadsheet)
		1	0.073286725
		Gamma CO32- (Initial value)	Gamma CO32- (PitzerXXL Spreadsheet)
		1	0.174028451

Example

First Step using initial value for activity coefficients of Ca^{2+} and CO_3^{2-} to obtain calcium concentration

$$[\text{Ca}^{2+}] = \frac{\Omega \times K_{sp}}{[\text{CO}_3^{2-}] \times \gamma_{\text{Ca}^{2+}} \times \gamma_{\text{CO}_3^{2-}}} \quad \text{with; } [\text{CO}_3^{2-}] = 0.00796 \text{ mol/L, } \Omega = 1.5 \text{ and } K_{sp} = 3.3 \times 10^{-9} \text{ mol}^2/\text{L}^2$$

Final Step using updated values for activity coefficients of Ca^{2+} and CO_3^{2-} , from PitzerXXL Spreadsheet, to obtain calcium concentration in carbonated pore solution of AAMs.

Figure 6.52 Calcium concentration in carbonated pore solution of AAMs

6.D Chloride diffusion transport models in alkali-activated mortars

Figures 6.53-6.55 present the curve fitting of the effective chloride diffusion data for alkali-activated mortars submerged in water and exposed to different temperatures in the laboratory.

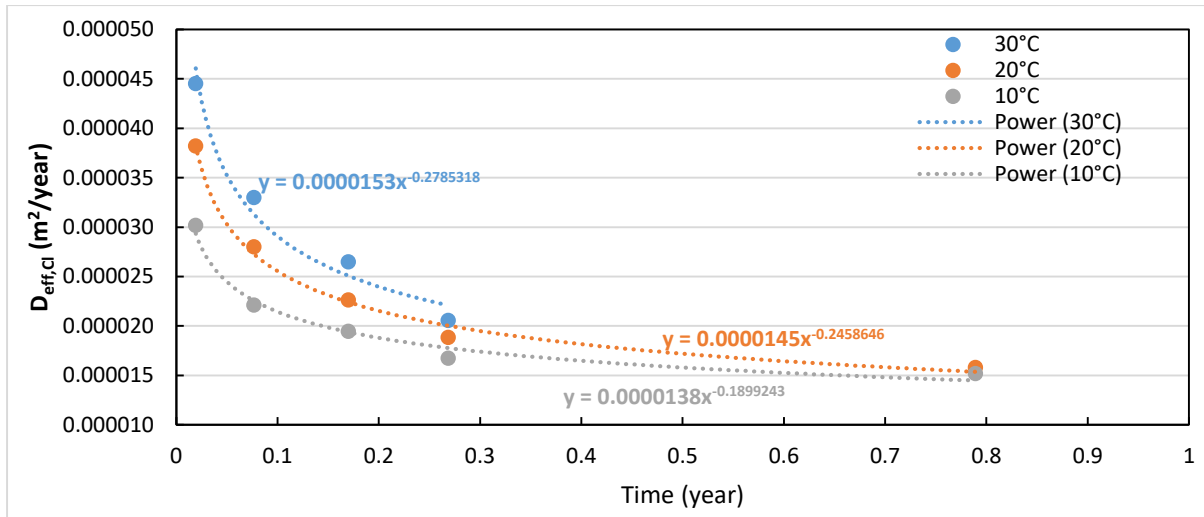


Figure 6.53 Chloride transport in 100SG mortar under submerged conditions and exposed to various temperatures of 30°C, 20°C and 10°C.

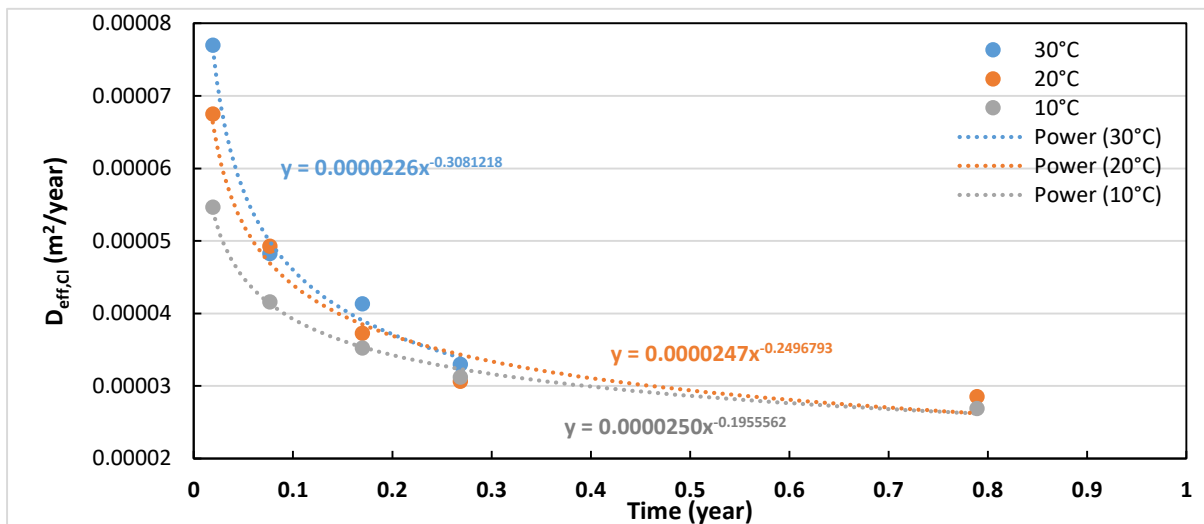


Figure 6.54 Chloride Transport in 75SG25FA mortar under submerged conditions and exposed to various temperatures of 30°C, 20°C and 10°C.

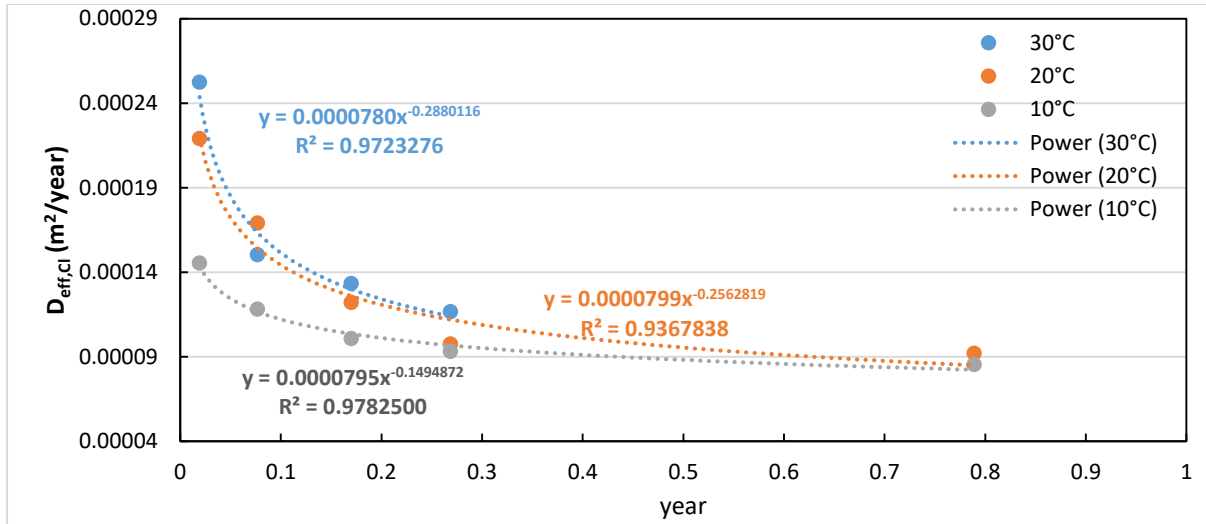


Figure 6.55 Chloride Transport in 50SG50FA mortar under submerged conditions and exposed to various temperatures of 30°C , 20 °C and 10 °C.

References

- [1] C. R. Gagg, "Cement and concrete as an engineering material: An historic appraisal and case study analysis," *Engineering Failure Analysis*, vol. 40, pp. 114-140, 2014, doi: 10.1016/j.engfailanal.2014.02.004.
- [2] J. L. Provis and J. S. Van Deventer, *Alkali activated materials: state-of-the-art report, RILEM TC 224-AAM*. Springer Science & Business Media, 2013.
- [3] G. Habert *et al.*, "Environmental impacts and decarbonization strategies in the cement and concrete industries," *Nature Reviews Earth & Environment*, vol. 1, no. 11, pp. 559-573, 2020, doi: 10.1038/s43017-020-0093-3.
- [4] K. Yang and C. E. White, "Multiscale pore structure determination of cement paste via simulation and experiment: The case of alkali-activated metakaolin," *Cement and Concrete Research*, vol. 137, p. 106212, 2020.
- [5] M. Xie, P. Dangla, and K. Li, "Reactive transport modelling of concurrent chloride ingress and carbonation in concrete," *Materials and Structures*, vol. 54, no. 5, pp. 1-19, 2021.
- [6] M. Nedeljković, Y. Zuo, K. Arbi, and G. Ye, "Carbonation resistance of alkali-activated slag under natural and accelerated conditions," *Journal of Sustainable Metallurgy*, vol. 4, no. 1, pp. 33-49, 2018.
- [7] H. Chang, S. Mu, and P. Feng, "Influence of carbonation on “maximum phenomenon” in surface layer of specimens subjected to cyclic drying-wetting condition," *Cement and Concrete Research*, vol. 103, pp. 95-109, 2018.
- [8] U. Angst, B. Elsener, C. K. Larsen, and Ø. Vennesland, "Critical chloride content in reinforced concrete—A review," *Cement and concrete research*, vol. 39, no. 12, pp. 1122-1138, 2009.
- [9] M. Alexander and H. Beushausen, "Durability, service life prediction, and modelling for reinforced concrete structures—review and critique," *Cement and Concrete Research*, vol. 122, pp. 17-29, 2019.
- [10] A. Wang *et al.*, "The Durability of Alkali-Activated Materials in Comparison with Ordinary Portland Cements and Concretes: A Review," *Engineering*, vol. 6, no. 6, pp. 695-706, 2020, doi: 10.1016/j.eng.2019.08.019.
- [11] N. B. 492, "Concrete, mortar and cement-based repair materials: chloride migration coefficient from non-steady-state migration experiments," *NordTest*, 1999.

- [12] A. S. F. T. O. MATERIALS, "Standart test method for water-soluble chloride in mortar and concrete: ASTM C 1218-92," *Annual Book of ASTM Standard*, 1993.
- [13] C. Astm, "1152, Standard test method for acid-soluble chloride in mortar and concrete," *American Society for Testing and Materials, EUA*, 1997.
- [14] X. Hu, C. Shi, X. Liu, and Z. Zhang, "Studying the effect of alkali dosage on microstructure development of alkali-activated slag pastes by electrical impedance spectroscopy (EIS)," *Construction and Building Materials*, vol. 261, 2020, doi: 10.1016/j.conbuildmat.2020.119982.
- [15] Y. Zuo, "Effect of chloride salt on the phase evolution in alkali-activated slag cements through thermodynamic modelling," *Applied Geochemistry*, vol. 136, p. 105169, 2022.
- [16] X. Ke, S. A. Bernal, J. L. Provis, and B. Lothenbach, "Thermodynamic modelling of phase evolution in alkali-activated slag cements exposed to carbon dioxide," *Cement and Concrete Research*, vol. 136, p. 106158, 2020.
- [17] V. J. Azad, C. Li, C. Verba, J. H. Ideker, and O. B. Isgor, "A COMSOL–GEMS interface for modeling coupled reactive-transport geochemical processes," *Computers & Geosciences*, vol. 92, pp. 79-89, 2016.
- [18] A. Michel, V. Marcos-Meson, W. Kunther, and M. R. Geiker, "Microstructural changes and mass transport in cement-based materials: A modeling approach," *Cement and Concrete Research*, vol. 139, p. 106285, 2021.
- [19] J. WHITING, "MANUFACTURE OF CEMENT. ," CHICAGO Patent 544,706, 1895.
- [20] V. Gluchovskij, "Gruntosilikaty," *Gosstrojizdat Kiev, Patent USSR*, vol. 245, p. 627, 1967.
- [21] F. Pacheco-Torgal, J. Labrincha, C. Leonelli, A. Palomo, and P. Chindaprasit, *Handbook of alkali-activated cements, mortars and concretes*. Elsevier, 2014.
- [22] J. S. van Deventer, J. L. Provis, P. Duxson, and D. G. Brice, "Chemical research and climate change as drivers in the commercial adoption of alkali activated materials," *Waste and Biomass Valorization*, vol. 1, no. 1, pp. 145-155, 2010.
- [23] J. Osio-Norgaard, J. P. Gevaudan, and W. V. Srubar, "A review of chloride transport in alkali-activated cement paste, mortar, and concrete," *Construction and Building Materials*, vol. 186, pp. 191-206, 2018, doi: 10.1016/j.conbuildmat.2018.07.119.
- [24] L. Baijnath, V. Gautam, and V. L. Yadav, "A comparative study of the removal efficiency of calcium hydroxide and sodium hydroxide as precipitating agents for chromium (III)," *Journal of Civil Engineering and Environmental Technology*, vol. 1, no. 1, pp. 17-20, 2014.

- [25] Z. Yan, Z. Sun, J. Yang, H. Yang, Y. Ji, and K. Hu, "Mechanical performance and reaction mechanism of copper slag activated with sodium silicate or sodium hydroxide," *Construction and Building Materials*, vol. 266, p. 120900, 2021.
- [26] C. Salocks and K. B. Kaley, "Sodium hydroxide," *Tech Support Doc Toxicol Clandest Drug Labs Methamphetamine*, vol. 1, pp. 1-9, 2003.
- [27] S. A. Bernal, "Advances in near-neutral salts activation of blast furnace slags," *RILEM technical letters*, vol. 1, pp. 39-39, 2016.
- [28] J. Péra, J. Ambroise, and M. Chabannet, "Properties of blast-furnace slags containing high amounts of manganese," *Cement and Concrete Research*, vol. 29, no. 2, pp. 171-177, 1999.
- [29] A. ASTM C618, "Standard specification for coal fly ash and raw or calcined natural pozzolan for use in concrete," *ASTM international*, 2019.
- [30] S. Mundra, D. P. Prentice, S. A. Bernal, and J. L. Provis, "Modelling chloride transport in alkali-activated slags," *Cement and Concrete Research*, vol. 130, p. 106011, 2020.
- [31] B. Walkley, S. J. Page, G. J. Rees, J. L. Provis, and J. V. Hanna, "Nanostructure of CaO-(Na₂O)-Al₂O₃-SiO₂-H₂O Gels Revealed by Multinuclear Solid-State Magic Angle Spinning and Multiple Quantum Magic Angle Spinning Nuclear Magnetic Resonance Spectroscopy," *The Journal of Physical Chemistry C*, vol. 124, no. 2, pp. 1681-1694, 2019, doi: 10.1021/acs.jpcc.9b10133.
- [32] H. Nguyen *et al.*, "Fiber reinforced alkali-activated stone wool composites fabricated by hot-pressing technique," *Materials & Design*, vol. 186, p. 108315, 2020.
- [33] J. Xie and O. Kayali, "Effect of superplasticiser on workability enhancement of Class F and Class C fly ash-based geopolymers," *Construction and Building Materials*, vol. 122, pp. 36-42, 2016.
- [34] P. Duxson and J. L. Provis, "Designing precursors for geopolymer cements," *Journal of the american ceramic society*, vol. 91, no. 12, pp. 3864-3869, 2008.
- [35] B. Walkley, G. J. Rees, R. San Nicolas, J. S. J. van Deventer, J. V. Hanna, and J. L. Provis, "New Structural Model of Hydrous Sodium Aluminosilicate Gels and the Role of Charge-Balancing Extra-Framework Al," *The Journal of Physical Chemistry C*, vol. 122, no. 10, pp. 5673-5685, 2018, doi: 10.1021/acs.jpcc.8b00259.
- [36] S. Sui, F. Georget, H. Maraghechi, W. Sun, and K. Scrivener, "Towards a generic approach to durability: Factors affecting chloride transport in binary and ternary cementitious materials," *Cement and Concrete Research*, vol. 124, p. 105783, 2019.

- [37] H. Beushausen and L. F. Luco, "Performance-based specifications and control of concrete durability," *RILEM TC*, pp. 66-72, 2016.
- [38] S. A. Bernal, J. L. Provis, and D. J. Green, "Durability of Alkali-Activated Materials: Progress and Perspectives," *Journal of the American Ceramic Society*, vol. 97, no. 4, pp. 997-1008, 2014, doi: 10.1111/jace.12831.
- [39] R. A. Robayo-Salazar, A. M. Aguirre-Guerrero, and R. M. de Gutiérrez, "Carbonation-induced corrosion of alkali-activated binary concrete based on natural volcanic pozzolan," *Construction and Building Materials*, vol. 232, p. 117189, 2020.
- [40] W. Tahri, X. Hu, C. Shi, and Z. Zhang, "Review on corrosion of steel reinforcement in alkali-activated concretes in chloride-containing environments," *Construction and Building Materials*, vol. 293, 2021, doi: 10.1016/j.conbuildmat.2021.123484.
- [41] S. Mundra, "Corrosion of steel in alkali-activated materials," University of Sheffield, 2018.
- [42] E. Deltombe, "Atlas of electrochemical equilibria in aqueous solutions," *section*, vol. 10, pp. 280-285, 1966.
- [43] E. McCafferty, "Thermodynamics of corrosion: Pourbaix diagrams. In Introduction to corrosion science (pp. 95-117)." *Springer*, pp. 95-117, 2010.
- [44] U. M. Angst, "Predicting the time to corrosion initiation in reinforced concrete structures exposed to chlorides," *Cement and Concrete Research*, vol. 115, pp. 559-567, 2019, doi: 10.1016/j.cemconres.2018.08.007.
- [45] S. Mundra and J. L. Provis, "Mechanisms of passivation and chloride-induced corrosion of mild steel in sulfide-containing alkaline solutions," *Journal of Materials Science*, vol. 56, no. 26, pp. 14783-14802, 2021, doi: 10.1007/s10853-021-06237-x.
- [46] P. Van den Heede, M. Maes, E. Gruyaert, and N. De Belie, "Full probabilistic service life prediction and life cycle assessment of concrete with fly ash and blast-furnace slag in a submerged marine environment: a parameter study," *International journal of environment and sustainable development*, vol. 11, no. 1, pp. 32-49, 2012.
- [47] M. D. Lepech, M. Geiker, and H. Stang, "Probabilistic design and management of environmentally sustainable repair and rehabilitation of reinforced concrete structures," *Cement and Concrete Composites*, vol. 47, pp. 19-31, 2014, doi: 10.1016/j.cemconcomp.2013.10.009.
- [48] C. Astm, "876-91 Standard test method for half-cell potentials of uncoated reinforcing steel in concrete," *Annual book of ASTM standards*, vol. 4, 1991.

- [49] A. Runci, J. L. Provis, and M. Serdar, "Revealing corrosion parameters of steel in alkali-activated materials," *Corrosion Science*, vol. 210, p. 110849, 2023.
- [50] C. Andrade and C. Alonso, "On-site measurements of corrosion rate of reinforcements," *Construction and building materials*, vol. 15, no. 2-3, pp. 141-145, 2001.
- [51] M. Babae and A. Castel, "Chloride-induced corrosion of reinforcement in low-calcium fly ash-based geopolymer concrete," *Cement and Concrete Research*, vol. 88, pp. 96-107, 2016, doi: 10.1016/j.cemconres.2016.05.012.
- [52] W. Tahri, X. Hu, C. Shi, and Z. Zhang, "Review on corrosion of steel reinforcement in alkali-activated concretes in chloride-containing environments," *Construction and Building Materials*, vol. 293, p. 123484, 2021.
- [53] P. Mangat, O. O. Ojedokun, and P. Lambert, "Chloride-initiated corrosion in alkali activated reinforced concrete," *Cement and Concrete Composites*, vol. 115, p. 103823, 2021.
- [54] S. Mundra, M. Criado, S. A. Bernal, and J. L. Provis, "Chloride-induced corrosion of steel rebars in simulated pore solutions of alkali-activated concretes," *Cement and Concrete Research*, vol. 100, pp. 385-397, 2017, doi: 10.1016/j.cemconres.2017.08.006.
- [55] M. Babae and A. Castel, "Chloride diffusivity, chloride threshold, and corrosion initiation in reinforced alkali-activated mortars: Role of calcium, alkali, and silicate content," *Cement and Concrete Research*, vol. 111, pp. 56-71, 2018.
- [56] O. Coussy, "Mechanics of porous continua," (*No Title*), 1995.
- [57] M. Mainguy, O. Coussy, and V. Baroghel-Bouny, "Role of air pressure in drying of weakly permeable materials," *Journal of engineering mechanics*, vol. 127, no. 6, pp. 582-592, 2001.
- [58] Z. Bažant and L. Najjar, "Nonlinear water diffusion in nonsaturated concrete," *Matériaux et Construction*, vol. 5, pp. 3-20, 1972.
- [59] C. Hall, "Anomalous diffusion in unsaturated flow: fact or fiction?," *Cement and Concrete Research*, vol. 37, no. 3, pp. 378-385, 2007.
- [60] S. Taylor, W. Hoff, M. Wilson, and K. Green, "Anomalous water transport properties of Portland and blended cement-based materials," *Journal of materials science letters*, vol. 18, no. 23, pp. 1925-1927, 1999.
- [61] N. M. Alderete, Y. V. Zaccardi, and N. De Belie, "Mechanism of long-term capillary water uptake in cementitious materials," *Cement and Concrete Composites*, vol. 106, p. 103448, 2020.

- [62] Z. Zhang and U. Angst, "A Dual-Permeability Approach to Study Anomalous Moisture Transport Properties of Cement-Based Materials," *Transport in Porous Media*, vol. 135, no. 1, pp. 59-78, 2020, doi: 10.1007/s11242-020-01469-y.
- [63] Z. Zhang and U. Angst, "Modeling Anomalous Moisture Transport in Cement-Based Materials with Kinetic Permeability," *Int J Mol Sci*, vol. 21, no. 3, Jan 28 2020, doi: 10.3390/ijms21030837.
- [64] F. Ren, C. Zhou, Q. Zeng, Z. Ding, F. Xing, and W. Wang, "The dependence of capillary sorptivity and gas permeability on initial water content for unsaturated cement mortars," *Cement and concrete composites*, vol. 104, p. 103356, 2019.
- [65] G. W. Scherer, "Drying, shrinkage, and cracking of cementitious materials," *Transport in Porous Media*, vol. 110, pp. 311-331, 2015.
- [66] I. Maruyama, T. Ohkubo, T. Haji, and R. Kurihara, "Dynamic microstructural evolution of hardened cement paste during first drying monitored by ¹H NMR relaxometry," *Cement and Concrete Research*, vol. 122, pp. 107-117, 2019.
- [67] C. Hall *et al.*, "Water anomaly in capillary liquid absorption by cement-based materials," *Journal of Materials Science Letters*, vol. 14, pp. 1178-1181, 1995.
- [68] Q. Zeng and S. Xu, "A two-parameter stretched exponential function for dynamic water vapor sorption of cement-based porous materials," *Materials and Structures*, vol. 50, no. 2, p. 128, 2017.
- [69] M. Babaei and A. Castel, "Water vapor sorption isotherms, pore structure, and moisture transport characteristics of alkali-activated and Portland cement-based binders," *Cement and Concrete Research*, vol. 113, pp. 99-120, 2018.
- [70] Z. Zhang, M. Thiéry, and V. Baroghel-Bouny, "A review and statistical study of existing hysteresis models for cementitious materials," *Cement and concrete research*, vol. 57, pp. 44-60, 2014.
- [71] W. Thomson, "4. On the equilibrium of vapour at a curved surface of liquid," *Proceedings of the Royal Society of Edinburgh*, vol. 7, pp. 63-68, 1872.
- [72] M. Feng and D. Fredlund, "Hysteretic influence associated with thermal conductivity sensor measurements," in *Proceedings from Theory to the Practice of Unsaturated Soil Mechanics in Association with the 52nd Canadian Geotechnical Conference and the Unsaturated Soil Group, Regina, Sask*, 1999, vol. 14, no. 2, pp. 14-20.
- [73] H. Pham, D. Fredlund, and S. L. Barbour, "A practical hysteresis model for the soil-water characteristic curve for soils with negligible volume change," *Geotechnique*, vol. 53, no. 2, pp. 293-298, 2003.

- [74] M. T. Van Genuchten, "A closed-form equation for predicting the hydraulic conductivity of unsaturated soils," *Soil science society of America journal*, vol. 44, no. 5, pp. 892-898, 1980.
- [75] D. G. Fredlund and A. Xing, "Equations for the soil-water characteristic curve," *Canadian geotechnical journal*, vol. 31, no. 4, pp. 521-532, 1994.
- [76] K. i. Kosugi, "Lognormal distribution model for unsaturated soil hydraulic properties," *Water Resources Research*, vol. 32, no. 9, pp. 2697-2703, 1996.
- [77] S. Whitaker, "Flow in porous media I: A theoretical derivation of Darcy's law," *Transport in porous media*, vol. 1, pp. 3-25, 1986.
- [78] Buckingham, E. (1907). Studies on the movement of soil moisture. *US Dept. Agric. Bur. Soils Bull.*, 38.
- [79] Z. Zhang, M. Thiery, and V. Baroghel-Bouny, "Investigation of moisture transport properties of cementitious materials," *Cement and Concrete Research*, vol. 89, pp. 257-268, 2016.
- [80] Z. Zhang, M. Thiéry, and V. Baroghel-Bouny, "Analysis of moisture transport in cementitious materials and modelling of drying-wetting cycles," in *International Conference: Numerical Modeling Strategies for Sustainable Concrete Structures, The French Association of Civil Engineering (AFGC), Aix-en-Provence, France, 2012*.
- [81] C. Antón, M. A. Climent, G. de Vera, I. Sánchez, and C. Andrade, "An improved procedure for obtaining and maintaining well characterized partial water saturation states on concrete samples to be used for mass transport tests," *Materials and structures*, vol. 46, no. 8, pp. 1389-1400, 2013.
- [82] V. Baroghel-Bouny, "Water vapour sorption experiments on hardened cementitious materials. Part II: Essential tool for assessment of transport properties and for durability prediction," *Cement and Concrete Research*, vol. 37, no. 3, pp. 438-454, 2007.
- [83] R. Millington, "Gas diffusion in porous media," *Science*, vol. 130, no. 3367, pp. 100-102, 1959.
- [84] M. Thiery, V. Baroghel-Bouny, N. Bourneton, G. Villain, and C. Stéfani, "Modélisation du séchage des bétons: analyse des différents modes de transfert hydrique," *Revue européenne de génie civil*, vol. 11, no. 5, pp. 541-577, 2007.
- [85] H. H. Gerke and M. T. Van Genuchten, "A dual-porosity model for simulating the preferential movement of water and solutes in structured porous media," *Water resources research*, vol. 29, no. 2, pp. 305-319, 1993.

- [86] H. H. Gerke and M. T. Van Genuchten, "Evaluation of a first-order water transfer term for variably saturated dual-porosity flow models," *Water Resources Research*, vol. 29, no. 4, pp. 1225-1238, 1993.
- [87] D. Smyl, F. Ghasemzadeh, and M. Pour-Ghaz, "Can the dual-permeability model be used to simulate unsaturated moisture flow in damaged mortar and concrete?," *International Journal of Advances in Engineering Sciences and Applied Mathematics*, vol. 9, pp. 54-66, 2017.
- [88] G. A. Scheffler and R. Plagge, "A whole range hygric material model: Modelling liquid and vapour transport properties in porous media," *International Journal of Heat and Mass Transfer*, vol. 53, no. 1-3, pp. 286-296, 2010.
- [89] R. Schirmer, "Die Diffusionszahl von Wasserdampf-Luft-Gemischen und die Verdampfungsgeschwindigkeit," VDI-Verlag, 1938.
- [90] P. Castro, O. T. De Rincon, and E. Pazini, "Interpretation of chloride profiles from concrete exposed to tropical marine environments," *Cement and Concrete Research*, vol. 31, no. 4, pp. 529-537, 2001.
- [91] I. M. Mills, "Dimensions of logarithmic quantities," *Journal of Chemical Education*, vol. 72, no. 10, p. 954, 1995.
- [92] Y. Mualem, "A new model for predicting the hydraulic conductivity of unsaturated porous media," *Water resources research*, vol. 12, no. 3, pp. 513-522, 1976.
- [93] J. Monteith and M. Unsworth, "Transport of Heat, Mass, and Momentum," *Principles of Environmental Physics*, pp. 25-35, 2013.
- [94] M. Balonis, B. Lothenbach, G. Le Saout, and F. P. Glasser, "Impact of chloride on the mineralogy of hydrated Portland cement systems," *Cement and Concrete Research*, vol. 40, no. 7, pp. 1009-1022, 2010.
- [95] B. Lothenbach and F. Winnefeld, "Thermodynamic modelling of the hydration of Portland cement," *Cement and Concrete Research*, vol. 36, no. 2, pp. 209-226, 2006.
- [96] L. Bertolini, B. Elsener, P. Pedferri, E. Redaelli, and R. B. Polder, *Corrosion of steel in concrete: prevention, diagnosis, repair*. John Wiley & Sons, 2013.
- [97] M. Khan, O. Kayali, and U. Troitzsch, "Chloride binding capacity of hydrotalcite and the competition with carbonates in ground granulated blast furnace slag concrete," *Materials and Structures*, vol. 49, no. 11, pp. 4609-4619, 2016.
- [98] A. Noushini, Q. D. Nguyen, and A. Castel, "Assessing alkali-activated concrete performance in chloride environments using NT Build 492," *Materials and Structures*, vol. 54, no. 2, pp. 1-15, 2021.

- [99] Provis, J. L., & Van Deventer, J. S. (Eds.). (2013). *Alkali activated materials: state-of-the-art report, RILEM TC 224-AAM* (Vol. 13). Springer Science & Business Media.
- [100] D. Bondar, Q. Ma, M. Soutsos, M. Basheer, J. L. Provis, and S. Nanukuttan, "Alkali activated slag concretes designed for a desired slump, strength and chloride diffusivity," *Construction and Building Materials*, vol. 190, pp. 191-199, 2018, doi: 10.1016/j.conbuildmat.2018.09.124.
- [101] P. S. Mangat, O. O. Ojedokun, and P. Lambert, "Chloride-initiated corrosion in alkali activated reinforced concrete," *Cement and Concrete Composites*, vol. 115, 2021, doi: 10.1016/j.cemconcomp.2020.103823.
- [102] X. Ke, S. A. Bernal, and J. L. Provis, "Chloride binding capacity of synthetic C-(A)-SH type gels in alkali-activated slag simulated pore solutions," in *Proceedings of the 1st international conference on construction materials for sustainable future, Zadar, Croatia, 2017*.
- [103] X. Ke, S. A. Bernal, and J. L. Provis, "Uptake of chloride and carbonate by Mg-Al and Ca-Al layered double hydroxides in simulated pore solutions of alkali-activated slag cement," *Cement and Concrete Research*, vol. 100, pp. 1-13, 2017.
- [104] P. Mangat and O. O. Ojedokun, "Free and bound chloride relationships affecting reinforcement cover in alkali activated concrete," *Cement and Concrete Composites*, vol. 112, p. 103692, 2020.
- [105] P. Mangat and O. O. Ojedokun, "Bound chloride ingress in alkali activated concrete," *Construction and Building Materials*, vol. 212, pp. 375-387, 2019.
- [106] O. B. Isgor and W. J. Weiss, "A nearly self-sufficient framework for modelling reactive-transport processes in concrete," *Materials and structures*, vol. 52, no. 1, pp. 1-17, 2019.
- [107] R. R. Lloyd, J. L. Provis, K. J. Smeaton, and J. S. van Deventer, "Spatial distribution of pores in fly ash-based inorganic polymer gels visualised by Wood's metal intrusion," *Microporous and Mesoporous Materials*, vol. 126, no. 1-2, pp. 32-39, 2009.
- [108] J. L. Provis, R. J. Myers, C. E. White, V. Rose, and J. S. Van Deventer, "X-ray microtomography shows pore structure and tortuosity in alkali-activated binders," *Cement and concrete research*, vol. 42, no. 6, pp. 855-864, 2012.
- [109] C. Fu, H. Ye, K. Zhu, D. Fang, and J. Zhou, "Alkali cation effects on chloride binding of alkali-activated fly ash and metakaolin geopolymers," *Cement and Concrete Composites*, vol. 114, p. 103721, 2020.

- [110] A. Runci, J. Provis, and M. Serdar, "Microstructure as a key parameter for understanding chloride ingress in alkali-activated mortars," *Cement and Concrete Composites*, vol. 134, p. 104818, 2022.
- [111] N. T. Build, "443," *Concrete, hardened: accelerated chloride penetration*, vol. 11, 1995.
- [112] T. Luping and L.-O. Nilsson, "Chloride binding capacity and binding isotherms of OPC pastes and mortars," *Cement and concrete research*, vol. 23, no. 2, pp. 247-253, 1993.
- [113] J. Zhang, C. Shi, and Z. Zhang, "Chloride binding of alkali-activated slag/fly ash cements," *Construction and Building Materials*, vol. 226, pp. 21-31, 2019, doi: 10.1016/j.conbuildmat.2019.07.281.
- [114] G. J. Gluth *et al.*, "RILEM TC 247-DTA round robin test: carbonation and chloride penetration testing of alkali-activated concretes," *Materials and Structures*, vol. 53, no. 1, pp. 1-17, 2020.
- [115] Y. Wang, S. Nanukuttan, Y. Bai, and P. A. M. Basheer, "Influence of combined carbonation and chloride ingress regimes on rate of ingress and redistribution of chlorides in concretes," *Construction and Building Materials*, vol. 140, pp. 173-183, 2017, doi: 10.1016/j.conbuildmat.2017.02.121.
- [116] K. Li, F. Zhao, and Y. Zhang, "Influence of carbonation on the chloride ingress into concrete: Theoretical analysis and application to durability design," *Cement and Concrete Research*, vol. 123, 2019, doi: 10.1016/j.cemconres.2019.105788.
- [117] K. Pasupathy, J. Sanjayan, P. Rajeev, and D. W. Law, "The effect of chloride ingress in reinforced geopolymer concrete exposed in the marine environment," *Journal of Building Engineering*, vol. 39, 2021, doi: 10.1016/j.jobbe.2021.102281.
- [118] S. Kashef-Haghighi, Y. Shao, and S. Ghoshal, "Mathematical modeling of CO₂ uptake by concrete during accelerated carbonation curing," *Cement and concrete research*, vol. 67, pp. 1-10, 2015.
- [119] S. A. Bernal, X. Ke, M. Criado, S. Mundra, and J. L. Provis, "Factors controlling carbonation resistance of alkali-activated materials," in *Special Publication 320: Proceedings of the 10th ACI/RILEM International Conference on Cementitious Materials and Alternative Binders for Sustainable Concrete*, 2017, no. SP 320: American Concrete Institute, pp. 36.1-36.10.
- [120] M. Nedeljković, B. Šavija, Y. Zuo, M. Luković, and G. Ye, "Effect of natural carbonation on the pore structure and elastic modulus of the alkali-activated fly ash and

- slag pastes," *Construction and Building Materials*, vol. 161, pp. 687-704, 2018, doi: 10.1016/j.conbuildmat.2017.12.005.
- [121] V. G. Papadakis, C. G. Vayenas, and M. N. Fardis, "Fundamental modeling and experimental investigation of concrete carbonation," *Materials Journal*, vol. 88, no. 4, pp. 363-373, 1991.
- [122] S. Martínez-Ramírez and L. Fernández-Carrasco, "Carbonation of ternary cement systems," *Construction and Building Materials*, vol. 27, no. 1, pp. 313-318, 2012.
- [123] B. Lothenbach *et al.*, "Cemdata18: A chemical thermodynamic database for hydrated Portland cements and alkali-activated materials," *Cement and Concrete Research*, vol. 115, pp. 472-506, 2019, doi: 10.1016/j.cemconres.2018.04.018.
- [124] H. Ye and A. Radlińska, "Carbonation-induced volume change in alkali-activated slag," *Construction and building materials*, vol. 144, pp. 635-644, 2017.
- [125] M. Criado, A. Palomo, and A. Fernández-Jiménez, "Alkali activation of fly ashes. Part 1: Effect of curing conditions on the carbonation of the reaction products," *Fuel*, vol. 84, no. 16, pp. 2048-2054, 2005.
- [126] A. E. Morandeau and C. E. White, "Role of magnesium-stabilized amorphous calcium carbonate in mitigating the extent of carbonation in alkali-activated slag," *Chemistry of Materials*, vol. 27, no. 19, pp. 6625-6634, 2015.
- [127] R. Van Santen, "The Ostwald step rule," *The Journal of Physical Chemistry*, vol. 88, no. 24, pp. 5768-5769, 1984.
- [128] A. Sarkar and S. Mahapatra, "Synthesis of all crystalline phases of anhydrous calcium carbonate," *Crystal growth & design*, vol. 10, no. 5, pp. 2129-2135, 2010.
- [129] S. A. Bernal, J. L. Provis, D. G. Brice, A. Kilcullen, P. Duxson, and J. S. van Deventer, "Accelerated carbonation testing of alkali-activated binders significantly underestimates service life: The role of pore solution chemistry," *Cement and Concrete Research*, vol. 42, no. 10, pp. 1317-1326, 2012.
- [130] M. Nedeljković, B. Ghiassi, S. Melzer, C. Kooij, S. van der Laan, and G. Ye, "CO₂ binding capacity of alkali-activated fly ash and slag pastes," *Ceramics International*, vol. 44, no. 16, pp. 19646-19660, 2018.
- [131] F. Puertas, R. Gutierrez, A. Fernández-Jiménez, S. Delvasto, and J. Maldonado, "Alkaline cement mortars. Chemical resistance to sulfate and seawater attack," *Materiales de Construcción*, vol. 52, no. 267, pp. 55-71, 2002.

- [132] X. Ke, M. Criado, J. L. Provis, and S. A. Bernal, "Slag-based cements that resist damage induced by carbon dioxide," *ACS Sustainable Chemistry & Engineering*, vol. 6, no. 4, pp. 5067-5075, 2018.
- [133] X. Ke, S. A. Bernal, O. H. Hussein, and J. L. Provis, "Chloride binding and mobility in sodium carbonate-activated slag pastes and mortars," *Mater Struct*, vol. 50, no. 6, p. 252, 2017, doi: 10.1617/s11527-017-1121-8.
- [134] S. A. Bernal *et al.*, "MgO content of slag controls phase evolution and structural changes induced by accelerated carbonation in alkali-activated binders," *Cement and Concrete Research*, vol. 57, pp. 33-43, 2014.
- [135] S. Y. Wang, E. McCaslin, and C. E. White, "Effects of magnesium content and carbonation on the multiscale pore structure of alkali-activated slags," *Cement and Concrete Research*, vol. 130, 2020, doi: 10.1016/j.cemconres.2020.105979.
- [136] R. Pouhet and M. Cyr, "Carbonation in the pore solution of metakaolin-based geopolymer," *Cement and Concrete Research*, vol. 88, pp. 227-235, 2016.
- [137] S. A. Bernal *et al.*, "Gel nanostructure in alkali-activated binders based on slag and fly ash, and effects of accelerated carbonation," *Cement and Concrete Research*, vol. 53, pp. 127-144, 2013.
- [138] M. Nedeljković, B. Ghiassi, S. van der Laan, Z. Li, and G. Ye, "Effect of curing conditions on the pore solution and carbonation resistance of alkali-activated fly ash and slag pastes," *Cement and Concrete Research*, vol. 116, pp. 146-158, 2019, doi: 10.1016/j.cemconres.2018.11.011.
- [139] S. A. Bernal, J. L. Provis, R. Mejía de Gutiérrez, and J. S. van Deventer, "Accelerated carbonation testing of alkali-activated slag/metakaolin blended concretes: effect of exposure conditions," *Materials and Structures*, vol. 48, no. 3, pp. 653-669, 2015.
- [140] B. E. 14630, "Products and systems for the protection and repair of concrete structures. Test methods. Determination of carbonation depth in hardened concrete by the phenolphthalein method," ed, 2006.
- [141] O. B. Isgor and A. G. Razaqpur, "Finite element modeling of coupled heat transfer, moisture transport and carbonation processes in concrete structures," *Cement and Concrete Composites*, vol. 26, no. 1, pp. 57-73, 2004.
- [142] K.-H. Yang, E.-A. Seo, and S.-H. Tae, "Carbonation and CO₂ uptake of concrete," *Environmental Impact Assessment Review*, vol. 46, pp. 43-52, 2014.

- [143] V. G. Papadakis, C. G. Vayenas, and M. Fardis, "A reaction engineering approach to the problem of concrete carbonation," *AICHE Journal*, vol. 35, no. 10, pp. 1639-1650, 1989.
- [144] V.-L. Ta, S. Bonnet, T. S. Kiese, and A. Ventura, "A new meta-model to calculate carbonation front depth within concrete structures," *Construction and Building Materials*, vol. 129, pp. 172-181, 2016.
- [145] R. J. Myers, S. A. Bernal, and J. L. Provis, "A thermodynamic model for C-(N-) ASH gel: CNASH_{ss}. Derivation and validation," *Cement and Concrete Research*, vol. 66, pp. 27-47, 2014.
- [146] A. Morandau, M. Thiery, and P. Dangla, "Investigation of the carbonation mechanism of CH and CSH in terms of kinetics, microstructure changes and moisture properties," *Cement and concrete research*, vol. 56, pp. 153-170, 2014.
- [147] M. Nedeljković, Y. Zuo, K. Arbi, and G. Ye, "Natural Carbonation of Alkali-Activated Fly Ash and Slag Pastes," Cham, 2018: Springer International Publishing, in *High Tech Concrete: Where Technology and Engineering Meet*, pp. 2213-2223.
- [148] P. Basheer, S. Chidiact, and A. Long, "Predictive models for deterioration of concrete structures," *Construction and Building Materials*, vol. 10, no. 1, pp. 27-37, 1996.
- [149] S. A. Bernal, R. San Nicolas, J. L. Provis, R. Mejía de Gutiérrez, and J. S. van Deventer, "Natural carbonation of aged alkali-activated slag concretes," *Materials and Structures*, vol. 47, no. 4, pp. 693-707, 2014.
- [150] V. Shah, K. Scrivener, B. Bhattacharjee, and S. Bishnoi, "Changes in microstructure characteristics of cement paste on carbonation," *Cement and Concrete Research*, vol. 109, pp. 184-197, 2018.
- [151] K. Pasupathy, M. Berndt, J. Sanjayan, P. Rajeev, and D. S. Cheema, "Durability of low-calcium fly ash based geopolymer concrete culvert in a saline environment," *Cement and Concrete Research*, vol. 100, pp. 297-310, 2017, doi: 10.1016/j.cemconres.2017.07.010.
- [152] I. Ismail *et al.*, "Influence of fly ash on the water and chloride permeability of alkali-activated slag mortars and concretes," *Construction and Building Materials*, vol. 48, pp. 1187-1201, 2013.
- [153] M. Criado and J. L. Provis, "Alkali activated slag mortars provide high resistance to chloride-induced corrosion of steel," *Frontiers in Materials*, vol. 5, p. 34, 2018.
- [154] K. Tuutti, *Corrosion of steel in concrete*. Cement-och betonginst., 1982.

- [155] M. Alexander and H. Beushausen, "Durability, service life prediction, and modelling for reinforced concrete structures – review and critique," *Cement and Concrete Research*, vol. 122, pp. 17-29, 2019, doi: 10.1016/j.cemconres.2019.04.018.
- [156] M. B. Otieno, H. D. Beushausen, and M. G. Alexander, "Modelling corrosion propagation in reinforced concrete structures—A critical review," *Cement and Concrete composites*, vol. 33, no. 2, pp. 240-245, 2011.
- [157] N. D. ADASOORIYA, S. SAMARAKOON, and O. T. Gudmestad, "Corrosion propagation phase and bond strength degradation of reinforced concrete structures: State of the art," *Materials Characterisation*, p. 47, 2018.
- [158] M. Collepardi, A. Marcialis, and R. Turriziani, "Penetration of chloride ions into cement pastes and concretes," *Journal of the American Ceramic Society*, vol. 55, no. 10, pp. 534-535, 1972.
- [159] J. M. Frederiksen, L. Mejlbro, and L.-O. Nilsson, "Fick's 2nd law-Complete solutions for chloride ingress into concrete—with focus on time dependent diffusivity and boundary condition," 2009.
- [160] T. Luping, "Engineering expression of the ClinConc model for prediction of free and total chloride ingress in submerged marine concrete," *Cement and Concrete Research*, vol. 38, no. 8-9, pp. 1092-1097, 2008.
- [161] C. Code, "Model code for service life design. Lausanne: Federation Internationale du Beton, fib," *Bulletin*, no. 34, 2006.
- [162] J. Marchand and E. Samson, "Predicting the service-life of concrete structures—Limitations of simplified models," *Cement and concrete composites*, vol. 31, no. 8, pp. 515-521, 2009.
- [163] I. Stipanovic Oslakovic, D. Bjegovic, and D. Mikulic, "Evaluation of service life design models on concrete structures exposed to marine environment," *Materials and structures*, vol. 43, no. 10, pp. 1397-1412, 2010.
- [164] J. Ožbolt, F. Oršanić, and G. Balabanić, "Modeling influence of hysteretic moisture behavior on distribution of chlorides in concrete," *Cement and Concrete Composites*, vol. 67, pp. 73-84, 2016.
- [165] J. L. Provis *et al.*, "RILEM TC 247-DTA round robin test: mix design and reproducibility of compressive strength of alkali-activated concretes," *Materials and Structures*, vol. 52, no. 5, pp. 1-13, 2019.

- [166] Z. Osmanovic, N. Haračić, and J. Zelić, "Properties of blastfurnace cements (CEM III/A, B, C) based on Portland cement clinker, blastfurnace slag and cement kiln dusts," *Cement and Concrete Composites*, vol. 91, pp. 189-197, 2018.
- [167] Y. Sun, Z. Liu, S. Ghorbani, G. Ye, and G. De Schutter, "Fresh and hardened properties of alkali-activated slag concrete: The effect of fly ash as a supplementary precursor," *Journal of Cleaner Production*, vol. 370, p. 133362, 2022.
- [168] X. Ke and V. A. Baki, "Assessing the suitability of alkali-activated metakaolin geopolymer for thermochemical heat storage," *Microporous and Mesoporous Materials*, vol. 325, p. 111329, 2021.
- [169] K. Yamada, S. Ogawa, and S. Hanehara, "Controlling of the adsorption and dispersing force of polycarboxylate-type superplasticizer by sulfate ion concentration in aqueous phase," *Cement and Concrete Research*, vol. 31, no. 3, pp. 375-383, 2001.
- [170] H. Ma, "Mercury intrusion porosimetry in concrete technology: tips in measurement, pore structure parameter acquisition and application," *Journal of porous materials*, vol. 21, no. 2, pp. 207-215, 2014.
- [171] K. Scrivener, R. Snellings, and B. Lothenbach, *A practical guide to microstructural analysis of cementitious materials*. Crc Press Boca Raton, FL, USA: , 2016.
- [172] Q. Zeng, K. Li, T. Fen-Chong, and P. Dangla, "Analysis of pore structure, contact angle and pore entrapment of blended cement pastes from mercury porosimetry data," *Cement and Concrete Composites*, vol. 34, no. 9, pp. 1053-1060, 2012.
- [173] M. M. a. T. S. Bjorn Van Belleghem, "Resistivity of repair materials for concrete repair prior to the application of a cathodic protection system," presented at the 75th RILEM Annual Week-International Conference on Advances in Sustainable Construction Materials and Structures, 2021.
- [174] R. J. Myers, B. Lothenbach, S. A. Bernal, and J. L. Provis, "Thermodynamic modelling of alkali-activated slag cements," *Applied Geochemistry*, vol. 61, pp. 233-247, 2015.
- [175] D. H. K. a. G. C. F. Harold C. Helgeson, "Theoretical prediction of the thermodynamic behavior of aqueous electrolytes by high pressures and temperatures; IV, Calculation of activity coefficients, osmotic coefficients, and apparent molal and standard and relative partial molal properties to 600 degrees C and 5kb," *American Journal of Science*, no. 281, pp. 1249-1516, 1981.
- [176] K. De Weerd, G. Plusquellec, A. B. Revert, M. Geiker, and B. Lothenbach, "Effect of carbonation on the pore solution of mortar," *Cement and Concrete Research*, vol. 118, pp. 38-56, 2019.

- [177] J. Crank, *The mathematics of diffusion*. Oxford university press, 1979.
- [178] G. D. Smith, G. D. Smith, and G. D. S. Smith, *Numerical solution of partial differential equations: finite difference methods*. Oxford university press, 1985.
- [179] Z. Zhang, M. Thiery, and V. Baroghel-Bouny, "Numerical modelling of moisture transfers with hysteresis within cementitious materials: Verification and investigation of the effects of repeated wetting–drying boundary conditions," *Cement and Concrete Research*, vol. 68, pp. 10-23, 2015.
- [180] R. D. Skeel and M. Berzins, "A method for the spatial discretization of parabolic equations in one space variable," *SIAM journal on scientific and statistical computing*, vol. 11, no. 1, pp. 1-32, 1990.
- [181] R. M. Corless, G. H. Gonnet, D. E. Hare, D. J. Jeffrey, and D. E. Knuth, "On the Lambert W function," *Advances in Computational mathematics*, vol. 5, pp. 329-359, 1996.
- [182] R. D. Morrison, "Forensic applications of subsurface contaminant transport models," in *Introduction to Environmental Forensics*: Elsevier, 2015, pp. 555-591.
- [183] S. Mundra *et al.*, "Application of electrochemical methods for studying steel corrosion in alkali-activated materials," *Materials and Corrosion*, 2023.
- [184] J. Frederiksen, L. Mejlbro, and E. Poulsen, "The HETEK model of chloride ingress into concrete made simpler by approximations," in *Second International RILEM Workshop on Testing and Modelling the Chloride Ingress into Concrete, 2000*: RILEM Publications SARL, pp. 317-336.
- [185] A. Lindvall, "Duracrete–probabilistic performance based durability design of concrete structures" in *2nd Int. PhD. Symposium in civil engineering*, 1998.
- [186] J. S. J. van Deventer, R. San Nicolas, I. Ismail, S. A. Bernal, D. G. Brice, and J. L. Provis, "Microstructure and durability of alkali-activated materials as key parameters for standardization," *Journal of Sustainable Cement-Based Materials*, vol. 4, no. 2, pp. 116-128, 2014, doi: 10.1080/21650373.2014.979265.
- [187] A. Dehghan, K. Peterson, G. Riehm, and L. H. Bromerchenkel, "Application of X-ray microfluorescence for the determination of chloride diffusion coefficients in concrete chloride penetration experiments," *Construction and Building Materials*, vol. 148, pp. 85-95, 2017.
- [188] R. J. Thomas, E. Ariyachandra, D. Lezama, and S. Peethamparan, "Comparison of chloride permeability methods for Alkali-Activated concrete," *Construction and*

- Building Materials*, vol. 165, pp. 104-111, 2018, doi: 10.1016/j.conbuildmat.2018.01.016.
- [189] C. Gunasekara, D. W. Law, and S. Setunge, "Long term permeation properties of different fly ash geopolymer concretes," *Construction and Building Materials*, vol. 124, pp. 352-362, 2016, doi: 10.1016/j.conbuildmat.2016.07.121.
- [190] C. Tennakoon, A. Shayan, J. G. Sanjayan, and A. Xu, "Chloride ingress and steel corrosion in geopolymer concrete based on long term tests," *Materials & Design*, vol. 116, pp. 287-299, 2017, doi: 10.1016/j.matdes.2016.12.030.
- [191] BSI, "BS EN 206-1: Concrete: Specification, performance, production and conformity," ed: BSI London, UK, 2000.
- [192] Y. Zhu, D. D. Macdonald, J. Yang, J. Qiu, and G. R. Engelhardt, "Corrosion of rebar in concrete. Part II: Literature survey and statistical analysis of existing data on chloride threshold," *Corrosion Science*, vol. 185, 2021, doi: 10.1016/j.corsci.2021.109439.
- [193] D. A. Kulik *et al.*, "GEM-Selektor geochemical modeling package: revised algorithm and GEMS3K numerical kernel for coupled simulation codes," *Computational Geosciences*, vol. 17, pp. 1-24, 2013.
- [194] P. T. Durdziński *et al.*, "Outcomes of the RILEM round robin on degree of reaction of slag and fly ash in blended cements," *Materials and Structures*, vol. 50, pp. 1-15, 2017.
- [195] M. Yang, S. R. Paudel, and E. Asa, "Comparison of pore structure in alkali activated fly ash geopolymer and ordinary concrete due to alkali-silica reaction using micro-computed tomography," *Construction and Building Materials*, vol. 236, p. 117524, 2020.
- [196] S. A. Bernal, R. Mejia de Gutiérrez, A. L. Pedraza, J. L. Provis, E. D. Rodriguez, and S. Delvasto, "Effect of binder content on the performance of alkali-activated slag concretes," *Cement and Concrete Research*, vol. 41, no. 1, pp. 1-8, 2011.
- [197] J. Zhang *et al.*, "Chloride diffusion in alkali-activated fly ash/slag concretes: Role of slag content, water/binder ratio, alkali content and sand-aggregate ratio," *Construction and Building Materials*, vol. 261, p. 119940, 2020.
- [198] Q. Ma, S. V. Nanukuttan, P. M. Basheer, Y. Bai, and C. Yang, "Chloride transport and the resulting corrosion of steel bars in alkali activated slag concretes," *Materials and Structures*, vol. 49, pp. 3663-3677, 2016.
- [199] G. J. G. Gluth *et al.*, "RILEM TC 247-DTA round robin test: carbonation and chloride penetration testing of alkali-activated concretes," *Materials and Structures*, journal article vol. 53, no. 1, p. #21, February 13 2020, doi: 10.1617/s11527-020-1449-3.

- [200] A. Noushini, Q. D. Nguyen, and A. Castel, "Assessing alkali-activated concrete performance in chloride environments using NT Build 492," *Materials and Structures*, vol. 54, no. 2, p. #57, 2021.
- [201] J. S. J. van Deventer, R. San Nicolas, I. Ismail, S. A. Bernal, D. G. Brice, and J. L. Provis, "Microstructure and durability of alkali-activated materials as key parameters for standardisation," *J. Sust. Cem.-Based Mater.*, vol. 4, no. 2, pp. 116-128, 2015.
- [202] CEN, "Concrete - Specification, performance, production and conformity (EN206:2013)." no. Brussels: European Committee for Standardization, 2013.
- [203] J. Gulikers, "A critical discussion on the usefulness and reliability of mathematical modeling for service life design of infrastructure," in *COMPLAS XII: proceedings of the XII International Conference on Computational Plasticity: fundamentals and applications*, 2013: CIMNE, pp. 542-553.
- [204] N. Ukrainczyk, "Simple model for alkali leaching from geopolymers: Effects of raw materials and acetic acid concentration on apparent diffusion coefficient," *Materials*, vol. 14, no. 6, p. 1425, 2021.
- [205] J. M. de Burgh and S. J. Foster, "Influence of temperature on water vapour sorption isotherms and kinetics of hardened cement paste and concrete," *Cement and Concrete Research*, vol. 92, pp. 37-55, 2017.
- [206] M. Mahmoudkhani and D. W. Keith, "Low-energy sodium hydroxide recovery for CO₂ capture from atmospheric air—Thermodynamic analysis," *International Journal of Greenhouse Gas Control*, vol. 3, no. 4, pp. 376-384, 2009.
- [207] Y. Gao, G. De Schutter, G. Ye, Z. Tan, and K. Wu, "The ITZ microstructure, thickness and porosity in blended cementitious composite: Effects of curing age, water to binder ratio and aggregate content," *Composites part b: engineering*, vol. 60, pp. 1-13, 2014.
- [208] H. M. Jennings, A. Kumar, and G. Sant, "Quantitative discrimination of the nano-pore-structure of cement paste during drying: New insights from water sorption isotherms," *Cement and Concrete Research*, vol. 76, pp. 27-36, 2015.
- [209] R. Helmuth, "Dimensional changes of hardened Portland cement pastes caused by temperature changes," *dynamics*, vol. 5, p. 1, 1961.
- [210] P. J. McDonald, O. Istok, M. Janota, A. M. Gajewicz-Jaromin, and D. A. Faux, "Sorption, anomalous water transport and dynamic porosity in cement paste: A spatially localised 1H NMR relaxation study and a proposed mechanism," *Cement and Concrete Research*, vol. 133, p. 106045, 2020.

- [211] J.-P. Thierry and G. Chanvillard, "Unifying Autogeneous and Drying Shrinkage of Cement Paste by the use of Isothermal Sorption/Desorption Curves."
- [212] V. Baroghel-Bouny, "Water vapour sorption experiments on hardened cementitious materials: Part I: Essential tool for analysis of hygral behaviour and its relation to pore structure," *Cement and Concrete Research*, vol. 37, no. 3, pp. 414-437, 2007.
- [213] M. D. Nguyen, "Modélisation des couplages entre hydratation et dessiccation des matériaux cimentaires à l'issue du décoffrage. Étude de la dégradation des propriétés de transfert," Ecole nationale des ponts et chaussées-ENPC PARIS/MARNE LA VALLEE, 2009.
- [214] L. Chica, C. Mera, L. M. Sepúlveda-Cano, and A. Alzate, "Porosity estimation and pore structure characterization of foamed cement paste using non-specialized image digital processing," *Materials and Structures*, vol. 55, no. 7, p. 189, 2022.
- [215] Z. Shi, C. Shi, S. Wan, N. Li, and Z. Zhang, "Effect of alkali dosage and silicate modulus on carbonation of alkali-activated slag mortars," *Cement and Concrete Research*, vol. 113, pp. 55-64, 2018.
- [216] W. Chen, B. Li, J. Wang, and N. Thom, "Effects of alkali dosage and silicate modulus on autogenous shrinkage of alkali-activated slag cement paste," *Cement and Concrete Research*, vol. 141, p. 106322, 2021.
- [217] E. P. Barrett, L. G. Joyner, and P. P. Halenda, "The determination of pore volume and area distributions in porous substances. I. Computations from nitrogen isotherms," *Journal of the American Chemical society*, vol. 73, no. 1, pp. 373-380, 1951.
- [218] S. M. Park, J. G. Jang, N. Lee, and H.-K. Lee, "Physicochemical properties of binder gel in alkali-activated fly ash/slag exposed to high temperatures," *Cement and Concrete Research*, vol. 89, pp. 72-79, 2016.
- [219] Z. Zhang, Y. Zhu, H. Zhu, Y. Zhang, J. L. Provis, and H. Wang, "Effect of drying procedures on pore structure and phase evolution of alkali-activated cements," *Cement and Concrete Composites*, vol. 96, pp. 194-203, 2019.
- [220] Q. Zeng, X. Wang, P. Yang, J. Wang, and C. Zhou, "Tracing mercury entrapment in porous cement paste after mercury intrusion test by X-ray computed tomography and implications for pore structure characterization," *Materials Characterization*, vol. 151, pp. 203-215, 2019.
- [221] S. Czarnecki and Ł. Sadowski, "Morphological properties of the cement skin: Understanding the effect of contact with formwork," *Case Studies in Construction Materials*, vol. 16, p. e01007, 2022.

- [222] Y. Zhang, M. Zhang, and G. Ye, "Influence of moisture condition on chloride diffusion in partially saturated ordinary Portland cement mortar," *Materials and Structures*, vol. 51, no. 2, 2018, doi: 10.1617/s11527-018-1162-7.
- [223] Y. Wang, Y. Bai, and Y. Xi, "Analytical solutions of moisture-chloride ion coupled transport in unsaturated concrete," *Journal of the American Ceramic Society*, vol. 104, no. 11, pp. 5883-5897, 2021.
- [224] Y. Xi, Z. P. Bazant, L. Molina, and H. M. Jennings, "Moisture diffusion in cementitious materials moisture capacity and diffusivity," *Advanced Cement Based Materials*, vol. 1, no. 6, pp. 258-266, 1994.
- [225] J. Larbi and J. Bijen, "Effects of water-cement ratio, quantity and fineness of sand on the evolution of lime in set portland cement systems," *Cement and Concrete Research*, vol. 20, no. 5, pp. 783-794, 1990.
- [226] A. W. Pope and H. M. Jennings, "The influence of mixing on the microstructure of the cement paste/aggregate interfacial zone and on the strength of mortar," *Journal of materials science*, vol. 27, pp. 6452-6462, 1992.
- [227] A. Brough and A. Atkinson, "Automated identification of the aggregate–paste interfacial transition zone in mortars of silica sand with Portland or alkali-activated slag cement paste," *Cement and Concrete Research*, vol. 30, no. 6, pp. 849-854, 2000.
- [228] R. San Nicolas, S. A. Bernal, R. M. de Gutiérrez, J. S. van Deventer, and J. L. Provis, "Distinctive microstructural features of aged sodium silicate-activated slag concretes," *Cement and Concrete Research*, vol. 65, pp. 41-51, 2014.
- [229] R. San Nicolas and J. L. Provis, "The interfacial transition zone in alkali-activated slag mortars," *Frontiers in materials*, vol. 2, p. 70, 2015.
- [230] G. Fang and M. Zhang, "The evolution of interfacial transition zone in alkali-activated fly ash-slag concrete," *Cement and Concrete Research*, vol. 129, p. 105963, 2020.
- [231] K. L. Scrivener, A. K. Crumbie, and P. Laugesen, "The interfacial transition zone (ITZ) between cement paste and aggregate in concrete," *Interface science*, vol. 12, pp. 411-421, 2004.
- [232] A. Lindvall, "Duracrete–probabilistic performance based durability design of concrete structures," in *2nd Int. PhD. Symposium in civil engineering*, 1998.
- [233] D. A. Kulik *et al.*, "GEM-Selektor geochemical modeling package: revised algorithm and GEMS3K numerical kernel for coupled simulation codes," *Computational Geosciences*, vol. 17, no. 1, pp. 1-24, 2013/02/01 2013, doi: 10.1007/s10596-012-9310-6.

- [234] T. Chrisp, G. Starrs, W. J. McCarter, E. Rouchotas, and J. Blewett, "Temperature-conductivity relationships for concrete: An activation energy approach," *Journal of materials science letters*, vol. 20, pp. 1085-1087, 2001.
- [235] Y. Zhang, Z. Yang, and G. Ye, "Dependence of unsaturated chloride diffusion on the pore structure in cementitious materials," *Cement and Concrete Research*, vol. 127, 2020, doi: 10.1016/j.cemconres.2019.105919.
- [236] R. E. Zeebe, "On the molecular diffusion coefficients of dissolved CO₂, HCO₃⁻, and CO₃²⁻ and their dependence on isotopic mass," *Geochimica et Cosmochimica Acta*, vol. 75, no. 9, pp. 2483-2498, 2011.
- [237] M. Criado, S. A. Bernal, P. Garcia-Trinanes, and J. L. Provis, "Influence of slag composition on the stability of steel in alkali-activated cementitious materials," *Journal of materials science*, vol. 53, pp. 5016-5035, 2018.
- [238] D. Ravikumar and N. Neithalath, "An electrical impedance investigation into the chloride ion transport resistance of alkali silicate powder activated slag concretes," *Cement and Concrete Composites*, vol. 44, pp. 58-68, 2013.
- [239] K. Vance, M. Aguayo, A. Dakhane, D. Ravikumar, J. Jain, and N. Neithalath, "Microstructural, mechanical, and durability related similarities in concretes based on OPC and alkali-activated slag binders," *International Journal of Concrete Structures and Materials*, vol. 8, pp. 289-299, 2014.
- [240] K. A. Snyder, X. Feng, B. Keen, and T. Mason, "Estimating the electrical conductivity of cement paste pore solutions from OH⁻, K⁺ and Na⁺ concentrations," *Cement and Concrete Research*, vol. 33, no. 6, pp. 793-798, 2003.
- [241] J. Skibsted and R. Snellings, "Reactivity of supplementary cementitious materials (SCMs) in cement blends," *Cement and Concrete Research*, vol. 124, p. 105799, 2019.
- [242] L. Arnaut and H. Burrows, *Chemical kinetics: from molecular structure to chemical reactivity*. Elsevier, 2006.
- [243] H. Darcy, *Les fontaines publiques de la ville de Dijon: exposition et application des principes à suivre et des formules à employer dans les questions de distribution d'eau... un appendice relatif aux fournitures d'eau de plusieurs villes au filtrage des eaux*. Victor Dalmont, éditeur, 1856.
- [244] P. C. Carman, "Fluid flow through a granular bed," *Trans. Inst. Chem. Eng. London*, vol. 15, pp. 150-156, 1937.

- [245] P. Rovnaník, P. Bayer, and P. Rovnaníková, "Characterization of alkali activated slag paste after exposure to high temperatures," *Construction and Building Materials*, vol. 47, pp. 1479-1487, 2013.
- [246] M. Thiery, P. Dangla, P. Belin, G. Habert, and N. Roussel, "Carbonation kinetics of a bed of recycled concrete aggregates: a laboratory study on model materials," *Cement and Concrete Research*, vol. 46, pp. 50-65, 2013.
- [247] M. Nedeljković, "Carbonation mechanism of alkali-activated fly ash and slag materials: In view of long-term performance predictions," 2019.
- [248] R. Sander, "Compilation of Henry's law constants (version 4.0) for water as solvent," *Atmospheric Chemistry and Physics*, vol. 15, no. 8, pp. 4399-4981, 2015.
- [249] Y. Zuo, M. Nedeljković, and G. Ye, "Pore solution composition of alkali-activated slag/fly ash pastes," *Cement and Concrete Research*, vol. 115, pp. 230-250, 2019/01/01/2019, doi: <https://doi.org/10.1016/j.cemconres.2018.10.010>.
- [250] F. Škvára, V. Šmilauer, P. Hlaváček, L. Kopecký, and Z. Cilova, "A weak alkali bond in (N, K)–A–S–H gels: evidence from leaching and modeling," *Ceramics–Silikáty*, vol. 56, no. 4, pp. 374-382, 2012.
- [251] B. Pinsent, L. Pearson, and F. Roughton, "The kinetics of combination of carbon dioxide with hydroxide ions," *Transactions of the Faraday Society*, vol. 52, pp. 1512-1520, 1956.
- [252] A. Korchef and M. Touaibi, "Effect of pH and temperature on calcium carbonate precipitation by CO₂ removal from iron-rich water," *Water and Environment Journal*, vol. 34, no. 3, pp. 331-341, 2020.
- [253] T. A. Gebrehiwet, G. D. Redden, Y. Fujita, M. S. Beig, and R. W. Smith, "The Effect of the CO₃²⁻ to Ca²⁺ Ion activity ratio on calcite precipitation kinetics and Sr²⁺ partitioning," *Geochemical Transactions*, vol. 13, no. 1, pp. 1-11, 2012.
- [254] J. Reyes-Santiago, L. García-Villanueva, G. Fernández-Villagómez, and P. Guzmán-Guadarrama, "Geochemical Characterization and Saturation Index (Si) in the Montebello Lagunar System Liquidamber Lagoon, Chiapas Mexico," *Nature Environment & Pollution Technology*, vol. 20, no. 4, 2021.
- [255] L. N. Plummer and E. Busenberg, "The solubilities of calcite, aragonite and vaterite in CO₂-H₂O solutions between 0 and 90 C, and an evaluation of the aqueous model for the system CaCO₃-CO₂-H₂O," *Geochimica et cosmochimica acta*, vol. 46, no. 6, pp. 1011-1040, 1982.

- [256] National Oceanic and Atmospheric Administration, "Carbon Dioxide Now More than 50% Higher than Pre-Industrial Levels." Available online: <https://www.noaa.gov/news-release/carbon-dioxide-now-more-than-50-higher-than-pre-industrial-levels> (accessed on 3 August 2023).
- [257] K. S. Pitzer and C. Press, *Activity coefficients in electrolyte solutions*. CRC press Boca Raton, FL, 1991.
- [258] P. J.L., "PitzerXXL Spreadsheet," 2010.
- [259] T. L. Bergman, T. L. Bergman, F. P. Incropera, D. P. Dewitt, and A. S. Lavine, *Fundamentals of heat and mass transfer*. John Wiley & Sons, 2011.
- [260] Y. Shen, B. Qu, K. Chen, C. Gong, and C. Han, "Environmental and energy benefits assessment of alkali-activated concrete (AAC) energy pile," *Journal of Building Engineering*, vol. 61, p. 105282, 2022.
- [261] S. A. Bernal, R. M. de Gutiérrez, A. L. Pedraza, J. L. Provis, E. D. Rodriguez, and S. Delvasto, "Effect of binder content on the performance of alkali-activated slag concretes," *Cement and concrete research*, vol. 41, no. 1, pp. 1-8, 2011.
- [262] E. Bentz and M. Thomas, "Life-365 Service Life Prediction Model™: User Manual," 2001.
- [263] S. Care, "Effect of temperature on porosity and on chloride diffusion in cement pastes," *Construction and Building Materials*, vol. 22, no. 7, pp. 1560-1573, 2008.
- [264] W. A. Al-Khaja, "Influence of temperature, cement type and level of concrete consolidation on chloride ingress in conventional and high-strength concretes," *Construction and Building Materials*, vol. 11, no. 1, pp. 9-13, 1997.
- [265] R. J. Myers, S. A. Bernal, R. San Nicolas, and J. L. Provis, "Generalized structural description of calcium–sodium aluminosilicate hydrate gels: the cross-linked substituted tobermorite model," *Langmuir*, vol. 29, no. 17, pp. 5294-5306, 2013.
- [266] B. S. EN, "197-1. Cement–Part 1: Composition, specifications and conformity criteria for common cements," *London: European Committee For Standardisation*, 2011.
- [267] C. Shi, D. Roy, and P. Krivenko, *Alkali-activated cements and concretes*. CRC press, 2003.